Nano Studies

3

2011

Nano Studies

3

2011

Nano Studies, 2011, v. 3

UDG [53 + 54 + 620.22] (051.2)
N – 21

Nano Studies is a biannual scientific journal published in Georgia.

Nano Studies' topics of interest include Nanoscience and related problems of Physics, Chemistry and Materials Science.

Nano Studies publish following categories of scientific articles: research papers, communications, reviews and discussions.

Nano Studies publish scientific articles in English and also in Georgian and in Russian.

Summaries of all the articles of **Nano Studies** are referred in **Georgian Abstracts Journal** and are accessible in **Tech Inform** (Georgia's Central Institute for Scientific and Technical Information) database: **http://www.tech.caucasus.net**

Full-texts of articles published in **Nano Studies** are free-accessible in **Nano Archive** database: **http://www.nanoarchive.org**

Editor-Founder: **Levan Chkhartishvili**
Editorial Assistant: **Tamar Berberashvili**

Address of Editorial Office: **Department of Physics**
Georgian Technical University
Campus 4, Room 307
77 Merab Kostava Avenue
Tbilisi, 0175, Georgia

E-mail: **chkharti2003@yahoo.com**
Phone: **995 322 37 19 42**
Mobile: **995 599 34 07 36**

Publishing House **Universal**
19, Ilia Chavchavadze Avenue, Tbilisi, 0179, Georgia
Phone: 995 322 22 36 09, Mobile: 995 599 17 22 30, E-mail: universal@internet.ge

ISSN 1987 – 8826

CONTENTS

NANOPARTICLES – NEW MEDICAL POTENTIAL – TODAY AND TOMORROW

T. Chachibaia

Responsible Nanotechnology Center
Tbilisi, Georgia
nanogeorgia@hotmail.com

Accepted February 8, 2011

1. Introduction

History of the drug formulations relied on nano-engineering is quite modern. The launch of products incorporating nanostructures particles is showing clear differentiation across sectors. The materials and products based on nanotechnology (NT) are regulated today within the existing network. Nanostructures are evaluated as 'chemicals with new uses' or as 'new chemicals'.

Healthcare and life sciences applications like nanostructured medical devices and nanotherapeutics have the longest time-to-market due to sector-specific regulation. In 2004, the US Food and Drug Administration (FDA) estimated that the proportion of all new drugs entering first phase trails that ultimately gain approval had fallen to 8 % from a historical average of about 14 %. The commonest factors resulting in project failure are lack of efficacy (25 %), clinical safety concerns (12 %), and toxicological findings in pre-clinical evaluation (20 %). Proposed Investigational New Drug Application (IND) needs to follow the way to FDA and EC approval passing through all stages of investigations lasting up to 10 – 15 years, starting 'in vitro' and ending third phase of clinical trials with subsequent approval of medication and pharmaceutical market entry.

The current applications of nanotechnology span a wide range of sectors. Current niche for such applications is in the areas where there is an overlap between medicines and cosmetics sectors. Many products are marketed as a means to enhance performance for different lifestyles and age groups, as an aid to health, beauty and wellbeing. Although such applications are relatively new and emergent, they appear to have started to make a global impact. Number one question is if quality of life will improve thanks to synthesis of new materials with new properties. How should people benefit from achievements of nanotechnology and nanoengineering? Answers to these and related questions are controversial, due to different approaches of regulation rules before market entry of the new products.

While FDA requirement are strict for novel medications, conversely, regulatory mechanisms for the cosmetics allow earlier market entry. Unlike medical and healthcare sectors, cosmetic industry outpaces commercial potential of nanoparticle containing product. To compare with the rate of released cosmetics, widely distributed worldwide, situation is quite unequal. Drugs, food packaging, and new chemical compounds, are required pre-market review

and approval, while in cases related to cosmetics and majority of consumer products, only sufficient is to apply post-market surveillance and monitoring [1].

Although the constituent materials used in cosmetic and personal care products should either be approved by FDA, at the same time there is no need in conducting long running clinical trials, as in the case of pharmaceutical drugs. But regulation mechanisms required revision when dealing with the ingredients processed to nanoscale dimension, while absolutely diverse chemical and physical properties are revealed. Particular interests pose cosmetics and personal care products. Recently there is widespread use of nanoparticle gold containing cosmetics like skin creams that are used on the whole body surface for appearance of shining glow, lipsticks, anti-aging face creams and many other products. Despite the big interest and widespread investigations performed for safety and efficacy studies for nanoparticle gold utilization in medical diagnostics or treatment there is obvious, that few if any are approved for these purposes. Overview of state-of-the-art exploration of nanoparticle gold compounds will handle us with special knowledge about differences in physical and chemical properties of this material, dependent on size, shape, charge, even solvent used in processing of this metal.

Gold nanoparticles are widely used in biomedical imaging and diagnostic tests. Based on their established use in the laboratory and the chemical stability, gold nanoparticles were expected to be safe. The recent literature, however, contains conflicting data regarding the cytotoxicity of gold nanoparticles.

2. Health monitoring issued concerning nondestructive use of nanoparticle gold compounds in medicine and cosmetology

'*All is not gold that glitters*'

Postindustrial gold rush reflects the hype of nanotechnologies, already ubiquitous in a wide range of consumer products, as diverse as electronics, medicine, environmental remediation, cosmetics, and solar energy. Discovering distinctive properties that many materials display at the extremely minuscule scale opens new opportunities for their conventional use [2]. Of particular interest to most nanotechnology applications are engineered nanoparticles (ENPs), which have much larger surface to mass ratios. Nano-sized ENPs have also been claimed to have a greater uptake, absorption and bioavailability in the body compared to bulk equivalents. This makes it possible to reduce the use of solvents in certain applications such as certain cosmetics and personal care products to allow the dispersion of water-insoluble colors, flavors and preservatives in low-fat systems. Nanosized water-insoluble substances can enable their uniform dispersion in aqueous formulations. This aspect alone has attracted a lot of commercial interest in the use of nano-sized ingredients [3].

Among other engineered nanoparticles interest to the gold is not diminished, on the contrary, increased enormously in recent years, particularly since early 80's, while mass production of nano-scaled chemical substances has been started, due to invention of the scanning tunneling microscope (STM) and the atomic force microscope (AFM). IBM scientist enabled manipulation even individual atoms to design and synthesize materials for desired features. Later in 2000's the IBM scientists precisely placing atom-by-atom 20 000 gold particles, each about 60 nanometers in diameter reproduced image of Robert Fludd's 17th century's

drawing of the Sun – the alchemists' symbol for gold. IBM scientists demonstrates a new nano "printing" bottom-up technique, that will lead to breakthroughs in ultra-tiny chips, lenses for optics, and biosensors for healthcare.

As gold is mostly studied chemical element it is characterized with most predictable behavior. But gold nano-particles may act absolutely diversely. Balk gold, which is usually characterized by its yellow color, while becoming processed to nano-dimensional scale the material is transforming its color to orange, purple, red or greenish tinge due to different particle size. The most well known cultural artifact is presented in the British Museum where is exhibited Lycurgus Cup dated in 4th century A.D., which is ruby red colored glass due to colloidal gold containing, which is changed in greenish color after light exposure. Nanogold already was used in medieval times in stained glass to attain almost all colors of rainbow. Today nobody argues that nano-sized gold particles don't act like bulk gold [4].

Traditionally bulk gold was considered as chemically inert and biocompatible material, due to this features it utilized widely in medical applications, e.g. in dental prosthesis, eyelid implants and etc. Throughout the history, gold was used to cure diseases. Finely ground gold particles in the size range 10 – 500 nm can be suspended in water. Such suspensions were used for medical purposes in ancient Egypt over 5 000 years ago. In Alexandria, Egyptian alchemists used fine gold particles to produce a colloidal elixir known as ''liquid gold'' that was intended to restore youth [5]. Dating back to Roman Empire, colloidal gold was thought to have healing properties. A colloid refers to a substance in which many fine particles are suspended in a stable condition in another substance. Gold nanoparticles traditionally used in Indian remedy curcumin [6]. German bacteriologist Robert Koch showed that gold compounds inhibit the growth of bacteria. He was awarded the Nobel Prize for Medicine in 1905.

With the development of pharmaceutical industry, first in 1935, gold salt containing drugs were reported to be effective for the treatment of rheumatoid arthritis. It is thought, that gold affects the entire immune response (phagocytes, leukocytes, T-cells) and reduce its potency and limit its oxidizing nature on joint inflammation and erosion. Effect is explained by the fact that administered gold compounds accumulate within body once absorbed into the cell and linked to anti-mitochondrial activity, induced apoptosis of proinflammatory cell. World Health Organization (WHO) classified gold salt containing compounds as an antirheumatic agent and included in its basic treatment scheme.

Due to prior long history of the use of gold inside the body, the safety issues seem to assume somewhat easier, though becoming more and more challenging, due to achievements of synthesis of new materials enabled by nanotechnology.

Properties of gold molecules processed to nanometer dimension almost thoroughly studied. Gold attains divergent physical and chemical characteristics while its molecules are processed to nanoscale dimension. Scientists revealed diverse properties of nanoparticle gold, which is dependent on various factors. Particularly, properties are becoming dependent not only on size of the gold nanoparticle, but also such other characteristics as particle shape, charge and composition or surface coating, which are also important. Respectively, health monitoring aspects are under greater concerns, then before.

When dealing with constraints of size below 100 nm, the laws of quantum physics supersede those of traditional physics, resulting in changes of a substance's properties. Quantum-size effects begin to significantly alter material properties, such as transparency, color of fluorescence, electrical conductivity, magnetic permeability, and other characteristics. All

these properties are of great interest for the industry and society as it enables new applications and products. Consequently, more attention is focused on determining ratio of efficiency versus toxicity, harm or benefit. There are some examples of conventional use of nanoscaled gold particles. For instance, Japanese scientists Dr. Masatake Haruta discovered, that while the particle diameter is turned in the size range of 3 – 5 nm gold exhibits unique catalytic performance, e.g. carbon monoxide (CO) oxidation and direct peroxide (H_2O_2) production at a temperature as low as – 77 °C [7]. In practice this invention was tested to prevent bad odor in rest rooms and are already in service in Japan. Thus gold nanoparticles can vanish smells produces by bacterial action. This is unusual feature for bulk god, but characteristic for nanoscaled gold particles. Another application for catalytic properties of nano-sized gold particles is utilized in fuel cells of hydrogen batteries.

One hundred and fifty years after one of the founders of chemistry Michael Faraday in 1850's first created gold nanoparticles and observed that these nanoparticles absorbed light, researchers in 20th century rediscovered that a mere flash of light can cause the gold particles to melt. Absorbed light is efficiently turned into extreme heat, which is capable of killing cancer cells. The externally applied energy may be mechanical, radio-frequency, laser, optical, near-infrared light – resultant therapeutic action is the same. Gold nanoparticles are also recognized in their ability to bind to DNA, which may be exploited within the treatment of disease, such as anticancer agents or within gene therapy, but may also contribute to genotoxicity, or block transcription [8]. Hammad–Shifferli et al. have demonstrated that transmitted radio signals influence integrity of DNA strand, while is bound to nanoparticles gold molecules. This discovery opens up the possibility to control more complex biological processes of living cells, such as enzymatic activity, protein folding and biomolecular assembly [9]. Furthermore, the ability of gold nanoparticles to bind to DNA is of concern, due to their potential cytotoxic or genatoxic consequences, which may be exploited within anticancer drugs, or gene therapy, which warrants further investigation. In addition, the ability of gold nanoparticles to interrupt transcription is of concern [10].

Naomi Halas of Rice University in Texas (Houston, USA) developed gold nanoshells in the 1990s. According to the study's lead authors, Rebekah Drezek and Jennifer West, nanoshells have a core of silica and a metallic outer layer of gold, or may be exchanged by cupper or iron. Nanoshells will preferentially concentrate in cancer lesion sites. In her interview with Nova, Naomi Halas describes a nanoshell as "essentially a nanolens" that captures light and then focuses it around itself [11]. Shining a near-infrared laser on the tumor site from outside the body (light can travel through tissue more than 10 cm); the nanoshells absorb the light and focus it on the tumor. The area around the nanoshells heats up and the tumor "cooks" until it is ablated. Halas points out that the nanoshells leave no "toxic trail" in the body the way conventional chemotherapeutic agents do, stated that "long-term studies have not indicated any toxicity or effect on the immune system".

The structure and properties of gold nanoparticles make them attractive for a wide range of biological applications. Nanoparticle gold is considered of low toxicity material and currently is widely used in cosmetology.

Actually, nanostructured gold particles possess various properties, which are under investigation and need longer time to final approval. Few if any of fabricated nanoparticle gold containing medication is yet approved by FDA. By the August of 2009 was released report of EU

7th Framework Program 'Engineered Nanoparticles: Review of Health and Environmental Safety' [12].

Particle size has been demonstrated to influence dermal penetration of gold nanoparticles [13]. Therefore, in general, greater effects are observed for smaller particles. The size of particles has been proven to be very influential to their behavior. Accordingly, smaller particles have a wider tissue distribution, penetrate further within the skin and internalized to a greater extent, and have a larger toxic potency. However, more extensive investigations, in the future, are required to more fully understand the tissue distribution and fate of metal particles, following exposure.

It was estimated that optimal size of interacting with the skin nanoparticles would be in the range of 50 nm. Smaller tend to penetrate the skin more easily than large particles, sometimes being taken up by lymphatic system and localizing in the lymph nodes [14]. Among other factors should be also considered particle concentration and charge state, which are in a causal relationship with their influence on the living cells. Goodman et al. [15] demonstrated gold cationic particles of 2 nm size as moderately toxic, whereas anionic particles were relatively non-toxic, observation data coincide with obtained data in different studies [16]. Toxicity, however, has been observed at high concentrations using these systems.

In one study the research group headed by Dr. Shuguang Wang [17] demonstrated cytotoxicity effect on human skin keratinocytes of gold nanomaterials of different sizes and shapes. It was shown that spherical gold nanoparticles of different sizes are not inherently toxic to human skin cells, conversely gold nanorods are highly toxic due to the presence of coating material CTAB, which is used in manufacturing process. This factor caused limitation on commercialization of gold nanorods for in-vivo and in-vitro applications due to toxicity. It is unreasonable to generalize from just a few studies, because in recent years company Nanopartz have announced about new manufacturing method, replacing undesirable organic molecule of CTAB with polyethylene glycol (PEG). PEG has low toxicity and is used in variety of products. Nanopods from one supplier may not be necessarily representative of toxicity of physical characteristics of all manufactures nanorods.

Besides more other nanocoating molecules like liposomes, dendrimers, biodegradable polymers, or albumin are capable to reduce the toxicity of the incorporated agent.

Major premise is relied on discovery of thiol (compound that contains the functional group composed of a sulfur atom and a hydrogen atom – SH) protected colloidal gold nanoparticles bound to cytokine – tumor necrosis factor (TNF). Buffering free TNF extreme activity, enhanced anti-tumor effect is attained by assembling into complex structure PEG with colloidal gold [18]. This new approach has significant advantages, that is under development in company CytImmune, elaborating results to achieve final approval over other alternatives.

Gold nanoparticles are also more biocompatible, than other types of optically active nanoparticles, such as cadmium containing quantum dots. Due to cadmium toxicity its use is restricted in the living cells. Why the process of nano-fabrication, in particular the making of gold nanodots or quantum dots, is well known. In 2007 Medal of Science, the USA's highest honor in the field, was awarded to the Egyptian-American chemist Professor Mostafa El-Sayed, director of the Laser Dynamics Laboratory of Georgia Institute of Technology, for his many outstanding contributions, among which using gold nanorods in cancer tumor treatment was the most recent. Gold nanoparticles are very good at scattering and absorbing light. For example, nanoparticles that are 36 nanometers wide, absorb light over 10 000 times better than

conventional organic dyes, making them potential candidates for optical imaging applications of small tumors. In the study, researchers found that the gold nanoparticles have 600 percent greater affinity for specific overexpressed surface receptors of cancer cells, rather, than for noncancerous cells.

As nanotechnology tend to develop in most responsible manner from the moment of its foundation, when US National Nanotechnology Initiative (NNI) established in 2000. It seems to have most regulation mechanisms for greener development, than any other known technology, social scientists are involved from the very beginning.

Green nanotechnology is developed in environmentally friendly manner. Dr. Jim Hutchinson's research group in the University of Oregon works at the cleaner and greener production of gold nanoparticles, a process that also reduces the cost of synthesizing these materials from 300 000 to 500 dollars per gram [19]. Actually, cost is one of the determining factors, next to safety and effectiveness.

Recent studies enabled synthesis of gold nanoparticles by means of certain bacterial strains e.g. Stenotrophomonas Malophilia was incubated for eight hours in the gold salt containing solution, resulting in the synthesis of gold nanoparticles that were about 40 nanometers in size [20]. The opportunity of this way of synthesis is that Au NPs are free of solvent, have hydrophilic properties and may be attained particles of various sizes in industrial quantities. This is new approach to green technology development.

A recent report by J. Davies from the Woodrow Wilson International Center of Scholars strongly criticized the current approach regulating cosmetics as wholly inadequate to dealing with the risks posed by nanotechnologies: "Although the Food, Drug and Cosmetic Act (FDCA) has a lot of language devoted to cosmetics, it is not too much of an exaggeration to say that cosmetics in the USA are essentially unregulated" [21].

David Rejeski, Director of the Project on Emerging Nanotechnologies, Woodrow Wilson International Center of Scholars, gives recommendations: 'for building confidence in nanotechnologies it is necessary to achieve greater transparency and disclosure; compulsory requirement is also pre-market testing, as well involvement of third party for additional testing and further research' [22]. Although, some cosmetic manufacturers may differ with such conclusions, based on unpublished propriety research, but do due diligence in tracing assertions back to primary sources [23].

In 2007, USA has listed gold and silver nanoparticles amongst a number of new chemicals and materials that the FDA had asked the National Toxicology Program (NTP) to study. This will seek to determine whether their use causes specific health problems. NTP should test the gold nanoparticles and, if so, what types of tests are warranted.

3. Summary

Thoroughly analyzing scientific achievements, exploring divergent features of gold nanoparticles, it was obviated that gold nanoparticles are considered as risky for human health. Experiments have shown that gold nanoparticles can result in uptake via the relevant exposure routes. The gold nanoparticles and the cell types used for their exposure are likely to influence the uptake, sub-cellular distribution, and toxicity of gold nanoparticles.

However, investigations of metal particulates are still in their infancy at this time, and have concentrated on revealing the toxicity, safety, tissue distribution, antibacterial properties and cellular uptake of gold nanoparticles. Consequently, more comprehensive studies are required to more fully understand the toxicity versus safety associated with metal particulate exposure.

Inevitably, any emerging technology requires extensive safety assessment before coming to market, including diagnostics, medications and cosmetics. While comparing and evaluating newly established properties at nanoscale, consumers may experience confusion concerning safety issues.

In the recent years responsibilities for the control and regulatory mechanisms increased to guard the utilization of nano-particles into cosmetic products.

On March 24, 2009, the European Parliament (EP) approved an update of EU legislation on cosmetics. As requested by the EP, the new regulation introduces a definition, safety assessment procedure and labeling requirement for all nanomaterials that are used in cosmetics.

References

1. M. C. Roco. Setting New Targets for Responsible Nanotechnology, 2003.
2. Technology Review's published by MIT of nanotech developments in 2005 (http://www.technologyreview.com/Nanotech-Materials/wtr_16096,318,pl.html).
3. Q. Chaudhry, L. Castle, R. Watkins. Nanotechnologies in Food. RSC Nanoscience & Nanotechnology, 2010, n. 14 (Royal Society of Chemistry: www.rsc.org).
4. M. Ratner, D. Ratner. Nanotechnology. New Jersey: Prentice Hall, 2003.
5. M. S. Amer. Raman Spectroscopy, Fullerenes and Nanotechnology. RSC Nanosci. & Nanotechnol., 2010, n. 13 (Royal Society of Chemistry: www.rsc.org).
6. R. Jagannathan et al. Functionalizing gold nanoparticles for biomedical applications: From catching crystals at birth to mature activity. In: 5th Int. Conf. Gold Sci., Technol. & Appl., 2009.
7. M. Haruta. Catalyst surveys of Japan 1:61 and references therein, 1997; M. Haruta. Catalysis Today, 1997, v. 36, p. 153.
8. Pan et al. Size-dependent cytotoxicity of gold nanoparticles. Small, 2007, v. 3, n. 11, pp. 1941- 1949 (http://www.virlab.virginia.edu).
9. K. Hamad–Schifferli, J. J. Schwartz, A. T. Santos, S. G. Zhang, J. M. Jacobson. Remote electronic control of DNA hybridization through inductive heating of an attached metal nanocrystal. Nature, 2002, v. 415, pp. 152-155.
10. Goodman et al. DNA-binding by functionalized gold nanoparticles: Mechanism and structural requirements. Chem. Biol. & Drug Design, 2006, v. 67, n. 4, pp. 297- 304.
11. N. Halas. Working with nanoshells: A conversation with Naomi Halas (Nova interview, February 3, 2005: http://www.pbs.org/wgbh/nova/sciencenow/3209/03-nanoshells.html).
12. Engineered Nanoparticles: Review Environmental Safety (International Collaborative Review – Project's co-coordinator Prof. Vicki Stone), 2008 – 2009 (http://nmi.jrc.ec. europa.eu/ project/ENRHES.htm.

13. Savanone et al. In vitro permeation of gold nano particles through rat skin and rat intestine: Effect of particle size. Colloids & Surfaces B: Biointerfaces, 2008, v. 65, n. 1, pp. 1-10.
14. G. Oberdorster et al. Environmental Health Perspective, 2005.
15. C. M. Goodman, C. D. mc Cusker, T. Yilmaz, V. M. Rotello. Toxicity of gold nanoparticles functionalized with cationic and anionic side chains. Bioconjug Chem., 2004, v. 15, pp. 897-900.
16. J. F. Hainfeld, D. N. Slatkin, H. M. Smilowitz. The use of gold nanoparticles to enhance radiotherapy in mice. Phys. Med. & Biol., 2004, v. 49, pp. 309-315.
17. Sh. Wang, W. Lu, O. Tovmachenko, U. Sh. Rai, H. Yu, P. Ch. Ray. Challenge in understanding size and shape dependent toxicity of gold nanomaterials in human skin keratinocytes. Chem. Phys. Letts., 2008, v. 463, pp. 145-149.
18. G. F. Paciotti, L. Meyer, D. Weinreich, D. Goia, N. Pavel, R.E. mc Laughlin, L. Tamarkin. Colloidal gold: A novel nanoparticle vector for tumor directed drug delivery. Drug Deliv., 2004, v. 11, pp. 169-183.
19. S. K. Ritter. Planning nanotech from the ground up. Chem. & Eng. News, April 17, 2006.
20. Y. Nangia, N. Wangoo, N. Goyal, G. Shekhawat, C. R. Suri. Bacterial strain used to synthesize gold nanoparticles. Gold Bulletin, 2009 (http://www.utilisegold.com/ news/2009/07/21/story/12536/bacterial_strain_used_to_synthesise_gold_nanoparticles.
21. J. Davies. Managing the effects of nanotechnology. Woodrow Wilson International Center for Scholars: Project on Emerging Nanotechnologies. Washington, 2006.
22. D. Rejeski. Nanotechnology: How much EH&S Research is enough? (Project on Emerging Nanotechnologies),Woodrow Wilson Center for Scholars, 2005.
23. T. E. Bell. Understanding Risk Assessment of Nanotechnology, 2006 (www.nano.gov/ Understanding_Risk_Assessment.pdf.

PHOTOELECTRIC PROPERTIES OF Cd- AND Pb-DOPED THULIUM SESQUISULFIDES THIN FILMS

Z. U. Jabua, K. D. Davitadze, A. V. Gigineishvili

Georgian Technical University
Tbilisi, Georgia
Z.Jabua@hotmail.com

Accepted February 13, 2011

1. Introduction

The sesquichalcogenides of rare earth elements (REEs) are characterized by combination of unique optical, luminescent, electro-optical and photoelectrical properties [1]. The REE sesquisulphides have the considerable photoconductivity (PC) and at the same time great by value the piezoelectric coefficients and they are considered to be the laser materials. In spite of this, all REE sesquisuphides have not been sufficiently studied.

Previously it has been studied the optical and photoelectric properties of Sm, Tm, Yb and Nd sesquisulphides [2-5]. In the present work, for the first time there is carried out the doping of thulium sesquisulphide thin films by atoms of Pb and Cd. An interpretation of received experimental data on the spectral and temperature dependences of PC and photo-electromotive force (PEMF) of doped films has been proposed.

2. Experimental details

High resistivity (~ 10^{10} Ohm · cm) of REEs sesquisulphides of stoichiometric composition considerably complicates the measurement of photoelectric properties what causes the necessity of doping of these materials. Plumbum and cadmium have been chosen as doping impurities for Tm_2S_3 films taking into account geometrical and electrochemical factors and relative simplicity of doping process.

The Tm_2S_3 thin crystalline films with thickness of 1 – 7 μm have been fabricated by two independent sources Tm and S on glass ceramics, fused quarts, leicosaphire and single-crystalline silicon substrates [3]. Obtained films had a cubic structure (cubic crystal system, Ta_2O_3 structural type) with lattice constant of 12.46 Å.

Doping of films with Pb atoms has been carried out in closed volume by the method of diffusion from steady source of impurities. Preliminarily, Tm_2S_3 films have been covered by the Pb layer of the thickness of 8 – 15 μm by means of vacuum evaporation at ~ 10^{-6} mm Hg. At the same time, the temperature of Tm_2S_3 was equal to 400 K and the temperature of the Pb evaporator was above ~ 1300 K. After the deposition of Pb, the films have been slowly cooled down to the room temperature in vacuum, and then for carrying out a diffusion annealing

process they were placed in a quarts ampoule which was pumped out to ~ 10^{-5} mm Hg and then filled with spectrally clean argon. We carry out the annealing at ~ 900 K for 18 – 25 hours. After diffusion annealing and cooling of films to the room temperature the above residual layer was removed by means of mechanical polishing using a diamond paste. The doped films had n-type conductance and value of resistivity of $(5 – 8) \cdot 10^2$ Ohm · cm.

As the pressure of saturated vapor of Cd is higher than that of Pb, we doped Tm_2S_3 films with Cd by means of vapor-diffusion from the vapor phase in a closed volume. Tm_2S_3 films were placed together with Cd on opposite ends of quarts ampoules pumped out to ~ 10^{-5} mm Hg. The ampoules were placed in a horizontal furnace and annealing was performed at ~ 870 K for ~ (40 – 45) hours. After annealing and cooling down to the room temperature, like the case of doping by Pb, we remove the excesses of condensed Cd from films' surfaces by means of mechanical polishing. After doping by Cd, like the case of Pb, the obtained films possess n-type conductance and the resistivity of $\sim (2 – 4) \cdot 10^2$ Ohm · cm. Electronographic and X-ray diffractometric investigations of phase composition for Tm_2S_3: Pb and Tm_2S_3: Cd did not reveal formation of an additional phase after doping.

The establishment of photoelectric and electric measurements and used methods of investigation are described in [6]. All numerical values of photoelectric parameters in the regions of photon energy of 0.3 – 3.3 eV and temperatures of 110 – 350 K have been calculated for the equal quantity of photons corresponding to the film irradiation intensity of 0.1 W / cm^2.

3. Results and discussion

In the Figures 1 and 2, there are represented the spectra of PC taken at various temperatures on the Tm_2S_3: Pb and Tm_2S_3: Cd films, respectively.

The abundance of structures in spectrum, their energetic states and high photosensitivity in a rather wide region allows us to suppose that the contributions to photo-processes give both the optical transitions of electrons from local levels and inter-band transitions. However, there is observed a difference between the spectral dependences of PC and PEMF (Figure 3) for the films doped with Pb and Cd (though in both cases the doping conditions lead to the n-type conductance) which does not allow us to explain all peculiarities of spectra taking into account only one impurity state and only one inter-band electron transition.

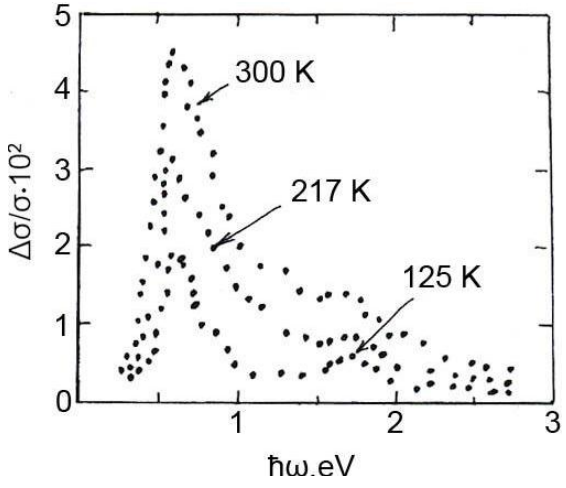

Figure 1. Spectral dependences of Tm_2S_3: Pb films photoconductivity at various temperatures.

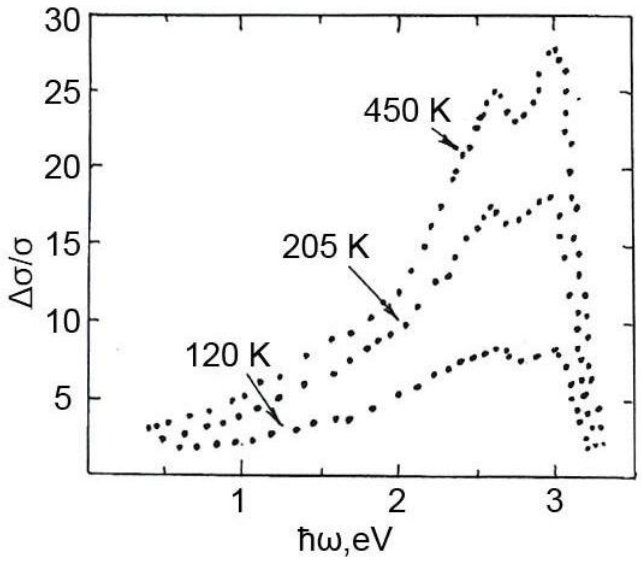

Figure 2. Spectral dependences of Tm_2S_3: Cd films photoconductivity at various temperatures.

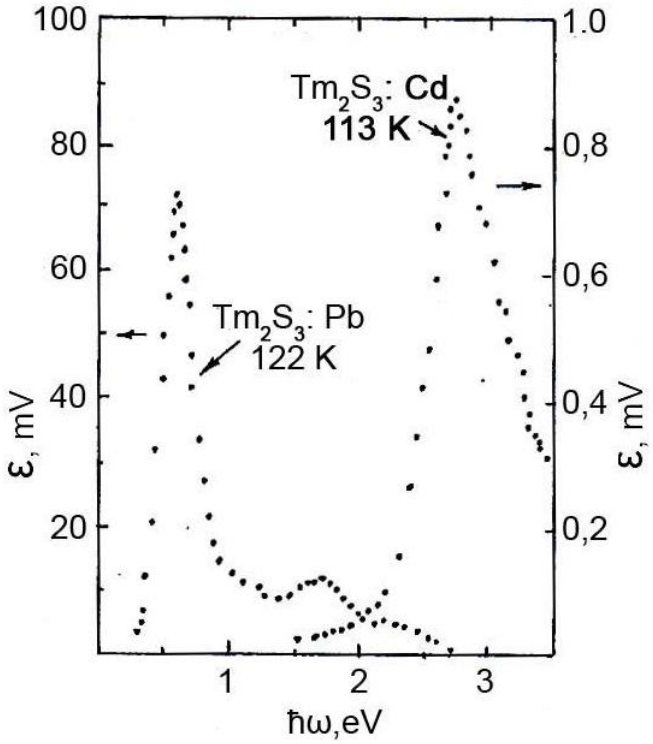

Figure 3. Spectral dependences of Tm_2S_3: Cd films photo-electromotive force at temperatures of 113 and 122 K.

As it is known in undoped dielectric materials not revealing any photo-activity, to which REE sesquisulphides belong, it is possible to achieve the considerable photosensitivity by creation the compensated acceptor states. In spite of the fact that in our case the impurity atoms of Pb and Cd introduced in the film form only donor centers, high photosensitivity and

formation of PEMF, like the previously studied Sm_2S_3: Pb [4] and Nd_2S_3: Pb [2] films, we ascribe it to the compensated acceptor levels availability in doped Tm_2S_3 films. It is known that in REE sesquisulphides each ninth node in the cations' sublattice is vacant [7]. Then, we suppose that these vacancies are responsible for creation of the deepest acceptor levels.

Based on interpretation of the experimentally derived spectral regularities we admit that there is available a deep acceptor level within forbidden gap of the undoped Tm_2S_3 and the photosensitivity is determined by introduction of donor impurities, being one of sources of photo-carriers, and all the time influencing photo-processes by the existing acceptor states participation.

As it is shown in Figures 1 and 3, Tm_2S_3: Pb films at any temperature revealed a PC and PEMF peaks with the energy maximum at ~ 0.510 eV, which probably corresponds to the Pb donor ground-state-energy. Besides, at 112 K and quantum energy of $\hbar\omega = 0.435$ eV the less intensive maximum is revealed, which gradually washed in diffused one during increase of temperature (Figure 4).

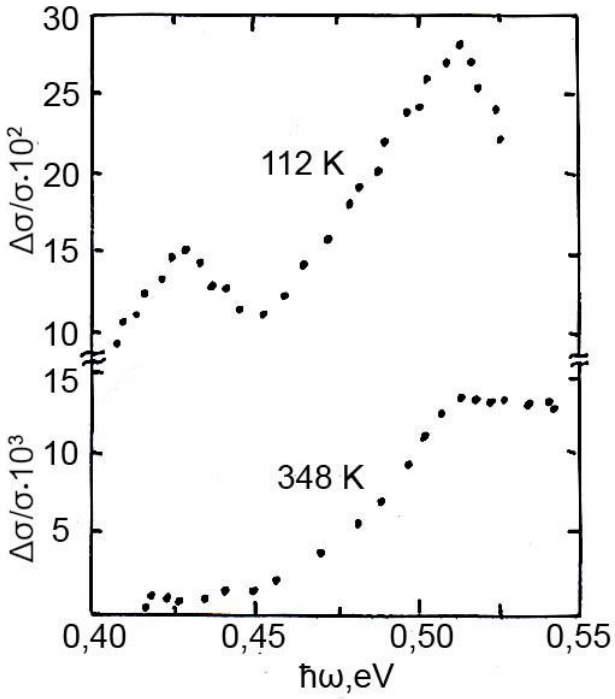

Figure 4. Thin structure of the Tm_2S_3: Pb films photoconductivity spectrum.

Ignoring any "chemical shifts", it is possible to suppose that the peak at 0.435 eV is related with a Pb donor excited state. Consequently, the energetic gap between the ground- and the first excited-states of this impurity in Tm_2S_3 equals to 0.075 eV.

PC and PEMF intensities of Tm_2S_3: Pb the main impurity maximum locate at the peak $\hbar\omega = 1.7$ eV, which we connect with electron excitation from the compensated acceptor level. Deriving this value from the impurity–electron inter-band transitions in Tm_2S_3 [3], we find the ionization energy of acceptor levels formed by Tm-vacancies: ~ 0.8 eV.

The considerable difference of spectral dependences of PC and PEMF of films doped with Cd from those doped with Pd is evidently related with the fact that cadmium creates

shallow donor state. This is testified by the fact that in long-wave region of spectrum it was not possible to find any structure up to 0.2 eV. Definitely, corresponding maximum is placed in far infrared region. Then, it may be admitted that even at temperature of 100 K there occurs a thermal ionization of the Cd donor state and its main part in photo-processes comes to compensation of acceptors, i.e. to increase of time-life of photo-carriers and growth of photosensitivity in intrinsic spectral region as it can be shown from experimental data represented in Figures 2 and 3.

The "tail" of PC and PEMF observed up to 22 eV apparently can be ascribed to the contribution of electron-transitions from compensated acceptor states and probably as well to the participation of electrons in indirect inter-band transition process.

We have already studied the influence of temperature on PC and PEMF during the irradiation of samples at fixed wave length lying both in impurity and intrinsic spectral regions. For all films there took place usual (being close to exponential) temperature-dependence of photosensitivity.

4. Conclusion

Doping of Tm_2S_3 by the Pb and Cd atoms has been carried out for the first time. The spectral dependences of PC and PEMF within the photon energy region of 0.3 – 3.3 eV and the temperature interval of 110 – 350 K have been investigated.

The supposition has been done that in photosensitivity the main part is played by the acceptor states connected with the vacancies in cations' sublattice which are compensated by the donor levels of Pb and Cd impurities.

High photosensitivity, especially for Tm_2S_3 films doped with Cd, testifies that application of REE sesquichalcogenides is promising for photosensitive structures formation.

References

1. M. Gasgnier. Rare earth compounds (oxides, sulfides, silicides etc) as thin films and thin crystals. Phys. Stat. Sol. A, 1989, **114,** 11.
2. Z. U. Jabua, T. O. Dadiani, A. V. Gigineishvili, M. I. Stamateli, K. D. Davitadze, G. N. Iluridze. Optical and photoelectric properties of nondoped and Cd and Pb doped thin films of neodymium sesquisulfide. Phys. Stat. Sol. A, 2006, **4,** 1397.
3. A. V. Gigineishvili, Z. U. Jabua, K. D. Davitadze, L. N. Glurjidze. Optical properties of thulium sesquisufide thin films. Thin Solid Films, 1995, **261,** 248.
4. L. N. Glurjidze, D. G. Gzirishvili, S. I. Koshoridze, Z. U. Jabua, V. V. Sanadze. Photoelectric properties of samarium sesquisulfides Pb and Cd doped thins films. Phys. Solid State, 1982, **24**, 1403.
5. L. N. Glurjidze, T. D. Kekhaiov, T. L. Bzhalava, Z .U. Jabua, V. V. Sanadze. Optical properties of samarium monosulfide thin films. Phys. Solid State, 1979, **21**3, 496.

6. L. N. Glurjidze, T. D. Kekhaiov, D. G. Gzirishvili, T. L. Bzhalava, V. V. Sanadze. Reflection, absorbtion, photoconductivity and photo emp spectrum of YbS thin films at 300 K. Phys. Solid State, 1980, **22,** 660.
7. A. V. Golubkov, E. V. Goncharova, V. P. Shuze, G. M. Loginov, V. M. Sergeeva, I. A. Smirnov. Physical properties of rare earth chalcogenides. 1973, Leningrad: Nauka, 105.

OPTICAL PROPERTIES OF SmSb and TmSb FILMS

A. V. Gigineishvili, L. N. Glurjidze, Z. U. Jabua

Georgian Technical University
Tbilisi, Georgia
Z.Jabua@hotmail.com

Accepted February 13, 2011

1. Introduction

Experimental investigation of various unusual physical properties of mixed-valence rare-earth (RE) compounds, heavy fermion systems, still arouse an increased interest. It is noteworthy that the number of such compounds is increasing continuously. They form a comparatively little studied class of materials including pnictides [1-3].

Making measurements on RE-materials' films often allows to avoid some experimental difficulties and, what is especially important, to reveal more reliably the RE-ion characteristic state and connect it with the macroscopic parameters of the sample. Hence, great attention is generally paid to thin crystalline RE compounds layers as a whole, and ours to pnictides.

In this paper, for the first time it is presented and discussed in details main optical parameters of samarium and thulium monoantimonides films and the effect of the RE-ion valence-state on their optical properties. Films electro-physical characteristics are also reported.

2. Experimental details

Single-phase polycrystalline partially grain-oriented SmSb and TmSb films, 0.1 – 1.0 μm in thick, were prepared by vacuum ($1.3 \cdot 10^{-3}$ Pa) thermal evaporation from two independent sources and deposition on fused sapphire, polycrystalline pyroceramic and monocrystalline silicon substrates. Used components contained 99.9 Sm or Tm and 99.999 % Sb. Films were prepared at the substrate temperature varying in a rather wide range. Magnitudes 1100 – 1120 and 1010 – 1060 K were found to be optimal for SmSb and TmSb, respectively. The evaporation rate was about 50 Å / s. According to the X-ray and electron diffraction investigations films had a well-developed NaCl-type cubic structure. The lattice parameters calculated from the experimental diffraction patterns were found to be 6.27 (SmSb) and 6.07 Å (TmSb). Films surface images obtained through secondary X-rays (on a Camebax-Microbeam X-ray microanalyzer) indicate homogeneous distribution of the components (Sm and Sb or Tm and Sb, respectively) within samples. The Auger spectra (obtained on a LAS–2000 Riber setup) usually contained two additional tracks indicating the insignificant presence of oxygen and carbon in the surface layers. However, with the increasing of thickness concentrations of these elements decrease rapidly – their traces virtually completely disappear after 60 min etching of the surface with the rate of 1 nm / min (using 4 keV Ar^+ ions).

Films of both compounds are rather stable in atmospheric conditions, don't decompose and change their colors spontaneously – a black color is characteristic of SmSb, whereas TmSb films can be prepared golden or violet-blue. Often the color variation is an evidence of the non-integer variable valency of the RE-ion [4, 5]. Samarium and thulium valencies in corresponding monoantimonides were determined using L_3 X-ray absorption spectra in accordance with the technique described in [5]. Investigation shows the correlation between the film color and the thulium ion valence-state does exist. The valence value ν is $+2.7 \pm 0.1$ for golden films and $+2.2 \pm 0.1$ for violet-blue ones. The samarium ion valency in SmSb films is approximately 3 (with error of 10 %). For galvano-magnetic (method of compensation, DC, a magnetic field up to 20 kOe, temperature range 80 – 440 K) and thermoelectric (absolute method with corrections for the EMF of copper) measurements the films were prepared in the Hall configuration with six ohmic contact areas deposited by copper (with a chromium underlayer to impove adhesion). Optical investigations included the detailed studying of the film reflection R and transmission T and were followed by the calculation of all main spectral parameters. The measurements of R and T were carried out at 300 K, on computer-controlled pair of spectrometers, point by point in the wavelength range 240 – 20 000 nm.

3. Results and discussion

Practically all of electro-physical parameters (resistivity, Hall R_H and Seebeck S coefficients) of the investigated films exhibit close to linear dependence on temperature and p-type conductance at sufficiently low temperature. Meantime, observed values of the Hall coefficient (often R_H was less than R_0 and it corresponded to one carrier per RE-ion), the low mobility $\sim 1 - 2$ cm^2 / V $\cdot$ s, and, finally, changes in the signs of R_H and / or S in the case of SmSb and $Tm^{+2.7}Sb$ indicate participation of both electrons and holes in the transport process. This is also confirmed by band structure calculations, the density-of-state value and the Fermi level position in these compounds [6, 7]. Indirect overlap of global extrema of the valence (Γ_{15}) and conduction (X_3) bands that is also crossed by a narrow band formed by a RE-ion *f*-state is observed; the overlap of wave functions of cation *f*-electrons and *p*-electrons of anion results in strong hybridization of states near the Fermi level, considerable and obvious dispersions of even bands mostly formed by *f*-electrons; the mobility region of carriers covers *pf*-, *f*- and *b*-bands which significantly differ in density-of-states and the degree of occupation. Simultaneously, the sensitivity of the Fermi level position to various excitations (according to the calculations given in [7] for example, the spin-orbit interaction in SmSb decreases the Fermi energy by ~ 1 eV), and, consequently, to insignificant variation of a RE-ion valence-state should be anticipated. It is in view of ale this that the correlation between the temperature of a substrate during evaporation of the SmSb film (affecting the lattice parameter) and the temperature of the change in the signs of the Hall and Seebeck coefficients (described in [1]) can be better understood.

Among mixed-valence RE-compounds, monopnictides optical spectra are characterized by the shift of the sharp and deep reflection minimum (E_0) toward the infrared region (from the visible region typical of metal-like chalcogenides [8]) and exhibition of the narrow minimum E_1 in the absorption coefficient spectrum, which agrees in energy position with the main reflection band E_2 (Figures 1 – 3, Table 1). The E_2 band in TmSb exhibits a fine structure

(especially clearly in films with $\nu = +2.2$) having at least two peaks (E_2, E_2') corresponding maxima in the dielectric function imaginary part spectrum. Within the absorption edge, the presence of some maxima in the spectrum of E_2 or R (E_3) can be also noted. With the increase of the thulium ion valency ($\nu = +2.7$) two peaks E_2 and E_2' smear and merge. Even higher valency of a RE-ion could be responsible for the absence of separated structures within the reflection band E_2 in SmSb. It should be noted that compared with samarium monoantimonide the optical spectra of TmSb have more singularities. This is probably due to the fact that in TmSb many of *f*-states are located below the Fermi level (even according to calculations taking into account the spin-orbit interaction [8]), whereas in SmSb the entire *f*-band and part of the *pf*-valence band are found to be placed above the Fermi level [6].

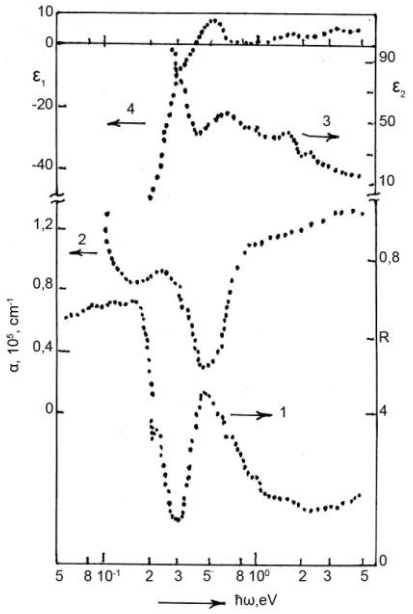

Figure 1. The reflection (1) and absorption coefficient (2),
real (3) and imaginary (4) parts of dielectric function of SmSb film.

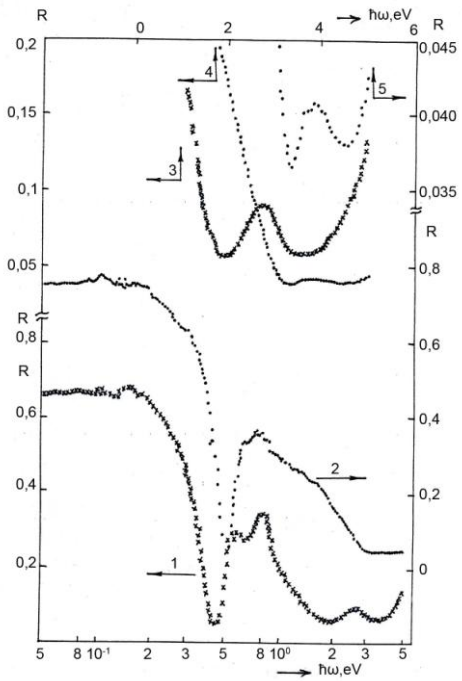

Figure 2. The reflection spectra of TmSb (1, 3 – $\nu = +2.2$; 2, 4, 5 – $\nu = +2.7$).

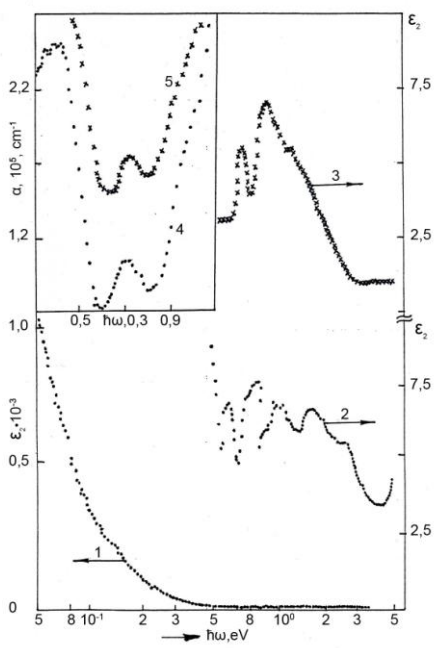

Figure 3. The imaginary part of the dielectric function and absorption coefficient spectra of TmSb (1, 2, 4 – ν = + 2.2; 3, 5 – ν = + 2.7).

Table 1. Structures positions in optical spectra (eV).

Structure	TmSb		SmSb
	ν = +2.2	ν = + 2.7	
E_0 (minimum R)	0.452	0.517	0.312
E_1 (minima α, ε_2)	0.58, 0.55	0.63, 0.56	0.40, 0.41
E_1 (maxima $\varepsilon_1, \varepsilon_1^b$)	0.60, 0.48	0.66, 0.64	0.45, 0.41
E_2 (maxima R, ε_2)	0.60, 0.87	0.65	0.45, 0.70
E_2' (maxima R, ε_2)	0.83, 1.07	0.78, 0.96	
E_3 (maximum R or α)	1.6	1.7	1.65
E_1' (maximum α)	0.700	0.710	
E'_0 (minimum R)	1.91	3.34	2.5
E_4 (maximum R)	2.7	3.8	

Calculations of the optical density-of-states and, correspondingly, optical constants spectral dependencies showed [6, 7] that it is possible to get rather good agreement between theory and experiment on the basis of the contribution of only direct electron transition between the nearest maxima of the density-of-states of mixed *pf*- and *fp*-bands, and *f*-band. This is confirmed by the calculated spectra ε_2 (SmSb) and R (TmSb) presented in Figures 1 and 2, respectively. Naturally, only one mechanism cannot describe all electron processes in materials with such complex band structure and valence electron configuration. The contribution of exciton states, for example, should be considered quite probable taking into account optical structures' small half-widths. Particularly, the maximum of resonance origin E_1' (with half-width of about 0.1 eV) was observed near the absorption edge (in the relative transmission window). Moreover, the hybridization of states at many points of the Brillouin

zone results in significantly less strict selection rules for optical transition of carriers. Thus, it exerts a considerable influence on the participation of concrete bands in energy shift and disappearance of the reflection maximum in the visible region caused by the RE-ion mixed (but varying within a certain range) valency. As investigation shows the reflection maximum E_4 with the amplitude about 4 % in $Tm^{+2.2}Sb$ is not only shifted towards short wavelengths by 1.1 eV in the case of $Tm^{+2,7}Sb$, but also disappears up to amplitude ~ 0.5 %, though preserving its well defined structure. The reflection maximum E_0, adjacent to the plasmon edge, also exhibits the expected short-wavelength shift with the increase of the various mechanisms of spectral sensitivity. It is highly probable that intraband transition, together with these free carriers, are responsible for a low energy ($\hbar\omega < 0.45$ eV) increase of the absorption coefficient and the presence of maxima in spectra.

Spectra of the real part of the dielectric function ε_1, loss function $\mathrm{Im}\varepsilon^{-1}$ and the results of separation of bound (ε_1^b) and free carriers (ε_1^f) contributions in $\varepsilon_1(\omega)$ are shown in Figure 4. The sharp positive maxima of ε_1, especially of ε_1^b, allow to specify the minimal energy of the fundamental interband electron transitions (E_1, Table 1). The presence of a great (but different for SmSb, $Tm^{+2.2}Sb$ and $Tm^{+2.7}Sb$) number of short-wavelength structures in the ε_1^b spectra indicates, on the one hand, the already mentioned existence of multiple critical points in the Brillouin zone and, on the other hand, the band reconstruction (at least in respect of the Fermi level) due to the change of the RE-ion valency. The reflection spectra, given in Figures 1 and 2, are characterized by a powerful long-wavelength reflection edge of the evident plasmon nature. The crossing of zero with a positive slope by the dependence $\varepsilon_1(\omega)$ or by $\varepsilon_1^b(\omega)$ (that increases accuracy), with accompanying maximum of $\mathrm{Im}\varepsilon^{-1}$ allows to determine of the characteristic energy of plasmons contributing to the optical constants dispersion. According to the measured data this energy of carriers' plasma oscillation is estimated at 1.5 eV for SmSb and 0.55 – 0.57 eV for TmSb.

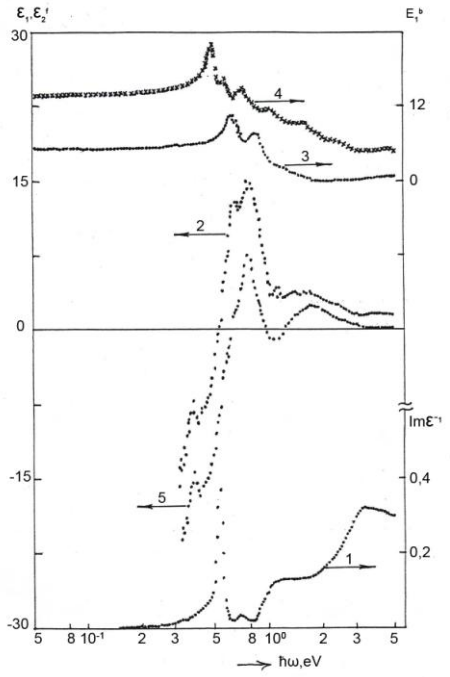

Figure 4. Loss function spectra (1), real part of dielectric function (2) and bound (3, 4) and free (5) carriers structures in $\varepsilon_1(\omega)$ for TmSb (4 – $\nu = +2.2$; 1-3, 5 – $\nu = +2.7$).

One of the characteristic features of the investigated reflection spectra is the presence of yet another (together with E_0) short-wavelength reflection minimum E_0, as well as the accompanying maximum E_4 in the case of TmSb (Figure 2, Table 1). Our earlier investigation carried out on SmS and DyS films [4, 7] revealed a certain regularity connected with the emergence, non-integer value of ν, while for TmSb this shift (both by the absolute and relative value) is considerably less than magnitudes observed in samarium and dysprosium monosulfides (see [4, 8]).

4. Conclusion

Single-phase crystalline films of samarium and thulium monoantimonides were prepared on various substrates by vacuum thermal evaporation from two independent sources. Electro-physical characteristics of main optical parameters are studied in detail and the sensitivity of the observed optical spectra singularities to the value of the RE-ion mixed valency determined by the characteristic L_3 X-ray absorption is shown. The reported experimental results agree well with and represent in many aspects the specific energy band structure of the investigated compounds.

References

1. L. N. Glurjidze, T. O. Dadiani, Z. U. Jabua, E. V. Dokadze, M. S. Taktakishvili, V. V. Sanadze. Electro-physical properties of samarium monoantidomide thin film. Phys. Solid State, 1986, **28**, 2860.
2. G. Vaitheeswaran, L. Petit, A. Svane, V. Kanchana, M. Rajagoplan. Electronic structure of praseodymium monopnictides and monochalcogenides under pressure. J. Phys.: Cond. Mat., 2004, **16**, 4429.
3. Z. U. Jabua, T. O. Dadiani, A. V. Gigineishvili, M. I. Stamateli, T. S. Lochoshvili. Preparation of thin films of praseodymium monoantimonide and their electro-physical properties. Georg. Eng. News, 2004, **3**, 36.
4. L. N. Glurjidze, A. V. Gigineishvili, N. J. Zurabishvili, T. L. Bzhalava, V. V. Sanadze. Reflection spectra of samarium monosulfide thin films at phase transition metal–semiconductor. Phys. Solid State, 1980, **22**, 1098.
5. L. N. Glurjidze, T. O. Dadiani, Z. U. Jabua, T. L. Plavisnkij, A. V. Gigineishvili, V. V. Sanadze, L. D. Finkelshtein, N. N. Efremova. Mixed valency of ytterbium in the ytterbium diantimonide thin films. Phys. Solid State, 1988, **30**, 1171.
6. K. R. Gegeshidze, G. P. Nijnikova, O. V. Farberovich, A. V. Gigineishvili, L. N. Glurjidze. Electronic properties of SmSb. Phys. Solid State, 1994, **36**, 1113.
7. K. R. Gegeshidze, G. P. Nijnikova, O. V. Farberovich, A. V. Gigineishvili, T. L. Plavinskij, L. N. Glurjidze. Energy bands structure and optical properties of TmSb. Phys. Solid State, 1992, **34**, 928.
8. L. N. Glurjidze, A. V. Gigineishvili, N. S. Zedginidze, V. V. Sanadze. Is the dysprosium monosulfide a compound with mixed valency? Phys. Solid State, 1983, **25**, 691.

This is an introductory paper in a series of four, devoted to outline mineral processing for nano-scientists — users of the final products.
Editor

MINERAL PROCESSING FOR NANO-SCIENTISTS

F. Habashi

Laval University
Quebec City, Canada
Fathi.Habashi@arul.ualval.ca

Accepted February 14, 2011

1. Introduction

People had inhabited the Earth for hundreds of thousands of years before they began to use metals. This was the Stone Age in which the only tools available were pieces of wood, bone, flint, or sea shells. The ancient peoples used only those metals that were available without mining or chemical treatment, for example, pieces of native gold, silver, and copper, and rare pieces of meteoric iron. These were too small in quantity to be of any consequence. Iron articles of meteoric origin can be easily identified by their nickel content.

Up to the Middle Ages, seven metals were only known and used by man. These were gold, silver, copper, iron, lead, tin, and mercury. During the Middle Ages the metalloids arsenic, antimony, and bismuth were isolated as well as zinc that was imported from the East. In the Eighteenth century mineral specimens were continuously supplied and analyzed, which resulted in the discovery of about a dozen new metals. With the discovery of electric current at the beginning of the nineteenth century the alkali metals were isolated and these were responsible for the isolation of new metals that were not possible to isolate before, such as aluminum, zirconium, titanium, etc. Once aluminum became available it was used to liberate other metals from their compounds. The industrial revolution in England introduced the Age of Steel while the discovery of X-rays towards the end of the century resulted in many more discoveries that changed our world in the twentieth century.

Shortly after the discovery of uranium fission in 1939, the possibility of harnessing atomic energy was realized. To achieve this goal metallic uranium would be required on a large scale. Since no rich deposits of the metal were known at that time, only poor ores had to be processed. This introduced the large scale application of ion exchange and solvent extraction in metallurgy. Also, the need for metals having special properties for their use in nuclear reactors resulted in the sudden interest in previously rarely used metals such as beryllium, zirconium, cadmium, sodium, potassium, thorium, and the rare earths. Thus, novel methods of extraction were devised and applied on a large scale, for example, chlorination, fluorination, and fused-salt electrolysis.

The improvement in the design of the jet engine, and the suitability of titanium and its alloys to meet the strains imposed by ultra-high speed flight, besides their exceptional high strength to weight ratio, resulted in the fast development of the commercial production of titanium. The discovery of the semi-conductive properties of germanium led not only to commercial production of this metal but also to the preparation of related metals such as silicon, selenium, and tellurium on a commercial scale. Further, the use of such metals for the electronic industry, called for very high purity, not known before. This resulted in the invention of new methods for metal refining like zone refining. If high purity had to be achieved, laboratory methods for determination of impurities, at such previously unknown low levels had to be devised. Polarography, activation analysis, atomic absorption spectroscopy, etc., were therefore either improved or invented to cope with the situation.

The competition in sending men to the moon was a strong reason to develop new alloys, new rocket fuels, and new materials of construction. The appearance of new ideas in chemical thermodynamics and kinetics by Nernst, Van't Hoff, Haber, Ostwald, Le Chatelier, Arrhenius, and others laid the foundation for a theoretical weapon to attack and solve problems related to metal recovery. The improvement in chemical engineering practice resu1ted in cheap and large scale production of important gases such as oxygen, chlorine, hydrogen, etc. in metal extraction The role played by refractories, and especially the basic refractories is also a milestone in the development of pyrometallurgical practice. Closely related to these achievements is the introduction of new unit operations such as flotation and fluidization.

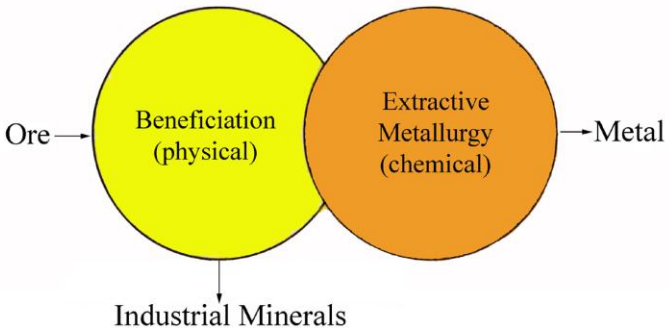

Figure 1. Mineral processing: metals from ores.

Mineral processing involves the treatment of ores to get metals (Figure 1). It involves two distinct operations: the first is physical called ***beneficiation*** the second is chemical called ***extractive metallurgy***. Both operations are overlapping since, in some cases, a physical method of separating the components of the material processed is inserted in the scheme of metal extraction. In few cases the mineral raw material is directly subjected to chemical treatment without being beneficiated.

2. Mineral beneficiation

Beneficiation is concerned with the enrichment of ores and separation of unwanted gangue minerals so that the subsequent treatment to get the metals by the extractive metallurgist is more efficient. The beneficiation engineer uses only mechanical, physical, and

physico-chemical methods for conducting his operations which are all done at normal temperature and pressure. These operations can be divided into two distinct steps:

● ***Liberation.*** In this operation the rock is broken down by mechanical means so that the individual mineral components become independent of each other, i.e., each is detached or liberated.

● ***Separation.*** In this operation the valuable minerals are separated from the rest by means of physical and physico-chemical methods making use of differences in specific gravity, magnetic properties, etc.

There is a group of some 300 minerals that are used as such or as a raw material for the chemical or other industries, i.e., they are not used for the production of metals. These are known as "industrial minerals." They may or may not be beneficiated. For example, clays, sands, and limestone are used in the construction industry. Sulfur, phosphate rock, fluorite are used in the chemical industry. Diamonds and other precious and semi-precious stones are used in jewellery.

The components of an ore are the valuable minerals and the waste or gangue minerals. The need to beneficiate ores by physical and mechanical means arises from the following facts:

● Transportation and handling costs can be greatly reduced if the unwanted gangue minerals were first removed.

● Size of reactors for treating such concentrates is also greatly decreased, which results in decreased capital cost, if the gangue minerals were removed.

● The ore may contain more than one valuable mineral, or certain undesirable impurity, and it is usually cheaper to separate them by physical rather than by chemical methods.

2.1. Aggregation of minerals

The reason for the above division is that minerals usually occur in ores in the following forms: detached, cemented, locked, and disseminated; each form has its own characteristics (Figure 2):

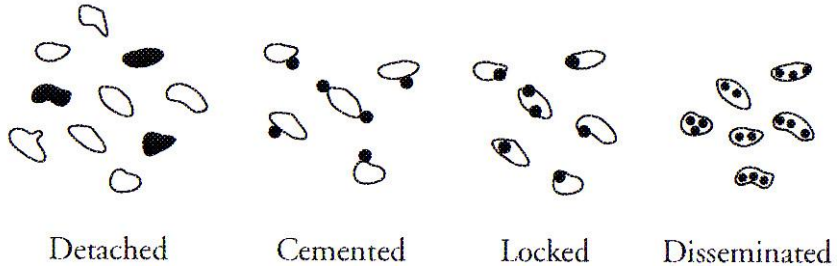

Figure 2. Mode of occurrence of minerals in nature.

● ***Detached.*** In this case the desired mineral is separate from the others and therefore easy to separate by physical methods. For example, gold particles and platinum metals in alluvial sand.

● ***Cemented.*** In this case the desired mineral is cemented with other mineral particles and separation would be possible if the particles are fractured at the grain boundaries. For example, apatite in phosphate rock and gibbsite in bauxite are usually cemented to clays.

● ***Locked.*** In this case the desired mineral is locked into other minerals and they cannot be separated by physical methods unless liberated by grinding. This is the case for most ore deposits.

● ***Disseminated.*** In this case finely divided mineral particles are dispersed in a matrix of another mineral. For example, the porphyry copper ores where finely divided copper minerals are dispersed in quartz, and the complex sulfides where copper, lead, and zinc sulfide minerals are dispersed in pyrite. These minerals can only be liberated by extensive grinding and under such conditions physical methods of separation usually fail and chemical methods must be applied.

A beneficiation plant is divided into two sections: liberation of the minerals from the rock and separation of the liberated minerals.

2.2. Liberation of minerals

Liberation of minerals by comminution is an expensive operation; the cost increases proportionally with decreased particle size of the product. On the other hand, the cost of any subsequent metallurgical operation, e.g., heating, leaching, etc., decreases with decreased particle size of the solid treated because of the increased surface area. Therefore, there must be a compromise between the cost of grinding and the ideal particle size required for a subsequent process. This is represented by the minimum in Figure 3. A relation between particle size and surface area is given in Figure 4. Excessive grinding may also be undesirable since it may cause problems in a subsequent step, e.g., during filtration if the ore or concentrate is treated by hydrometallurgical methods. Comminution of ores is usually done in three steps as shown in Table 1 (Figures 5-8).

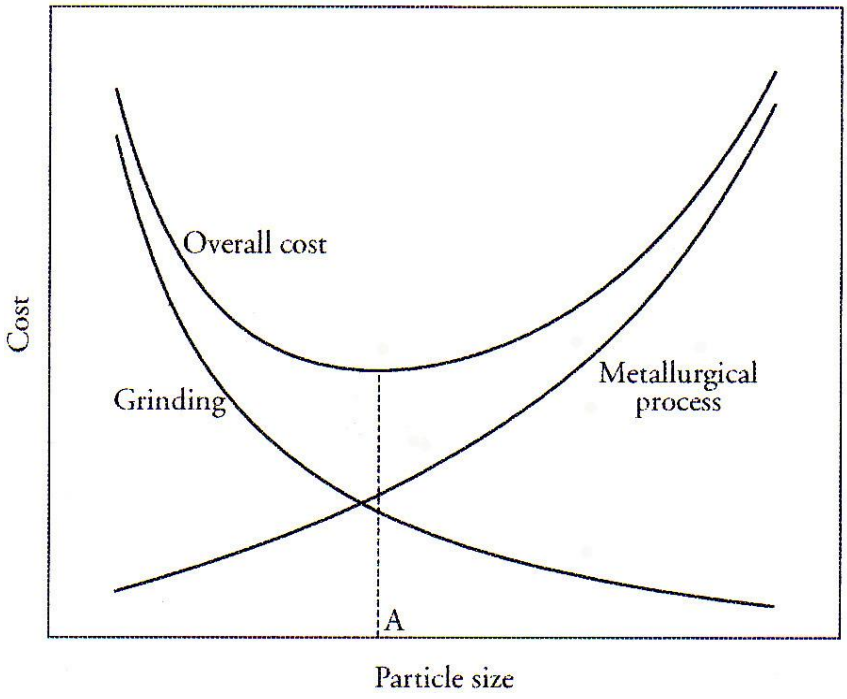

Figure 3. Relation between cost and particle size.
Point A represents the most economic particle size.

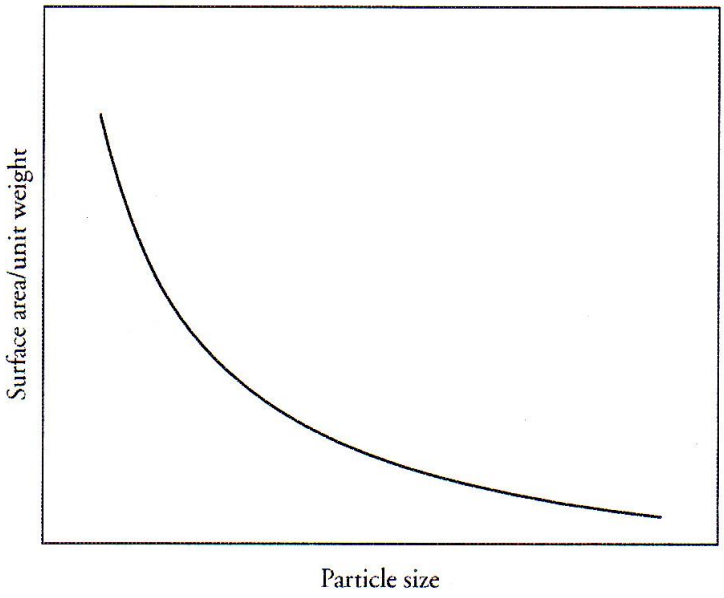

Figure 4. A relation between particle size and surface area.

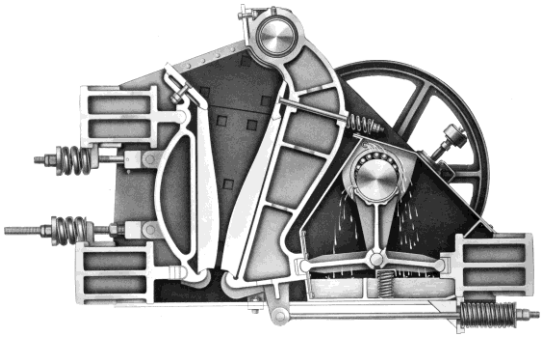

Figure 5. Jaw crusher.

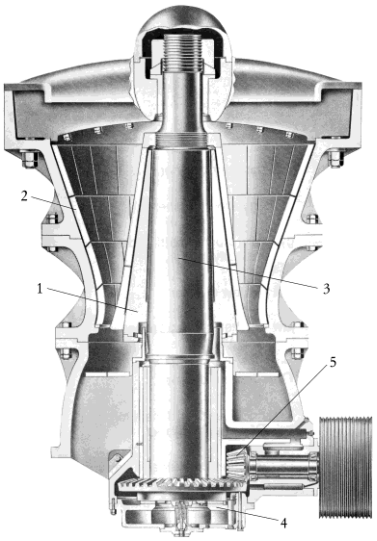

Figure 6. Gyratory crusher.

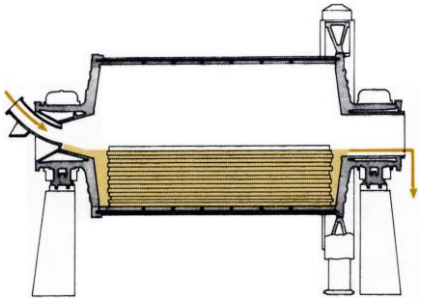

Figure 7. Rod mill.

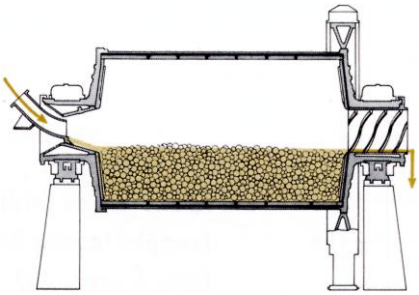

Figure 8. Ball mill.

Table 1. Data on crushing and grinding industrial operations.

Operation	Equipment used	Feed size, mm	Product size, mm
Coarse or primary crushing	Jaw or gyratory crusher	100 – 300	10 – 50
Fine or secondary crushing	Rod mill	10 – 50	2 – 10
Grinding	Ball mill	10 – 20	0.005

2.3. Attrition grinding and mechanochemistry

Mechanochemical phenomena have been utilized since ancient times in making fire by rubbing pieces of wood against each other or by using flint to generate a spark that ignites dry bush. In mineral processing attrition grinding mills have been used to produce a product more susceptible to reaction and also to reduce the energy required for grinding. A vertical mill with an agitating screw suspended into the grinding chamber, supported by spherical roller bearings, and driven by a fixed-speed motor through a planetary gearbox typically handles feed sizes ranging from 6 mm and less, while grinding material to under 20 μm in size. The mill has a screw that pulls media up the centre of the mill before cascading over the edge of the screw, creating a downward flow of media at the mill perimeter (Figure 9). The vertical mill does not use impact to break material, which wastes energy. In another design cemented carbide balls are used as attrition medium (Figure 10).

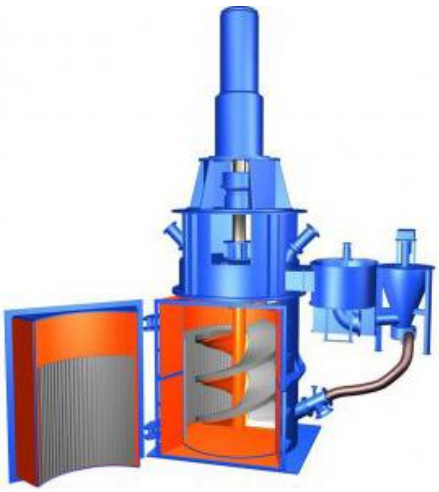

Figure 9. Vertical attrition mill with a screw [Metso].

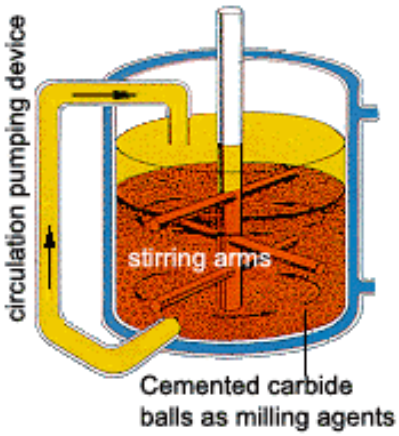

Figure 10. Attrition mill with silicon carbide balls.

2.4. Separation of minerals

Separation of minerals is based on differences in their physical or physico-chemical properties. Among the physical properties that are extensively exploited are the specific gravity, magnetic and electrostatic properties, and radioactivity. Physico-chemical methods are based on

the surface properties of the minerals. These methods are not very effective, but they are cheap and rapid.

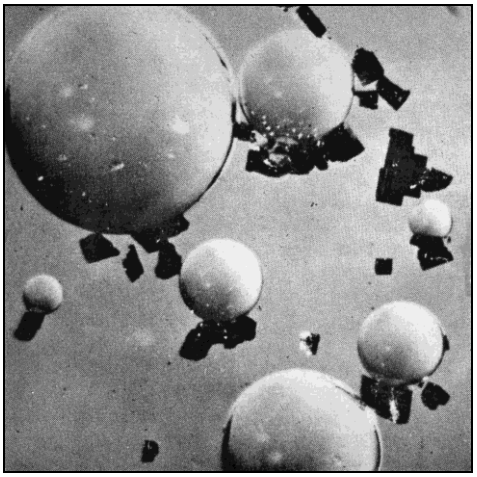

Figure 11. Photomicrograph of fine mineral particles floated by tiny air bubbles.

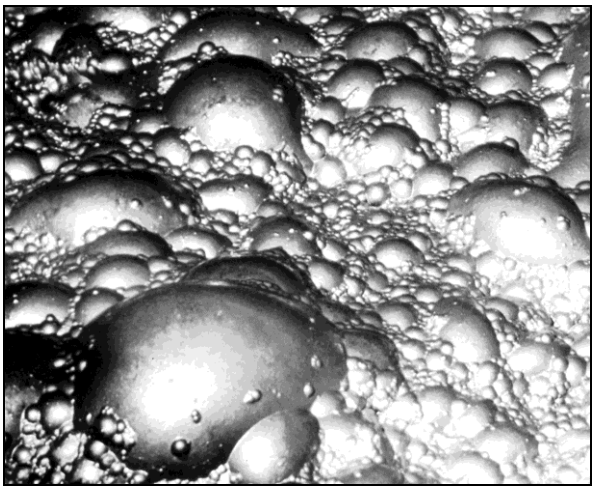

Figure 12. Foam from a flotation cell containing a mineral concentrate. Tiny mineral particles, about 40 μm, are adhering to air bubbles.

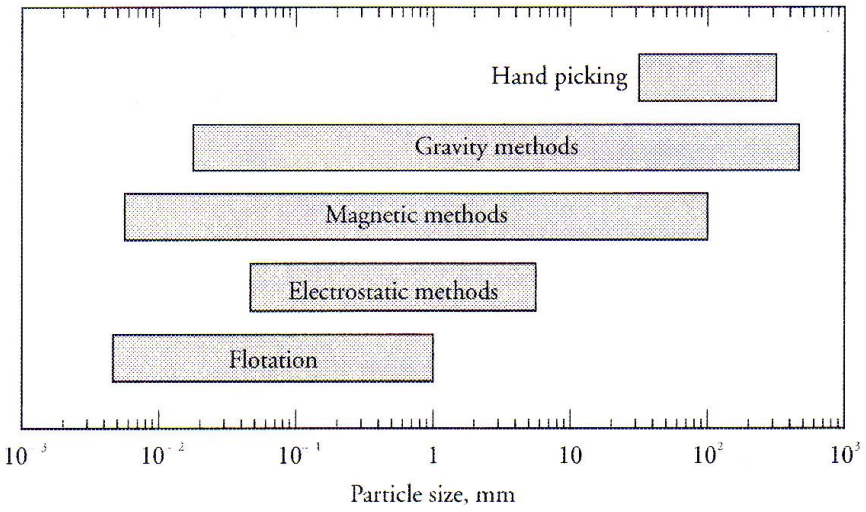

Figure 13. Optimum particle size for separating minerals.

Separation based on the surface properties of minerals is the basis of the flotation process which is now the most important concentration method; more ores are treated by this method than by any other. The process depends upon the ability to selectively render some minerals un-wetted by water while others remain wetted. The un-wetted particles adhere to air bubbles which float to the surface and are removed as a concentrate in the froth (20 – 40 % solids) as shown in Figure 11, while the wetted particles do not adhere to the air bubbles and remain behind. The particles in the froth (Figure 12) are then subjected to filtration to get a "flotation

concentrate." The specific gravity of the minerals is not the determining factor, for the minerals floated are usually heavier than the minerals which are not floated.

For each property on which a separation process is based there is an optimum particle size of the feed at which the process functions most effectively. Figure 13 gives the optimum range of particle size for various methods. For example, flotation can be most effectively conducted when the mineral particles are 1 to 0.01 mm; particles larger than 1 mm will be too heavy to be lifted by the air bubble and all particles smaller than 0.01 mm will be floated because at this small size loose agglomeration takes place. Usually, more than one process is used to effect a separation. In magnetic methods, both low and high magnetic fields are used.

2.5. Recovery and grade

Two parameters have to be determined in any separation process:

- ***Recovery.*** This is the percentage of the metal values recovered in the concentrate.
- ***Grade.*** This is the content of the metal in the concentrate expressed in percent.

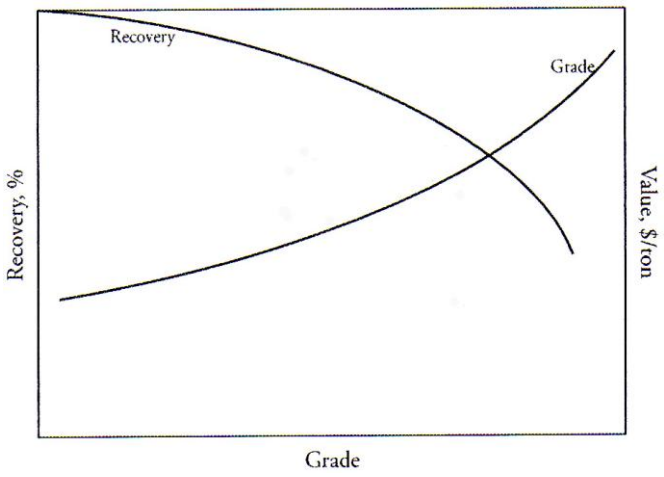

Figure 14. Relation between recovery of a certain mineral grade of the concentrate obtained, and its value.

The connection between these parameters are the following (Figure 14):

- There is an inverse relation between recovery and grade. To obtain a high grade concentrate, the metal values lost in the tailings will be high and therefore the recovery is low. A 100 % recovery is only possible by not concentrating the ore.
- There is a direct relation between the value of a concentrate and its grade. This is because the cost of extracting metal values from a concentrate is determined largely by the cost of rejecting the valueless material still present. For example, the lower the grade of a copper sulfide concentrates the more energy the concentrate will require when treated by pyrometallurgical methods.

Thus, the production of a high-grade concentrate will result in the loss in some values, but the value of the concentrate would be higher. Therefore, a compromise is generally sought between the metal values lost in the tailings and the ease of subsequent metallurgical treatment of the concentrate. Physical and physico-chemical properties on which separation of minerals is based are the following.

3. Extractive metallurgy

While the beneficiation engineer uses only mechanical, physical, and physico-chemical methods, the extractive metallurgist uses chemical methods. Another important difference is that while all beneficiation operations are conducted at normal temperature and pressure, extractive metallurgical processes are seldom conducted at ambient conditions — usually at high temperature, and sometimes also at high pressure. In its modern form extractive metallurgy is broadly divided into three areas: pyro-, hydro-, and electrometallurgy.

● ***Pyrometallurgy.*** This is the oldest sector of extractive metallurgy and involves dry methods usually conducted at high temperature, such as oxidation, reduction, chlorination, melting, slagging, etc., and often involving the melting of the minerals and the separation of the valuable components in the liquid state. Typical ores treated by this technology are those of iron, copper, and lead.

● ***Hydrometallurgy.*** This is a relatively new sector of extractive metallurgy and involves the wet methods, usually conducted at room temperature or near the boiling point of water. It includes the leaching of ores or the precipitation of a metal or its compounds from aqueous solutions, as well as methods of isolation and purification such as ion exchange and solvent extraction. Typical ores treated by this technology are those of gold, uranium, and aluminum.

● ***Electrometallurgy.*** This is the newest domain of extractive metallurgy and involves all processes based on the use of electric current for metal recovery or refining either in aqueous solution or in a fused salt. Typical metals produced by this technology are aluminum, copper, and zinc.

These areas, however, cannot be considered isolated one from the other, because a combination of these processes is generally used in the production of a single metal.

3.1. Pyro- versus hydrometallurgy

Pyrometallurgy was most successful when high grade massive ores were treated in a blast furnace, because such a furnace has maximum heat economy being itself a heat exchanger: the cold charge descending from the top is preheated by the hot gases ascending in the furnace. Dust problems were also minimal because the ore was in the form of large lumps. With the exhaustion of such raw material, metallurgists turned their attention towards the treatment of low-grade ores. This necessitated extensive grinding and flotation, which resulted in finely divided concentrates as raw material. These, naturally, could not be charged to a blast furnace because if charged they will block the movement of the ascending gases — hence the birth of the fossil-fired horizontal reverberatory furnace for melting sulfide concentrates. This was a turning point for the worst with respect to pollution of the environment, high energy consumption, and excessive dust formation.

Treatment of sulfide ores

Pyrometallurgical treatment of sulfide ore is plagued by the problem of sulfur dioxide generation. If it is in high enough concentration, it must be used for making acid and a nearby market for this acid must be found. If the sulfur dioxide concentration is too low for making acid, disposal methods must be found. These are available but expensive. As a result, in many cases, sulfur dioxide is simply emitted to the atmosphere. On the other hand, sulfides can be

treated by hydrometallurgical methods without generating sulfur dioxide thus eliminating the need to manufacture sulfuric acid. The sulfur can be recovered in the elemental form which can be easily stock-piled, or transported at low cost.

Material handling

In pyrometallurgical processes, the metallurgist is forced to transfer molten slag and matte from one furnace to the other in large, heavy, refractory-lined ladles. Besides the inconvenience and the cost of handling these materials, there is also the inevitable gas emission from them because they are usually saturated with sulfur dioxide and during transfer they cool down a little, resulting in decreased gas solubility and emission, hence the inconvenient working condition. In hydrometallurgical plants, solutions and slurries are transferred by pipelines without any problem.

Energy

Because of the high temperature involved in pyrometallurgical processes, usually around 1500 °C, the reaction rates are high but much fuel is needed. To make a process economical, heat recovery systems are essential. Heat can be readily recovered from hot gases, but rarely from molten material like slag or metal. Thus, a great deal of energy is lost. Further, the equipment needed for heat economy is bulky and expensive. Further, in a horizontal furnace heat is mainly transferred from the ceiling of the furnace by radiation and has to penetrate a thick layer of slag which has a low thermal conductivity; that is why it is inefficient. In hydrometallurgical processes, on the other hand, less fuel is needed because of the low temperature involved (usually below 100 °C). Heat economy is usually no problem.

Dust

Combustion of fossil fuels in a horizontal furnace results in the formation of a large volume of gases that carry over large amounts of dust. This must be recovered to abate pollution and because the dust itself is also a valuable material. The technology of dust recovery is well established but the equipment is bulky and expensive. In hydrometallurgical processes this is no problem because wet material is usually handled.

Treatment of complex ores

Treatment of complex ores by pyrometallurgical method is unsuitable because separation is difficult; complex ores can be treated more conveniently by hydrometallurgy.

Treatment of low-grade ores

Treatment of low-grade ores by pyrometallurgy is unsuitable because of the large amount of energy required to melt the gangue minerals. On the other hand it is especially suitable to use hydrometallurgy since a selective leaching agent that can solubilize the valuable minerals, and not the gangue, is usually available.

Economics

The economics of a pyrometallurgical process is usually suitable for large scale operations and this requires a large capital investment. On the other hand, hydrometallurgical processes are suitable for small scale operations and low capital investment. The hydrometallurgical units can be increased in number when the need arises without any economic disadvantage.

Residues

Many residues of pyrometallurgical processes are coarse and harmless. For example, slag which is a silicate phase can be stored in piles exposed to air and rain without the danger of dissolution and contaminating the streams. It is just unacceptable from the aesthetic point of view. On the other hand most residues of hydrometallurgical processes are finely divided solids.

If they are dry, they create dust problems when the wind blows and when wet they will gradually release metal ions in solution which will contaminate the environment. Hence well prepared storage sites must be created.

3.2. Pyro- versus electrometallurgy

The competition between pyro- and electrometallurgy is mainly between metallothermic reduction processes for producing metals, i.e., liberating a metal from its compounds by heating with another more reactive metal, and the electrolysis of fused salts. While both routes require using pure materials and their handling under strict anhydrous conditions, the metallothermic reduction usually involves more handling steps than the electrolytic route. On the other hand, electrolytic processes require cheap electric power.

The first metallic aluminum produced commercially was prepared by a pyrometallurgical route, namely, by the reduction of aluminum chloride with metallic sodium. The process, however, gave way when the electrolytic reduction of Al_2O_3 process was invented. While the choice between pyro- and electrometallurgy has been settled for the aluminum industry long time ago, this is not the case for other metals like beryllium and magnesium. For these two metals, both routes are used. On the other hand, the production of titanium by metallothermic reduction is still unchallenged by the electrometallurgical route.

4. Progress and problems in mineral processing

The present tendency in mineral processing is focused towards solving the following problems:

4.1. Processing of low-grade ores

It is evident that rich ores will first be exploited. These have been practically exhausted and the metallurgist is now faced with deposits containing low metal content from which the metal has to be recovered by economical means.

4.2. Processing of complex ores

Extractive metallurgists are also faced with ores containing numerous valuable metals thus making difficult their separation and recovery, for example, pyrite containing disseminated lead, zinc, and copper sulfides, or pyrrhotite containing nickel, cobalt, and copper sulfides. These ores also contain gold, silver, and platinum group metals.

4.3. Preparation of high-purity metals

At one time a metal 99.9 % pure was sufficient for many applications. Today to meet the demands of the more specialized industry such as the electronic or the nuclear industry, the extractive metallurgist is now preparing metals 99.999 % pure. New techniques have to be developed and new methods of chemical analysis have to be devised. Electrolytic methods, for

example, are used to prepare the common metals copper, nickel, zinc, gold, and silver, in a pure form. High purity nickel is produced on large scale by the carbonyl process while zirconium and hafnium are usually purified by the iodide process.

To produce a reactor-grade uranium, the yellow cake (sodium or ammonium uranate) produced at the mine has to be dissolved in nitric acid and purified by organic solvents until a very pure uranyl nitrate is obtained which can then be processed further to metal. To prepare germanium for the electronic industry, germanium tetrachloride is thoroughly purified by fractional distillation before reduction to metal and the preparation of single crystals of germanium. Zone melting is used to purify low melting point metals while electron beam melting is used for high melting point metals. Polarography, spectrophotometry, and emission spectography were at one time the most sensitive methods for analyzing impurities in metals. Now, atomic absorption and neutron activation methods have taken over.

4.4. Increased demand for metals

As a result of the growing population, there is an increased demand for metals, hence the necessity for increased production. This requires the design of larger reactors of unprecedented size capable of satisfying the increased demand. Today a blast furnace produces 10 000 t / d iron. To produce this amount of iron, about 17 000 tons of ore, 5 000 tons of coke, 2 500 tons of limestone, 20 000 tons of air, 3 000 tons of slag, 500 tons of dust, and 30 000 tons of blast furnace gas must be handled daily. The engineering problems associated with handling these materials are no doubt enormous. In 1960, the production of aluminum exceeded that of copper for the first time. Aluminum is now the first nonferrous metal in terms of tonnage produced which exceeds 20 million tons / year.

4.5. Conservation of mineral resources

Natural resources are limited and it is necessary to conserve them. This can be only achieved by:

- ***Utilization of scrap metal.*** Processing of scrap metal not only conserves the metal but utilizes much less energy. Production of steel from scrap consumes only 25 % of the energy that would be used to produce the same steel from an iron ore. In the case of aluminum the energy consumed is even much less (about 4 %).
- ***Recovery of metals that would be otherwise lost during processing.*** For example phosphate rock contains on the average 100 ppm uranium. During processing the rock for the production of fertilizers, the major part of uranium goes into the phosphoric acid produced as an intermediate product. Since about 100×10^6 tons of rock are processed every year, about 10 000 tons of uranium would therefore be lost in the fertilizers. Some plants are recovering this uranium from the acid before manufacturing the fertilizers. This is usually done by extraction with organic solvents.
- ***Converting mineral waste into useful products.*** The metallurgical industry produces large amounts of tailings, slags, and residues which accumulate through the years. While some tailings are returned to the mine as a filling in case of underground exploitation, in case of open pit mining the tailings is usually piled in the neighborhood. For example, in the asbestos producing areas in Quebec about 20 million tons are rejected every year. These tailings are

mainly magnesium silicates. At present, there are about 600 million tons of tailings that have already accumulated and are a source of pollution when the wind blows. Efforts are under way to recover magnesium from this source; however, the problems have not yet been solved.

Metallurgical slags may be used in road construction, and in cement manufacture. However, much slag piles are still accumulating around metallurgical plants for a variety of economical, technological, or transportation reasons. Some slags may be radioactive if the ore contains uranium or thorium. For example, niobium ores usually contain some uranium and thorium; in the production of ferroniobium the slag contains the radioactive metals.

In the production of alumina from bauxite a red mud is produced which contains principally Fe_2O_3, SiO_2, and TiO_2. For every ton Al_2O_3 produced about one ton of red mud is produced. A small amount is used for making refractory bricks but the great part is usually piled occupying large areas of land. While this residue may be relatively harmless, other residues, for example those from zinc or uranium ore treatment may contain traces of metals that may be solubilized by the combined action of air and rain causing contamination of surface waters.

4.6. Pollution abatement

At one time the metallurgical industry cared less about emitting its waste products in rivers and lakes or in the atmosphere. Now, with increased government regulations, it is no longer acceptable to dump waste solutions in rivers or lakes, or emit sulfur dioxide or fluorine-containing gases in the atmosphere. The extractive metallurgist is now trying to cope with this problem by adding new equipment in existing plants that would abate pollution. He is even forced in some cases to develop new costly processes but less polluting than the conventional processes.

4.7. Decreasing expenditure of energy

Fuel, heat, and electricity are costly items in a metallurgical process and should be used with great efficiency to decrease production costs. To this end, the recent trend is focused towards the following goals:

An increased use of heat recovery systems

Heat from an exhaust fluid is to be used for preheating the entering fluid. For example, exhaust hot gases from a furnace can be used to preheat the air and / or the fuel (gas or liquid) used in the furnace, or to generate steam in a waste heat boiler. This steam can be used in the plant for various purposes or for generating electricity. Recently, gases leaving a steelmaking converter have been collected to recover their calorific value. A 200 tons steel converter contains about 8.4 tons of carbon which are oxidized during oxygen blowing to CO. At one time this gas was left to burn to CO_2 at the mouth of the converter. Introducing air-tight hoods prevents this combustion, and CO can now be cleaned of its dust content and directed to a gas holder, from which it can be used on demand as a fuel.

An increased use of oxygen instead of air

It has been realized that the cost of separating oxygen from the air is less than the cost of using large equipment utilizing air either in hydro- or in pyrometallurgy. Air contains only 21 % oxygen and the rest is nitrogen which plays no useful role in metallurgical processes; on the opposite, nitrogen must be heated before entering the reactor and then as much as possible

of this heat must be recovered when it gets out of the reactor. The increased use of oxygen resulted in a tremendous decrease in its price. It also resulted in a parallel increase in production of argon which is present in air to the extent of 1 %. New applications for argon were thus created, for example, in the refining of steel.

Improved equipment design

Electric heating is more efficient than heating by burning carbonaceous material. There is no flue gases to worry about recovering there sensible heat or remove their dust content. That is why more electric furnaces are being used in extractive metallurgy. Improved furnace design may also be achieved by using direct instead of indirect heating. For example, zinc and magnesium were once produced by the reduction of their oxides in retort furnaces where heat was supplied to the charge in the retort from the outside. Naturally this is not an efficient way of heating because of the slow rate of heat transfer and the rapid deterioration of the retorts. These processes were later abandoned in favor of direct heating, i.e., heat is generated directly inside the charge, for example, by electric heating or by burning the carbonaceous fuel in direct contact with the charge.

Improved process design

Copper, lead, and nickel sulfides concentrates are common in one respect: the molten sulfide can be treated by air to produce the metal in a single step; the process is exothermic. However, until recently these metals were produced by a multi-step process, including one that is endothermic. It was therefore thought that if all the operations were conducted in one reactor instead of two or three then there will be great saving in energy. For the production of copper this concept was applied, using reactors in which one region is a strongly oxidizing atmosphere to permit partial oxidation and melting of the sulfide, slagging of the iron, and converting the copper sulfide, and another region where the slag is tapped is a reducing atmosphere to permit decreasing the copper content in the slag. The same principle is applied to lead sulfide. For nickel sulfide the situation was slightly different but it was possible to solve the standing problems.

Improved methods of operation

Operating a vertical furnace is usually susceptible to channeling, i.e., the ascending gases penetrate unequally through the bed due to the presence of channels. This causes inefficient operation because certain parts of the bed undergo reaction while others, where the gas does not penetrate, descend without reaction. The main reason of channeling is the unequal particle size of the charge. Agglomeration of the charge and sieving to a narrow range results in preventing channeling. This has been demonstrated and applied in iron blast furnace.

4.8. Efficient process control

Metal production suffered from the difficulty of controlling the quality of the product because of fluctuations in raw material processed. Nowadays, with the advent of computer systems and physical methods of chemical analysis, it became possible to improve the quality and to control its composition. For example, steel samples are taken and transported pneumatically to the laboratory where X-ray fluorescence analysis or emission spectrographic analysis is conducted for a large number of elements, results of which are conveyed in a printed form via a computer to the operator within minutes.

In electrolytic plants it is essential to make sure that the designed anode–cathode distance is respected otherwise the voltage will change and will result in excess energy consumption and / or electrodeposition of undesirable impurities. In aluminum reduction cells sensors have been introduced to automatically control this variable. In copper and zinc electrolytic plants this was formerly checked by workers using a voltmeter. Nowadays, scanning infrared cameras are used to photograph the cells from the top. Any hot zones due to a narrow anode–cathode distance will be revealed and at once corrected.

4.9. Minimum utilization of manpower

Many metallurgical processes are conducted batchwise. This needs a large number of operators. To decrease the manpower operating a plant, the process should be conducted on continuous basis. This proved sometimes to be not only a saving in manpower but also a saving in energy. For example, steel was at one time cast in ingots and when solidified it was removed and put in a furnace to be heated to a certain temperature before transporting it to the rolling mills. Naturally, this meant many times handling a batch as well as loss of heat during the cooling step. Introducing continuous casting where the molten metal is directly cast solved this problem. Few years later the same technique was introduced in the nonferrous industries. The production of copper was for many years a batch process: the sulfide concentrate was melted in a furnace to separate the gangue then the matte is transferred to another reactor to remove the iron, and to get the copper. In recent years a Japanese process was introduced in which the molten material is continuously transferred from one furnace to the other by gravity, thus saving manpower.

5. Summary

In the past centuries pyrometallurgy was the only route to extract metals from ores and this required a large capital investment many countries could not afford to raise. This situation encouraged marketing of concentrates. Today, metallurgists have the option to use the hydrometallurgical route to process ores and concentrates at a reasonable capital investment. This opened the way to the possibility of processing ores locally. When need arises to increase production new units can be added economically. This is not possible with pyrometallurgical processes because one large furnace is more economical than a number of small furnaces with the same capacity due to heat radiation losses. In summary, mineral processing has made great progress in the past thirty years but there are still some standing problems that need to be solved.

Suggested readings

1. P. Balaz. Extractive Metallurgy of Activated Minerals. 2000, Amsterdam: Elsevier.
2. F. Habashi (Ed.). A History of Metallurgy. 1994, Quebec City: Métallurgie Extractive Québec (distributed by Laval University Bookstore “Zone”. www.zone.ul.ca).

3. F. Habashi. Metallurgical Chemistry. 1987, Washington: American Chemical Society, 279 pp. + 5 cassettes (1 hr. each) (re-issued by Métallurgie Extractive Québec in 2007 (book & CD); distributed by Laval University Bookstore "Zone". www.zone.ul.ca).
4. F. Habashi. Extractive Metallurgy Today. Progress and Problems. 2000, Quebec City: Métallurgie Extractive Québec (distributed by Laval University Bookstore "Zone". www.zone.ul.ca).
5. F. Habashi. Metals from Ores. An Introduction to Extractive Metallurgy. 2003, Quebec City: Métallurgie Extractive Québec (distributed by Laval University Bookstore "Zone". www.zone.ul.ca).
6. F. Habashi (Ed.). Handbook of Extractive Metallurgy. 4 volumes, 2500 pp. 1997, Weinheim: Wiley–VCH.
7. F. Habashi. Extractive Metallurgy Today. Progress and Problems. 2000, Quebec City: Métallurgie Extractive Québec (distributed by Laval University Bookstore "Zone". www.zone.ul.ca).
8. F. Habashi. Pollution Problems in the Mineral and Metallurgical Industries. 1996, Québec City: Métallurgie Extractive Québec (distributed by Laval University Bookstore "Zone". www.zone.ul.ca).
9. A. Z. Juhaśz, L. Opoczk. Mechanical Activation of Minerals by Grinding. 1990, Budapest: Akadémiai Kiadó.

This is the second paper in a series of four, devoted to outline mineral processing for nano-scientists — users of the final products. The first paper was a general outline of mineral processing. The next two will be on hydrometallurgy and electrometallurgy.
Editor

PYROMETALLURGY FOR NANO-SCIENTISTS

F. Habashi

Laval University
Quebec City, Canada
Fathi.Habashi@arul.ualval.ca

Accepted February 23, 2011

Pyrometallurgical processes involve a preliminary step to render the ore or concentrate more amenable to further processing. This is then followed by a reduction or a conversion step to liberate the metal and finally a refining step to get the pure metal for the market. When the flotation process was introduced it permitted the utilization of low great ores which resulted in fine particles that cannot be introduced into shaft furnaces in use. As a result new unit operations were invented to cope with the situation. Although fine particles may be desirable because of the large surface area and the rapid rate of reaction they have the disadvantage of generating undesirable dust. Fine particles are crucial for roasting and flash smelting technologies.

1. Introduction

Pyrometallurgy is as ancient as our civilization. The use of fire made it possible for ancient people to produce gold articles by melting and casting tiny particles found in rocks, or loose in the ground (Figure 1). Pyrometallurgy is that branch of extractive metallurgy dealing with the extraction of metals from their ores by thermal methods. Because of the extensive use of carbon as a fuel and as a reducing agent, pyrometallurgy can be called the ***technology of carbon***, in analogy to organic chemistry, the ***chemistry of carbon***. More than 50 % of the coal mined today is used by the metallurgical industry.

Figure 1. Ancient Egyptian wall painting showing the use of bellows to blow air in a fire.

Pyrometallurgy is the most important division of extractive metallurgy, since it is involved in the recovery of most metals and primarily in the ferrous industry. It is based on two important principles:

- The formation of immiscible molten layers during the melting of ores.
- The different energetics of liberation of metals from their compounds at high temperature.

2. Formation of immiscible molten layers

During the melting of an ore or a concentrate, the silicates, sulfides, arsenides, and metals produced coalesce, each forming an individual molten layer. Because of the differences in specific gravity, it is usually possible to allow the material to settle and to separate each layer (Figure 2). The silicate layer on the top is called ***slag***, the sulfide layer next is called ***matte***, and the arsenide layer next, is called ***speiss***. Table 1 gives the properties of the different layers formed when melting lead oxide (obtained by the oxidation of a lead sulfide concentrate) in the presence of carbon to get impure metallic lead called ***bullion***. The separation is, however, not sharp; each layer will contain some impurities from the other layers in contact with it. Not all four layers are necessarily formed in a process. Most common are the slag–matte or slag–metal layer that form. The case of lead is a particular example.

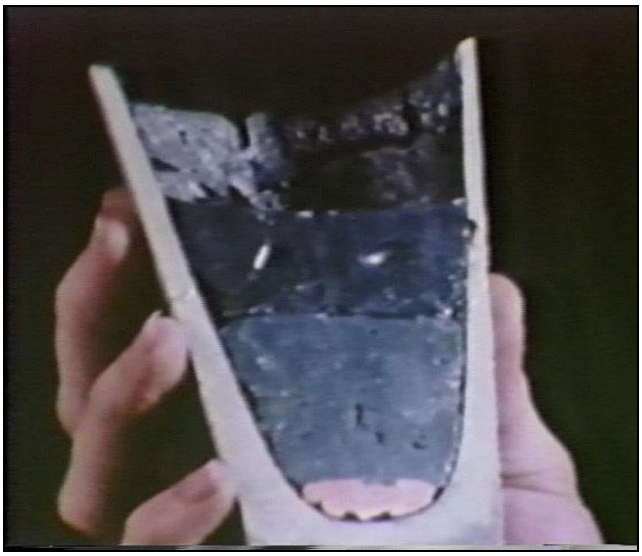

Figure 2. Formation of three immiscible layers: slag, matte, and metallic copper when melting copper sulfide concentrate under certain conditions.

Table 1. Immiscible molten layers formed during the production of lead.

Phase	Specific gravity	Common name	Metal present	
			Major	Minor
silicate	3.6	slag	Ca, Si, Al, Mg, Zn, Fe	Mn, Sn
sulfide	5.2	matte	Cu	Fe
arsenide	6.0	speiss	As, Sb	Co, Ni
metal	10.0	bullion	Pb	Au, Ag

Hot gases leaving the furnace are loaded with dust particles. These are mainly components of the charge as well as volatile components formed during melting, e.g., cadmium and indium. In a pyrometallurgical plant, provision is always made to separate the dust from the gas for recovery and to avoid pollution of the environment.

2.1. Fluxes

To facilitate the melting process, a ***flux*** is usually added to combine with the high-melting point components and form the slag having a low melting point. For example, an ore containing limestone as gangue mineral, when heated, will result in the formation of CaO, which has a melting point of 2580 °C. To melt such material, a large amount of fuel will be consumed to achieve this temperature. This approach is not only uneconomical but also will necessitate the construction of a furnace that can withstand such high temperatures. If, however, a flux such as silica (melting point 1728 °C) is added to the ore, then on heating, a reaction between CaO and SiO_2 will take place to form calcium silicate, i.e., a slag whose melting point may be as low as 1500 °C. In this way the gangue minerals are separated from the other valuable ore components in the form of a low-melting slag. If on the other hand, the gangue mineral was SiO_2, then CaO should be added as a flux to aid in the formation of the slag. Figure 3 shows the phase diagram SiO_2 – CaO.

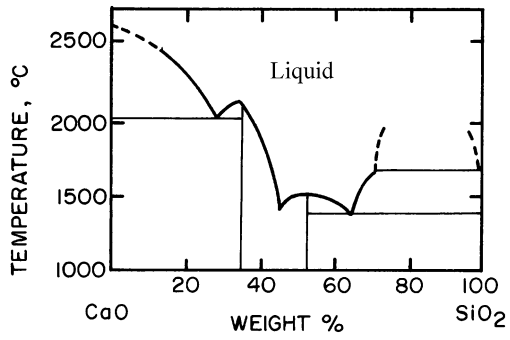

Figure 3. Simplified phase diagram of SiO_2 – CaO system.

In pyrometallurgy, SiO_2 is considered an acidic oxide and CaO as basic oxide. This concept was introduced long ago when it was observed that some oxides dissolve in water forming an acid, and others when dissolved form a base. For example, P_2O_5 dissolves in water to form phosphoric acid and CaO dissolves to form calcium hydroxide. Silica is insoluble in water; it was regarded as the anhydride of various silicic acids: ortho H_4SiO_4, meta H_2SiO_3, and poly H_4SiO_8, in which the hydrogen atoms can be replaced by metals to form silicates. This is true for a limited number of silicates such as those of the alkali metal group. Recent research, however, has shown that the structure of other silicates is not so simple. Thus, it was found that SiO_2 is composed of a large network in which the fundamental structural unit is the tetrahedral group SiO_4; the central silicon ion is linked with four oxygen ions.

In terms of recent theories, an oxide MO is called a basic oxide because it provides oxygen ions:

$MO \rightarrow M^{2+} + O^{2-}$.

An acidic oxide, on the other hand, will absorb ions provided by a basic oxide, e.g.:

$SiO_2 + 2O^{2-} \rightarrow SiO_4^{4-}$.

When CaO dissolves in molten silica, the Si – O bonds are steadily broken down, until eventually the melt is composed of discrete SiO_4^{4-} groups and Ca^{2+} ions. A slag, therefore, is a silicate network of various compositions. It is considered an acid slag when it is rich in silica, and basic slag when poor in silica, i.e., rich in basic oxides. An acid slag will be capable of dissolving basic oxides while a basic slag, on the other hand, will be capable of dissolving acidic oxides.

There is, however, another group of undesirable components in ores that have the ability to combine with either the acid or basic flux. These are called ***amphoteric oxides***. For example, Al_2O_3 can combine with SiO_2 to form aluminum silicates, e.g.:

$3Al_2O_3 + 2SiO_2 \rightarrow Al_6[Si_2O_{13}]$.

Or it can react with a basic oxide such as CaO to form calcium aluminate:

$Al_2O_3 + CaO \rightarrow Ca[Al_2O_4]$.

This information is important not only when conducting a melting or a refining process involving slags but also has to be considered when selecting the refractory lining of a furnace or a ladle handling slags.

2.2. Slags

In pyrometallurgy, slags are produced in large quantities, either during the melting of ores or the refining of pig iron to make steel. They are usually disposed of in either one of the following ways:

- Collected in pots which are then transported on rails and poured into a dumping area.
- Allowed to flow into a large volume of water so that they are granulated and granulated material is transported by mechanical conveyors to the dumping area.

A slag must be sufficiently fluid to permit entrained globules of the layer underneath to settle rapidly and also to flow easily from the furnace. Fluidity of a slag is a function of:

- ***Temperature.*** The higher the temperature the more fluid the slag. However, at high temperature, corrosion of the refractory lining becomes more severe.
- ***Composition.*** Some oxides when dissolved in a slag increase its viscosity while others decrease it. Slags have slight electric conductivity: this demonstrates their ionic character. This property is utilized in industry for heating purposes; thus when electrodes are immersed in a molten slag layer and a current is passed, the temperature of the slag increases thus permitting melting of the charge.

3. Chemical aspects of pyrometallurgy

The chemical aspects of metal production from ores by thermal methods can be conveniently divided into three steps: preliminary treatment of ore, metal separation, and refining (Figure 4). It is not necessary that all steps be exactly followed, e.g., high- grade iron ores can be directly reduced to metal without any preliminary treatment. It is quite often that a hydrometallurgical or a mineral beneficiation process is inserted, usually after the preliminary treatment. If the refined metal is in the molten state, it will be cast into ingots, and if it is in powder form, it will be hot-pressed.

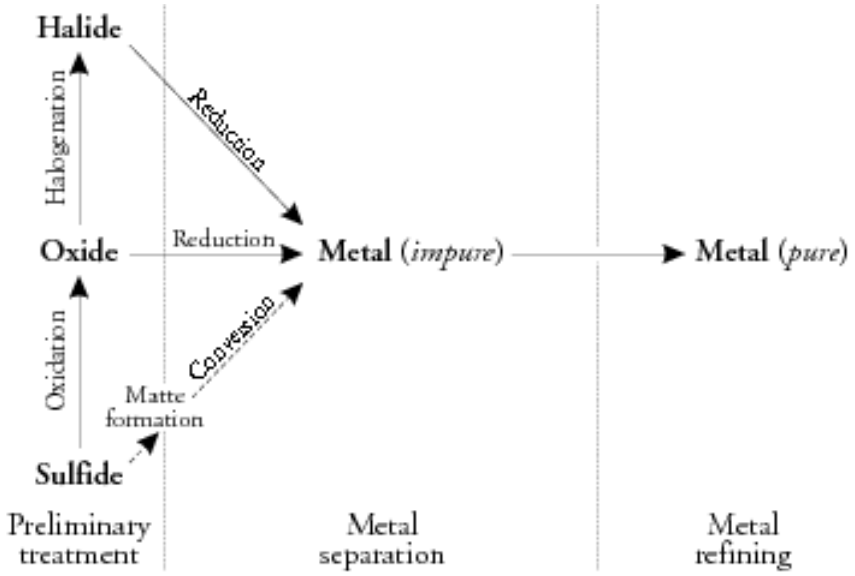

Figure 4. Schematic representation of metal production from ores. Dashed line is for special cases: conversion of Cu_2S, PbS, and Ni_3S_2.

3.1. Preliminary treatment

The preliminary treatment step may apply to an ore or a concentrate to break down the mineral structure so that it is rendered easily amenable to further treatment either by hydrometallurgical or by pyrometallurgical methods (Table 2 and Figures 5-7).

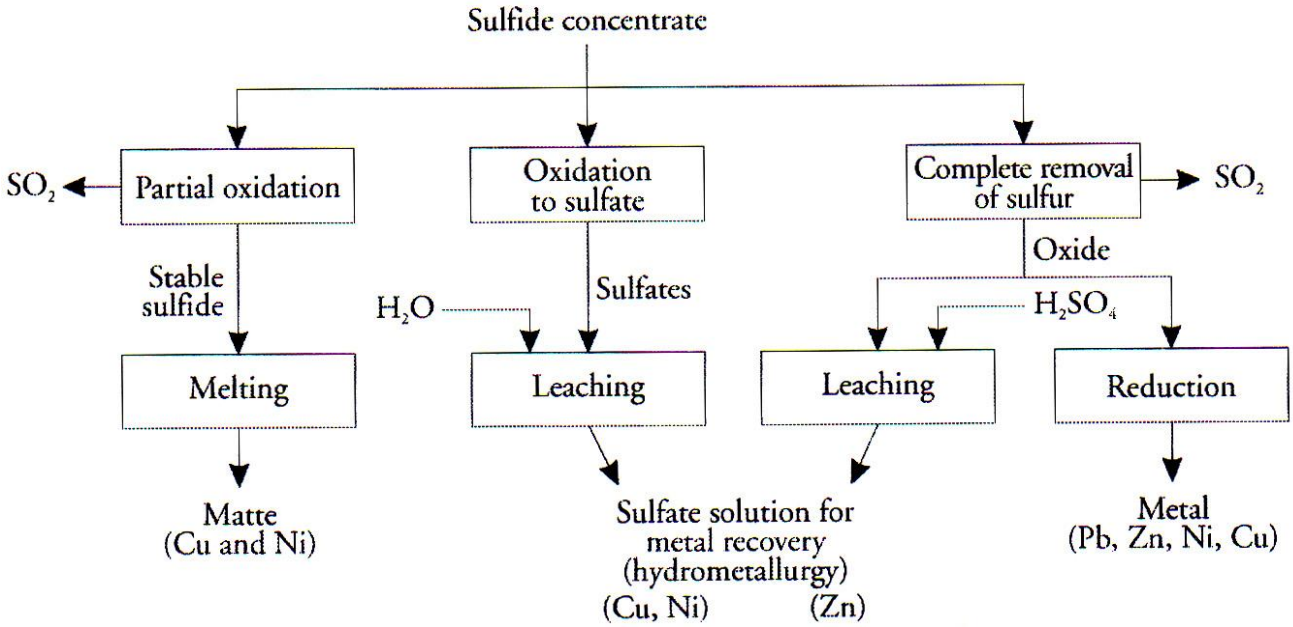

Figure 5. Oxidation of sulphides.

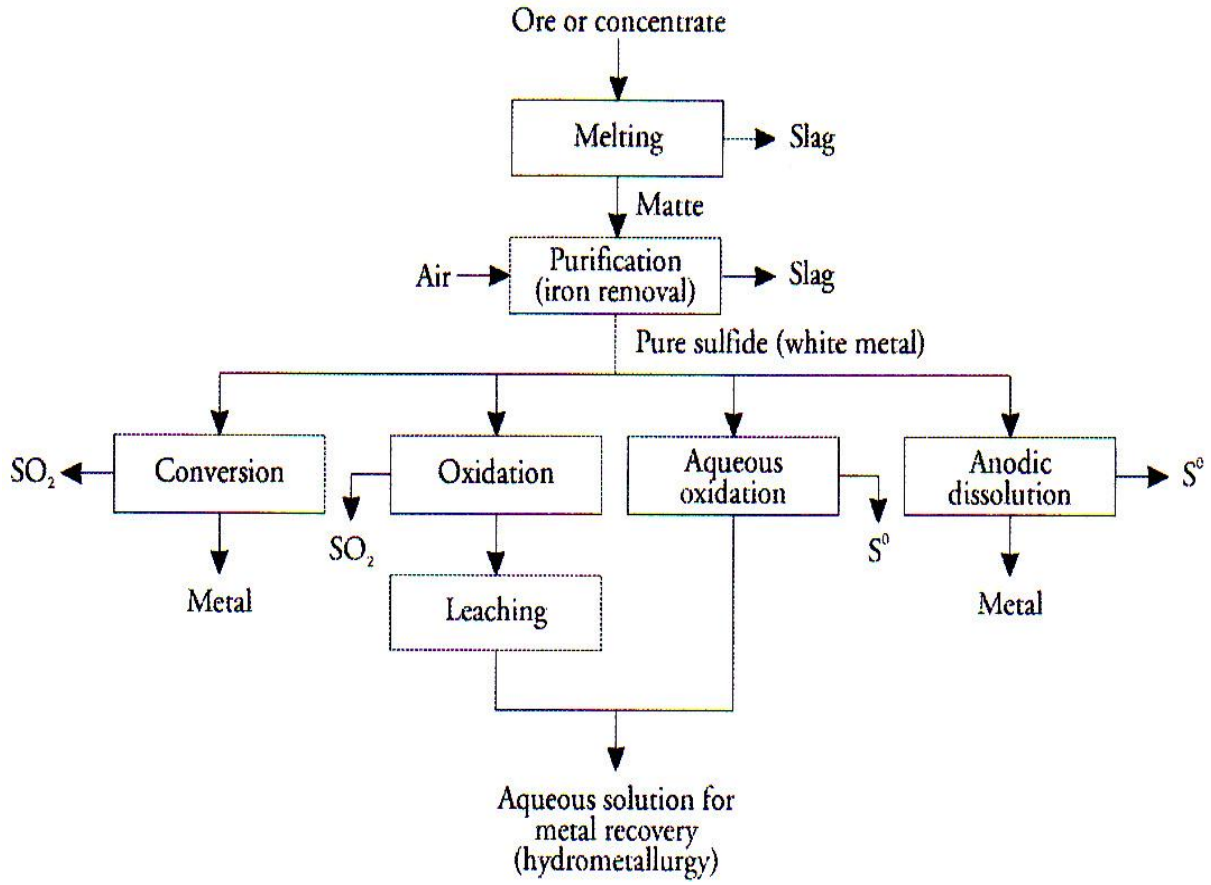

Figure 6. General methods for processing mattes.

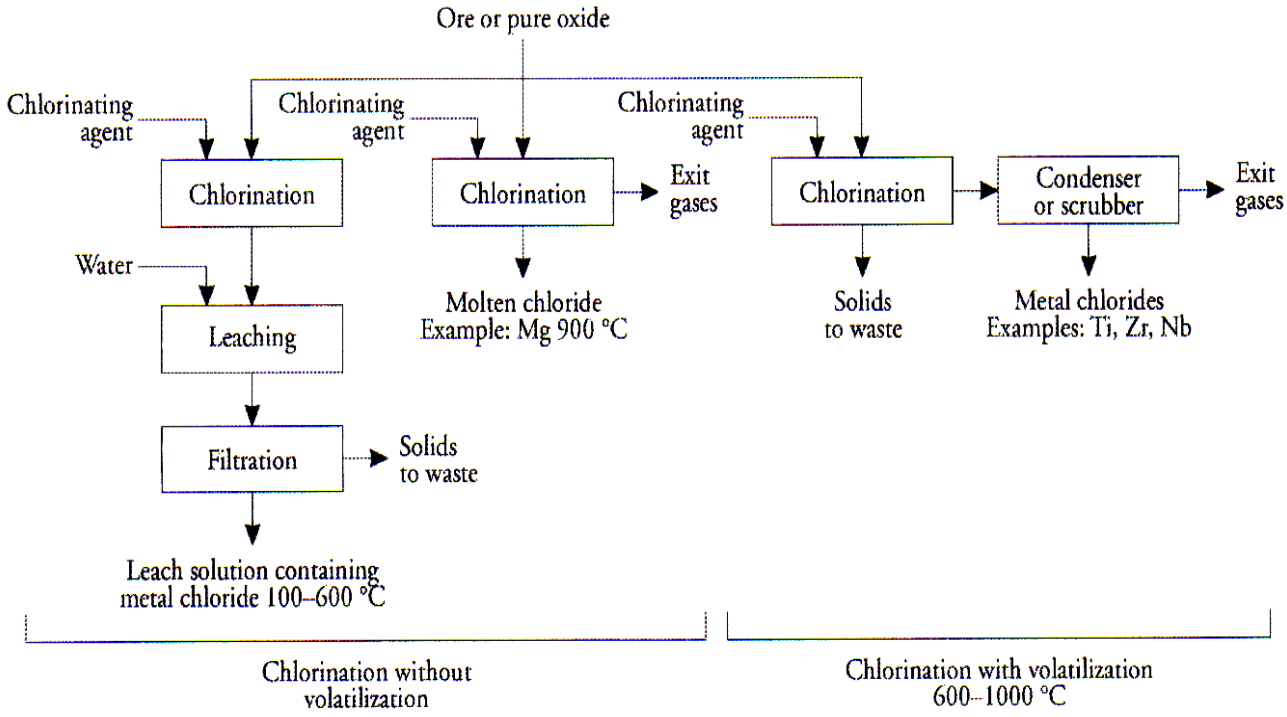

Figure 7. Chlorination of oxides.

Table 2. Preliminary treatment of ores or concentrated.

Process	Example	Application
thermal pretreatment (no reagent added)	phase transformation	Spodumene, $LiAl(Si_2O_6)$, is a hard mineral (density 3.15) not attacked by hot concentrated acid. When, however, it is heated to 1100 °C, it is converted into β-spodumene that has a density of 2.4. Due to the volume change the product can then be easily crushed to a fine powder and reacted with acid.
	melting and quenching	Beryl, $Be_3Al_2(Si_6O_{18})$, is a refractory mineral that is not attacked by hot concentrated acids. When, however, it is melted and the molten mass is quenched in water, an amorphous glassy product is obtained from which beryllium can be leached by dilute acids leaving a porous siliceous matrix.
alkali fusion	The ore is heated in the presence of alkaline reagents, e.g., Na_2CO_3 or NaOH.	Niobium and tantalum complex oxides are fused with alkali and the product is then leached with water to remove the soluble sodium salts and recover the metal values.
oxidation of sulfides	Sulfides oxidized to sulfates or to oxides.	Cu, Ni, Co, Zn, Pb sulfides (see Figure 5)
matte formation	Metal values in an ore are separated from the gangue minerals in the form of a molten sulfide phase known as a matte.	Cu, Ni sulfides (see Figure 6)
chlorination	Applied to ores and concentrates to isolate the metal values or convert them into a more amenable form. It is also applied to pure oxides to convert them to chlorides, since chlorides are easier to reduce to metals than the corresponding oxides.	Ti, Zr, Nb (see Figure 7)
fluorination	Applied to ores or concentrates as a means for breaking down the mineral for the recovery of metal values, as well as to pure oxides to convert them to fluorides for subsequent reduction to metals.	$BeO + 2HF \rightarrow BeF_2 + H_2O$ $UO_2 + 4HF \rightarrow UF_4 + 2H_2O$ $UF_4 + F_2 \rightarrow UF_6$

Oxidation of sulfides to remove a certain amount of sulfur to be able to melt the product to a matte. These reactions are conducted under a limited supply of air and the temperature is usually about 500 °C. Sulfides treated in this manner are those that lose a part of their sulfur on heating in an inert atmosphere. The oxidizing atmosphere is simply used to furnish the oxygen necessary to burn the sulfur liberated, and the heat generated from this reaction partly supplies the energy required to heat the raw material to the required temperature. This route is usually followed for copper and nickel sulfides:

$2CuS + O_2 \rightarrow Cu_2S + SO_2$,

$3NiS + O_2 \rightarrow Ni_3S_2 + SO_2$.

Pyrite which is usually present in such ores is transformed to ferrous sulfide:

$FeS_2 + O_2 \rightarrow FeS + SO_2$.

Sulfides may also be completely converted to oxides:

$MS + {}^3/_2O_2 \rightarrow MO + SO_2$.

The oxides may be leached and the solution electrolyzed or reduced to metal.

3.2. Halogenation

As shown earlier in Figure 4 chlorination and fluorination are used to transform oxides that cannot be reduced to metals into a more amenable compound that could be readily reduced. A general scheme of chlorination is shown in Figure 7. Fluorination is similar to chlorination and is applied mainly for beryllium and uranium.

3.3. Metal separation

The metal separation step involves the liberation of the metal from its compounds. This can be achieved mainly by reduction or conversion and to a minor extent by oxidation and thermal decomposition.

Reduction is the addition of electrons to an ion or group of ions. For example:

$M^{2+} + e^- \rightarrow M^+$,

$M^{2+} + 2e^- \rightarrow M$.

This method is applied to a variety of compounds: oxides, chlorides, fluorides, and others except sulfides. For oxides, carbon is commonly used as a reducing agent, e.g.:

$2Fe_2O_3 + 3C \rightarrow 4Fe + 3CO_2$.

However, in some cases when an oxide is heated with carbon, carbide is formed instead of a metal. In this case, other reducing agents have to be used, e.g., hydrogen:

$WO_3 + 3H_2 \rightarrow W + 3H_2O$.

When hydrogen is not effective, metals such as Al, Ca, Mg, and Na are used as reducing agents. For example:

$3Nb_2O_5 + 10Al \rightarrow 6Nb + 5Al_2O_3$.

When oxides do not yield metals by reduction, they are usually halogenated, then reduced. Reduction of halides is usually effected by metals, e.g.:

$UF_4 + 2Mg \rightarrow U + 2MgF_2$.

These types of reactions are known as metallothermic reactions.

Reduction of sulfides is thermodynamically unfavorable and this is why this process has not yet found technical application. To obtain a metal from its sulfide, the sulfide is usually oxidized and the oxide formed is reduced to metal.

The three sulfides that undergo conversion reaction are shown in Table 3, the overall reaction being:

$MS + O_2 \rightarrow M + SO_2$.

This is an exothermic reaction and can be represented by:

$M^{2+} + 2e^- \rightarrow M$,

$S^{2-} + O_2 \rightarrow SO_2 + 2e^-$.

Table 3. Sulfides that undergo conversion reaction.

Sulfide	Reaction
copper sulfide	$Cu_2S + O_2 \rightarrow 2Cu + SO_2$
lead sulfide	$PbS + O_2 \rightarrow Pb + SO_2$
nickel sulfide	$Ni_3S_2 + 2O_2 \rightarrow 3Ni + 2SO_2$

3.4. Refining

The physical, mechanical, and electrochemical properties of a metal are greatly influenced by the level of impurities. Thus electrical conductivity, ductility, and corrosion resistance improve remarkably with increased purity. Zinc, for example, cannot be rolled unless its tin content is less than 20 ppm. The castability of metals and alloys, particularly their ability to fill a mould, is influenced by the presence of a trace amount of oxygen in the molten material. Zinc of ultra high purity (99.999 %) retains its bright surface for many years in ordinary room air, but even a few parts per million of a metallic impurity reduce the corrosion resistance of a zinc–aluminum alloy sufficiently to make it useless. Refining is, therefore, an important metallurgical operation and processes vary considerably from one metal to the other. The purity called for depends on the use for which the metal is intended.

If the feed material to the metal separation step is an ore or concentrate, the liberated metal will be in a crude form usually of 90 to 95 % purity. Such material will require extensive refining before reaching the consumer. If, on the other hand, the feed material is a purified compound, then the liberated metal will be fairly pure and will require only a minimum of refining. Steelmaking is essentially an iron refining process though it is different in concept from the refining of other metals. In making steel, the aim is to produce iron containing between 0.1 and 1.5 % of carbon and not pure iron. In the refining of other metals, on the other hand, the aim is to remove as much as possible of the impurities. Decreasing the impurity level beyond a certain value is a prohibitively expensive operation since unconventional techniques have to be used. Some metals such as copper, lead, and zinc are usually refined to a 99.9 % purity. Others, such as germanium and gallium are always refined to a higher level.

Pyrometallurgical refining is mostly done when the metals are in the molten state. It is classified in three categories: chemical, physico-chemical, and physical methods (Figure 8).

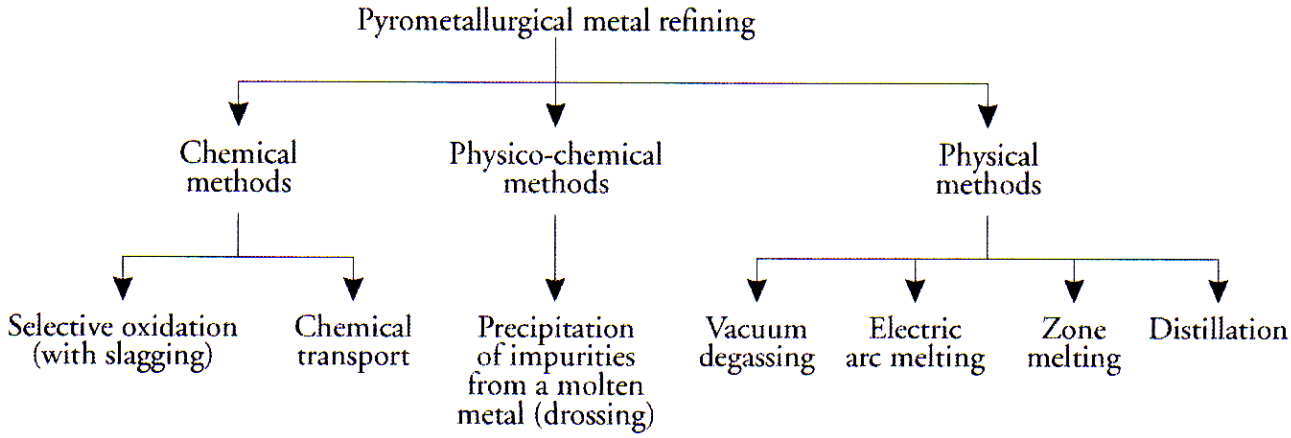

Figure 8. Summary of pyrometallurgical metal refining operations.

3.5. Selective oxidation

This is the most important process and is applied in the production of steel and copper.

Steel

Strictly speaking the production of steel from pig iron is not a refining step because the goal is not to remove all the impurities. Pig iron consists of iron containing about 7 % of its weight as impurities such as carbon, silicon, manganese, sulfur, and phosphorus. Due to the presence of these impurities it is brittle and has no practical value. Steel is an alloy of iron containing not more than 1.5 % carbon. It has important mechanical properties and is of great technical value. It is produced by getting rid of most of the impurities in pig iron. During the refining operation, oxygen combines with the impurities with the exception of sulfur, and unavoidably with some of the iron, to form oxides. Carbon monoxide escapes as a gas while other oxides are combined with a dosed amount of calcium oxide which acts as a flux to form a slag that floats on the surface of steel. Because of the affinity of sulfur to calcium oxide, it will also enter the slag layer.

At the end of this operation, the steel will contain a small amount of oxygen, in the form of ferrous oxide, FeO, which renders it brittle. This oxygen is then removed by a process called ***deoxidation***, which involves the addition of a stoichiometric amount of a metal that has a strong affinity for oxygen. The metal added is usually in the form of a ferroalloy such as ferromanganese. This forms an oxide layer that can be skimmed off the deoxidized steel.

Copper

Refining of copper is more complicated than that of iron; some operations are however similar from the chemical point of view. Thus, most of the impurities in raw copper are oxidized by selective oxidation and slagging, then the excess oxygen is also removed by a deoxidation process. This, however, is not enough since the copper produced is still not suitable for the market. More impurities have to be removed, this time by electrolytic methods. In the electrolytic method, precious metals, selenium, and tellurium impurities drop at the bottom of the cell as slimes. These are collected and treated for recovery. Finally, the refined copper is melted and cast for shapes suitable for the consuming industries.

3.6. Chemical transport reactions

This method involves the formation of a volatile compound of the metal to be refined by means of a reactive gas followed by its decomposition to yield the pure metal and to regenerate the reactive gas for recycle. The metal is thus transported from the impure solid as a gas and then re-deposited in another vessel as a pure metal leaving the impurities behind in the first reactor. Two processes are used industrially: the carbonyl and the iodide processes (Table 4).

Table 4. Refining by chemical transport.

Process	Transporting gas	Compound transported	Temperature, °C		Example
			Formation	Decomposition	
carbonyl	CO	$M(CO)_n$	50	180	$Ni(CO)_4$
			120	140	$Fe(CO)_5$
iodide	iodine vapor	MI_4	200	1000	TiI_4
			340	1200	ZrI_4
			300	1400	HfI_4
			460	1750	ThI_4

3.7. Physico-chemical methods

These involve the precipitation of impurities from the molten metal, sometimes called *drossing* and apply mainly to lead. Refining of lead is complex because of the numerous processes involved and the variety of techniques. Lead produced in the blast furnace contains up to 4% impurities, mainly copper, tin, antimony, arsenic, bismuth, and silver. These impurities render it hard, thus interfering with the malleability required for rolling it into sheet and forming it into pipe. In addition, sufficient silver is usually present to render its recovery profitable. Refining involves the precipitation of impurities form the melt. This is achieved in two steps: softening and desilverization.

Softening

In this process the impurities rendering lead hard are removed, hence the operation is known as "softening." These impurities are mainly copper, tin, antimony, arsenic, and bismuth. These are removed principally by forming dross which is an intermetallic compound formed as a solid phase that separates from the molten bath and floats on its surface to be skimmed off. This is simply achieved by cooling the molten lead to about 350 °C — copper in solution precipitates as a copper–lead dross; being lighter than lead it floats and is skimmed off. Not all the copper is removed in this way; the last traces are removed by adding a dosed amount of elemental sulfur to the molten metal to form copper sulfide, which is again skimmed off. Other impurities are removed by oxidation and slagging.

Desilverization

This is also a dross formation process, but in this case a foreign metal is added to the molten bath to precipitate the silver. The most suitable metal for these propose is zinc; it is lighter than lead, has a limited solubility in lead, and has a strong affinity for silver. Zinc

associated with the silver in the dross is removed by heating under vacuum at 600 °C leaving behind a silver–lead alloy. Silver is recovered from this alloy by a process called cupellation, which is a selective oxidation process; lead oxidizes to lead oxide while silver resists oxidation and remains behind. Zinc that dissolves in lead in removed by heating under vacuum.

3.8. Physical methods

These methods of refining are used for two purposes:

- The refining of raw steel to prepare specialty alloys of certain ranges of physical and mechanical properties.
- Increasing the purity of certain metals used for special purposes.

The use of vacuum plays an important role in the majority of these processes. Great improvements in vacuum pumps and vacuum technology were developed to satisfy the needs of this industry. Table 5 gives a summary of these processes.

Table 5. Refining by physical methods.

Method	Description
Vacuum degassing To remove dissolved gases and volatile impurities thereby improving the mechanical properties.	Transferring molten metal from one ladle to another in a vacuum chamber. If the metal is solid, melting and degassing take place in an induction furnace under vacuum, or in an electron beam furnace.
Electric arc melting Used for reactive metals with high melting points, such as Ti, Ta, Zr, Mo and special alloy steels.	• Non-consumable electrode process: electric arc is struck between an electrode and the compacted metal in an evacuated vessel. • Consumable electrode process: the metal to be refined is compacted and made anode, when electric arc is struck the metal melts and impurities evaporate. • Electroslag melting: similar to previous process, but in the presence of a slag.
Zone melting Based on segregation of impurities between a molten and a solid part of a metal, used for Ge, Se, Te.	A portion of the ingot is melted and moved along: pure metal will concentrate in the cooling portion while impurities will be carried forward in the molten portion.
Distillation	Used for purifying metals that has high vapor pressure at moderate temperature, e.g., mercury and zinc.

4. Engineering aspects of pyrometallurgy

The engineering aspects of pyrometallurgy can be conveniently divided into six unit operations (Table 6):

Table 6. Engineering aspects of pyrometallurgical processes.

Unit operation	Application
heat transfer	all processes
solid–gas separation	accessory to all furnaces
compaction of powders	feed to shaft and fluidized-bed furnaces
oxidation of a solid phase	sulfide ores
oxidation in molten phase	steelmaking, copper, and nickel industries
metallothermic reactions	preparation of reactive metals by reduction of their oxides and halides by other metals

4.1. Heat transfer

When rich massive deposits were exploited, the vertical furnace was used because of its high thermal efficiency (Figure 9). The lump ore was charged at the top and the hot reducing or oxidizing gases at the bottom in a counter-current flow. There was, therefore, an excellent heat transfer: the charge was gradually heated and the hot gases gradually lost their heat. There was little dust and heat recovery problems with the exit gases were minor. When low-grade ores had to be processed, they had to be finely ground and enriched by physical methods to prepare concentrates. It was not possible to introduce such material in the vertical furnace because the pressure drop would be very high. Consequently, two routes were proposed:

- The finely divided concentrates had to be agglomerated and introduced into the furnace.
- A new furnace that accepts powders had to be designed.

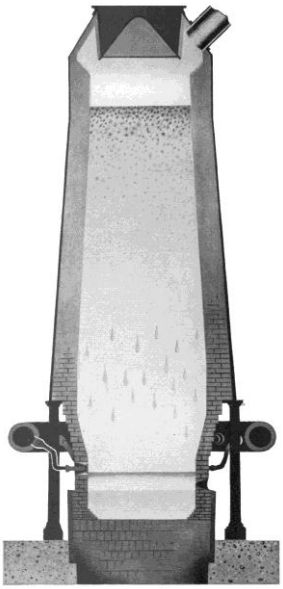

Figure 9. A vertical furnace.

The iron industry chose the first option in treating taconites the low-grade iron oxide ores, while the copper industry chose the second option in treating porphyry copper ores — hence the adoption of the horizontal furnace (Figure 10) which proved to be a catastrophe to the industry. It is an energy intensive reactor: heat transfer by radiation from the roof is not efficient and heat recovery system and dust removal from hot flue gases are mandatory; these were expensive and required bulky equipment. Gases contained small amounts of SO_2 which was not economical to recover and therefore were emitted to the environment causing much damage. The horizontal furnace remained unchallenged for about a century when finally the flash smelting furnace emerged as a result of pressing needs to economize in production costs.

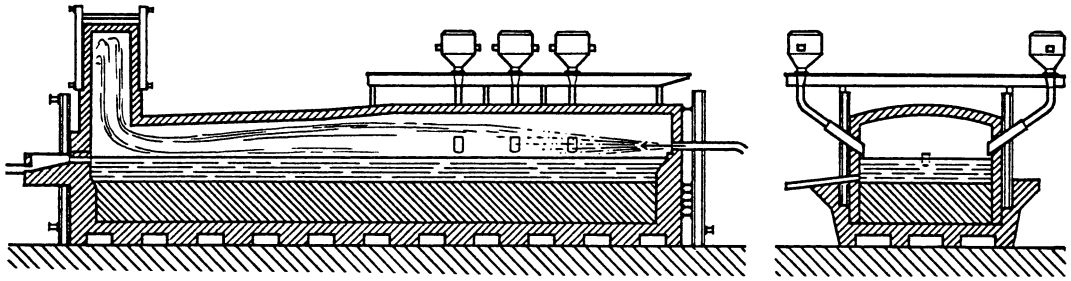

Figure 10. A horizontal furnace for melting flotation concentrates. The finely divided concentrate is introduced at the top and carbonaceous fuel burned to supply the necessary heat.

Using oxygen or oxygen-enriched air

Air is composed of 21 % oxygen and 79 % nitrogen. The advantages gained by using pure oxygen or oxygen-enriched air in oxidation processes offset the cost of liquefaction of air and separating the nitrogen. The reasons for that are the following:

● Nitrogen acts as a diluent and absorbs large amounts of the combustion heat. When oxygen or oxygen-enriched air is used, the amount of heat lost by nitrogen is therefore decreased. As a result, the temperature of the furnace rises, the rate of combustion is accelerated, and consequently more fuel can be burned per furnace, i.e., production is increased. Or, fuel consumption / ton of material processed are reduced.

● The total volume of gases passing through the furnace would be considerably less than in normal practice. It is therefore to be anticipated that the erosion of the refractories should be reduced and the size of furnace and dust collecting units reduced.

This principle is now extensively applied in most furnaces burning carbonaceous fuels. The same principle has been also extended too many oxidation processes in pyrometallurgy as well as in the chemical industry. Of particular importance are the following:

● The oxidation of impurities in pig iron to make steel. This had been achieved by using oxygen lance in a top-blown converter and the bottom-blown converters. As a result, the steel industry has become one of the largest users of oxygen.

● The oxidation of nonferrous metal sulfides, e.g., lead, zinc, and nickel sulfides, and the conversion of white metal.

4.2. Solid–gas separation

Fine particles of material treated in furnaces are partially carried out of the unit in the exit gas. This dust must be captured to recover its valuable metal content and to prevent

pollution of the environment. Methods of dust removal depend mainly on particle size of the dust, temperature and moisture content of the gas. The equipment used can be broadly classified as either dry or wet collectors. The dry collectors include the gravity and baffle chambers, cyclones, filters, and electrostatic precipitators. In the wet collectors dust particles are made to collide with water which then makes their removal as slurry possible. Wet cleaning is preferred to dry cleaning because of the excessive wear and the difficulty in handling the fine dust removed in the dry methods. Wet methods must be followed by filtration, drying of filter cake, and recycle of water. Equipment used for wet methods are known as scrubbers.

Usually two or three sets of equipment are connected in a series to remove first the large and then the small dust particles. The range of application for each type of equipment is shown in Figures 11 and 12, from which it can be seen that gravity chambers and cyclones are only suited for separating the large particles while the filters, scrubbers, and electrostatic precipitators are most suited for separating the small particles.

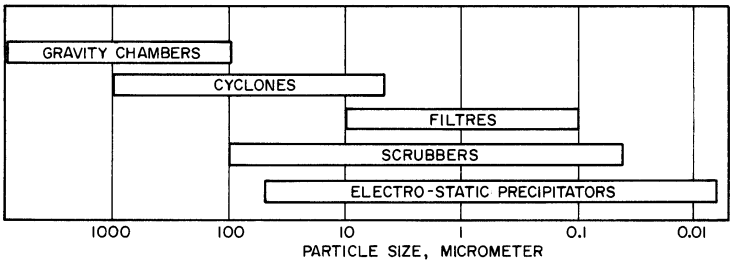

Figure 11. Range of application of solid–gas separating equipment.

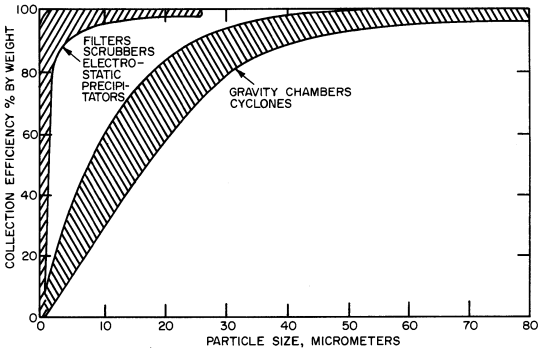

Figure 12. Collection efficiency of solid–gas separating equipment.

4.3. Compaction of powders

Although finely divided ores and concentrates possess large surface area and therefore high chemical reactivity, they are usually compacted in larger agglomerates before treatment. This is because of their inconvenient handling and storage characteristics such as dusting, uncontrolled agglomeration, segregation, and high bulk volume. Strong and uniform agglomerates of any required size can be readily obtained. This unit operation is not restricted to metallurgy; it is extensively used in other industries as well, e.g., coal, pharmaceuticals, fertilizers, animal feed, and others. Two methods are used: briquetting and agglomeration. The first involves the application of mechanical pressure, while the second involves either heating

or curing at room temperature after adding certain additives (Table 7). The product from each method has different appearance as shown in Figure 13.

Table 7. Methods of compacting powders.

Method	Equipment	Product
briquetting	briquetting machine	briquettes
agglomeration	rotary kiln	nodules
	moving grate furnace	sinter
	balling and heat treatment	pellets
	balling and curing	pellets

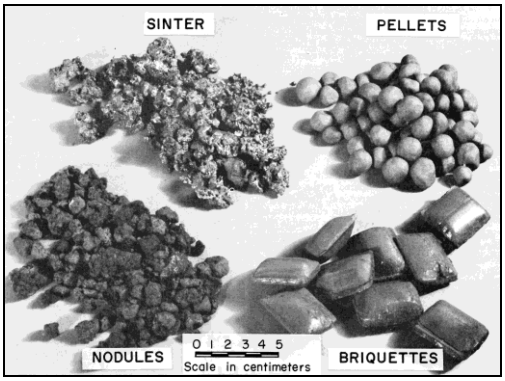

Figure 13. Different types of compacted iron ores.

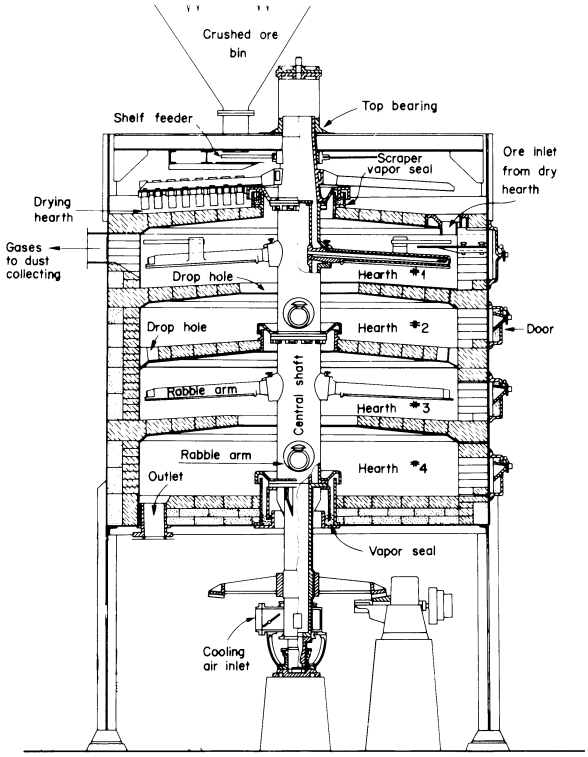

Figure 14. A multiple hearth furnace.

4.4. Oxidation of a solid phase

The multiple hearth furnace (Figures 14 and 15) was first introduced for the oxidation of sulfides. Ore or concentrate fed to the top hearth is raked the full area of the hearth to the center where it falls through openings to the second hearth. In the second hearth the rakes are set to move the ore to the periphery, and from these it is discharged through openings to the next hearth. Hot gas is introduced at the lowest hearth and comes into contact with the ore in the hearths in a counter-current flow, leaving the furnace at the top while the calcined material leave at the bottom heart.

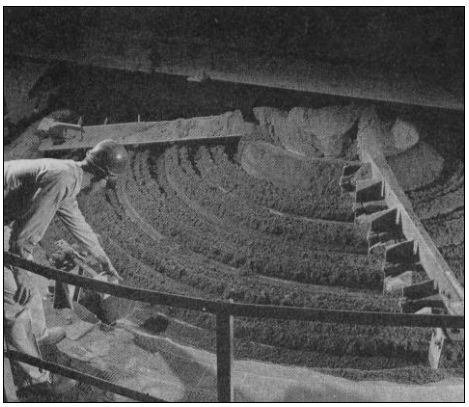

Figure 15. Sulfide concentrate is raked on the top hearth.

In using this furnace it was observed that a large portion of sulfur was eliminated while the charge was dropping from hearth to hearth rather than during the raking action. This led to the removal of some of the intermediate hearths to open up a large combustion chamber and thus improve the oxidation (Figure 16).

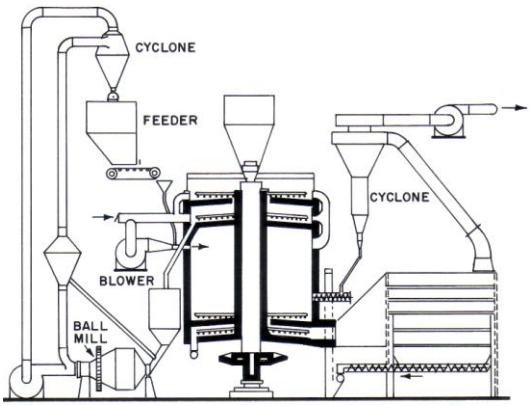

Figure 16. Removing intermediate hearths resulted in increased productivity.

This led to the introduction of the so-called "flash" oxidation (Figure 17). In this process finely divided sulfide concentrate is sprayed in a heated chamber in a stream of air. Because of the intimate solid–gas contact, the reaction is very rapid resulting in "flashing" of the combustible constituents. The exothermic heat is usually sufficient to keep the chamber heated. The oxidation product settles down at the bottom of the chamber where it is collected and discharged.

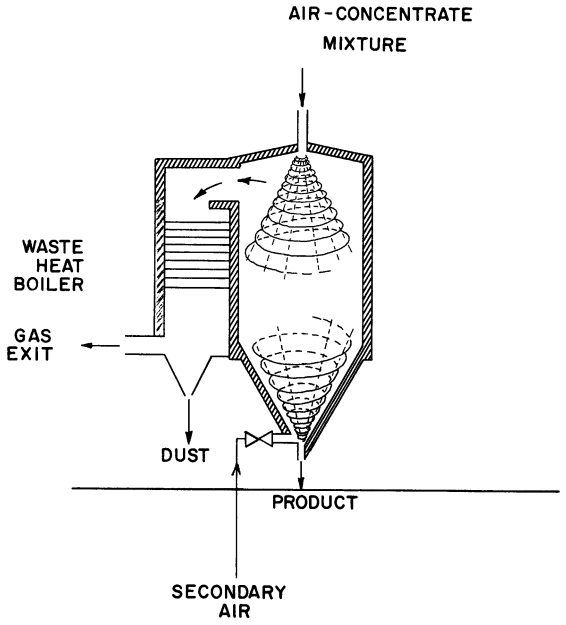

Figure 17. Flash oxidation.

Conditions of oxidation may be so adjusted that the exothermic heat of oxidation of part of the sulfides would be enough to melt the remainder of the charge forming matte and slag (Figure 18). The matte separates as an immiscible phase from the other molten components of the ore, that is, the gangue minerals which form a slag. Being heavier than slag, the matte forms as a layer underneath in which the metal values are enriched.

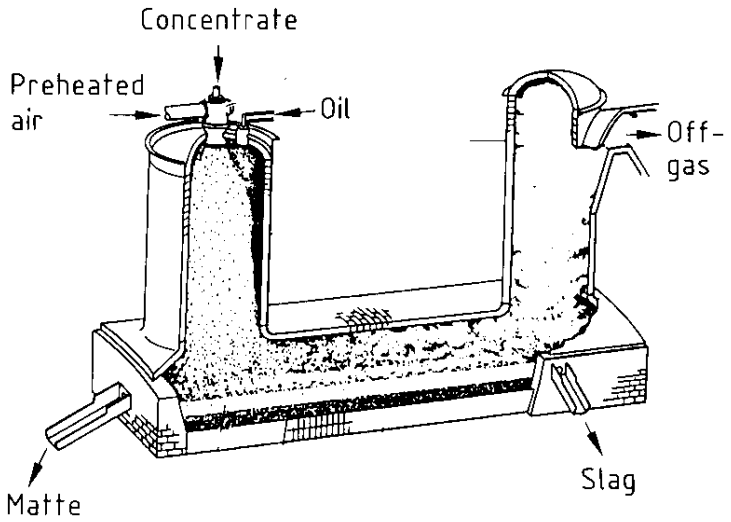

Figure 18. Flash smelting furnace.

When sulfides are heated rapidly in air they ignite at a certain temperature and glow like pieces of coal. Table 8 gives the ignition temperature of some sulfide minerals at various particle size ranges. It can be seen that the ignition temperature increases with decreasing sulfur content and with increased particle size; chalcopyrite, however, seems to be an exception. In all these cases, the reaction products are an oxide, SO_2 and small amounts of SO_3. When, however, heating is conducted gradually, numerous intermediate reactions can be identified, which varies from one sulfide to another.

Table 8. Ignition temperature of pure sulfide minerals.

Particle size, mm	Ignition temperature, °C				
	Pyrite 53.4 % S	Pyrrhotite 36.4 % S	Chalcopyrite 34.5 % S	Sphalerite 32.9 % S	Galena 13.4 % S
0.10 – 0.15	422	460	364	637	720
0.15 – 0.20	423	465	375	644	730
0.20 – 0.30	424	471	380	646	730
0.30 – 0.50	426	475	385	646	735
0.50 – 1.00	426	480	395	646	740
1.00 – 2.00	428	482	410	646	750

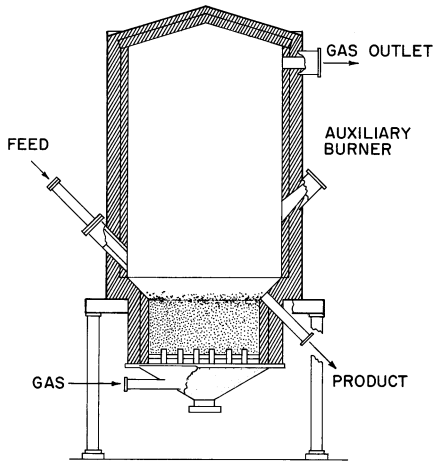

Figure 19. Fluidized bed reactor.

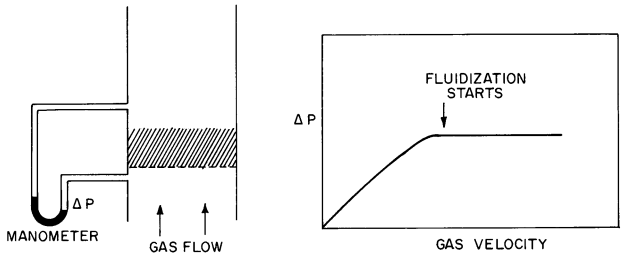

Figure 20. Minimum fluidization velocity.

Fluidized bed

A fluidized-bed furnace is an efficient method of conducting oxidation of sulfides. The reactor consists of a large vertical brick-lined steel cylindrical vessel into which the gaseous reactant is blown beneath a perforated steel grate at the base. The powdered solids are admitted at one side by a screw conveyor, and the reaction product continuously overflow from another

opening (Figure 19). It is suitable for conducting numerous reactions, e.g., oxidation, reduction, chlorination, etc. It has the following characteristics:

● There is a minimum velocity of the gas which effects fluidization; below this value no fluidization takes place. The pressure drop in a fluidized bed shown in Figure 20 demonstrates this property. As the gas velocity increases the pressure drop increases gradually until a constant value is reached when fluidization starts. This is the minimum velocity to achieve fluidization. If the velocity of gas increases greatly, the solids will be blown out of furnace.

● A fluidized bed behaves in a manner similar to a boiling liquid.

● Because of the intense gas–solid contact, chemical reactions and heat transfer are extremely rapid. This permits close control of reaction temperature thus preventing any local overheating or fusion of the solids.

● Gases leaving the bed through a duct at the top usually carry an appreciable amount of dust. This is separated in cyclones and collected as product. Dust losses can be minimized by pelletizing the feed material.

● When an exothermic process is conducted in such a furnace, the reaction first has to be started by an auxiliary flame, which is then extinguished when the reaction proceeds. When endothermic reactions are conducted, the gas has to be preheated to a temperature slightly above the reaction temperature. Also, electrical resistive heating using graphite electrodes has been suggested.

4.5. Oxidation in molten phase

Typical processes involving the oxidation of a component of a molten phase are shown in Table 9. Early equipment used for this purpose was the horizontal furnace. The process was slow and inefficient because the contact between the oxidizing atmosphere and the molten phase was at the stagnant interface whose area was not large and no use was made of the fact that the oxidation reactions were exothermic and as a result heat had to be supplied to the system to keep the batch molten.

Table 9. Oxidation in a molten phase.

Process	Molten phase	Component to be oxidized	Products
steelmaking	pig iron	C, S, P, Si, Mn	CO, slag, steel
purification	matte	FeS	SO_2, slag, white metal
conversion	Cu_2S	S	SO_2, Cu
	Ni_3S_2	S	SO_2, Ni

In 1856, Henry Bessemer in England and William Kelly in the USA were independently able to oxidize the impurities in pig iron to make steel by blowing air through the molten iron. This technique resulted in the tremendous increase in steel production and in displacing the older methods of steelmaking. The equipment used for this operation is called the “converter,” which is a brick-lined reactor that handles molten material (Figure 21). Air for oxidation can be blown into the molten phase either from the bottom or the side of the converter.

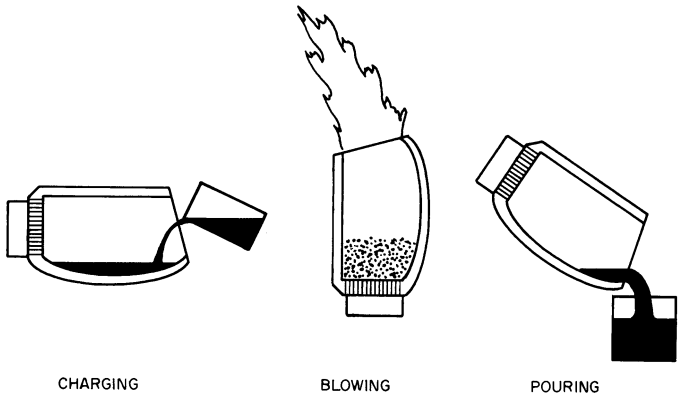

Figure 21. Bottom-blown converter using air.

4.6. Metallothermic reactions

This unit operation is concerned with the preparation of metals and alloys by reduction of their oxides or halides with metal. These reactions can be expressed in general by the equation:

$$AX + B \rightarrow A + BX,$$

where X is oxygen, chlorine, or fluorine, and A and B are two metals. The method is characterized by the fact that the reducing metal is converted to a solid or a liquid product and not to a gas as in other reduction processes, e.g., by carbon or hydrogen where $CO + CO_2$ and H_2O are formed, respectively. In fact this method is used when reduction by carbon and hydrogen or by electrowinning from aqueous solutions is not possible. The most commonly used reducing metals are aluminum, calcium, ferrosilicon, magnesium, and sodium. The choice of a reducing metal is based on many factors including thermodynamic considerations. Metallothermic reactions are batch processes involving numerous steps (Figure 22) that is why it has been challenged by fused salt electrolysis.

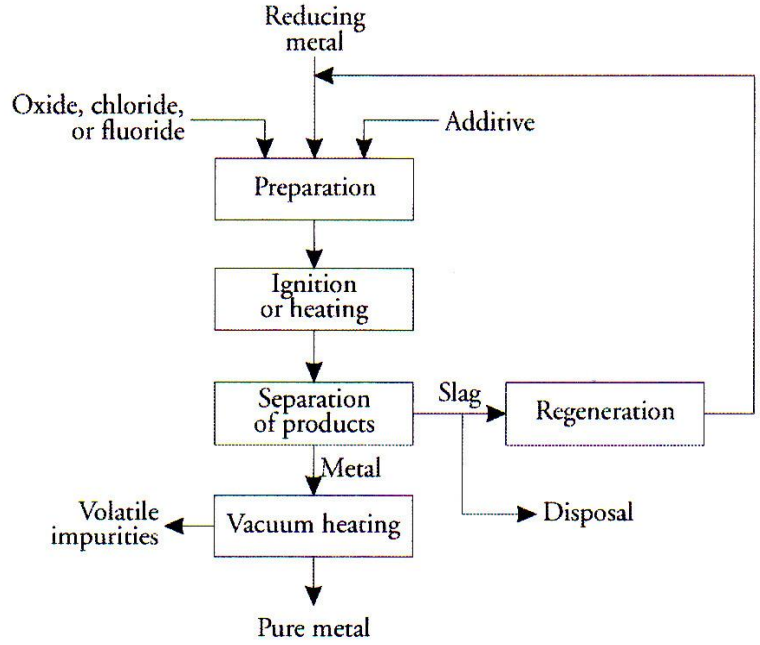

Figure 22. General scheme of metallothermic reduction.

5. Summary

Pyrometallurgy is an ancient art that developed in recent years to become a highly advanced science. Mathematical modeling, instrumentation, and methods of control have been introduced to achieve smooth and efficient operation. As an example, an iron blast furnace few decades ago produced 2 to 3 thousand tons of pig iron per day. Today a large blast furnace produces 10 000 tons per day. To produce this amount of iron, about 17 000 tons of ore, 5 000 tons of coke, 2 500 tons of limestone, 20 000 tons of air, 3 000 tons of slag, 500 tons of dust and 30 000 tons of blast furnace gas must be handled. The engineering problems associated with handling these materials are enormous.

Suggested reading

1. F. Habashi. Textbook of Pyrometallurgy. 2002, Quebec City: Métallurgie Extractive (distributed by Laval University Bookstore, www.zone.ul.ca).

This is the third paper in a series of four, devoted to outline mineral processing for nano-scientists — users of the final products. The first paper was a general outline of mineral processing, the second on pyrometallurgy. The last one will be on electrometallurgy.
Editor

HYDROMETALLURGY FOR NANO-SCIENTISTS

F. Habashi

Laval University
Quebec City, Canada
Fathi.Habashi@arul.ualval.ca

Accepted February 25, 2011

Hydrometallurgy is a relatively recent subject. Major hydrometallurgical processes started at the end of the 19th century for the leaching of gold ores using a cyanide solution and for leaching of bauxite by sodium hydroxide to get pure aluminum oxide for the expanding aluminum industry. At the beginning of the 20th century leaching of low grade copper oxide ore and leaching of zinc oxide calcines by dilute sulfuric acid were introduced on large scale. It was, however, during World War II that new hydrometallurgical techniques such as ion exchange and solvent extraction were developed for the recovery of uranium for the manufacture of atomic bombs. These new technologies as well as others revolutionized hydrometallurgy. Hydrometallurgical processes are now competing with the ancient pyrometallurgical routes.

1. Introduction

Hydrometallurgy is the art and science of treating ores by aqueous solutions to get pure metals or their compounds. In general it involves two distinct steps (Figure 1):

- Leaching: Selective dissolution of metal values from an ore.
- Precipitation: Selective recovery of these metal values from the solution.

Between these two steps, the leach solution must be filtered, purified, and sometimes concentrated. Also, an oxidizing agent may be needed in certain leaching steps. Hydrometallurgical processing may be used for:

- The direct production of metals in a pure form suitable for the market after a subsequent minor treatment, for example, nickel and copper.
- The production of metals in a lesser degree of purity which has to be subsequently refined, for example copper, gold, and cadmium.
- The production of a pure compound which can be subsequently used for producing the pure metal by other methods. For example, pure compounds of aluminum, magnesium,

uranium, and beryllium are produced by hydrometallurgical methods but the metals themselves are produced by pyrometallurgy or electrometallurgy.

● Chemical beneficiation of ores: In this case, the undesirable components of the raw material are leached away and the remaining solids are the valuable product that can be used for producing the metal, for example, the treatment of ilmenite to produce what is known as synthetic rutile.

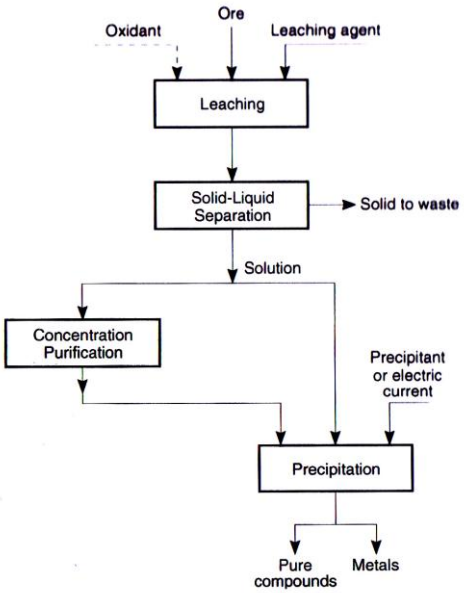

Figure 1. An outline of hydrometallurgical processes.

2. Leaching

2.1. Raw materials for leaching

● Metals leached range from native metals such as gold, silver, copper, and platinum group metals, to metals obtained by the reduction of their ores such as those of copper, nickel, and cobalt.

● Oxides and hydroxide ores such as bauxite, laterites, copper oxides ores, uranium ores, zinc ores and calcines, and manganese ores and nodules.

● Complex oxides such as chromite, niobite and tantalite, pyrochlore, ilmenite, wolframite, and scheelite.

● Sulfide concentrates such as those of copper, zinc, and nickel.

● Selenides and tellurides such as those found in the anodic slimes of copper electrorefining.

● Arsenides such as those of cobalt and nickel ores or the speiss formed in the smelting of lead concentrates.

● Phosphates, mainly phosphate rock and monazite concentrates.

● Silicates such as clays and nepheline–syenite for production of alumina and beryllium ores for the production of beryllium oxide.

● Chlorides and sulfates formed during the processing of pyrite cinder by either the chloride or sulfate process to extract its nonferrous metal values.

2.2. Reagents

To treat such diversified chemical compounds a variety of leaching agents are used:

● ***Water.*** Used for leaching water-soluble sulfates and chlorides.

● ***Acids.*** These are the most common reagents. Although sulfuric acid is the cheapest acid especially at smelters where it must be produced as a result of treating sulfide ores, yet hydrochloric and nitric acids are sometimes preparable although more expensive. Hydrofluoric acid is specifically used for leaching niobium and tantalum ores because they form soluble complex fluorides. Aqua regia which is a mixture of hydrochloric and nitric acids is used for treating platinum ores and for refining gold bullion because of the presence of chlorine and nitrosyl chloride in the acid mixture which solubilizes these metals.

● ***Bases.*** Sodium hydroxide is used to extract aluminum from bauxite while ammonium hydroxide is used to extract nickel from laterites or from nickel sulfide concentrates.

● ***Aqueous salt solutions.*** Sodium carbonate solutions are used for leaching scheelite which is a tungsten ore. Sodium carbonate together with an oxidant is used for leaching uranium ores. Sodium cyanide is specifically used for leaching gold and silver ores because they form soluble complex cyanides.

● ***Oxidizing agents.*** Many leaching processes require an oxidizing agent to solubilize the minerals. The most common reagent is air or oxygen. It can be used in acidic or basic medium. Ferric ion is also used but only in acidic medium. During leaching, the ferric ion is reduced to ferrous, which after separation, should be reoxidized for recycle.

● ***Reducing agents.*** Reducing agents such as SO_2 or ferrous ion are sometimes used to solubilize certain minerals in acidic medium, e.g., MnO_2.

2.3. Leaching of metals

The dissolution of gold in cyanide solution was one of the puzzles that faced metallurgists for many years for two reasons: gold, the most noble metal that dissolved only in aqua regia, dissolved readily in a very dilute solution of sodium cyanide and although gold did not tarnish in air, air was essential for its dissolution. This puzzle was solved when it was recognized that the dissolution of gold is an oxidation–reduction process in which cyanide ion forms a strong complex with Au^+ ion and the reduction of oxygen on the surface of metal to form hydrogen peroxide stage as follows (Figure 2):

Oxidation	$Au \rightarrow Au^+ + e^-$,
Complex formation	$Au^+ + 2CN^- \rightarrow [Au(CN)_2]^-$,
Reduction	$O_2 + 2H_2O + 2e^- \rightarrow H_2O_2 + 2OH^-$,
Overall reaction	$2Au + 4CN^- + O_2 + 2H_2O \rightarrow 2[Au(CN)_2]^- + H_2O_2 + 2OH^-$.

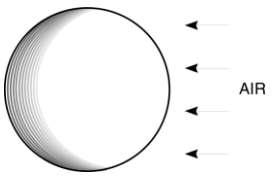

Figure 2. A gold bead embedded in potassium cyanide gel corroded at the surface less exposed to the air; an illustration of the electrochemical phenomenon during the dissolution of gold.

According to this stoichiometry, 1 gram mole of oxygen and 4 gram moles of NaCN should be present in solution. At room temperature and at atmospheric pressure, 8.2 mg O_2 are dissolved in 1 liter of water. This corresponds to $0.27 \cdot 10^{-3}$ mol / L. Accordingly, gold dissolution should occur at a concentration of NaCN equal to $4 \cdot 0.27 \cdot 10^{-3} \cdot 49 = 0.05$ g / L or 0.005 %. Thus a very dilute sodium cyanide solution would be enough for dissolving gold. The fact that oxygen was necessary for dissolution was not readily recognized because as seen from the above calculations, oxygen in solution as a result of air solubility is enough to bring about the reaction.

2.4. Leaching of oxides and hydroxides

Sulfuric acid is the usual leaching agent for oxidized copper ores; copper is recovered from the leach solution by solvent extraction followed by electrolysis. The spent electrolyte is recycled in the leaching circuit. The use of sodium hydroxide to leach bauxite is a process for obtaining pure aluminum hydroxide which can be calcined to pure Al_2O_3 suitable for processing to metal. About 90 million tons of bauxite are treated annually by this process. About 2 tons bauxite yield 1 ton Al_2O_3 from which 0.5 ton aluminum is produced. Also 2 tons bauxite produce 1 ton waste minerals called ***red mud***. The reactions in leaching are the following:

$Al(OH)_3 + OH^- \rightarrow [AlO(OH)_2]^- + H_2O$,

$AlOOH + OH^- \rightarrow [AlO(OH)_2]^-$.

2.5. Leaching of sulfides

Sulfide minerals are insoluble in water even at high temperature. They can be solubilized, however, by a variety of methods:

● ***Under reducing conditions*** (***absence of oxidizing agents***). Some sulfides dissolve in acid medium forming H_2S, others dissolve in basic medium forming sulfide ion.

● ***Under oxidizing conditions***. Elemental sulfur usually forms but because of its instability in neutral or basic media it oxidizes to sulfates. In acid medium, however, there is a narrow region where elemental sulfur can form.

These data are summarized in the stability diagram shown in Figure 3, which is valid in the temperature region 25 to 150 °C. Above 150 °C, however, the narrow stability region of elemental sulfur disappears and no sulfur can form. Hydrometallurgy is the only way to get elemental sulfur from sulfide concentrates thus avoiding the formation of SO_2 in smelting processes.

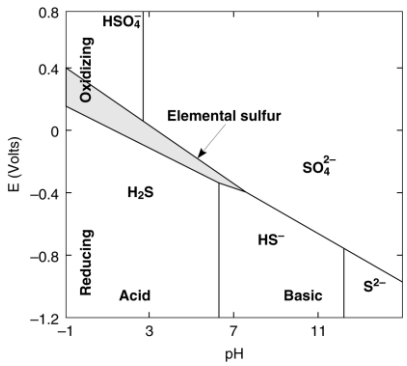

Figure 3. Potential–pH diagram for sulfur at 100 °C.

3. Methods and equipment

The method used for leaching an ore depends on the grade of the ore and the ease with which the mineral values are dissolved in a particular reagent. The most common methods of leaching are the following (Table 1):

Table 1. Leaching methods and equipment.

Method	Pressure, kPa	Temperature, °C	Agitation	Ore size	Time of leaching	Equipment	Examples
leaching in place	ambient	ambient	none	lumps	years	none	copper, uranium
heap or dump leaching	ambient	ambient	none	lumps	months	none	copper, uranium, gold
percolation or vat leaching	ambient	ambient	none	sandy	days	vats with false bottom	copper, uranium, gold
agitation or pulp leaching	ambient	< 100	mechanical, compressed air	fine	hours	Pachuca tanks, Dorr agitators, tanks	copper, gold, ZnO, phosphates
	1000–1200	110–200	mechanical, high-pressure steam, rotation	fine	hours	autoclaves	bauxite, laterites, nickel sulfide, scheelite
baking	ambient	200	none	fine	hours	digesters, rotary kilns, pugmills	anodic slimes, monazite sand, ilmenite

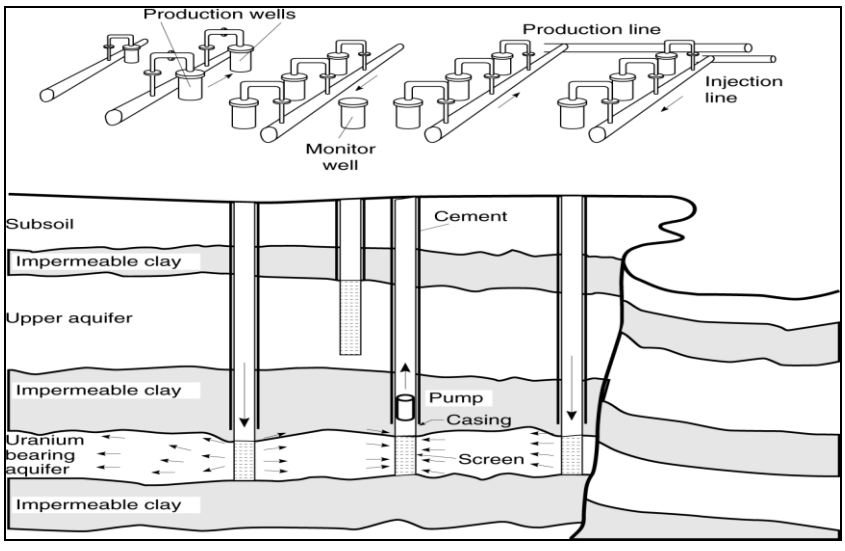

Figure 4. Leaching in place.

3.1. Leaching in place

This method is also known as leaching in situ or solution mining (Figure 4). The ore is simply shattered and leached in place over long periods of time because it is usually too low in grade to justify mining and transportation expenses. Recently, however, because of its success, the method has been used for high grade ores as well. The basic criteria required for an underground deposit to be considered suitable for leaching in place are: the ore body must be enclosed between impermeable strata that will prevent the loss of solution, and it must be permeable to the leaching solution. The following solvents are generally used:

● Water for leaching potash and trona and other water-soluble salts. Dilute sulfuric acid for leaching copper ores. When copper sulfide minerals are also present, these are solubilized by the combined action of air and water. The presence of pyrite enhances the leaching because of its oxidation and the formation of sulfuric acid and ferric sulfate. The oxidation reactions are exothermic and the heat generated facilitates continued oxidation.

● Dilute sulfuric acid and sodium chlorate, or ammoniacal ammonium carbonate and hydrogen peroxide are used for leaching uranium deposits.

Two techniques are used: spraying when the one body is exposed, and injection when it is buried.

3.2. Heap or dump leaching

In this method an area is first cleared from all vegetation then leveled at a slight inclination, compacted, and covered with an asphalt layer or a flexible plastic sheet. The crushed ore is then transported from the mine to the prepared site by dump trucks to a level of 10 – 15 m high. The leaching agent is then sprayed at the top of the dump through which it percolates and the leach solution is collected in streams at the bottom (Figure 5). When the material is fully leached, the dump is either abandoned or loaded on trucks for disposal and the site re-used for leaching another batch.

Figure 5. Heap leaching.

3.3. Percolation or vat leaching

This process is suited to cases where the material is porous and sandy, and is inapplicable to material which tends to pack into impervious masses. Regularity in the size of the particles rather than their actual size is the chief factor governing good percolation. The idea is that where the particles are of unequal size, the small ones pack in the openings between the larger ones, thereby clogging the channels. Extraction becomes slow, and channeling of solutions through the bed takes place. The method is therefore unsatisfactory if much slime is present. The material to be leached is placed in a tank equipped with a false bottom covered with a filtering medium. The leach solution is added at the top of the tank and is allowed to percolate through the material.

3.4. Agitation or pulp leaching

In this method, the leaching agent is added to the finely ground raw material such that the mixture forms a pulp that has to be agitated continuously to prevent the solids from settling, and to terminate the leaching process in the shortest possible time. It is generally used under the following conditions:

- Raw material is of moderate or high grade.
- The metal values are of fine grain size and disseminated in the host rock therefore extensive crushing and grinding are necessary before leaching to expose the maximum surface of the solids to the solution.
- The metal values are difficult to dissolve and that is why intensive agitation is needed to increase the rate.

The equipment used are numerous and expensive, and high recoveries are mandatory. Leaching conditions may be mild using dilute solutions at ambient conditions or it may be severe using concentrated solutions (either acidic or basic) and at high temperature and pressure. Agitation may be mechanical — in this case motor-driven impellers are used, or pneumatic — in this case compressed air or high pressure steam is used when heating is desired.

3.5. High pressure leaching

High-pressure leaching necessitates the use of pressure reactors (or autoclaves). One should distinguish between two types of pressure leaching:

- ***In absence of air or oxygen.*** In this case the rate of leaching at ambient or moderate temperature is low and a temperature higher than the boiling point of the solution must be used. Consequently the reaction must be conducted in a closed vessel to prevent the escape of vapors. The pressure generated is the result of the vapor pressure of the solution. This method is mainly used for leaching bauxite, scheelite, ilmenite, and laterites.
- ***In presence of air or oxygen.*** In this case leaching at ambient or moderate temperature is not possible unless air or oxygen is present as oxidizing agent. In both cases, it is the oxygen partial pressure that has the controlling factor on the rate of leaching. At a certain temperature the rate increases with increasing oxygen partial pressure. The use of oxygen instead of air is more advantageous because for the same oxygen requirement the total pressure in the autoclave

is low, and as a result the autoclave design will be less demanding, or decreased in size. When ammonium hydroxide is used as a leaching agent, the vapor pressure due to the volatility of NH_3 should be taken into consideration. This method is mainly used for leaching sulfides, selenides, and tellurides.

Autoclaves

According to their shape, autoclaves may be in form of cylinders vertically mounted or horizontally laid, spherical, or in form of a long horizontal tube (Figures 6-9). Method of agitation in an autoclave may be affected by injecting high-pressure steam, mechanically, or by rotating the whole autoclave. Vertical autoclaves are usually steam- agitated, sometimes mechanically agitated, the horizontal are agitated mechanically by impellers and sometimes rotating, while the spherical are agitated by rotating the whole autoclave slowly around its horizontal axis. Some horizontal autoclaves are also agitated by rotation. Steam-agitated and rotating autoclaves have minimum maintenance costs while autoclaves agitated by mechanical impellers are usually expensive to maintain because of the rotating shafts.

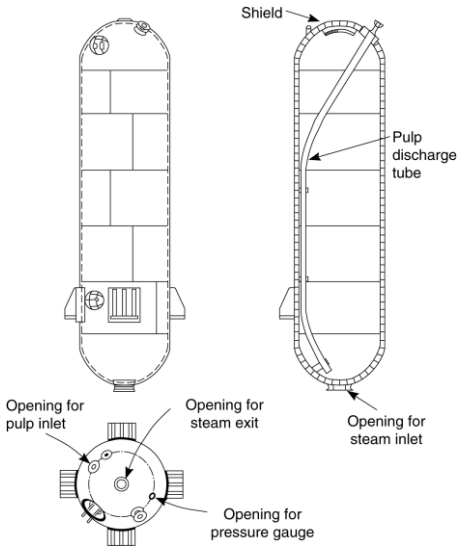

Figure 6. Vertical autoclave.

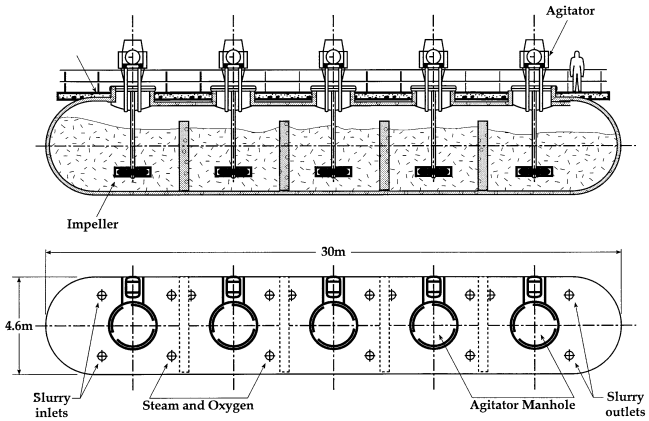

Figure 7. Horizontal autoclave.

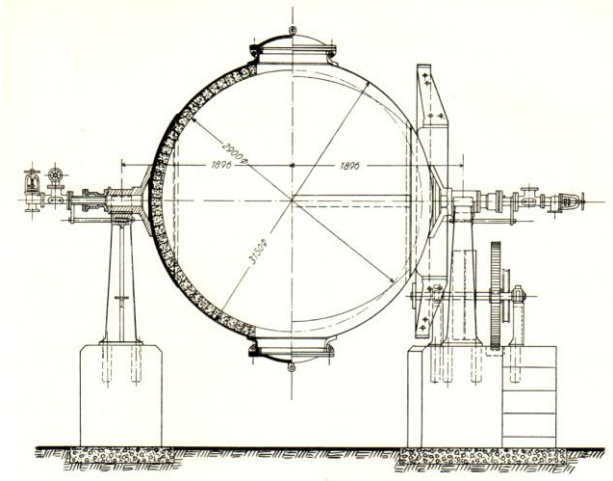

Figure 8. Rotating autoclave.

Figure 9. Tube autoclave.

In tube autoclaves, the slurry is pumped through one end and is discharged through the other. The system is applied for the continuous leaching of bauxite. The slurry is pumped into an externally heated thick-walled tube about 30 cm in diameter and 30 to 50 m long. The system is characterized by extremely short residence time 2 – 3 minutes, high thermal efficiency, and low capital investment.

Pressure leaching plant

A typical pressure leaching plant is shown in Figure 10.

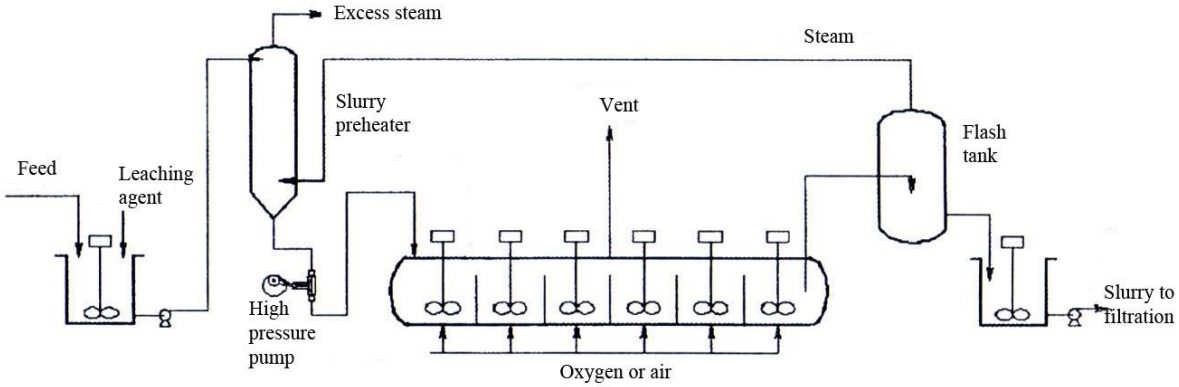

Figure 10. A typical pressure leaching plant.

A high-pressure membrane piston pump is used for introducing pulps into autoclaves. Flash evaporators are large vertical tanks usually installed after an autoclave. This equipment serves three purposes:

- Decreasing the pressure and temperature of the slurry.
- Recovery of heat in form of low-pressure steam.
- Concentration of the solution as a result of the flash evaporation of water.

Slurries to be introduced in an autoclave are preheated by the steam generated in the flash evaporator.

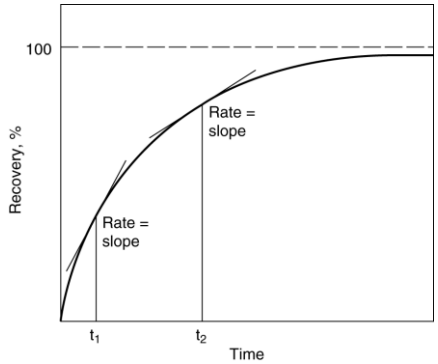

Figure 11. Recovery and rate of leaching.

3.6. Engineering aspects

In conducting a leaching process certain factors must be considered since they directly influence the cost of operation. For any leaching process, the percent recovery is a major concern. It is determined from a material balance based on the analysis of solids and solutions. The

rate of a leaching process is followed by knowing the percent recovery as a function of time (Figure 11). The rate at any moment is the quantity of metal recovered per unit time. It is the slope of the curve at that moment. It can be seen that at the beginning of the process the rate is high and then it decreases gradually with time. Therefore, a compromise should be made between the percent recovery and the residence time in the reactor to achieve maximum productivity. The rate of leaching depends on the following factors:

- ***Particle size.*** The rate increases with decreased particle size of solids, i.e., increased grinding since the smaller the particles, the larger is the surface area per unit weight. However, increased grinding is not only a costly item, but also may cause a filtration problem. Extremely fine particles are sometimes difficult to settle and to filter.
- ***Concentration of leaching agent.*** Increased concentration of leaching agent increases the rate of leaching. But, it may also cause the dissolution of undesirable minerals thus leading to increased reagent consumption and increased impurities in solution.
- ***Agitation.*** Increased agitation usually increases the rate of leaching. But, this again may be a costly item due to increased capital cost of the agitator and operating cost due to the power consumed to effect agitation.
- ***Pulp density.*** Rate of leaching increases with decreasing pulp density, i.e., when a large volume of leaching agent is added to a small weight of solids. But this will result in dilute solutions that will make handling and recovery more difficult. High pulp density results in concentrated solutions, but, on the other hand, is usually associated with high erosion of equipment, e.g., pumps, agitators, etc.
- ***Temperature.*** Rate of leaching increases with increased temperature. However, increased temperature may result in increased dissolution of other minerals thus causing increased reagent consumption and increased impurities in solution.

Therefore, a compromise is always made between the increased rate of leaching and the negative effect of any of the factors influencing this increase.

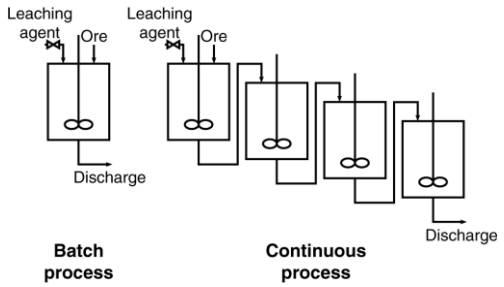

Figure 12. Batch and continuous leaching.

3.7. Batch and continuous processes

A leaching process may be conducted batchwise or continuously (Figure 12). In a batch process, the solids and the solution are charged in a reactor and agitated for a certain time until reaction is complete. The slurry is then discharged for filtration and washing, and the process is repeated, i.e., charging, agitation, and discharging. In a continuous system, a number of reactors must be available through which the solids and the solutions flow from one to the other continuously. The number of the leaching tanks is such that in the last reactor the reaction

should be complete. In a batch process the capital investment is therefore low but the operating cost is high while in a continuous process the reverse is usually true. In general, for large plants, continuous processes are usually more economical because the reactors are effectively utilized: no time is lost in charging and discharging, the possibility of fully automating the circuit, and a minimum of manpower will be required.

3.8. Filtration and washing

Slurries obtained after leaching are usually filtered to recover the leach solution then washed to remove entrained solution. Very clear solutions can only be obtained if sophisticated and expensive solid–liquid separation plant is installed. The finer the grind required either to liberate the metal values or to increase the rate of leaching the more expensive is the filtration plant. In a conventional gold or uranium ore leaching plant, for example, the clarification and filtration steps account for a significant proportion of the overall operating cost. The following procedures are usually practiced:

● When the undissolved material is small as that obtained in leaching concentrates, it is usually washed directly on the filter. Intensive washing increases the recovery of soluble metal values but decreases their concentration and also results in large volumes of solutions to be handled. Therefore a compromise must be made between the metal recovered and the cost of washing.

● When the undissolved material is moderate in volume, the slurry is filtered, the filter cake is repulped in water, and the solids separated while washing counter-currently in thickeners. This is usually the case of leaching zinc oxide calcines.

● When the undissolved material is voluminous as that obtained in leaching low-grade ores, extensive washing is necessary. This is usually conducted in counter-current washing in thickeners followed by filtration. This is usually the case of gold, copper oxide, and uranium ores (Figures 13).

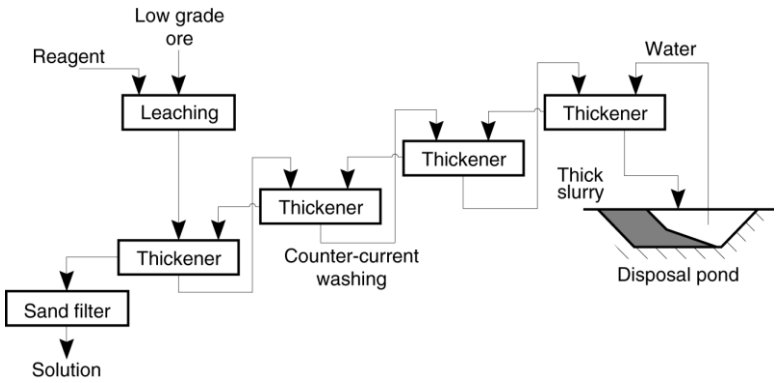

Figure 13. Filtration and washing of low-grade ore.

The thickener consists of a flat-bottomed tank of large diameter as compared with the depth (Figure 14). It has a central shaft on which slowly revolving arms with plow scrapers are fixed. The slurry from agitators is fed to a central well at the top of the shaft. Clear liquid containing the soluble matter overflows into a channel around the circumference of the tank. The solids separate at the bottom of the tank and are gradually removed by the scrapers to the center, where they are withdrawn. Organic coagulating agents such as glue are sometimes added to facilitate the settling of fine slimes.

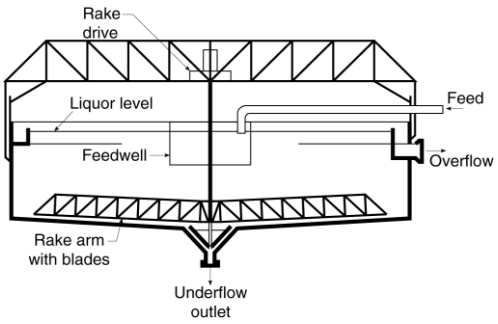

Figure 14. A thickener.

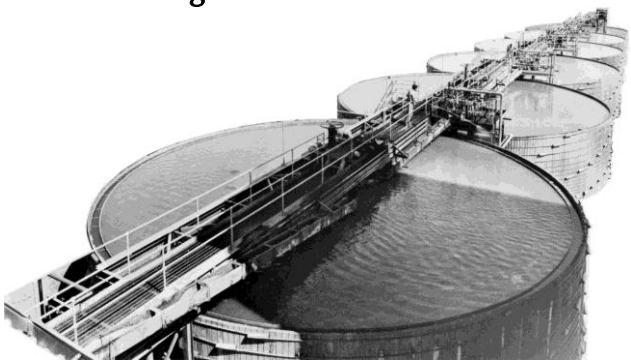

Figure 15. Thickeners operating in counter-current decantation system.

Thickeners are usually installed at graded elevation so that the overflow moves by gravity from one thickener to the other (Figure 15) while the underflow is pumped by a slurry pump and moves from one thickener to the other in a counter-current direction until finally discharged in disposal ponds. Slurry pumps are generally mounted on the edge of the thickener. Overflow from the thickeners may contain about 500 ppm solids; these are removed in sand filters to obtain a clear solution suitable for further processing, for example, when ion exchange, solvent extraction, or precipitation are used.

3.9. Residue disposal

Solid residue, usually wet, is transported by conveyer belts or trucks to disposal site. Thick slurry from the last thickener underflow is pumped to large disposal ponds where long-term settling takes place (Figure 16). Clarified water is pumped back to the washing circuit.

Figure 16. Disposal pond.

3.10. Regeneration and recycle of leach solution

In many leaching operations, it is desirable and is usually possible to regenerate the leaching agent after the metal recovery step. The following examples may be cited:

● After leaching a copper oxide ore with dilute sulfuric acid, copper is usually recovered from the solution by electrolysis. During this process, dilute acid is formed according to:

Cathodic reaction: $Cu^{2+} + 2e^- \rightarrow Cu$,

Anodic reaction: $H_2O \rightarrow 2H^+ + {}^1/_2O_2 + 2e^-$.

This acid is usually recycled to the leaching step. Since only copper was precipitated at the cathode, other metal ions remain in solution. Therefore, when the leaching agent is recycled, impurities will accumulate in the circuit and may contaminate the product. To keep a certain safe limit of impurities in the recycled solution, a part of the solution is usually discharged to waste; it is known as ***bleed solution*** (Figure 17). A similar situation exists in the treatment of gold ores by cyanide solution. Measures should be taken to prevent polluting the environment by this solution.

● In some cases, the solution must be concentrated by evaporation before recycling. This is usually the case when the metal values are precipitated by hydrolysis, e.g., in treatment of bauxite by NaOH.

● In leaching ilmenite by hydrochloric acid, the acid is regenerated from the ferrous chloride solution by oxyhydrolysis.

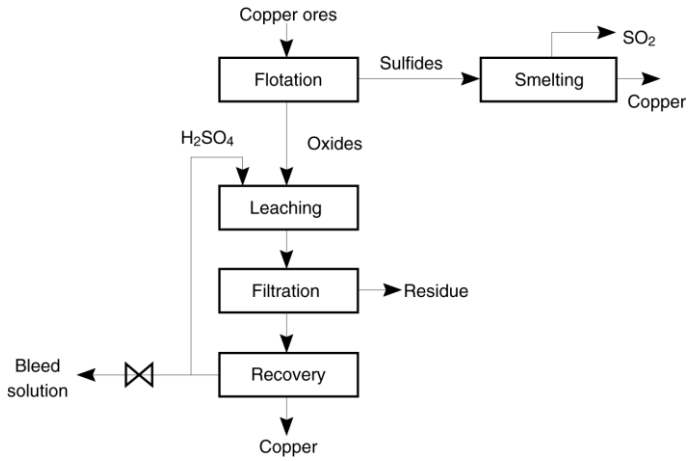

Figure 17. Flowsheet showing the treatment of copper oxide ore and discarding a bleed solution.

3.11. Role of microorganisms

Certain microorganisms known as ***Thiobacillus thiooxidans*** and ***Thiobacillus ferrooxidans*** isolated from mine water and others isolated from sulfur-bearing hot springs are capable of accelerating the rate of dissolution of sulfide minerals (Figure 18). These bacteria can also accelerate the oxidation of elemental sulfur, ferrous ion, sulfite ion, and thiosulfate ion. These microorganisms are minute, unicellular microscopic organisms 0.5 – 2 μm in size that reproduce by binary fission. They are known as autotrophic because they live on inorganic matter in contrast to heterotrophic microorganisms that live on organic matter.

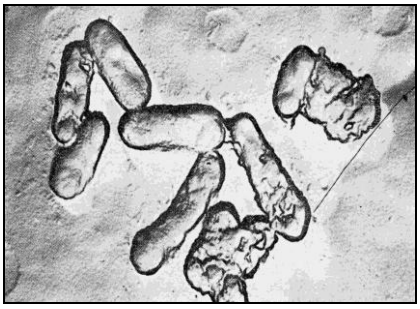

Figure 18. Photomicrograph of ***Thiobacillus ferrooxidans***. Magnification 40 000 x.

Autotrophic bacteria have the following characteristics:

● They must have oxygen to carry out their function, i.e., the oxidation of mineral substances with release of energy which is necessary for their growth.

● They utilize CO_2 as the principal source of carbon required for the synthesis of organic compounds composing the cell. In this respect they resemble plants.

● They absorb certain nutrient from solution, e.g., PO_4^{3-} ion that is necessary for their metabolic function.

● They have resistance to high concentrations of metal ions in solution, e.g., Cu^{2+} which are usually extremely toxic to most other forms of life.

● They adapt to live and grow in strongly acidic environments (pH 1.5–3).

● They are destroyed by light, particularly ultraviolet light. Total darkness has a positive effect on their action.

Their maximum activity occurs at a certain temperature. For ***Thiobacillus ferrooxidans***, for example, this occurs at 35 °C while for those isolated from sulfur-bearing hot springs (the thermophilic bacteria) the temperature may be as high as 85 °C. Below these temperatures they are dormant while above, they are destroyed.

● They manufacture enzymes and with their aid they catalyze the oxidation processes:

$S^{2-} + 2O_2 \rightarrow SO_4^{2-}$,

$S + {}^3/_2O_2 + H_2O \rightarrow 2H^+ + SO_4^{2-}$,

$2Fe^{2+} + 2O_2 + 2H^+ \rightarrow 2Fe^{3+} + H_2O$.

The adherence of the microorganisms on the sulfide surface makes possible the rapid oxidation of S^{2-} ions liberated by the mineral and catalyzed by the enzymes (Figure 19).

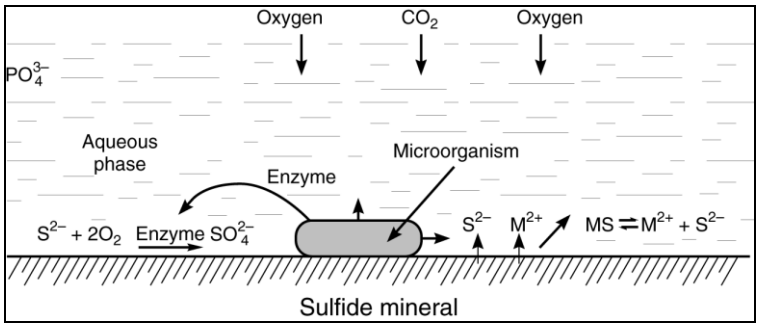

Figure 19. Schematic representation of the action of microorganisms adhering on the surface of a sulfide mineral.

4. Purification and concentration of solutions

Leach solutions may be directly treated to precipitate the metal values, or they may first be purified and concentrated prior to precipitation. The methods used are: adsorption on activated charcoal, sorption on ion exchange resins, and extraction by organic solvents (Table 2). They are common in one respect: the same scheme of loading, washing, and elution is used in all three operations. In the elution step, the material is simultaneously regenerated for another cycle. While the first two materials (activated charcoal and ion exchange resins) are solids and particularly suitable for very dilute solutions the third material is a liquid phase and is suitable for more concentrated solutions. By these techniques it is possible to purify and concentrate dilute solutions with great efficiency.

Ion exchange and solvent extraction are used in the recovery of not only expensive metals such as uranium, vanadium, niobium, tantalum, zirconium, hafnium, beryllium, tungsten, and the rare earths, but also for cheap metals such as copper and zinc. Both techniques are competing with each other. Solvent extraction can be used continuously but the leach solution should be clear. On the other hand, ion exchange is not well adapted for continuous operation, but can be used for turbid solution, thus there is great saving in by-passing the filtration step.

Table 2. Comparison between the different concentration–purification processes.

	Adsorption on activated charcoal	Ion exchange	Solvent extraction
Maximum efficiency	dilute solution	dilute solution	concentrated solution
Speed	slow	slow	rapid
Capacity	low	high	high
Clarity of solution	clear or turbid	clear or turbid	clear
Method of operation	batch or semi-continuous	batch, semi-continuous, or continuous	continuous
Cost	low	high	moderate
Main application	gold and silver from cyanide solution	uranium lanthanides	U, Cu, Zn, Be, B, V, Cr, Fe, Co, Ni, Zr, Hf, Nb, Ta, Mo, W, As, Pt-metals, Au, Th, Pu, lanthanides
Mechanism	physical	physico-chemical	chemical

4.1. Adsorption on activated charcoal

This process is particularly used for separation of gold and silver from cyanide leach solutions. Charcoals, are prepared by carbonization of solid carbonaceous material such as coal,

wood, nut shells, sugar, and synthetic resins at about 600 °C in the absence of air followed by activation by steam at about 800 °C. In the carbonization step, volatilization of component elements other than carbon takes place as well as other complex reactions such as dehydration with formation of double bonds, polymerization, and condensation. In the activation step pores are created by burning away some of the remaining material and existing pores are enlarged. The large surface area as well as the complex organic structure formed is responsible for the adsorption of metal ions. Charcoal is usually used as pellets 2 – 5 mm diameter.

4.2. Ion exchange

Ion exchangers are usually available in the form of spherical particles of 0.5 – 2.0 mm diameter. Synthetic resins consist of an elastic three-dimensional network of hydrocarbon chains which carry fixed ionic groups. The charge of the groups is balanced by mobile counter-ions. The introduction of groups such as sulfonic acid, $-SO_3^-H^+$, makes the hydrocarbon macromolecule soluble in water. But ion exchange resins containing such groups are made insoluble by cross-linking, that is, interconnecting the various hydrocarbon chains. The degree of cross-linking determines the physical properties of the resin.

Ion exchangers can be compared to a sponge with counter-ions floating in the pores. When the sponge is immersed in a solution, the counter-ions can leave the pores and float out. In order to preserve electrical neutrality in the sponge, a stoichiometric number of other ions from the solution enters the pores (Figure 20).

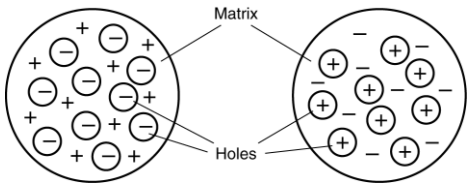

Figure 20. Sponge model of exchangers.

The functional groups, either anionic or cationic, are incorporated either in the monomer before polymerization, or into the polymer itself. Ion exchangers are two types:

● Cationic exchangers can be represented as follows:

$R^-Y^+ + B^+ \rightarrow R^-B^+ + Y^+$

or simply:

$Y^+_{(r)} + B^+_{(aq)} \rightarrow B^+_{(r)} + Y^+_{(aq)}$.

● Anionic exchangers:

$R^+X^- + A^- \rightarrow R^+A^- + X^-$

or simply:

$X^-_{(r)} + A^-_{(aq)} \rightarrow A^-_{(r)} + X^-_{(aq)}$.

4.3. Solvent extraction

Extraction by organic solvents is a chemical process in which metal species in the aqueous phase react with an organic reagent to form an organometallic ***complex***; thus, the

metal species leave the aqueous phase and enter the organic phase. The metal in the organic phase is not bound to carbon atoms as in organometallic ***compounds*** but to oxygen, nitrogen, sulfur, or hydrogen by a coordination (dative) bond. For example, the copper complex formed by extraction of copper ion from aqueous solution by β-hydroxyoxime–copper complex is shown in Figure 21.

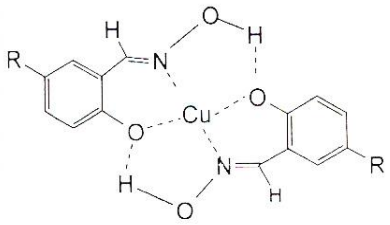

Figure 21. β-hydroxyoxime–copper complex.

Solvent extraction involves two operations:

● ***Extraction.*** The metal values in the aqueous phase are extracted by agitation with an organic solvent immiscible in that phase. The two phases are then allowed to separate; the aqueous phase is usually discarded and the loaded organic phase saved.

● ***Stripping.*** Recovery of the metal values from the loaded organic phase by agitation with a small volume of suitable solution; a concentrated solution containing the metal values in a relatively pure form is obtained and the stripped solvent is then recycled.

An extractant is seldom used in pure form, it is usually diluted with a cheap organic solvent in order to improve its physical properties, such as its viscosity, density, etc. This organic solvent, called ***diluent***, has no capacity to extract metal ions from solution; however, it may influence the extracting power of the extractant. The solution of the extractant in the organic solvent composes the organic phase and is often referred to as the solvent. Commonly used diluents are: hydrocarbons such as n-hexane, kerosene, benzene, toluene, and xylene, or substituted hydrocarbons such as chloroform and carbon tetrachloride.

Extractants

A variety of extractants are available. They may be divided into the following groups:

● ***Ethers.*** Simple ethers are light, volatile, and highly flammable liquids having the general formula R.O.R. They are no longer used because they are susceptible to oxidation, forming peroxides that are liable to explode on distillation. Thioethers, also known as organic sulfides having the formula R.S.R., are selective extractants for palladium and gold.

● ***Alcohols.*** Monohydric alcohols may be primary, secondary, or tertiary. The lower members are soluble in water, and the solubility decreases with increasing molecular weight. Octyl alcohol (or 1-octanol), $CH_3(CH_2)_7OH$ is used in separating cobalt from nickel.

● ***Ketones.*** Commonly used ketones are methyl isobutyl ketone, known as hexone, and acetyl acetone, which is a diketone.

● ***Oximes.*** These are compounds containing the group = N – OH, and have been used for many years in analytical chemistry as precipitants for metals. The alpha-hydroxyoximes are well known as specific for precipitating copper; they are also used for extracting copper.

● ***Oxines.*** These are derived from 8-hydroxyquinoline. Keelex 100 is a trade name for a commercial extractant from this group that is widely used for extracting copper.

● ***Organic acids.*** These may be fatty acids, having the formula R – COOH. The low molecular weight members of this group are soluble in water and the solubility decreases with

increasing molecular weight. These are in use under the trade name Versatic Acid. Alpha-substituted acids, for example, alpha-bromolauric contains 12 carbon atoms have also been suggested because of their increased strength. Naphthenic acids are carboxylic derivatives of cycloparaffin hydrocarbons. They are derived from crude petroleum oils and have a variable composition. The molecular weight varies from 170 to 330.

● ***Phenols.*** In this category a hydroxyl group is attached to an aromatic nucleus; they are more strongly acidic than alcohols. An example is polyol which is used on commercial scale for boron extraction.

● ***Esters.*** These are formed by the reaction of alcohols with inorganic acids. Those used in extractive metallurgy are derived from phosphoric acid and can be classified into acidic esters or neutral esters or neutral esters. Phosphoric acid is introduced in the form of P_2O_5 or $POCl_3$. A mixture of products is generally obtained.

● ***Amines.*** These may be primary, secondary, or tertiary. The use of simple amines is limited to those of molecular weight between 250 and 600. Amines of molecular weight lower than 250 are appreciably soluble in water, and those of molecular weight higher than 600 are either not easily available or have low solubility in the organic phase. Most of these are commercial products which are mixtures of compounds in isomeric or homologous series. Quaternary ammonium compounds are closely related to amines, but they are significantly different in behavior. While the simple amines are ineffective at high pH, the strong-base quaternary ammonium compounds are effective over a wide pH range. Solubility of the amines in aqueous and organic solutions, as well as phase-separation properties, depends on the structure of the amine and the nature of the solvent. Water immiscibility decreases with increasing length of the aliphatic chain.

5. Precipitation

Precipitation methods which are the final steps in any hydrometallurgical process are: crystallization, hydrolysis, ionic precipitation, and reduction. While crystallization is a physical process, the others are chemical.

5.1. Crystallization

Crystallization is a common procedure for obtaining pure compounds. Solubility of salts in water usually increases with increased temperature. Thus, on cooling a hot solution, crystals form:

$$M(H_2O)_x^{n+} + A(H_2O)_y^{m-} \rightarrow MA_{(solid)}.$$

This method is used occasionally for recovering some metals from solutions, for example $CuSO_4 \cdot 5H_2O$, $NiSO_4 \cdot 4H_2O$, $FeCl_2 \cdot 4H_2O$, etc. These processes are usually slow and apply for soluble salts. During the crystallization of pairs of salts with a common anion such as two sulfates or two chlorides, three types of crystals may be obtained.

Heterogeneous mixture

In this case a mixture composed of the two original salts is obtained; they can be either anhydrous or hydrated. For example, when a mixture of NaCl and KCl are dissolved in water

and the solution allowed crystallizing, the solids obtained will be a mixture of NaCl and KCl, i.e., each salt has preserved its identity during dissolution and crystallization.

Mixed crystals

In this case a homogeneous mixture is obtained in which the ratio of the component salts do not conform to a simple stoichiometric ratio. For example, when a mixture of $FeSO_4$ and $CuSO_4$ are dissolved in water and the solution allowed to crystallize, a crystalline solid is obtained in which the copper and iron are irregularly distributed in the crystal lattice, i.e., there will be crystals of $CuSO_4 \cdot nH_2O$ incorporating iron in their structure and $FeSO_4 \cdot mH_2O$ crystals incorporating copper in their structure. This is also known as a solid solution and may be represented by $(Cu,Fe)SO_4 \cdot nH_2O$. The X-ray diffraction pattern of the mixed crystal will be similar to the original salts but the diffraction lines are slightly shifted. In this case, the two salts did not completely preserve their identity during crystallization.

Double salt

This is a compound formed from the two salts which has a distinct X-ray diffraction pattern and chemical properties. For example, when $FeSO_4$ and $(NH_4)_2SO_4$ are dissolved in water and the solution allowed to crystallize, a compound, ferrous ammonium sulfate, having the formula $FeSO_4 \cdot (NH_4)_2SO_4 \cdot H_2O$ is obtained, while ferrous sulfate oxidizes readily in the air. Ferrous ammonium sulfate is quite stable, that is why it is usually used in analytical chemistry to prepare solutions of ferrous ion. Double salts are more exactly represented by the formula $M^{I}_2M^{II}(SO_4)_2 \cdot nH_2O$. A group known as alums which has the general formula $M^{I}M^{III}(SO_4)_2 \cdot 12H_2O$ is sometimes made use of in hydrometallurgy, for example, separation of aluminum or chromium from leach solutions by forming the corresponding alums: $(NH_4)_2SO_4 \cdot Al_2(SO_4)_3 \cdot 24H_2O$ or $NH_4Al(SO_4)_2 \cdot 12H_2O$ and $(NH_4)_2SO_4 \cdot Cr_2(SO_4)_3 \cdot 24H_2O$ or $NH_4Cr(SO_4)_2 \cdot 12H_2O$.

5.2. Hydrolysis

Hydrolysis is the reaction of metal ions with water:

$$M^{x+} + x\,H_2O \leftrightarrows M(OH)_x + x\,H^+.$$

This usually takes place on diluting the solution. For example, on diluting a solution of titanyl sulfate, titanium dioxide is precipitated:

$$TiO^{2+} + H_2O \leftrightarrows TiO_2 + 2H^+.$$

The reaction is usually slow and may be accelerated by adding a small amount of finely divided titanium dioxide which acts as a seed on which precipitation takes place. This is the basis of production of titanium dioxide pigment by the sulfate process. Similarly, in the precipitation of aluminum hydroxide from sodium aluminate solution, the solution is diluted and a seed of aluminum hydroxide is added to accelerate the hydrolytic reaction:

$$[Al(OH)_4]^- + H_2O \leftrightarrows Al(OH)_3 + OH^-.$$

This is the basis of the preparation of aluminum oxide for aluminum production. The difference in the two processes is the hydrolysis of titanyl ion takes place in acid medium while that of the aluminate ion is in basic medium. Additional examples on precipitation by hydrolysis are given in Table 3. It can be seen that not only hydroxides and oxides are formed but also hydrated oxides, oxysalts, and hydroxy salts as well, depending on the conditions of hydrolysis.

Table 3. Summary of hydrolytic and ionic precipitation methods.

Precipitate	Precipitating agent	Examples
oxides, hydrated oxides, hydroxides	H_2O	TiO_2, $Al(OH)_3$, $Be(OH)_2$
	OH^-	$Nb_2O_5 \cdot nH_2O$, $Ta_2O_5 \cdot nH_2O$, Cu_2O, $Mg(OH)_2$, $Co(OH)_2$
hydroxy salts	OH^- + anion	$Cu(OH)_2 \cdot CuCO_3$
polyacids and their salts:		
vanadates	H^+	$Na_4V_6O_{17}$, $(NH_4)_4[V_4O_{12}]$
molybdates	H^+	$(NH_4)_4[H_2Mo_6O_{21}] \cdot 3H_2O$
tungstates	H^+	$Na_{10}W_{12}O_{41} \cdot 28H_2O$
uranates	OH^-, MgO	$(NH_4)_2U_2O_7$, $Na_2U_2O_7$, MgU_2O_7
dialuminates	OH^- + cation	$LiAl_2(OH)_7 \cdot 2H_2O$
sulfides	S^{2-}	CuS, NiS, CoS, ZnS
carbonates	CO_3^{2-}	Li_2CO_3
chlorides	Cl^-	CuCl, $(NH_4)_2PtCl_6$, K_2TiCl_6
cyanides	CN^-	CuCN
fluorides	F^-	PuF_3, $UF_4 \cdot nH_2O$
oxalates	$(C_2O_4)^{2-}$	$Th(C_2O_4)_2$, $Ln_2(C_2O_4)_3$*
peroxides	O_2^{2-}	$UO_4 \cdot 2H_2O$, PuO_4
sulfites	$(NH_4)_2SO_3$	copper ammonium sulfites
metalloids	H^+	selenium from selenosulfate solution

* Ln = lanthanide or rare earth metal

5.3. Ionic precipitation

Ionic precipitation is characterized by adding an anionic reagent A^{y-} that selectively precipitates the metal compound:

$$yM^{x+} + xA^{y-} \rightarrow M_yA_{x(s)}.$$

Precipitation usually takes place rapidly because the compound formed has low solubility and is attached together by electrostatic forces. For example, the addition of sulfide ion or hydrogen sulfide to a cupric sulfate solution results in the immediate precipitation of copper sulfide:

$$Cu^{2+} + S^{2-} \rightarrow CuS_{(s)}.$$

Additional examples of ion precipitation are given in Table 3. It can be seen that hydroxides, salts of polyacids like uranates and molybdates, sulfides, carbonates, chlorides, cyanides, fluorides, oxalates, peroxides, and sulfites can be precipitated using the proper reagents. All these methods are applied technically.

5.4. Reduction

Precipitation by reduction involves electron transfer and four types can be identified:

Ionic

In this case a reducing agent is added which results in the precipitation of a metal:

M^{x+} + reduced species → M^o + oxidized species.

For example, gold is precipitated from industrial chloride leach solutions by reduction with ferrous ion as follows (Figure 22):

$Au^+ + Fe^{2+} \rightarrow Au^o + Fe^{3+}$.

This is an oxidation–reduction couple:

$Au^+ + e^- \rightarrow Au$,

$Fe^{2+} \rightarrow Fe^{3+} + e^-$.

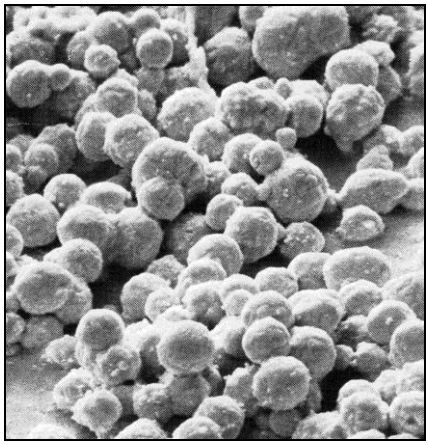

Figure 22. Scanning electron micrograph of gold powder precipitated from gold chloride solution by ferrous sultate. Magnification 1000 x (courtesy Gold Bulletin).

Similarly the precipitation of elemental selenium from selenious acid by sulfurous acid is the industrial method for recovering selenium from its solution as follows:

$H_2SeO_3 + 2SO_2 + H_2O \rightarrow Se + 2H_2SO_4$.

Table 4. Precipitation by non-ionic reduction.

Reducing agent	Reaction	Application
hydrogen	$H_2 \rightarrow 2H^+ + 2e^-$	$Ni^{2+} + 2e^- \rightarrow Ni$
carbon monoxide	$CO + H_2O \rightarrow CO_2 + 2H^+ + 2e^-$	$Ag^+ + e^- \rightarrow Ag$ $Cu^{2+} + 2e^- \rightarrow Cu$
formaldehyde	$HCHO + H_2O \rightarrow HCOOH + 2H^+ + 2e^-$ $HCHO + 3OH^- \rightarrow HCOO^- + 2H_2O + 2e^-$	$Cu^{2+} + 2e^- \rightarrow Cu$
hydrazine	$H_2N \cdot NH_2 \rightarrow N_2 + 4H^+ + 4e^-$ $2H_2N \cdot NH_2 \rightarrow N_2 + 2NH_4 + 4e^-$	$Cu^{2+} + 2e^- \rightarrow Cu$

Non-ionic

Hydrogen, carbon monoxide, formaldehyde, and hydrazine are non-ionic reducing agents (Table 4). Hydrogen displaces copper from $CuSO_4$ solution and nickel from $NiSO_4$ solution:

$M^{2+} + 2e^- \rightarrow M$,

$H_2 \rightarrow 2H^+ + 2e^-$.

In both cases, a temperature of about 200 °C and a hydrogen partial pressure of about 3500 kPa are needed. In the case of nickel, ammonia must be added continuously to neutralize the acid liberated. These reactions are applied commercially. For the reaction:

$M^{2+} + H_2 \rightarrow M + 2H^+$

the equilibrium constant is given by:

$$K = \frac{[H^+]^2}{[M^{2+}] \cdot p_{H_2}}$$

therefore:

$\log[M^{2+}] = -2pH - (\log K + \log p_{H2})$.

This means that when precipitation is carried out at constant hydrogen pressure and constant temperature, then at equilibrium there is a linear relation between $\log [M^{2+}]$ and the pH of the solution, and the slope of this straight line equals – 2. This was confirmed for the precipitation of nickel from $NiSO_4$ solution (Figure 23) and for cobalt (Figure 24).

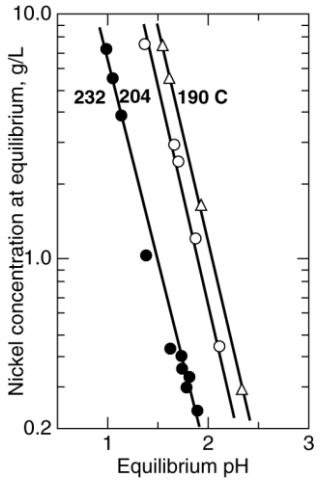

Figure 23. Precipitation of nickel from nickel sulfate solution by hydrogen at 3500 kPa, $[(NH_4)_2SO_4]$ = 112 g / L, equilibrium conditions.

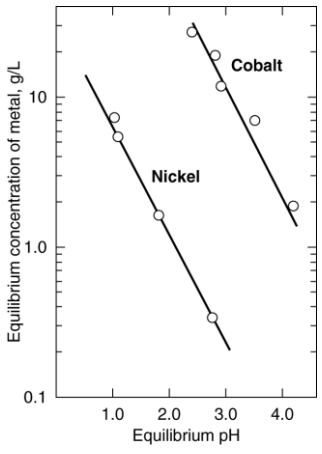

Figure 24. Precipitation of cobalt and nickel from acid solution, temperature 190 °C, H_2 pressure 3500 kPa, $[(NH_4)_2SO_4]$ = 112 g / L

Nucleation

In some cases, the presence of a solid surface for precipitation is essential; such a solid is termed a *catalys*.

● If no catalyst were provided, the internal surface of the autoclave itself acts as a catalyst and deposition of metals takes place on the walls or on stirrers. Deposition of metal on the internal surface of the reactor is undesirable because it causes operating difficulties in collecting the metal.

● A catalyst may be needed in one medium but not in another. For example, a catalyst is needed for precipitating cobalt and nickel from an ammoniacal sulfate but not from an acid medium. Nickel is precipitated catalytically from an ammoniacal sulfate medium but not from an ammoniacal carbonate medium.

● Precipitation of a metal may be autocatalytic. Thus, while copper can be precipitated from ammoniacal solution without the need of a catalyst, yet the deposited metal accelerates the process. A difference between the two processes however is that in non-catalyzed reduction, the rate depends on the initial metal ion concentration, while in catalyzed reduction it does not, but depends on the surface area of the catalyst.

● The commercial precipitation of nickel from the ammonium sulfate system nucleation is induced by adding a small amount of ferrous sulfate which, upon heating to the reaction temperature, hydrolyzes to ferrous hydroxide thus furnishing the catalytic surface required. Nickel deposited in the first step acts as a catalyst for the next. After each reduction, the nickel particles are allowed to settle to the bottom of the autoclave, while the spent solution is drawn off and replaced with fresh pregnant solution. In this way, the nickel particles grow to the desired size, at which point the suspension is discharged and the nickel powder then separated.

● There is no need for the ferrous sulfate catalyst in the ammonium carbonate system; as a result, the nickel powder produced in this medium has a lower sulfur and iron impurity level than powder produced from the ammonium sulfate system.

Role of additives

The presence of certain organic or inorganic substances in the aqueous phase greatly affects the physical nature of metal precipitated. It is possible to precipitate metal powder of certain physical property by simply adding a certain amount of additive. However, when organic additives are used, the carbon content in the powder produced is increased and a special heat treatment is necessary to lower it to 0.01 %. Additives may be used for the following purposes:

● ***Anti-agglomeration.*** Agglomeration of the precipitated metal particles may take place, especially at high temperature. This is undesirable because the agglomerated particles entrap solution causing an impure product. Reagents are therefore added to control the particle size. These are the same as those commonly used to promote uniform growth of cathodes in the electrowinning of metals, e.g., ammonium polyacrylate, arabic gum, gelatin, dextrin, dextrose, and fatty acids such as oleic and stearic. These additives are adsorbed on the individual particles, thus preventing their agglomeration.

● ***Smooth surface formation.*** When anthraquinone or its derivatives is added during reduction, nickel particles produced are smooth and regular because of uniform deposition while in the absence of anthraquinone, they are coarse and irregular (Figure 25). Anthraquinone has no effect on the precipitation of cobalt. The addition of this additive to ammoniacal nickel sulfate or carbonate solutions also accelerates the precipitation, and this effect increases with increasing anthraquinone concentration up to a certain value, beyond which it has no further effect.

● ***Crystalline product.*** Figure 26 shows hexagonal platelets of metallic cobalt precipitated in presence of a suitable additive.

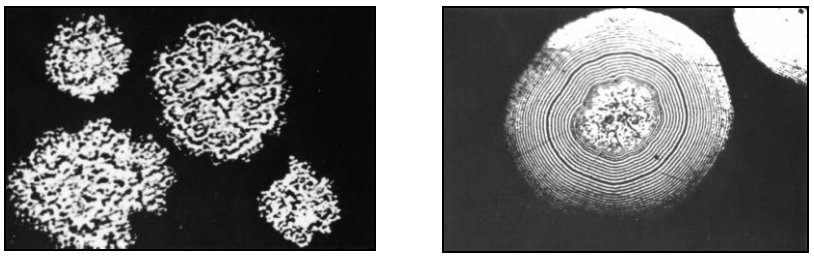

(a) (b)

Figure 25. Effect of anthraquinone on the shape on nickel powder (320 ×); (a) no anthraquinone, (b) in presence of anthraquinone, cross section through smooth nickel sphere after 40 successive depositions.

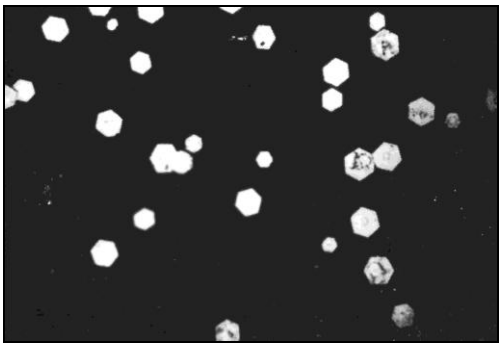

Figure 26. Hexagonal crystals of cobalt powder.

Electrochemical

In this case a less noble metal is used to precipitate another metal M from its solution

$M^{x+} + X \rightarrow M + X^{x+}$.

These are also oxidation–reduction processes. For example for the precipitation of copper from copper sulfate solution by metallic iron, the reaction can be represented by:

$Cu^{2+} + 2e^{-} \rightarrow Cu$,

$Fe \rightarrow Fe^{2+} + 2e^{-}$.

This differs from the previous case in being electrochemical: metallic iron in contact with copper sulfate solution will exchange electrons at the interface. Being a conductor, iron gives away its electrons at one position, and ferrous ion leaves the surface at another. One should recall the electrochemical series of metals. In this series, metals are classified into three categories: reactive, less reactive or base metals, and non-reactive or noble. Each metal at the top can displace any metal below it in the series. Thus, while iron displaces copper from copper sulfate solution, it is true as well that copper can displace silver from silver nitrate solution:

$2Ag^{+} + Cu \rightarrow 2Ag + Cu^{2+}$.

In the same way zinc can displace cadmium from cadmium sulfate solution which is the standard method for recovering cadmium from leach solutions:

$Cd^{2+} + Zn \rightarrow Cd + Zn^{2+}$.

Activated charcoal is also capable of precipitating a metal from its aqueous solution by an electrochemical mechanism. This applies however, only for gold chloride solutions as shown by the oxidation–reduction couple:

$Au^{3+} + 3e^- \rightarrow Au$,

$C + 2H_2O \rightarrow CO_2 + 4H^+ + 4e^-$.

Gold precipitated on the surface of charcoal can be recovered by burning the charcoal.

Precipitation by metals

Precipitation of a metal from an aqueous solution of its salts by another metal is known as ***cementation***, because the precipitated metal powder is usually adhering loosely on the surface of the precipitating metal. The process can be predicted in terms of electrode potentials: The metal with the more positive (oxidation) potential will pass into solution and displace a metal with a less positive potential provided the solutions are dilute and the metal ion is un-complexed. The process is electrochemical in nature as shown in Figure 27.

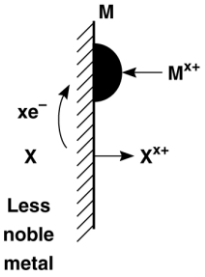

Figure 27. Displacement of a metal by another metal.

A metal may also be recovered from an aqueous suspension of one of its insoluble salts by this method, e.g., silver from silver chloride:

$2\,AgCl + Fe_{(s)} \rightarrow 2Ag_{(s)} + FeCl_{2(aq)}$.

Although AgCl is insoluble in water, yet a certain amount of Ag^+ ions do exist in solution and their continuous removal by metallic iron shifts the equilibrium:

$AgCl_{(s)} \rightarrow Ag^+ + Cl^-$

to the right resulting in the ultimate disappearance of AgCl. Similarly, copper may be recovered from cuprous chloride suspensions by metallic iron:

$Cu_2Cl_2 + Fe_{(s)} \rightarrow Cu_{(s)} + FeCl_{2(aq)}$.

In some cases, the metal to be precipitated exists in solution as a complex ion, e.g., gold or silver in cyanide solution exist as the complex cyanide ions $[Au(CN)_2]^-$ and $[Ag(CN)_2]^-$ respectively. Precipitation by metallic zinc takes place as a result of displacing the equilibrium of the complex ion according to:

$[Au(CN)_2]^- \rightarrow Au^+ + 2CN^-$,

$2Au^+ + Zn \rightarrow 2Au + Zn^{2+}$,

$Zn^{2+} + 4CN^- \rightarrow [Zn(CN)_4]^{2-}$.

Overall reaction: $2[Au(CN)_2]^- + Zn \rightarrow 2Au + [Zn(CN)_4]^{2-}$.

Factors affecting the physical properties of precipitated metals

For the cementation of copper by iron, a finer powder is obtained at high Cu^{2+} ion concentration, as shown in Table 5. Further, at a constant Cu^{2+} ion concentration, a fine powder is obtained at high H_2SO_4 concentration, as shown in Table 6. Also, the form of the metal precipitated depends on the precipitating metal as shown in Figure 28.

Table 5. Effect of Cu^{2+} concentration on the particle size of copper precipitated by iron.

Screen analysis, %	Cu^{2+} concentration, g / L		
	3.7	15.0	27.0
100 mesh	7.7	4.1	1.6
100 to 150	11.6	9.2	6.0
150 to 200	15.7	11.3	11.3
200 to 270	14.0	10.8	12.2
270 to 325	5.4	5.1	6.5
325	45.6	59.5	62.4

Table 6. Effect of H_2SO_4 on the particle size of copper precipitated by iron.

Screen analysis, %	H_2SO_4 concentration, g / L		
	8.9	16.4	29.9
100 mesh	3.5	4.6	3.3
100 to 150	8.6	8.8	2.9
150 to 200	13.4	12.0	11.9
200 to 270	13.4	12.3	11.4
270 to 325	6.5	5.8	6.4
325	54.6	56.5	64.1

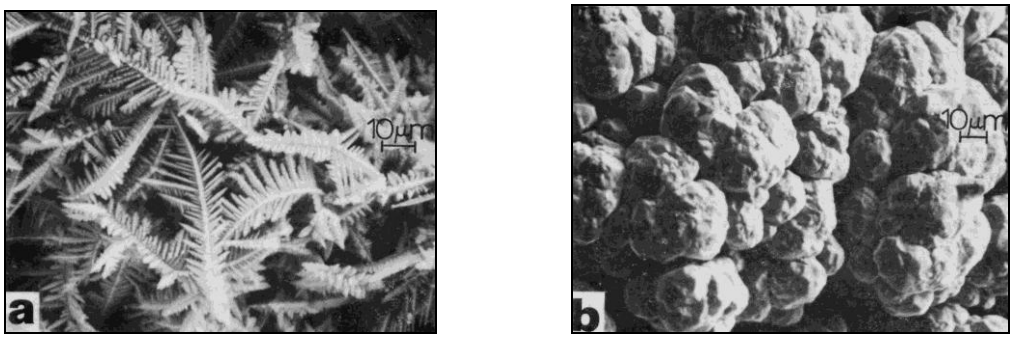

Figure 28. Morphology of copper precipitate from sulfate solution (*a*) aluminum, (*b*) iron.

Electrolytic

In this case, precipitation of a metal from its aqueous solution is effected by imposing an outside electromotive force from a direct current source:

$M^{x+} + x\,e^- \rightarrow M$.

For example copper, zinc, cadmium, and nickel are recovered industrially from leach solutions by this method — a process called electrowinning. The aqueous solutions are electrolysed using inert electrodes; the pure metal is deposited on the cathode.

6. Summary

Table 7 gives a summary of metal production by hydrometallurgical route.

Table 7. Summary of precipitation methods.

Method	Characteristics	Reactions	Examples
crystallization	slow, high solubility of salt	$yM^{x+} + xA^{y-} + nH_2O \rightarrow M_yA_x{\cdot}nH_2O_{(s)}$	$Cu^{2+} + SO_4^{2-} + 5H_2O \rightarrow CuSO_4{\cdot}5H_2O$
ionic precipitation	fast, low solubility of precipitate	$yM^{x+} + xA^{y-} \rightarrow MA_{(s)}$	$Cu^{+} + Cl^{-} \rightarrow CuCl$
ionic reduction	homogeneous, involves oxidation–reduction, reagent in ionic form	M^{x+} + Reduced species →M+Oxidized species	$Au^{+} + e^{-} \rightarrow Au$ $Fe^{2+} \rightarrow Fe^{3+} + e^{-}$ $Au^{+} + Fe^{2+} \rightarrow Au + Fe^{3+}$
			$SO_3^{2-} + H_2O \rightarrow SO_4^{2-} + 2H^{+} + 2e^{-}$ $SeO_3^{2-} + 6H^{+} + 4e^{-} \rightarrow Se + 3H_2O$ $SeO_3^{2-} + 2H^{+} + 2SO_3^{2-} \rightarrow Se + 2SO_4^{2-} + H_2O$
non-ionic reduction	homogeneous, involves oxidation–reduction, reducing agent is non-ionic	$M^{x+} + {}^{x}/_{2}H_2 \rightarrow M + xH^{+}$	$Ni^{2+} + 2e^{-} \rightarrow Ni$ $H_2 \rightarrow 2H^{+} + 2e^{-}$ $Ni^{2+} + H_2 \rightarrow Ni + 2H^{+}$
	substitution in organic medium, 200°C, 100 kPa	$RM_{(org)} + H_{2(org)} \rightarrow RH_{2(org)} + M_{(s)}$	
electrochemical reduction	heterogeneous, involves oxidation–reduction	$4M^{+} + xC + 2xH_2O \xrightarrow[\text{charcoal}]{\text{activated}} 4M + xCO_2 + 4xH^{+}$	$Au^{3+} + 3e^{-} \rightarrow Au$ $C + 2H_2O \rightarrow CO_2 + 4H^{+} + 4e^{-}$ $4Au^{3+} + 3C + 6H_2O \rightarrow 4Au + 3CO_2 + 12H^{+}$
		$M^{n+} + X \rightarrow M + X^{n+}$ (less noble metal)	$Cu^{2+} + 2e^{-} \rightarrow Cu$ $Fe \rightarrow Fe^{2+} + 2e^{-}$ $Cu^{2+} + Fe \rightarrow Cu + Fe^{2+}$
electrolytic reduction	imposed EMF	$M^{x+} + x\,e^{-} \rightarrow M$	$Cu^{2+} + 2e^{-} \rightarrow Cu$

Suggested reading

1. F. Habashi. Textbook of Hydrometallurgy, 2nd edition. 1999, Quebec City: Métallurgie Extractive (distributed by Laval University Bookstore, www.zone.ul.ca).

This is the last paper in a series of four, devoted to outline mineral processing for nano-scientists — users of the final products. The first paper was a general outline of mineral processing, the second on pyrometallurgy, and the third was on hydrometallurgy.
Editor

ELECTROMETALLURGY FOR NANO-SCIENTISTS

F. Habashi

Laval University
Quebec City, Canada
Fathi.Habashi@arul.ualval.ca

Accepted June 28, 2011

Electrometallurgy is applied in three major industries: refining of copper, recovery of zinc, and production of aluminum. Which copper and zinc are processed in aqueous solutions, the production of aluminum takes place from molten salt. Electrowinning of zinc and aluminum are energy intensive operations while electrorefining of copper is not. Electrometallurgy cannot be isolated from other areas of extractive metallurgy because of its dependence on the feed material as well the final processing of the products and the secondary products like anodic slimes. There is a competition between electrometallurgy and pyrometallurgy in connection with the production of reactive metals such as beryllium and magnesium.

1. Introduction

Electrometallurgy is that branch of extractive metallurgy in which electric energy is used for extracting or refining metals. Metallurgical processes using electric energy for heating purposes are known as ***electrothermic*** processes and are a part of pyrometallurgy. Metallurgical processes using mercury as a cathode or an amalgam as an anode are a special field of electrometallurgy known as ***amalgam metallurgy***. Electrometallurgy is dependent on the other areas of mineral processing as shown in Figure 1.

2. Electrometallurgical plants

An electrometallurgical plant consists of a cell that is the reactor where the electrochemical reaction takes place, a source of current supply (alternating current converted to direct current by a mercury rectifier), electrodes immersed in the cell to conduct the electric current to the material inside the cell, and an electrolyte. The electrode where deposition of metals takes place is called the ***cathode*** while the other electrode is called the ***anode***. The

material inside the cell is the ***electrolyte***. An electrochemical reaction is a heterogeneous chemical process involving the transfer of charge to or from an electrode, generally a metal or a semiconductor. The charge transfer may be a cathodic or an anodic process. In a cathodic process a stable species is reduced by the transfer of electrons from an electrode.

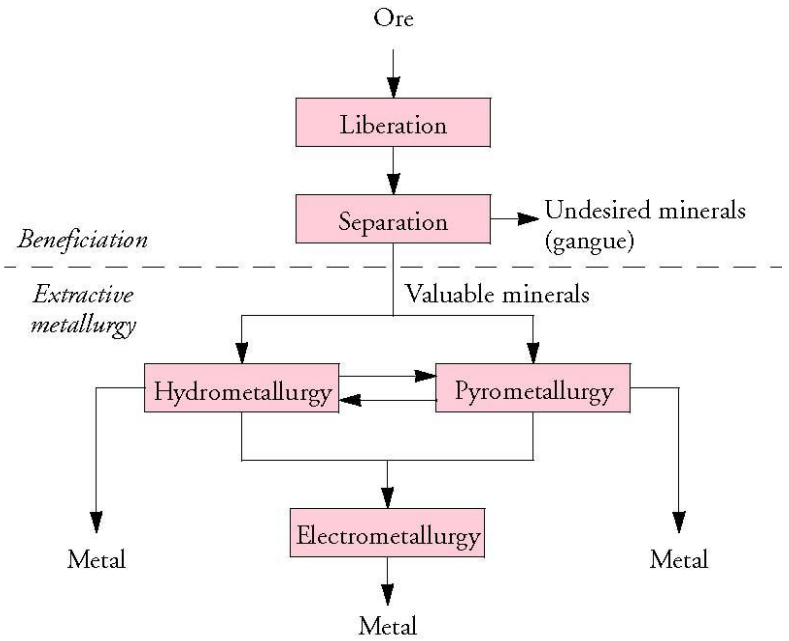

Figure 1. Electrometallurgy in relation to other areas of mineral processing.

Table 1. Summary of electrolytic reduction processes.

Electrode	Electrolyte		Examples	Remarks
inert electrodes	aqueous	cathodic	$Cu^{2+} + 2e^- \rightarrow Cu$	industrial scale for Cu, Zn, Ni, Co, Au, Ag, Mn, Cr, Cd, Te
		anodic	$H_2O \rightarrow {}^1/_2O_2 + 2H^+ + 2e^-$	
	fused salt (chloride)	cathodic	$Mg^{2+} + 2e^- \rightarrow Mg$	industrial scale for Mg, Ga, Na, Li laboratory scale for Al, Ti, Nb, Ta
		anodic	$2Cl^- \rightarrow Cl_2 + 2e^-$	
	fused salt (sulfide)	cathodic	$Pb^{2+} + 2e^- \rightarrow Pb$	laboratory scale
		anodic	$S^{2-} \rightarrow S^o + 2e^-$	
consumable electrode	aqueous	cathodic	$Cu_2S + 2e^- \rightarrow Cu + S^{2-}$	laboratory scale
		anodic	$H_2O \rightarrow {}^1/_2O_2 + 2H^+ + 2e^-$	
	fused salt (fluoride)	cathodic	$Al^{3+} + 3e^- \rightarrow Al$	Industrial scale
		anodic	$O^{2-} + C \rightarrow CO + 2e^-$	
mercury cathode	aqueous	cathodic	$Na^+ + Hg + e^- \rightarrow Na(Hg)$	industrial scale for Na, Ga
		anodic	$2Cl^- \rightarrow Cl_2 + 2e^-$	
	fused salt (chloride)	cathodic	$Be^{2+} + nHg + 2e^- \rightarrow Be(Hg)_n$	laboratory scale
		anodic	$2Cl^- \rightarrow Cl_2 + 2e^-$	

Table 1 gives a summary of electrolytic reduction processes using inert, consumable, and mercury cathodes. In either case, the electrolyte may be an aqueous solution or a fused salt. In

the anodic oxidation processes, examples are given for a metal consumable electrode in either an aqueous electrolyte or a fused salt, a sulfide consumable electrode in an aqueous electrolyte, and an amalgam anode in a fused chloride (Table 2). The scale of operation, whether industrial or laboratory, is indicated.

Table 2. Summary of anodic oxidation process.

Electrode	Electrolyte		Examples	Remarks
metal consumable anode	aqueous	anodic	$Cu_{(impure)} \rightarrow Cu^{2+} + 2e^-$	industrial scale for Cu, Ni, Co, Pb, Sn, Au, Ag, Sb, Bi, In
		cathodic	$Cu^{2+} + 2e^- \rightarrow Cu_{(pure)}$	
	fused salt (fluoride)	anodic	$Al_{(impure)} \rightarrow Al^{3+} + 3e^-$	industrial scale
		cathodic	$Al^{3+} + 3e^- \rightarrow Al_{(pure)}$	
sulfide consumable anode	aqueous	anodic	$Ni_3S_2 \rightarrow 3Ni^{2+} + 2S + 6e^-$	industrial scale
		cathodic	$Ni^{2+} + 2e^- \rightarrow Ni$	
amalgam anode	fused salt (chloride)	anodic	$In(Hg)_n \rightarrow In^{3+} + nHg + 3e^-$	industrial scale
		cathodic	$In^{3+} + 3e^- \rightarrow In$	

The amount of reduction at the cathode and oxidation at the anode must be equal. The total chemical change in the cell is determined by adding the two individual electrode reactions. Thus the chemical change taking place when electrolyzing a copper sulfate solution is:

$Cu^{2+} + 2e^- \rightarrow Cu$,

$H_2O \rightarrow {}^1/_2O_2 + 2H^+ + 2e^-$.

Overall reaction $Cu^{2+} + H_2O \rightarrow Cu + {}^1/_2O_2 + 2H^+$ or $CuSO_4 + H_2O \rightarrow Cu + {}^1/_2O_2 + H_2SO_4$.

3. Laws of electrochemical reactions

The laws governing electrochemical reactions were formulated by Michael Faraday in 1830 and are known as Faraday laws:

● The amount of chemical change produced by an electric current, i.e., the amount of any substance deposited or dissolved, is proportional to the quantity of electricity passed.

● The amounts of different substances deposited or dissolved by the same quantity of electricity are proportional to their chemical equivalent weights.

Electrode processes, therefore, differ from other heterogeneous reactions in that the velocity is directly proportional to the current:

● Weight of metal w deposited in time t is proportional to the current I:

$w \sim I$.

● At constant current I, the weight of metal deposited is proportional to the time of electrolysis:

$w \sim t$.

● At a constant current I, and within a certain time t, the weight of metals deposited are proportional to their equivalent weights:

$$w \sim \frac{W}{n},$$

where W is the atomic weight of the metal in question and n is its valency. Therefore:

$$w = kIt\,\frac{W}{n},$$

where k is the proportionality constant. It follows from this equation that:

$$t = \frac{1}{kI}\frac{w}{W/n}.$$

Further, the time required to deposit one gram equivalent of any metal, that is, when $w = W/n$, on passing a current of 1 ampere, was found to be 26 hours and 48 minutes or 96 500 seconds. Therefore:

$$k = \frac{1}{96\,500}.$$

Substituting the value of k as given above and arranging terms, we get:

$$\frac{w/W}{t} = \frac{I}{96\,500\,n}$$

or, the rate of metal deposition in gram atom per second equals:

$$\text{Rate} = \frac{I}{nF},$$

where $F = 96\,500$, the faraday. The unit of F is ampere second, or coulomb. Faraday's law is independent of temperature or pressure, and is applicable to aqueous, nonaqueous, and fused salts; to cathodic deposition as well as anodic dissolution. That is, 1 faraday will deposit one equivalent weight of a substance at an electrode. Since 1 equivalent weight of an element involves a transfer of $6.023 \cdot 10^{23} = N$ electrons in the process of a chemical reaction, it follows then that 1 faraday will supply N electrons in the electrolysis of a substance in solution. Calculations in electrochemical reactions can be treated in the same way as the stoichiometric relations in chemical reactions if the faraday is considered as "one mole of electrons".

4. Electrode progress

Reactions occurring at an electrode are heterogeneous; they differ from other heterogeneous reactions in that electric current is passing at the solid–liquid interface. Similar to other heterogeneous reactions, a boundary layer also exists at the interface of the electrode and as a result, diffusion processes may be superimposed on the electrode process. For example, the discharge of hydrogen ions at the cathode may be represented by the following steps:

- Diffusion of ions through the boundary layer,
- Dehydration of the ions,
- Discharge of the ions,
- Formation of hydrogen molecules,
- Desorption of gaseous hydrogen from the electrode,
- Diffusion of hydrogen away from the electrode.

Any one of these stages may be the rate-determining step. Since the first and last steps are diffusion processes, therefore like any heterogeneous reaction, an electrode process may be diffusion-controlled, chemically controlled, or intermediate-controlled.

4.1. Types

Consider a solid–liquid reaction (Figure 2) in which the solid is a plate of surface area A, and the concentration of the reagent is C, its concentration at the interface, C_i, and the thickness of the boundary layer δ. Three cases are possible:

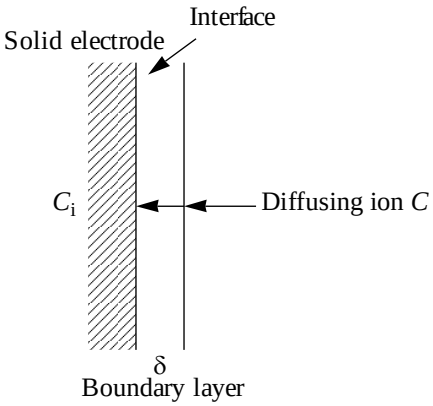

Figure 2. Electrode processes.

Diffusion-controlled

When the rate of chemical reaction at the interface is much faster than the rate of diffusion of reactants to the interface, then $C_i = 0$. These reactions are therefore called diffusion-controlled reactions:

$$\text{Rate} = \frac{D}{\delta} A(C - C_i),$$

where D is the diffusion coefficient, δ is the thickness of the boundary layer, and A the surface area of the electrode exposed to the electrolyte.

Chemically controlled

When the rate of chemical reaction is much slower than the rate of diffusion then the process will be chemically controlled:

$$\text{Rate} = k_2 A C_i^n,$$

where n is the order of reaction.

Intermediate-control

When both rates are of the same magnitude the process is intermediate control; this is the general case. In this case a concentration gradient is formed across the boundary layer, i.e., $C_i \neq 0$:

$$\text{Rate} = k_1 A(C - C_i) = k_2 A C_i^n.$$

Assuming $n = 1$, therefore:

$$k_1 A(C - C_i) = k_2 A C_i^n,$$

$$C_i = \frac{k_1}{k_1 + k_2} C .$$

Substituting the value of C_i in the above equation:

$$\text{Rate} = \frac{k_1}{k_1 + k_2} AC = kAC ,$$

where

$$k = \frac{k_1}{k_1 + k_2} .$$

If $k_1 < k_2$, then $k = k_1 = D/\delta$, i e., the process is diffusion-controlled. If $k_2 < k_1$, then $k = k_2$, i.e., the process is chemically controlled.

4.2. Deposition of metals

The rate of metal deposition, according to Faraday's laws, depends only on the current applied and not on other factors such as temperature, concentration, etc. The character of metal deposit is, however, a direct function of these factors. Metal deposits are always crystalline, but they vary from large-grained coarse adherent deposits to fine-grained loosely adhering powder. The form of the deposit depends on many factors. Two processes are taking place during electrodeposition:

- Nucleation,
- Crystal growth.

When the rate of nucleation is much larger than the rate of crystal growth, the product will be fine powder. On the other hand, when the rate of crystal growth is much larger than the rate of nucleation, the product will be coarse-grained. When C_i, the concentration of metal ion at the interface, tends to zero, i.e., when the process becomes diffusion-controlled, the rate of nucleation becomes much greater than the rate of crystal growth, thus favoring the deposition of powders. In other words powder formation occurs when the electrode process is diffusion-controlled and coarse grain deposits occur when the process is chemically controlled. The following factors influence the value of C_i and therefore influence the nature of metal deposited:

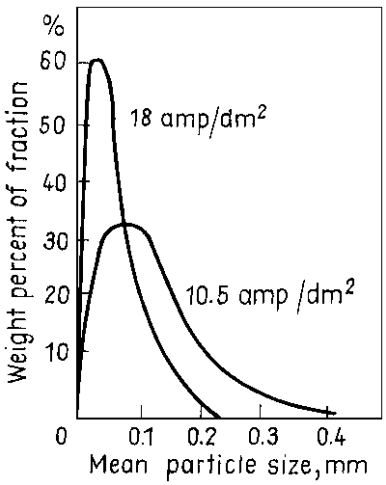

Figure 3. Effect of current density on particle size of copper powder.

● ***Current density.*** At low current density, the discharge of ions is slow, i.e., the process is chemically controlled. The rate of crystal growth is much greater than the rate of nucleation. Therefore the product will be a coarse deposit. At high current density, the opposite is true. Figure 3 shows the effect of current density on particle size distribution. It can be seen that at 10.5 A / dm^2 the most common particle size of electrodeposited copper powder is 0.1 mm while at 18 A / dm^2 it is only 0.05 mm.

● ***Concentration of electrolyte.*** At low electrolyte concentration, the rate of diffusion is slow and usually governs the whole process, i.e., the process becomes diffusion-controlled and powder formation is favored. The opposite is true at high electrolyte concentration. Table 3 shows that the more dilute the electrolyte the more fine particles of the metal are electrodeposited.

Table 3. Effect of electrolyte concentration on particle size of copper powder.

$[Cu^{2+}]$, g / L	Apparent density of powder, g / cc	Particle size analysis, %	
		< 74 μm	< 44 μm
5	0.420	82.3	62.4
10	0.663	68.2	33.9
20	0.776	66.9	32.8
30	1.060	59.0	25.1
40	2.040	47.7	21.0
45	2.440	29.2	11.8

● ***Temperature.*** Increasing the temperature increase the rate of diffusion and the rate of crystal growth. Both factors favor the formation of coarse deposits. Therefore increasing the temperature results in the formation of coarse deposits.

● *Stirring of bath.* The higher the speed of stirring, the coarser the deposited particles (Table 4), because under these conditions, the thickness of the boundary layer is decreased, resulting in an increased rate of diffusion. The process becomes chemically controlled.

Table 4. Effect of speed of stirring on particle size of copper powder.

Speed of stirring, rpm	Percentage of fraction			
	160 – 140 μm	112 – 160 μm	80 – 112 μm	< 80 μm
300	9.7	12.2	35.6	40.5
600	21.6	16.2	27.4	41.5
900	23.3	18.8	31.5	24.5
1 500	46.6	15.2	14.5	16.6
2 200	43.0	18.9	20.6	14.8

● ***The presence of an indifferent electrolyte.*** An indifferent electrolyte does not react at the cathode but decreases the transference number of the cation deposited. A decrease in the transference number will decrease the diffusion process to such an extent that it becomes rate-controlling, thus favoring powder formation.

● ***Presence of colloidal substances in electrolyte.*** Small additions of gelatin, agar, glue, gums, peptones, sugars, etc., result in the formation of a smooth fine-grained deposit. If, however, the concentration of such colloids exceeds about 0.05 g / liter, a loose deposit is obtained. The reason is that such colloids are adsorbed on the nuclei of metal crystals, thus preventing their growth, and the ions are compelled to start new nuclei.

The previous discussion is simplified only because usually side reactions are superimposed. For example, when the conditions are already favorable for powder deposition, and when the process has progressed for some time, the effective surface area of the cathode increases, resulting in a decreased current density. Consequently, the conditions may be shifted toward coarse-grain deposition. Also, the nature of the electrolyte may affect the type of deposit. For example, lead deposited from nitrate solution is rough, while from silicofluoride solution it is smooth. Silver deposited from nitrate solution is coarse, while from cyanide solution it is smooth. Thus the complexing state of metal ion in solution plays an important role. In the case of silver, the free Ag^+ ions are extremely small due to the equilibrium:

$Ag^+ + 2CN^- \leftrightarrows [Ag(CN)_2]^-$.

No powder is formed, but an extremely smooth and bright deposit is obtained instead.

If during deposition, hydrogen is evolved, the solution at the immediate vicinity of the interface will be depleted of H^+ ions thus becoming alkaline and causing precipitation of colloidal hydroxides. This may inhibit crystal growth, thus favoring powder formation. On the other hand, the stirring action due to hydrogen bubble movements may favor the production of large grain size deposits. While powders are formed at low electrolyte concentrations and low temperature, sponge formation is favored at low electrolyte concentration and high temperature.

4.3. Diffusion-controlled processes

As a result of the discharge process at the cathode, the concentration of the metal ion is decreased at the interface. This loss is compensated by diffusion of a fresh supply of metal ions from the body of the solution. The rate of diffusion is given by:

$$\text{Rate of diffusion} = \frac{D}{\delta} A(C - C_i) .$$

The rate of discharge of the ions by the current is given by:

$$\text{Rate of discharge} = \frac{I}{nF} .$$

At the steady state, the two rates are equal, i.e.:

$$\frac{I}{nF} = \frac{D}{\delta} A(C - C_i)$$

or

$$I = \frac{nFDA}{\delta}(C - C_i) .$$

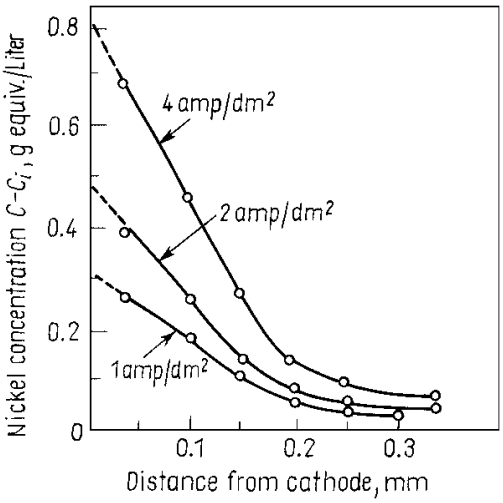

Figure 4. Concentration of nickel on the cathode diffusion layer at different current densities. $I/A = (C - C_i)\, nFD/\delta$, i.e., when I/A increases, $C - C_i$ increases (hence C_i will decrease).

● With increasing current density, I/A, the value $C - C_i$ should increase, since the metal ions at the interface, C_i, will be rapidly depleted. This is verified in Figure 4 for nickel deposition. At 1 A / dm^2, $C - C_i$ is 0.3 g equivalent / 1 while at 4 A / dm^2 it is 0.8.

● At constant current density, when the electrolyte is stirred, thus decreasing the thickness of the boundary layer, δ, the difference $C - C_i$ should decrease, i.e., C_i increases. This is verified in Figure 5 for copper deposition; for a stationary cathode $C_i = 43.5$ g / L while for a rotating cathode $C_i = 47$ g/ L.

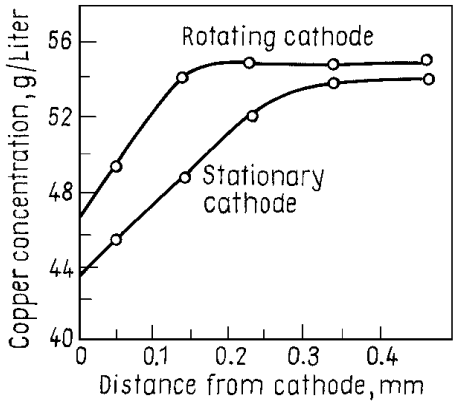

Figure 5. Effect of stirring on copper concentration of the cathode interface. $I/A = (C - C_i)\, nFD/\delta$, i.e., for rotating electrode, δ decreases, hence $C - C_i$, therefore, C_i, increases.

In electrolytic deposition of metals, vertical cathodes are usually used. The depleted solution at the cathode interface, being of lower density than the body of the bath, is forced upward by the more dense solution. Thus, along with the horizontal flow of solution toward the cathode, there also occurs a vertical flow. The convection currents in the vicinity of the cathode, therefore, have both a horizontal and a vertical component.

Optical methods, among others, have been used for studying the diffusion layer. These are based on making the diffusion layer visible and having a color different from that of the body of the bath. For example, when a platinum wire is made anode in a solution containing both potassium iodide and sodium thiosulfate, the thiosulfate prevents the body of the bath from being colored by the iodine liberated electrolytically. A dark anode diffusion layer can therefore be observed due to the iodine when the current passes. It forms more rapidly than it dissipates. When the circuit is broken, the layer gradually disappears. Interferometric method is based on the difference in the refractive index of the solution at the cathode–electrolyte interface and that in the body of the bath. In another method, when a beam of light is passed to a cathode, it's bending from the less dense solution at the interface toward the body of the bath yields a shadow, the width of which is indicative of the thickness of the cathode diffusion layer.

5. Electrolytic reduction

In electrolytic reduction, the basic reaction is the discharge of a metal ion in an aqueous solution or a fused salt at the surface of a cathode:

$M^{n+} + n\,e^- \rightarrow M$.

5.1. The cathode

● ***Inert solid.*** In this case, it may be either the same metal as that to be deposited or a different metal. For example, copper is usually deposited on thin sheets of pure copper cathodes, while zinc is usually deposited on cathodes made of a lead alloy. In the first case, when the cathode is removed from the bath, it is simply washed and melted. In the second case, the deposited metal must be stripped off the cathode before melting; the cathode will be again ready for re-use.

● ***Molten pool of the metal to be deposited.*** This takes place when the process is conducted in a fused salt and the metal to be deposited has a low melting point, e.g., aluminum. In this case, the deposited molten metal is removed periodically from the cell by siphoning into an evacuated reservoir.

● ***Mercury.*** This type of cathode is used when it is not possible to deposit the metal on a solid cathode from an aqueous solution, e.g., metallic sodium. The deposited metal may be recovered from the amalgam by distilling off the mercury under vacuum.

5.2. The anode

● ***Inert solid.*** In this case, it should be able to withstand the discharge of a gas like oxygen or chlorine at its surface without disintegration.

● ***Consumable solid.*** In this case, it reacts electrochemically with the discharging ion. Thus, the carbon anode in the electrolytic cell for aluminum production reacts with the oxide ion in the fused bath forming carbon dioxide:

$2O^{2-} + C \rightarrow CO_2 + 4e^-$.

This type of anode is used when no suitable inert material is available. Research, however, is under way to develop such inert anode.

6. Anodic oxidation

In anodic oxidation, an impure metal, an amalgam, or a sulfide are made anodes in a cell containing an aqueous or a fused salt electrolyte. On passing the electric current, decomposition of the anode takes place, forming metal ions in solution according to:

$M_{(impure)} \rightarrow M^{n+} + ne^-$,

$M_{(Hg)} \rightarrow M^{n+} + Hg + ne^-$,

$MS \rightarrow M^{2+} + S + 2e^-$.

The metal ions then migrate to the cathode where they discharge as a pure metal leaving behind the impurities in the cell, either in solution or as an insoluble deposit at the bottom of the cell. In the case of sulfides, elemental sulfur remains adhering at the anode, which can be separated and recovered.

Processes using inert electrodes are usually called ***electrowinning*** processes while those using consumable electrodes are called electrolytic refining or simply ***electrorefining***. Electrolytic reduction processes using consumable electrodes, for example, aluminum production and anodic oxidation processes using consumable anode, for example, metal sulfide are however considered recovery processes.

Mercury is usually used as a cathode when the wanted metal cannot be deposited on a solid cathode from an aqueous solution, due to the reactive nature of the metal. For example, the electrodeposition of metallic sodium from brine solution is only possible when a mercury cathode is used since electrodeposited sodium dissolves in the mercury, forming an amalgam.

7. Electrolytic reactions in aqueous media

Aqueous solutions are the most convenient and the easiest to handle electrolytes. They usually have high electrical conductivity and low vapor pressure. They are usually utilized at room temperature or slightly above (40 – 60 °C) and in general represent no hazard during handling. The most important properties that determine whether a metal can be deposited from aqueous solution are the following:

7.1. Discharge of ions

● The application of electrical potential causes the ions in an electrolyte to move, the positive ions in the direction of the current and the negative ions in the opposite direction. Also, the applied potential causes the movement of electrons from the anode to the cathode outside the cell. The flow of electrons is thus accompanied by a removal of electrons from the anode and their transfer through the connecting wire to the cathode. The supply of electrons at the anode is provided by the negatively charged anions, while the same number of electrons at the cathode are removed by the positively charged cations. Examples of anodic reactions are the following:

$2Cl^- \rightarrow Cl_2 + 2e^-$,

$2OH^- \rightarrow H_2O + {}^1/_2O_2 + 2e^-$.

Examples of cathodic reactions are the following:

$Cu^{2+} + 2e^- \rightarrow Cu$,

$2H^+ + 2e^- \rightarrow H_2$.

● Some anions, however, such as sulfate and nitrate are not discharged from aqueous solutions. In such cases, other processes accompanied by the removal of electrons take place at the anode. One of these, is the removal of electrons from the atoms of the metal constituting the anode. The atoms are thus converted into the corresponding positively charged cations which pass into solution, i.e., the anode is solubilized:

$M \rightarrow M^{n+} + ne^{-}$.

The ions carrying the current are not necessarily the ones discharged at the anode or the cathode. The discharge of an ion is determined by the reversible potential of that particular ion in the given solution. In a sulfuric acid solution of copper sulfate, for example, the current is carried toward the anode almost exclusively by sulfate ions, and toward the cathode largely by hydrogen ions and to some extent by cupric ions. Nevertheless, cupric ions only are discharged at the cathode, while at an insoluble anode such as platinum, hydroxyl ions are discharged, although they play a negligible part in the carriage of current and they are present in extremely low concentration. The reason is that hydroxyl ions have the higher oxidation potential.

● If an electrolyte contains a number of different positive and negative ions then each ionic discharge will take place as the appropriate potential is reached. The cations that are discharged most readily are those having the largest reduction potential, which corresponds to the smallest oxidation potential. Hence, the lower the oxidation potential, the more easily will the metallic ion is discharged. This means that for solutions of approximately equivalent ionic concentrations, metals lower in Table 5 will be deposited before those higher in the table. Consider, for example, the electrolysis of a solution containing molar amounts of zinc and copper sulfates. The oxidation potentials of the respective metals in these solutions are + 0.76 and – 0.34 volt, respectively. It follows, therefore, that the cupric ions will be discharged first and metallic copper will be deposited. If the electrolysis is prolonged to such an extent that the copper ions in the solution are almost exhausted, the cathode potential will increase until that for zinc deposition is attained.

● If two metals have potentials that are not very different in the particular electrolyte then simultaneous deposition of both metals occurs in the form of an alloy. Such is the case, for example, for copper and zinc in a solution containing their complex cyanides. Although the potentials of these metals differ considerably in sulfate solutions, the ionic concentrations are so changed in the complex cyanide solutions as to bring their respective potentials close together. When these solutions are electrolyzed, an alloy of zinc and copper, i.e., brass is deposited on the cathode. Other alloys can be obtained in an analogous manner.

● The behavior at an anode is, in general, analogous to that at a cathode. The process associated with the largest negative free energy change whether it be solution of metallic anode to form cations or the discharge of anions, will take place first. The reaction taking place at the anode is always an oxidation, and so anodic processes take place in order of decreasing oxidation potential since ΔF is equal to $-nFE$. For solutions of approximately the same ionic concentration, the order of anodic processes is that of the potentials in Table 5. The higher the process in this table, the more easily does it occur at an anode. For example, if a copper electrode is placed in an acid solution of 1 M $CuSO_4$, three anodic processes are possible:

– Dissolution of copper to form cupric ions at a potential of – 0.34 volt.

– Discharge of hydroxyl ions at about – 1.2 volts.

– Discharge of sulfate ions probably at a very high negative potential, e.g., about – 2 volts.

Table 5. The electrochemical series of metals.

Group	Metals
reactive metals	lithium potassium calcium sodium lanthanum cerium magnesium yttrium scandium thorium beryllium uranium hafnium aluminum titanium zirconium manganese vanadium chromium
less reactive metals	zinc gallium iron cadmium indium thallium cobalt nickel tin lead
	hydrogen
least reactive metals (noble)	copper mercury silver gold platinum group metals

It is evident, therefore, that when an external EMF is applied to the copper anode, the first process to occur will be that of the anode passing into solution as cupric ions since the reaction

$Cu \rightarrow Cu^{2+} + 2e^{-}$

has the highest oxidation potential. The next possible process is the discharge of hydroxyl ions, but this will not occur unless for some reason the solution of the anode is prevented. At an insoluble anode such as platinum, hydroxyl ions would be discharged and oxygen evolved. The discharge of SO_4^{2-} ions is highly improbable.

7.2. Electrode potential

Metals having deposition potentials very much less noble than hydrogen cannot be deposited, because hydrogen is discharged preferentially and the cathode potential required for their deposition cannot be attained. Thus reactive metals, like sodium or calcium, cannot be deposited. It is true that due to the phenomenon of overpotential, hydrogen does not discharge on many metals until the cathode potential is several tenths of a volt less noble than the reversible potential of hydrogen. That is why, for example, the deposition of zinc or manganese is possible from an aqueous medium although they are deposited at about 0.5 volt more negative (less noble) than the equilibrium potential of hydrogen. However, many metals are apparently so much less noble than hydrogen that even the resistance of hydrogen overvoltage does not suffice to enable their deposition potentials to be attained.

7.3. Ionic size

When ions are extremely small, which is also usually associated with a large positive charge, they are excessively hydrated. Dehydration prior to neutralization of the charge at the cathode may be an extremely slow step, so that hydrolysis, instead, takes place, resulting in the precipitation of the hydroxide instead of the metal. For this reason, beryllium and aluminum, for example, cannot be deposited from aqueous solutions. It is therefore apparent that the exclusion of water from such an electrolytic system may result in better chances for metal deposition. Non-aqueous electrolytes usually have low conductivity and are sometimes hazardous to handle; that is why they are not commonly used in metallurgy. Fused salts are more difficult to handle and, therefore, they are used only when aqueous electrolytes cannot be used.

8. Electrolytic reactions in fused salts

Electrometallurgical reactions involving fused salts as electrolytes must be maintained at high temperature and in the absence of moisture. Different types of electrolytes are used. The guidelines for choosing an electrolyte are: low melting point, low vapor pressure, high electrical conductivity, low corrosive action, low viscosity, and low surface tension. Salts satisfying these requirements are usually the fluorides and the chlorides, or sometimes a mixture of the two. A mixture of two or more fluorides, two or more chlorides, or a fluoride and chloride always has a melting point and a vapor pressure lower than that of the individual salt at the same temperature. In conducting reactions of this type, the following points should be taken into consideration:

- The cathode is usually a molten pool of the metal to be recovered because of its low melting point. If the melting point of the metal to be deposited is high, then provision must be

made to deposit it at a solid cathode. This will be more difficult from the engineering point of view (for example, separating the deposited metal from the electrolyte) but has been realized, for example, for the electrowinning of beryllium from beryllium chloride–sodium chloride eutectic. Electrowinning from fused salts can be made continuously only when the metal electrodeposited at the cathode is in the molten state.

● Temperature in the cell is usually maintained by resistive heating, for example, by an increase in the electrode spacing.

● Solubility of the metal in the electrolyte at the elevated temperature is often a source of inefficiency.

The metal to be recovered may be present in the electrolyte in any of the following forms:

● A salt that is one of the components of the electrolyte. For example, aluminum may be recovered by electrolyzing an aluminum chloride–sodium chloride eutectic:

$Al^{3+} + 3e^- \rightarrow Al$,

$2Cl^- \rightarrow Cl_2$.

Similarly, the production of magnesium from magnesium chloride–calcium chloride eutectic.

● An oxide that goes into solution in the electrolyte. For example, the production of aluminum by the electrolytic reduction of aluminum oxide dissolved in a fused cryolite (Na_3AlF_6) bath. As a result of the dissociation of aluminum oxide, then during electrolysis, aluminum ion is carried to the cathode, where it is discharged and collected in a pool of metal while the oxide ion is carried to the anode, where it reacts to form carbon monoxide and carbon dioxide:

$Al^{3+} + 3e^- \rightarrow Al$,

$O^{2-} + C \rightarrow CO + 2e^-$,

$2O^{2-} + C \rightarrow CO_2 + 2e^-$.

A modern cell for the production of aluminum is shown in Figure 6.

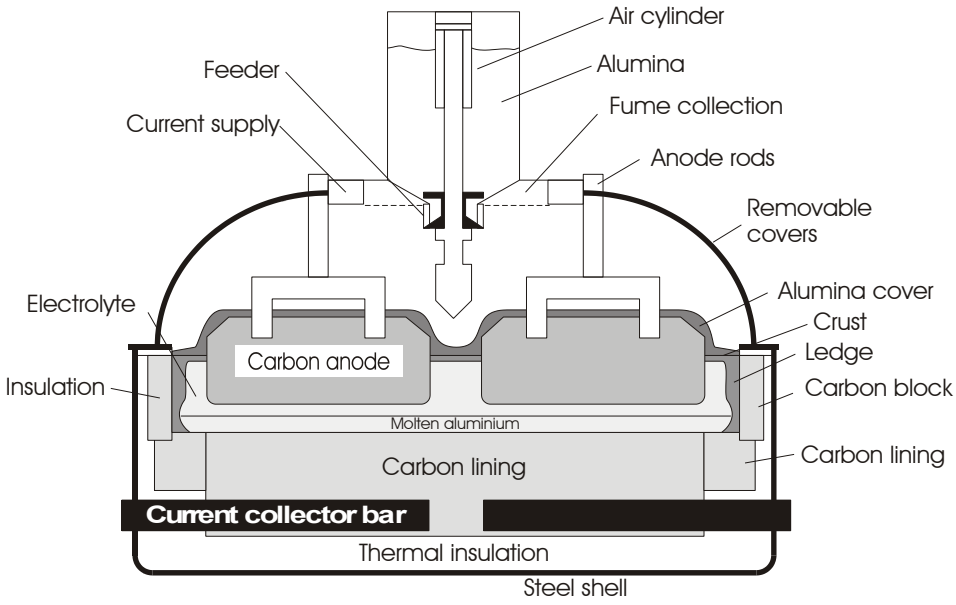

Figure 6. A modern cell for the production of aluminum.

9. Engineering aspects

Transforming a carbonaceous fuel into an electrical energy is a process with only 37% efficiency. In spite of that, the use of electrical energy in metallurgy is still economical as compared to some pyrometallurgical operations. Electrowinning and electrorefining operations are conducted for a large variety of metals. Electrolytic production of aluminum became the largest electrochemical operation worldwide with about 50 million tons produced annually by this route. Electrowinning of zinc surpassed the tonnage by the pyrometallurgical route. Electrometallurgy is also being preferred to other routes, e.g., solvent extraction–electrowinning of copper has now displaced the cementation route. Electrorefining of copper has been perfected during its 150 years operation, and new other electrometallurgical processes are being introduced.

Electrometallurgical processes, however, are capital intensive processes. Electrowinning and electrorefining in aqueous solutions require a large space (Figure 7). The tank house in electrorefining contains a large inventory in form of anodes and electrolyte, hence, the operation requires a large capital investment. Operating cost is also high because of the large number of electrodes that are involved. For example, in a large copper refinery producing ~ 500 tons of copper per day, about 2 000 new anodes, 2 000 spent anodes, 4 000 starter sheets, and 4 000 finished cathodes must be handled every day. A floor area of about 6 000 m^2 will be required.

Figure 7. View of a typical electrolytic plant.

Provisions must be made for:

- Continuous supply of fresh electrolyte.
- Continuous withdrawal of the spent electrolyte.
- Supply of electrical energy to cathodes and anodes.
- Periodic supply of new cathodes.
- Periodic removal of finished cathodes.
- Periodic supply of soluble anodes.

● Periodic removal of spent anodes (anode scrap).

● Periodic removal of anodic slimes.

Although direct current is necessary for many industrial purposes such as electrolytic processes and for many motor applications such as for rolling mills, elevators, etc., at least 95 % of the electrical energy is generated as alternating current. This is because alternating current generators can be built in large units and generates energy at high voltage. When the voltage is high the current can be low, which means small losses. Hence, they are economical and efficient. That is why it is more economical to generate power in bulk as alternating current, transmit it, and then convert it to direct current when it is needed through transformers and amplifiers.

9.1. Electrowinning versus electrorefining

Energy requirement for an electrowinning operation is intensive while for electrorefining it is negligible. For the electrowinning of a divalent metal M from H_2SO_4 solution:

Anodic reaction: $H_2O \rightarrow O_2 + 2H^+ + 2e^-$ $\quad E^\circ = x$,

Cathodic reaction: $M^{2+} + 2e^- \rightarrow M$ $\quad E^\circ = y$,

Total potential $= x + y$.

For the electrorefining of the same metal:

Anodic reaction: $M \rightarrow M^{2+} + 2e^-$ $\quad E^\circ = y$,

Cathodic reaction: $M^{2+} + 2e^- \rightarrow M$ $\quad E^\circ = -y$,

Total potential = 0.

In electrorefining, the energy is mainly consumed in solubilizing the impurities and in both cases energy is also consumed due to the resistance in the electrolyte.

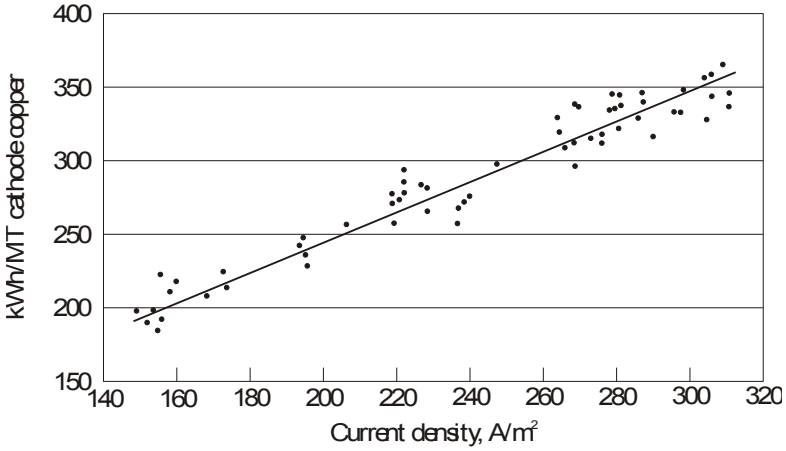

Figure 8. Power consumption vs. current density for copper electrolysis.

9.2. Productivity and energy requirement

Cell design is dictated by two factors: productivity and cell voltage. Increased current density increases the productivity which is highly desirable because of lower capital investment per ton of metal produced. However, there are drawbacks:

● Lower quality of cathodic product as a result of increased operating potential, i.e., increased number of secondary reactions causing the possible deposition of impurities.

● Decreased current efficiency as a result of the secondary reactions, e.g., anode passivity.

● Increased operating potential, i.e., increased electrical energy consumption (Figure 8).

Hence, a compromise should be made between these factors.

9.3. Cell design and electrical circuits

There are a large variety of cells used industrially. The cell design depends on a number of factors:

● The electrolyte whether aqueous or fused salt.

● Electrical conductivity of $CuSO_4$ solution in different H_2SO_4 acid concentrations.

● The cathode whether liquid or solid.

● The process itself whether electrowinning or electrorefining.

While some generalizations can be made regarding cell design in electrowinning and electrorefining in aqueous solutions, other cells vary widely. Electrolytic cells for most of these applications are nearly the same: The anodes and cathodes are suspended vertically facing each others. In case of nickel a special precaution is made in introducing the feed electrolyte to avoid contamination by impurities. In gold and silver refining, horizontally laid electrodes are used because the refined metal is recovered in a powder form.

In fused salts, the situation is different because the metal deposited at the cathode may be a liquid which may be lighter or heavier than the electrolyte. As a result, the cell design is more complex and depends on each particular case as will be shown later in the proper place. The production of aluminum is again different from other fused salt operations because the anodes are consumable.

9.4. Current density

Current density is the current supplied to a cell per unit area of electrode — hence there are anodic and cathodic current densities. They need not be equal. Further, in processes conducted in aqueous solutions, current densities are usually 100 – 200 A / m^2 while in fused salts 10 000 – 15 000 A / m^2. The increased current density in fused salts is due to the increased conductivity at high temperature. Current density represents the rate at which an electrolytic reaction takes place schematic of a copper busbar.

9.5. Anodes

Figure 9 shows a summary of the anodes generally used. Insoluble anodes for electrowinning must resist the attack of gases evolved at the anode:

● Graphite is cheap and resists chlorine but not oxygen.

● Lead containing a small amount of silver is expensive and must be used when oxygen is evolved.

Soluble anodes for electrorefining are prepared either in the casting wheel or by continuous casting. Both methods are continuous.

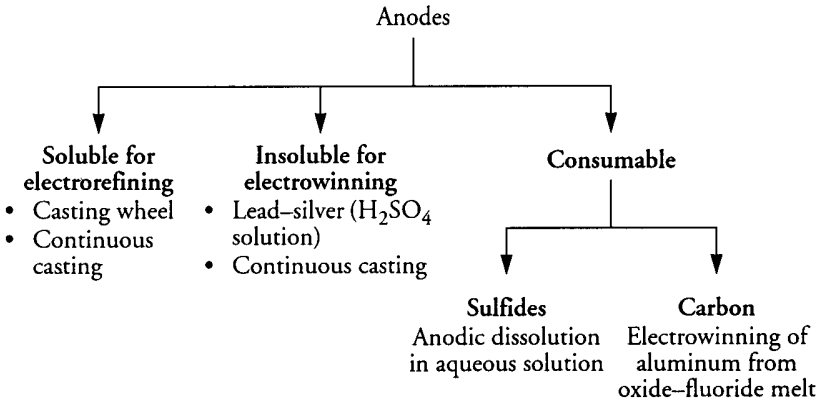

Figure 9. Anode systems.

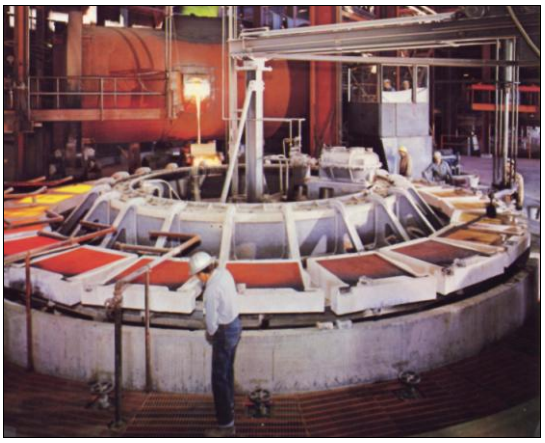

Figure 10. Anode-casting machine.

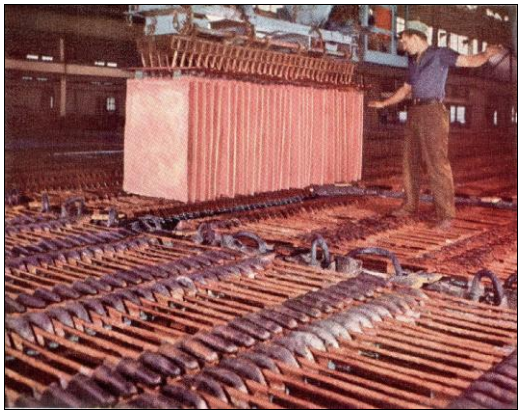

Figure 11. Anodes handling system.

Casting wheel

A typical anode-casting machine is a rotating table with 24 horizontal molds placed around its perimeter (Figure 10). The wheel slowly revolves, bringing the molds through a spray of mold wash, allowing them to be filled with molten metal, and then passing through a water-sprayed cooling section.

The solidified anodes are partially lifted in the mold by lifting pins located in the bottom of the mold and subsequently removed by a pickup device. Automatic mold-filling systems are

used so that the molds are filled with a pre-weighed amount of metal for smooth operation during electrolysis. Cast anodes often have imperfections on the surface, i.e., blisters, fins, and edge rims, which can cause shorting with the cathodes. These are usually manually corrected by chipping. Anodes cast from the impure metal are usually 80 – 100 cm wide, 90 – 110 cm long, and 3 – 6 cm thick. Figure 11 shows anodes handling system.

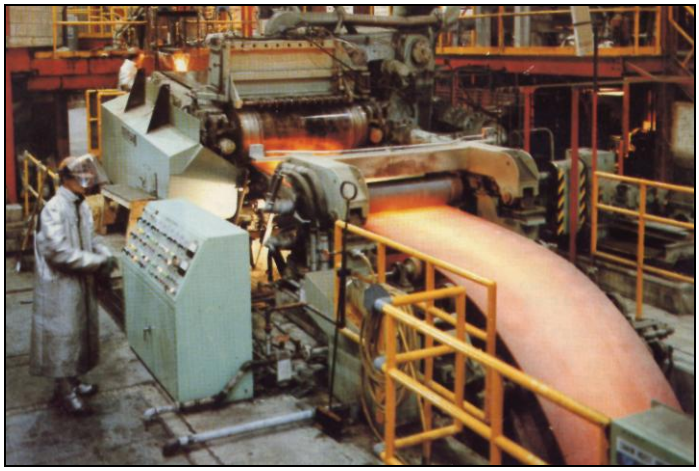

Figure 12. Hazelett machine for manufacturing copper anodes for refining.

Continuous strip casting machine

This is known as the Hazelett machine (Figure 12) and is used principally in copper electrorefining. Molten copper from the anode furnaces is fed into the machine. As it passes between two water-cooled stainless steel belts, it solidifies and emerges as precise strip, 1 150 mm wide and 16 mm thick. The hot copper strip is fed to a large blanking press, where two 145 kg anodes are formed simultaneously.

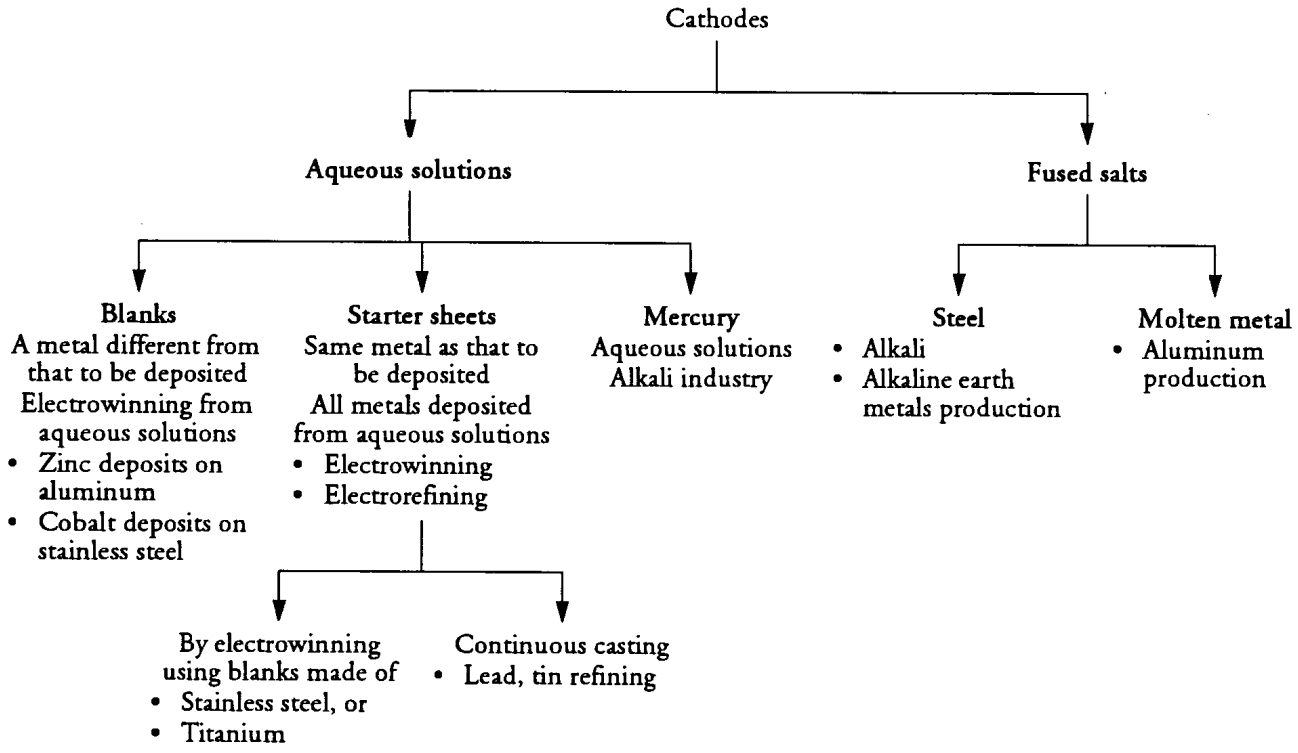

Figure 13. Cathode systems.

9.6. Cathodes

Cathodes may be solid or liquid (Figure 13). Solid cathodes in electrowinning operations from aqueous solutions are two types: blanks or starter sheets. In both cases, when the metal is deposited, the cathodes are washed, then stripped and / or stacked for preparation for melting and casting.

Blanks

These are pieces of metal different from that to be deposited. The deposited metal is then stripped from these blanks, either manually (Figure 14) or mechanically (Figure 15). The stripped metal is then melted and cast in form of ingots, while the blanks are re-used for another deposition. For example, zinc is electrodeposited on blanks made of aluminum, while cobalt on blanks made of stainless steel. To facilitate stripping, the blanks are first covered by a thin layer of oil or anodically polished to maintain a smooth surface.

Figure 14. Manual stripping of zinc cathodes from blanks.

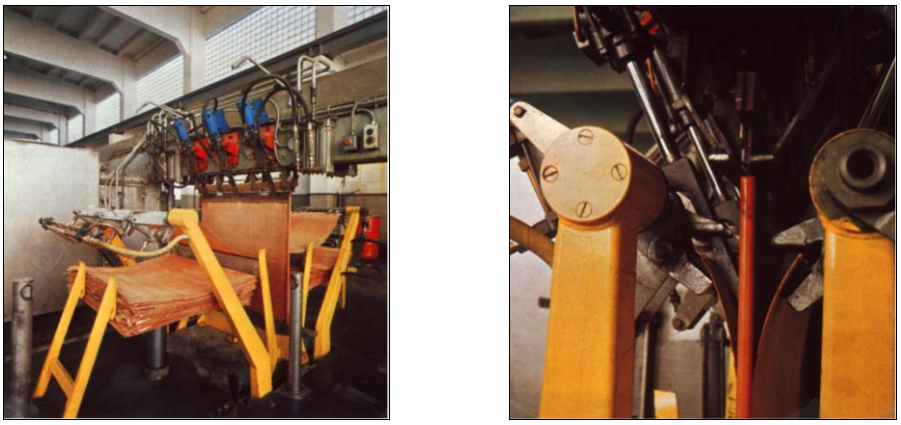

Figure 15. Mechanical stripping machines. Left: general view. Right: details.

Starter sheets

These are made of the same metal as that to be deposited. When deposition is complete, the cathodes are then melted, without stripping, and cast in the desired form for the market. Starter sheets are prepared in two ways:

Electrodeposition on blanks. The starter sheets are prepared by deposition for 1 or 2 days on sheets of the same metal to be deposited or sometimes on stainless steel, or titanium blanks in an independent electrowinning plant operating at a low current density for maximum purity. The blanks are either masked on the edges with cemented plastic strips or have a groove along the edges where the deposit may be easily broken. Starter sheets are stripped from the blanks manually or by various automatic stripping machines. To permit easy stripping the stripper blanks are wetted with a solution of soap, with a water emulsion of mineral oil, or other reagents. Stripped sheets are then processed through a starting sheet machine, where they are straightened, trimmed, suspension loops (with pre-inserted suspension bars) attached by punching, and embossed with a shallow pattern to give them mechanical rigidity.

Continuous casting. Starter sheets used in refining lead and tin are conveniently prepared by the continuous casting of these low-melting point metals, using a water-cooled drum.

Dimensions of solid cathodes are always somewhat larger than anode dimensions so that current density at cathode edges is not excessive. Liquid cathodes may be:

- Mercury, e.g., in the alkali industry, or
- A molten metal, e.g., in the production of aluminum from fused salts.

9.7. Diaphragms

The diaphragm increases the electrical resistance of the electrolyte because of the greater the path of electrolyte within the diaphragm, hence the greater the potential drop across it. An ideal diaphragm must be:

- Permeable to ions but not gas bubbles.
- Of high void fraction to minimize electrical resistance.
- Of small mean pore size to prevent the passage of gas bubbles and minimize diffusion.
- Homogeneous to ensure even current distribution.
- Nonconducting to prevent action as an electrode.
- Chemically resistant to the reactants and products.
- Mechanically strong.

Chemical stability is a constant problem especially if the anolyte is acid and the catholyte alkaline and most diaphragms have a relatively short life requiring frequent renewal. Many scores of materials have been used in the past of which porous concrete, asbestos and asbestos mixtures (all alkaline resistant), ceramics, quartz and fire clay (all acid resistant). Microporous rubber, linen and metal gauzes have also been commercially applied.

9.8. Electrolyte

In refining cells the electrolyte is circulated for the following reasons:

- Adjust the concentrations of the main electrolyte components.
- Maintain a suitable cell temperature.
- Provide a steady supply of reagents.
- Correct electrolyte composition by removing the soluble impurities. This is done by treating a small portion of this recirculation stream.

9.9. Labor cost

Labor costs are one of the highest in the electrorefining operation. Improvements in mechanical handling over the past few years have brought significant reduction in labor costs. Labor is required for:

- Systematic inspection of cells for short-circuiting.
- Preparation of starting sheets.
- Casting of anodes.
- Changing of anodes and cathodes.
- Treatment of slimes.

9.10. Handling of scrap anodes

Scrap anodes are removed from the cell, washed thoroughly to remove anodic slimes and electrolyte, and then transported to the furnace for remelting.

10. Summary

Table 6 gives a summary of electrometallurgical processes.

Table 6. Summary of electrometallurgical processes.

Process	Electrode	Electrolyte	Examples	Remarks
electrolytic reduction	inert electrodes	aqueous	cathodic: $Cu^{2+} + 2e^- \rightarrow Cu$ anodic: $H_2O \rightarrow {}^1/_2O_2 + 2H^+ + 2e^-$	industrial scale; also for An, Ni, Co, Au, Ag, Mn, Cr, Cd, Te.
		fused salt (chloride)	cathodic: $Mg^{2+} + 2e^- \rightarrow Mg$ anodic: $2Cl^- \rightarrow Cl_2 + 2e^-$	industrial scale; also for Be, Na, Li laboratory scale for Al, Ti, Nb, Ta
		fused salt (sulfide)	cathodic: $Pb^{2+} + 2e^- \rightarrow Pb$ anodic: $S^{2-} \rightarrow S^o + 2e^-$	laboratory scale
	consumable electrode	aqueous	cathodic: $Cu_2S + 2e^- \rightarrow 2Cu + S^{2-}$ anodic: $H_2O \rightarrow {}^1/_2O_2 + 2H^+ + 2e^-$	laboratory scale
		fused salt (Al_2O_3 dissolved in cryolite)	cathodic: $Al^{3+} + 3e^- \rightarrow Al$ anodic: $O^{2-} + C \rightarrow CO + 2e^-$	industrial scale
	mercury cathode	aqueous	cathodic: $Na^+ + Hg + e^- \rightarrow Na(Hg)$ anodic: $2Cl^- \rightarrow Cl_2 + 2e^-$	industrial scale; also for Ga
		fused salt (chloride)	cathodic: $Be^{2+} + nHg + 2e^- \rightarrow Be(Hg)_n$ anodic: $2Cl^- \rightarrow Cl_2 + 2e^-$	laboratory scale
anodic oxidation	metal consumable anode	aqueous	anodic: $Cu_{(impure)} \rightarrow Cu^{2+} + 2e^-$ cathodic: $Cu^{2+} + 2e^- \rightarrow Cu^o_{(pure)}$	industrial scale; also for Ni, Co, Pb, Sn, Au, Ag, Sb, Bi, In
		fused salt (fluoride)	anodic: $Al_{(impure)} \rightarrow Al^{3+} + 3e^-$ cathodic: $Al^{3+} + 3e^- \rightarrow Al^o_{(pure)}$	industrial scale
	sulfide consumable anode	aqueous	anodic: $Ni_3S_2 \rightarrow 3Ni^{2+} + 2S^0 + 6e^-$ cathodic: $Ni^{2+} + 2e^- \rightarrow Ni$	industrial scale
	amalgam anode	fused salt (chloride)	anodic: $In(Hg)_n \rightarrow In^{3+} + nHg + 3e^-$ cathodic: $In^{3+} + 3e^- \rightarrow In$	industrial scale

Suggested reading

1. F. Habashi. Principles of Extractive Metallurgy. Volume 4: Amalgam and Electrometallurgy. 1998, Quebec City: Métallurgie Extractive (distributed by Laval University Bookstore, www.zone.ul.ca).

SHORT DICTIONARY ON NANOCHEMISTRY AND NANOTECHNOLOGY. Part I

Ts. Ramishvili, V. Tsitsishvili

Ivane Javakhishvili Tbilisi State University
Petre Melikishvili Institute of Physical & Organic Chemistry
Tbilisi, Georgia
rtsiuri@yahoo.com

Accepted February 16, 2011

Recently many new terms have been created in the rapidly developing fields of science, nanochemistry and nanotechnology, mostly coming from English, and relating to the names of compounds and materials. Table 1 lists some of such terms in English, German, and Russian taken from dictionaries and scientific periodic chemical publications [1-19], and the corresponding terms in Georgian.

Table 1. English, German, Russian, and Georgian terms used in nanochemistry and nanotechnology.

Terms			
in English	**in German**	**in Russian**	**in Georgian**
Actuator Actuators	Aktor m, Aktuator m Aktoren pl, Aktuatoren pl	Актюатор, актуатор Актюаторы, актуаторы	აქტორი აქტორები (ლათ. act – მოქმედება. მოწყობილობა, რომელიც სიგნალის მიხედვით გარკვეულ მოქმედებას ასრულებს ერთი სახის ენერგიის (ელექტრული, მაგნიტური, სითბური, ქიმიური) მეორე სახის ენერგიაში, ძირითადად მექანიკურში გარდაქმნისას)
Armchair SWNT Armchair SWCNT	Achirales, sesselförmiges SWNT Achirales, sesselförmiges SWCNT	Кресельная структура SWNT Кресельная структура SWCNT	SWNT / SWCNT-ის “სავარძლისებრი” სტრუქტურა (ნახშირბადის ნანომილაკის ერთ-ერთი სტრუქტურა)

Atomic force microscopy (AFM), scanning force microscopy (SFM)	Atomkraftmikroskopie (AFM) f Rasterkraftmikroskopie (RKM) f	Атомно-силовая микроскопия (АСМ)	ატომურ-ძალური / ატომურ ძალთა მიკროსკოპია
Atomic manipulation Atomic manipulations	Atom-Manipulation f Atom-Manipulationen pl	Манипуляция атомами Манипуляции атомами	მანიპულირება ატომებით მანიპულირებები ატომებით (ცალკეული ატომებით მანიპულირების იდეა ეკუთვნის Richard Feynman-ს, ამერიკელ მეცნიერს, ნანომეცნიერების ფუძემდებელს. ზედაპირზე გადაადგილებით ატომების და მოლეკულების მიმართული გადანაცვლება და დაფიქსირება, რითაც შესაძლებელია მოწესრიგებული ნანოსტრუქტურების აწყობა, პირველად განხორციელდა D. Eigler-ის მიერ 1989 წ. მან Ni -ის მონოკრისტალის ზედაპირზე მოათავსა ქსენონის 35 ატომი კომპანია IBM-ის ლოგოტიპის ფორმით და ამისთვის გამოიყენა მასკანირებელი ტუნელური მიკროსკოპიის მეთოდი; ამ მიზნებისთვის აგრეთვე იყენებენ ლაზერულ “ხაფანგს” – ოპტიკურ პინცეტს)
Atomic / scanning force microscope (Atomic force microscope or scanning force microscope)	Atomkraftmikroskop n Rasterkraftmikroskop n	Атомно-силовой микроскоп	ატომურ-ძალური / ატომურ ძალთა მიკროსკოპი, მასკანირებელი ძალური მიკროსკოპი

Azafulleroids	Azafulleroide n pl	Азафуллероиды	აზაფულეროიდები
Band gap	Bandlücke f	Щель энергетическая	ენერგეტიკული ღრეჩო
Bingel reaction	Bingel-Reaktion f	Бингеля реакция	ბინგელის რეაქცია (ფულერენების ციკლოპროპანირების რეაქცია)
Biomimetic nanomaterials, bioinspired nanomaterials	Biomimetische Nanomaterialien n pl	Биомиметические наноматериалы	ბიომიმეტიკური მასალები (ხელოვნური ნანომასალები, შექმნილი ცოცხალ ბუნებაში რეალიზებული პრინციპების საფუძველზე ან ბიომასალების თვისებების მიბაძვით; მაგ., მწებავი მასალა Velcro შეიქმნა მცენარე ბირკას ნაყოფის კაკვების მსგავსად, რომლებსაც შეუძლია ქსოვილზე ან ბეწვზე გამოდება, მიწებება)
Biomimetics, bionics, biomimicry, bio-inspiration, biognosis, bionical creativity engineering	Biomimetik f Biomimese f Bionik f Biomimikry	Биомиметика Бионика Биомимикрия	ბიომიმეტიკა ბიომიმეზია ბიონიკა ბიომიმიკრია (ბერძნ. bios – სიცოცხლე, mimesis – მიბაძვა)
Bionanotechnology	Bionanotechnologie f	Бионанотехнология	ბიონანოტექნოლოგია
Buckminsterfullerene Backy ball	Buckminster-Fulleren n Fußballmolekül n	Бакминстерфуллерен	ბაკმინსტერფულერენი (C_{60}) (სფერული ფულერენების ოჯახის პირველი წევრი, C_{60} მოლეკულისთვის ვან დერ ვაალსის დიამეტრია 1.1 ნმ, ნახშირბადის ატომთა შორის ქიმიური ბმა კოვალენტურია)

Buckyball Bucky ball Carbonballs Carbonspheres Buckyballs (spherical fullerenes)	Buckyball m Hohle Kohlenstoff-kugel f Kohlenstoffkugeln pl	Бакисфера Бакиболы, букиболы	ბაკიბურთი (C_{60}) ბაკიბურთები (სფერული ფულერენები)
Buckypaper	Buckypapier n	Бумага повышенной упругости (Бакибумага)	ბაკიქაღალდი (ნახშირბადის ნანომილაკებისაგან დამზადებული მაღალი დრეკადობის ქაღალდი, რომელიც ფოლადზე ათჯერ უფრო მსუბუქი და 500-ჯერ უფრო მტკიცეა, ატარებს დენს და სითბოს)
Cantilever	Cantilever f Messspitze f Freitagenderausleger m Freiträger m Kragträger m Kragbalker m Klagarm m	Кантилевер, консольная балка	კანტილევერი (ინგლ. “Cantilever” – ბრჯენი. კანტილევერი (კ) მასკანირებელი ზონდური მიკროსკოპის (მ.ზ.მ.) ერთ-ერთი ძირითადი ნაწილია; ის მიკროზომების ამწეს ჰგავს, რომლის კოჭი – საკუთრივ კ, შესაბამისად 0.03 და 0.1 – 0.5 ნმ სისქის და სიგანისაა და ღუნვადია; მ.ზ.მ.-ში კ-ით ხდება საკვლევი ზედაპირის და მასზე განლაგებული მოლეკულების “მოსინჯვა”, რამდენიმე ნანომეტრის მანძილზე მათი მექანიკური გადაადგილება და ქიმიური ცდების ჩატარებაც კი. ნანოპოზიციონირების სისტემით კ-ის წვეროში მოთავსებული ნემსი-ზონდი ზედაპირზე მოძრაობისას არ ერჭობა მასში, არამედ იღუნება მისი სირბილის გამო; კ-ის გადახრის სიდიდე ან რხევების სიხშირე განისაზღვრება მისი ურთიერთქმედების ძალით ნიმუშის ზედაპირზე არსებულ ატომებსა და მოლეკულებთან. ზონდი მზადდება Si-, Si_3N_4-, ალმასისგან ლითოგრაფიულად ან ქიმიური და ფიზიკური ამოჭმით)

Carbon fibre (fiber) Carbon fibres (fibers), carbon filaments (CF)	Kohlenfaser f Kohlenstofffaser f Carbonfaser f Carbon-Fasern pl Kohlenstofffasern pl Kohlefasern pl	Углеволокно Волокно углеродное Углеволокна Волокна углеродные	ნახშირბადის ბოჭკო ნახშირბადის ბოჭკოები
Carbon nanobud (CNB) Carbon nanobuds (CNBs)	Kohlenstoff-nanobud m Carbon nanobud (CNB) Kohlenstoff-nanobuds pl Carbon Nanobuds pl (CNBs) Carbon NanoBuds pl	Углеродный наноросток Углеродные наноростки	ნახშირბადის ნანოკვირტი (ნანოღივი) ნახშირბადის ნანოკვირტები (ნანოღივები) (ფულერენის მოლეკულები –“ნანოკვირტები” კოვალენტურად არის შეკავშირებული ერთკედლიანი ნანომილაკის გარე ზედაპირთან)
Carbon nanocone (CNC) Carbon nanocones (CNCs)	Carbon Nanocone m Hohler Kohlenstoff (Carbon) Kegel m Kohlenstoff (Carbon) nanocones pl Hohle Kohlenstoff nanocones pl	Углеродный наноконус Углеродные наноконусы	ნახშირბადის ნანოკონუსი ნახშირბადის ნანოკონუსები
Carbon nanofoam	Kohlenstoffnano-schaum m	Углеродная нанопена	ნახშირბადის ნანოქაფი
Carbon-Nanorods	Carbon-Stäbchen n pl	Углеродные наностержни	ნახშირბადის ნანოღეროები
Carbon nanotube (CNT), tubulene, buckytube, tubular fullerene Carbon nanotubes (CNTs), tubulenes, Buckytubes, tubular fullerenes	Kohlenstoffnanoröhre (CNT) f Kohlenstoff-Nanoröhre f Kohlenstoffnano-röhrchen n Kohlenstoffnano-röhren pl Kohlenstoff-Nano-röhrchen pl Kohlenstoffnano-röhrchen pl	Нанотрубка, углеродная (УНТ) Нанотрубки, углеродные (Тубулены) Бакитрубки	ნახშირბადის ნანომილაკი, ტუბულენი, ბაკიმილაკი, მილაკოვანი ფულერენი ნახშირბადის ნანომილაკები, ტუბულენები, ბაკიმილაკები, მილაკოვანი ფულერენები

Carbon nanotube film (CNF) Carbon nanotube films, nanofilms (CNF)	Kohlenstoff-Nanoröhren-Schicht f Kohlenstoff-Nanoröhrchen (Nanoröhren)-Film m Kohlenstoff-Nanoröhren-Schichten pl Kohlenstoff-Nanoröhrchen (Nanoröhren)-Filme, Nanofilme pl	Углеродная наноплёнка Углеродные наноплёнки	ნახშირბადის ნანომილაკის აფსკი ნახშირბადის ნანომილაკის აფსკები (ნანოაფსკები ორგანზომილებიანი ობიექტებია, მათი ზომები 100 ნმ-მდეა)
Carbon nanotube peapod (Nano-peapod) Carbon nanotube peapods (Nano-peapods)	Kohlenstoffnanoröhren Peapod m Carbon Nano Erbsenschote f Kohlenstoffnanoröhren Peapods pl Carbon Nano Erbsenschoten pl	Наноуглеродный стручок Наноуглеродные стручки	ნახშირბადის ნანომილაკის პარკი ნახშირბადის ნანომილაკების პარკები (ფულერენიანი ტუბულენები; ფულერენიანი ნახშირბადის ნანომილაკები) (ნახშირბადის ნანომილაკებში კაფსულირებული ფულერენის ან ლითონფულერენის მოლეკულები)
Chiral SWNT Chiral SWCNT	Chirales SWNT Chirales SWCNT	Хиральная структура SWNT Хиральная структура SWCNT	SWNT / SWCNT-ის “ქირალური” სტრუქტურა (ნახშირბადის ნანომილაკის ერთ-ერთი სტრუქტურა)
Cluster Clusters	Cluster m Cluster pl	Кластер Кластеры	კლასტერი კლასტერები
Colloidal nanoparticle Colloidal nanoparticles	Kolloidnanopartikel f Kolloidnanopartikeln pl	Коллоидная наночастица Коллоидные наночастицы	კოლოიდური ნაწილაკი კოლოიდური ნაწილაკები

Cryochemical synthesis, cryochemical processing, cryoprocessing	Kryochemische Synthese f	Синтез, криохимический	კრიოქიმიური სინთეზი
Cryogel Cryogels	Kryogel n Kryogele pl	Криогель Криогели	კრიოგელი კრიოგელები
Dendrimer Dendrimers	Dendrimer n Dendrimere pl	Дендример Дендримеры	დენდრიმერი დენდრიმერები
Dialkynylmethano-fullerene	Dialkynylmethano-fulleren n	Диалкинилметан-фуллерен	დიალკინილმეთან-ფულერენი
Dispersity	Dispersität f	Дисперсность	დისპერსულობა
DNA nanotubes (DNA-wrapped carbon nanotubes, Grafting single-walled carbon nanotubes with highly hybridizable DNA)	DNA-Nanoröhren f pl	Привитые к нанотрубкам ДНК Намотанная на углеродную нанотрубку ДНК	დნმ-ნანომილაკები (ნანომილაკებზე დახვეული დნმ)
Doping agent Dopant	Dotierungsstoff m Dotiermittel n Dotierungsmittel n Dotand (Dopant) m	Допинг-агент	მადოტირებელი (მალეგირებელი) საშუალება, სადოპირებო აგენტი დოტანდი (ლათ. dotare – მომარაგება, მოწყობა, გაწყობა)
Double-walled / wall-carbon-nanotube (DWCNT)	Doppelwandige Kohlenstoffnanoröhre f Doppelwandiges Kohlenstoffnano-röhrchen n	Нанотрубка двухстенная, углеродная (ДСНТ)	ნახშირბადის ორკედლიანი ნანომილაკი (DWCNT)

Double-walled / wall-carbon-nanotubes (DWCNTs)	Doppelwandige Kohlenstoff-nanoröhren pl Doppelwandige Kohlenstoff-nanoröhrchen pl	Нанотрубки двухстенные, углеродные (ДСНТ)	ნახშირბადის ორკედლიანი ნანომილაკები (DWCNTs)
Effect of particle (grain) size Effects of particle (grain) size	Auswirkung der Partikelgröβe f Auswirkungen der Partikelgröβe pl	Размерный эффект Размерные эффекты	ზომის ეფექტი ზომის ეფექტები (მაკრომასალებისაგან განსხვავებით ნანოსტრუქტურებში მასალის ფიზიკურ-ქიმიური თვისებების პირდაპირი კავშირი სტრუქტურული ელემენტების ზომებთან არის ზომის ეფექტი. ის შეიძლება იყოს სტრუქტურული, ქიმიური, მექანიკური ან ფიზიკური. ნანოსტრუქტურულ მასალებს (ორ განზომილებაში მათი ზომები არ აღემატება 100 ნმ-ს) აქვს ნიმუშის ზედაპირის მოცულობასთან შეფარდების დიდი მნიშვნელობა და ამის გამო მაკრომასალისაგან სრულიად განსხვავებული, ახალი ტექნიკისთვის მნიშვნელოვანი თვისებები, რაც იძლევა ნანოტექნოლოგიაში ელექტრონული მოწყობილობების მინიატურიზაციის შესაძლებლობას)
Endohedral fullerene Endohedral fullerenes	Endohedrales Fulleren n Endohedrale Fullerene pl	Эндоэдральный фуллерен Эндофуллерен Эндоэдральные фуллерены	ენდოედრული ფულერენი ენდოედრული ფულერენები

	Endohedrale Komplexe m pl	Эндоедральные комплексы	ფულერენის ენდოედრული კომპლექსები $M_m@C_n$, $X@C_n$ (ფულერენის ღრუს შიგნით რომელიმე ლითონის ატომის ჩანერგვით მიღებული ფულერენის ნაერთი)
Endohedral metallofullerenes	Endohedrale Metallofullerene n pl	Эндометалло-фуллерены (ЭФ, ЭМФ)	ენდოედრული ლითონფულერენები (მაგ. $La@C_{80}$)
Exohedral fullerene Exohedral fullerenes	Exohedrales Fulleren n Exohedrale Fullerene pl Exohedrale Addukte n pl	Экзоэдральный фуллерен Экзоэдральные фуллерены Продукты экзоэдрального (внешнесферного) присоединения	ეგზოედრული ფულერენი ეგზოედრული ფულერენები (მაგ., $C_{60}F_{48}$, $C_{60}H_2$, $C_{60}H_{36}$, მიიღება ფუნქციური ჯგუფების შეერთებით ფულერენის ორმაგ ბმებთან)
Field emission microscopy (FEM)	Feldelektronen-mikroskopie f (Feldemissions-mikroskopie f)	Микроскопия, полевая эмиссионная	ველის ემისიური მიკროსკოპია
Field ion microscopy (FIM)	Feldionenmikroskopie f	Микроскопия, полевая ионная (ПИМ)	ველის იონური მიკროსკოპია
Fulleran Fullerans	Fulleran n Fullerane pl	Фуллеран Фуллераны	ფულერანი ფულერანები (სრულად ჰიდრირებული ფულერენები, მაგ., $C_{60}H_{60}$, $C_{70}H_{70}$)
Fullerene(backyball) Fullerenes	Fulleren n Fullerene pl	Фуллерен Фуллерены, бакиболы, букиболы	ფულერენი ფულერენები (ნახშირბადის პოლიედრული კოლოიდური კლასტერები

			– C_n, $n \geq 20 – 540$; სფერული ფულერენები ბაკიბურთებია, ცილინდრული – ტუბულენები, ნანომილაკები)
Fullerene-doped polymer	Fulleren-dotiertes Polymer n	Допированный фуллереном полимер	ფულერენით დოტირებული პოლიმერი
Fullerenes cyclopropanation reaction	Cyclopropanierung (Cycloprpylation) von Fullerenen	Циклопропаниро-вания реакция фуллеренов	ფულერენების ციკლოპროპანირების რეაქცია
Fulleride Fullerides	Fullerid n Fulleride pl	Фуллерид Фуллериды	ფულერიდი ფულერიდები (Na_3C_{60}, K_3C_{60}. ფულერენების მყარ ფაზაში – ფულერიტებში მოლეკულებს შორის დიდი ზომის სიცარიელეებია, რომლებშიც შეიძლება ჩაინერგოს, ჩაისვას მცირე ზომის მოლეკულები, ლითონები, მეტალოცენები. მიღებული ჩანერგვის (ინტერკალირებული) ნაერთები ფულერიდებია; განსაკუთრებით მნიშვნელოვანია ლითონშემცველი ფულერიდები, მაგ., K_3C_{60}, რომელიც ზეგამტარია)
Fulleride anion Fulleride anions	Fullerid Anion n Fullerid Anionen pl	Фуллерид-анион Фуллерид-анионы	ფულერიდ ანიონი ფულერიდ ანიონები
Fullerite Fullerites	Fullerit n Fullerite pl	Фуллерит Фуллериты	ფულერიტი ფულერიტები (მყარი ფულერენები – ფულერიტები ფულერენების მოლეკულებისაგან შედგენილი მოლეკულური კრისტალებია)

Fulleroid Fulleroids	Fulleroid n Fulleroide pl	Фуллероид Фуллероиды	ფულეროიდი ფულეროიდები (ფულეროიდებია: ჰეტერო-, ნორ-, ჰომო-, სეკოფულერენები)
Functional nanomaterial (NFM) Functional nanomaterials	Funktionsmaterial n Funktionales Material n Funktionsmaterialien pl Funktionale Nanomaterialien pl Nano-funktionelle Materialien pl	Функциональный наноматериал Функциональные наноматериалы	ფუნქციური ნანომასალა ფუნქციური ნანომასალები
Fused fullerenes	Fused Fullerene n pl Verschmolzene Fullerene pl	Конденсированные фуллерены	კონდენსირებული ფულერენები
Graphane Graphanes	Grafan n Grafane pl	Графан Графаны	გრაფანი გრაფანები (ჰიდრირებული გრაფენი)
Graphene Graphenes	Graphen n Graphene pl	Графен Графены	გრაფენი გრაფენები (გრაფიტის ერთი მონოატომური სისქის შრე)
Graphene nanoribbons (nano-graphene ribbons) GNRs	Graphen Nanobänder, (Nano-Graphen Bänder) GNRs n pl	Графеновые нанолenты	გრაფენის ნანოლენტები
Grey goo/Gray goo	Grauer Schleim m	Серая слизь / жижа	რუხი ლორწო
Heterofullerene Heterofullerenes	Heterofulleren n Heterofullerene pl	Гетерофуллерен Гетерофуллерены	ჰეტეროფულერენი ჰეტეროფულერენები
Heterostructure Heterostructures	Heterostruktur f Heterostrukturen pl	Гетероструктура Гетероструктуры	ჰეტეროსტრუქტურა ჰეტეროსტრუქტურები

Hybrid nanomaterial Hybrid nanomaterials	Hybrid-Nanomaterial n Hybrid-Nanomaterialien pl	Гибридный наноматериал Гибридные наноматериалы	ჰიბრიდული ნანომასალა ჰიბრიდული ნანომასალები (ერთდროულად არაორგანული და ორგანული შემადგენელი ნივთიერებების ნანონაწილაკების შემცველი ერთგვაროვანი კომპოზიტები, რომლებშიც ძირითადი ნივთიერება განაწილებულია მეორე ნივთიერების – მატრიცის მოცულობაში; მაგ., არაორგანული ბოჭკოები, განაწილებული პოლიმერში; ასეთი მასალა რბილი, დრეკადი და ამავე დროს მექანიკურად მტკიცეა შესაბამისად ორგანული და არაორგანული შემადგენლის ხარჯზე)
Hydrated fullerene	Hydratisiertes (hydratiertes) Fulleren n	Гидратированный фуллерен	ჰიდრატირებული ფულერენი ((HyFn), $C_{60}@\{H_2O\}_n$)
Inorganic fullerene-like nanostructure (IF) Inorganic fullerene-like nanostructures (IF)	Anorganische Fullerenartige Nanostruktur f Anorganisches Fullerenartiges Nanomaterial n Anorganische Fullerenartige Nanostrukturen / Nanomaterialien pl	Неорганическая фуллереноподобная структура Неорганический фуллереноподобный материал Неорганические фуллереноподобные структуры / материалы	არაორგანული, ფულერენის მსგავსი ნანოსტრუქტურა არაორგანული, ფულერენის მსგავსი ნანოსტრუქტურები
Inorganic fullerene-like material (nano-structure), IFLM	Anorganisches Fulleren-artiges Material n	Неорганический фуллереноподобный материал (наноструктура)	ფულერენის მსგავსი არაორგანული მასალა (ნანოსტრუქტურა)

Inorganic fullerene-like materials (nano-structures) IFLMs	Anorganische Fulleren-artige Materialien pl	Неорганические фуллереноподобные материалы (наноструктуры)	ფულერენის მსგავსი არაორგანული მასალები (ნანოსტრუქტურები) (ნახშირბადისაგან განსხვავებული ატომების შემცველი, ფულერენის მსგავსი სტრუქტურის ნაერთების ნანონაწილაკები. მაგ., ოქსიდები: Cs_2O, TiO_2, SnO_2 და სხვ., გარდამავალ ლითონთა დიქალკოგენიდები: WS_2, MoS_2, ZrS_2 და სხვ.)
Inorganic nanocages	Anorganische Nanocages	Неорганические наноячейки, наноклети	არაორგანული ნანოღრუები / ნანოფიჭა / ნანოფიტი (კეთილშობილ ლითონთა, მაგ., Au, Ag, Pd ნანოღრუიანი ნაწილაკები)
Inorganic nanotube (INT) Inorganic nanotubes (INTs)	Anorganische Nanoröhre f Anorganische Nanoröhren pl	Неорганическая нанотрубка Неорганические нанотрубки	არაორგანული ნანომილაკი არაორგანული ნანომილაკები (ცილინდრული ფორმის ფულერენის მსგავსი ნაერთებია, არ შეიცავს ნახშირბადს, წარმოქმნილია სხვადასხვა არაორგანული ნაერთებისაგან: W-ის, Mo-ის, Ti-ის, Nb-ის სულფიდები, B-ის და Si-ის ნიტრიდები, ტიტანატები და სხვ.)
Intercalation compound Intercalation compounds	Einlagerungsver-bindung f Intercalationsver-bindung f Einlagerungsver-bindungen pl Intercalationsver-bindungen pl	Соединение внедрения Соединения внедрения	ჩანერგვის ნაერთი ჩანერგვის ნაერთები (ლათ. intercalatus – ჩადგმული, დამატებული, ჩანერგილი; ინტერკალაცია არის მოლეკულების,

			იონების ან ატომების ჩანერგვა შექცევადად სხვა ტიპის მოლეკულების ან ატომების ჯგუფებს (შრეებს) შორის; ასეთი ნაერთებია მაგალითად, ფულერიდები)
Lab-on-a-chip (LOC), micro total analysis system, μTAS	Lab-on-a-chip (LOC), Labor auf dem Chip n	Лаборатория на чипе, микросистемы полного анализа	ლაბორატორია ჩიპზე (სრული ანალიზის მიკროსისტემები)
Langmiur–Blodgett film Langmiur–Blodgett films	Langmuir–Blodgett-Schicht (LB-Schicht, LB-Film m) f Langmuir–Blodgett-Schichten (LB-Schichten, LB-Films) pl	Пленка Ленгмюра-Блоджет Пленки Ленгмюра-Блоджет	ლენგმიურ–ბლოჯეტის აფსკი ლენგმიურ–ბლოჯეტის აფსკები
Laser ablation	Laserablation f	Лазерная абляция	ლაზერული აბლიაცია (ლათ. “ablatio” – წართმევა, მოცილება. მყარი სხეულის ზედაპირიდან ან მოცულობიდან ლაზერის სხივით ნივთიერების მოცილების პროცესი. იყენებენ ნანოკლასტერების, ნანოაფსკების, ჰეტეროსტრუქტურების მისაღებად)
Low-energy electron microscopy (LEEM)	Niederenergetische Elektronen-mikroskopie f	Микроскопия медленных электронов	დაბალი ენერგიის (ნელი) ელექტრონების მიკროსკოპია
Magnetic fluid (ferrofluid, magnetic liquid)	Magnetische Flüssigkeit f	Магнитная жидкость (феррожидкость), МЖ	მაგნიტური სითხე, ფეროსითხე (მაღალდისპერსული – 5 – 50 ნმ ფერო- და ფერიმაგნიტური ნაწილაკების მდგრადი კოლოიდური სისტემა სითხეში)

Magnetic force microscopy (MFM)	Magnetkraft-mikroskopie (MKM) f	Магнито-силовая микроскопия	მაგნიტურ ძალთა მიკროსკოპია
Metallofullerene Metallofullerenes	Metallofulleren n Metallofullerene pl	Металлофуллерен Металлофуллерены	ლითონფულერენი მეტალფულერენი ლითონფულერენები მეტალფულერენები
Metamaterial Metamaterials	Metamaterial n Metamaterialien pl	Метаматериал Метаматериалы	მეტამასალა მეტამასალები (ხელოვნურად მიღებული სტრუქტურებია უარყოფითი გარდატეხის მაჩვენებლით, ისინი ჩვეულებრივი მასალების ანტიპოდებია)
Methanofullerenes	Methanofullerene f	Метанофуллерены	მეთანფულერენები
Micelle Micelles	Mizelle f Mizellen pl Assoziationskolloide n pl	Мицелла Мицеллы	მიცელა მიცელები
Microbalance	Mikrowaage f	Микровесы	მიკროსასწორი
Military nano-technology Military nano-technologies	Militärnano-technologie f Militärnano-technologien f	Военная нанотехнология Военные нанотехнологии	სამხედრო ნანოტექნოლოგია სამხედრო ნანოტექნოლოგიები
Molecular assembler Molecular assemblers	Molekularer Assembler m Molekulare Assembler pl	Наноассемблер Наноассемблеры	მოლეკულური ასემბლერი * მოლეკულური ასემბლერები (ჰიპოტეტური მოლეკულური რობოტი, რომელიც მანიპულირებს ცალკეული ატომებით და

* მოლეკულური ასემბლერის ბევრი სხვა იდეის ავტორია Drexler, Kim Eric (1955 –) – ამერიკელი ინჟინერი და მეცნიერი, მოლეკულური ნანოტექნოლოგიის პიონერი და პოპულარიზატორი.

			მოლეკულებით, და რომლითაც შეიძლება ბუნებაში არარსებული სტრუქტურების დასინთეზება. ნანოტექნოლოგიის მიზანია პროგრამირებადი, თვითპროდუცირებადი ასემბლერის შექმნა)
Molecular beam epitaxy (MBE)	Molekularstrahl-epitaxie f	Молекулярно-лучевая эпитаксия	მოლეკულურ-სხივური ეპიტაქსია
Molecular electronics	Molekulare Elektronik f	Молекулярная электроника	მოლეკულური ელექტრონიკა
Molecular imprinting (stamping)	Molecular imprinting Molekulares Prägen n	Молекулярный импринтинг	„მოლეკულური ანაბეჭდების“ მიღება – მოლეკულური იმპრინტინგი („მოლეკულური ანაბეჭდების“ მიღების მეთოდი, რომელიც ეფუძნება ფუნქციური მონომერების პოლიმერიზაციას თარგების – ტემპლეტების თანაობისას. მიღებული პოლიმერები „მოლეკულური ანაბეჭდებით“ მაღალი შერჩევითობის სორბენტებია, რომლებშიც პოლიმერები ნანო დონეზე სტრუქტურულ შესაბამისობაშია სამიზნე სორბატთან)
Molecular nanotechnology	Molekulare Nanotechnologie (MNT) f	Молекулярная нанотехнология	მოლეკულური ნანოტექნოლოგია
Molecular recognition	Molekulare Erkennung f	Молекулярное распознавание	მოლეკულური გამოცნობა
Molecular switch	Molekularer Schalter m	Молекулярный переключатель	მოლეკულური გადამრთველი

Multi-walled / wall carbon nanotube (MWCNT) Multi-walled / wall carbon nanotubes (MWCNTs)	Mehrwandige Kohlenstoffnanoröhre f Mehrwandiges Kohlenstoffnanröhrchen n (MWCNT) Mehrwandige Kohlenstoffnanoröhren pl Mehrwandige Kohlenstoffnanoröhrchen pl (MWCNTs)	Нанотрубка многостенная, углеродная (МСНТ) Нанотрубки многостенные, углеродные (МСНТ)	ნახშირბადის მრავალკედლიანი ნანომილაკი ნახშირბადის მრავალკედლიანი ნანომილაკები
Nano / microfiber Nano / microfibers	Nano / mikrofaser f Nano / mikrofasern pl	Нано / микроволокно Нано / микроволокна	ნანო / მიკრობოჭკო ნანო / მიკრობოჭკოები
Nanoactuator Nanoactuators	Nanoaktuator / Nanomotor m Nanoantrieb m Nanoaktuatoren / Nanomotoren pl Nanoantriebe pl	Наноактю(у)атор Наноактю(у)аторы	ნანოაქტორი, ნანოძრავა ნანოაქტორები, ნანოძრავები (მოლეკულური ძრავა ნანომოწყობილობებისთვის)
Nanobalance	Nanobalance n	Нановесы, атомные весы	ნანოსასწორი
Nanobattery Nanobatteries	Nanobatterie f Nanobatterien pl	Нанобатарейка Нанобатарейки	ნანობატარეა ნანობატარეები
Nanobelt Nanoribbon Nanobelts Nanoribbons	Nano-Gürtel m Nanoband n Nano-Gürtel pl Nanobänder(n) pl	Нанопояс Наноленты Наноремешки, наноремни / наноленты	ნანოსარტყელი ნანოლენტა (ზოლი) ნანოსარტყელები / ნანოლენტები
Nanocage Nanocages	Hohle Nanopartikel f Nanocage Hohle Nanopartikeln pl Nanocages pl	Наноклеть Наноклети	ნანოღრუ / ნანოუჯრედი ნანოღრუები / ნანოფიჭა / ნანოფიტი
Nanocapsule Nanocapsules	Nanokapsel n Nanokapseln pl	Нанокапсула Нанокапсулы	ნანოკაფსულა ნანოკაფსულები

Nanocatalyst Nanocatalysts	Nanokatalysator m Nanokatalysatoren pl	Нанокатализатор Нанокатализаторы	ნანოკატალიზატორი ნანოკატალიზატორები
Nanoceramic Nanoceramics	Nanokeramik f Nanokeramiken pl	Нанокерамика	ნანოკერამიკა (კერამიკული ნანოსტრუქტურული მასალა)
Nanochemistry	Nanochemie f	Нанохимия	ნანოქიმია (ქიმიური მეცნიერების დარგი; ნანონაწილაკების – ნანოფხვნილების, ნანოკლასტერების, ნანოკრისტალების ქიმია)
Nanocluster Nanoclusters	Nanocluster m Nanocluster pl	Нанокластер Нанокластеры	ნანოკლასტერი ნანოკლასტერები
Nanocomposite Nanocomposites	Nanokomposit m, n Nanoverbundwerkstoff m Nanokomposite pl Nanoverbundwerkstoffe pl	Нанокомпозит Нанокомпозиты	ნანოკომპოზიტი ნანოკომპოზიტები
Nanocrystal Nanocrystals	Nanokristall n Nanokristalle pl	Нанокристалл Нанокристаллы	ნანოკრისტალი ნანოკრისტალები
Nanodiamond Nanodiamonds	Nanodiamant m Nanodiamanten pl	Наноалмаз, НА Наноалмазы Ультрадисперсные алмазы, УНА	ნანოალმასი ნანოალმასები
Nanodispersion	Nanodispersion f	Нанодисперсия	ნანოდისპერსია
Nanodispersity	Nanodispersität f	Нанодисперсность	ნანოდისპერსულობა
Nanodrugs	Nanopartikuläre Arzneistoffe pl	Нанолекарства	ნანოწამლები
Nanoeducation	Nano-Bildung f	Нанообразование	ნანოგანათლება

Nanoelectronics	Nanoelektronik f	Наноэлектроника	ნანოელექტრონიკა
Nanoemulsion Nanoemulsions	Nanoemulsion f Nanoemulsionen pl	Наноэмульсия Наноэмульсии	ნანოემულსია ნანოემულსიები
Nanoenergetics	Nanoenergetik f	Наноэнергетика	ნანოენერგეტიკა
Nanofibre (CF) Nanofibres	Nanofaser f / Nanofaden m Nanofasern pl / Nanofäden pl	Нановолокно Нановолокна	ნანობოჭკო ნანობოჭკოები
Nanofiller Nanofillers	Nanofüller m Nanofüllstoff m Nanofüllstoffe pl	Нанонаполнитель Нанонаполнители	ნანოშემავსებელი ნანოშემავსები ნანოშემავსებლები
Nanofluid Nanofluids	Nanofluid n Nanoflüssigkeit f Nanofluide pl Nanoflüssigkeiten pl	Наножидкость Наножидкости	ნანოსითხე ნანოსითხეები (ნანონაწილაკების კოლოიდური ხსნარები თხევად გამხსნელში)
Nanoglass Nanoglasses	Nanoglas n Nanogläser pl	Наностекло Наностёкла	ნანომინა ნანომინები
Nanoglue	Nanoglue m	Наноклей	ნანოწებო
Nanohardness	Nanohärte f	Нанотвердость	ნანოსიმაგრე / ნანოსისალე
Nanoindentor	Nanoindenter (Nanoindentor) m	Наноиндентер	ნანოინდენტორი, ნანოანალიზატორი (ნანოინდენტორით (ნ.ი.) განისაზღვრება ნანომასალების სიმაგრე; ნ.ი. წარმოადგენს ალმასის სამ- ან ოთხწახნაგა პირამიდას. ნანოინდენტირებას ახდენენ ზედაპირის სიღრმეზე, რომელიც არ აღემატება რამდენიმე ნმ-ს)

Nanomarket	NanoMarket m	Рынок нанопродуктов	ნანოპროდუქტების ბაზარი
Nanomaterial Nanomaterials (NanoMat)	Nanomaterial n Nanomaterialien pl	Наноматериал Наноматериалы	ნანომასალა ნანომასალები
Nanomedicine	Nanomedizin f	Наномедицина	ნანომედიცინა
Nanomembrane Nanomembrans	Nanomembran(e) f Nanomembranen pl	Наномембрана Наномембраны	ნანომემბრანა ნანომემბრანები
Nanometer	Nanometer n	Нанометр	ნანომეტრი (10^{-9} მ)
Nanometrology	Nanometrologie f	Нанометрология	ნანომეტროლოგია
Nanomodifier Nanomodifiers	Nanomodifikator m Nanomodifikatoren pl	Наномодификатор Наномодификаторы	ნანომოდიფიკატორი ნანომოდიფიკატორები
Nano-onion Nested nanoparticle	Nano-Zwiebel f	Нанолуковица Многослойный фуллерен Луковичная форма углерода Наноматрёшка	ნანოხახვი, მრავალშრიანი ფულერენი (ნანოგანზომილების ნახშირბადიანი სტრუქტურა, რომელიც წარმოადგენს ერთმანეთში ჩადგმულ ნახშირბადის (გრაფენის) სფეროებს)
Nanopaper	Nanopapier n	Нанобумага	ნანოქაღალდი (მიღებულია ცელულოზის ნანობოჭკოებისაგან, ტიტანის ოქსიდის ნანომილაკებისაგან; უკანასკნელი თერმომდგრადია 700 °C-მდე, არატოქსიკური და არალპობადია)

Nanoparticle Nanoparticles	Nanopartikel f Nanoteilchen n Nanopartikel(n) pl Nanoteilchen pl	Наночастица Наночастицы	ნანონაწილაკი ნანონაწილაკები (ნანოგანზომილების ნაწილაკები (ნ.ნ.); მათში არჩევენ 1. ნანოკლასტერებს, რომელთა ზომებია 1 – 5 ნმ, შეიცავს 1000 ატომამდე; 2. საკუთრივ ნ.ნ.-ებს ზომებით 5 – 100 ნმ, შეიცავს 10^3 – 10^8 ატომს. ხაზოვანი ზომების მიხედვით განასხვავებენ ნულ-, ერთ-, ორ- და სამგანზომილებიან ნ.ნ.-ებს. ნ.ნ.-ებს (შესაბამისად,0D-,1D-,2D- და 3D-ნანონაწილაკები; D განზომილებას აღნიშნავს, ინგლ. dimension – განზომილება) იღებენ ორი მეთოდით: “ქვემოდან ზემოთკენ” (Bottom-up) – იგულისხმება ნ.ნ.-ების აწყობა ცალკეული ატომებისაგან; “ზემოდან ქვემოთკენ” (Top-down) – ნ.ნ.-ები მიიღება მსხვილი ნაწილაკების ნანოზომამდე დანაწევრებით)
Nanopharmacology	Nanopharmakologie f	Нанофармакология	ნანოფარმაკოლოგია
Nanophysics	Nanophysik f	Нанофизика	ნანოფიზიკა
Nanopolishing	Nano-Polieren n	Нанополирование	ნანოგაპრიალება (მყარი სხეულის ზედაპირის დამუშავება ფიზიკური, ქიმიური და ელექტროქიმიური მეთოდებით მაღალი ხარისხის სიგლუვემდე, როდესაც ნარჩენი სიმქისე მხოლოდ რამდენიმე ნანომეტრია)
Nanopowder Nanopowders	Nano-Pulver n Nano-Pulver pl	Нанопорошок Нанопорошки	ნანოფხვნილი ნანოფხვნილები

Nanorings	Nanoringe f	Нанокольца	ნანორგოლები
Nanorobot, nanobot Nanorobots (nanobots, nanoids, nanites, nanomachines or nanomites)	Nanoroboter m Nanobots (Nanorobotern, Naniten) pl Nanoroboter pl	Наноробот Нанороботы (наноботы)	ნანორობოტი ნანორობოტები (იგივეა, რაც მოლეკულური ასემბლერი. სიტყვა “რობოტ”-ის ავტორია ჩეხი დრამატურგი კ. ჩაპეკი, რომელმაც 1920 წ. “ robota ” უწოდა ადამიანის მსგავს არსებებს, რომელთაც აქვს მაღალი ინტელექტი და არ აქვს სული. “ robota ” ნიშნავს იძულებით შრომას)
Nanorod Nanorods	Nanostäbchen n Nanostäbchen pl	Наностержень Наностержни	ნანოღერო ნანოღეროები (ერთგანზომილებიანი ანუ 1D-ჭრუვიანი ღეროები, რომელსაც აქვს სიგრძის დიამეტრთან ფარდობის ყველაზე მცირე 10-ის ტოლი მნიშვნელობა, მათი სიგრძე კი არის 1 – 100 ნმ)
Nanoscale Nano area	Nanobereich m (Nanometerbereich) m Nanomaßstab m	Нанодиапазон	ნანომასშტაბი
Nanoscale material Nanoscale materials	Nanoscaliges Material n Nanoscalige Materialien pl	Наноматериал Наноматериалы	ნანომასშტაბური მასალა ნანომასშტაბური მასალები
Nanoscale particle Nanoparticle Nanoscale particles Nanoparticles	Nanoscaliges Teilchen n Nanopartikel f, n Nanoteilchen n Nanoscalige Teilchen pl Nanoteilchen pl Nanopartikel (f, n) pl	Наночастица Наночастицы	ნანომასშტაბური ნაწილაკი ნანომასშტაბური ნაწილაკები (მათი ზომები ნანომეტრული რიგისაა: 1 ნმ =10^{-9} მ, 1 ნ დნმ-ის ორმაგი სპირალის რადიუსის ტოლია)

Nanoscale phenomenon Nanoscale phenomena	Nanoscaliges Phänomen n Nanoscalige Erscheinung f Nanoscalige Phänomene pl	Наномасштабное явление Наномасштабные явления	ნანომასშტაბური მოვლენა ნანომასშტაბური მოვლენები
Nanoscale research Nanoresearch Nanoscale researchs	Nanoforschung f Nanoforschungen pl	Нано-исследование Нано-исследования	ნანო-გამოკვლევა ნანო-გამოკვლევები (ნანომასშტაბური მოვლენების გამოკვლევა)
Nanoscience	Nanowissenschaft f	Нанонаука	ნანომეცნიერება (“მეცნიერება და ტექნიკა მასალების, ფუნქციური სტრუქტურების და მოწყობილობების ატომურ, მოლეკულურ და ნანომეტრულ დონეზე შექმნის, დამზადების, დახასიათების და რეალიზაციის შესახებ”[13])
Nanosensor Nanosensors	Nanosensor m Nanosensoren pl	Наносенсор Наносенсоры	ნანოსენსორი ნანოსენსორები
Nanoshell Nanoshells	Nanoshell f Nanoschale f Nanokugel f Nanoschalen pl Nanokugeln pl	Нанооболочка Наносфера Нанооболочки Наносферы	ნანოგარსი ნანოსფერო / ბურთულა ნანოგარსები ნანოსფეროები / ბურთულები
Nanostructure Nanostructures	Nanostruktur f Nanostrukturen pl	Наноструктура Наноструктуры	ნანოსტრუქტურა ნანოსტრუქტურები (კომპლექსური ნანოსკოპიური სტრუქტურის ერთეულოვანი ელემენტი)

Nanotechnology Nanoengineering Nanotech Nanotechnologies Nano technologies	Nanotechnologie f Nanotechnik f Nanotech Nano-Technologien pl	Нанотехнология Нанотехнологии	ნანოტექნოლოგია * ნანოტექნოლოგიები (დისციპლინათშორისი დარგი მასალების, სისტემების და მოწყობილობების ატომურ და მოლეკულურ დონეზე მანიპულირების მეთოდებისა და ხერხების შესახებ. მოიცავს სტრუქტურებს, რომელთა სულ მცირე ერთი განზომილება 100 ნმ-ზე ნაკლებია)
Nanotechnology instrument Nanotechnology instruments	Nanotechnologie Instrument n Nanotechnologie Instrumente pl	Инструмент нанотехнологии Инструменты нанотехнологии	ნანოტექნოლოგიის ინსტრუმენტი ნანოტექნოლოგიის ინსტრუმენტები (ელექტრონული, მასკანირებელი ზონდური და სხვა მიკროსკოპები, ნანოპინცეტი, ოპტიკური პინცეტი, ნანოსასწორი, ნანოშპრიცი და სხვა)
Nanothermometer	Nanothermometer n	Нанотермометр	ნანოთერმომეტრი
Nanotoxicity	Nanotoxizität f	Нанотоксичность	ნანოტოქსიკურობა
Nanotoxicology	Nanotoxicologie f	Нанотоксикология	ნანოტოქსიკოლოგია
Nanotribology	Nanotribologie f	Нанотрибология	ნანოტრიბოლოგია
Nanotube	Nanoröhre f Nanoröhrchen n	Нанотрубка	ნანომილაკი

* ნანოტექნოლოგიის მამამთავარია Richard Feynman (1918 – 1988) – ამერიკელი ფიზიკოსი, ნობელის პრემიის ლაურეატი ფიზიკაში (1965). სიტყვა “ნანოტექნოლოგია” სამეცნიერო ენაში 1974 წ. შემოიტანა Norio Taniguchi-იმ (1912 – 1999), იაპონელმა ფიზიკოსმა და მასალათმცოდნემ. ძვ. ბერძნ. “ნანოს” – ჯუჯა, “ტექნო” – ხელოვნება, “ლოგოს” – სწავლება.

Nanotubes	Nanoröhren pl Nanoröhrchen pl Nanotubes pl	Нанотрубки Тубулярные наноструктуры Нанотубулены	ნანომილაკები
Nanotube membrane Nanotube membranes	Nanotube-Membrane f Nanotube-Membranen pl	Мембрана из нанотрубок Мембраны из нанотрубок	ნანომილაკებიანი მემბრანა ნანომილაკებიანი მემბრანები
Nanotweezer	Nanopinzette f	Нанопинцет	ნანოპინცეტი (ნანოობიექტებით მანიპულირების მოწყობილობა; პირველად ის შექმნეს 1999 წელს ჰარვარდის უნივერსიტეტში (აშშ); შედგება ნახშირბადის მრავალკედლიანი 50 ნმ დიამეტრის ნანომილაკებისგან, რომლებიც იმართება ელექტრული ძაბვით; ძაბვის მიწოდებისას მილაკების ბოლოები ერთმანეთს უახლოვდება და შეუძლია კლასტერების ნაწილაკების წატაცება და გადაადგილება)
Nanoweb	Nanoweb n	Интернет-сайты о нанотехнологиях	Nanoweb (ინტერნეტ-გვერდები ნანოტექნოლოგიებზე. მაგ., http://www.nano.org.uk)
Nanowire / Nanowhisker Nanowires / Nanowhiskers	Nanodraht m Nanodrähte pl	Нанопроволока / нановискер Нанопроволоки / нанонити / нановискеры	ნანომავთული / ნანოვისკერი ნანომავთულები / ნანოვისკერები
Near-field scanning optical microscopy (SNOM / NFSOM in USA)	Optische Rasternahfeld-mikroskopie (SNOM) f	Сканирующая ближнепольная оптическая микроскопия (СБОМ)	ახლო ველის მასკანირებელი ოპტიკური მიკროსკოპია

Non-metal doped fullerenes	Mit Nichtmetall dotierten Fullerene n pl	Допированные неметаллом фуллерены	არალითონით დოტირებული ფულერენები ($N@C_{60}$ $He@C_{60}$)
Norfullerene Norfullerenes	Norfulleren n Norfullerene pl	Норфуллерен Норфуллерены	ნორფულერენი ნორფულერენები
Open-cage fullerene	Open-Käfig Fullerene n pl	Фуллерен с открытыми клетками	ფულერენები ღია / გახსნილი ღრუებით / უჯრედებით
Optical tweezer Optical trap Light tweezer Optical tweezers Optical traps Light tweezers	Optische Pinzette f Lichtpinzette f Optische Pinzetten pl Lichtpinzetten pl	Оптический пинцет Лазерный пинцет Оптическая ловушка Оптические пинцеты Лазерные пинцеты Оптические ловушки	ოპტიკური პინცეტი ოპტიკური პინცეტები (ოპტიკური მოწყობილობა (“ლაზერული ხაფანგი”) ლაზერის სხივში დაფოკუსებული მიკრო- და ნანოზომების ობიექტების სივრცეში შესაკავებლად და გადასაადგილებლად. ამით შეიძლება მოწესრიგებული სტრუქტურების აწყობა კოლოიდური ნაწილაკებისაგან, რაც დღეისათვის ხორციელდება “ხელით” ატომების მცირე რიცხვისთვის ოპტიკური პინცეტით ან მასკანირებელი ზონდური მიკროსკოპით; ატომებით მანიპულირება (იდეის ავტორია ნობელიანტი ამერიკელი ფიზიკოსი რ. ფეინმანი, 1960) პრაქტიკულად შესაძლებელი გახდა სინათლის წნევის მეშვეობით (A. Ashkin, S. Chu, აშშ, 1986); პირველად 1989 წ. D. Eigler-მა და მისმა ჯგუფმა (აშშ) Ni-ის მონოკრისტალზე განალაგა Xe-ის 35 ატომი კომპანია IBM-ის ლოგოტიპის ფორმით)

Particle size analysis, granulometry	Korngrößenanalyse f Partikelgrößenanalyse f Granulometrie f Teilchengrößenanalyse f	Гранулометрический анализ, гранулометрия	გრანულომეტრია
Polyfluorfullerene Polyfluorfullerenes	Polyfluorfulleren n Polyfluorfullerene pl	Полифторфуллерен Полифторфуллерены	პოლიფტორფულერენი პოლიფტორფულერენები ($C_{60}F_n$, n = 15 –20)
Prato reaction	Prato Reaktion f	Реакция Прато	პრატოს რეაქცია
Probe microscopy	Sondenmikroskopie f	Зондовая микроскопия	ზონდური მიკროსკოპია
Pyrrolodino-fullerene	Pyrrolodino-fullerene pl	Фуллеро-пирролидины	ფულერო-პიროლიდინები
Quantum dot Quantum dots	Quantenpunkt m Quantenpunkten pl	Квантовая точка Квантовые точки	ქვანტური * წერტილი ქვანტური წერტილები
Quantum effects	Quanteneffekte m pl	Квантово-размерные эффекты	ქვანტურ-ზომითი ეფექტები
Quantum wire Quantum wires	Quantendraht m Quantendräte pl	Квантовый провод Квантовые провода Квантовые нити	ქვანტური მავთული / ძაფი ქვანტური მავთულები ქვანტური ძაფები
Reflection electron microscopy (REM)	Reflexionselektronen mikroskopie f	Микроскопия, электронная отражательная (ОЭМ)	არეკვლითი ელექტრონული მიკროსკოპია
Retro-Bingel reaction	Retro-Bingel-Reaktion f	Ретро-Бингеля реакция	რეტრო-ბინგელის რეაქცია

* დამკვიდრებული “კვანტური”-ს მიუხედავად [14], სწორად მიგვაჩნია “ქვანტური” ლათინური “quantum”-ის შესაბამისად.

Retro-Prato reaction, retro cycloaddition	Retro-Reaktion Prato, retro-Cycloaddition f	Ретро-реакция Прато, ретроцикло-присоединение	რეტრო-პრატოს რეაქცია, რეტრო-ციკლოშეერთება
Scanning electron microscope	Rasterkraftmikrokop n (*technisch*-Rastermikroskop n Rasterelectronen-mikroscop n)	Микроскоп, сканирующий электронный, растровый электронный микроскоп	რასტრული (მასკანირებელი) მიკროსკოპი
Scanning electron microscopy (SEM)	Rasterelectronen-mikroscopie (REM) f	Микроскопия, сканирующая электронная (СЭМ, РЭМ)	რასტრული (მასკანირებელი) ელექტრონული მიკროსკოპია
Scanning Near-Field Acoustic Microscope (NSAM)	Akustischesrasternah-feldmikroskop (SNAM oder NSAM) n	Микроскоп, сканирующий ближнепольный акустический	ახლო ველის მასკანირებელი აკუსტიკური მიკროსკოპი
Scanning probe microscope	Rastersonden-mikroskop n	Микроскоп, сканирующий зондовый	მასკანირებელი ზონდური მიკროსკოპი
Scanning probe microscopy (SPM)	Rastersonden-mikroskopie f (RSM)	Микроскопия, зондовая сканирующая (СЗМ)	მასკანირებელი ზონდური მიკროსკოპია
Scanning tunneling microscope (STM)	Rastertunnel-mikroskop n (Rastertunnelelectronen-mikroskop n (RTM) Tunnelelektronen-mikroskop n (STM)	Микроскоп, сканирующий туннельный	მასკანირებელი (რასტრული) ტუნელური მიკროსკოპი
Scanning tunnel microscopy (STM)	Rastertunnel-mikroskopie f (RTM)	Микроскопия, сканирующая туннельная (СТМ)	მასკანირებელი (რასტრული) ტუნელური მიკროსკოპია

Self-assembled monolayer (SAM)	Selbstorganizierende Monoschicht (SAM) f Selbstorganizierte Monoschicht (SAM) f Selbstassemblierte Monolage f	Самоорганизованный монослой	თვითორგანიზებული/ თვითორგანიზებადი / თვითაწყობილი / თვითაწყობადი მონოშრე, მონოფენა
Self-assembly (SA)	Selbst-Assemblierung f	Самосборка	თვითაწყობა
Self-organization	Selbstorganisation f Selbstanordnung f Selbstzusammenbau m	Самоорганизация	თვითორგანიზება
Sensor (transducer) Sensors (transducers)	Sensor (Messfühler, Fühler, Aufnehmer) m Transducer m Sensoren (Messfühler, Fühler, Aufnehmer) pl	Датчик, сенсор Датчики, сенсоры	სენსორი სენსორები
Sensory nanocomposite Sensory nanocomposites	Sensorische Nanokomposite f Sensorische Nanokompositen pl	Сенсорный нанокомпозит (композиционный материал) Сенсорные нанокомпозиты	სენსორული ნანოკომპოზიტი სენსორული ნანოკომპოზიტები
Single electron transistor	Einzel-Elektronen-Transistor m	Одноэлектронный транзистор	ერთელექტრონიანი ტრანზისტორი
Single-walled / wall carbon nanohorn (SWCNH) Single-walled / wall carbon nanohorns (SWCNHs)	Einwandiges Kohlenstoff-Nanohörn n (CNH) Einwandige Kohlenstoff-Nanohörner pl (CNH)	Нанорожок одностенный, углеродный Нанорожки одностенные, углеродные	ნახშირბადის ერთკედლიანი ნანორქა ნახშირბადის ერთკედლიანი ნანორქები (ნანორქა არის მოკლე, ერთკედლიანი, კონუსის ფორმის ნახშირბადის ნანომილაკი ერთი ღია

			ბოლოთი; ნანორქები ვან დერ ვაალსის ძალების მოქმედებით ერთიანდება და 100 ნმ მცირე დიამეტრის სფერული ყვავილის ფორმას იღებს, რომელიც წყალში ხსნადია, სხვა ნახშირბადიანი მასალებისაგან განსხვავებით, რასაც იყენებენ უჯრედის შიგნით წამლების ტრანსპორტირებისთვის)
Single-walled / wall carbon nanotube (SWCNT) Single-walled/wall carbon nanotubes (SWCNTs)	Einwandige Kohlenstoffnanoröhre f Einwandiges Kohlenstoff-nanoröhrchen n (SWCNT) Einwandige Kohlenstoff-nanoröhren pl Einwandige Kohlenstoff-nanoröhrchen pl (SWCNTs)	Нанотрубка одностенная, углеродная (ОСНТ) Нанотрубки одностенные, углеродные (ОСНТ)	ნახშირბადის ერთკედლიანი ნანომილაკი (SWCNT) ნახშირბადის ერთკედლიანი ნანომილაკები (SWCNTs)
Single-walled / wall nanotube (SWNT) Single-walled/wall nanotubes (SWNTs)	Einwandige Nanoröhre f Einwandiges-Nanoröhrchen n (SWNT) Einwandige Kohlenstoff-nanoröhren pl (SWCNTs) Einwandige Nanoröhrchen pl (SWNTs)	Нанотрубка одностенная (ОСНТ) Нанотрубки одностенные (ОСНТ)	ერთკედლიანი ნანომილაკი (SWNT) ერთკედლიანი ნანომილაკები (SWNTs)
Smart materials	Smart materials pl Schlaue Stoffe m pl Smarte Werkstoffe m pl Intelligente Materialien n pl	Умные материалы (интеллектуальные материалы)	გონიერი / ჭკვიანი / საზრიანი მასალები, სმარტმასალები

Soft chemistry (Chimie douce)	Sanfte Chemie f (Chimie douce)	“Мягкая химия”	ფაქიზი (ნატიფი) ქიმია (მყარფაზიანი მასალების, მაგ., ნანოფხვნილების, მიღების ქიმიური მეთოდები, რომლებიც გულისხმობს მაღალი წნევისა და ტემპერატურის მინიმალურად გამოყენებას)
Sol-gel technology (Sil-gel process)	Sol-gel technologie f	Золь-гель технология (Золь-гель процесс)	ზოლ-გელის ტექნოლოგია (ნანონაწილაკების მიღების ხერხი, რომელიც ეფუძნება არაორგანული და არაორგანულ-ორგანული ჰიბრიდული მასალების კოლოიდური ნაწილაკების სინთეზს; ეს ხერხი მოიცავს ზოლის მიღებას და შემდგომ გელში მის გადაყვანას)
Space elevator	Weltraumlift m	Космический лифт	კოსმოსური ლიფტი
Spherical aromaticity	Sphärische Aromatizität f	Сферическая ароматичность	სფერული არომატულობა (სფერულ შეუღლებულ არომატულ სისტემაში)
Spray drying	Sprühtrocknung f Zerstäubung-strocknung f	Распылительная сушка	შრობა გაფრქვევით
Substitutional doping	Substitutionelles Doping n	Заместительное допировапние	ჩანაცვლებითი დოტირება (C_{60}-ში N-ით და B-ით დოტირების პროდუქტებია მაგ., $C_{59}N$, $C_{48}N_{12}$, $C_{59}B$, ისინი ჩანაცვლებული ფულერენებია და მიიღება ფულერენებში ნახშირბადის ატომის სხვა ატომით ჩანაცვლებისას)

Supperlatice Supperlatices	Űbergitter n Űbergittern pl	Сверхрешётка Сверхрешётки	ზეგისოსი ზეგისოსები
Supramolecular catalysis	Supramolekulare Katalyse f	Супрамолекулярный катализ	სუპრამოლეკულური კატალიზი
Supramolecular chemistry	Supramolekulare Chemie f	Супрамолекулярная химия	სუპრამოლეკულური ქიმია (1978 წ. ნობელიანტმა ფრანგმა მეცნიერმა J. M. Lehn-მა შემოიტანა ტერმინი “სუპრა-მოლეკულური ქიმია” (ს.ქ.) და მისი განმარტება: “მოლეკულური ანსამბლების და მოლეკულათშორისი ბმების ქიმია”; ნანოტექნოლოგიებში გამოყენებული ნანოსისტემების და მოლეკულური მოწყობილობების სინთეზისთვის გამოიყენება სწორედ სუპრამოლეკულური სტრუქტურები, რომლებშიც მოლეკულური ანსამბლების თვითაწყობა სუპრამოლეკულურია, ე.ი. არაკოვალენტური ურთიერთქმედებითაა მოლეკულების დიდი რიცხვი ურთიერთ-შეკავშირებული. ს.ქ. მეთოდებით არის მიღებული სხვადასხვა არქიტექტურის ნანოანსამბლები, რომლებსაც იყენებენ ინოვაციურ ნანოტექნოლოგიებში ნანოელექტრონიკასა და კომპიუტერებში)
Surface active compound Surfactant	Oberflächenaktiver Stoff m, Grenzflächen-aktive Substanz f, Tensid n	Поверхностно-активное вещество	ზედაპირულად აქტიური ნივთიერება

Surface active compounds Surfactants	Oberflächenaktive Stoffe pl Oberflächenaktive / grenzflächenaktive Substanzen pl Tenside pl	Поверхностно-активные вещества	ზედაპირულად აქტიური ნივთიერებები
Template Templates	Template n Vorlage f Schablone f Vorlagen pl Schablonen pl	Темплейт, шаблон, матрица Шаблоны	თარგი, ტემპლეტი, შაბლონი, მატრიცა. თარგები, ტემპლეტები, შაბლონები, მატრიცები (თარგის, ტემპლეტის, მაგ., ტუტე ლითონების იონების, დიდი სივრცითი სტრუქტურების მაკრო-მოლეკულების გარშემო ქიმიური სინთეზის დროს ხდება დაბალმოლეკულურ ნივთიერებათა ორგანიზება და სივრცითი, ნანო- და სუპრამოლეკულური სტრუქტურების წარმოქმნა)
Template effect	Templat effect m	Эффект темплатный	თარგის ეფექტი (თარგის თანაობისას სუპრამოლეკულური კომპლექსის სინთეზის რეაქციაში გამოსავლიანობის მრავალჯერადი გადიდება)
Template technique	Template Technik f	Темплатный метод	თარგის ტექნიკა, ტემპლეტის ტექნიკა (თარგის ტექნიკა ნიშნავს რაიმეს შექმნას თარგის, შაბლონის, ტემპლეტის ანუ მატრიცის მიხედვით. ქიმიურ ნანო-ტექნოლოგიაში თარგებს იყენებენ ერთი ქიმიური ნაერთის მიერ მეორის კრისტალიტების ან მიცელების ფორმის

			“კოპირებისთვის”. მაგ., შეიძლება არაორგანული მატრიცის შექმნა, რომელიც იმეორებს ორგანული მიცელების, ცილების ან დნმ-ის სპირალის ფორმას. თარგი ამ შემთხვევაში არის ცენტრი, რომლის გარშემო ხდება საჭირო ნივთიერების (მოლეკულების ან ატომების) ძირითადი სტრუქტურული ერთეულების ორგანიზება. თარგის ტექნიკას იყენებენ ნანოლითოგრაფიასა და ნანობეჭდვაში)
Thermal spraying	Thermische Trocknung f	Термическая сушка	თერმული შრობა
Thin films	Dünne Schichten f	Тонкие пленки	თხელი აფსკები/ფირები
Transmission electron microscope	Transmissionsel-ektronen-Mikroskop n	Микроскоп, электронный просвечивающий	გაშუქებითი ელექტრონული მიკროსკოპი
Transmission electron microscopy (TEM)	Transmissionsel-ektronen-Mikroskopie (TEM) f (Transmissions-Elektronen-mikroskopie f)	Микроскопия, электронная просвечивающая (ПЭМ) Микроскопия, трансмиссионная электронная (ТЕМ)	გაშუქებითი ელექტრონული მიკროსკოპია
Tri-metal nitride fullerenes	Trimetallnitrid-fulleride n pl	Триметаллонитрид-эндофуллерены (ТМН, ЭФ)	ტრილითონნიტრიდ-ფულერიდები (მაგ., $Sc_3N@C_{80}$)
Wet chemical methods	Methoden der Nasschemie f Nasschemie f	Мокрые химические методы “Мокрая” химия	“სველი” ქიმიური მეთოდები (მყარფაზური მეთოდის საპირისპიროდ

			ფხვნილების და მასალების მიღების მეთოდების – ზოლ-გელის მეთოდის, ჰიდროთერმული სინთეზის, კრიოქიმიური სინთეზის და სხვ. ჯგუფური სახელწოდება; ამ დროს ერთ-ერთ საფეხურზე აუცილებლად იყენებენ ხსნარს)
Zigzag SWNT / Zigzag SWCNT	Zickzackförmiges SWNT / Zickzackförmiges SWCNT	Зигзагообразная структура SWNT / Зигзагообразная структура SWCNT	SWNT / SWCNT-ის იკანკლური / ზიგზაგური სტრუქტურა (ნახშირბადის ნანომილაკის ერთ-ერთი სტრუქტურა)

The aim of our work was to present a first attempt to collect just used and to create the new Georgian terms in accordance with acknowledged in nanochemistry and nanotechnology foreign-language terms. The paper presents app. 215 terms in Georgian. Authors are continuing work on the second part of the dictionary and will respond on essential remarks and offers with pleasure.

References

1. Словарь нанотехнологических и связанных с нанотехнологией терминов. Электронный словарь. РОСНАНО. 2009. http://thesaurus.rusnano.com
2. Linguee.de- Das Web als Wörterbuch. http://www.linguee.de/
3. Dictionary of nanotechnology (Nanodictionary). http://www.nanodic.com/
4. ENZYKLO.Online Enzyklopädie. http://www.enzyklo.de/Begriffe/
5. M. Hirner. Űberblick über die Terminologie der Nanotechnologie. 2005, Wien Universität.
6. http://en.wikipedia.org/wiki/Science; http://en.wikipedia.org/wiki/Fulleren; http://en.wikipedia.org/wiki/Nanochemistry
7. http://de.wiktionary.org/wiki/Wiktionary:Deutsch
8. Нанотехнологии. Азбука для всех (под ред. Ю. Д. Третьякова). 2009, Москва: Физматлит.
9. Ч. Пул-мл., Ф. Оуэнс. Нанотехнологии. 3-е издание. 2007, Москва: Техносфера.
10. Г. Б. Сергеев. Нанохимия. 2007, Москва: Университет. Книжный дом.
11. У. Хартман. Очарование нанотехнологии. 2008, Москва: БИНОМ. Лаборатория знаний.

12. http://www.britannica.com/EBchecked/topic/221927/fulleride
13. Encyclopedia of Nanoscience and Nanotechnology. 10-Volume set. (Edited by Hari Singh Nalwa, Editor-in-Chief, Journal of Nanoscience and Nanotechnology). 2004, Valencia, California, USA: American Scientific Publishers. http://www.aspbs.com/enn.html
14. ტექნიკური ტერმინოლოგია. ქართულ–რუსული ნაწილი (რ. დვალის და რ. ღამბაშიძის რედაქციით). 1982, თბილისი: მეცნიერება.
15. ვ. თოფურია, ი. გიგინეიშვილი. ქართული ენის ორთოგრაფიული ლექსიკონი. 1968, თბილისი: განათლება.
16. რუსულ–ქართულ–ინგლისურ–გერმანული ქიმიური ლექსიკონი (რედაქტორები და გამომცემლები: ვ. დოლიძე, ვ. ციციშვილი). 2004, თბილისი: უნივერსალი.
17. http://www.dict.cc
18. სულხან–საბა ორბელიანი. ლექსიკონი ქართული. I, II. 1993, თბილისი: მერანი.
19. ა. ღლონტი. ქართულ კილო–თქმათა სიტყვის კონა. 1984, თბილისი: განათლება.

REGULATION OF DEFECT CREATION IN ZnO p-TYPE FILMS BY RBQE METHOD

T. Butkhuzi, M. Sharvashidze, T. Khulordava, N. Gapishvili, E. Kekelidze, N. Bukhsianidze, L. Aptsiauri, L. Trapaidze, R. Melkadze, I. Kamkamidze, L. Gapishvili

Ivane Javakhishvili Tbilisi State University
Tbilisi, Georgia
tamazbutkhuzi@yahoo.com

Accepted February 24, 2011

In order to obtain impurity p-type conductivity in ZnO nano-films we carried out following experiment: n-type ZnO was implanted with F^+ ions at the concentration 10^{20} cm^{-3} at the energy $E = 110$ keV and at the dose $D = 10^{16}$ cm^{-2}. Healing of the created defects in the implanted ZnO crystals were carried out by Radical Beam Quasi Epitaxy (RBQE) method. According to the measurements with van der Pauw method the hole mobility, hole concentration and resistivity were found as 270 $cm^2 / V \cdot s$, $1.0 \cdot 10^{19}$ cm^{-3} and $2.3 \cdot 10^{-3}$ $\Omega \cdot cm$, respectively. In photoluminescence (PL) spectrum (recorded at $T = 70$ K) of p-type ZnO:F layers maxima at $\lambda = 369.1$, 374.5, 382.4, 389.9 and 401 nm were observed.

Here we demonstrate the ability of the RBQE technology for control of electrical and optical properties of ZnO material.

ZnO has a wide band gap (3.3 eV at room temperature) and lattice constants that are similar to those of GaN are currently the key materials for blue and ultraviolet (UV) photonics [1, 2]. The exciton binding energy of ZnO is 60 meV, much larger than that of GaN (25 meV). Therefore, it is expected that a ZnO-based light emitter should be much brighter than a corresponding GaN light emitter. Furthermore, low material cost, high crystalline quality, and high radiation resistance make it a promising material to compete with GaN-based technologies [1, 3-5]. However, ZnO is more difficult to dope p-type than the nitrides [6-8]. This is because oxygen is more electronegative than N; therefore, ZnO has a lower valence-band maximum than GaN [9]. Consequently, acceptor levels are deep in ZnO, and following the "doping limit rule" [7], it will be much more difficult to dope ZnO p-type than to dope GaN p-type. The p-type doping bottleneck has so far hindered the full utilization of ZnO as a novel optoelectronic material [1]. The difficulty of doping a wide-gap semiconductor such as ZnO is often related to either low dopant solubility or high defect ionization energy, so the defect is not ionized at normal operating temperature [8]. The low solubility of the dopants can be overcome by using nonequilibrium growth techniques [10, 11].

Theoretical calculation predicted that fluorine (F) impurity is a best candidate for producing shallow acceptor levels in ZnO [12]. According to authors calculation the transition energies of complex pair V_{Zn} – F_O acceptor is 0.16 eV.

The RBQE (Radical Beam Quasi Epitaxy) technological method was developed to solve issue of control of electrical and optical properties of ZnO [13-16]. We separately investigated how effectively RBQE controls the electrical and optical characteristics of ZnO layers doped by fluorine.

Hall effect measurements (with van der Pauw method) show that p-type ZnO:F layers obtained by RBQE method have excellent characteristic: in PL spectrum of p-type ZnO:F layers maxima at $\lambda = 369.1$, 374.5, 383.5, 392.5 and 401 nm ($T = 70$ K) were observed.

RBQE enables the growth of quasi-epitaxial layers of ZnO on the surface of binary compounds such as ZnO, ZnS and ZnSe. The difference between RBQE and well-known gaseous-phase epitaxy is that during the formation of new layers, the non-metal component comes from the gaseous phase and the metal-component from the basic crystal. The second significant difference is that the basic crystal is placed in the area of maximum temperature of the reactor. This profile of temperature distribution promotes the movement of uncontrollable impurities towards the colder areas of the reactor. The formation of new layers takes place in the temperature range 300 to 1100 K, and experiment shows that p-type ZnO is obtained from thermal treatment at temperatures bellow 300 – 600 °C [13]. The RBQE method produces single crystalline layers of ZnO on the basic crystal of ZnO. The concentration of oxygen radicals was about $n_O \approx 10^{14} – 5 \cdot 10^{15}$ cm^{-3} [14, 16].

Accordingly of defect creation mechanism under RBQE method the concentration of V_{Zn} increases in the basic crystals. The concentration of oxygen vacancies in the basic n-type ZnO crystal was very high. Due to the increase of V_{Zn} concentration the Fermi level decreases to the valence band edge and a transfer of electrons from V_O^+ to V_{Zn} takes place, resulting in the creation of V_{Zn}^- and V_o^{+2}. With increased concentration of V_{Zn}^- and V_O^{+2} the probability of creation of (V_{Zn}^- – V_O^{+2}) increases too. Also is important that increasing of concentration of V_{Zn} and V_O^{+2} increases the probability of creation (V_{Zn} – V_O^{+2}). The creation energy of V_{Zn} defect near V_O is low as creation energy of V_{Zn} defect in the area where structural defects do not exist. So, predominant defects are V_{Zn}^-, V_O^{+2}, V_{Zn} (V_{Zn}^- – V_O^{+2}) and (V_{Zn} – V_O^{+2}). This model agrees with experimental data [14].

Using the first-principles band-structure method, authors [12] had demonstrated that the acceptor transition energies of V_{Zn} – O_O can be reduced by introducing F_O, because F is more electronegative than O.

Table 1.

Number and type	Treatment temperature $T_{Treatment}$, °C	Treatment time t, h	Investigation temperature $T_{Investigation}$, K	Carrier mobility μ, cm^2 / V · s	Carrier concentration n, cm^{-3}	Resistivity ρ, Ω · cm
1. n	400	3	300	1500	$1.5 \cdot 10^{19}$	2,7x10^{-4}
2. p	400	4	300	220	$1.6 \cdot 10^{18}$	1,8x10^{-2}
3. p	400	6	300	270	$1.0 \cdot 10^{19}$	2,3x10^{-3}
4. p	400	6	300	250	$7.7 \cdot 10^{18}$	1,8x10^{-3}

In order to obtain impurity p-type conductivity in ZnO we carried out following experiment: n-type ZnO (produced by Cermet, Inc.) was implanted with F^+ ions at the concentration 10^{20} cm^{-3} at the energy $E = 110$ keV and at the dose $D = 10^{16}$ cm^{-2}. Healing of the

created defects in the implanted ZnO crystals carried out by RBQE method. The duration of RBQE treatment was 3, 4 and 6 hours. As a result we obtain new ZnO:F quasiepitaxial layers. According to Hall measurement (with van der Pauw method) epitaxial ZnO:F layers obtained in 4 and 6 hours showed p-type conductivity. The measurement was performed at $T = 300$ K. Hall measurements are summarized in Table 1.

$I-V$ characteristics before and after annealing of ZnO:F (sample 4 by Cermet Inc.) treated by RBQE was investigated. $I-V$ investigation result (Figures 1 and 2) shows that p-i-n junction on the basis of ZnO / ZnO:F structure was obtained.

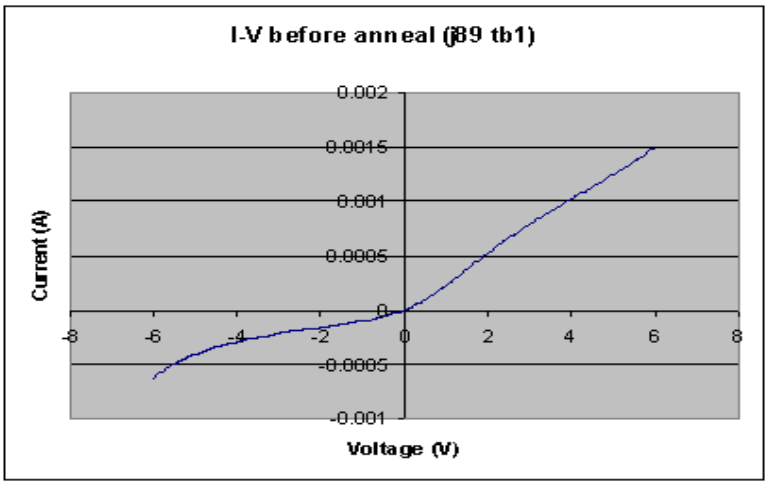

Figure 1. $I-V$ characteristic before annealing of ZnO:F (sample 4) treated by RBQE.

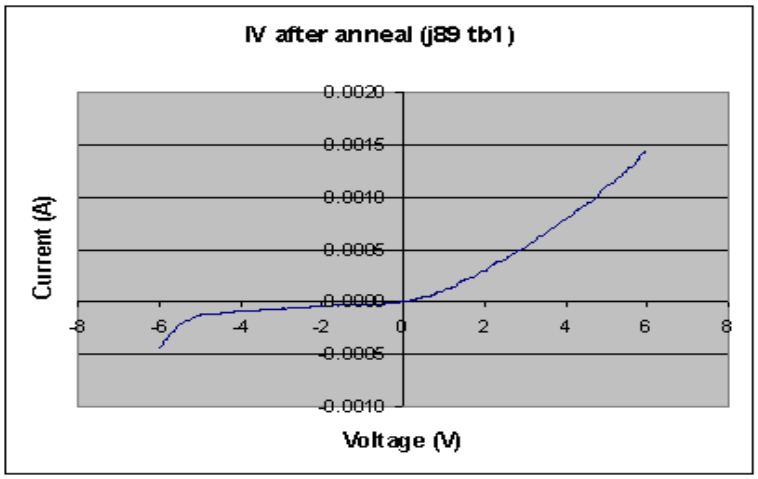

Figure 2. $I-V$ characteristic after annealing of ZnO:F (sample 4) treated by RBQE.

We have studied photoluminescence (PL) spectra of the initial n-type ZnO crystals and of new epitaxial p-type ZnO layers obtained by the RBQE method at temperatures of 70 K. The PL investigation was carried out with a FS 920 luminescence spectrometer (excitation source was $\lambda_{Excitation} = 313$ nm). The PL spectrum (recorded at $T = 70$ K) for the initial n-type ZnO gave maxima at $\lambda = 369.1$, 374.5, 383.5 and 392.5 nm (Figure 3a), while the quasiepitaxial p-type ZnO layers had maxima at $\lambda = 369.1$, 374.5, 382.4, 389.9 and 401 nm (Figure 3b).

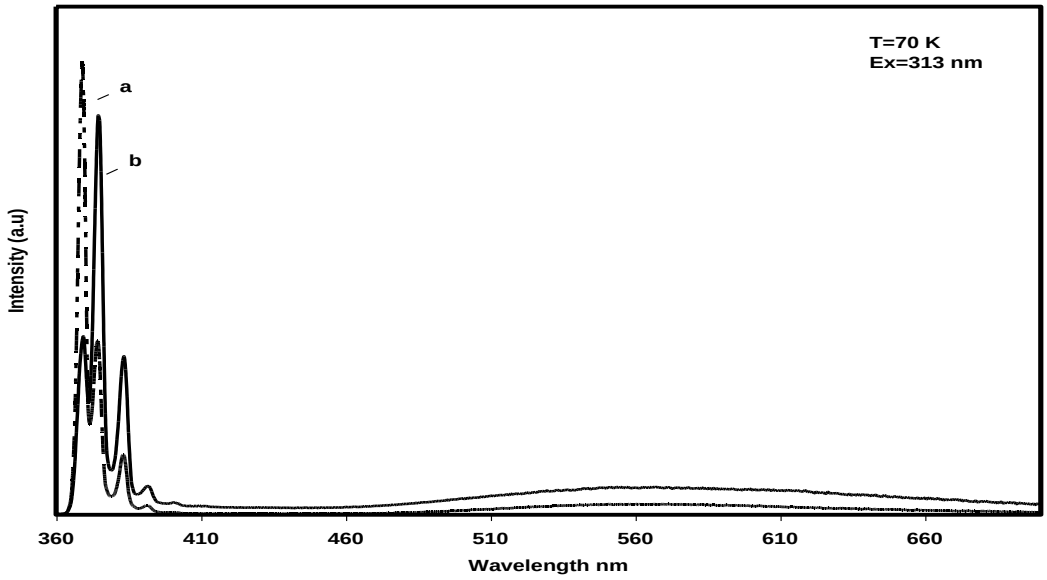

Figure 3

(b) p-type ZnO
(a) n-type ZnO

The Hall Effect and thermo-EMF measurements were made and showed the hole conductivity of the ZnO layers. Table 1 summarizing Hall measurements, demonstrates that obtained results depend on time of treatment. According to the investigation results we conclude that when the time of treatment is 3 hours ($T_{Treatment} = 400$ °C) the diffusion process of Zn atoms is very active through radioactive defects. As a result the concentration of Zn atoms in new epitaxial layers is very high and obtained layers (to 150 nm) have n-type characters. The time of treatment 3 hours is nonsufficient for healing of radiation defect created under implantation.

When we increased the time of the treatment to 4 and 6 hours, conductivity type has changed to p-type and our investigation demonstrated that the higher the treatment time the better the electric characteristics of new layers become. The time of treatment 4 hours is just sufficient for healing of radiation defects created under implantation and obtained layers (to 150 nm) have p-type characters.

The specific mechanism of defect creation takes place in ZnO under the RBQE treatment and associate ($V_{Zn} - V_O^{+2}$) is obtained. Consequently when we implant ZnO sample with fluorine and then treat it by the RBQE associative defects ($V_{Zn} - F_O^{+2}$) are created [12]. Accordingly, these are the defects which are responsible for p-type conductivity in new constructed layers. Correspondingly the better electric properties obtained under RBQE treatment for 6 hours is due to the higher concentration of created associate ($V_{Zn} - F_O^{+2}$).

Observation of acceptor bound exciton in p-type ZnO layers obtained by RBQE also demonstrates high purity and perfect structure.

In order to identify the defects responsible for the bands observed in the PL spectra we considered the specific mechanism of defect creation in ZnO under RBQE.

The maximum $\lambda = 401$ nm band in the PL spectrum (at $T = 70$ K) must be connected to the V_{Zn}^- level (Figure 3b). The low intensity of this line may be explained by the low electron capture cross-section [17]. The peak at $\lambda = 382.4$ nm is connected to the associated ($V_{Zn}^- - V_O^{2+}$) level [15, 18], which for p-type conductivity is in good agreement with theoretical and experimental estimations for acceptor centers [14]. The peak $\lambda = 389.9$ nm could be connected

to the ($V_{Zn} - F_o^{2+}$) (Figure 3b). In work [19] authors identified the peak in PL spectrum of ZnO co-doped with fluorine and with phosphor. In Pl spectrum the level 3.180 eV (389.6 nm) was observed and identified as free electron to donor–acceptor pair (DAP) transitions ($T = 8.5$ K).

The high intensity $\lambda = 374.5$ nm band observed corresponds to acceptor bound excitation (Figure 3a). The peak at $\lambda = 369.1$ nm in the PL spectrum of initial n-type ZnO samples is more intensive than that at $\lambda = 374.5$ nm (Figure 3a). The peak positions at $\lambda = 369.1$ and 374.5 nm correspond to donor bound excitons [20, 21] and acceptor bound excitons [22, 23], respectively. Results for the acceptor bound exciton in p-type ZnO layers obtained by RBQE demonstrate the high purity and perfect structure and a significantly reduced number of residual defects.

The RBQE method provides control of the defect creation mechanism in the production of ZnO wide-gap semiconductors, and consequently the determination of the electrical and optical properties of the samples. In particular, the RBQE method has the following important advantage: for fixed oxygen concentration it is possible to regulate the concentration of Zn extracted from the basic crystal by variation of temperature. The method allows control of the stoichiometric composition both in the growing of ZnO layers and in the basic ZnO crystal. The acceptor bound exciton in the p-type ZnO layers obtained by RBQE exhibits high purity and perfect structure. This result is one of the most important achievements for production of non-degradation diode on the basic of ZnO / ZnO.

By means of the RBQE method it is possible to produce n- and p-type stoichiometric layers of ZnO with thickness from a few atomic layers to 25 μm. The size of basic crystals in the RBQE reactor changes from 1 to 4 cm^2 and with modernized of the RBQE reactor can be increased.

By the RBQE method we were obtained the blue light emitting diode on the basis of Au–ZnO–ZnSe–In system [16].

Acknowledgement

The authors are very grateful to the Science and Technology Department of Georgia for the financial assistance. “The designated project has been fulfilled by financial support of the Georgia National Science Foundation (Grants # GNSF/ST07/4-192, # GNSF/ST07/4-187). Any idea in this publication is possessed by the author and may not represent the opinion of the Georgia National Science Foundation itself”.

References

1. D. C. Look, B. Claflin, Y. I. Alivov, S. J. Park. Phys. Status Solidi A, 2004, **201**, 2203.
2. H. Morkoc. Nitride Semiconductors and Devices. 1999, New York: Springer.
3. D. M. Bagnall, Y. F. Chen, Z. Zhu, T. Yao, S. Koyama, M. Y. Shen, T. Goto. Appl. Phys. Lett., 1997, **70**, 2230.
4. Z. K. Tang, G. K. L. Wong, P. Yu, M. Kawasaki, A. Ohtomo, H. Koinuma, Y. Segawa. Appl. Phys. Lett., 1998, **72**, 3270.

5. D. K. Hwang, S. H. Kang, J. H. Lim, E. J. Yang, Y. J. Oh, J. H. Yang, S. J. Park. Appl. Phys. Lett., 2005, **86**, 222101.
6. S. J. Pearton, F. Ren, A. P. Zhang, K. P. Lee. Mat. Sci. & Eng. B, 2000, **30**, 55.
7. S. B. Zhang, S.-H. Wei, A. Zunger. J. Appl. Phys., 1998, **83**, 3192.
8. S.-H. Wei. Comp. Mat. Sci., 2004, **30**, 337.
9. S.-H. Wei, A. Zunger. Appl. Phys. Lett., 1998, **72**, 2011.
10. Y. Yan, S. B. Zhang, S. T. Pantelides. Phys. Rev. Lett., 2001, **86**, 5723.
11. S. B. Zhang, S.-H. Wei. Phys. Rev. Lett., 2001, **86**, 1789.
12. J. Li, S.-H. Wei, S.-S. Li, J. B. Xia. Phys. Rev. B, 2006, **74**, R 081201.
13. T. Butkhuzi., T. Khulordava, B. Tsekvava, T. Chelidze, D. Djashiashvili. Phys. Rev. B, 1998, **58**, 10692.
14. T. V. Butkhuzi, M. Sharvashidze, T. Khulordava, N. Kekelidze, E. Kekelidze, Kh. Gelovani. Semicond. Sci. & Technol., 2001, **16**, 575.
15. T. V. Butkhuzi et al. In: International Conference on Solid State Crystals Epilayers and Heterostructures in Optoelectronics and Semiconductor Technology, 1998, 53.
16. T. V. Butkhuzi, T. G. Khulordava, A. N. Georgobiani, A. N. Buryaev. J. Crystal Growth, 1992, **117**, 1055.
17. A. Kohan, G. Cender, C. van de Walle. Phys. Rev. B, 2000, **61**, 1519.
18. V. V. Ursaki et al. Semicond. Sci. & Technol., 2004, **19**, 851.
19. F. X. Xiu, Z. Yang, L. J. Mandalapu, J. L. Liu, W. P. Beyermann. Appl. Phys. Lett., 2006, **88**, 052106.
20. A. Teke, U. Ozgur, S. Dogan. Phys. Rev. B, 2004, **70**, 1.
21. S. F. Chichibu et al. J. Appl. Phys., 2003, **93**, 759.
22. A. B. M. A. Ashrafi et al. Jpn. J. Appl. Phys. (Part 2), 2002, **41**, LI 281.
23. D. C. Look et al. Appl. Phys. Lett., 2002, **81**, 1830.

FARADAY ROTATION IN ULTRAFINE MAGNETIC STRUCTURES

L. Kalandadze

Shota Rustaveli State University
Batumi, Georgia
lali62@mail.ru

Accepted March 6, 2011

In this work, we consider Faraday rotation in magnetic fluids based on particles of magnetic oxides, for the optical constants of the material of which, n and k, the relation $k^2 << n^2$ holds. In this work the Faraday rotation is represented within the theoretical Maxwell–Garnett model. A theoretical analysis has shown that Faraday rotation for magnetic fluids is related to the Faraday rotation on the material of particles by the simple relation. According to this result in specific experimental conditions the values of the Faraday rotation prorate to q, which is the occupancy of the volume of the magnetic fluid with magnetic particles and spectral dependences of the Faraday rotation in magnetic fluid and in the proper bulk magnetic are similar. We would like to underline that this result are expected to be suitable to all magnetic ultrafine medium with the same relation between optical constants: $k^2 << n^2$.

1. Introduction

Nowadays, magneto-optical research methods are widely used for examination of ultrafine magnetic structures with insertions that have the sizes of structural and magnetic heterogeneities less than 1000 Å. Magneto-optical investigation of these types of structures are subject of overall interest, which is conditioned by both theoretical and practical importance.

In general, the magneto-optical properties of magnetic fluids are very different from the properties of the bulk ferromagnetic. This fact causes the changes in spectral and angular dependences of the magneto-optical effects. The reason for this is that magnetic fluids represent an example of a magnetic ultrafine medium composed with magnetic particles, the sizes of which are much less than the light wavelength. Therefore, it is important to define clearly the conditions of the magneto-optical experiment to make easier the interpretation of the magneto-optical spectra, which in its turn, provides with the information of surface layer of magnetized magnetic fluids, electronic energy structure of fine magnetic particles, as well as of the properties of carrier fluids. Besides, it is significant to examine the electronic energy structures of fine magnetic particles not only to investigate the temporary stability of magnetic fluids, but also to analyze the chemical processes on the surface of the magnetic particles. On the other hand, in some cases the fine magnetic particles could be used as a probe.

2. Theory

In [1] using magnetite magnetic fluids as examples, it was considered the magneto-optical reflection effect for magnetic fluids based on particles of magnetic oxides, for the optical constants of the material of which, n and k, the relation $k < n$ holds. In this research the equatorial Kerr effect is represented within the theoretical Maxwell–Garnett model. A theoretical analysis has shown that in the case of magnetic oxides, for which the condition $k^2 << n^2$ is fulfilled, the equatorial Kerr effect $\delta_e(q)$ for magnetic fluids with the ratio of the volume occupied by magnetic particles is related to the equatorial Kerr effect δ_m on the material of particles by the following simple relation:

$$\delta_e(q) = q\delta_m . \tag{1}$$

We did analogous researches for Faraday rotation. When considering the magneto-optical effects, which are odd function of magnetization, in magnetic fluids, it should be kept in mind that magnetic fluid is a variety of the ultrafine media [2].

The magneto-optical properties of ultrafine media were analyzed in [3]. It was shown that when considering the magneto-optical properties of medium consisting of magnetic colloidal particles the sizes of which are much less than the light wavelength, one should introduce the tensor of the effective dielectric permittivity:

$$\varepsilon_{eff} = \begin{bmatrix} \varepsilon_{eff} & -i\varepsilon'_{eff} & 0 \\ i\varepsilon'_{eff} & \varepsilon_{eff} & 0 \\ 0 & 0 & \varepsilon_{0eff} \end{bmatrix}, \tag{2}$$

where $\varepsilon_{eff} = \varepsilon_{1eff} - i\varepsilon_{2eff}$, $\varepsilon_{0eff} = \varepsilon_{01eff} - i\varepsilon_{02eff}$ and $\varepsilon'_{eff} = \varepsilon'_{1eff} - i\varepsilon'_{2eff}$.

In this case, the tensor components depend on both the properties of magnetic colloidal particles themselves and the properties of the medium in which they find themselves.

Diagonal component of (1) is connected to reflective index n_{eff} and absorption index k_{eff} of ultrafine media by formula:

$$\varepsilon_{eff} = (n_{eff} - ik_{eff}) . \tag{3}$$

For magnetic fluids with a low concentration of magnetic colloidal particles and consequently, with no interaction between them, the tensor components of the effective dielectric permittivity within the framework of the theoretical Maxwell–Garnett model of an effective medium can be written as:

$$\varepsilon_{eff} = \frac{2q(\varepsilon_m - \varepsilon_0) + (\varepsilon_m + 2\varepsilon_0)}{(\varepsilon_m + 2\varepsilon_0) - q(\varepsilon_m - \varepsilon_0)}, \tag{4}$$

$$\varepsilon'_{eff} = \frac{9q\varepsilon_0^2\varepsilon'_m}{(\varepsilon_m(1-q) + \varepsilon_0(2+q))^2}, \tag{4'}$$

where $\varepsilon_m = \varepsilon_{1m} - i\varepsilon_{2m}$ and $\varepsilon'_m = \varepsilon'_{1m} - i\varepsilon'_{2m}$ are the diagonal and non-diagonal tensor components of the dielectric permittivity of the material of magnetic colloidal particles, ε_0 is the dielectric permittivity of the fluid phase, and q is the ratio of the volume, occupied by magnetic particles, to the total volume of the magnetic fluid.

In the research, the Faraday rotation is represented within the framework of the theoretical Maxwell–Garnett model.

The Faraday effect is related to the tensor components of the effective dielectric permittivity as follows [2]:

$$\alpha_F = \frac{\pi}{\lambda} \mathrm{Re} \frac{\varepsilon_{eff}^{'}}{\sqrt{\varepsilon_{eff}}}, \tag{5}$$

where $\varepsilon_{eff} = \varepsilon_{1eff} - i\varepsilon_{2eff}$ and $\varepsilon_{eff} = \varepsilon_{1eff}^{'} - i\varepsilon_{2eff}^{'}$.

In this case, considering the following relation $k^2 << n^2$ and formula (2), Faraday rotation can be expressed in this way:

$$\alpha_F = \frac{\pi}{\lambda n_{eff}^2} (\varepsilon_{1eff}^{'} n_{eff} + \varepsilon_{2eff}^{'} k_{eff}). \tag{6}$$

Taking into account formulas (3) for real and imaginary parts of the tensor of the effective dielectric permittivity $\varepsilon_{eff}^{'}$ together with $k^2 << n^2$ and $k_{eff}^2 << n_{eff}^2$ formula (5) takes the form:

$$\alpha_F = \frac{\pi q n_0^2}{\lambda} \frac{\varepsilon_1^{'} n_0 + 4yk\varepsilon_2^{'}}{(y(n^2 - n_0^2) + n_0^2)^2}, \tag{7}$$

where $y = (1-q)/3$ and n_0 is the reflective index of liquid carrier.

If $n_0 \approx n$, then

$$\alpha_F = \frac{\pi q}{\lambda n^2} (\varepsilon_1^{'} n + 4yk\varepsilon_2^{'}). \tag{8}$$

Note that we have the following correlation: when $q < 0.4$, then $4y \approx 1$. Thus the expression for the Faraday rotation could be written down in the simpler way:

$$\alpha_F(q) = q\alpha_{FM}, \tag{9}$$

where $\alpha_F(q)$ is Faraday rotation for magnetic fluids with the ratio of the volume occupied by magnetic particles q; α_{FM} – Faraday rotation on the material of particles.

It is necessary to say that received results (9) represent truth if only these two conditions are followed: (1) $k^2 << n^2$; (2) $n_0 \approx n$.

It follows from the relation obtained that in the specific experimental conditions the amount of Faraday effect is proportional to q and therefore to magnetization itself. Also, the character of spectral dependences of magneto-optical effects, are similar for the magnetic fluids and the substance of particles.

3. Results and discussion

Figure 1 represents the results of calculations of $\alpha_F(q)$ made by means of the formula (5) for magnetite particles in the air (a) and in the liquid silicon-organic compound (b), and by the formula (9). Calculations were carried out for different q. From the Figure 1 it is obvious that the magneto-optical maxima for magnetite particles shift to the side of large energies. If we increase ε_0, this shift diminishes, and for the liquid silicon-organic compound ($\varepsilon_0 = 2.56$) the shift approximates to the zero. The results derived from our research indicate that calculations conducted according to (5) for large ε_0 ($\varepsilon_0 = 2.56$), coincide with the calculations carried out by the simplified formula (9).

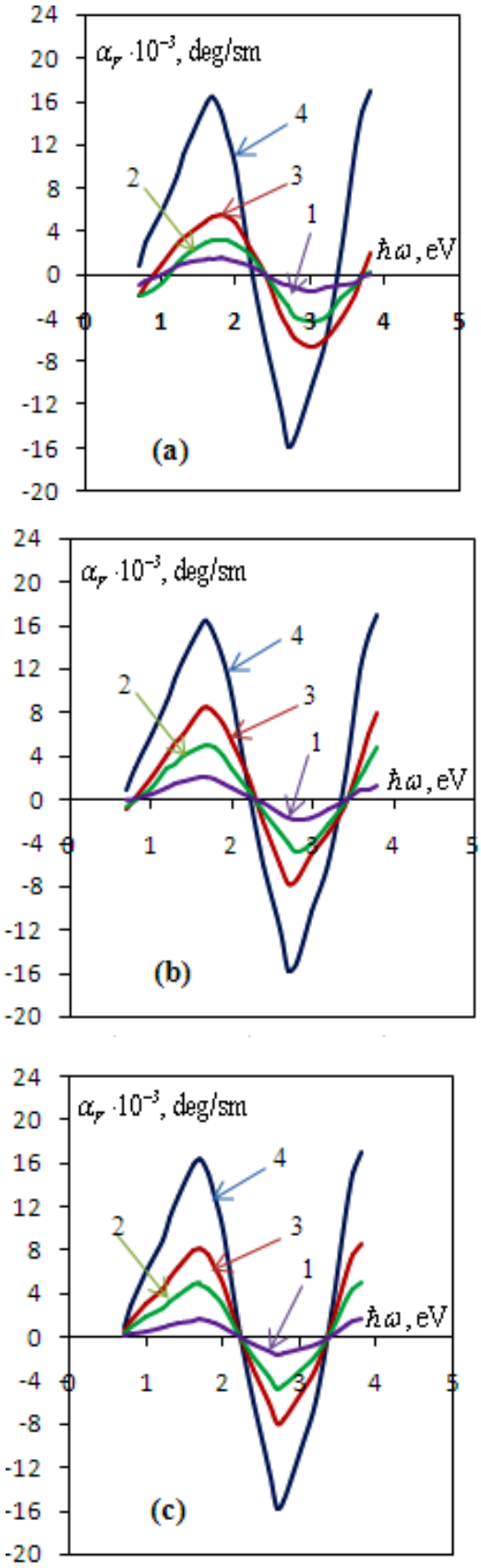

Figure 1. Dependences of the Faraday rotation on the quantum energy of incident light $\hbar\omega$, calculated by formula (5) for magnetite particles in the air (a) and in the liquid silicon-organic compound (b); and by the formula (9) (c) with $q = 0.1 - 1$, $0.3 - 2$, $0.5 - 3$ and $1 - 4$.

We did analogous calculations using formulas (5) and (9) for magnetite particles in order to verify the linear dependence of Faraday rotation on q. Figure 2 shows the correlations of Faraday rotation to q for magnetite particles, which are calculated by formulas (5) and (9) at the quantum energy of incident light $\hbar\omega = 1.7$ eV.

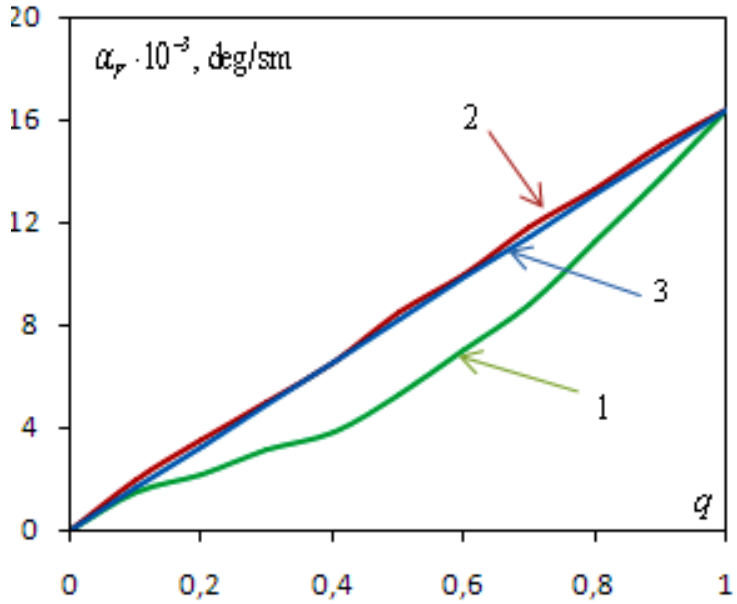

Figure 2. Dependences of the Faraday rotation on q, calculated by formula (5) for magnetite particles in the air – 1 and in the liquid silicon-organic compound – 2, and by the formula (9) – 3 at $\hbar\omega = 1.7$ eV.

From the Figure 2 it is obvious that the linear dependences of Faraday rotation on q have been observed only for large ε_0 ($\varepsilon_0 = 2.56$).

Our results are in a good relation with the experiments [4], where Faraday rotation has been studied in magnetite magnetic fluids with different concentrations.

4. Conclusion

In the present paper, on the example of magnetite magnetic fluids we considered Faraday rotation in magnetic fluids based on particles of magnetic oxides. Within the framework of the theoretical Maxwell–Garnett model the simple relation between the Faraday rotation for ultrafine medium and bulk material is revealed. The conditions of the magneto-optical experiment were defined for the essential analytical simplification of the subsequently received results.

In conclusion, we would like to underline that this result are expected to be suitable to any magnetic ultrafine medium with the same relation between optical constants: $k^2 << n^2$.

References

1. L. Kalandadze. J. Phys.: Conf. Ser., 2010, **200**, 072043.
2. L. V. Nikitin, L. G. Kalandadze, M. Z. Akhmedov, S. A. Nepijko. J. Magn. & Magn. Mat., 1995, **148** , 279.
3. G. S. Krinchik, L. V. Nikitin, O. V. Kasatkina. Surf.: Phys., Chem. & Mech., 1985, **7**, 140.
4. A. Akram Rousan, M. Hassan El-Ghanem, A. Yusuf. IEEE Trans. Magn., 1989, **25**, 3121.

ვეივლეტ ტექნოლოგიები ნანომედიცინაში

ი. მ. ჩხეიძე, ლ. შ. ტოკაძე

საქართველოს ტექნიკური უნივერსიტეტი
თბილისი, საქართველო
irmikh2002@mail.ru

მიღებულია 2011 წლის 7 მარტს

1. შესავალი

ვეივლეტ-ტექნოლოგიები თანამედროვე ელექტრონულ ბიო–მედიცინაში განიხილება როგორც ინფორმაციული გრიდ-ტექნოლოგიების (HealthGrid) ინოვაციური გამოყენების მაგალითი. ელექტრონული გრიდ-ტექნოლოგიების [1] ძირითადი გამოყენების სფეროს წარმოადგენს სამედიცინო გამოსახულებათა დამუშავება და ანალიზი, ასევე გრიდ-ტექნოლოგიები გამოიყენება ფარმაცევტიკაში, გენომიკაში და ბიოინფორმატიკაში. ყველა ეს მიმართულება უკავშირდება ნანოტექნოლოგიას და ნანომედიცინას. დისკრეტული ვეივლეტ ტექნოლოგიის [2] გამოყენება სხვადასხვა სახის ინფორმაციის ციფრული მეთოდებით დამუშავებისას განპირობებულია ვეივლეტ გარდაქმნების უნიკალური თვისებებით: ინფორმაციის შეკუმშვის უნარით და აღდგენის მაღალი ხარისხით, გამოსახულებაში საინტერესო არეების გამოყოფისა და შეცდომებიანი სიგნალიდან და გამოსახულებიდან შეცდომების აღმოფხვრის უნარებით.

წინამდებარე გამოკვლევის მიზანია ბიო–სამედიცინო და ნანოსამედიცინო ინტროსკოპიის სფეროში ვეივლეტ-ტექნოლოგიების გამოყენების ეფექტურობის შეფასება. სამედიცინო ინტროსკოპიის კომპიუტერული ტომოგრაფიის [3] მეთოდების სახესხვაობები მოცემულია ცხრილში 1.

ცხრილი 1.

მეთოდი	სიმკვრივე
რენტგენული გამოსხივება. კომპიუტერული რენტგენული ტომოგრაფია (კრტ)	რენტგენული გამოსხივების კოეფიციენტის შემცირება
γ-გამოსხივება. ერთფოტონიანი ემისიური კომპიუტერული ტომოგრაფია	რადიოაქტიური იზოტოპით ნიშანდებული ნივთიერების კონცენტრაცია
პოზიტრონული გამოსხივება. ორფოტონიანი პოზიტრონული ემისიური კომპიუტერული ტომოგრაფია	პოზიტრონებით ნიშანდებული ნივთიერების კონცენტრაცია
მაგნიტური ველი. მაგნეტო-ბირთვული რეზონანსის საფუძველზე აგებული კომპიუტერული ტომოგრაფია	პროტონების სიმკვრივე
ულტრაბგერა. ულტრაბგერული კომპიუტერული ტომოგრაფია	აკუსტიკური წინაღობა
მძიმე ნაწილაკები (იონები, α-ნაწილაკები, პროტონები და ა.შ.)	შთანთქმის განივი კვეთა
ინფრაწითელი გამოსხივება	ტემპერატურის სივრცული განაწილება
ზემაღალსიხშირული გამოსხივება	დიელექტრიკული შეღწევადობის და გამტარობის განაწილება

2. ვეივლეტ ტექნოლოგიების რეალიზაცია

ვეივლეტ ტექნოლოგიების რეალიზაციისათვის გამოვიყენეთ *Mathcad* პროგრამული გარემო [4], რომელშიც ვეივლეტ ტექნოლოგიების საფუძვლებზე აგებული ალგორითმები გამოირჩევიან სიმარტივით, რეალიზაციის სწრაფქმედებით და მაღალი სიზუსტით.

კვლევის ობიექტად ავირჩიეთ აკადემიკოს ა. მ. სარაჯიშვილის სახელობის კლინიკური ნევროლოგიისა და ნეიროქირურგიის ინსტიტუტიდან მოწოდებული ჯანმრთელი და ავადმყოფი ადამიანების ინტროსკოპიული გამოსახულებები (მათი სურათები მოცემულია ფიგურებზე 1-3) და სიგნალი, რომელიც მიღებულია მაგნიტო-ბირთვული რეზონანსული ტომოგრაფიით [3].

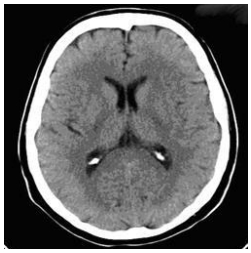

ფიგურა 1. ჯანმრთელი თავის ტვინი.

ფიგურა 2. ჰემორაგია.

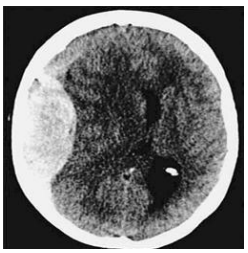

ფიგურა 3. ეპიდურული სისხლჩაქცევა.

პირველ შემთხვევაში, ჩვენი მიზანი იყო ინფორმაციის შეკუმშვის ანალიზი. შეკუმშვის კოეფიციენტი C განისაზღვრება ფორმულით

$$C = \frac{N_1 \cdot N_2 \cdot 8bit}{N_1 \cdot N_2 \cdot n\% \cdot 8bit}, \qquad (1)$$

სადაც n არის შენარჩუნებული კოეფიციენტების რაოდენობა, ხოლო N_1 და N_2, შესაბამისად, სტრიქონებისა და სვეტების რაოდენობაა გამოსახულებაში; $8bit$ არის ორობითი ერთეულების ის რაოდენობა, რომელიც საჭიროა ერთი ანათვალის გადასაცემად. ჩვენს შემთხვევაში $n = 5$, 10 ან 15 %-ს, ხოლო

$$C = \frac{2^8 \cdot 2^8 \cdot 8bit}{2^8 \cdot 2^8 \cdot n\% \cdot 8bit}. \qquad (2)$$

ყოველ შეკუმშვას შეესაბამება გამოსახულების აღდგენის შესაბამისი ხარისხი, რომელიც ფასდება სიგნალ / ხმაურის პიკური ფარდობით:

$$\text{სხპფ} = -10\log\left\{\frac{\frac{1}{256^2}\sum_{m=0}^{m=255}\sum_{n=0}^{n=255}\left[f(m,n) - f'(m,n)\right]^2}{255^2}\right\}, \qquad (3)$$

სადაც $f(m,n)$ (m,n) -კოორდინატებზე საწყისი გამოსახულების ანათვალის ინტენსივობაა, $n = 0,\ldots,255$ და $m = 0,\ldots,255$; $f'(m,n)$ აღდგენილი გამოსახულების ანათვალის ინტენსივობაა იგივე კოორდინატებზე; ხოლო $N_1 = 256$ და $N_2 = 256$, შესაბამისად, სტრიქონებისა და სვეტების რაოდენობებია გამოსახულებაში.

გამოვიყენეთ ორი სახის ვეივლეტ ფუნქცია: ჰაარის და დაუბეშ 4-ის ფუნქციები, რომელთაც აქვთ ფიგურებზე 4 და 5 ნაჩვენები სახეები.

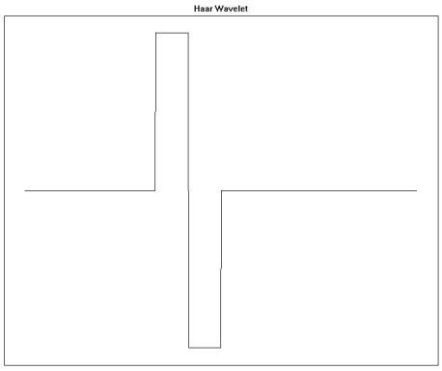

ფიგურა 4. ვეივლეტის ფუნქცია Haar.

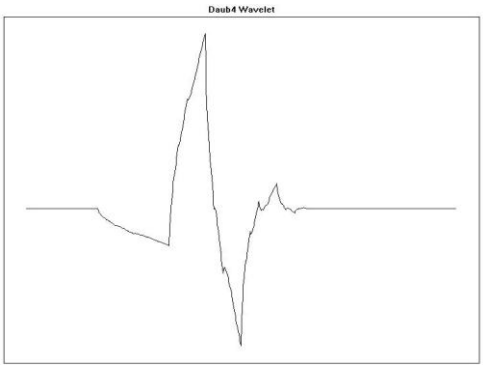

ფიგურა 5. ვეივლეტის ფუნქცია D4.

ჯანმრთელი ადამიანის თავის ტვინის მახასიათებლები მოყვანილია ცხრილში 2.

ცხრილი 2.

გამოსახულების დასახელება	ვეივლეტი	სხპფ
ჯანმრთელი თავის ტვინი	Haar 10 %	29.6400
	D4 5 %	27.7658
	D4 10 %	31.6137
	D4 15 %	34.2339

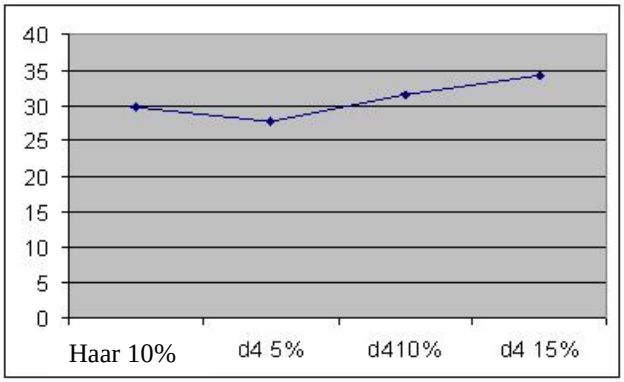

ფიგურა 6. აღდგენილი გამოსახულების დამოკიდებულება შენარჩუნებული კოეფიციენტების რაოდენობაზე.

ამ შედეგების საფუძველზე იქნა აგებული გრაფიკი (ფიგურა 6), საიდანაც ჩანს, რომ დაუბეშ ფუნქციამ უკეთესი შედეგი მოგვცა. ამიტომ ამავე მეთოდით იყო დამუშავებული ორი დაავადების მქონე ადამიანის თავის ტვინის გამოსახულება (ჰემორაგია და ეპიდურული სისხლჩაქცევა). შესაბამისი ცხრილი და გრაფიკები მოცემულია ქვემოთ (ცხრილი 3 და ფიგურა 7).

ცხრილი 3.

გამოსახულების დასახელება	ვეივლეტი		
	D4 5 %	D4 10 %	D4 15 %
ჯანმრთელი თავის ტვინი	27.7658	31.6137	34.2339
ჰემორაგია	22.4093	25.0711	27.2266
ეპიდურული სისხლჩაქცევა	25.0444	28.0297	30.4001

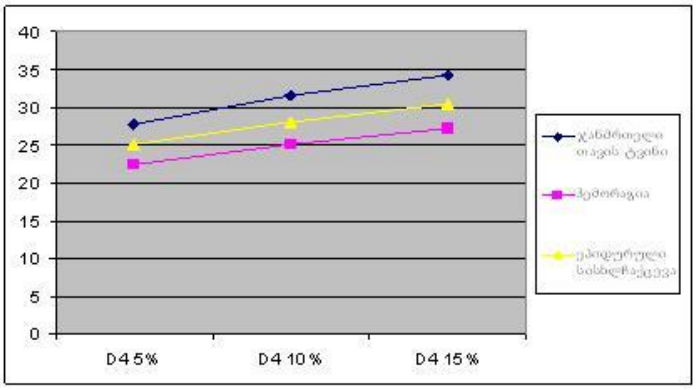

ფიგურა 7. აღდგენილი გამოსახულების დამოკიდებულება ტრანსფორმანტში შენარჩუნებული კოეფიციენტების რაოდენობაზე.

მეორე ექსპერიმენტი ეხებოდა მაგნიტო-ბირთვული რეზონანსის საფუძველზე მიღებული კომპიუტერული ტომოგრაფიის სიგნალს. გვაინტერესებდა ვეივლეტ გარდაქმნის მეორე უნიკალური თვისების შემოწმება: გარდაქმნის უნარი აღმოფხვრას ხმაური, რომელიც ყოველთვის ახლავს სიგნალს. სასარგებლო სიგნალის გამოყოფა ხმაურიანი სიგნალიდან ხდებოდა დონოჰიუსა და ჯონსოუნის მეთოდით [2]. ეს მეთოდი გამოვიყენეთ ბირთვულ მაგნეტო-რეზონანსის (რეალურად მიღებული) სიგნალისათვის, რომლის ფორმაც მოცემულია ფიგურაზე 8.

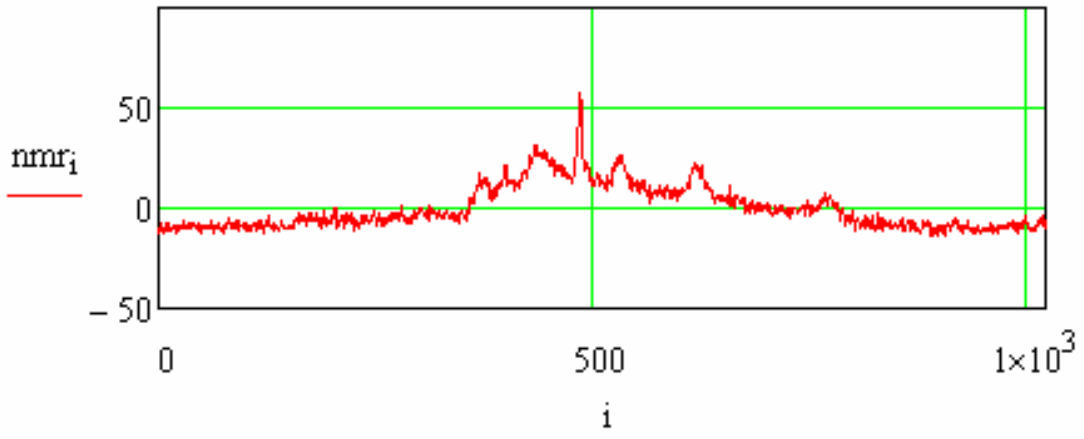

ფიგურა 8. ხმაურდადებული სიგნალი.

როგორც ნახაზიდან ჩანს, სიგნალს თან ახლავს ხმაური, რომელიც ისე უნდა აღმოიფხვრას, რომ სასარგებლო სიგნალის ყველა დამახასიათებელი ამპლიტუდური

ნახტომი (მკვეთრი გაზრდა ან შემცირება) იქნას შენარჩუნებული. მიღებული შედეგი ასახულია ფიგურაზე 9. ვხედავთ, რომ აღდგენილ გამოსახულებაში შენარჩუნებულია სასარგებლო სიგნალისათვის დამახასიათებელი მკვეთრი და იმპულსური ხასიათის ცვლილებები.

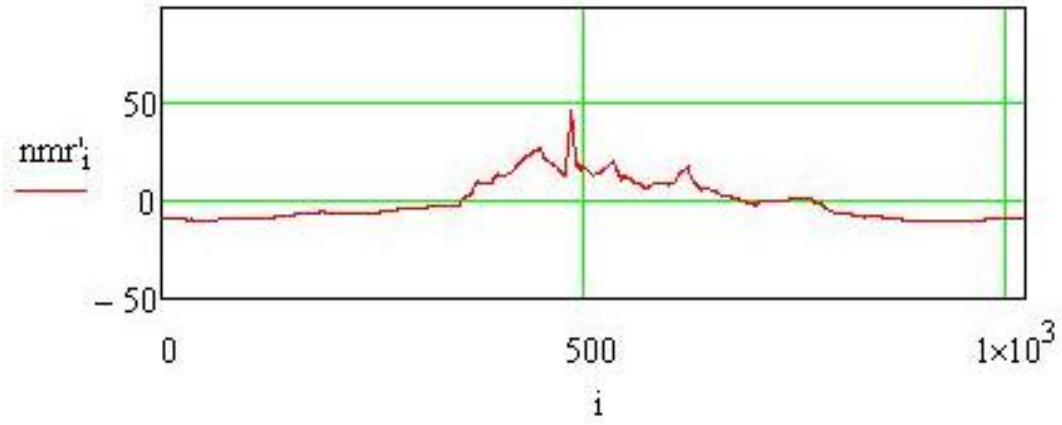

ფიგურა 9. სიგნალის სახე შეცდომების აღმოფხვრის შემდეგ.

ამრიგად, *waveshrink* ფუნქციის საშუალებით შესაძლებელი გახდა ხმაურის აღმოფხვრა ამ სიგნალის განმსაზღვრელი მახასიათებლის შენარჩუნებით.

შემდეგი ექსპერიმენტი ეხებოდა *Mathcad* პროგრამულ გარემოში არსებული ოპერაციების საფუძველზე გამოსახულებაში კვლევის ობიექტის დეტალებისა და კონტურების გამოყოფას (ფიგურები 10-14). გამოსახულებაში კონტურების გამოყოფა ხდებოდა *Canny* (*M*, *sigma*, *low*, *high*) ფუნქციის საშუალებით, ხოლო "მორფოლოგიური" ოპერაციების და ნიღაბის შექმნის გამოყენებით სამედიცინო გამოსახულების სეგმენტირება – მორფოლოგიური ოპერაციებისა და *masking* ფუნქციის მეშვეობით.

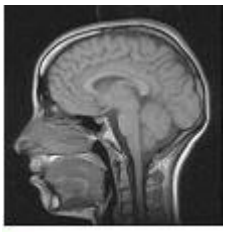

ფიგურა 10. საწყისი გამოსახულება.

ფიგურა 11. გამოსახულებაში კონტურების გამოყოფა.

ფიგურა 12. საწყისი გამოსახულება.

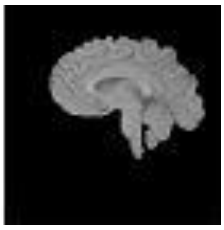

ფიგურა 13. ობიექტის გამოყოფა.

ფიგურა 14. შავ-თეთრი ობიექტი.

3. დასკვნა

კომპუტერულმა ექსპერიმენტულმა შემოწმებამ აჩვენა, რომ

1. შეკუმშვის შედეგად მიღებული აღდგენილი გამოსახულების სიგნალ / ხმაურის პიკური მნიშვნელობა მცირდება: შემცირება შეადგენს 7 dB-ს ჰემორაგიის დროს 15 %-იანი კოეფიციენტების შენარჩუნების პირობებში, მაშინ როდესაც ეპიდურული სისხლჩაქცევის დროს იგი უდრის 4 dB-ს. აღდგენილი გამოსახულების ხარისხის დამაკმაყოფილებელი შედეგი მიიღება მაშინაც, როდესაც გამოსახულების აღდგენაში მონაწილეობს მხოლოდ 10 % ტრანსფორმანტის კოეფიციენტისა (სხპფ = 28.33 dB).

2. მაგნიტო-ბირთვული რეზონანსის სიგნალზე შემოწმებული იქნა ვეივლეტ გარდაქმნის უნარი შეცდომებიანი სიგნალიდან სასარგებლო სიგნალის გამოყოფისა. ექსპერიმენტის შედეგებმა გვიჩვენეს, რომ დონოჰიუსა და ჯონსოუნის მეთოდის გამოყენებით შესაძლებელი გახდა მოგვეხდინა ხმაურის იმგვარი ფილტრაცია, რომ საბოლოო სიგნალში შენარჩუნდა ყველა ის საჭირო მახასიათებელი, რომელიც მონაწილეობს დიაგნოსტიკაში. ამავე დროს სიგნალი გაიწმინდა ხმაურისაგან, რომელიც უშლიდა ხელს დიაგნოზის დასმას. ნაჩვენებია, რომ *Mathcad* პროგრამულ გარემოში ვეივლეტ-ტექნოლოგიის საფუძველზე აგებული ალგორითმები გამოირჩევიან სიმარტივით, რეალიზაციის სწრაფქმედებით და მაღალი სიზუსტით.

3. *Mathcad* პროგრამულ გარემოში არსებული ფუნქციებისა და მოდულების ანალიზმა და ექსპერიმენტულმა შემოწმებამ აჩვენა, რომ მათი მისადაგება ადამიანის ტვინის გამოსახულებებში კონტურებისა და კვლევის ობიექტების საზღვრების და ფორმების გამოყოფისათვის ექიმებს დაეხმარება სწორი დიაგნოზის დადგენაში და სასარგებლო იქნება დიაგნოსტიკის პროცესის ავტომატიზაციისათვის.

დამოწმებანი

1. А. М. Ходжибаев, Ф. Т. Адылова. Новейшие ГРИД-технологии в электронной медицине. Ukr.z.telemed.med.telemat. 2005, **3**, 23. http://www.telemed.org.ua
2. М. Хофер. Компьютерная томография (CT Teaching Manual). 2008, Москва: Медицинская литература.
3. С. Уэлстид. Фракталы и вейвлеты для сжатия изображений в действии. 2003, Москва: Триумф.
4. В. Дьяконов. Mathcad 2001 (Учебный курс). 2001, Санкт-Петербург: Питер.

IRRADIATION-INDUCED METAL-LIKE NANOINCLUSIONS' INFLUENCE ON SILICON CONDUCTIVITY

T. Pagava, N. Maisuradze, M. Beridze, N. Kharshiladze

Georgian Technical University
Tbilisi, Georgia
tpagava@gtu.ge

Accepted March 22, 2011

1. Introduction

The effect of disordered regions (DRs) on the electric properties of semiconductors manifests itself first of all in a change in the mobility of majority charge carriers [1].

According to Gossik's model [2], a DR is a macroscopic spherical inclusion, the core of which contains a high concentration of vacancies and their associations ($10^{18} – 10^{20}$ cm^{-3}) and the conductivity of which differs from the conductivity of the undamaged part of the crystal. This brings about the formation of a spherical space-charge region around a particular DR. Therefore, DRs influence the mobility of majority carriers in two ways. On the one hand, DRs have a geometrical effect, blocking the flows of majority charge carriers and, thus, decreasing the effective cross section of the sample; on the other hand, DRs have an electrical effect, manifesting themselves as charge inclusions, the field of which is responsible for extra scattering of free charge carriers [3].

According to the model proposed in [4], a DR consists of a core filled with multivacancy complexes and a shell containing complexes of monovacancies with impurity atoms. DR shells are formed upon diffusion of monovacancies of the core into the matrix, where the monovacancies are involved in a quasi-chemical reaction with impurity atoms arranged around the DR core. The penetration depth of monovacancies into the matrix and, hence, the dimensions of the DR shells are controlled by the concentration of impurities in the sample.

From the experimental data obtained by Hall and photo-Hall measurements, the authors of [5-7] established that, in the n- and p-Si samples irradiated with protons with the energies 25, 30, and 640 MeV, the DR shell (atmosphere) consisted of secondary radiation defects (A- and E-centers, divacancies, oxygen–divacancy complexes, and so on). By analyzing the experimental results reported in [6, 7], we could suggest that the DR cores are formed of not only multivacancy defects, but interstitial atoms as well.

The authors of [8, 9] observed a sharp increase in the effective (i.e. measured) mobility of electrons μ_{eff} in the n-Si crystals when irradiated with 25 MeV protons. This observation gives direct proof of the fact that the inclusions with a relatively high-conductivity and ohmic junctions at interfaces with the semiconductor matrix, the so-called metal-like inclusions, are basically formed in the n-Si crystals irradiated with high-energy protons. The authors of [8, 9] believe that such inclusions may be clusters of interstitial (intrinsic and / or extrinsic) atoms or

associations of them, as suggested in [6, 7]. Hypothetically, these inclusions are atomic nanoclusters.

The aim of this study was to determine the DR dimensions, to analyze the effect of these DRs on the conductivity, i.e. mobility, of electrons in the n-Si crystal, and to establish the nature of the DRs formed in the n-Si crystals upon irradiation with 25 MeV protons.

2. Experimental

We here studied n-type silicon single crystals grown by the floating zone method and doped with phosphorus to the concentration $N_P = 6 \cdot 10^{13}$ cm^{-3}. The density of growth dislocations did not exceed $10^3 - 10^4$ cm^{-2}. As determined from infrared absorption studies, the concentration of oxygen was $\sim 2 \cdot 10^{16}$ cm^{-3}. Bar-shaped samples $1 \times 3 \times 10$ mm in dimensions were irradiated with 25 MeV protons at room temperature. The irradiation dose was varied in the range $(1.8 - 8.1) \cdot 10^{12}$ cm^{-2}. The Hall constant R_H and the concentration of electrons N in irradiated crystals were determined by the Hall method, and the conductivity σ was determined by the two-probe method. The Hall mobility was calculated by the formula $\mu_{eff} = \sigma R_H$. The measurements were conducted in the range of temperatures $T = 77 - 300$ K. In the measurements of the above-mentioned quantities, the error was no larger than ~ 10 %.

3. Results and discussion

The temperature dependences of the concentrations of electrons $N(T)$ are shown in Figure 1. In the curve $N(T)$ obtained after irradiation of the crystals with the integrated proton flux $8.1 \cdot 10^{12}$ cm^{-2}, we observe an exponential portion corresponding to depletion of acceptor centers with the energy $E_i = E_c - 0.36$ eV (Figure 1, Curve 5). In the samples irradiated with the dose $5 \cdot 10^{12}$ cm^{-2}, we find $E_i = E_c - 0.42$ eV (Figure 1, Curve 4), whereas, in the samples irradiated with the doses $1.8 \cdot 10^{12}$ cm^{-2} or $2.7 \cdot 10^{12}$ cm^{-2}, we observe deionization of A-centers in the temperature range 77 – 300 K (Figure 1, Curves 2 and 3). In the samples irradiated with the dose $5 \cdot 10^{12}$ cm^{-2} and then naturally aged for 90 days at 300 K, the dependence $N(T)$ exhibits an exponential portion corresponding to the depletion of acceptor levels with the energy $E_i = E_c - 0.36$ eV at temperatures 140 – 170 K (Figure 1, Curve 4').

It is known [5] that the energy of electrostatic interaction of electrons in the chain of dangling bonds at dislocations E depends on the occupancy of these dangling bonds and can be represented by the expression

$$\mathrm{E} \approx \mathrm{E}_0 F_s \left(\frac{3}{2} \ln \frac{F}{F_s} - 0.866 \right). \qquad (1)$$

Here, $\mathrm{E}_0 = e^2 / \varepsilon s$ ($\mathrm{E}_0 \approx 0.5$ eV for Si), F is the Fermi function, $F_s = s(\pi(N_d - N_a - N))^{1/3}$ is the occupancy of dangling bonds at dislocations, N_d and N_a are the concentrations of donor and acceptors, respectively; ε is the permittivity, s is the spacing between dangling bonds; and N is the concentration of electrons in the conduction band after the crystal was strained and annealed.

Let *s* be comparable to the spacing between complexes in the impurity–defect shell around metal inclusions formed in the n-Si crystals on irradiation. Then, disregarding the second term in parenthesis in expression (1) and using it for the atmosphere of complexes, we obtain $E \approx 0.03$ eV. However, since the occupancy of deep centers in the atmosphere around metal-like inclusions tends toward unity, transformation of the atmosphere itself is needed and the interaction energy can reach the quantity $E \approx E_0$ comparable to the ionization energy of deep complexes (~ 0.5 eV). Electrostatic interaction can increase or decrease the ionization energy of the centers, since the n-Si crystals under study contain positively charged donor impurity atoms, apart from negatively charged acceptor radiation defects (RDs). In addition, the sign of interaction between different negatively charged RDs responsible for different energy levels depends on the directions of spins of electrons trapped by acceptor centers.

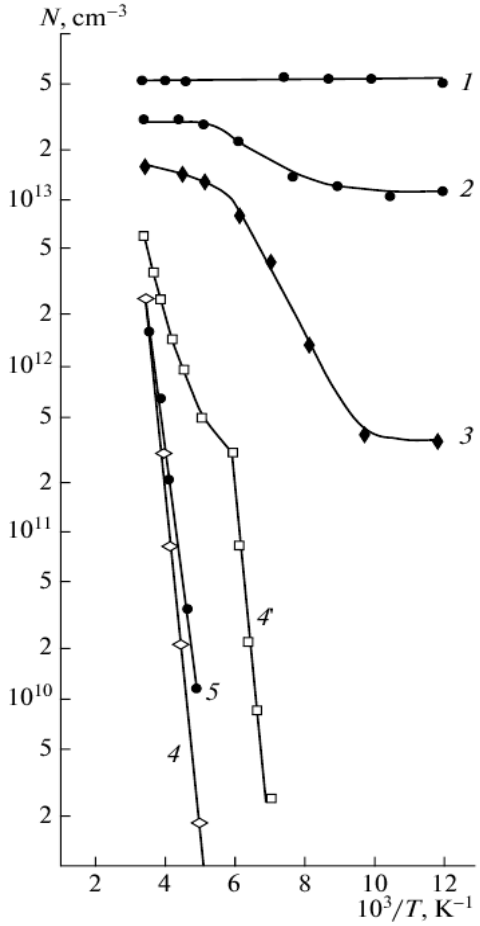

Figure 1. The temperature dependence of the concentration of electrons in the n-Si samples (1) before and (2 – 5, 4') after irradiation with 25 MeV protons at different irradiation doses equal to (in 10^{12} cm^{-2}) (2) 1.8, (3) 2.7, (4, 4') 5.0, and (5) 8.1. Curve 4' is obtained after natural aging of the sample at 300 K over 90 days.

Proton irradiation increases the fraction of electrostatically interacting centers (A- and E-centers, divacancies, etc.), since the irradiation creates primary defects arranged along the tracks and capable of condensing with the formation of closely located vacancy complexes and clusters [5]. Curve 5 in Figure 1 corresponds to depletion of divacancies or E-centers, although the ionization energy of these centers is reduced by electrostatic interaction between charged

centers to 0.36 eV. As the irradiation dose is decreased ($5 \cdot 10^{12}$ cm^{-2}), the concentration of electrostatically interacting centers decreases and the ionization energy increases to 0.42 eV (Figure 1, Curve 4). It is not inconceivable that the level $E_c - 0.42$ eV arises from superposition of divacancies in the charge state –1 ($E_c - 0.39$ eV) and E-centers ($E_c - 0.44$ eV); i.e., the V_2 + E-centers are formed. The fraction of divacancies commonly corresponds to ~ 0.9 [10].

In Curve 4' (Figure 1) obtained for the samples irradiated with the dose $5 \cdot 10^{12}$ cm^{-2} and then naturally aged at 300 K, the temperature range of depletion (140 – 170 K) corresponds to A-centers, although the ionization energy of these centers is increased by electrostatic interaction to 0.36 eV.

At high irradiation doses ($5 \cdot 10^{12}$ and $8.1 \cdot 10^{12}$ cm^{-2}), all electrons from the conduction band are captured by deep centers (E-centers, divacancies, unknown defects with the levels at $E_c - 0.57$ [10] and $E_c - 0.54$ eV [11]). Consequently, the A-centers are in the neutral state and unobservable in Hall measurements.

In the samples irradiated with low doses of protons ($1.8 \cdot 10^{12}$ and $2.7 \cdot 10^{12}$ cm^{-2}), the total concentration of electrons captured by RDs is $N_{RDs} < N_P$. Therefore, at 77 K, all acceptor RDs are charged, including A-centers. Curves 2 and 3 in Figure 1 correspond to depletion of A-centers.

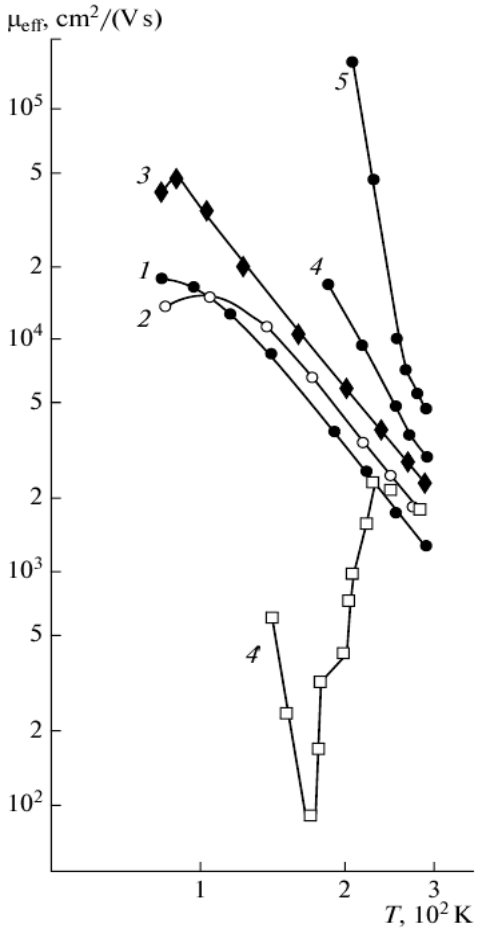

Figure 2. The temperature dependence of the Hall mobility of electrons in the n-Si samples (1) before and (2 – 5, 4') after irradiation with 25 MeV protons at different irradiation doses equal to (in 10^{12} cm^{-2}) (2) 1.8, (3) 2.7, (4, 4') 5.0, and (5) 8.1. Curve 4' is obtained after natural aging of the sample at 300 K over 90 days.

Figure 2 shows the temperature dependences of the experimental Hall mobility $\mu_{eff}(T)$ for samples irradiated with different doses of protons. For the initial sample, the temperature dependence of the Hall mobility (Figure 2, Curve 1) is described by the expression $\mu_{eff} \sim 1/T^{\alpha}$ with $\alpha \approx 2.6$. This suggests that, in the measurement temperature range (77 – 300 K), the phonon mechanism of scattering of electrons prevails. In the samples irradiated with the dose $8.1 \cdot 10^{12}$ cm^{-2}, the dependence $\mu_{eff}(T)$ is shifted upward and the exponent α of the temperature dependence of the mobility reaches value of $\alpha \approx 13$ (Figure 2, Curve 5). As the irradiation dose is lowered, the dependence $\mu_{eff}(T)$ shifts downward and α tends to its initial value (Figure 2, Curves 2-4).

In the crystals irradiated with the dose $5 \cdot 10^{12}$ cm^{-2} and then naturally aged at 300 K during 90 days, we observe anomalously strong scattering of electrons, with a minimum of the mobility at 170 K (Figure 2, Curve 4'). The high mobilities determined from Hall measurements (Figure 2, Curves 2-5) are evidence of the formation of relatively high-conductivity inclusions with ohmic junctions at interfaces with the semiconductor matrix of the n-Si samples.

From the experimental data, it is possible to calculate the volume fraction f and the radius R of metal-like inclusions in the n-Si samples under study.

According to the effective-medium theory, the Hall concentration of electrons is essentially defined by their concentration in the relatively low-conductive matrix, whereas the effective Hall mobility is an increasing function of the volume fraction of inclusions f. If the inclusions are spherical, we have

$$\frac{\mu_{eff}}{\mu_H} = \frac{1+3f}{1-6f}, \tag{2}$$

where μ_H is the Hall mobility in the matrix [12]. In silicon at room temperature, point RDs can influence the mobility only slightly; therefore, the corresponding Hall mobility of electrons in the initial material, 1400 cm^2 / V · s, can be used as the parameter μ_H. In the samples irradiated with the dose $8.1 \cdot 10^{12}$ cm^{-2}, the room-temperature Hall mobility of electrons is $\mu_{eff} \approx 4500$ cm^2 / V · s. Hence, we obtain $f \approx 0.1$, a reasonable estimate of the total volume fraction of agglomerates of interstitial atoms typical of the real structure of silicon irradiated with light ions and subjected to heat treatments [13, 14].

Knowing the volume fraction of metal-like inclusions f, we can determine their radius R. The number of inclusions in the sample is $N_{DRs}V$, where N_{DRs} is the concentration of inclusions (i.e. DRs) and V is the volume of the sample under study. The volume occupied by inclusions is fV and the volume of one inclusion is $v = fV / N_{DRs}V = f / N_{DRs}$. If the inclusions are spherical, we have $v = 4\pi R^3 / 3 = f / N_{DRs}$. Hence, we obtain

$$R = \left(\frac{3f}{4\pi N_{DRs}} \right)^{1/3}. \tag{3}$$

According to the estimates we obtained on the basis of the data reported in [1, 14-16], upon irradiation of Si crystals with protons with the energy 25 MeV ($\approx 10^{13}$ cm^{-2}), the concentration of agglomerates formed in the bulk of the sample under study is $N_{DRs} \approx 5 \cdot 10^{13}$ cm^{-3}. Substituting the values of f and N_{DRs} into formula (3), we obtain $R \approx 80$ nm.

For similar samples subjected to annealing at 90 °C and aging during 30 days at 300 K, the volume fraction f' of quasi-insulator inclusions is $f' \approx 0.3$ [9]. From formula

$$R' = \left(\frac{3f'}{4\pi N_{DRs}} \right)^{1/3}, \qquad (3')$$

similar to formula (3), we obtain the radius R' of these inclusions $R' \approx 100$ nm.

We have the ratio $R'/R \approx 1.25$. In reality, the value of R' for quasi-insulator inclusions is substantially smaller than the radius of purely metal-like inclusions. It is known [10] that, during thermal annealing or aging, vacancy-type defects and interstitial defects can annihilate each other. In the samples under study, quasi-insulator inclusions are formed upon interaction of nonequilibrium vacancies with agglomerates of interstitial atoms. A certain fraction of these vacancies enters into the quasi-chemical reaction with impurity atoms and form impurity–defect shells around the agglomerates. Some nonequilibrium vacancies recombine with interstitial atoms of the agglomerates and, thus, decrease their radius. Thus, the ratio R'/R can be quite different from 1.25.

As the dose of protons decreases, the concentration of metal-like inclusions decreases. With this effect, it is possible to interpret the experimentally observed decrease in the effective mobility of conductivity electrons μ_{eff} in the n-Si samples, since the Hall mobility is an increasing function of the volume fraction of metal-like inclusions f (Figure 2, Curves 2-5) [12].

Like dislocations in crystals, the agglomerates of interstitial atoms produce elastic strains. Nonequilibrium vacancies that are emitted from vacancy-type DRs upon annealing and natural aging of the sample [9] move toward these agglomerates. Some of these vacancies recombine with interstitial atoms. Other vacancies enter into a quasi-chemical reaction with impurity atoms and create a shell of acceptor centers around the agglomerates [4]. As the measurement temperature is lowered, the occupancy of deep centers around metal inclusions apparently tends to unity. Consequently, metal-like inclusions gradually transform into quasi-insulator inclusions, i.e., nontransparent inclusions playing the role of scattering centers for electrons. Therefore, as the temperature is lowered, the values of μ_{eff} start to decrease (Figure 2, Curve 4').

To estimate the volume fraction of quasi-insulator inclusions f' in a rather rough approximation, we can use an expression similar to formula (2):

$$\frac{\mu_{eff}}{\mu_H} = \frac{1-f'}{1+f'}, \qquad (2')$$

In our samples irradiated with protons with the energy 25 MeV and the dose $5 \cdot 10^{12}$ cm^{-2}, the volume fraction of the metal-like inclusions turned into quasi-insulator ones and their impurity–defect shells, is $f' \approx 0.46$ at 170 K, as calculated by formula (2'). The concentration of inclusions is $N_{DRs} \approx 10^{13}$ cm^{-3}. Consequently, the radius of inclusions is $R' \approx 220$ nm.

At the temperature 170 K, the quantity E in the shell of the agglomerate reaches a value comparable with the ionization energy of deep centers. Electrons transit from the corresponding deep levels to the conduction band and are immediately captured by deep centers located in the crystal matrix, wherein E is smaller than that in the shells around metal-like inclusions (we assume that the concentration of RDs N_{RDs} and, correspondingly, the quantity E in the impurity–defect shell around metal-like inclusions is larger than that in the

crystal matrix). Deionization of RDs in the shell of DRs is bound to yield a decrease in R'. In fact, at 140 K, $f' \approx 0.25$ and $R' \approx 180$ nm. Correspondingly, the degree of screening of metal-like inclusions decreases and, at temperatures below 170 K, the mobility μ_{eff} begins to increase.

Apparently, the nonmonotonic dependence $\mu_{eff}(T)$ can be attributed to the nonmonotonic variation in the degree of screening of metal-like inclusions in the course of measurements of μ_{eff} of irradiated crystals in the range from 77 to 300 K. In the ranges from 240 to 170 K and from 170 to 140 K, the inclusions behave as quasi-insulator inclusions and metal-like inclusions, respectively.

It is known [1, 12, 14] that insulator inclusions are responsible for the decrease in μ_{eff}, whereas metal inclusions are responsible for the increase in μ_{eff}. As a consequence, the dependence $\mu_{eff}(T)$ has a minimum at 170 K.

4. Conclusions

Thus, on irradiation of the n-Si samples with protons with the energy 25 MeV, the so-called metal-like inclusions consisting of interstitial atoms are apparently formed along with points RDs and insulator inclusions. On interaction between insulator inclusions and metal-like ones, shells that are composed of acceptor RDs and are nontransparent to conductivity electrons are formed. The charge state of these defects varies with measurement temperature. Correspondingly, the degree of screening of inclusions varies as well. This may be the cause of the experimentally observed nonmonotonic temperature dependence of the effective Hall mobility of electrons.

The radius of metal-like inclusions formed in n-Si irradiated with protons with the energy 25 MeV and the dose ~ 10^{13} cm^{-2} is ~ 80 nm, and the volume fraction of these inclusions in the crystal bulk is ~ 0.1.

On the basis of the experimental data obtained in the study, it can be inferred that irradiation of the n-Si crystals with 25 MeV protons brings about the formation of atomic nanoclusters (nanoinclusions) with relatively high conductivity and ohmic junctions at interfaces with the semiconductor matrix. It is known [17-19] that doping of semiconductor materials with atomic clusters by proton irradiation opens up fresh opportunities for controlling the properties of semiconductors and for developing semiconductor-based microelectronic and nanoelectronic devices.

References

1. R. F. Konopleva, V. L. Litvinov, N. A. Ukhin, Radiation Damage of Semiconductors by Energetic Particles. 1971, Moscow: Atomizdat.
2. B. R. Gossick. J. Appl. Phys., 1959, **30**, 1214.
3. I. D. Konozenko, A. K. Semenyuk, V. I. Khivrich. Radiation Effects in Silicon. 1974, Kiev: Naukova dumka.
4. N. A. Ukhin. Semicond., 1972, **6**, 804.

5. L. S. Milevskij, T. M. Tkacheva, T. A. Pagava. JETP, 1975, **42**, 1084.
6. V. I. Kuznetsov, P. F. Lugakov. Semicond., 1979, **13**, 369.
7. V. I. Kuznetsov, P. F. Lugakov, Semicond., 1980, **14**, 1146.
8. T. A. Pagava, L. S. Chkhartishvili. Ukr. J. Phys., 2003, **48**, 232.
9. T. A. Pagava, N. I. Maisuradze. Semicond., 2010, **44**, 151.
10. I. V. Antonova, S. S. Shaimiev, S. A. Smagulova. Semicond., 2006, **40**, 543.
11. V. S. Vavilov, V. F. Kiselev, B. N. Mukashev. Defects in Bulk and at Surface of Silicon. 1990, Moscow: Nauka.
12. E. V. Kuchis. Galvanomagnetic Effects and Methods of Their Investigation. 1990, Moscow: Radio Svyaz'.
13. A. Aseev, L. Fedina, D. Hoehl, H. Barch. Clusters of Interstitial Atoms in Silicon and Germanium. 1994, Berlin: Academy Verlag.
14. R. F. Konopleva, V. I. Ostroumov. Interaction of High-Energy Charged Particles with Germanium and Silicon. 1975, Moscow: Atomizdat.
15. L. Palmetshofer, J. Reisinger. J. Appl. Phys., 1992, **72**, 21676.
16. P. Hazdra, J. Vobeeky. Solid State Phenom., 1999, **69 / 70**, 545.
17. M. G. Mil'vidskij, V. V. Chaldyshev. Semicond., 1998, **32**, 457.
18. V. V. Kozlovskij, V. A. Kozlov, V. I. Lomasov. Semicond., 2000, **34**, 123.
19. V. A. Kozlov, V. V. Kozlovskij. Semicond., 2001, **35**, 735.

ОЦЕНКА ВЛИЯНИЯ КОНЦЕНТРАЦИИ МАГНИТНЫХ ЧАСТИЦ НА МАГНИТООПТИЧЕСКИЕ СВОЙСТВА УЛЬТАДИСПЕРСНЫХ СРЕД МЕТОДОМ ДИСПЕРСИОННОГО АНАЛИЗА

Л. Г. Каландадзе

Государственный университет им. Шота Руставели
Батуми, Грузия
lali62@mail.ru

Принята 24 марта 2011 года

Магнитооптические эффекты отражения широко применяются при решении различных задач в области физики магнитных явлений. С их помощью наблюдаются домены и доменные границы, исследуются процессы намагничивания, изучается электронная энергетическая структура твердых тел [1].

Сравнительно недавно нечетные по намагниченности магнитооптические эффекты отражения были успешно применены для исследования процессов, протекающих в тонком приповерхностном слое магнитных жидкостей. С их помощью было установлено, что внешнее магнитное поле приводит к изменению концентрации магнитных частиц в тонком приповерхностном слое магнитных жидкостей, вызывает образование поверхностных слоев, намагниченных против внешнего магнитного поля, активизирует поверхностное расслоение магнитных жидкостей [2, 3].

Магнитооптические свойства магнитных жидкостей в самом общем случае существенно отличаются от свойств массивных ферромагнетиков, что приводит к изменению дисперсионных и угловых зависимостей величины магнитооптических эффектов по сравнению с аналогичными зависимостями для массивных образцов. Это связано с тем, что магнитные жидкости представляют собой пример ультрадисперсной магнитной среды, состоящей из окруженных жидкостью-носителем малых магнитных частиц, размеры которых значительно меньше длины волны света.

В связи с этим весьма существенным является вопрос о рассмотрении условий магнитооптического эксперимента, при которых упрощается расшифровка экспериментально наблюдаемых магнитооптических спектров, дающих информацию, как о намагниченности тонкого приповерхностного слоя магнитных жидкостей, так и об электронной энергетической структуре малых магнитных частиц и свойствах жидкости-носителя. Следует отметить, что исследование электронной энергетической структуры малых магнитных частиц важно не только для изучения процессов временной стабильности магнитных жидкостей, но и для анализа химических процессов, протекающих на поверхности частиц, так как в некоторых случаях малые магнитные частицы могут выступать в качестве своеобразного зонда.

В работе [4] рассмотрен нечетный по намагниченности экваториальный эффект Керра в магнитных жидкостях на основе частиц магнитных окислов в рамках

теоретической модели Максвелла–Гарнетта, распространенной на случай магнитных сред. Сформулированы условия эксперимента, позволяющие существенно упростить выражение для определения намагниченности тонкого приповерхностного слоя магнитной жидкости и исследования электронной энергетической структуры малых магнитных частиц. Получено простое соотношение для экваториального эффекта Керра

$$\delta_q = q\delta_m, \qquad (1)$$

где δ_q – экваториальный эффект Керра на магнитной жидкости, q – коэффициент объемного заполнения магнитных жидкостей магнитными частицами, δ_m – экваториальный эффект Керра на материале частиц.

Необходимо отметить, что выражение (1) является строгим только при выполнении следующих трех условий: (1) $k_m^2 << n_m^2$, где k_m и n_m показатели поглощения и преломления материала частиц, соответственно; (2) угол падения света на образец $69\,° < \varphi < 72\,°$; (3) $n_0 \approx n_m$, где n_0 – показатель преломления жидкости-носителя.

Соотношение (1) показывает, что при проведении эксперимента удовлетворяющее перечисленным выше условиям величина экваториального эффекта Керра на магнитных жидкостях пропорциональна коэффициенту объемного заполнения магнитных жидкостей магнитными частицами, а следовательно и намагниченности. При этом дисперсионные зависимости экваториального эффекта Керра на магнитной жидкости и материале частиц подобны.

С целью оценки влияния фактора q на вариацию экваториального эффекта Керра относительно других факторов (размер магнитных частиц, их расположение, свойства жидкости-носителя и др.), мы решили применить правило сложения дисперсий. Количественная оценка влияния q фактора на магнитооптические свойства магнитных жидкостей докажет важность этого фактора и справедливость соотношений (1).

Согласно правилу сложения дисперсий, общая дисперсия равна сумме средней из внутригрупповых и межгрупповой дисперсий:

$$\sigma_0^2 = \overline{\sigma^2} + \delta^2, \qquad (2)$$

где

$$\overline{\sigma^2} = \frac{\sum_{i=1}^{i=n} f_i \sigma_i^2}{\sum_{i=1}^{i=n} f_i}$$

– средняя из внутригрупповых дисперсий,

$$\sigma_i^2 = \frac{\sum_{j=1}^{j=n} f_i (X_{ji} - \overline{X_i})^2}{f_i}$$

– внутригрупповая дисперсия в i-й группе,

$$\delta^2 = \frac{\sum_{i=1}^{i=n} f_i (\overline{X_i} - \overline{X_0})^2}{\sum_{i=1}^{i=n} f_i}$$

– межгрупповая дисперсия, f_i – число единиц в i-й группе, $\overline{X_i}$ – частная средняя по i-й группе, $\overline{X_0}$ – общая средняя по совокупности единиц.

Отметим, что σ_0^2 характеризует вариацию признака как результат влияния всех факторов, определяющих индивидуальные различия единиц совокупности. Вариацию, обусловленную влиянием фактора, положенного в основу группировки, характеризует межгрупповая дисперсия δ^2, а вариацию, обусловленную влиянием прочих факторов, средняя из внутригрупповых дисперсий.

Отношение δ^2 / σ_0^2 показывает ту часть от общей вариации, которая обусловлена влиянием фактора, положенного в основу группировки.

Экспериментальные данные мы взяли из работ [3, 4], в которых исследованы дисперсионные зависимости экваториального эффекта Керра (угол падения света на образец $\varphi = 70\ °$) в магнетитовых магнитных жидкостях и их осадков на основе воды, керосина и разных кремний-органических соединений с различными коэффициентами объемного заполнения q. Эти исследования дали возможность разбить экспериментальные данные на группы, положив в основу группировки интересующий нас фактор – коэффициент объемного заполнения магнитных жидкостей магнитными частицами.

Расчеты проводились для энергии квантов падающего света $\hbar\omega =$ 2 eV. Экспериментальные данные, разложенные по q, приведены в Таблице 1.

Таблица 1.

q	δ_q		
0.05 – 0.1	$0.35 \cdot 10^{-3}$	$-0.15 \cdot 10^{-3}$	$0.2 \cdot 10^{-3}$
0.1 – 0.3	$1.1 \cdot 10^{-3}$	$0.28 \cdot 10^{-3}$	$0.8 \cdot 10^{-3}$

Расчеты, выполненные по этим данным, показали, что влияние фактора q на вариацию дисперсионных зависимостей экваториального эффекта Керра составляет 53 %. Отсюда можно сделать вывод, что в рассмотренном случае q фактор имеет преобладающее влияние на вариацию эффекта и определяет магнитооптические свойства ультрадисперсных сред.

Таким образом, в работе количественно определено влияние q фактора на магнитооптические свойства ультрадисперсных сред на примере магнетитовых магнитных жидкостей. Отметим, что полученный результат будет справедливым для всех ультрадисперсных сред, оптические константы которых удовлетворяют соотношение $k_m^2 << n_m^2$.

Ссылки

1. Г. С. Кринчик. Вестн. МГУ (Сер. мат., мех., астр., физ. и хим.), 1957, **6**, 87.
2. Л. В. Никитин, А. А. Тулинов. Изв. АН СССР (Сер. физ.), 1991, **1**, 112.
3. L. B. Nikitin, A. A. Tulinov. J. Magn. & Magn. Mat., 1990, **85**, 89.
4. L. Kalandadze. J. Phys.: Conf. Ser., 2010, **200**, 072043.

РЕГУЛЯРНЫЕ РЕШЕТКИ И НИТИ НАНОЧАСТИЦ МЕТАЛЛОВ В ЦЕОЛИТНЫХ КАНАЛАХ

А. А. Капанадзе, Г. В. Ртвелиашвили, Г. Д. Табатадзе

Грузинский технический университет
Тбилиси, Грузия
nodar@iname.com

Принята 27 марта 2011 года

В последнее время в связи с поисками новых материалов для твердотельной электроники была создана и исследована целая группа объектов, свойства которых отличаются от свойств массивных тел за счет увеличения роли поверхности. К числу таких объектов принадлежат несмачивающие жидкие металлы, внедренные в полости цеолитов типа NaX, NaA и NaM. Цеолиты типа NaX и NaA представляют собой алюминосиликаты каркасной структуры, в которых в трех направлениях имеются строго одинаковые и регулярные полости, размеры которых 11.4 – 12 Å. Введение несмачивающих жидкостей в каналы столь малых размеров должно требовать энергии порядка теплот испарения, т.е. 10 – 100 ккал / моль. В пересчете на давление это порядка 5 – 50 кбар, т.е. практически весьма реальная величина.

Введение жидких металлов в каналы цеолита можно наблюдать как по скачку объема системы цеолит–металл, так и по скачку проводимости цеолитной прессовки, находящейся в контакте с жидким металлом [1-3]. При критическом давлении жидкие металлы проникают в полости цеолитов и образуют регулярные решетки, повторяющие конфигурацию каналов и полостей цеолитной матрицы – в случае цеолита NaA кубическую, а в случае цеолита NaX – структуру типа алмаза. Оценки скачка объема показывают, что в каждой полости находятся 16 – 20 атомов. В результате заполнения жидким металлом полостей цеолитной матрицы кристаллы цеолита, каркас которого является хорошим диэлектриком типа кварца, приобретают металлическую проводимость, что указывает на достаточно сильное взаимодействие между кластерами. Изучение температурной зависимости галлия и ртути в цеолитах показало, что на 80 – 100 K ниже точек плавления массивного металла под давлением наблюдаются скачки проводимости, которых можно приписать отвердиванию и плавлению цеолитного металла. Если внешнее давление снять, проводимость исчезает. При этом часть металла уходит из полостей. Данные по плотности свидетельтвуют, что число атомов в полости сокращается до 10 – 15, что, по-видимому, приводит к ослаблению взаимодействия между кластерами и исчезновению металлического состояния. Рентгеновский анализ показал, что в каркасе цеолита возникают напряжения, которые исчезают при удалении металла из полостей. Структура цеолита сохраняется, но наблюдать капельные решетки не удается. Однако, и в такой диэлектрической системе кластеров, зафиксированной в пространстве полостями каркаса цеолитов, наблюдаются острые пики теплоемкости при температурах, соответствующих плавлению цеолитного металла. По мере уменьшения содержания металла этот пик закономерно уменьшается по величине и сдвигается в низкотемпературную область, что указывает на равномерность распределения металла в полостях цеолита. В точке плавления резко изменяется также магнитная проницаемость диэлектрической системы металлических кластеров. В частности, в кластерах Hg_{13} магнитным полем свыше 25 кЭ в точке плавления возбуждается новое сильное

парамагнитное состояние. Этот факт указывает на то, что кластеры можно рассматривать, как квазиатомы, заполнение уровней которых осуществляется в соответствии со спектроскопическими правилами [4-5].

Следует отметить, что расположение атомов металла в сферической полости цеолитов существенно отличается от их расположения в кристаллическом массиве. Однако, резкость переходов в точках плавления и отвердивания указывает на то, что во всех полостях число атомов в кластере одно и то же и, кроме того, их конфигурация одинакова и определяется строгой одинаковостью полостей цеолита. Остается невыясненным, в чем заключается плавление таких капель – кластеров, фиксированных в полостях матрицы, и как это отражается на проводимость.

Известно, что фазовый переход в отдельном кластере, состоящем из $10-20$ атомов металла, должен быть сильно размыт флуктуациями. Экспериментально обнаруженные фазовые переходы носят резкий характер и можно утверждать, что флуктуационное уширение, естественное для малых частиц, в данном случае подавлено взаимодействием кластеров друг с другом либо непосредственно (кластерные металлы при $P > P_c$), либо через диэлектрическую матрицу (кластерные диэлектрики при $P < P_c$), а также высокой степенью упорядочения системы. Проявление коллективных свойств в процессе разового перехода указывает на то, что металл в цеолите можно рассматривать как кристалл, созданный диэлектрической матрицей цеолита. Число кластеров в кристалле ($5 \cdot 10^{20}$ см$^{-3}$), период и правильность его решетки определяются диэлектрической матрицей. Поэтому, в зависимости от наполнителя и типа использованного цеолита, как диэлектрической матрицы, можно получить разные по свойству трехмерные сверхрешетки – кластерные металлы или диэлектрики на основе веществ в ультрамелкодисперсном состоянии.

Для создания одномерных металлических нитей путем вдавливания металла в диэлектрическую матрицу идеальными являются структуры типа морденита, в которых каналы имеют размеры, допускающие проникновение металла в виде одноатомных цепочек, располагающихся достаточно близко друг к другу так, чтобы между ними могло существовать взаимодействие. В таких системах взаимодействие атомов металла с диэлектрической матрицей будет, вероятно, достаточно слабым, обеспечивая требуемую квазиодномерность. Роль физического контакта с матрицей сводится лишь к стабилизации металлических нитей в пространстве. Синтетический цеолит Na – морденит (NaM) своей структурой соответствует этим требованиям. В его каркасе отсутствуют пустоты «больших» диаметров, имеются лишь пересекающиеся каналы с диаметрами 6.6 и 2.8 Å. Поэтому этот цеолит можно считать обладающим практически одномерной системой каналов. Опыт показал, что критические давления, при которых происходит проникновение металлов (ртути и висмута) в каналы цеолита NaM, соответственно равны 29 и 20 кбар, величины скачка объема соответственно равны 3.6 и 6 %. После снятия внешнего давления ртуть, введенная в каналы цеолита NaM, по-видимому, полностью вытекает наружу. На это указывает измерение плотности данных материалов.

Ссылки

1. В. Н. Богомолов. ФТТ, 1971, **13**, 815.
2. В. Н. Богомолов, Т. И. Волконская, А. И. Задорожний, А. А. Капанадзе. ФТТ, 1975, **17**, 1707.
3. В. Н. Богомолов, А. И. Задорожний, А. А. Капанадзе, Э. Л. Луценко. ФТТ, 1976, **18**, 3050.
4. В. Н. Богомолов, А. А. Капанадзе. ФТТ, 1978, **20**, 104.
5. В. Н. Богомолов, А. И. Задорожний, А. И. Панина. ПЖЭТФ, 1980, **31**, 371.

DEPENDENCE OF ENERGY-GAP WIDTH ON PRESENCE OF SHALLOW IMPURITIES IN SEMICONDUCTORS WITH TETRAHEDRAL SYMMETRY

Z. Gogua, A. Gigineishvili, G. Kantidze, G. Iluridze, G. Rtveliashvili

Georgian Technical University
Tbilisi, Georgia
zgogua@gmail.com

Accepted March 27, 2011

It's known that implantation of the large amount of impurities in semiconductors can cause significant distortions in their band structure. The "large amount" means such concentration of impurities N, for which average distance between neighboring impurity centers $1/N^{1/3}$ becomes less than Bohr orbit radius $1/N^{1/3} \ll a_B$, where $a_B = (m/m^*)\varepsilon a_0$. m^* is the effective mass of electron in semiconductor under the consideration, m is the free electron's mass, ε is the dielectric constant, a_0 is the Bohr orbit radius in a hydrogen atom. In these conditions, there appears an impurity band. In case of donor impurities it joins the conduction band, while in case of acceptor impurities – the valence band. This causes the significant changes in the density-of-states. At the appropriate band edge there appear a tail of the density-of-states and it drags this edge into the energy-gap and causes narrowing of the energy-gap. Studies of this process began about 50 years ago and it continues even today. First papers about this topic appeared when it became possible to perform experiments defining band structures. These works were contra-positive and mutually exclusive, e.g., reflection measurement experiments showed [1] that the increase in impurities' concentration causes the increment of effective mass of electron, but the calculations of [2] don't approve these results. Pankov [3] investigated the spectral dependence of absorption coefficient for interband optical transitions in germanium heavily doped with shallow impurities and calculated the dependence of the energy-gap width on the concentration of impurities. He defined that increasing of the impurity concentration causes decrease of the energy-gap in germanium. In case of impurity concentration of $4.5 \cdot 10^{-19}$ cm^{-3}, the band width decreases by 0.1 eV. These experiments were performed at 4.2 K. Haas provided [4] with similar calculations for germanium heavily doped with phosphorus and arsenic at 80 K. He also defined the decrease of the energy-gap width when increased the impurity concentration, but not so much as in [3]. Other authors, e.g. [5], said that the reason of the difference is the wrong extrapolation of the absorption by unrecombinated carriers in the Haas's main absorption region. Besides, it's quite difficult to compare these results because mentioned experiments were performed on heavily doped p-type germanium. The fact of reduction of the energy-gap width was also investigated in [6], where it was performed some investigations of infrared absorption in germanium heavily doped with gallium at temperatures 80 and 293 K. At 80 K, authors obtained that the difference between direct and indirect transitions energies is 0.16 eV. But, according them this fact takes place because of heavy doping Fermi energy enters in the valence band and then interband transitions begin there. The value of energy-gap width reduction in such case (with impurity concentration of ~ 10^{19} cm^{-3}) was calculated to be of 0.05 eV. In heavily doped and compensated germanium narrowing of the energy-gap was theoretically determined by Keldish & Proshko

[7]. They followed the conception of random distribution of impurities and calculated the value of energy-gap width reduction caused by the fluctuations of the impurity potential. This potential was represented as a Coulomb-like potential. The band width reduction formula found is

$$\Delta E_g = 2\left(\frac{e^2}{a_0}\right)\frac{1}{\varepsilon}\left(\frac{m}{m_v}\left(1+\frac{m_v}{m_e}\right)\varepsilon\right)^{1/5}(na_0^3)^{2/5}\sqrt{\left(\frac{m_v}{m_c}\right)^{2/5}-1}\,, \qquad (1)$$

where m_e and m_v are effective masses of free electrons and holes, respectively, and n denotes the concentration of free carriers. The values of energy-gap width reduction, calculated using formula (1), are small, e.g., for germanium when n~10^{19} cm^{-3}, ΔE_g~10^{-3} eV. These values are also small when Hamman's formulas [8] are used for germanium and silicon. They are based on Coulomb-like potential for an impurity center. Hamman calculated the decrease of energy-gap energy in semiconductors using the variational method. Taking into account the Fermi energy μ changes caused by the charge carrier concentration increment and without it (n_0), he proposed following formulas for Ge and Si (n (or n_0) and ΔE_g are given in cm^{-3} and eV, respectively):

Ge: $\Delta E_g(\mu,n) = \Delta E_g(n) - 6.63(n/10^{18})^{2/3}$,

$$\Delta E_g(n) = 0.741 - 4.89(n_0/10^{18})^{1/3} - 8.2(n_0/10^{18})^{1/4} - 3\,; \qquad (2)$$

Si: $\Delta E_g(\mu,n) = \Delta E_g(n) - 3.34(n/10^{18})^{2/3}$,

$$\Delta E_g(n) = 1.156 - 6.47(n_0/10^{18})^{1/3} - 13.1(n_0/10^{18})^{1/4} - 8.1. \qquad (3)$$

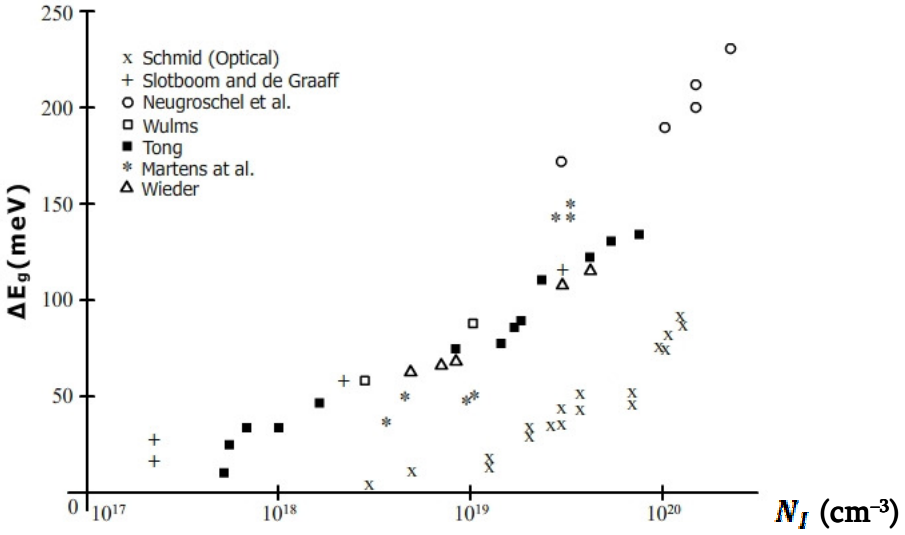

Figure 1. Electrical and optical energy-gap narrowing vs. donor doping density, the points are experimental data.

Here $\Delta E_g(\mu,n)$ is the value of energy-gap reduction. When the impurities are ionized, gas of free carriers is too much disturbed and the chemical potential enters the band gap. $\Delta E_g(n)$ is the energy-gap width reduction value without taking this fact into account, so it is the distance from one band's edge to another. This method also gives small values, e.g. for Ge with $n = 5\cdot 10^{19}$ cm^{-3}, $\Delta E_g(n)$~ 0.02 eV. In papers by van Overstraeten & Mertens (see e.g. [9]), there are gathered a lot of results of calculations on the relation between impurity concentration and the energy-gap width. They used electronic measurements in their experiments. In these papers there are shown results of six various authors and presented in the Figure 1. As one can see, reduction of the energy-gap is not small: in Si it's almost 0.25 eV.

There is low concentration of electrons at low temperatures when it makes sense to measure the energy-gap width in heavily doped germanium and silicon. According to the theories, which were considered above, the neutral impurities can't take part in changing energy-gap narrowing process. We (Z. Gogua, A. Gerasimov and A. Tsertsvadze) offered [10] the impurity center model, where the impurity atom in the first coordination sphere with radius of r_0 is considered as the free atom in vacuum and outside it – as usual, within the continuum approximation for dielectric constant. According to this conception, the impurity center potential's formula is

$$\Phi(r) = n^* \sqrt{\frac{E_I}{E_H}} \frac{e}{r} \Theta(r_0 - r) + \frac{Ze}{\varepsilon r} \Theta(r - r_0). \quad (4)$$

where n^* is the principal quantum number of the valence layer of the impurity atom, which is calculated using Slater's rule [11], E_I is the ionization energy of the corresponding electron state in isolated impurity atom, E_H is the ionization energy of the isolated hydrogen atom, Z is the impurity center charge number and $\Theta(r)$ is Heaviside step-function. As the dielectric constant spatial dependence is limited by the first coordination sphere, the potential (4) needs some corrections. Corresponding dependency $\varepsilon \to \varepsilon(r)$ can be described well with simple function

$$\frac{1}{\varepsilon(r)} = \frac{1}{\varepsilon} + e^{-\alpha r}, \quad (5)$$

where α equals to 0.0625 and 0.0833 / Å for Ge and Si, respectively, and $\alpha = 2/a_B$ for both cases. After this correction formula (4) will transform into

$$\Phi(r) = n^* \sqrt{\frac{E_I}{E_H}} \frac{e}{r} \left(\frac{1}{\varepsilon} + e^{-\alpha r}\right) \Theta(r_0 - r) + \frac{Ze}{\varepsilon r} \Theta(r - r_0). \quad (6)$$

Parameters n^* and E_I automatically describe individualities of each impurity. This model was successfully applied in investigations of charge carriers' scattering by ionized impurity centers, also emissive and non-emissive electron transitions and other problems [11-13].

We tried to use that impurity center's common model and investigate the dependence of energy-gap narrowing vs. impurity density. We assume that the impurity is randomly distributed and the potential (4) is screened according to Debye mechanism:

$$\Phi(r) = n^* \sqrt{\frac{E_I}{E_H}} \frac{e}{r} \left(\frac{1}{\varepsilon} + e^{-\alpha r}\right) \Theta(r_0 - r) + \frac{Ze}{\varepsilon r} e^{-qr} \Theta(r - r_0). \quad (7)$$

Here q is the inverted value of Debye radius in substance as whole. The correlation function of potential energy of impurities randomly distributed in volume V is

$$\langle u(\vec{r_1})\, u(\vec{r_2})\rangle = \frac{N}{V} \int d\vec{r}\, u(\vec{r} + \vec{r_1})\, u(\vec{r} + \vec{r_2}), \quad (8)$$

where $u(r) = e\Phi(r)$. If we insert their Fourier transforms instead $u(\vec{r} + \vec{r_1})$ and $u(\vec{r} + \vec{r_2})$ functions in (8) we'll get the formula

$$\langle u(\vec{r_1})\, u(\vec{r_2})\rangle = \frac{N_I}{(2\pi)^3} \int e^{i\vec{k}(\vec{r_1} - \vec{r_2})}\, u(\vec{k}) u(-\vec{k}) d\vec{k}, \quad (9)$$

where $N_I = N/V$ is the concentration of impurities, while $u(\vec{k})$ is the Fourier transform of the $u(\vec{r})$ function:

$$u(\vec{k}) = e^2 n^* \sqrt{\frac{E_I}{E_H}} \left(\frac{1 - \cos kr_0}{\varepsilon k^2} - \frac{k - (\alpha \sin kr_0 + k \cos kr_0) e^{-\alpha r_0}}{k(k^2 + \alpha^2)}\right) +$$
$$+ \frac{e^2 Z}{\varepsilon} \frac{e^{-qr_0}}{k^2 + q^2} \left(\frac{q}{k} \sin kr_0 + \cos kr_0\right). \quad (10)$$

As we see $u(\vec{k}) = u(-\vec{k})$, so at the $\vec{r_1} = \vec{r_2}$ point for potential energy fluctuation there will be work the formula:

$$\langle u^2(r)\rangle = \frac{N_I}{(2\pi)^3} \int |u(k)|^2 d\vec{k}. \quad (11)$$

If we insert formula (10) into (11) and take into account relation $\Delta E_g(N_I) = \sqrt{\langle u^2(r)\rangle}$, after tedious, but simple transformations we'll get:

$$\Delta E_g(N_I) = \sqrt{4\pi\left(n^{*2}\left(1-\frac{2}{\varepsilon}\right)E_I E_H N_I a_0^3\right) + \left(\frac{z}{\varepsilon}\right)^2 N_I e^2 \frac{e^{-2\alpha r_0}}{2a_0}}. \quad (12)$$

This formula shows that the impurity center's inner area, as well as the outer one, affects the energy-gap narrowing process. Besides, the universality of our conception is that formula (12) reveals the difference between individual impurities and their different influence on the energy-gap narrowing process.

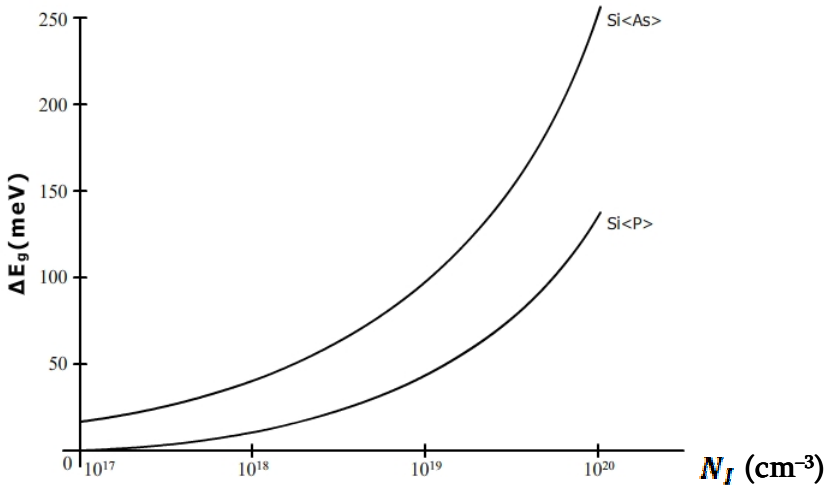

Figure 2. Results of formula (13) for energy-gap narrowing value.

Energy-gap width reduction at absolute zero temperature according to (12) will be:

$$\Delta E_g(N_I) = 2n^* \sqrt{\pi\left(1-\frac{2}{\varepsilon}\right)E_I E_H N_I a_0^3}\,. \quad (13)$$

Numerical results for Si<P> ($n^* = 3$ and E_I =8 eV) and Si<As> ($n^* = 3$ and E_I =2 eV) obtained according to the formula (13) are presented in Figure 2. If we compare these results with the experimental data obtained in [9] we'll find a satisfying similarity.

References

1. M. Cordona, H. Simmers. Phys. Rev., 1961, **122**, 1382.
2. W. Spitzer. J. Appl. Phys., 1961, **32**, 1828.
3. J. Pankov. Phys. Rev. Lett., 1960, **11**, 20.
4. E. Haas. Phys. Rev., 1961, **123**, 1965.
5. В. И. Фистуль. Сильно легированные полупроводники. 1967, Москва: Наука.
6. В. С. Багаев, Г. П. Прошко, А. П. Шотов. ФТТ, 1962, **4**, 3228.
7. Л. В. Кельдиш, Г. П. Прошко. ФТТ, 1963, **5**, 3778.
8. G. D. Mahan. J. Appl. Phys., 1980, **51**, 2635.
9. R. J. van Overstraeten, R. P. Mertens. Solid State Electr., 1987, **30**, 1077.
10. А. Б. Герасимов, З. Г. Гогуа, А. А. Церцвадзе. ЖТФ, 1982, **52**, 137.
11. П. Гомбаш. Проблема многих тел в квантовой механике. 1953, Москва: ИЛ.
12. A. B. Gerasimov, Z. G. Gogua, V. N. Svanidze. Phys. Status Solidi B, 1987, **141**, K83.
13. A. B. Gerasimov, Z. G. Gogua, V. N. Svanidze, D. A. Kimeridze. Phys. Status Solidi B, 1987, **144**, K99.

NANOSTRUCTURED ELECTRODES FOR ENERGY CONVERSION DEVICES

A. N. Tavkhelidze

Ivane Javakhishvili Tbilisi State University
Tbilisi, Georgia
avtotav@gmail.com

Accepted April 14, 2011

1. Introduction

Low work function (WF) electrodes [1] are essential for cold emission and room temperature operation of thermionic [2-6] and thermotunnel [7-13] energy converters and coolers. Such devices consist of plain emitter and collector electrodes, separated by the thin vacuum gap. Electrons absorb heat energy inside the emitter electrode, overcome the vacuum barrier (or tunnel through it) and release heat energy inside the collector electrode. Electrodes require materials with work function $e\phi = 0.2 - 0.4$ eV (here, e is electron charge and ϕ potential). For most metals $e\phi > 4$ eV, and only some compounds show $e\phi = 2 - 3$ eV. This is one order of magnitude higher than required. WF values of about 1 eV were obtained in sophisticated systems like Mo–Cs and Ag–O–Cs. However, these types of electrodes have a short lifetime even in good vacuum conditions. To overcome difficulties, quantum mechanical tunneling was utilized. Tunneling through vacuum nanogap allows sufficiently large currents from the electrodes, having relatively high $e\phi$ values. It was found that image force reduces potential barrier and increases tunneling current, giving a cooling power of 100 W / cm^2 for $e\phi \approx 1$ eV [7] in mixed thermotunnel and thermionic regime. Electrons were filtered by collector coating, to increase the cooling coefficient [8] and conformal electrode growth technology was developed [9]. However, vacuum nanogap device appears extremely difficult to fabricate [9-11] as it requires an electrode spacing of 5 – 10 nm. If an $e\phi < 1$ eV electrode could be obtained, poor thermionic regime can be realized at increased electrode spacing. Fabrication of wide vacuum gap, using conformal electrode technology, is much more straightforward. Low WF energy converters are essential for heat to electricity direct conversion in the temperature range 400 – 1000 K in which waste heat is available from the combustion sources. Low WF coolers are essential for integrated circuit cooling and other applications where low weight and ecological purity are major requirements.

Here, we offer to reduce $e\phi$ using surface nanostructuring. The electrode is coated by the metal nanostructured quantum well (NQW) layer. Its operation is based on the effect of quantum state depression. Periodic ridges, fabricated on the layer surface, impose additional boundary conditions on the electron wave function. Supplementary boundary conditions forbid some quantum states for free electron, and the quantum state density in the energy $\rho(E)$ reduces. According to Pauli's Exclusion Principle, electrons rejected from the forbidden

quantum states, have to occupy the states with higher energy E. As result the Fermi energy E_F increases and $e\phi$ decreases [14].

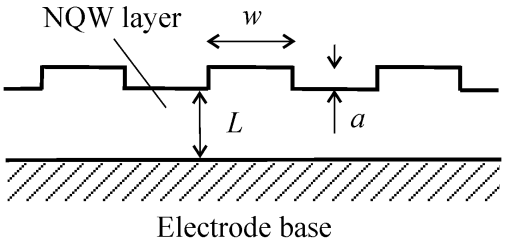

Figure 1. Cross section of electrode coated by nanostructured quantum well.

The quantum state density in the NQW (Figure 1) reduces G times

$$\rho(E) = \rho_0(E)/G\,, \tag{1}$$

where $\rho_0(E)$ is the density of states in a conventional quantum well layer of thickness L ($a = 0$) and G is the geometry factor introduced in [15]. For the case $a << L, w$ and within the range $5 < G < 10$, the following approximate expression (obtained in [16]) can be used

$$G \approx L/a\,, \tag{2}$$

where a is the ridge height and L is the NQW layer thickness. Density of forbidden quantum states is

$$\rho_{FOR}(E) = \rho_0(E) - \rho_0(E)/G = \rho_0(E)\times(1-G^{-1})\,. \tag{3}$$

To determine the number of rejected electrons n_{REJ}, equation (3) should be integrated over the energy region in which the electrons are confined to the NQW:

$$n_{REJ} = \int\limits_{CON} dE\,\rho_{FOR}(E) = (1-G^{-1})\times\int\limits_{CON} dE\,\rho_0(E) = (1-G^{-1})\times n_{CON}\,. \tag{4}$$

Here, $n_{CON} = \int\limits_{CON} dE\,\rho_0(E)$ is the number of quantum states (per unit volume) within electron confinement energy region (which depends on substrate and NQW band structures and band offset). The NQW retains quantum properties at G times more width with respect to the conventional quantum well. Previously, quantum state depression was studied theoretically [15] and experimentally [17] in nanostructured metal films.

The objective of this work is to calculate $e\phi$ in the metal NQW layer, grown on semiconductor and metal substrates, and find out how it depends on ridge geometry and electron confinement. In the beginning we calculate $e\phi$ values in the metal NQW forming Schottky barrier or ohmic contact with a semiconductor substrate. Next, we calculate $e\phi$ in the metal NQW grown on a metal substrate. Finally, the possibility of realization of such electrodes using conventional thermionic and other materials is discussed. Analysis was made within the limits of parabolic band, wide quantum well and degenerate electron gas approximations.

2. Work function of metal NQW grown on semiconductor substrate

To maintain the uniform vacuum nanogap over the whole area, electrodes should have plane geometry and smooth surface. The simplest solution is to use semiconductor substrate as an electrode base [8] and grow a thin metal NQW layer on it.

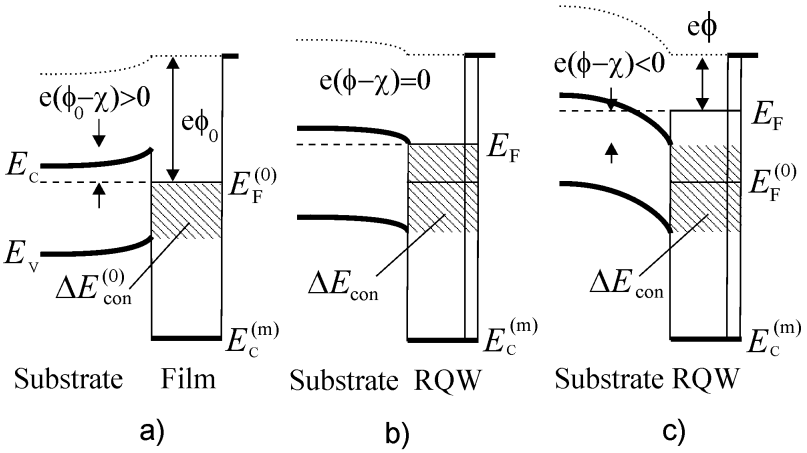

Figure 2. a) Energy diagram of metal-semiconductor contact in the case $e(\phi_0 - \chi) > 0$ without periodic ridges on the surface or $G = 1$, b) with ridges at $G = G_0$, c) with ridges at $G > G_0$. Hatch depicts confinement energy region.

The Energy diagram of the metal film grown on n^+-type semiconductor substrate is shown in Figure 2a. We begin from the case when the difference between metal initial work function $e\phi_0$ and semiconductor electron affinity $e\chi$ is positive, i.e. $e(\phi_0 - \chi) > 0$. We presume that electron gas in metal layer is degenerate, so that all quantum states are occupied below Fermi energy E_F and are empty above E_F. Further, suppose that the semiconductor band gap $E_g = E_C - E_V$ is wide enough, so that $e(\phi_0 - \chi) < E_g$ is satisfied. Then, electrons having energies within the region

$$\Delta E_{con}^{(0)} = E_g - e(\phi_0 - \chi) \tag{5}$$

are confined to the metal film. Within $\Delta E_{con}^{(0)}$, quantum states for electrons are filled in the metal film and forbidden in the semiconductor substrate. Next, we fabricate ridges on the metal film surface (Figure 2b). Additional vertical lines near the vacuum boundary in Figures 2b and 2c depict extra boundary conditions, imposed by the ridges. Owing to quantum state depression, supplementary boundary conditions reduce the quantum state density G times, within the energy region $e(\chi_m - \chi) - E_g < E < e(\chi_m - \chi)$, having width $\Delta E_{QSD} = E_g$. Here, we measure energies from the metal conduction band bottom $E_C^{(m)}$ and depict $e\chi_m \equiv E_F^{(0)} + e\phi_0$ as a metal conduction band width. G electrons, rejected from the forbidden quantum states within $\Delta E_{con}^{(0)}$, occupy the empty states above $E_F^{(0)}$. The Fermi level and the semiconductor band edges E_C and E_V move up on the energy scale. At the same time, $e\phi$ decreases and the energy region $\Delta E_{con} = E_g - e(\phi - \chi)$ (equation (5)) gets extended. As $e\phi$ decreases, the semiconductor band edge curving follows the $e(\phi - \chi)$ value and reverses its curving direction at $e(\phi - \chi) = E_C - E_F^{(0)}$.

The $e\phi$ value was calculated using electron number conservation in the NQW conduction band. The number of electrons rejected from the forbidden quantum states was equal to number of electrons accommodated above the initial Fermi level n_{ACC}. The rejected electron number n_{REJ}, according to equation (4) was

$$n_{REJ} = (1 - G^{-1}) \times \int_{CON} dE \rho_0(E) = (1 - G^{-1}) \times \int_{e(\chi_m - \chi) - E_g}^{e(\chi_m - \varphi_0)} dE \rho_0(E). \tag{6}$$

In equation (6), we take into account that electrons were rejected from the energy interval $e(\chi_{\mathbf{m}}-\chi)-E_{\mathbf{g}}<E<e(\chi_{\mathbf{m}}-\phi_{\mathbf{0}})$. They were accommodated in the interval $E_{\mathrm{F}}^{(0)}<E<E_{\mathrm{F}}$ or $e(\chi_{\mathbf{m}}-\phi_{\mathbf{0}})<E<e(\chi_{\mathbf{m}}-\phi)$. If n_{REJ} was low, the last interval fit within the ΔE_{QSD} (Figure 2b) where the density of states is reduced (equation (1)). The accommodate electron number was equal to the number of empty quantum states between $E_{\mathrm{F}}^{(0)}$ and E_{F}

$$n_{\mathbf{ACC}}=\int_{E_F^{(0)}}^{E_F} dE\rho(E)=\int_{e(\chi_m-\varphi_0)}^{e(\chi_m-\varphi)} dE\rho(E)=(1/G)\times\int_{e(\chi_{\mathbf{m}}-\phi_0)}^{e(\chi_{\mathbf{m}}-\phi)} dE\rho_0(E). \tag{7}$$

Using condition $n_{\mathrm{REJ}}=n_{\mathrm{ACC}}$ and putting in $\rho_0(E)\propto E^{1/2}$, which is true within the limit of parabolic band approximation, we found after integration and simplification that

$$\underset{\mathbf{e\phi\geq e\chi}}{e\phi}=e\chi_{\mathbf{m}}-e\left[G\left(\chi_{\mathbf{m}}-\phi_{\mathbf{0}}\right)^{3/2}-(G-1)\left(\chi_{\mathbf{m}}-\chi-E_{\mathbf{g}}/e\right)^{3/2}\right]^{2/3}. \tag{8}$$

Here, we use 3D density of states $\rho_0(E)\propto E^{1/2}$ (wide quantum well). Further, if n_{REJ} was high enough, $e(\phi-\chi)$ changed sign as shown in Figure 2c. n_{REJ} was calculated using equation (6) again. However, in this case, electrons were accommodated in quantum states from two different energy intervals. The primary interval $e(\chi_{\mathbf{m}}-\phi_{\mathbf{0}})<E<e(\chi_{\mathbf{m}}-\chi)$ was above $E_{\mathrm{F}}^{(0)}$ and within the energy region ΔE_{QSD} where density of states was reduced, and the secondary interval $e(\chi_{\mathbf{m}}-\chi)<E<e(\chi_{\mathbf{m}}-\phi)$ was above $E_{\mathrm{F}}^{(0)}$ and out of ΔE_{QSD}. The two intervals differ by density of states. The density was equal to equation (1) in the primary interval and $\rho_0(E)$ in the secondary one. Consequently, n_{ACC} was

$$\int_{E_{\mathbf{F}}^{(0)}}^{E_{\mathbf{F}}} dE\rho(E)=\int_{e(\chi_m-\phi_0)}^{e(\chi_m-\phi)} dE\rho(E)=(1/G)\times\int_{e(\chi_m-\phi_0)}^{e(\chi_m-\chi)} dE\rho_0(E)+\int_{e(\chi_m-\chi)}^{e(\chi_m-\phi)} dE\rho_0(E). \tag{9}$$

Further, equalizing equations (6) and repeating the above described steps we found

$$\underset{e\phi<e\chi}{e\phi}=e\chi_{\mathbf{m}}-e\left\langle\left(\chi_{\mathbf{m}}-\phi_{\mathbf{0}}\right)^{3/2}+\left(1-G^{-1}\right)\left[\left(\chi_{\mathbf{m}}-\chi\right)^{3/2}-\left(\chi_m-\chi-E_{\mathbf{g}}/e\right)^{3/2}\right]\right\rangle^{2/3} \tag{10}$$

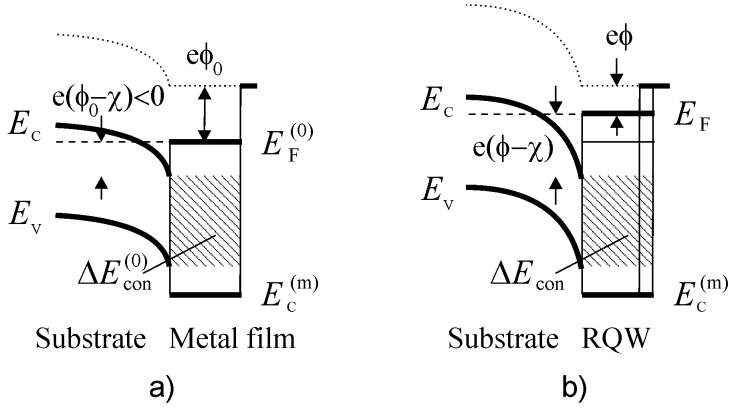

Figure 3. Energy diagram of metal–semiconductor contact for $e(\phi_0-\chi)<0$, a) without periodic ridges on the surface, b) with ridges. Hatch depicts confinement energy region.

Next, we consider the case when the difference between $e\phi_{\mathbf{0}}$ and $e\chi$ was negative, i.e., $e(\phi_{\mathbf{0}}-\chi)<0$ from the beginning (Figure 3a). Here, $\Delta E_{\mathrm{con}}^{(0)}=E_{\mathrm{g}}$. When ridges were fabricated (Figure 3b), the rejected electrons reduced $e\phi$. As $e\phi$ reduced $e(\phi-\chi)$ also reduced and got

even more negative. Semiconductor bands curve in the direction of $E_C^{(m)}$. At the same time, ΔE_{con} width remains constant. Electrons were rejected from the interval $e(\chi_m - \chi) - E_g < E < e(\chi_m - \chi)$, and their number was calculated by applying this interval to equation (4). Electrons were accommodated in the interval $e(\chi_m - \phi_0) < E < e(\chi_m - \phi)$ and their number was

$$\int_{e(\chi_m-\phi_0)}^{e(\chi_m-\phi)} dE\rho_0(E). \tag{11}$$

Using $n_{REJ} = n_{ACC}$, and repeating the above steps, we found that equation (10) is true for the case $e(\phi_0 - \chi) < 0$ as well.

Finally, equation (8) allows the calculation of geometry factor value G_0, at which an ideal ohmic contact was obtained or $e(\phi - \chi) = 0$. Inserting this in equation (8), we found

$$G_0 = \left[(\chi_m - \chi)^{3/2} - (\chi_m - \chi - E_g/e)^{3/2}\right] \times \left[(\chi_m - \phi_0)^{3/2} - (\chi_m - \chi - E_g/e)^{3/2}\right]^{-1}. \tag{12}$$

Analysis of metal – NQW / semiconductor contact shows that in the case $e(\phi_0 - \chi) \geq 0$, metal NQW layer $e\phi$ was calculated using equation (8) if $G \leq G_0$ (or $e\phi \geq e\chi$) and equation (10) if $G > G_0$ (or $e\phi < e\chi$). For opposite case, $e(\phi_0 - \chi) < 0$, $e\phi$ was calculated using equation (10) for all G values (note that $G > 1$ by definition).

3. Work function of metal NQW grown on metal substrate

In the case of metal – NQW / metal contact, electrons are confined to the material having wider conduction band (Figure 4). Within $\Delta E_{con}^{(0)}$, quantum states for electrons are filled in the metal film and forbidden in the metal substrate (MS). There are no quantum states below MS conduction band bottom $E_C^{(S)}$ except core levels which are at ≈ -100 eV and do not fall within $\Delta E_{con}^{(0)} < 10$ eV (values 100 and 10 eV are typical for metals). Let us begin from the case $e\phi_S > e\phi_0$, where $e\phi_S$ is the MS work function. Owing to WF difference, the contact potential emerges and the bottoms of conduction bands curve near the contact as shown in Figure 4a.

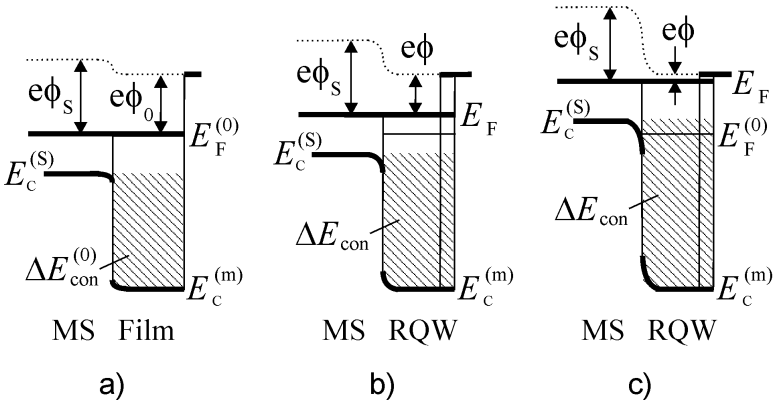

Figure 4. Energy diagram of metal–metal contact for the case $e\phi_S > e\phi_0$. a) Without periodic ridges, b), c) with ridges. MS depicts metal substrate. Hatch depicts confinement energy region.

When ridges are fabricated on the surface (Figures 4b and 4c), some electrons are rejected from $\Delta E_{\mathrm{con}}^{(0)}$ and accommodated above $E_{\mathrm{F}}^{(0)}$. Fermi level moves up on energy scale. The $E_{\mathrm{C}}^{(\mathrm{S})}$ follows the Fermi level (Figure 4b). The electron confinement energy region $\Delta E_{con} = E_{\mathrm{C}}^{(\mathrm{S})} - E_{\mathrm{C}}^{(\mathrm{m})}$ increases. This leads to rejection of even more electrons and $e\phi$ reduction amplifies. However, with rising E_{F}, number of states $\int dE\,\rho_0(E) \propto E^{3/2}$ above E_{F} increase more rapidly than n_{REJ} (as $E_{\mathrm{F}} > E_{\mathrm{C}}^{(\mathrm{S})}$) and at some $e\phi$ value, equilibrium is maintained.

Let us consider the case of low n_{REJ} or $E_{\mathrm{C}}^{(\mathrm{S})} < E_{\mathrm{F}}^{(0)}$ in the beginning (Figure 4b). To find $e\phi$, we use electron number conservation in NQW conduction band again. Electrons were rejected from the energy region $0 < E < E_{\mathrm{C}}^{(\mathrm{S})}$ or $0 < E < e(\chi_{\mathbf{m}} - \phi + \phi_S - \chi_S)$, where $e\chi_S \equiv E_{\mathbf{F}}^{(\mathbf{S})} + e\phi_S$ was the width of the substrate conduction band ($E_{\mathrm{F}}^{(\mathrm{S})} = E_{\mathrm{F}} - E_{\mathrm{C}}^{(\mathrm{S})}$ was substrate Fermi energy). The n_{REJ} was calculated by applying the last region to equation (4). Electrons were accommodated in the energy interval $E_{\mathrm{F}}^{(0)} < E < E_{\mathrm{F}}$ or $e(\chi_{\mathbf{m}} - \phi) < E < e(\chi_{\mathbf{m}} - \phi_0)$, where density of state was $\rho_0(E)$. The n_{ACC} was calculated via equation (11). Using $n_{\mathrm{REJ}} = n_{\mathrm{ACC}}$ and integrating, we obtain the following equation for ϕ

$$\left(1 - G^{-1}\right) \times \left(\chi_{\mathrm{m}} - \phi + \phi_S - \chi_S\right)^{3/2} = \left(\chi_{\mathrm{m}} - \phi\right)^{3/2} - \left(\chi_{\mathrm{m}} - \phi_0\right)^{3/2} . \qquad (13)$$

In the case of high n_{REJ} or $E_{\mathrm{C}}^{(\mathrm{S})} > E_{\mathrm{F}}^{(0)}$ (Figure 4c), electrons were rejected from the interval $0 < E < e(\chi_m - \phi_0)$ and we applied this interval to equation (4). They were accommodated in two intervals having diverse density of states. The primary interval $e(\chi_{\mathbf{m}} - \phi_{\mathbf{0}}) < E < e(\chi_{\mathbf{m}} - \phi + \phi_S - \chi_S)$ was above $E_{\mathrm{F}}^{(0)}$ and within the ΔE_{con}, and the secondary one $e(\chi_{\mathbf{m}} - \phi + \phi_S - \chi_S) < E < e(\chi_{\mathbf{m}} - \phi)$ was above $E_{\mathrm{F}}^{(0)}$ and out of ΔE_{con}. The two intervals differ in the density of states. Density was equal to equation (1) in the primary interval and $\rho_0(E)$ in the secondary one. The accommodated electron number was

$$\int_{E_{\mathbf{F}}^{(0)}}^{E_{\mathbf{F}}} dE\,\rho(E) = \int_{e(\chi_m - \phi_0)}^{e(\chi_m - \phi)} dE\,\rho(E) = (1/G) \times \int_{e(\chi_m - \phi_0)}^{e(\chi_m - \phi + \phi_S - \chi_S)} dE\,\rho_0(E) + \int_{e(\chi_m - \phi + \phi_S - \chi_S)}^{e(\chi_m - \phi)} dE\,\rho_0(E) . \qquad (14)$$

Using $n_{\mathrm{REJ}} = n_{\mathrm{ACC}}$ and integrating, we obtain equation (13) again for the last case.

Analysis of equation (13) shows that in some cases $e\phi$ can be reduced to zero and even acquire negative values, hypothetically. However, negative $e\phi$ cannot be realized since, in that case, at least one electron leaves NQW to vacuum. Simultaneously, the electrode as a whole charges positively, owing to electrical neutrality. This leads to shifting down of band bottoms $E_{\mathrm{C}}^{(\mathrm{m})}$ and $E_{\mathrm{C}}^{(\mathrm{S})}$ on the energy scale. At the same time, their difference $\Delta E_{con} = E_{\mathrm{C}}^{(\mathrm{S})} - E_{\mathrm{C}}^{(\mathrm{m})}$ does not increase and no additional electron is rejected. Naturally, vacuum level retains its position, which implies that both the conduction bands widen a little bit as their bottoms shift down. In the wider band, a fresh quantum state emerges at the band top. The electron that left returns (following image force) and occupies the emerged quantum state. As result, $e\phi$ increases back to zero value. Some details on this mechanism can be found in [15]. Related mechanisms were studied in negative electron affinity semiconductors [18].

The energy diagram for the opposite case $e\phi_S < e\phi_0$ is shown in Figure 5a. Initially, the vacuum level curves in the opposite direction, the contact potential has opposite sign and the conduction band bottoms curve in opposite directions. In this case, a small reduction in $e\phi$ results in the flattening of the conduction band bottoms. The width of ΔE_{con} reduces instead of

increasing. If initial n_{REJ} (rejected from $\Delta E_{con}^{(0)}$) was low, the system remains in the state $e(\phi_S - \phi_0) < 0$. However, if initial n_{REJ} was high enough to reduce $e\phi$ below $e\phi_S$, the band bottom curving direction changes (Figure 5b). Energy diagram becomes analogous to the one shown in Figure 4a and $e\phi$ can be calculated using equation (13) again. Further, we seek the initial n_{REJ}, required to change the sign of $\phi_S - \phi$. The following approximation was used to determine this number. It was assumed that the charge depletion depth has the same values in the two metals and is much less than the thickness of the NQW layer (electron concentration is thought to be equal in two metals). Within this approximation the electric field distribution around the contact area was symmetric and electron confinement energy region was $E_C^{(m)} < E < E_C^{(S)} + e\phi^{(-)}$, where $\phi^{(-)} \approx (\phi_0 - \phi_S)/2$. Here, we did not take into account the quantum states inside the triangular quantum well below $E_C^{(m)}$, assuming that the triangular well width was low with respect to NQW. Electrons, rejected from the above interval, should fill the interval $F_F^{(0)} < E < F_F^{(0)} + e(\phi_0 - \phi_S)$ to equalize WFs and flatten bang bottoms. According to equation (4)

$$\left(1 - G^{-1}\right) \times \int_{E_C^{(m)}}^{E_C^{(S)} + e\phi^{(-)}} dE\, \rho_0(E) = \int_{E_F^{(0)}}^{E_F^{(0)} + e(\phi_0 - \phi_S)} dE\, \rho_0(E). \tag{15}$$

Integrating equation (15) and simplifying, we found threshold geometry factor

$$G_{th} = \frac{\left(\chi_m - \chi_S + \phi_S/2 - \phi_0/2\right)^{3/2}}{\left(\chi_m - \chi_S + \phi_S/2 - \phi_0/2\right)^{3/2} + \left(\chi_m - \phi_0\right)^{3/2} - \left(\chi_m - \phi_S\right)^{3/2}}. \tag{16}$$

If $G \geq G_{th}$ system ends with reduced $e\phi$ in the NQW, and if $G < G_{th}$ system remains in the initial state $e(\phi_S - \phi_0) < 0$. Analysis of metal – NQW / metal contact show that if initially $e\phi_S > e\phi_0$, $e\phi$ of NQW layer was reduced and its value was calculated using equation (13). If initially opposite relation $e\phi_S < e\phi_0$ was realized, the last was true only in the case $G \geq G_{th}$. Otherwise the reduction was irrelevant.

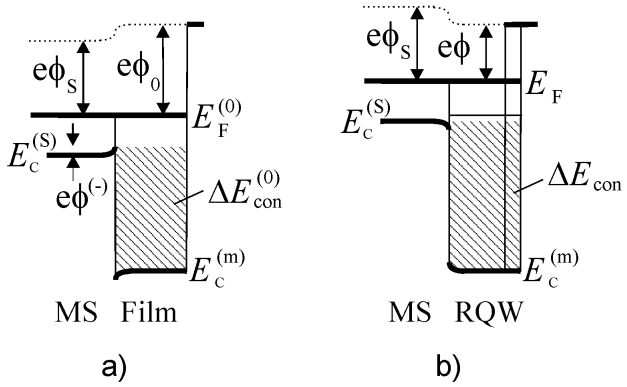

Figure 5. Energy diagram of metal–metal contact for the case $e\phi_S < e\phi_0$. a) Without periodic ridges, b), c) with ridges. MS depicts metal substrate. Hatch depicts confinement energy region.

4. Material pairs for NQW coated electrode

The thickness of a conventional metal quantum well is only 1 – 5 nm [19]. Periodic ridge fabrication on such thin layer surface seems complicated. However, owing to reduced quantum

state density, metal NQW layer retains quantum properties at G times more thickness (as found in [16]) with respect to a conventional metal quantum well. This makes ridge fabrication straightforward. In some cases, layer thickness can be increased even more than G times. As Figures 3-5 show, confined electrons have energies $E < E_{\mathbf{F}}^{(0)} - K_{\mathbf{B}}T$ (here, K_{B} is Boltzmann constant and $K_{\mathrm{B}}T \approx 25$ meV $<< E_{\mathrm{F}}^{(0)}$ for $T = 300$ K). For these energies, Fermi–Dirac distribution function $f(E, E_F, T) \approx 1$. Consequently, electron scattering on phonons and lattice defects is limited. Such scattering requires the exchange of a small portion of energy with environment, which is quantum mechanically restricted as all nearby quantum states are occupied. The mean free path of such electrons is very large and is limited only by structural defects, such as grain boundaries. In epitaxial films, such electrons allow phase coherence at large distances (in transverse direction) and metal NQW thickness can be increased. In this work, we do not concentrate on thermal processes in the metal NQW by following reasons. Transport coefficients in NQW have the same values as in a conventional quantum well (having the same value of E_F) [14]. In vacuum device, temperature gradient is applied mainly to the vacuum gap and only significant thermal process inside the electrode is Joule heating [20]. Such heating inside the metal NQW is negligible. We regard only n^+ semiconductor substrates (Figures 2-3), in which the difference $E_{\mathrm{C}} - E_{\mathrm{F}}$ is low and, heat absorption or release at the metal / semiconductor interface is insignificant.

Table 1. Parameters of electrode base materials.
The P_{d} and ∇T are given for 1 mm thick substrate.

Substrate material	E_g, eV	$e\chi$, eV	N_{D}, cm^{-3}	r, $\Omega \cdot \mathrm{cm}$	P_{d}, mW at 10 A / cm	κ, W / cm · K	∇T, K at 10 W / cm
Si	1.12	4.05	$8 \cdot 10^{20}$	$2 \cdot 10^{-4}$	2	1.6	0.6
GaAs	1.42	4.07	$8 \cdot 10^{19}$	$1 \cdot 10^{-4}$	1	0.5	2.0
GaN	3.20	4.10	$1 \cdot 10^{19}$	$7 \cdot 10^{-3}$	70	5.0	0.2
Mo				$5.3 \cdot 10^{-6}$	$5.3 \cdot 10^{-2}$	1.4	0.7
Ni				$6.2 \cdot 10^{-6}$	$6.2 \cdot 10^{-2}$	0.9	1.1

Regular semiconductor materials can be used as base substrate. Thermionic and thermotunnel converters are high current low voltage devices. Consequently, the main limitation is electrical conductivity. Equations (8) and (10) show that wide band gap material allows more reduction in $e\phi$. Unfortunately, it is problematic to achieve low resistivity in such materials. The most promising seems GaN in which relatively low resistivity was obtained. Other possible substrate materials are GaAs and Si. Table 1 shows possible donor concentrations N_{D} for GaN [21], Si, GaAs [22] and corresponding electrical resistivity r and heat conductivity κ. Metals, Ni and Mo, are also included since they are frequently used in thermionic converters. Table 1 also shows the dissipated power per cm^2 area P_{d}, and temperature gradient ∇T over 1 mm thick substrate, calculated for typical current density ($10\ \mathrm{A} / \mathrm{cm}^2$) and heat flux ($10\ \mathrm{W} / \mathrm{cm}^2$). Power dissipation in GaN substrate is considerable (note that ∇T is low for GaN). On the other hand, GaN has a wide band gap and allows lower $e\phi$ values. Possible solution is to

grow thin GaN epitaxial layer on the GaAs or Si substrates. Such bi-layer substrate ensures low power loss together with low $e\phi$ in the metal NQW layer. Fortunately, GaN can be grown epitaxially on both GaAs and Si substrates [23].

Most technological metals have $e\phi_0 > 4$ eV and form Shottky barriers with above semiconductor materials i.e. $e(\phi_0 - \chi) > 0$. Table 2 shows parameters of some metals frequently used as electrode materials (other interesting metals are included as well), collected from the literature: $e\phi_0$ from [24] and $E_F^{(0)}$ from [25]. It also contains data on E_F^{Band}, which is the Fermi energy obtained from *ab initio* calculations and experiments [26-31]. Parameter E_F^{Band} differs more or less from $E_F^{(0)}$. We used E_F^{Band} instead of $E_F^{(0)}$ for Mo, W, Ni and Pt since no $E_F^{(0)}$ data was found. This substitution is acceptable as far as a parabolic band is good approximation for these metals. The $e\phi$ values presented in the table were calculated using equation (10). WF values were reduced by ≈ 1, 1.2 and 2.3 eV on Si, GaAs and GaN substrates, respectively. Reduction is limited by the ΔE_{con} scale. The last can only be increased by increasing band gap. However, wide band gap substrates have high resistivity and were not acceptable for thermotunnel and thermionic devices. Obviously 1 – 2.3 eV reduction in $e\phi$ was not enough for cold emission, but it was still interesting since the plain Mo and Ni electrodes, coated with ultra thin layer of Cs atoms, show very low WF (1 – 1.5 eV). WF reduction by less than mono layer of Cs atoms is a surface effect. At the same time, quantum state depression is not a surface effect. Most probably, the two mechanisms of WF reduction will sum up and result in an $e\phi$ considerably less than 1 eV. The same is true for Ag – Ba and W – Li electrodes.

Table 2. Characteristic energies for some metals and values of $e\phi$, calculated for $G = 10$.

NQW material	$e\phi_0$, eV	$E_F^{(0)}$, eV	E_F^{Band}, eV	$e\phi$, eV on		
				Si	GaAs	GaN
Ag	4.26	5.48	7.5[a]	3.32	3.10	2.02
Nb	4.30	5.32	5.5[b]	3.36	3.14	2.06
W	4.55		6.7[c]	3.58	3.34	2.14
Cu	4.65	7.0	9.1[a]	3.65	3.43	2.20
Mo	4.60		5.0[d]	3.63	3.41	2.32
Au	5.10	5.53	9.4[a]	4.09	3.85	2.64
Ni	5.15		5.0[e]	4.14	3.90	2.81
Pt	5.65		10[f]			2.95

[a] [26]
[b] [27]
[c] [28]
[d] [29]
[e] [30]
[f] [31]

Borides have $e\phi_0 < 4$ eV and for them $e(\phi_0 - \chi) < 0$ (Figure 3). The most frequently used is lanthanum hexaboride LaB_6, which shows $e\phi = 2 - 3.2$ eV. Fermi energy for LaB_6 is $E_F^{Band} = 10$ eV [32]. Inserting these values in equation (10) gave $e\phi = 0 - 0.85$, $0.94 - 2.05$ and $1.15 - 2.28$ eV for nanostructured LaB_6 layer on GaN, substrate, GaAs and Si substrates, respectively ($G = 10$ was used in all cases). These values were low enough for thermotunnel and thermionic devices operating at room temperatures.

Geometry factors, at which ideal ohmic contact was obtained, were calculated using equation (12). They were in the range $G_0 = 1 - 5$ for most material pairs. Such G_0 can easily be obtained in practice. Exceptions were Ni / Si ($G_0 = 59$) and Au/Si ($G_0 = 16$) pairs.

Next, we consider metal substrates (Figures 4 and 5). Electron confinement energy region emerges only if E_F^{Band} of a substrate material is less than that of a NQW material. Nickel and molybdenum were good choices for substrates as they have low E_F^{Band}. Au, Pt, Cu materials were suitable for NQW. They have high E_F^{Band} and at the same time can be grown epitaxially on Ni substrate [33-35]. The $e\phi$ in NQW depends on material parameters and G according to equation (13). To determine the geometry factor, needed for $e\phi = 0.5$ eV in NQW, material parameters from Table 2 together with $e\phi = 0.5$ eV were put in equation (13). Results were $G = 8.2$, 7.8 and 6.5 for cases of Cu / Ni, Au / Ni and Pt / Ni, respectively. These values were low enough to be realized in practice. One more interesting NQW material is TiN since it has high E_F^{Band} (in fact it has two bands) [36]. However, lattice mismatch introduces problems in TiN epitaxial growth. Threshold geometry factor G_{th} for Ni and Mo substrates was calculated using equation (16). We got $G_{th} = 1.1$, 1.3 and 1.6 for Pt / Ni, Au / Mo and Pt / Mo, respectively. For other pairs, $G_{th} = 1$.

Analysis, made on the basis of material parameters, shows that low $e\phi$ electrodes can be obtained using NQW layer made from conventional thermionic materials. Both semiconductor and metal substrates can be used to obtain low $e\phi$. However, metal substrate is preferable as it allows low $e\phi$ for a broad range of materials. Dissipated power and temperature gradient calculations show that both semiconductor and metal substrates, coated with metal NQW layer, can be used as electrodes for thermionic and thermotunnel converters.

5. Conclusions

Low work function was obtained in the metal nanostructured quantum well having reduced quantum state density. Metal NQW layers, grown on semiconductor and metal substrates, were analyzed. Electron confinement to the NQW was essential in both cases. When using semiconductor substrate, wide band gap material allows more electron confinement and lower values of resulting $e\phi$. Dependence of $e\phi$ on the band gap was analyzed for a number of cases and the corresponding formulae derived. When using metal substrate, materials with low Fermi energy allow more electron confinement and lower values of resulting $e\phi$. If initial $e\phi_0$ in the metal layer was less than in the substrate, $e\phi_0 < e\phi_S$, considerable $e\phi$ reduction was obtained for all metal pairs, ensuring electron confinement. In the opposite case, $e\phi_0 > e\phi_S$, low $e\phi$ was obtained only if the geometry factor exceeded some threshold value.

Acknowledgements

The author thanks L. Tsakadze for useful discussions and the Physics Department of NY University, where part of this work was done, for their hospitality.

References

1. S. Yamamoto. Reps. Prog. Phys., 2006, **69,** 181.
2. T. Zeng. Appl. Phys. Lett., 2006, **88,** 153104.
3. H. J. Goldsmid. In: Thermoelectrics (22nd Int. Conf. on Themoelectrics), 2003, 433.
4. G. Despesse, T. Jager. J. Appl. Phys, 2004, **96**, 5026.
5. G. Wachutka, Y. C. Gerstenmaier. AIP Conf. Proc., 2007, **890**, 349.
6. W. S. Koh, L. K. Ang. Nanotechnology, 2009, **19,** 235402.
7. Y. Hishinuma, T. H. Geballe, B. Y. Moyzhes, T. W. Kenny. Appl. Phys. Lett., 2001, **78**, 2572.
8. A. Tavkhelidze, V. Svanidze, L. Tsakadze. J. Vac. Sci. &Technol. A, 2008, **26,** 5.
9. A. Tavkhelidze, G. Skhiladze, A. Bibilashvili, L. Tsakadze, L. Jangidze, Z. Taliashvili, I. Cox, Z. Berishvili. In: 21st Int. Conf. on Themoelectrics, 2002, 435.
10. Y. Hishinuma, T. H. Geballe, B. Y. Moyzhes. J. Appl. Phys., 2003, **94,** 4690.
11. E. Enikov, T. Makansi. Nanotechnology, 2009, **19,** 075703.
12. M. F. O'Dwyer, T. E. Humphrey, R. A. Lewis, C. Zhang. J. Phys. D: Appl. Phys., 2009, **42,** 035417.
13. T. L. Westover, T. S. Fisher. Phys. Rev. Lett. B, 2008, **77,** 115426.
14. A. Tavkhelidze. Nanotechnology, 2009, **20,** 405401.
15. A. Tavkhelidze, V. Svanidze, I. Noselidze, J. Vac. Sci. & Technol. B, 2007, **25,** 1270.
16. A. Tavkhelidze, V. Svanidze. Int. J. Nano Sci., 2008, **7,** 333.
17. A. Tavkhelidze, A. Bibilashvili, L. Jangidze, A. Shimkunas, P. Mauger, G. F. Rempfer, L. Almaraz, T. Dixon, M. E. Kordesch. J. Vac. Sci. & Technol. B, 2006, **24,** 1413.
18. J. F. Prins. Semicond. Sci. & Technol., 2003, **18,** S125-S130.
19. W. B. Su, C. S. Chang, T. T. Tsong. J. Phys. D: Appl. Phys., 2010, **43**, 013001.
20. Y. Hishinuma, B. Y. Moyzhes, T. H. Geballe. Appl. Phys. Lett., 2002, **81**, 4242.
21. C. J. Eiting, P. A. Grudowski, R. D. Dupuis. J. Electr. Mat., 1998**, 27,** 206.
22. S. M. Sze, K. K. Ng. Physics of Semiconductor Devices. 2007, NJ: Wiley–Interscience.
23. J. W. Yu, H. C. Lin, Z. C. Feng, L. S. Wang, B. S. Tripathy, S. J. Chua. Thin Solid Films, 2006, **498,** 108.
24. D. R. Linde. CRC Handbook of Chemistry and Physics (71st ed.), 1990 / 1991, 12.
25. N. E. Ashkroft, N. D. Mermin. Solid State Physics. 1976, NY: Saunders.
26. T. mc Avoy, J. ZhangJ, C. Waldfried, D. N. mc Ilroy, P. A. Dowben, O. Zeybek, T. Bertrams, B. S. Barrett, Eur. Phys. J.l B, 2000, **14,** 747.
26. U. Mizurani. Electron Theory of Metals. 2001. Cambridge: Cambridge University Press.
27. Ch. E. Lekka, M. J. Mehl, N. Bernstein, D. A. Papaconstantopoulos. Phys. Rev. B, 2003, **68,** 035422.

28. E. Lassner, W.-D. Schubert. Tungsten: Properties, Chemistry, Technology of the Element, Alloys, and Chemical Compounds. 1999, NY: Kluwer Academic / Plenum Publ.
30. A. Yamasaki, T. Fujiwara. J. Phys. Soc. Jpn., 2003, **72,** 607.
31. S. Baud, C. Ramseyer, G. Bihlmayer, S. Blügel, C. Barreteau, M. C. Desjonquères, D. Spanjaard, N. Bernstein. Phys. Rev. B, 2004, **70**, 235423.
32. M. A. Uijttewaal, G. A. de Wijs, R. A. de Groot. J. Phys. Chem. B, 2006, **110***,* 18459.
33. W. D. Luedtke, U. Landman. Phys. Rev. B, 1991, **44, 5970**.
34. A. Tesauro, A. Aurigemma, C. Cirillo, S. L. Prischepa, M. Salvatoand, C. Attanasio. Supercond. Sci. & Technol.**,** 2005**, 18,** 1.
35. H. Kenneth, L. Mayat, N. J. Lonergan. J. Phys. Chem. B, 2005, **109,** 14557.
36. A. Vojvodic, C. Ruberto, B. I. Lundqvist. Surf. Sci., 2006, **600**, 3619.

MAGNETOPLASTIC EFFECT IN LiF CRSTALS X-RAYED IN A WEAK MAGNETIC FIELD

M. Galustashvili, M. Abramishvili, D. Driaev, V. Kvatchadze, S. Tsakadze

Ivane Javakhishvili Tbilisi State University
Elevter Andronikashvili Institute of Physics
Tbilisi, Georgia
maxsvet@yahoo.com

Accepted April 15, 2011

1. Introduction

At present there exists ample amount of experimental evidence of weak magnetic field (MF) effect (for nonmagnetic materials $B \leq 10$ T at room temperature) upon physical and mechanical characteristics of diamagnetic crystals, the so called magnetopastic effect [1-3]. To explain the phenomenon the theory of spin-dependent processes, causing magnetoplastic effect (MPE) particularly, is engaged.

In diamagnetic crystals two types of MPE, which can manifest themselves both separately and simultaneously [4], are observed. Both of these effects can be attributed to MF induced spin-dependent transitions in pairs of nonequilibrium paramagnetic defects, representing a two-spin nanoreactor: impurity point defect–dislocation or several impurity paramagnetic ions, forming metastable clusters of point defects. The first type effect, referred to as dynamic, is the radical change of dislocation–paramagnetic center (stopper) configuration as a result of the exclusion removal for specific spin transition by external magnetic field. The second type effect consists in transformation of stoppers and does not need dislocation existence at the moment of magnetic field application. This effect is referred to as static one. The mobility of dislocations in this case is the indirect indicator of changes in crystal defect structure in MF.

The necessary condition for MPE is existence in the crystal of nonequilibrium defects, with X-raying being one of the generation options for it. As it was shown in alkali-haloid crystals [5] magnetosensitive defects are already formed at very low doses of X-raying (5 s). When applying MF to the crystal during its irradiation, it can affect both electron excitations generated by ionizing irradiation and processes of structural defects initiation during their decay; in that way composition of generated defects will change which in its turn should affect both plastical characteristics of the crystal and optical absorption spectra of sample irradiated in MF.

The goal of presented paper is to study both types of MPE in LiF crystals with magnetosensitive defects, including those generated by X-rays.

2. Samples and methods

The investigations were carried out in LiF single crystals (Karl Zeiss, Germany) containing Ni ($6 \cdot 10^{-4}$ wt %), as well as Fe, Pb, Si, Mn and Ca (each not more than 10^{-4} wt %). The samples with dimensions of $8 \times 8 \times 0.5$ mm^3 were cleaved from single crystal ingot along the cleavage plane (100). The yield stress was determined in the deformation machine (DY–22), all parts of it being made of non-magnetic materials in the region of the magnetic field action. The compressive deformation was carried out at the constant rate of $3 \cdot 10^{-5}$ / s. The magnetic field ($B = 0.7$ T), with the vector of magnetic induction $\vec{B}$ directed perpendicular to the axis of sample compression, was formed by a permanent magnet. The optical absorption spectra were measured in the range of 195 – 1100 nm by spectrophotometer SF–29. All experiments were carried out at room temperature.

The samples were irradiated on X-ray equipment URS–55M (Fe anode, $\lambda = 1.94$ Å), the voltage and current in the tube were $U = 50$ kV and $I = 20$ mA correspondingly. Two samples, irradiated simultaneously, were located at the opposite outputs of X-ray beam; the magnetic field $\vec{B}$, with vector parallel to the big face of sample (perpendicular to the direction of X-ray beam) was applied to one of them.

3. Results and discussion

The magnetoplastic effect in the samples under investigation was registered by the changes of yield stress σ_y – one of the main microplastic characteristics of LiF. The measurements of σ_y were carried out in two runs of experiments differing by MF application at different stages of experiment. In that way the defects of various types and states were affected by the field.

In similar investigations carried out earlier, each curve of deformation was plotted for separate sample showing its individual properties and inevitable spread in σ_y values. To exclude such spread, all dependencies in each run of experiments were obtained on one sample multiply loaded up to the yield stress. To prevent the deformation hardening accompanied by formation of dislocation “forest”, the measurements were carried out at the beginning of the easy glide stage in the narrow interval of deformations near the yield stress σ_y. At the minimum three samples were tested in each run.

The dislocation pattern was revealed by chemical etching of the deformed samples surface. It was registered that MPE was observed only in case when a pair of slip planes, in which the dislocation lines $\vec{L}$ were perpendicular to the vector of magnetic induction $\vec{B}$, was active in the process of deformation; which is in full agreement with the conclusion of the authors who discovered the magnetoplastic effect first [1] and the others [2, 3]. Note that in our experiments, at fields less than 0.7 T and at the rate of deformation more than $3 \cdot 10^{-5}$ / s, MPE was not replicated reliably.

In the first run of experiments, the sample was deformed until the initial stage of plastic flow, the initial yield stress $\sigma_y = 3.5 \pm 0.1$ MPa was registered. Then the sample was placed in

MF and anew the yield stress was measured. Further on, the field was removed and after some intervals of time σ_y was measured repeatedly (Figure 1).

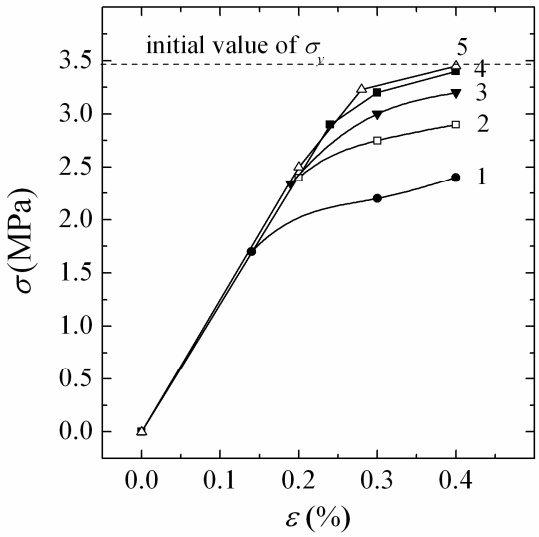

Figure 1. $\sigma(\varepsilon)$ diagrams for LiF crystal: Curve 1 – the initial sample deformed without magnetic field; Curve 2 – deformation of the same sample in magnetic field (0.7 T); Curves 3-5 – deformation of the sample in 0.5, 2 and 10 hours after MF removal, respectively.

The experiments showed that in the region of elastic deformation, MF does not lead to the change of the $\sigma(\varepsilon)$ diagram slope, while the yield stress decreases more than twice. At room temperature σ_y relaxes to the initial value. The process is a two stage one: the first is a short phase (< 1 h), when almost a full recovery of σ_y takes place, and the second is a slow relaxation during 24 hours to the initial value of σ_y (Figure 2).

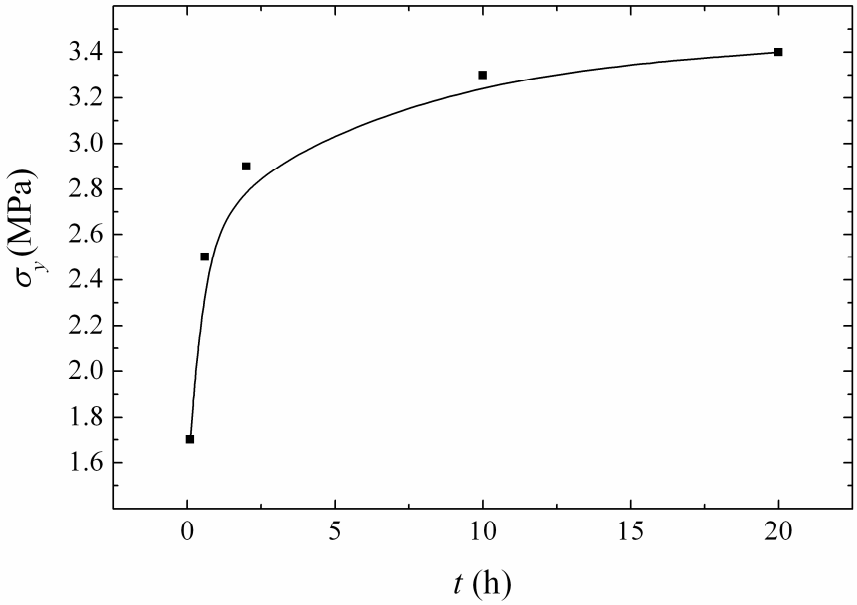

Figure 2. Dependence of yield stress σ_y for LiF crystals on time passed after tests in magnetic field (the lower point on the curve corresponds to MF test).

These experiments were as well carried out under the conditions, when the necessary orientation of magnetic induction vector $\vec{B}$ with respect to the dislocation line $\vec{L}$ is given and retained in the process of deformation (2 – 3 %) with high reliability. The sample was deformed by a pure shear in one system of slip planes (Figure 3) by the technique developed in-house [6]. The results fully confirmed the data obtained in the first run of experiments.

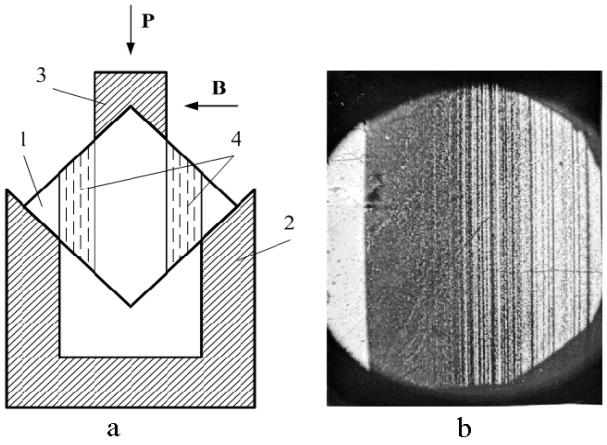

Figure 3. a) Scheme of the device for deformation of LiF crystals by simple shear in one slip system: 1 – sample, 2 – support, 3 – forcer, 4 – system of active slip planes; b) Etching pattern of deformed sample (left side of sample).

In the second run, the initial sample (without preliminary deformation) was placed in the magnetic field and its yield stress was registered. Then, the field was removed and, as in the first case σ_y was measured after some intervals of time. Unhardening of the sample in this run of experiment is less (1.5 times), but the initial value of σ_y has been restored for the same period of time, as in the first case. The much higher degree of unhardening in the first run of experiments is probably caused by nonequilibrium formed by deformation prior to the magnetic field application.

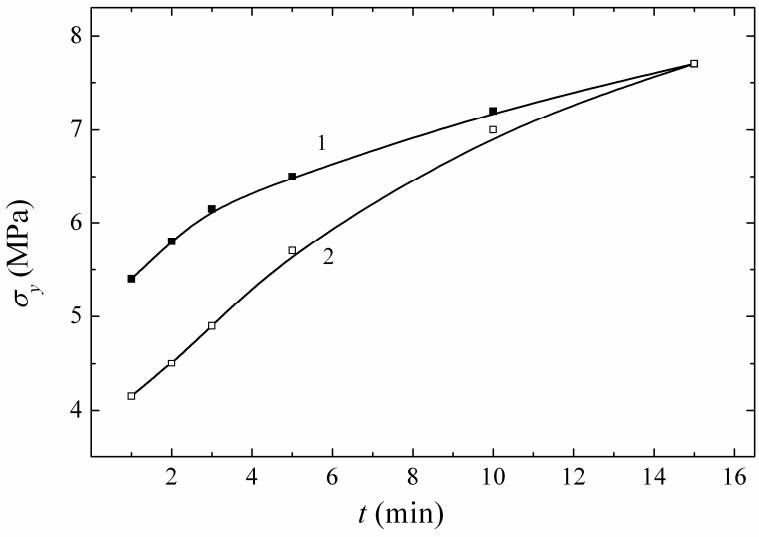

Figure 4. Dependence of yield stress σ_y on the time of X-raying: irradiation without MF (Curve 1) and in MF (Curve 2).

After experiments having registered "dynamic" MPE in the initial crystals, the tests for the second type MPE were performed. In this case potential stoppers were born and changed both under X-raying only and under combined action of X-rays and magnetic field. The yield stress was measured after irradiation (without MF application), results given in Figure 4.

At the irradiation time up to $t = 15$ min, the samples irradiated in MF show the lower yield stress: the maximum difference in the yield stress makes about 25 % and with the increase of a dose it vanishes. Thus, the effect of MF on the process of radiation hardening of the crystal is observed only at small doses of X-ray irradiation. This result and the data of other authors [7] give evidence that the new magneto-sensitive defects are already originated at the very first stages of X-ray irradiation, and at the same stages MF affects the process of crystal radiation hardening.

The fact, that at the early stages of irradiation process causing crystal unhardening prevails, and then as radiation defects are accumulated, this effect decreases to zero, indicates the existence of two types of potential stoppers for moving dislocations. The first type is represented by intrinsic radiation defects whereas the second type stoppers are impurity complexes, being in the crystal primordially and modified by magnetic field (in process of irradiation); as it was noted in [7] the irradiation makes the impurity more magnetosensitive. The latter can lead to lowering of local barriers for dislocation motion and consequently to yield stress decrease. As dose rises concentration and hardening role of intrinsic radiation defects increase too, whereas the role the impurity complexes is diminished. Competition of these two processes eventually in time ~ 10^3 s reduces to zero total effect of MF upon radiation hardening of LiF crystal.

In contrast to yield stress, MF combined with X-ray radiation ($B = 0.7$ T) does not lead to quantitative or qualitative changes in optical absorption electron spectra of samples. At small doses used, only F-band was observed in spectra.

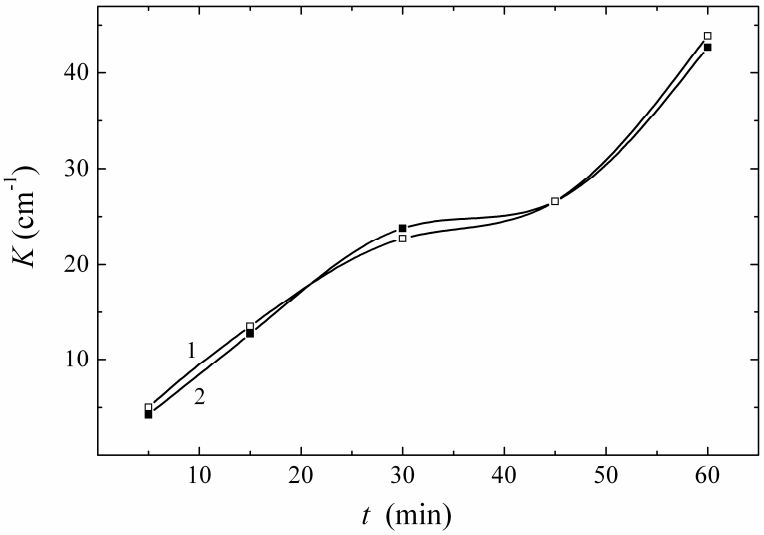

Figure 5. Dependence of absorption coefficients for F-centers (250 nm) on the time of crystals exposure in the X-ray field: irradiation without MF (Curve 1) and in MF (Curve 2).

Figure 5 shows the dependencies of absorption coefficients for F-centers (250 nm) on the time of crystal exposure in the X-ray field in a free state (Curve 1) and in MF (Curve 2). Almost a complete coincidence of these dependencies is seen in the whole interval of irradiation doses.

4. Conclusions

● When deforming LiF crystal in magnetic field the yield stress σ_y decrease is observed; after magnetic field removal the yield stress restores its former value in twenty-four hours.

● The X-raying of crystals in MF at the early stages of irradiation (~ 10^3 s) leads to sample unhardening caused by modification of impurity complexes (stoppers) configuration.

● The effect of MF on the accumulation process of F-centers was not observed at the given regime of combined action.

Acknowledgements

The designated study has been fulfilled by financial support of the Georgian National Science Foundation (Grants # GNSF/ST08/4-414 and GNSF/ST07/4-194).

References

1. V. I. Alshits, E. V. Darinskaya, M. V. Koldaeva, E. A. Petrzhik. In: Dislocations in Solids (Ed. J. P. Hirth). 2008, Amsterdam: Elsevier, 333.
2. Yu. I. Golovin. Phys. Solid State, 2004, **46**, 769.
3. R. B. Morgunov. Uspekhi Phys. Nauk, 2004, **174**, 131.
4. R. B. Morgunov. Phys. Solid State, 2011, **53**, 733.
5. A. L. Buchachenko. JETP, 2006, **129,** 909.
6. M. V. Galustashvili, D. G. Driaev, I. A. Politov, Z. K. Saralidze. Phys. Solid State, 1988, **30,** 1533.
7. V. A. Alshits, E. V. Darinskaya, O. L. Kazakova. JETP Lett., 1995, **62**, 352.

ერთელექტრონიანი ნანოსისტემები

ა. პ. ბიბილაშვილი

ივანე ჯავახიშვილის სახელობის თბილისის სახელმწიფო უნივერსიტეტი
თბილისი, საქართველო
amiran.bibilashvil@tsu.ge

მიღებულია 2011 წლის 26 აპრილს

1. შესავალი

მიკროელექტრონიკის რთული ტექნიკური ამოცანისადმი ზოგადმა და სისტემურმა მიდგომამ და მისმა უპრეცენდენტოდ სწრაფი ტემპებით განვითარებამ ხელსაწყოთა მინიატურიზაციის მიმართულებით წარმოშვა მეცნიერებისა და ტექნიკის ახალი სწრაფად მზარდი და პერსპექტიული დარგი – ნანოელექტრონიკა. მისი კვლევების მთავარი მიზანია ახალი პრინციპების საფუძველზე ზემინიატურული და სუპერსწრაფქმედი ნანოსისტემების და მოწყობილობების შემუშავება. ამ ამოცანის გადაწყვეტის ერთ-ერთი შესაძლო გზაა განსაზღვრული რაოდენობის, კერძოდ, ერთი ელექტრონის გადაადგილების მაკონტროლებელი ხელსაწყოს შექმნა. ასეთ სისტემებში ინფორმაცია ერთადერთ ელექტრონს გადააქვს და ამიტომაც ნანოელექტრონიკაში ისინი ფართო პერსპექტივებს შლიან. მათში ელექტრონების გადაადგილება ხდება სათითაოდ, უშუალოდ გვირაბგასვლით. რადგანაც ელექტრონის გვირაბგასვლის დრო საკმაოდ მცირეა, ამიტომ თეორიულად ერთელექტრონიანი ხელსაწყოს სწრაფქმედების ზღვარი ძალიან მაღალია. მეორეს მხრივ, ერთი ელექტრონის გადაადგილებაზე შესრულებული მუშაობა მცირეა და შესაბამისად, ერთელექტრონიან სისტემებში ენერგომოთხოვნებიც დაბალია. ამიტომაა მკვლევარებისთვის ერთელექტრონიანი ნანოსისტემების შესწავლა და სრულყოფა ძალიან მნიშვნელოვანი, როგორც ფუნდამენტული, ასევე გამოყენების თვალსაზრისით. წინამდებარე ნაშრომში განხილულია ერთელექტრონიანი სტრუქტურის და მის ბაზაზე შექმნილი ნანოტრანზისტორის მოქმედების ფიზიკური პრინციპი.

2. ელექტრონული გვირაბგასვლის პროცესი

ელექტრონული გვირაბგასვლის პროცესი ელექტრონის ტალღური ბუნების გამოვლენის ტიპიური შემთხვევაა და მდგომარეობს იმაში, რომ ელექტრონს პოტენციალური ჯებირის გავლა შეუძლია მაშინაც კი, როდესაც მისი ენერგია ნაკლებია პოტენციალური ჯებირის სიმაღლეზე. ეს ეფექტი არსებითად კვანტურია და მას კლასიკურ მექანიკაში ანალოგი არ გააჩნია. კლასიკური მექანიკის თანახმად, ნაწილაკი არ შეიძლება იმყოფებოდეს U_0 სიმაღლის პოტენციალური ჯებირის შიგნით, თუკი მისი

ენერგია $E < U_0$, რადგან ამ დროს ნაწილაკის კინეტიკური ენერგია ხდება უარყოფითი, ხოლო იმპულსი – წარმოსახვითი:

$$\frac{\vec{p}^2}{2m} = E - U_0 < 0 . \qquad (1)$$

აქ $\vec{p}$ ნაწილაკის იმპულსია, ხოლო m მისი მასაა. გარდა ამისა, თუ ნაწილაკი ენერგიით $E < U_0$, უახლოვდება პოტენციალურ ჯებირს, მაშინ ის მისგან აირეკლება და დაიწყებს მოძრაობას საპირისპირო მიმართულებით. მაგრამ თუ $E > U_0$, მაშინ ნაწილაკი გააგრძელებს მოძრაობას თავდაპირველი მიმართულებით. კვანტურ მექანიკაში სურათი სხვაგვარია. კვანტური მექანიკის მიხედვით, ელექტრონული გვირაბგასვლის პროცესი შესაძლებელია ნაწილაკის იმპულსსა და მის კოორდინატს შორის არსებული განუზღვრელობის პრინციპის წყალობით [1]. ამ პრინციპის თანახმად, იმპულსის და კოორდინატის ერთდროულად ზუსტად განსაზღვრა შეუძლებელია, რაც მათემატიკურად ასე ჩაიწერება:

$$\Delta x \Delta p_x \geq \hbar , \qquad (2)$$

სადაც Δx ნაწილაკის x კოორდინატის განსაზღვრის ცდომილებაა დროის მოცემულ მომენტში, ხოლო Δp_x – იმპულსის ვექტორის x ღერძზე პროექციის განსაზღვრის ცდომილება იმავე მომენტში. ამიტომ ჯებირის შიგნით ნაწილაკის კოორდინატის ფიქსაცია იმპულსს ხდის განუზღვრელს და იგი შეიძლება აღმოჩნდეს ჯებირის გარეთ.

ამრიგად, თუ ზუსტადაა ცნობილი ელექტრონის კოორდინანტი, საერთოდ არ იქნება ცნობილი მისი იმპულსი (ან სიჩქარე) და პირიქით. ამიტომ აზრს კარგავს კლასიკურ მექანიკაში მიღებული მიკრონაწილაკის მდებარეობის განმსაზღვრელი ტრაექტორიის ცნება და მექანიკური ენერგიის დაყოფა კინეტიკურ და პოტენციალურ ენერგიებად. კვანტურ მექანიკაში აზრი აქვს მიკრონაწილაკის მოცემულ მომენტში სივრცის მოცემულ წერტილში ყოფნის ალბათობას და, შესაბამისად, მიკრონაწილაკი აღიწერება სტატისტიკური მახასიათებლებით. ჩნდება ნაწილაკის მიერ პოტენციალური ჯებირის განჭოლვის ალბათობა. იმავროულად შეინარჩუნება მიკრონაწილაკის ისეთი მახასიათებლები, როგორიცაა მასა, ენერგია და იმპულსის მომენტი.

ელექტრონის გვირაბგასვლის კვანტური და კლასიკური პროცესები ნაჩვენებია ფიგურაზე 1.

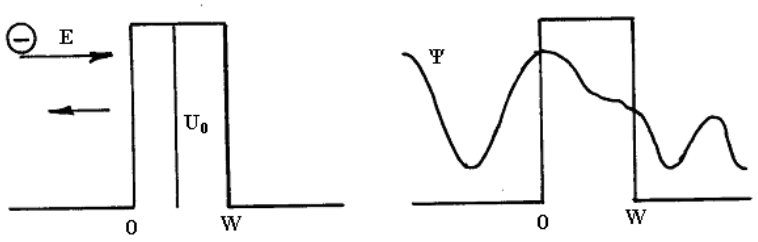

ა) ბ)

ფიგურა 1. ელექტრონის პოტენციალურ ჯებირში გავლის ალბათობა კლასიკურ (ა) და კვანტურ (ბ) შემთხვევებში.

გვირაბგასვლის ეფექტი აღმოაჩინა გ. გამოვმა [2]. ამ ფაქტმა ბევრი იმ დროისათვის დაგროვილი ექსპერიმენტული ფაქტი ახსნა. განსაკუთრებით უნდა აღინიშნოს ბირთვიდან ნაწილაკების ამოფრქვევის მოვლენა – თანამედროვე ატომური მეცნიერებისა და ტექნიკის ძირითადი საფუძველი. გამოვი მართლაც იმსახურებდა

ნობელი პრემიას, მაგრამ მისი აღმოჩენიდან მხოლოდ ოცდაათი წლის შემდეგ, როცა ის უკვე ცოცხალი აღარ იყო, დამზადდა გვირაბგასვლის ეფექტზე პირველი ისეთი ხელსაწყოები, როგორიცაა გვირაბული დიოდი, ტრანზისტორი, გადამცემები, ზედაბალი ტემპერატურის გამზომი თერმომეტრები და ბოლოს, მასკანირებელი გვირაბული მიკროსკოპი [3], რომელმაც დაუდო საფუძველი ნანოტექნოლოგიის წარმოშობას.

ერთელექტრონული გვირაბგასვლის შესაძლებლობა თეორიულად იწინასწარმეტყველა კ. ლიხარიოვმა [4], რომელიც რამდენიმე წლის შემდეგ დამტკიცდა ექსპერიმენტულად [5]. ვთქვათ, ელექტრონს შეუძლია იმყოფებოდეს რომელიმეში ორი A და B წერტილიდან. კვანტური მექანიკის თანახმად, სივრცის ამ ორ სხვადასხვა წერტილში ელექტრონის მოხვედრის ალბათობები დროში იცვლებიან უწყვეტად, მაგრამ ისე, რომ მათი ჯამი ყოველთვის 1-ის ტოლია. ასე, მაგალითად, თუ დროის საწყის $t=0$ მომენტში ელექტრონი იმყოფება A კვანტურ წერტილში P_{A} ალბათობით, მაშინ მისი აქ აღმოჩენის ალბათობა ერთის ტოლია, ხოლო B-ში აღმოჩენის ალბათობა P_{B}, საითკენაც ის შეიძლება მოძრაობდეს, – ნულის. ეს ნიშნავს, რომ A კვანტურ წერტილში მუხტი ტოლია $-e$-ის ხოლო B-ში – 0-ის. დროთა განმავლობაში P_{A} მონოტონურად მცირდება ნულამდე, ხოლო P_{B} იზრდება ერთამდე, ისე, რომ ყოველთვის $P_{\mathrm{A}}+P_{\mathrm{B}}=1$. დროის ნებისმიერ t მომენტში A და B წერტილებში მუხტი ტოლი იქნება $-eP_{\mathrm{A}}$ და $-eP_{\mathrm{B}}$-ის, შესაბამისად. ეს ნიშნავს, რომ მათი აბსოლუტური მნიშვნელობები შეიძლება ნაკლები იყოს ელემენტარულ მუხტზე. თუმცა, გაზომვისას დაიმზირება, რომ ყოველ კვანტურ წერტილში მუხტი ან ნულია ან $-e$ და არა რაღაც სიდიდე მათ შორის [6].

განვიხილოთ გვირაბგასვლა ორ მეტალური გამტარებლობის ფირფიტას შორის მოთავსებულ თხელ დიელექტრიკულ ფენაში. როგორც ცნობილია, გამტარში დენი განპირობებულია ატომური მესერის უძრავ იონებს შორის ელექტრონების მოძრაობით. თითოეულ ელექტრონს გადააქვს დისკრეტული, ერთეულოვანი მუხტი, ხოლო გადატანილი საერთო მუხტი იცვლება მონოტონურად, უწყვეტად. ორ გამტარს შორის მოთავსებულ თხელ დიელექტრიკიან სტრუქტურაში დენი იცვლება კომბინირებულად – უწყვეტად გამტარში და დისკრეტულად დიელექტრიკის გავლით. ამგვარი პროცესები სქემატურად გამოსახულია ფიგურაზე 2 [7]. გვირაბგავლის ეს პროცესები კ. ლიხარიოვმა შეადარა წყლის ბოლომდე კარგად დაუკეტავ ონკანს.

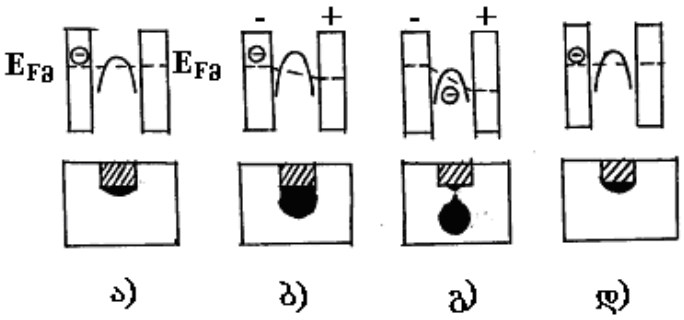

ფიგურა 2. ერთელექტრონიანი გვირაბგასვლა.

დასაწყისში, პროცესის პირველ სტადიაზე, მეტალ–დიელექტრიკის გამყოფი საზღვარი ელექტრულად ნეიტრალურია. დიელექტრიკის ორივე მხარეს, მეტალურ შემონაფენებში ფერმის დონეები ერთსა და იმავე სიმაღლეზეა (ა). მეორე სტადიაზე,

მეტალურ შემონაფენებს მოედება ელექტრული ველის მცირე მუდმივი პოტენციალი, რაც იწვევს მათში ფერმის დონეების ურთიერთწანაცვლებას, დიელექტრიკის საზღვრებამდე დენის უწყვეტ გავლას და ამ საზღვრებზე მუხტის დაგროვებას (ბ). აღწერილი პროცესი მსგავსია იმისა, თუ როგორ გროვდება წვეთი ბოლომდე კარგად დაუკეტავ ონკანზე. მესამე სტადიაზე დაგროვილი მუხტის სიდიდე აღწევს იმ მნიშვნელობას, როდესაც ადგილი აქვს ერთი ელექტრონის გვირაბგასვლას დიელექტრიკში, ანუ წვეთის მოწყვეტას (გ) გვირაბგასვლის აქტის შემდეგ – მეოთხე სტადიაზე სისტემა უბრუნდება საწყის მდგომარეობას (დ) და პროცესი თავიდან იწყება.

ელექტრონი დიელექტრიკის გავლით გვირაბგავლის უნარს იძენს მაშინ, როცა დაგროვილი მუხტი აღემატება $+e/2$-ს (გვირაბგასვლა „პირდაპირი“ მიმართულებით) ან ნაკლებია $-e/2$ -ზე (გვირაბგასვლა „უკუ“ მიმართულებით), რადგანაც მხოლოდ ამ პირობებში მცირდება სისტემის ელექტროსტატიკური ენერგია. დიელექტრიკის გავლით ელექტრონს შეუძლია გვირაბგასვლა რაღაც ზღურბლური ძაბვის მიღწევის შემდეგ. ამ ძაბვამდე გვირაბგასვლა შეუძლებელია გამტარში არსებულ ელექტრონზე სხვა მოძრავი ან უძრავი მუხტების კულონური ზემოქმედების გამო. აღწერილ მოვლენას კულონური ბლოკადა ეწოდება. გვირაბგასვლას თან სდევს სტრუქტურის წინაღობის შემცირება.

3. ელექტრონის ერთგვირაბული გასვლის სტრუქტურის სისტემა

ელექტრონის ერთგვირაბული გასვლის სტრუქტურა [8] წარმოადგენს ბრტყელ კონდენსატორს C ტევადობით, რომელზედაც შეიძლება დაგროვდეს Q მუხტი. ასეთ კონდენსატორში არსებული ელექტროსტატიკური ველის ენერგია ტოლია

$$\mathrm{E} = \frac{Q^2}{2C}. \qquad (3)$$

კონდენსატორის ენერგია დისკრეტულად იცვლება და ენერგიის ის მინიმალური ცვლილება, რომელიც გამოწვეულია ერთი ელექტრონის მიერ ელემენტარული მუხტის გადატანით შეადგენს

$$\Delta\mathrm{E} = \frac{e^2}{2C}. \qquad (4)$$

ელექტროსტატიკური ენერგიის ცვლილება გარე ძაბვის მოდებისას, ერთი ელექტრონის გვირაბგასვლის პროცესში, წარმოადგენს ენერგიის ამ ცვლილებისა და წყაროს მიერ შესრულებელი მუშაობის სხვაობას

$$\Delta\mathrm{E} = \frac{e^2}{2C} - eV, \qquad (5)$$

სადაც, V კონდენსატორზე მოდებული გარეშე ძაბვაა. გვირაბგასვლა შესაძლებელია მხოლოდ მაშინ, როცა ეს ენერგია მინიმალურია, ანუ $\Delta\mathrm{E} < 0$. აქედან გამოდის, რომ როგორც ერთ, ისე მეორე მხარეს გვირაბგასვლის ზღურბლური ძაბვა ტოლია

$$|V_{th}| = \frac{e}{2C}. \qquad (6)$$

სიდიდეს $e/2C$ კულონური ღრეჩო ეწოდება. ფიგურაზე 3 მოცემულია ერთგვირაბული სტრუქტურის ექვივალენტური სქემა (ა) და მისი ვოლტ-ამპერული მახასიათებელი (ვამ) (ბ).

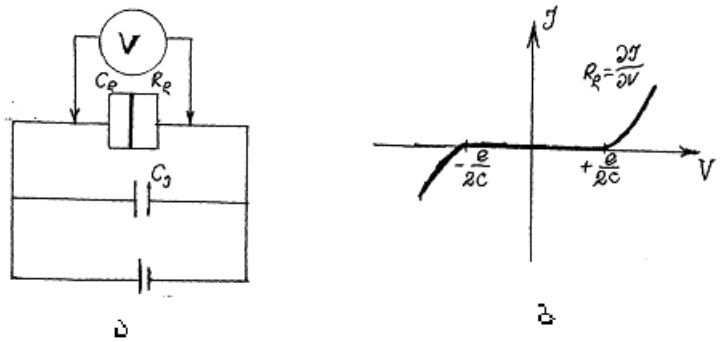

ფიგურა 3. ერთგვირაბული სტრუქტურის ექვივალენტური სქემა (ა) და მისი ვამ (ბ).

ასეთი სტრუქტურის ძირითადი ელემენტია დიელექტრიკით შექმნილი C_d ტევადობა და გვირაბული ანუ დიელექტრიკის R_d წინაღობა, რომელიც მას აქვს გარე ძაბვის მოდების გარეშე. C_{eff} ეფექტური ტევადობა ითვალისწინებს ნიმუშის კონტაქტების და დენის წყაროს ტევადობებს. ცხადია, რომ საერთო C ტევადობა, რომელიც შედის (5) ფორმულაში, ტოლია მათი ჯამისა: $C = C_d + C_{eff}$. დენი სტრუქტურაში გაივლის მხოლოდ V_{th} -ზე უფრო მაღალი ძაბვის მოდებისას. ეს გარემოება მის ვამ-ზე აისახება (ბ). პირდაპირი ძაბვისას დენს კი R_d განსაზღვრავს.

ზემოთაღნიშნული პროცესების ექსპერიმენტული რეალიზებისათვის საჭიროა, რომ სითბური ენერგიის ფლუქტუაცია იყოს მინიმალური, ანუ $kT << e^2/2C$, საიდანაც გამომდინარეობს, რომ

$$C << \frac{e^2}{2kT}. \qquad (7)$$

მეორეს მხრივ, ჰაიზენბერგის განუზღვრელობის პრინციპის თანახმად, $\Delta t \Delta E \geq \hbar$ ანუ $e^2/2C << \hbar/R_d C$ და, მაშასადამე, კულონური ბლოკადისათვის საჭიროა, რომ სტრუქტურის გვირაბული წინაღობა აღემატებოდეს წინაღობის კვანტურ ერთეულს:

$$R_d > \frac{\hbar}{e^2} \approx 25.813 \text{ k}\Omega \qquad (8)$$

(7) და (8) პირობების შესრულება შესაძლებელია დაბალ ტემპერატურაზე ნანოზომის სტრუქტურებში. ასე მაგალითად, 4.2, 77 და 300 K ტემპერატურებისათვის საჭიროა შეიქმნას ისეთი ტევადობები, რომ $C << 2 \cdot 10^{-16}$, $2 \cdot 10^{-17}$ და $3 \cdot 10^{-18}$ F, შესაბამისად. ერთგვირაბული გასვლის სისტემაში ერთელექტრონიანი გვირაბგასვლის პროცესის განხორციელება შეუძლებელია, რადგან ამ შემთხვევაში ფლუქტუაცია მუხტის საჭირო ცვლილებისათვის უნდა იყოს ძალზე მცირე, რათა მოხერხდეს მისი მდგრადი ლოკალიზება კვანტურ წერტილში [9]. ასეთი სტრუქტურის კვანტურ წერტილში მუხტი უფრო ფართო დიაპაზონში ლოკალიზდება, ვიდრე ელექტრონის ერთგვირაბგასვლისას. გარდა ამისა, რეალურ პირობებში შეუძლებელია 10 – 15 F-ზე უფრო ნაკლები მაშუნტირებელი ტევადობის მიღება, რაც ორი რიგით მეტია საჭიროზე. მაშასადამე, თანამედროვე ტექნოლოგიით ერთი გვირაბით ელექტრონის გასვლის რეგულირება პრობლემურია. ამ მიზნით შემოთავაზებულია ორი მიმდევრობით ჩართული გვირაბებისაგან შედგენილი კონსტრუქცია.

4. ელექტრონის ორგვირაბული გასვლის სტრუქტურა

ახალი სწრაფქმედი ხელსაწყოს მუშაობის პრინციპი დამყარებულია კვანტური განზომილებების მქონე შრეებში ელექტრონის გავლაზე. ცხადია, ასეთი შრეების სისქე იმდენად მცირე უნდა იყოს, რომ ელექტრონმა გამოავლინოს თავისი ტალღური ბუნება. ასეთი შრეების შექმნა მხოლოდ თანამედროვე ტექნოლოგიითაა შესაძლებელი, კერძოდ, მოლეკულურ-სხივური ეპიტაქსიით [10]. სწორედ ამ მეთოდით მიიღეს მრავალშრიანი თხელფიროვანი სტრუქტურები, თითოეული რამდენიმე ათეული და ერთეული ნანომეტრის რიგის სისქით. ამ თანამედროვე ხელსაწყოს შესაქმნელად საინტერესოა არა ერთგვირაბული, არამედ ორგვირაბული სტრუქტურის გამოყენება. ტოპოლოგიურად იგი შედგება ორი მიმდევრობით შეერთებული ერთგვირაბული სტრუქტურისაგან. მისი ექვივალენტური სქემა მოცემულია ფიგურაზე 4.

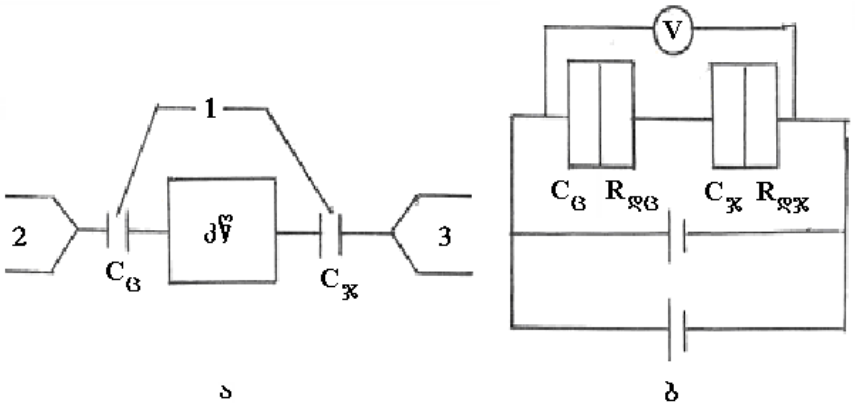

ფიგურა 4. ორგვირაბული სტრუქტურის ექვივალენტური სქემა (კვანტური წერტილის) კუნძულის (ა) და ორი ერთგვირაბული სტუქტურის შეერთებისას (ბ): 1 –გვირაბგასვლა; 2 – გამომდენი და 3 – ჩამდენი.

ეს შეიძლება იყოს მეტალის გამტარი, ორმხრივ კონტაქტში მყოფი ნახევარგამტარის ან მეტალის ნანონაწილაკებთან (კუნძულებთან). ასეთი კუნძული, თავის ზომით და თვისებებით წარმოადგენს კვანტურ წერტილს, რომელიც ატარებს განსაზღვრული რაოდენობის მუხტს. მას აქვს ტევადობითი კავშირი მარჯვენა და მარცხენა ელექტროდებთან, შესაბამისი C_{right} და C_{left} ტევადობების მეშვეობით. თვით კუნძულის ტევადობა C ტოლია C_{right} და C_{left} ტევადობების ჯამისა. როგორც ერთგვირაბულისათვის, აქაც, ე.ი. ორგვირაბული სტრუქტურისათვისაც არსებობს ძაბვის გარკვეული დიაპაზონი, რომელშიც დენი არ აღიძვრება ელექტრონის გადატანის კულონური ბლოკადის გამო ელექტრული. დასაშვები ელექტრული დონეების განსხვავებულობის გამო კუნძულში ელექტროდების მახლობლად და უშუალოდ კუნძულის შიგნით ვამ-ის სიმეტრიულობა, როგორც ეს იყო ერთგვარაბული სტრუქტურისათვის, ახლა დარღვეული იქნება. ეს ეფექტი შეიძლება აიხსნას კუნძულის და ელექტროდების ელექტროქიმიური პოტენციალების ცნებებში. მართლაც, მცირე ზომების მქონე კუნძულისთვის ფერმის ენერგია მის შიგნით და ელექტროდებზე განსხვავებულია და ეს იძლევა განსხვავებას მათ ელექტრულ პოტენციალებს შორის

$$\Delta\mu = \mu_{island} - \mu_{right} = \mu_{island} - \mu_{left} = e\Delta V_0 , \qquad (9)$$

რაც ჩანს ფიგურიდან 5, რომელზედაც გამოსახულია ორგვირაბული სტრუქტურის ექვივალენტური ენერგეტიკული სქემა (ა) და შესაბამისი ვამ (ბ). განსხვავების მიზეზი ისაა, რომ კუნძულში მუხტის გადანაწილება დამახასიათებელია მხოლოდ μ_{island}-სათვის, რომელიც e/C -ის ჯერადია, ხოლო მაკროსკოპული ნიმუშისათვის C დიდია, შესაბამისად e/C ფარდობა ძალზე მცირეა და განსხვავება ფერმის დონეების მდებარეობებს შორის შეუმჩნეველია.

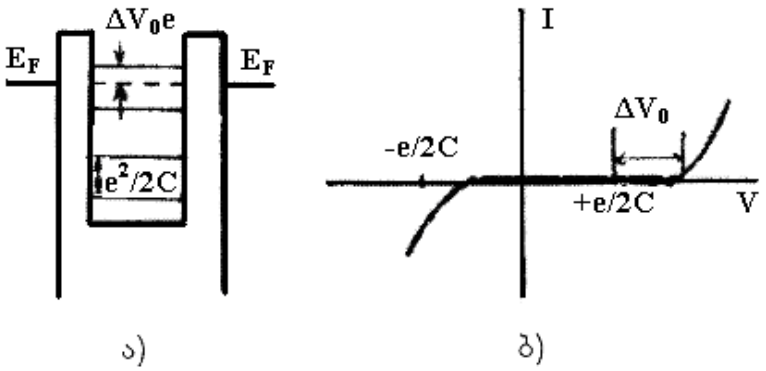

ფიგურა 5. ორგვირაბული სტრუქტურის ექვივალენტური ენერგეტიკული სქემა (ა) და შესაბამისი ვამ (ბ).

ნანონაწილაკებში წონასწორობის დამყარებას მივყავართ იქამდე, რომ ფერმის ეს დონეები, ერთმანეთთან რამდენადაც ეს შესაძლებელია ახლოს აღმოჩნდებიან განლაგებული. მაგრამ ΔV_0 -ის მნიშვნელობა მაინც გარკვეულ დიაპაზონში იქნება: $\Delta V_0 < e/2C$. ეს გარემოება იწვევს ორ გვირაბს შორის განსხვავებას, გაჟონვის კოეფიციენტების მიხედვით, და სტრუქტურის ვამ-ის ასიმეტრიულობას.

ელექტრონის ენერგეტიკული დონეების დისკრეტულება კუნძულში განპირობებულია იმით, რომ მისი მუხტის ცვლილება შეიძლება მხოლოდ ერთი ელექტრონის მუხტის ჯერადი ულუფების მიღებით ან გაცემით. ამ დისკრეტულობის ბიჯია $e^2/2C$. 0 K ტემპერატურაზე ელექტრონული მდგომარეობები ფერმის დონის ქვემოთ მთლიანად შევსებულია. ამიტომ რჩება ΔV_0 სხვაობა იმ დონეთა შორის, რომლისგანაც ხდება ელექტრონის ინჟექცია და რომელიც მან უნდა დაიკავოს კუნძულში (უახლოესი დონე). ერთი ელექტრონის მოსვლით სისტემის ელექტროსტატიკური ენერგია შეიცვლება სიდიდით:

$$\Delta \mathrm{E} = \frac{C}{2}\left(\left(\frac{e}{C} + \Delta V_0\right)^2 - \Delta V_0^2\right). \qquad (10)$$

კუნძულზე მარცხენა ელექტროდიდან მისული ელექტრონი, პოლარიზების მექანიზმით ინდუცირებს მარჯვენა ელექტროდში მუხტს სიდიდით eC_{right}/C . შესაბამისი პოტენციალის გადასალახავად და კულონური ბლოკადის დასაძლევად საჭიროა მოდებული იყოს გარეშე ძაბვა სიდიდით

$$V > \frac{C}{C_{right}}\left(\frac{e}{2C} + \Delta V_0\right). \qquad (11)$$

სწორედ ეს გარემოება განაპირობებს ვამ-ის ასიმეტრიულობას (ფიგურა 5ბ).

5. ერთელექტრონიანი ტრანზისტორის მუშაობის პრინციპი

ერთელექტრონიანი ტრანზისტორის მუშაობის პრინციპი კარგად იხსნება ორგვირაბგასვლის სტრუქტურის მაგალითზე. ერთელექტრონიანი ტრანზისტორი _ ესაა სამგამოსავლიანი ხელსაწყო, სადაც ელექტრონები სათითაოდ გადაადგილდებიან გამომდენიდან ჩამდენისაკენ, მათი გამყოფი კვანტური წერტილის გავლით, და რომელშიც კვანტური წერტილის ელექტრული მდგომარეობები ჩამკეტით ელექტროსტატიკურად კონტროლდება. ასეთი ტრანზისტორის სტრუქტურის ფორმირების პროცესი, ექვივალენტური სქემა და შესაბამისი ვამ მოცემულია ფიგურაზე 6.

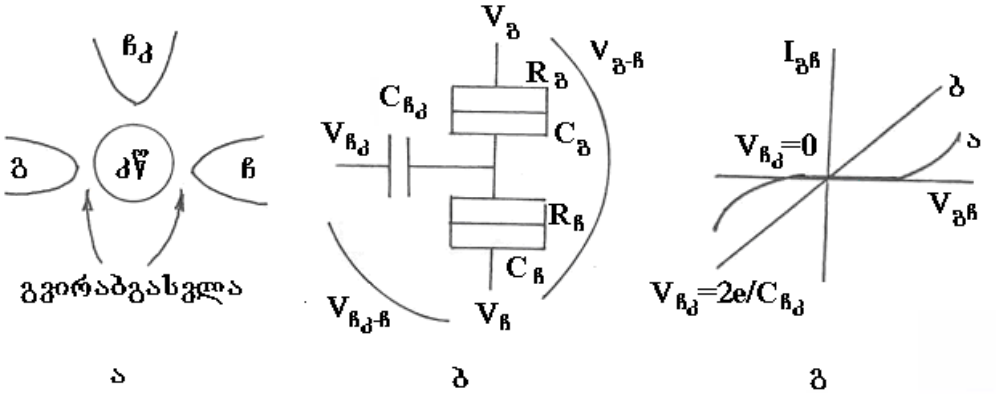

ფიგურა 6. ერთელექტრონიანი ტრანზისტორის სტრუქტურა (ა), ექვივალენტური სქემა (ბ) და შესაბამისი ვამ (გ).

ერთელექტრონიანი ტრანზისტორის მუშაობა შეიძლება ნათლად აღიწეროს, თუ მის სტრუქტურაში გარკვეული წესით გამოვყოფთ ორ ერთელექტრონიან უჯრედს. ერთი მათგანი დაკავშირებულია გამომდენთან, მეორე კი – ჩამდენთან. ვამ მიიღება ისე, როგორც ელექტრონის ორგვირაბიანი გავლისას, როცა $V_{gate} = 0$ (ფიგურა 6გ, მრუდი ა). მაგრამ როცა $V_{gate} = e/2C_{gate}$, მაშინ კულონური ბლოკადა მოიხსნება და დენი იწყებს უწყვეტად დინებას (ფიგურა 6გ, მრუდი ბ).

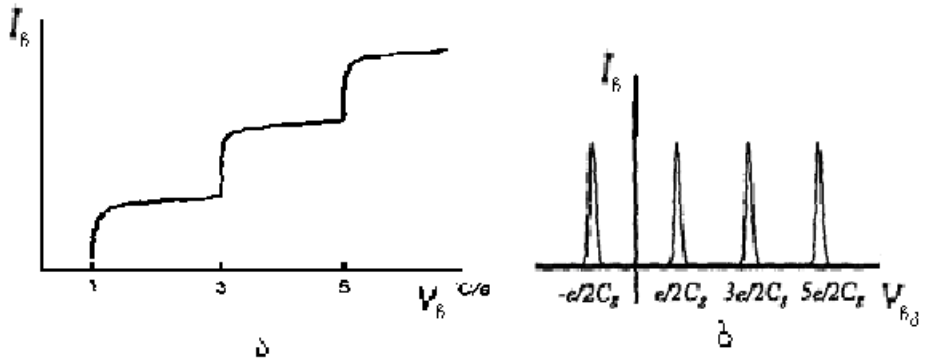

ფიგურა 7. ერთელექტრონიანი ტრანზისტორის გამოსავლითი (ა) და გარდამავალი ვამ-ები (ბ).

ერთელექტრონიანი ტრანზისტორის ჩამკეტზე ძაბვის ცვლილებისას შუალედში 0-დან $e/2C_{gate}$-მდე კულონური ბლოკადა არსებობს და ამ პირობებში ელექტრონი,

რომელიც გადადის გამომდენიდან კვანტურ წერტილში, ვეღარ გადადის ჩამდენში. ჩამკეტზე $e/2C_{gate}$ -ის ჯერადი ძაბვის მოდებისას კულონური ბლოკადა მოიხსნება, გამომდენ–ჩამდენის დენი ხდება სიდიდით შესამჩნევი, ხოლო ფორმით და საფეხურისებრი. ამგვარ ვოლტ–ამპერულ მახასიათებელს კულონური კიბე ეწოდება (ფიგურა 7ა). ამის მსგავსად დაიმზირება ჩამდენის დენის ოსცილაცია $I_{drain-gate}(V_{gate})$ დამოკიდებულებაზე, როცა იცვლება ჩამკეტზე მოდებული ძაბვა $ne/C_{gate} - e/2C_{gate}$ (n მთელი რიცხვია), რაც გამოსახულია ფიგურაზე 7ბ.

ერთელექტრონიანი ტრანზისტორის სრული სახე მოცემულია ფიგურაზე 8.

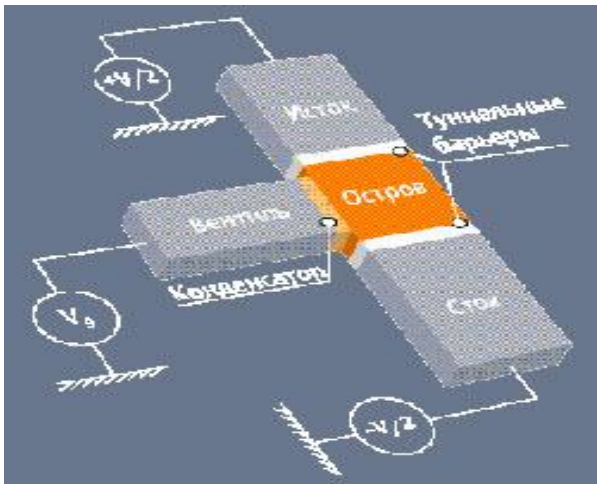

ფიგურა 8. ერთელექტრონიან ნანოტრანზისტორის სრული სახე.

ერთელექტრონიან ტრანზისტორში გამომდენი–ჩამდენის დენის ($I_{source-drain}$) გამოთვლა შესაძლებელია კვანტურ წერტილში ელექტრონის გვირაბით შემოსვლის სიჩქარისა და მისგან გასვლის ალბათობის სიდიდეების გამოყენებით.

ერთელექტრონიან ტრანზისტორში კვანტურ წერტილად Au_{55}-ის ლიგანდური ჯაჭვის გამოყენება პერსპექტიულია სტაბილიზაციისა და ტემპერატურაში მოგების თვალსაზრისით. ამ მიზნით მცირე რაოდენობის ოქროს ატომები იფარება ბუნებრივი, ე.წ. იზოლირებული ლიგანდის ~ 0.7 nm სისქის გარსით. გვირაბგასვლა ხდება ორ მეზობელ – ლიგანდურ და სტაბილიზირებულ არეებს შორის, რა დროსაც ეს გარსი პოტენციალური ჯებირის როლშს ასრულებს. ექსპერიმენტმა აჩვენა, რომ ელექტრონის გასვლა ჯაჭვურ ლიგანდში სოლიტონის მოძრაობის მსგავსად ხორციელდება. გამოთვლების მიხედვით, ამ დროს ნაწილაკთა ურთიერთტევადობა 10 – 18 F-ია, ხოლო მათ შორის წინაღობა – 100 mΩ.

ჩვენი ინტერპრეტაციით, ერთელექტრონიანი ტრანზისტორის მუშაობის პრინციპი შეიძლება აიხსნას ჰიდრავლიკური მოდელის საფუძველზეც, რომელიც მოცემულია ფიგურაზე 9. ბოლომდე კარგად დაუკეტავი ონკანიდან, ანუ გამომდენიდან მოედინება წვეთები, რომლებიც ჩაედინებიან წყლის ავზში. ავზიდან კი ჩამკეტისა და სარქველის მოქმედების შედეგად წყლის წვეთები მხოლოდ სათითაოდ გაედინებიან დროის გარკვეული შუალედებით. ამ შუალედის სიდიდე დამოკიდებულია გამომდენის, ჩამკეტის და სარქველის პარამეტრებზე.

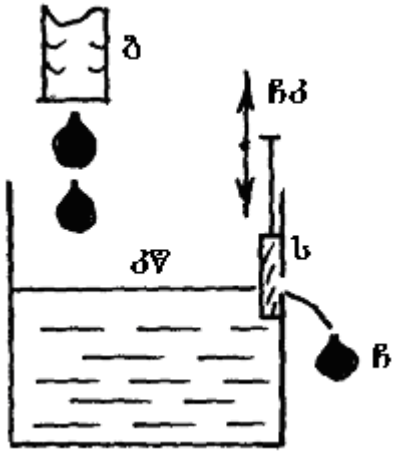

ფიგურა 9. ერთელექტრონიანი ტრანზისტორის მუშაობის „ჰიდრავლიკური“ მოდელი: გ – გამომდენი (ონკანი); ჩკ – ჩამკეტი და მასთან დაკავშირებული ს – სარქველი; ჩ – ჩამდენი; კწ – კვანტური წერტილი (ავზი წყლის რამდენიმე წვეთით).

ერთელექტრონიანი ტრანზისტორის უპირატესობაა ის, რომ მას აქვს ძალიან მცირე (რამდენიმე ატომისაგან შედგენილი სისტემის რიგის) ზომები და ამასთან დაკავშირებული დიდი ინტეგრაცია, აგრეთვე ძალზე მცირე სიმძლავრის მოთხოვნილება და ფართო ფუნქციონალური შესაძლებლობები. მაგრამ მხედველობაში უნდა მივიღოთ მისი უარყოფითი მხარეებიც. ეს უპირველეს ყოვლისა გამოიხატება შემდეგში: 1) ერთელექტრონიანი ტრანზისტორის მუშაობის შესაძლებლობა შემოიფარგლება მხოლოდ დაბალი ტემპერატურებით. ოთახის ტემპერატურაზე მათი მუშაობისათვის საჭიროა, რომ კვანტური წერტილის ზომები 10 nm-ზე ბევრად ნაკლები იყოს; 2) ერთელექტრონიან ტრანზისტორებს, გვირაბული გადასვლის დიდი წინააღმდეგობის გამო, რომელიც ბევრად აღემატება $\hbar/e^2 \approx 25.8$ kΩ-ს, აქვთ გამოსავალის დიდი იმპედანსი; 3) ერთელექტრონიანი ტრანზისტორისათვის გამომდენი–ჩამდენზე მოდებული ძაბვა ჩამკეტი ძაბვის ამპლიტუდაზე ნაკლები უნდა იყოს – ეს საჭიროა იმისათვის, რომ გადამრთველ ხელსაწყოებში, კვანტური წერტილის პოტენციალის გამომდენი–ჩამდენზე მოდებული ძაბვით ადვილად მართვით ერთელექტრონიანი ტრანზისტორი გამოყენებულ იქნას როგორც ჩამკეტი; და 4) კუნძულთან ახლოს არაკონტროლირებად მუხტის გაჩენასთან დაკავშირებულია ერთელექტრონიანი ხელსაწყოს მახასიათებლების დადგენისა და მათი განმეორადობის სირთულეები. ასეთი მუხტის აღსაძვრელად საკმარისია კუნძულის გარემომცველ დიელექტრიკში მინარევული ნივთიერების თუნდაც ერთი ატომის არსებობა. მინარევის მუხტი იწვევს კუნძულის პოლარიზებას და ამით ცვლის კულონური ბლოკადის პირობებს.

უკანასკნელ ხანს იაპონიის ნანოელექტრონიკის ცენტრ Tsukuba-ში თანამედროვე ნანოტექნოლოგიის გამოყენებით მიიღეს ოთახის ტემპერატურაზე მომუშავე ერთელექტრონიანი ნანოტრანზისტორი, კვანტური წერტილის ანუ კუნძულის ზომით 2 nm. ამ ნანოტრანზისტორის ბაზაზე კი შექმნეს ლაბორატორიული ერთკრისტალიანი ნანოსისტემა (chip), რომელიც გამოსახულია ფიგურაზე 10.

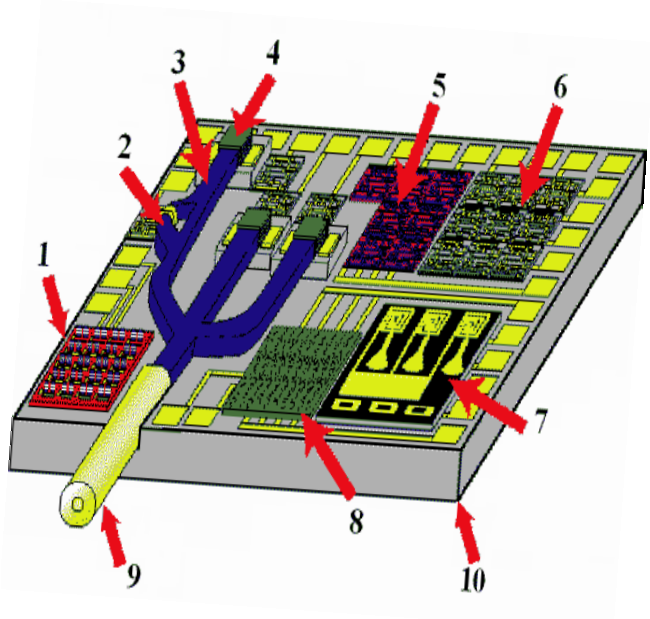

ფიგურა 10. ერთკრისტალიანი ნანოსისტემა: 1 – გარდამქმნელი; 2 – ოპტიკური მოდულატორი; 3 – დიელექტრიკული ფენა; 4 – ოპტიკური დეტექტორი; 5 – ერთელექტრონიანი გარდამქმნელი; 6 – კომპლემენტალური მდნ (მეტალი–დიელექტრიკი–ნახევარგამტარი) მოწყობილობა; 7 – გადამცემი მოდული; 8 – ნანოელექტრონული ელემენტი; 9 – სადენი და 10 – სილიციუმის ფუძეშრე.

ბოლო წლებში ნანოელექტრონიკაში მკვლევარებს შორის დიდ ინტერესს იწვევს მეტალურ შემონაფენებს შორის, განსხვავებული დიელექტრიკული მუდმივას (ε) მქონე ორი დიელექტრიკის გამოყენება [11]. დიელექტრიკის სისქის შემცირებისას, როგორც ცნობილია, იზრდება გაჟონვის დენის სიდიდე და ამიტომ მის შესამცირებლად შუალედური ε_1-ის მქონე d_1 სისქის დიელექტრიკს ეფინება მაღალი ε_2-ის მქონე მეორე d_2 სისქის დიელექტრიკული ფენა. ამ დროს, დიელექტრიკის ეფექტური სისქე იქნება

$$d_{eff} = d_1 + \frac{\varepsilon_1}{\varepsilon_2} d_2 . \qquad (12)$$

ასე მაგალითად, თუ აღებულია შუალედური დიელექტრიკული მუდმივას მქონე SiO_2-ის ($\varepsilon_1 = 3.9$) ფენა სისქით $d_1 = 0.5$ nm და მასზე ეფინება $\varepsilon_2 = 30$-ის ტოლი დიელექტრიკული მუდმივას მქონე $d_2 = 5$ nm სისქის დიელექტრიკი, მაშინ ეფექტური სისქე იქნება $d_{eff} = 0.65$ nm. გაუსის თეორემის თანახმად, დიელექტრიკის ფენებს შორის სხვაობა დიელექტრიკული მუდმივობას მიხედვით იწვევს კონდენსატორში ველის არათანაბარ გადანაწილებას. დიდი დიელექტრიკული მუდმივას მქონე დიელექტრიკულ ფენაში ველი უფრო მცირე იქნება. ამიტომ მასში გაჟონვის დენიც მცირე იქნება, რაც გაჟონვის დენს ბლოკირებას ნიშნავს.

უკანასკნელ ხანს, SiO_2 დიელექტრიკის ნაცვლად იყენებენ სილიციუმის ოქსინიტრიდს (SiO_xN_y) დიელექტრიკული მუდმივათი 7. მისი უპირატესობა ისაა, რომ იგი სილიციუმთან უფრო სრულყოფილ გამყოფ საზღვარს ქმნის, ვიდრე SiO_2 და, გარდა ამისა, ხასიათდება დიელექტრიკში მცირე დადებითი მუხტის არსებობით. მაღალი დიელექტრიკული მუდმივას მქონე დიელექტრიკებად გამოდგება Ta_2O_5, HfO_2, ZrO_2 და ა.შ., რომლებისთვისაც დიელექტრიკული მუდმივას მნიშვნელობები ხვდებიან

დიაპაზონში 25 – 30 და რომლებიც ტემპერატურის ზემოქმედებით ან დროთა განმავლობაში საკუთარ სტრუქტურას არ იცვლიან.

ნანოტექნოლოგიის განვითარების თანამედროვე ტემპები და მიღწევები მის გამოყენებაში იძლევა იმის გარანტიას, რომ უახლოეს მომავალში შესაძლებელი გახდება რთული ნანოხელსაწყოებისა და ნანოსისტემების სერიული წარმოების დაწყება.

დამოწმებანი

1. И. Г. Неизвестный, О. В. Соколова, Д. Г. Шамирян. МЭ, 1999, **28**, 83.
2. Г. Гамов, Д. Иваненко, Л. Ландау. Журн. Русс. физ.-хим. общ. (Часть физ.), 1928, **60**, 13.
3. Ю. И. Головин. Введение в нанотехнику. 2007, Москва: Машиностроение.
4. D. V. Averin, K. K. Likharev. J. Low Temp. Phys., 1986, **62**, 345.
5. T. A. Filton, G. J. Dolan. Phys. Rev. Lett., 1987, **59**, 109.
6. К. К. Лихарев. МЭ, 1987, **16**, 195.
7. K. K. Likharev, T. Glaeson. Sci. Amer., 1992, **6, 50.**
8. В. Е. Борисенко. Соросовский образовательный журнал, 1997, **5**, 100.
9. В. П Драгунов, И. Г. Неизвестный, В. А. Гридчин. Основы наноэлектроники. 2006, Москва: Логос.
10. www.meit.ru/nanonewsnet.ru
11. V. Mikhelashvili, Y. Shneider, A. Zeidler, B. Meyler, S. Yofis, J. Salzman, M. Garbrecht, T. Cohen–Hyams, W. Kaplan, M. Lisiansky, Y. Roizin, G. Eisenshtein. In: Int. Sci. Conf. “Modern Issues of Applied Physics”. 2011, Tbilisi: GTU, 71.

РЕШЕТОЧНАЯ ТЕПЛОЕМКОСТЬ ТВЕРДЫХ ТЕЛ ВНЕ ФОНОННОЙ КОНЦЕПЦИИ

А. Герасимов, Л. Чхартишвили, Д. Буачидзе

Грузинский технический университет
Тбилиси, Грузия
aleksi.gerasimovi@gmail.com,
chkharti2003@yahoo.com,
davidbuachidze@gmail.com

Принята 3 мая 2011 года

1. Введение

В рамках стандартной теории решетечной теплоемкости твердых тел (см., например, [1]) структура, построенная из колеблющих атомов, представляется свободным газом бозонных квазичастиц – фононов. Подобный подход позволяет найти лишь наиболее общее объяснение зависимости теплоемкости твердого вещества на атом c от температуры T, но не в состоянии обеспечить количественное согласие с имеющимися экспериментальными данными.

Так например, при попытке описания $c(T)$ зависимости, измеренной для β-ромбоэдрического бора, на основе модели Дебая, основная константа модели – температура Дебая T_D, определяемая предельной частотой фононных колебаний в материале, на деле оказывается очень сильно зависящей от температуры. Достаточно сказать, что значение T_D меняется от 880 до 1810 K, пройдя через два хорошо выраженных максимума и один пологий минимум [2].

Исходя из генеральной идеи [3, 4] об определяющей роли в формировании тепловых свойств твердых тел электронных конфигураций составляющих вещество атомов и природы химических связей между ними, в настоящей работе предложена новая теория теплоемкости, в которой поглощение тепла атомной решеткой связывается не с возбуждением фононных волн, а с возбуждением колебаний находящихся в потенциальных ямах конечной глубины реальных атомов, энергии которых непрерывно меняются внутри полос конечной ширины. Таким способом было получено общее выражение температурной зависимости теплоемкости твердых тел.

2. Основные соотношения

Пусть макроскопический образец твердого вещества содержит N_i атомов i-типа, $i = 1,2,3,\ldots,I$. Тогда их сумма

$$N = \sum_{i=1}^{i=I} N_i \qquad (1)$$

дает полное число атомов N в физической системе. Здесь I обозначает количество различных типов атомов. Подчеркнем, что мы будем различать друг от друга не только химические элементы, но и изотопы одного и того же элемента и даже атомы одного и того же изотопа, если те занимают сруктурно-неэквивалентные атомные узлы. При этом будем считать, что все особенности данного типа атомов отражены в пространственном распределении потенциальной энергии атомов в самосогласованном стационарном поле, которого создают все другие атомы системы. Те же особенности должны быть отражены в энергетическом спектре атома данного типа в соответствующем самосогласованном поле.

Далее, формально будем считать, что спин S_i атома любого типа равен нулю,

$$S_i = 0 \qquad (2)$$

и, следовательно, отсутствует спиновое вырождение уровней энергий E_i атомов – соотвествующий фактор вырождения $\eta_i = 2S_i + 1$ для атома любого типа равен единице:

$$\eta_i = 1 \ , \qquad (3)$$

а заполнение энергетических уровней с ростом температуры осуществляется согласно функции распределения Бозе–Эйнштейна $f_{B-E}(E_i)$ с нулевым химическим потенциалом:

$$f_{B-E}(E_i) = \frac{1}{\exp\left(\frac{E_i}{kT}\right) - 1} \qquad (4)$$

(k – постоянная Больцмана). Разумеется, что при таких допущениях все спиновые и магнитные эффекты считаются включенными в то самосогласованное поле, которое действует на атом данного типа, а также – в энергетический спектр атома в этом поле.

И наконец, воспользуемся тем обстоятельством, что колебательные (и тем более, поступательные) движения атомов в твердых телах в хорошем приближении квазиклассичны и приходящую на атом энергию ε твердого вещества выразим взвешенной суммой интегралов по фазовым пространствам от произведений энергий атомов различного типа на соответсвующие функции распределения по энергии:

$$\varepsilon = \sum_{i=1}^{i=I} \nu_i \iint\limits_{(\vec{r}_i, \vec{p}_i)} \frac{d\vec{r}_i \, d\vec{p}_i}{(2\pi\hbar)^3} \frac{E_i}{\exp\left(\frac{E_i}{kT}\right) - 1} \qquad (5)$$

($\hbar$ – постоянная Планка). Здесь ν_i – относительные концентрации атомов i-типа,

$$\nu_i = \frac{N_i}{N} . \qquad (6)$$

Из соотношений (1) и (6) следует, что они нормированы на единицу:

$$\sum_{i=1}^{i=I} \nu_i = 1 . \qquad (7)$$

Переменные интегрирования $\vec{r}_i$ и $\vec{p}_i$ являются, соответственно, радиусом-вектором и импульсом атома i-типа. Интегрирование ведется по тем областям фазовых пространств $(\vec{r}_i, \vec{p}_i)$, которые разрешены областями допустимых значений энергий E_i.

Если выражение (5) энергии решетки на атом продифференцировать по температуре, то найдем решеточную теплоемкость на атом:

$$c = \frac{d\varepsilon}{dT} = \frac{k}{32\pi^3\hbar^3}\frac{1}{(kT)^2}\sum_{i=1}^{i=I}\nu_i \iint\limits_{(\vec{r}_i,\vec{p}_i)} \frac{d\vec{r}_i\, d\vec{p}_i\, E_i^2}{\sinh^2\left(\frac{E_i}{2kT}\right)}. \qquad (8)$$

3. Общий вид температурной зависимости

Энергия атома i-типа, находящегося в самосогласованном поле, которое стационарно, принимает определенное значение E_i из области допустимых значений. В квазиклассическом приближении ее можно представить суммой потенциальной P_i и кинетической K_i энергий, которые зависят соответственно только от радиуса-вектора $\vec{r}_i$ и только от импульса $\vec{p}_i$ атома:

$$E_i(\vec{r}_i, \vec{p}_i) = P_i(\vec{r}_i) + K_i(\vec{p}_i). \qquad (9)$$

В общем случае потенциальные функций $P_i(\vec{r}_i)$ неизвестны. Для их нахождения потребуется, во-первых, конкретизация структуры и химического состава твердого тела и, во-вторых, проведение вычислений с учетом особенностей химических связей, реализующихся в данном веществе. Решение подобных задач выходит далеко за рамки рассматриваемой и оно не менее, если не более сложно, чем нахождение общей формы температурной зависимости теплоемкости твердых тел. По этой причине для получения возможности продвижения вперед нам придется ограничиться модельными потенциалами, которые однако будут обладать главными особенностями реальных потенциалов: во-первых, потенциал, действующий на атом твердого тела является совокупностью чередующихся в пространстве потенциальных ям (и потенциальных барьеров) и, во-вторых, глубины этих ям (и высоты этих барьеров) конечны.

Наиболее простая потенциальеая функция, удовлетворяющая этим требованиям, это – чередование центрально-симметричных относительно атомных узлов потенциальных ям с радиальной степенной зависимостью внутри соответствующих сфер Вигнера–Зейтца:

$$P_i(r_i) = P_{0i}\left(\frac{r_i}{r_{0i}}\right)^{m_i} \qquad 0 \le r_i \le r_{0i}. \qquad (10)$$

Здесь $m_i > 0$ – показатель степени радиальной зависимости потенциальной энергии атома в данной яме, P_{0i} – глубина потенциальной ямы, r_{0i} – радиус сферы Вигнера–Зейтца. Как следует из определения этой сферы, обратная величина ее объема равна концентрации n_i атомов i-типа:

$$n_i = \frac{3}{4\pi r_{0i}^3}. \qquad (11)$$

Такой выбор потенциала позволяет интеграл, взятый по всему объему твердого тела, заменить суммой объемных интегралов, взятых по сферам Вигнера–Зейтца от центрально-симметричных функций. Интегрирование по направлениям в конфигурационном пространстве даст множитель 4π . Так что, в подинтегральном выражении следует произвести замены $d\vec{r}_i \to 4\pi N_i r_i^2 dr_i$. Следует подчеркнуть, что дальнейшее интегрирование не ведется по всей сфере Вигнера–Зейтца (т.е. по всему интервалу $0 \le r_i \le r_{0i}$), а лишь по той ее части, где полная механическая энергия атома может иметь определенное значение E_i.

Что же касается зависимости кинетической энергии атома от его импульса, то ее явный вид известен:

$$K_i(\vec{p}_i) = \frac{p_i^2}{2M_i}, \tag{12}$$

где M_i – масса атома i-типа. Лишный раз подчеркнем, что поскольку в используемом подходе рассматривается движение реальных частиц – атомов, закон дисперсии (12) точен, указанные параметры есть реальные массы, а не т.н. эффективные массы квазичастиц. Далее, поскольку кинетическая энергия не зависит от направления импульса, интегрирование по направлениям в импульсном пространстве даст еще один множитель 4π . И таким образом в подинтегральном выражении мы должны произвести замены $d\vec{p}_i \to 4\pi p_i^2 dp_i$. В принципе величина импульса атома любого вида может принять любое значение от нуля до бесконечности. Однако и в этом случае интегрирование не ведется по всему интервалу $0 \le p_i < \infty$, а лишь по той его части, в которой полная механическая энергия атома может иметь определенное значение E_i.

С учетом сделанных замечаний общее выражение теплоемкости твердого тела на атом (8) можно переписать в следующей приближенной форме:

$$c \approx \frac{k}{2\pi\hbar^3}\frac{1}{(kT)^2}\sum_{i=1}^{i=I}\nu_i N_i \iint\limits_{(r_i,p_i)} \frac{dr_i\, dp_i\, r_i^2 p_i^2 E_i^2}{\sinh^2\left(\dfrac{E_i}{2kT}\right)}. \tag{13}$$

Ввиду взаимооднозначного соответствия между парой переменных интегрирования (r_i, p_i) и (P_i, K_i) возможен прямой переход от интегрирования по длинам радиуса-вектора и вектора импульса к интегрированию по потенциальной и кинетической энергиям:

$$c = \frac{3k}{4\sqrt{2}\,\pi^2\hbar^3}\frac{1}{(kT)^2}\sum_{i=1}^{i=I}\frac{\nu_i M_i^{\frac{3}{2}}}{n_i m_i P_{0i}^{\frac{3}{m_i}}} \iint\limits_{(P_i,K_i)} \frac{dP_i\, dK_i\, P_i^{\frac{3}{m_i}-1} K_i^{\frac{1}{2}} E_i^2}{\sinh^2\left(\dfrac{E_i}{2kT}\right)}. \tag{14}$$

Удобно еще раз произвести замену переменных интегрирования: пару переменных (P_i, K_i) заменить парой (E_i, P_i). Дело в том, что поскольку интегрирование ведется по состояниям с определенной энергией, то при подобном выборе переменных границы интегрирования возможно записать в явной форме.

Для нашей модели потенциальная энергия атома i-типа может принимать значения из интервала $0 \le P_i \le P_{0i}$. С другой стороны, поскольку полная энергия атома E_i складывается из потенциальной и кинетической энергий, а кинетическая энергия может

принимать значения от нуля до бесконечности, отсюда следует, что интервал интегрирования по потенциальной энергии таков: $0 \le P_i \le \min(P_{0i}, E_i)$. С целью уточнения границ интегрирования заметим, что движения отдельных атомов, возбужденных в состояниях с энергией $E_i \ge P_{0i}$ будут инфинитными – соответствовать их миграции по всей решетке. Когда же доля таких высокоэнергетичных атомов сильно возрастет, твердое тело начнет сначала плавиться, а потом – испаряться. По это причине при изучении тепловых свойств твердого тела, возбуждения атомов в состояниях с энергиями $E_i \ge P_{0i}$ следует исключить из рассмотрения. Таким образом интервал интегрирования по потенциальной энергии есть $0 \le P_i \le E_i$.

Атом i -типа может находиться в любой из N_i эквивалентных потенциальных ям конечной глубины. По этой причине его энергетический спектр будет состоять не из дискретных уровней, как это имело бы место для атома в уединенной потенциальной яме бесконечной глубины (например, для независимого атомного осциллятора в модели Эйнштейна), а из полос с непреривным в пределе $N_i \to \infty$ распределением допустимых значений энергии. Вовсе необъязательно чтобы число подобных энергетических полос было бесконечным, как это имеет место для дискретных уровней частицы в потенциальной яме бесконечной глубины. Даже при квадратичной радиальной зависимости потенциальной энергии внутри потенциальных ям ($m_i = 2$) соответствующие края энергетических полос не будут эквидистантными, как это имеет место для дискретных энергетических уровней в гармоническом потенциале. Таким образом, используемый нами модельный потенциал при любом допустимом значении параметра m_i приводит к энергетическому спектру, который существенно отличается от спектра гармонического осциллятора.

Пусть индекс $j = 1,2,3,\ldots,J$ нумерует отмеченные выше энергетические полосы в направлении повышения энергии. Здесь J будет обшим числом подобных полос. Обозначим через E'_{ij} и E''_{ij} соответственно нижний и верхний границы j -й полосы для атома i -типа ($E'_{ij} < E''_{ij}$). Посколку рассматриваем квазиклассические движения атомов, наиболее низколежащие полосы должны включать нулевую энергию, т.е. $E'_{i1} \equiv 0$. С другой стороны, как было указано выше, даже наиболее высоколежащая полоса допустимых атомных энергий в твердом теле не должна выходить из потенциальной ямы, т.е. $E''_{iJ} < P_{0i}$. Понятно, что определение численных значений параметров E'_{ij} и E''_{ij} есть еще одна дополнительная задача, которая должна решаться после разрешения проблемы самосогласованных потенциалов в твердом теле. По этой причине при построении общей теории этих параметров, наряду с параметрами модельного потенциала, будем считать заданными, а при сопоставлении теории с эксперименетом используем их в качестве подгоночных параметров. Будем иметь:

$$c = \frac{3k}{4\sqrt{2}\,\pi^2\hbar^3}\frac{1}{(kT)^2}\sum_{i=1}^{i=I}\frac{\nu_i M_i^{\frac{3}{2}}}{n_i m_i P_{0i}^{\frac{3}{m_i}}}\sum_{j=1}^{j=J}\int_{E'_{ij}}^{E''_{ij}}\frac{dE_i\,E_i^2}{\sinh^2\left(\frac{E_i}{2kT}\right)}\int_0^{E_i} dP_i\;P_i^{\frac{3}{m_i}-1}\,(E_i - P_i)^{\frac{1}{2}}\,. \qquad (15)$$

Сначала соотношением

$$y_i = \frac{P_i}{E_i} \tag{16}$$

введем безразмерную переменную интегрирования во внутренний интеграл. В результате верхняя граница области интегрирования во внутреннем интеграле станет константой,

$$c = \frac{3k}{4\sqrt{2}\,\pi^2\hbar^3}\frac{1}{(kT)^2}\sum_{i=1}^{i=I}\frac{\nu_i M_i^{\frac{3}{2}}}{n_i m_i P_{0i}^{\frac{3}{m_i}}}\sum_{j=1}^{j=J}\int_{E'_{ij}}^{E''_{ij}}\frac{dE_i\, E_i^{\frac{3}{m_i}+\frac{5}{2}}}{\sinh^2\left(\frac{E_i}{2\,kT}\right)}\int_0^1 dy_i\; y_i^{\frac{3}{m_i}-1}(1-y_i)^{\frac{1}{2}}, \tag{17}$$

а сам внутренний интеграл превратится в бета-функцию

$$\mathrm{B}(a,b) = \int_0^1 dt\, t^{a-1}(1-t)^{b-1} \qquad a,b>0, \tag{18}$$

зависящую лишь от констант, т.е. в постоянный множитель, которого можно вынести перед знаком интегрирования. Одновременно, с целью более отчетливого выделения характера температурной зависимости, другую безразмерную переменную интегрирования соотношением

$$x_i = \frac{E_i}{2kT} \tag{19}$$

введем и в оставшийся внешний интеграл:

$$c = \frac{6k}{\pi^2\hbar^3}\sum_{i=1}^{i=I}\frac{\nu_i M_i^{\frac{3}{2}}}{n_i m_i}\mathrm{B}\left(\frac{3}{m_i},\frac{3}{2}\right)\left(\frac{2}{P_{0i}}\right)^{\frac{3}{m_i}}(kT)^{\frac{3}{m_i}+\frac{3}{2}}\sum_{j=1}^{j=J}\int_{\frac{E'_{ij}}{2kT}}^{\frac{E''_{ij}}{2kT}}\frac{dx_i\, x_i^{\frac{3}{m_i}+\frac{5}{2}}}{\sinh^2 x_i}. \tag{20}$$

Входящий сюда интеграл аналитически не вычисляется, его можно представить только с помощью разности бесконечных степенных рядов верхних и нижних границ интеграла. Из полученного выражения (20) видно, что при многообразии различных типов атомов в твердом теле и при возможности одновременного теплового возбуждения нескольких энергетических полос атомных колебаний решеточная теплоемкость твердого тела может довольно сложно зависеть от температуры.

4. Предельные случаи

Детально проанализируем наиболее простой случай, когда твердое тело состоит из одного типа атомов ($I=1$, $\nu_i=\nu_1=1$, $n_i=n_1\equiv n$, $m_i=m_1\equiv m$, $M_i=M_1\equiv M$, $P_{0i}=P_{01}\equiv P$, $x_i=x_1\equiv x$) и термически возбуждается единственная – наиболее низколежащая энергетическая полоса ($E'_{ij}=E'_{11}=0$, $E''_{ij}=E''_{11}\equiv E$). Теперь выражение (20) примет более простой вид:

$$c \approx \frac{6k}{\pi^2\hbar^3}\frac{M^{\frac{3}{2}}}{n\,m}\mathrm{B}\left(\frac{3}{m},\frac{3}{2}\right)\left(\frac{2}{P}\right)^{\frac{3}{m}}(kT)^{\frac{3}{m}+\frac{3}{2}}\int_0^{\frac{E}{2kT}}\frac{dx\, x^{\frac{3}{m}+\frac{5}{2}}}{\sinh^2 x}. \tag{21}$$

Если температура настолько низка, что $E/2kT >> 1$, то верхнюю границу интеграла можно заменить на бесконечность ∞. Интеграл превращается в множитель, значение которого не зависит от температуры:

$$c \approx \frac{6k}{\pi^2\hbar^3}\frac{M^{\frac{3}{2}}}{nm}\,\mathrm{B}\left(\frac{3}{m},\frac{3}{2}\right)\left(\frac{2}{P}\right)^{\frac{3}{m}}\int_0^{\infty}\frac{dx\,x^{\frac{3}{m}+\frac{5}{2}}}{\sinh^2 x}\,(kT)^{\frac{3}{m}+\frac{3}{2}} \equiv A\,T^{\frac{3}{m}+\frac{3}{2}}, \qquad (22)$$

Здесь A – некоторый независящий от температуры коэффициент пропорциональности. Таким образом, в низкотемпературной области следует ожидать степенного роста теплоемкости твердого вещества. В частности если взять $m = 2$, то получается известный закон T^3, нередко наблюдаемый на экспериментах. Отметим естественность этого значения показателя степени в модельном потенциале для низкотемпературной области, так как именно оно отвечает малым колебаниям атомов около своих положений равновесия. Выше уже говорилось о тех принципяльных различиях, которые имеются между нашим модельным потенциалом с показателем степени $m = 2$, с одной стороны, и с гармоническим потенциалом в модели независимых осциллятором Эйнштейна, с другой стороны.

Противоположный предельный случай будет соответствовать настолько высоким темпепатурам, что $E/2kT << 1$. При этом переменная интегрированрия оказывается малой во всей области интегрирования, $x << 1$. Данное обстоятельство позволяет разложить знаменатель подинтегральной функции в степенный ряд по x и ограничиться только первыми тремя членами разложения. Дальнейшее упрощение подинтегральной функции достигается опять-таки посредством использования малости переменной x и позволяет представление искомого интеграла линейной комбинацией интегралов от степенных функций, которые вычисляемы в явном виде. Окончательно получим:

$$c \approx \frac{\sqrt{2}\,k}{\pi^2\hbar^3}\frac{(M\,E)^{\frac{3}{2}}}{n(m+2)}\left(\frac{E}{P}\right)^{\frac{3}{m}}\mathrm{B}\left(\frac{3}{m},\frac{3}{2}\right)\left(1-\frac{m+2}{7m+6}\left(\frac{E}{2kT}\right)^2\right) \equiv B-\frac{C}{T^2}, \qquad (23)$$

где B и C положительтные параметры, независящие от температуры. Следовательно, теплоемкость твердого вещества должна возрастать и в высокотемпературной области, но горазде медленнее, снизу приближаясь к некоторой постоянной величине. Это вполне разумное поведение, часто реализуемое в условиях эксперимента. Хотя, насыщение теплоемкости твердых тел, как правило, не наступает – еще задолго до достижения необходимой для этого температуры наступает точка плавления вещества, где его теплоемкость увеличивается скачкообразно.

5. О проблеме подгонки теоретической кривой к экспериментальным данным

Таким образом выражение решеточной теплоемкости твердого тела, как функции температуры, полученное нами в рамках нового подхода (без привлечения концепции фононов) – непосредственным анализом теплового возбуждения атомных колебаний, в состоянии качественно хорошо описать как низко- так и высокотемпературное поведение этой характеристики. Для получения ответа на вопрос, в какой степени спасобно то же самое выражение количественно опысать экспериментальные температурные зависимоси

теплоемкостей конкретных твердых веществ в целом, необходимо осуществить подгонку теоретической кривой (20) к эксперменталным точкам.

Рассмотрим упрощенную форму (21). В роли подгоночных параметров будут выступать параметры использованного модельного потенциала и энергетических состояний атомов в этом потенциале: m, P и E. Если теория в представленной форме действительно «работает» для данного вещества, подгонка должна дать физически разумные значения этих величин: должно быть $m \sim 2$, чтобы при низких температурах выполнялся закон T^3; P должен иметь порядок энергии связывания, приходящей на один атом данного твердого тела; величина E должна коррелировать с энергией нижней полосы инфракрасного поглощения в материале.

Что же касается параметров M и n, то они являюся константамы материала и по этой причине их значения считаются заданными.

Хотя может быть оправданным использование отличающихся друг от друга по значениям наборов параметров подгонки в разных температурных интервалах. Дело в том, что, строго говоря, перечисленные выше параметры (за исключением M) вовсе не являются константами и в большей или меньшей мере изменяются с температурой. Так например, тепловое расширение уменшает среднюю концентрацию атомов в веществе n; уменьшает глубину P потенциальнх ям с атомами; удлиняя химические связы, уменьшает их жесткость и таким путем меняет параметр формы m потенциальной ямы; с повышением температуры верхняя граница возбужденной энергетической полосы E тоже сдвигается вверх. Но оценки важности подобных эффектов, это – тема дальнейших исследований.

Прежде всего зафиксируем значение параметра m, равное 2, обеспечивающее правильное никзотемпературное поведение температурной зависимости теплоемкости. Тогда из выражения (21) получим,

$$c = \frac{3M^{\frac{3}{2}}k(kT)^3}{2\sqrt{2}\pi\hbar^3 n P^{\frac{3}{2}}}\int_0^{\frac{E}{2kT}}\frac{dx\,x^4}{\sinh^2 x}. \qquad (24)$$

Из оставшихся параметров два, n и P, сюда входят в произведении. Так что, они по сути эквивалентны одному параметру. Температурная зависимость n связана с тепловым расширением твердого тела и, следовательно, очень слаба. Ею всегда можно пренебречь по сравнению с температурной зависимости P. Вместо них введем

$$\alpha = \frac{3M^{\frac{3}{2}}k^4}{2\sqrt{2}\pi\hbar^3 n P^{\frac{3}{2}}}, \qquad (25)$$

а вместо E – еще один новый параметр

$$\beta = \frac{E}{2k}. \qquad (26)$$

Таким образом теплоемкость элементпрного вещества представляется функцией

$$c = \alpha T^3\int_0^{\frac{\beta}{T}}\frac{dx\,x^4}{\sinh^2 x}, \qquad (27)$$

которая зависит от температуры как явно, так и – через указанные два параметра.

Поскольку выражение (27) содержит два параметра, его подгонку к результатам измерений мы осуществим по парам экспериментальным точкам, а полученные таким путем значения α и β сопоставим середине соответствующего температурного интервала.

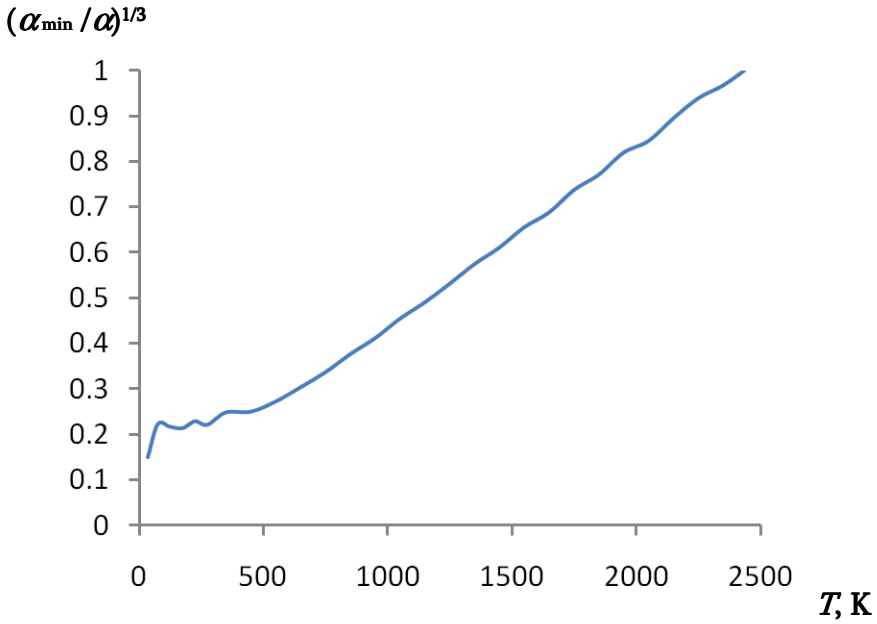

Рисунок 1. Температурная зависимость приведенного параметра $(\alpha_{min}/\alpha)^{1/3}$ функции теплоемкости β-ромбоэдрического бора.

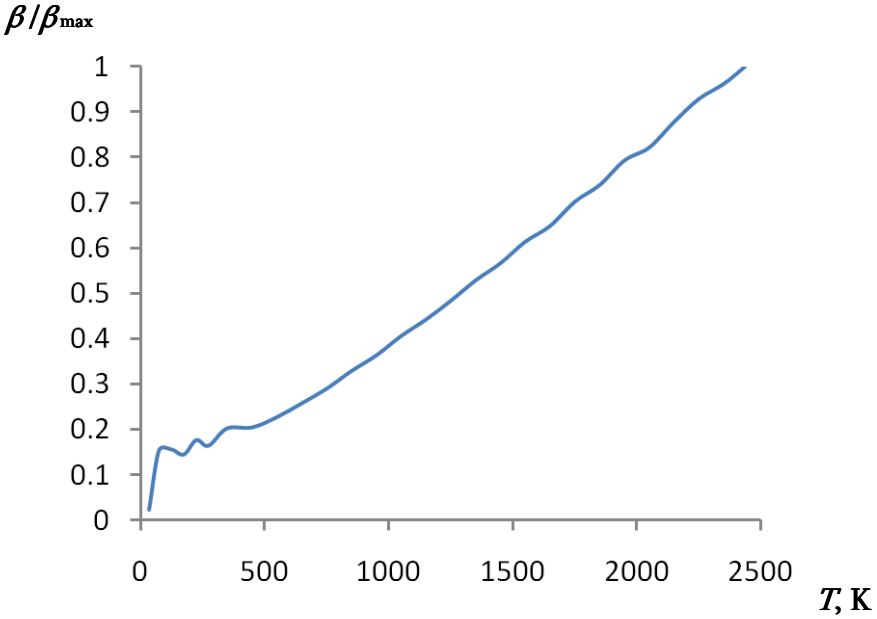

Рисунок 2. Температурная зависимость приведенного параметра β/β_{max} функции теплоемкости β-ромбоэдрического бора.

На рисунках 1 и 2 представлены полученные таким путем температурные зависимости $1/\alpha^{1/3}$ и β для β-ромбоэдрического кристалла бора. При этом была использована сглаженная кривая, учитывающая множество измерений теплоемкости этого материала [2]. Они оба практически линейны: $(\alpha_{min}/\alpha)^{1/3} = 6.043 \cdot 10^{-2} + 3.859 \cdot 10^{-4}\ T$ и $\beta/\beta_{max} = 2.555 \cdot 10^{-3} + 4.096 \cdot 10^{-4}\ T$, соответсвенно (за исключением слабых флуктуаций

при низких темиературах, которые связываются с большой относительной погрешностью измерений теплоемкости в этих условиях), что находит разумное качественное объяснение: параметр $1/\alpha^{1/3}$ по своей температурной зависимости эквивалентен импульсу волны низкотемпературных упругих колебаний, а β – усредненной энергии колебаний атомов при высоких температурах.

Ссылки

1. Ch. Kittel. Introduction to Solid State Physics. 2005, NJ: John Wiley & Sons, Inc.
2. Г. В. Цагарейшвили, Д. Ш. Цагарейшвили. Термические и упругие свойства бора. 1990, Тбилиси: Мецниереба.
3. A. Gerasimov, B. Gerasimov, A. Gerasimov–Titov. Correlation between heat-conductivity of solid states and electron configurations of atoms constituting them. Bull. Georg. Acad. Sci., 2005, **171**, 1, 40-43.
4. A. Gerasimov, D. Buachidze, G. Chuchulashvili. Correlation between thermal capacity of simple solids with atomic bonding rigidity. Bull. Georg. Acad. Sci., 2005, **172**, 1, 48-50.

NANOBORON (AN OVERVIEW)

L. Chkhartishvili

Georgian Technical University
Tbilisi, Georgia
chkharti2003@yahoo.com

Accepted May 3, 2011

1. Introduction

Elemental boron possesses a variety of nano-structured forms, which can find applications in number of techniques and technologies. Present overview aims to describe in brief methods of producing, atomic structures, and available data on physical properties of nano-structured species of boron: molecules and clusters; crystals stabilized by intrinsic imperfections; amorphous films and powders; dispersed crystals; filaments and fibers; nanowires, nanoribbons, and nanobelts; planar and quasi-planar sheets, nanotubes, cages and fullerenes; as well as quasi- and nanocrystals.

Boron B belongs to the least abundant chemical elements. It constitutes only a minute fraction of the Matter (Earth crust and Ocean water contain different amounts of boron, around 0.001 and 0.015 wt %, respectively). As for the role of boron in forming of the various molecular and condensed phases, it is incommensurable great if compared with boron abundance. In the final analysis, understanding of the diversity of boron structures reduces to the electronic structure of an isolated boron atom. Valence-shell configuration peculiar to the free B atom is $2s^2 2p$. In multi-atomic networks, adding an electron it becomes at first in the energetically more favorable configuration $2s^2 2p^2$, which then tends to most stable one $2s2p^3$. Thus, boron is strongly distinct acceptor and, consequently, elemental boron structures have to be electron-deficient. It is a reason why all boron forms, both molecular and condensed phases, exhibit very complex, clustered structures. For them, an icosahedron B_{12} with 12 boron atoms at vertexes serves as a main structural unit. For instance, crystalline unit cell of the β-rhombohedral boron (β-B), which was believed to be a ground-state structural modification of boron, consists of 105 regular atomic sites forming number of slightly distorted icosahedra and joined icosahedral fragments.

Since carbon nanosystems were discovered, it has triggered interest in other materials, including bare boron, which may also exhibit nanostructures. Due to its rich chemistry, boron is a natural choice for constructing nanosystems, like the clusters, nanowires, nanotubes etc. And indeed, relatively recently they were synthesized. A boron atom of the given icosahedron is bonded with 5 neighboring atoms and, usually, is linked with an atom from the neighboring icosahedron. This fact explains why the average coordination number of atomic sites in β-B

lattice, as well as in all solid-state forms of boron, is almost 6. But, a free regular boron icosahedron still remains electron-deficient: it needs 2 extra electrons to saturate all dangling B – B bonds. In boron crystals and amorphous boron, electron-deficiency is compensated by the presence of intrinsic point defects (vacancies in form of only partially occupied boron sites and self-interstitials) and / or certain impurity atoms in very high concentrations.

In addition to solid-state modifications, constructed from inter-connected icosahedra, elemental boron forms diboron molecule B_2 and molecular clusters B_n ($n > 2$). At relatively low n, boron clusters are planar or quasi-planar, but at sufficiently high n, they can take polyhedral, nearly spheroidal, cage-like shapes, in particular, icosahedral shape, if dangling bonds at the boron atom are saturated by hydrogen or other foreign atoms. Thus, most boron atoms should be surrounded by 6 nearest neighbors (they usually have 5 intra-icosahedral plus 1 inter-icosahedral or outward bonds). This circumstance leads to the possibility to synthesize fragments of planar or quasi-planar nanosheets in form of surfaces with triangular 6-coordinated 2D-lattices, which can be rolled up cylindrically or spherically forming nanotubular and fullerene-like materials. There is known number of other nano-structured forms of boron: amorphous and micro-crystalline thin films and powders, fine-dispersed crystalline powders, filamentary and fibrous materials, nanowires, nanobelts, nanoribbons, quasi-crystals etc. They reveal many interesting features in addition to the complex of useful properties characteristic of the macro-crystalline (bulk) boron. Strong B – B bonds make all these high-temperature materials highly resistive against aggressive environments and cause their unusual semiconducting properties.

There exist three earlier monographs by late Prof. Guri V. Tsagareishvili and co-workers devoted to the various aspects of boron issue: semiconducting properties [1], thermal and elastic properties [2], and producing techniques and atomic structure [3]. They partially cover micro-structured boron studies, but (and it is clear) not the last decade achievements in the field of nano-structured boron. According to the recent review [4], many of the fundamental questions regarding the solid-state chemistry of boron are still unsolved, more than 200 years after its discovery and boron is an elementary challenge both for experimenters and theoreticians. The theoretical work on the existence and stability of known and new modifications of this element combined with high-pressure and high-temperature experiments have revealed some new aspects of the problem. A lot has also happened over the last few years in the field of reactions between boron and other chemical elements. Physical properties such as hardness, superconductivity, neutron scattering length, and thermoelectricity have made boron-rich compounds attractive for applications as well. The greatest challenges to boron chemistry, however, are still the synthesis of monophasic products in macroscopic quantities and in the form of single crystals, the unequivocal identification and determination of crystal structures, and a thorough understanding of their electronic situation. Linked polyhedra are the dominating structural elements of the boron-rich compounds. In many cases, their structures can be derived from those that have been assigned to modifications of the element.

Present paper is an overview shortly summarizing available data on methods of fabrication, structural forms, and some physical properties of all nano-structured boron species.

2. Boron clusters

Clusters as systems of a finite number of bound atoms or molecules are physical objects occupying an intermediate position between atomic particles (atoms and molecules), on the one hand, and macroscopic atomic systems (solids and liquids), on the other hand [5]. One of the most interesting features of elemental boron and many boron binary compounds is the occurrence of highly symmetric icosahedral clusters (Figire 1). The variety of boron crystalline modifications and boron-rich solids can be constructed from the interconnected boron icosahedra. The same short-range structure is characteristic of amorphous boron. However, boron icosahedra do not lend themselves to the construction of an ideal 3D-framework, and various degrees of compromise in the pattern of icosahedral linkage give rise to the observed proliferation of boron polymorphs. For instance, within the rhombohedral lattice icosahedral atoms lying along the rhombohedral axes tend to positions themselves closer to the center of the icosahedron relative to the other atoms. The 3-center bonding and crystal structures of icosahedral boron-rich solids, the refractory materials, produce many exceptional properties [6]: some of these compounds are, for example, very high-temperature thermoelectric etc.

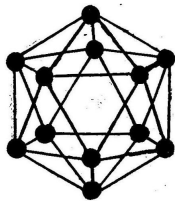

Figure 1. Boron icosahedron B_{12}.

Then, in bare boron structures most of B atoms usually are members of almost regular triangles. This circumstance leads to possibility of the new kind of boron-based materials in form of planar, quasi-planar or convex boron surfaces with triangular 2D-lattices. The rich chemistry of boron also is dominated by 3D-cage structures. Consequently, it seems very important to gain deeper insight in boron clusters – "building blocks" of nano-, micro-, and macro-structured boron. However, elemental boron clusters have been only scarcely studied experimentally and their structures and chemical bonding are not fully elucidated theoretically.

Boron has still remained the last elemental material (having stable natural isotopes) with unknown ground-state crystalline phase. It has been a subject of long-standing controversy, if α-rhombohedral boron (α-B) or β-B is the thermodynamically stable phase at ambient pressure and temperature. In [7], this enigma has been resolved based on the α-B-to-β-B phase boundary line which has been experimentally established in the high-pressure interval (from ~ 4 to 8 GPa) and linearly extrapolated down to ambient pressure. In a series of high-pressure high-temperature experiments authors heve synthesised single crystals of the three boron phases – α-B, β-B, and γ-B – and provided evidence of higher thermodynamic stability of α-B. This

result opens a way for reproducible synthesis of α-B, an optically transparent direct band gap semiconductor with very high hardness, thermal and chemical stability.

Boron is an element of fascinating chemical complexity. Controversies have shrouded this element since its discovery. Today there are known at least 16 boron polymorphs. Boron's complexities arise from frustration: situated between metals and insulators in the Periodic Table, boron has only 3 valence electrons, which would favour metallicity, but they are sufficiently localized that insulating states emerge. However, this subtle balance between metallic and insulating states can be shifted by pressure, temperature and impurities. The [8] reported the results of high-pressure experiments and *ab initio* evolutionary crystal structure predictions that explore the structural stability of boron under pressure and, strikingly, revealed a partially ionic high-pressure boron phase γ-B. This new phase is stable between 19 and 89 GPa and can be quenched to ambient conditions. It has a structure consisting of 2 icosahedral B_{12} clusters and 2 B_2 pairs (i.e., 28 atoms in the unit cell) in a NaCl-type arrangement. The ionicity of the phase is found to affect its electronic bandgap, infrared (IR) adsorption and dielectric constants, and arise from the different electronic properties of the B_2 pairs and B_{12} clusters and the resultant charge transfer between them.

Measurements of the hardness of a new high-pressure boron phase, orthorhombic γ-B_{28}, were reported in [9]. According to the data obtained, γ-B_{28} has the highest hardness (~ 50 GPa) of all known crystalline modifications of boron. In [10], the orthorhombic boron phase was synthesized at pressures above 9 GPa and high-temperature, and demonstrated to be stable at least up to 30 GPa. The structure, determined by single-crystal X-ray diffraction, consists of B_{12} icosahedra and B_2 dumbbells. The charge density distribution obtained from experimental data and *ab initio* calculations suggest mainly covalent chemical bonding in this phase. Strong covalent interatomic interactions explain the low compressibility value (at 300 K bulk modulus is 227 GPa) and high hardness of high-pressure boron (with Vickers hardness of 58 GPa), after diamond the second hardest elemental material.

The recently characterized crystal structure of metastable γ-B_{28} has been analyzed from a crystal chemical point of view, and the electron requirement of its building units and that of their linkage determined [11]. The structure consists of unique B_2 dumbbells and B_{12} icosahedra, which are connected through 2- and 3-center, 2-electron bonds. The different bonding motifs are ascertained by theoretical calculations of difference charge distributions. Chemical bonding in γ-B_{28} bears great resemblance to α-B_{12} (which is the simplest boron modification). The above mentioned previous description of γ-B_{28} as ionic in terms of $(B_2)^{\delta+}$ and $(B_{12})^{\delta-}$ was not supported.

The structure, bonding and charge transfer in γ-B_{28} was also considered in [12]. It has been stated that the crystal structure of the hardest known phase of boron, γ-B, now is firmly established, but the intriguing relationships among the structure, chemical bonding, charge transfer and physical properties in such phase raised a lot of interest. γ-B is stable between 19 and 89 GPa and can be visualized as a NaCl type arrangement of B_{12} icosahedra and B_2 pairs. The exciting characteristic of γ-B_{28} is that it shows a non-negligible charge transfer between the B_2 and B_{12} clusters. Although γ-B_{28} may be formally envisaged as a NaCl-type arrangement of B_{12} icosahedra and B_2 pairs, one should nonetheless remind that (1) there is only a partial charge

transfer of about $0.3 - 0.5$ electrons between the two clusters; (2) the Cl^--like groups are covalently linked between each other, and (3) the Na^+-like and the Cl^--like groups interact together not only through 2 long polar bonds, but also with 1 normal covalent bond. So, the chemical bonding in γ-B_{28} is predominantly covalent but with a partially polar nature, leading to unexpected physical properties for an elemental phase.

Most of boron crystals contain extra atoms in the 3D-network, such as chains with different number of atoms. For example, the chains are constructed by 2 boron atoms, in recently synthesized γ-B_{28}, etc. In [13], the structural, electronic and mechanical properties of hypothetical boron crystals which are formed by inserting extra boron atoms between icosahedra in α-B, B_n ($n = 13, 14$) were investigated by using plane-wave (PW) density functional theory (DFT). It was studied that how does structural parameters of the crystals change, as increasing number of atoms in inter-icosahedral chain. Cohesive energies were calculated to discuss nergetic stability of the purposed structures and then mechanical stabilities were investigated. The detailed micro hardness analysis was presented with the individual bond hardnesses and Mulliken populations. The results were compared with α-B (B_{12}) and B_{15}.

2.1. Bare boron clusters

According to the mass-spectrometric analysis [14] of the boron cluster ions detached from the high-purity (99.99995 % B) target-source in process of growing of amorphous boron thin and massive films, there are some complicated (due to natural isotopic composition of boron) peaks corresponding to the interval $B_2^+ - B_8^+$.

Bonding of small boron cluster cations from B_2^+ to B_{13}^+ was examined [15] (see also [16]) by measurement of appearance potentials and fragmentations patterns for collision (with Xe atoms) induced dissociation. Cluster stabilities were generally found to increase with increasing size. However, there are large fluctuations from the overall trend. The lowest energy fragmentation channel for all size cluster ions is loss of a single B atom. Clusters, smaller than 6 atoms, preferentially lose B^+ ion, while for the larger clusters the charge remains on the B_{n-1}^+ fragment. Obtained results were used to estimate cluster ionization potentials (IPs) and geometries. It was also reported *ab initio* calculations of geometries, IPs, charge distributions, dissociation energies, and bonding characters for both neutral and single-positive ionic clusters from B_1 to B_6 and from B_1^+ to B_6^+, respectively.

The boron clusters B_n, $n = 2 - 52$, formed by ablation of hexagonal boron nitride with a 532 nm laser were discovered in [17]. Creating species were ionized with a 193 nm ultra-violet (UV) laser and analyzed with a time-off-light (TOF) mass spectrometer.

The geometries, electronic structures and energies of the neutral and cationic boron clusters (B_{2-12} and B_{2-12}^+) have been also investigated by the *ab initio* molecular orbital (MO) method [18]. The geometries of boron-cluster cations B_{3-12}^+ are essentially the same as those of the neutral clusters, planar (or pseudo-planar) cyclic structures. Clusters of $8 - 11$ atoms characteristically have the most stable structure of a cyclic form with one atom in the middle. The capped pentagonal B_6, B_7 and B_7^+ and the trigonal bipyramidal B_{12} and B_{12}^+ are exceptions.

The same problem was considered [19] for the neutral and cationic clusters B_{12} and B_{13}. Several planar and non-planar stationary structures were optimized for neutrals and cations of each cluster size. A characteristic cyclic form with one atom in the middle was found to be stable for each cluster, while the icosahedral B_{12}^+ was found to be the most stable. The triplet icosahedral B_{12} was stable but energetically unfavorable than the cyclic B_{12}. All the 3D-structures analyzed for B_{13} and B_{13}^+ clusters were unstable.

Some symmetrical clusters of boron and carbon as well were discussed [20] by introducing the concept of conjugate polyhedra. If a polyhedron of carbon (boron) is given, its conjugate polyhedron of boron (carbon) can be obtained by interchange of numbers *n* and *f* with *I* being kept constant; and a conjugate polyhedra should have the same symmetry.

The geometrical structures and properties of small cationic boron clusters B_n^+ ($n = 2 – 14$) were investigated [21] using local-spin-density (LSD) formalism including a nonlocal correction. The linear search for minima on the potential energy surface (PES) was performed using the analytical gradients of the total LSD energy. Most of the final structures of the cationic boron clusters prefer planar or quasi-planar atomic arrangements and can be considered as fragments of a planar surface or as segments of a sphere. The calculated adiabatic IPs of B_n exhibited features that are analogous to those of measured IPs for boron clusters. Most of the calculated normal modes of the cationic clusters have frequencies that are around 1000 / cm and have strong IR intensities. They correspond quite well with analogous properties of solid boron.

A linear search for minima on PESs based on analytical gradient methods and the determination of binding energies of small boron clusters B_n ($n = 2 – 14$) have been made using the *ab initio* Hartree–Fock (HF) and self-consostent-field (SCF) configuration interaction (CI) quantum chemical (QC) methods as well as by means of DFT at the LSD and non-local corrections to the exchange-correlation levels of theory [22]. According to this *ab initio* SCF–CI and DFT comparative study, following results were obtained. The final optimized HF-topologies of the neutral boron clusters are identical with those derived with the LSD approximation. The most stable boron clusters have convex or quasiplanar structures. The convex clusters seem to be segments of the surface of a sphere.

The geometries of B_n^+ clusters for $n \leq 14$ were optimized in [23] applying DFT. The calculation suggested that the experimental results for the $B_n^+ \rightarrow B^+ + B_{n-1}$ fragmentation energies are too small, while experimental $B_n^+ \rightarrow B + B_{n-1}^+$ fragmentation energies for B_4^+, B_5^+, and B_{13}^+ are too large. Then, the fragmentation energies were calibrated based on coupling cluster theory. Overall corrected fragmentation energies were found to be in reasonable agreement with experiment. The most stable structure for each cluster was found to be planar or quasi-planar. The larger clusters are derived from fusing 6- and / or 7-membered atomic rings, which share 4 atoms for the 6 – 6 and 6 – 7 rings and 5 atoms for the 7 – 7 rings.

The structures and energies of B_{13}^+, observed experimentally to be an unusually abundant species among cationic boron clusters, have been studied systematically with DFT in [24]. The most thermodynamically stable B_{12}^+ and B_{13}^+ clusters are confirmed to have planar or quasiplanar rather than globular structures. However, the computed dissociation energies of the

3D B_{13}^+ clusters are much closer to the experimental values than those of the planar or quasi-planar structures. Hence, planar and 3D B_{13}^+ may both exist.

Based on *ab initio* QC methods, accurate calculations on small boron clusters B_n ($n = 2 - 14$) were carried out in [25] to determine their electronic and geometric structures. The geometry optimization with a linear search to local minima on the PES was performed using analytical gradients in the framework of the restricted HF SCF approach. Most of the final structures of the boron clusters with $n > 9$ are composed of 2 fundamental units: either of hexagonal or pentagonal pyramids. Using "Aufbau principle" one can easily construct various highly stable boron species. The resulting quasi-planar and convex structures can be considered as fragments of planar surfaces and segments of nanotubes or hollow spheres, respectively.

Again based on *ab initio* QC and HF approximations, and DFT and linear-muffin-tin-orbitals (LMTO) methods within the atomic-sphere-approximation (ASA) in [26] the geometric and electronic structures of some atomic-scaled boron clusters were determined. The starting structures were constructed with help of "Aufbau Principle" proposed for boron clusters.

Using *ab initio* QC methods, different structures of B_{32} clusters was investigated in [27]. The most stable isomers have quasi-planar or tubular structures often containing dove-tailed hexagonal pyramids. In contrast, hollow spheres are less stable. Their stability can be understood as a competition between a curvature strain (favoring quasi-planar clusters) and elimination of dangling bonds (favoring tubular and cage structures). Note that atomic coordination number in these structures is larger than in carbon clusters.

The curiously stable cationic B_{13}^+ cluster and its neutral and anionic counterparts were examined [28] though the use of DFT. Several different isomers were studied and compared with a special emphasis given to the electronic structure of the lowest lying isomers. Included among the isomers were 3 ones. While no minima that corresponded to the filled icosahedron could be found for the cluster, an intriguing atom-in-cage structure was found that is a local minimum on the cationic, neutral, and anionic surfaces. In the structure found for the B_{13}^- anionic cluster, the 12 external boron atoms are arranged as 3 6-membered rings back-to-back. The planar and quasi-planar structures were seen to be more stable than 3D isomers, but their ordering by stability changes depending on the charge state. Relative energies, selected geometric features, IPs, and electron affinities (EAs) were reported for these structures and some justification for the differences seen among the isomers was given. It was found that planar structures benefit from π-delocalization and in the case of the global minimum of the B_{13}^+ cationic cluster this delocalization is reminiscent of aromaticity.

The electronic structure and chemical bonding of boron clusters B_5^- and B_5 were investigated [29] using anion photoelectron spectroscopy and *ab initio* calculations. Vibrationally resolved photoelectron spectra were obtained for B_5^- and compared with theoretical calculations performed at various levels of theory. Extensive searches were carried out for global minimum of B_5^-, which was found to have a planar structure with a closed-shell ground-state. Excellent agreement was observed between *ab initio* detachment energies and the experimental spectra, firmly establishing the ground-state structures for both B_5^- and B_5. The chemical bonding in B_5^- was investigated and compared to that in Al_5^-. While both B_5^- and Al_5^-

have a similar planar structure, their bonding orbitals are different. In Al_5^-, a bonding orbital previously was observed to delocalize over only the 3 central atoms in the ground-state structure, whereas a similar orbital was found to completely delocalize over all 5 atoms in the B_5^-. Such bonding in B_5^- makes it more rigid towards butterfly out-of-plane distortions.

The electronic structure and chemical bonding of B_6^- and B_6 were investigated using anion photoelectron spectroscopy and *ab initio* calculation [30]. Vibrationally resolved photoelectron spectra were obtained for B_6^- and compared to calculations performed at various levels of theory. Extensive searches were carried out for the global minimum of B_6^-, which was found to have a planar structure with a doublet ground state. Good agreement was observed between *ab initio* detachment energies and the experimental spectra, establishing that the ground-state structure of B_6^- is planar, in contrast to the 3D structures for the valence-isoelectronic Al_6^- and Al_6 species. The chemical bonding in B_6^- was interpreted in terms of linear combinations of MOs of two B_3^- fragments. The antiaromatic nature of chemical bonding was established for B_6^- and B_6^{2-}, based on the analysis of orbital contributions to overall paratropic ring currents.

In [31], there are reported experimental and theoretical evidences that small boron clusters prefer planar structures and exhibit aromaticity and antiaromaticity according to the Hückel rules, akin to planar hydrocarbons. The planar boron clusters are thus the only series of molecules other than the hydrocarbons to exhibit size-dependent aromatic and antiaromatic behavior and represent a new dimension of boron chemistry. The stable aromatic boron clusters may exhibit similar chemistries to that of benzene (forming sandwich-type metal compounds).

Experimental and computational simulations revealed [32] that boron clusters, which favor 2D structures up to 18 atoms, prefer 3D structures beginning at 20 atoms. Using global optimization methods, it was found that the B_{20} neutral cluster has a double-ring tubular structure with diameter of ~ 5.2 Å. For the B_{20}^- anion, the tubular structure is shown to be isoenergetic to 2D structures, which were observed and confirmed by photoelectron spectroscopy. The 2D to 3D structural transition observed at B_{20}, reminiscent of the ring-to-fullerene transition at C_{20} in carbon clusters, suggests that it may be considered as the embryo of the thinnest single-walled boron nanotubes. The experiments were carried out using a magnetic-bottle TOF photoelectron spectroscopic apparatus equipped with a laser vaporization supersonic cluster source. B_n^- cluster anions were produced by laser vaporization of a disk target made of enriched ^{10}B isotope (99.75 %) in the presence of a helium carrier gas and analyzed with TOF mass-spectrometer. Selected B_{20}^- clusters were decelerated before irradiation by a photo-detachment laser beam. Measured vertical detachment energies were calibrated and then compared with calculated values.

Small boron clusters as individual species in the gas phase were reviewed in [33]. Free boron clusters have been characterized using photoelectron spectroscopy and *ab initio* calculations, which have established the planar or quasi-planar shapes of small boron clusters. This was surprised as the chemistry of boron has been diversely featured by 3D structures. Further the planarity of the species has been elucidated on the basis of terms of multiple aromaticity, multiple antiaromaticity, and conflicting aromaticity.

The electronic and geometric structures, total and binding energies, harmonic frequencies, point symmetries, and highest occupied MO–lowest unoccupied MO (HOMO–LUMO) gaps of small neutral boron B_n clusters ($n = 2 - 12$) have been investigated in [34] using DFT. Linear, planar, convex, quasi-planar, 3D-cage and open-cage structures have been found. None of the lowest energy structures and their isomers have an inner atom, i.e., all the atoms are positioned at the surface. Within the size range, the planar and quasi-planar (convex) structures have the lowest energies. The first and the second energy differences were used to obtain the most stable sizes. A growth path was also discussed with the sizes and isomers.

Issues of observation and confirmation of hepta- and octa-coordinated boron in molecular wheels of aromatic 8 and 9 atom boron cluster compounds were considered in [35] based on photoelectron spectra and *ab initio* calculations.

In order to elaborate a direct experimental method available for structural determination of boron clusters, photoelectron spectroscopy of size-selected cluster anions has combined with quantum calculations to probe the atomic and electronic structures and chemical bonding of small boron clusters up to 20 atoms [36]. Based on this method the experimental and theoretical evidences were presented showing that small boron clusters prefer planar structures and exhibit aromaticity and antiaromaticity according to the Hückel rules, akin to hydrocarbons. Aromatic boron clusters possess more circular shapes whereas antiaromatic boron clusters are elongated. It was found that for neutral boron clusters the planar to 3D structural transition occurs at B_{20}, which possesses a double-ring structure, even though the B_{20}^- anion remains planar. The stability of the double-ring structure suggests the possible existence of all-boron nanotubes.

The paper [37] has devoted to study of the ErB_{12} anisotropy emission properties. The emission properties of ErB_{12} (100) and (110) single crystals have been studied by using pulse current take-off method. An annealing results in decrease of electron work function (WF) for both types of the ErB_{12} single crystals. X-ray phase analysis and scanning-electron-microscophic (SEM) study of ErB_{12} emitting surfaces after emission tests showed boron depletion and appearance of ErB_4 inclusions. The model describing the electron WF anisotropy of ErB_{12} single crystals is proposed. The explanation is the boron-depletion of the ErB_{12} surface.

Using *ab initio* QC and DFT methods, it was investigated the structural transition from planar 2D boron clusters into 3D double-ring system and then from double-ring into triple-ring system [38]. The first structural transition occurs by B_{19} and B_{20} clusters, while the second transition occurs between B_{52} and B_{54} clusters. The effect of the repulsive Coulomb forces in boron clusters when they are multi-ionized also was studied. It was appointed the related fragmentation channels, ionization energies and Coulomb explosion and determined the critical charge for the metastability and Coulomb explosion. Further, the stability of different boron clusters in form of nanotubes and sheets were compared with the unit-cells of α- and γ-B. The noninteracting free-standing triangular buckled-sheet was confirmed to be more stable than Boustani's γ-sheet and the α-sheet, proposed earlier. In contrast, however, when these sheets are considered as infinite periodic systems, then the α-sheet remains the most stable one. The experimentally observed physical manifestations of a number of these clusters and nanostructures and related properties are consistent with suggested theoretical models.

Some of the major aims of the current research in field of boron clusters, which are developing, simulating, modeling, and predicting new boron structures to build pre-selected, uniform nanostructural materials with specific properties, e.g. superhardness, superconductivity, super-lightness, and propellance, were reviewed in [39]. According to these and other results obtained by Isah Boustani and co-workers (see detailed references), one can conclude that most structures of boron clusters can be classified into 4 groups: (1) quasi-planar, (2) tubular, (3) convex, and (4) spherical clusters. The transition of the quasi-planar surfaces into tubules may be pictured by rolling the surfaces and forming cylinders. The closure of boron quasi-planar surfaces into tubules goes through an energy barrier path.

2.2. Boron icosahedron

The electron structure of a regular icosahedron of boron atoms was investigated [40] theoretically by the method of MOs. It was found that 30 bonding orbitals are available for holding the icosahedron together, besides the 12 outward-pointed equivalent orbitals of the separated atoms. These results can be used to interpret the stability of crystal structures of elementary boron too.

In [41], the energy spectrum of boron icosahedron in the α-B structure was studied using MO–linear-combinations-of-atomic-orbitals (LCAO) method. In spite of regular boron icosahedron, real one is an electron-deficient structure. Besides, in distorted in crystalline field icosahedron the bond lengths are different and there is no 5-fold symmetry axis. It was found that molecular levels placed at – 9.35 eV should be half-filled, while all lower energy levels should be filled. They form the valence band. Band gap was (under)estimated as 0.9 eV. When inter-icosahedral interaction is introduced in theory, it provides with better agreement between the calculated band structure and experimental data available on α-B X-ray emission spectrum.

Using an expansion of 2870 PWs in [42] it has been performed *ab initio* calculations of the energy bands, equilibrium lattice constants, atomic positions, and cohesive energy of boron icosahedron B_{12}. It was found an indirect gap of 1.427 eV and direct gap of 1.780 eV. The theoretical lattice constants and atomic positions were found to be in good agreement with X-ray data. As for the calculated charge-density contour plots, they revealed strong intra-icosahedral and inter-planar inter-icosahedral bonding but weak intra-planar bonding.

Based on the well-known group properties of a regular icosahedron, its normal vibrational modes had been pictured [24]. There were found 8 distinct frequencies for the 30 normal modes with 1-, 3-, 4-, and 5-fold degeneracies. Icosahedral oscillations were pictured in terms of three equilibrium descriptions: first involves 2 parallel regular pentagons and 2 polar atoms; second has 2 polar triangles and an equatorial puckered hexagon; while the third consists of 6 pairs of atoms on opposite faces of a cube. Such visualization should prove useful in application to spectra interpretation, substituting atom location, polaron formation and hopping, and possibly heat conduction in solid elemental boron and boron-rich solids which contain groups of 12 boron atoms at the vertexes of approximately-regular icosahedra.

It was shown [44] that by the interaction between electron and pair of phonons (which are the slightly modified two breathing modes of the isolated icosahedron B_{12}) the electron trapping level is generated, which influences the boron-rich solids essentials.

Occurrence of the first-order polar vibrations for the icosahedra B_{12} and also α-B crystal (α-B_{12}) was demonstrated [45] within the harmonic approximation, by using the shell model. The dynamical effective charges were expressed by both the normal and Cartesian coordinates, while the tensor nature of the effective charges was emphasized. Numerical estimations have been made for the examined B_{12} cluster and α-B. It was shown that the effective charge of the B_{12} is very small (≈ 0.01), while that of α-B is enhanced by the deformation of the icosahedra. The non-central core–shell force had the dominant effect on this enhancement. The calculation provided leads to relationship between the frequencies and Raman and IR bands and the intensity of IR bands. Presented consideration explained, why boron crystals exhibit polar vibrations, despite the fact that crystal is composed of the same chemical species.

The metallic–covalent bonding conversion in boron icosahedral cluster solids have been discussed [46, 47] in relation to the occupation by an atom the center of clusters by using the electron density distribution according to electronic state calculations or X-ray diffraction (XRD) data analysis. In addition, the change of the electron localization due to the occupation of an atom the center of the clusters was quantitatively estimated by using electron localization indicator (ELI), $0 \le ELI \le 1$. ELI ~ 1 means that electron is well localized, which corresponds to covalent bonding; while ELI ~ 0.5 corresponds to the metallic bonding and electron gas-like behavior. The distributions of the ELI were compared for the pair of clusters B_{12}^{+} and B_{13}^{-}. The occupation of the center by atom found to cause the electrons delocalization in B – B bonds. The comparison of B_{12} and B_{13} clusters revealed that the bonding conversion from covalent to metallic one involved a decrease in both the electron density and ELI between boron.

The nearest-neighbor antiferromagnetic Heisenberg model was considered for spins 1/2 and 1 located on the vertices of the icosahedron [48]. Taking into account the permutational and spin-inversion symmetries of the Hamiltonian results in a drastic reduction of the dimensionality of the problem, leading to its full diagonalization. There is a strong signature of the frustration present in the system in the low-energy spectrum for spin of 1/2, where the first excited state is singlet. For spin of 1 the system again has singlet excitation. The specific heat of the icosahedron has a two-peak structure as a function of temperature.

The kinetic mechanism of spontaneous self-assembly of viral proteins into icosahedral capsid proteins was studies using molecular dynamics simulations of coarse-grained models [49].

2.3. Boron-based clusters with foreign atoms

Boron hydrides and their derivatives present very interesting objects for valence theory in general. Most of these compounds are essentially non-ionic and have the physical properties of ordinary covalent compounds. However, for lack of enough valence electrons they can not be assigned the “classical” covalent structures. In boron cluster compounds like the B_2H_6, B_5H_9, and $B_{10}H_{14}$, the boron atoms have 5 or 6 ligands as in the main boron-rich solids: elementary

boron structural modifications, boron carbide, metallic hexaborides etc. The experimental basis for the extended Hückel theory, the first widely applicable use of MO theory to study chemical bonding, is formed by the W. N. Lipscomb Jr's works on boranes [50].

The nature of bonding in electron-deficient compounds of boron was discussed [51] with reference to their intermediate position as a class between ordinary covalent compounds and the metals. In particular, the bond lengths, which vary widely (e.g. B – H = 1.15 to 1.40, B – B = 1.66 to 1.93 Å), were successfully correlated with Pauling's semi-empirical equation $r(n) \approx r(1) - 0.3 \log n$, with best $r(1)$ for boron about 0.80 Å, in a way which can also used for molecules of unknown structure to obtain additional structural information from incomplete data. There were also calculated atomic charges and polarizabilities.

The results of the above quoted theoretical investigation (performed by MO-method) of the electron structure of a regular icosahedron of boron atoms by Longuet–Higgins & de Roberts [40] can be used to interpret the chance of existence of a boron hydride $B_{12}H_{12}$ too.

The symmetry properties of the icosahedral vibration modes and molecular vibrations of the $B_{12}H_{12}^{2-}$ molecule were discussed in [52]. It was found strong and angular-dependent forces pointing outward from the icosahedron. However, the intra-icosahedral forces should be relatively weak and much less angle-dependent. Altogether obtained results support the idea that within the icosahedron, the binding is metal-like, whereas the outward bonds are more covalent. Then, the Raman and IR data for $B_{12}H_{12}^{2-}$ molecule and icosahedron-based elemental boron solids were analyzed using various valence-force-field model potentials.

Ab initio HF calculations, extended by many-body perturbation theory corrections for electron correlations, were made [53] on small boranes. The dissociation energy of B_2H_6 was calculated and reaction energies of B_3H_7 for the formation of B_3H_9 were also reported.

The structures of boron cluster B_{14}, its anion B_{14}^{2-} and boron-hydride cluster $B_{14}H_{14}^{2-}$ in octahedral symmetry were investigated [54] by *ab initio* calculations. The relationship of MOs has been analyzed and it was found that the number of valence bonding orbitals of a high borane obeys the Wade's $n + 1$-rule: number of the framework bonding orbitals of $B_nH_n^{2-}$ equals to $n + 1$. The similarities and differences between boron and carbon clusters were also discussed.

Computational calculations by the 3-parameter hybrid method using correlation functional have been performed [55] on $B_{12}H_{12}^{2-}$ dodecaborane anions with different boron isotopic composition. This was done in order to investigate isotopic dependence of vibrational spectral properties of B_{12} icosahedra, and for comparison of the optical vibrational properties of the icosahedral molecule with those characteristic of boron-rich crystals.

Hydrogen-terminated icosahedral cluster $B_{12}H_{12}^{2-}$ is known as the most stable molecule among the various polyhedral boranes. Meanwhile, the isolated B_{12} without hydrogen has been determined to be quasi-planar with 6 delocalized π-electrons. To understand the type of structure that is preferentially formed in $B_{12}H_x$ clusters ($x = 1 - 11$), in [56, 57] it have been considered the formation of icosahedral $B_{12}H_8^+$ through ion–molecule reactions of the ^{11}B isotopically enriched decarborane ion ($B_{10}H_x$, $x = 6 - 14$) with diborane (B_2H_6) molecules in an external quadruple static attraction field of ion trap. The hydrogen content mass-spectrum analysis has revealed $B_{12}H_8^+$ as the main product. *Ab initio* calculations showed that it

preferentially forms an icosahedral structure rather than a quasi-planar structure. The energies of the formation reactions of $B_{12}H_{14}^+$ and $B_{12}H_{12}^+$ between $B_{10}H_x^+$ ($x = 6, 8$) ions (which were considered to be involved in the formation of $B_{12}H_x^+$) and a B_2H_6 molecule were also calculated. The calculations of the detachment pathway of H_2 molecules and H atoms from the product ions, $B_{12}H_{14}^+$ and $B_{12}H_{12}^+$, indicated that the intermediate state has a relatively low energy, enabling the detachment reaction to proceed owing to the sufficient reaction energy. This auto-detachment of H_2 accounts for the experimental result that $B_{12}H_8^+$ is the most abundant product, even though it does not have the lowest energy among $B_{12}H_x^+$. *Ab initio* calculations indicated that icosahedral structure is more stable for $B_{12}H_x^+$ clusters with $x = 6 - 12$, but planar configuration is more stable for clusters with $x = 0 - 5$. It was reported the energy barriers of structure transition by detaching H atoms from icosahedral $B_{12}H_6^+$ cluster to planar $B_{12}H_5^+$, planar $B_{12}H_4^+$, icosahedral $B_{12}H_5^+$, or icosahedral $B_{12}H_4^+$ clusters. It was performed DFT calculations to explore the energy barriers and the reaction path of the structure transition. The resultant energy barriers are almost the same, enabling the transition to proceed and suggesting that the structure of $B_{12}H_x^+$ clusters is controlled by the number of hydrogen atoms x.

A theoretical assessment of doping α-B with hydrogen was presented in [58]. Dissimilar to other impurities, H is unique because its site is the most stable one well suited to the 3-center bond. The formation energy was calculated for configurations $B_{12}H$, $B_{12}H_2$, $B_{12}H_{1/3}$, and $B_{12}H_{2/3}$.

The [59] reported the formation of icosahedral $B_{12}H_8^+$ through ion–molecule reactions of the decaborane ion $B_{10}H_x^+$ ($x = 6 - 14$) with diborane B_2H_6 molecules in an external quadrupole static attraction ion trap. The hydrogen content n of $B_{12}H_n^+$ was determined by the analysis of the mass spectrum. The result reveals that $B_{12}H_8^+$ is the main product. *Ab initio* calculations indicated that $B_{12}H_8^+$ preferentially forms an icosahedral structure rather than a quasiplanar structure. The energies of the formation reactions of $B_{12}H_{14}^+$ and $B_{12}H_{12}^+$ between $B_{10}H_x^+$ ions ($x = 6, 8$), which are considered to be involved in the formation of $B_{12}H_n^+$ and B_2H_6 molecule were calculated. The calculations of the detachment pathway of H_2 molecules and H atoms from the product ions, $B_{12}H_{14}^+$ and $B_{12}H_{12}^+$, indicated that the intermediate state has a relatively low energy, enabling the detachment reaction to proceed owing to the sufficient reaction energy. This auto-detachment of H_2 accounts for the experimental result that $B_{12}H_8^+$ is the most abundant product, even though it does not have the lowest energy among $B_{12}H_n^+$.

In addition to the discussion of [46, 47] on the metallic–covalent bonding conversion in boron icosahedral cluster solids, the change of the electron localization due to the occupation of an atom at the center of the clusters was quantitatively estimated by using ELI. In particular, the distributions of the ELI were compared for the pair of clusters $B_{12}H_{12}^{2-}$ and $B_{13}H_{12}$. The occupation of the center by atom found to cause the electrons delocalization in B – B bonds.

In spite of numerous theoretical examinations of bonding situation in closo-hydroborates $B_nH_n^{2-}$ there is lack of experimental data. But, it has become possible to obtain some model substances for studying the multi-center bonding within a boron cluster. For this reason, the conventional X-ray determination of the crystal structures was followed up [60] by charge density analysis on multipole refinements. These were complemented by topological analysis according to the atoms-in-molecules (AIM) method. The experimental data were supplemented

by *ab initio* calculations. Interatomic interactions can be described as the appearance of bond-, ring-, and cage-critical points and corresponding values for the electron density in these points. Careful analysis of both experimental data, and charge density calculations and topological data permits, in particular, to show the distribution of the electron density in multi-center bonds of the $B_6H_6^{2-}$ cluster. Analysis of the critical points shows the attractive interaction of cation and anion. It was also discovered truly rhomboidal almost planar B – B – B – H rings.

Under the right conditions, and using the appropriate synthetic strategies, single-cluster boron hydride species can fuse together to form large multi-cluster agglomerations that are often referred to as "macro-polyhedral" compounds. The most outstanding example of this phenomenon is the fusion of two closo-$[B_{10}H_{10}]$ polyhedra to form the anti- and syn-isomers of $B_{18}H_{22}$. These isomers are very different species in terms of their optical and chemical properties. Both isomers are very acidic and form stable mono- and dianions that can be react with and incorporate a variety of different *p*-block elements into its macro-polyhedral structure. The boron hydride cage $B_{18}H_{22}$ can also be functionalized by halogens or by reactive organic species. Future development of their applications requires strict control of various chemical and physical properties of cluster borane compounds. The chemistry of such large borane species has been discussed in [61].

The [62] has presented the formation of hydrogen-content-controlled $B_{12}H_n^+$ clusters through the decomposition and ion–molecule reactions of the decaborane $B_{10}H_{14}$ and diborane B_2H_6 molecules in an external quadrupole static attraction ion trap. The hydrogen- and boron contents of the $B_{10-y}H_x^+$ cluster are controlled by charge transfer from ambient gas ions. In process of ionization, a certain number of hydrogen and boron atoms are detached from decaborane ions by the energy caused by charge transfer. The energy caused by the ion–molecule reactions also induces H-atom detachment. Ambient gas of Ar leads to the selective generation of $B_{10}H_6^+$. The $B_{10}H_6^+$ clusters react with B_2H_6 molecules, resulting in the selective formation of $B_{12}H_8^+$ clusters. Ambient gas of Ne (He) leads to the generation of $B_{10-y}H_x^+$ clusters with $x = 4 - 10$ and $y = 0 - 1$ (with $x = 2 - 10$ and $y = 0 - 2$), resulting in the formation of $B_{12}H_n^+$ clusters with $n = 4 - 8$ ($n = 2, 4 - 8$). The introduction of ambient gas also increases the production of clusters. In addition, DFT calculations were conducted to investigate the structure and the mechanism of formation of $B_{10-y}H_x^+$ and $B_{12}H_n^+$ clusters.

Hydrogen-terminated icosahedral $B_{12}H_{12}^{2-}$, which has the same structure as the unit in solids, is the most stable molecule among the various polyhedral boranes synthesized so far. On the other hand, small boron clusters strongly favor planar or nearly planar structures, on the basis of systematic *ab initio* calculations and experiments. The fact that the stable structure of boron clusters depends on the hydrogen contents is fascinating, because it means that the structure is tunable through the control of the number of hydrogen atoms. In [63], there was presented the formation of hydrogen-content-controlled $B_{12}H_n^+$ clusters through the decomposition and ion–molecule reactions of the decaborane ($B_{10}H_{14}$) and diborane (B_2H_6) molecules in an external quadrupole static attraction ion trap. In the process of ionization, a certain number of hydrogen and boron atoms are detached from decaborane ions by the energy caused by charge transfer from ambient gas ion to decaborane molecule. The energy caused by

the ion-molecule reactions also induces H atom detachment. The mechanism of the charge transfer and following detachment of hydrogen and boron atoms were investigated by DFT.

Now let us concern the boron-based clusters containing other than hydrogen elements.

Like the boron hydride $B_{12}H_{12}$ cluster, electron structure of a regular icosahedron of boron atoms theoretically established in [40] by the method of MOs can be used to interpret the stability of crystal structure of boron carbide $B_{12}C_3$.

The [64] focused on the understanding gained from the investigation of the physical properties of boron carbides with theoretical methods based on DFT. Examination of the total energies of various atomic configurations in the unit cell together with vibrational or nuclear-magnetic-resonance (NMR) spectra has lead to the determination of the atomic structure of $B_{12}C_3$ as C – B – C chains linking mostly $B_{11}C$ icosahedra, and a few percents of $B_{10}C_2$ icosahedra. In the icosahedron, the carbon C atom was found to be in the polar site: $B_{12}C_3{}^P$. When there are 2 carbon atoms, they were found to be in antipodal polar positions. At carbon concentrations others than ~ 20 %, 4 structural models have a negative formation energy with respect to a formation from α-B plus diamond. Moreover, they all have positive formation energy with respect to $B_{12}C_3{}^P$, showing a tendency to decompose into $B_{12}C_3{}^P$ plus α-B or $B_{12}C_3{}^P$ plus diamond. Such metastability explains actual difficulties in the synthesis of clean (i.e., not carbon-contaminated) boron samples, in particular for $B_{13}C_2$. Finally, results on the strength of the electron–phonon coupling constants obtained in $B_{13}C_2$ were presented.

The electronic structure, total energy, and vibrational properties of carborane $C_2B_{10}H_{12}$ molecules and C_2B_{10} clusters formed when the hydrogen atoms are removed from carborane molecules were studied using DFT methods and a semi-empirical model [65]. Computed vibrational spectra for carborane molecules were shown to be in close agreement with previously published measured spectra taken on carborane solids. Semiconducting boron carbide films were prepared by removing hydrogen from the 3 polytypes of $C_2B_{10}H_{12}$ deposited on various surfaces. Results from X-ray and Raman scattering measurements on these films were also reported. 11 vibrationally stable structures for C_2B_{10} clusters were described and their energies and HOMO–LUMO gaps tabulated. Calculated Raman and IR spectra were reported for the 6 lowest-energy clusters. Good agreement with the experimental Raman spectra was achieved from theoretical spectra computed using a Boltzmann distribution of the 6 lowest-energy free clusters. The agreement can be further improved if the computed frequencies are scaled by a factor of 0.94, a discrepancy which could easily arise from comparing results of two different systems: zero-temperature free clusters and room-temperature films. Calculated energies for removal of hydrogen pairs from carborane molecules were reported as well.

It has been discovered [66] that reactive boron-carbon clusters called carborynes, $C_2B_{10}H_{10}$, which are in effect 3D versions of benzyne, can exist in 2 resonance forms that exhibit significantly different reactivity patterns. Carborynes are best described as resonance hybrids with bonding and biradical forms: the bonding form reacts with aromatics to give cyclo-addition products, whereas the biradical form undergoes C–H insertions with aliphatic ethers.

Mixed clusters of B and N have been produced by sputtering BN with Cs or Rb [67]. The atom ordering in assumed linear species has been deduced from measurements of the mass

distribution of both the positive and negative products from the fragmentation of the anionic clusters in a gas target. The existence of the anions BBN, BNN, BBBN, BBBBN, BBNN, and BBBNN has been demonstrated. The structural isomer with the largest EA is usually the dominant species produced in the sputter source.

In [68], three different approaches have been discussed to understand and control the properties of ammonia borane NH_3BH_3 and other boron-based materials to be practical in terms of reduced dehydrogenation temperatures, accelerated H_2 release kinetics and / or minimized borazine release. In the first approach, a new family of metal borohydride ammonia borane complexes has been developed. The mixed-metal amidoboranes $Na_2Mg(NH_2BH_3)_4$ and $Li_2(BH_4)_2NH_3BH_3$ and $Ca(BH_4)_2(NH_3BH_3)_2$ are some examples. More than 11 wt % hydrogen can be released from these new complex boron-metal hydrides. In the second approach, the effect of nano-confinement and catalytic activity of various metal-organic-frameworks on the hydrogen release of ammonia borane was explored. It was found that intercalating ammonia borane into 1D pores improves the hydrogen release kinetics and inhibits unwanted byproducts such as amonia and borazine, thus putting one a step closer for using ammonia borane based materials for hydrogen storage. In the third approach, a new nanoporous material, so called graphene oxide framework (GOF), formed of layers of graphene oxide connected by benzene-1,4-diboronic acid pillars, were designed and synthesized as a potential storage medium for hydrogen and other gases. These findings seem to be useful as a guideline and inspiration for the design and synthesis of other boron based complex hydrides for hydrogen storage.

The ternary and quaternary metal borides with a new cage structure compounds were synthesized from the elements [69]. They crystallize in the cubic system. Their crystal structures, determined by means of single-crystal XRD, are characterized by 3D frameworks of composition $Pt_{18}B_{12}$ or $Ir_{18}B_{12}$ approximating the shape of the periodic minimal surface. This framework separates 2 identical, interpenetrating labyrinths with large, 6-armed cages accommodating arrays of Ba or Li atoms, the latter combined with various other elements as well. In all compounds mixed or partially occupied sites were observed.

Metallaboranes constitute an attractive class of compounds intermediate between borane cages, on one hand, and transition metal clusters, on the other hand. While carbon substitution into a borane cage is rather common and gives rise to an entire class of metallaheteroborane compounds, other main-group atom substitution is rather rare. Theoretical calculations of DFT-type were carried out [70] to study the geometries, energetics and bonding properties in these compounds, aiming at completing their characterization, in particular establishing the exact number of hydrogens in the structures.

Ab initio HF calculations, extended by many-body perturbation theory corrections for electron correlations was made in [53] on 4 optimized structures of $Be(BH_4)_2$.

Stable positions of a metal ion relative to an icosahedral borane were found in [71]. It was considered a series of configurations of the neutral complex Mg – $B_{12}H_{12}$, including those in which the Mg is internal to the icosahedral B_{12} cage. A SCF MO calculation to determine the total cluster energy was carried out as the Mg atom is moved from the center of the borane to a position ~ 10 Å from the center (i.e., outside the borane cage). Two energy minima were found

as a function of position. One is outside the borane cage, at 3.0 – 3.5 Å from the center; the second is at the center of the borane cage. In the region in which Mg atoms near the plane of B atoms making up the triangular face are in equilibrium, authors were unable to calculate the height of the activation barrier for penetration of the Mg through the face. As for the central minimum, it was found to be deeper if Mg 3*d* orbitals are included in the basis set. There are known many atoms which have a low ionization energy and are, as ions, of appropriate "size" to fit inside a B_{12} cage. Incorporation of such ions into B_{12} cage in solids may offer significant flexibility in development of refractory boron-based semiconductors.

DFT-calculations have been performed to investigate the electronic structures of $B_{12}H_n$ cages up to $n \le 12$ and $AlB_{12}H_n$ up to $n \le 13$ [72]. Moreover, the computations has been extended to the charged clusters of $[B_{12}H_{12}]^q$, $[AlB_{12}H_{12}]^q$ and $[AlB_{12}H_{13}]^q$ where $q = \pm 1$ and ± 2. Their energetics was calculated and structural analysis has been carried out. Cage-form of the B_{12} remains stable against to hydrogen adsorptions. The binding energies of $B_{12}H_n$ and $AlB_{12}H_n$ are in a decreasing trend with n. The HOMO–LUMO energy gaps show that $B_{12}H_{11}$ has relatively higher chemical hardness, while $B_{12}H_2$, $B_{12}H_4$, $B_{12}H_7$ and $B_{12}H_{10}$ are the energetically more stable clusters. $AlB_{12}H_3$, $AlB_{12}H_8$, $AlB_{12}H_{10}$ and $AlB_{12}H_{12}$ clusters are also obtained as relatively more stable. In the charged $AlB_{12}H_n$ clusters structural orientations are observed for $n = 12$ and 13.

DFT has been employed to optimize the structures of AlB_n ($n = 1 - 14$) microclusters [73]. Analysis of the energetic and structural stability of these clusters and their various isomers were presented. Total and binding energies of the clusters have been calculated. Their harmonic frequencies, point symmetries, and the HOMO–LUMO energy gaps have been determined. Results were evaluated by comparing to the previous similar works. An Al atom single doped in hardly affects the shape of the host boron clusters. Further investigation may be needed to realize the truth of that the planar / quasi-planar metal-boron compound is more stable than any 3D isomers. The AlB_8, AlB_{11} and AlB_{13} clusters are of the magic sizes, i.e., these clusters possess relatively high stability among the AlB_n clusters up to $n = 14$. HOMO–LUMO gaps demonstrate the relatively higher chemical hardnesses at the AlB_8, AlB_{11} and AlB_{13} clusters. IP calculations show that AlB_9 also has a chemical hardness.

The change of the electron localization due to the occupation of an atom at the center of the boron-based clusters was quantitatively estimated in [46, 47] by using ELI-conception. The distributions of the ELI were compared for the pair of clusters $B_{48}H_{36}$ and $VB_{48}H_{36}$ and found that in the case of vanadium doping into B_{48} cluster surrounding the doping site, in β-B the electron density increases in some parts of the cluster and decreased in other parts.

To optimize hydrogen release from materials containing the BH_4^- anion requires an understanding of the thermal decomposition mechanism. In particular, it is important to identify any stable intermediates with a lower hydrogen-to-boron ratio that may form in the course of the decomposition of borohydrides. One such intermediate is the $B_{12}H_{12}^{2-}$ anion, which has been indentified in previous studies of borohydride decomposition. In [74], the transmission IR spectroscopy has been used to characterize the temperature dependence of the vibrational spectra of $LiBH_4$, $NaBH_4$, KBH_4 and $K_2B_{12}H_{12}$. The high symmetry of the icosahedral $B_{12}H_{12}^{2-}$ anion leads to only 3 IR active fundamentals, which are observed at 716, 1076 and

2485 / cm for $K_2B_{12}H_{12}$. Upon heating to 550 K, the IR spectrum of KBH_4 shows transformation into a new species with IR peaks at 716, 1074 and 2450 / cm. The changes in the spectrum provide good evidence for the formation of $B_{12}H_{12}^{2-}$ as an intermediate in the decomposition of the BH_4^- anion.

Within the last several decades there are considerable interests on bare boron clusters and clusters of their compounds due to extraordinary properties such as the ability to build highly strong and directional bonds with electron donor atoms. Boron can link 3 or more atoms due to hybridization of the valence s^2p electrons to sp^2 form. In [75], the recent studies on Al doped B_n (n = 1 – 14) and hydrogenated cage $AlB_{12}H_n$ clusters has been presented. In addition, continuing studies on TiB_n (n = 1 – 15) clusters and hydrogenated cage structures of $MB_{12}H_n$ complexes (for M = Ti, Cr, Fe, Co and for $n \leq 13$) were presented. For the computations of these systems DFT has been utilized. Energetic properties such as binding energies, HOMO-LUMO energy gaps and interaction energies of H, 2H, H_2 have been analyzed. Structural parameters, frequencies and point groups of the optimized geometries have been determined. One of these findings shows that the metal-coated cage structure of B_{12} is stable against to H-adsorption.

Synthesis techniques, including the transition metal-promoted oxidative fusion of boron cage compounds, allows the systematic construction of boranes, carboranes, and metalloboranes, which exhibit unusual structural features and / or properties such as cage fluxionality. Among them are carbon-rich carboranes and metallocarboranes having up to 14 cluster vertexes. Although these materials have complicated cage geometries, the study them is greatly facilitated by a powerful technique of 2D ^{11}B – ^{11}B NMR spectroscopy, which reveals the pattern of bonding within the boron framework. Based on these data, the multiple-decked sandwich complexes incorporating $R_2C_2B_4H_4^{2-}$ and / or $R_2C_2B_3H_5^{2-}$ carboranes units, transition metal ions, and planar aromatic hydrocarboranes had been prepared and characterized [76]. Species of this type exhibit high electron delocalization and may lead to new types of low-dimensional electrically conducting polymers.

To study the free and undistorted boron cage, a compound would be appropriate containing cations without considerable coordinating influence. Also, the absence of solvent molecules would be desirable. For this reasons, the crystal structure of the otherwise well-known compound $[N(C_2H_5)_3H]_2[B_{10}H_{10}]$ have been determined and characterized spectroscopically [77]. These findings were compared with data on new compounds with the closo-$[B_{10}H_{10}]^{2-}$-anion, $Rb_2[B_{10}H_{10}]$ and $Cs_2[B_{10}H_{10}]$.

Review on complex hydrides for hydrogen storage including tetrahydroborate ($LiBH_4$ and $NaBH_4$) and other borohydrides was given in [78].

2.4. Applications of boron and boron-based clusters

Although mostly observed in gas phase, pure boron clusters are promising molecules for coordination chemistry as potential new ligands and for materials science as new building blocks. The use of pure boron species as novel ligands has commenced, suggesting many new chemistries are ahead. Boron-based clusters can serve also as models to simulate silicon-based

materials. General properties such as high structural stability and high molecular boron content make the isomers $B_{18}H_{22}$ attractive compounds for ion-implantation of boron into silicon wafers in the making of p-type semiconductors.

Functionalized carboranes can feature extensively in the synthesis of polymers, ceramics, catalysts, and radio-pharmaceuticals.

Interest in the use of hydrogen as a transportation fuel has driven extensive research into novel gas storage materials. Many efforts have been focused on boron-containing hydrogenous materials primarily due to the light constitutional elements and the resulting high hydrogen storage capacities. Among many promising hydrogen-rich boron-containing materials ammonia borane NH_3BH_3 has received much attention because of its satisfactory air stability, relatively low molecular mass and remarkably high energy storage densities. However, the direct use of pristine ammonia borane as a hydrogen energy carrier in on-board / fuel-cell applications is prevented by its very slow dehydrogenation kinetics and the concurrent release of detrimental volatile by-products such as ammonia, borazine and diborane.

Metal borohydrides are also of interest as hydrogen storage materials as BH_4^- is 27 % hydrogen by weight. When the borohydride anion is paired with a light weight cation such as Li^+ or Na^+, the compound has a hydrogen weight percentage that is sufficiently high to be of potential practical importance for hydrogen storage. Boron and metallo-boron clusters have been actively studied, offering new opportunities for searching materials which are suited for the hydrogen storage.

Polyhedral boron compounds (boron clusters) are interested for creation of medicines for neutron capture therapy (NCT). Synthesis of these compounds is expensive and labour consuming because of necessary high enrichment degree with ^{10}B stabile nuclide. Therefore, information about influence of substitutes on biological properties of polyhedral boron compounds is too actual. However, systematic investigations of this problem was never conducted. In NCT clinical practice mercapto-closo-dodecaborate (weak acid of dodecaborate anion) is available. Two liposomal forms of medicines are widely used. These forms are capable to actively penetrate into tumor cells. Objects of studies presented in [79] were amphiphyle derivatives of boron cluster anions in the form of sodium salts. Obtained data are indicated that boron clusters derivatives with lipophylic substitutes of various structure are of moderate toxicity. The general targets of biological influence were organs of digestive system. It is possible that such feature of biological effect is generally caused by toxic influence of a lipid-like molecular fragment gave more significant contribution into toxicity of final compound.

Interaction of polyhedral boron compounds with albumin has been considered in [80]. The albumin is transport form binding xenobiotics and transferring their into liver for subsequent destruction and elimination of catabolic products from organism. Chemical compounds basing on polyhedral boron compounds are potential medicines for ^{10}B-NCT. These compounds are classic xenobiotics. Therefore, it is necessary to study an interaction of polyhedral boron with albumin for truly creation of extensive pharmacokinetic model. Such model would be described the features of polyhedral boron distribution in organs and tissues. It was developed the method of that investigation and the device for its realization. The base of

device consists of dialyzing camera possessing membrane with pores of diameter providing only polyhedral boron penetration through membrane and non-penetrated for albumin. There were presented the results of investigation of albumin binding with synthezied hybrid trisdioxymat-closo-borate complexes on the base of closo-borate anion, total formula is $Na_{12}CoN_6O_{18}C_{38}H_{120}B_{64}$. It is well water soluble, contains significant boron quantity (64 atoms) and is a chromophore center. The presence of transitive metal allows correcting of the obtained data in correlation of X-ray fluorescent analysis technique. The separate positive feature, capable to provide specific biological activity, is factor that complex is nano-sized object similar in its physical properties to negative charged lyposomes.

3. Structurally stabilized boron crystals

Boron crystalline structures are open networks (with many crystallographic voids) in which icosahedra can be linked together in a variety of ways. It is a reason, why icosahedron is the basic building block in the boron amorphous form too. In the Periodic Table, boron is neighbor of carbon and its chemical richness is second only to carbon due to its 3 valence electrons instead of 4. Boron and carbon independently have very stable structures formed from sp^2 hybridized bonds, but they have very different lattice structures. The preference for icosahedral B_{12} cluster amongst elemental boron and polyhedral boranes as well was elucidated by Jemmis & Prasad [81] based on an optimized overlap model. The ingenious ways in which elemental boron and boron-rich solids achieve icosahedron-related structures were explained by a fragment approach. Namely, the Jemmis' *mno*-rule was used to get the electron requirements: a polyhedral atomic structure with m polyhedra, n vertexes and o single-atom bridges between polyhedra requires $m + n + o$ electron pairs for stability. Intrinsic point imperfections, extra occupancies and vacancies, which are peculiar for β-B structures, were shown to be inevitable results of these electron requirements.

The structural connections between the compounds of boron and carbon have been extended using the *mno*-rule [81]. In particular, an interesting electronic structural relationship between the B_{84} fragment of the β-B and the fulleride anion, C_{60}^{12-}, is derived by replacing the 12 pentagonal pyramidal B_6^{4-} units by isoelectronic C_5^- units and removing the central B_{12} from the electron-deficient B_{84} unit.

The β-B and other icosahedral boron-rich solids, which are materials containing boron-rich units where atoms reside at 12 vertexes of icosahedra, are known for their exceptional bonding properties and corresponding unusual structures. Emin has described [83] how the unusual bonding generates other distinctive and useful effects in elemental boron and boron-rich materials. In particular, in boron-rich solids radiation-induced atomic vacancies and interstitials spontaneously recombine to produce the "self-healing" that underlines these materials' extraordinary radiation tolerance. Furthermore, boron carbide, the best-investigated icosahedral boron compound, possesses unusual electronic, magnetic and thermal properties. The charge carriers, holes, due to significant polaron effect (electron–phonon interaction)

should be localized as singlet pairs on icosahedral dangling bonds (the unusual origin of this localization is indicated by the absence of a concomitant photoionization effect). The thermally assisted hopping of singlet pairs, named as bipolarons, between icosahedra produced Seebek coefficient that is unexpectedly large and only weakly dependent on carrier concentration.

Starting from the statement that boron and boron-rich solids are strong electron–phonon coupling systems one can conclude that therefore they potentially have high-T_c superconductivity. Special superconductivity research on boron and boron-rich solids has been performed in [84, 85]. It was emphasized that for realizing high transition temperature T_c a careful control of the valence electrons is necessary, which requires detailed understanding of the electronic structure. By critically reviewing recent development in this field, along with the situation in heavily doped materials similar with boron by strong electron–phonon coupling, it was shown that a promising route to the high T_c in boron-rich system is doping. Although both α- and β-B become metallic and exhibit superconductivity at high pressure, the strong covalent character still remains, which significantly limits their T_c achieved by applying high pressure. Heavy doping is preferable, as long as the basic electronic structure is retained. But it is extremely difficult at normal conditions. A promising method to achieve this is high pressure synthesis. To design high-pressure experiment, the role of theory is important through predicting the phase diagram, which was constructed for boron by authors at the first time.

It was demonstrated by Schmechel & Werheit [86] that for β-B the concentrations of point structural defects and electronic gap states are quantitatively correlated. In this way the theoretically determined valence electron deficiencies are exactly compensated. The metallic character of these materials resulting in the theoretical calculations on hypothetical idealized structure is changed to the experimentally proved semiconducting behavior. Obviously, the structural defects in this crystal are the necessary consequence of the valence electron deficiency. It was also suggested that this correlation holds for icosahedral boron-rich solids too. Later the present knowledge of electronic properties and charge transport in icosahedral boron-rich solids were described in details [87, 88]. As it is known, B_{12} icosahedra or related structure elements determine the different modifications of elementary boron and numerous boron-rich compounds from α-B with 12 to YB_{66}-type with about 1584 atoms per unit cell. They are characterized by typical well-defined high density intrinsic defects: Jahn–Teller distorted icosahedra, vacancies, incomplete occupancies, statistical occupancies and antisite defects. The correlation between intrinsic point imperfections and electron deficiencies solves the discrepancy between theoretically predicted metal and experimentally proved semiconducting character. The electron deficiencies generate split-off valence states, which are decisive for the electronic transport, a superposition of band-type and hopping-type conductions. Their share depends on actual conditions like temperature or pre-excitation. According to H. Werheit, D. Emin's theoretical model of bipolaron hopping is incompatible with experiments.

Unusual structures and chemical bonds realized in pure boron and many boron-rich borides having local icosahedra in their crystals has been studied [89] by visualization of the electron density distributions. It was used maximum entropy method / Rietvald analysis of powder XRD-data in order to discuss the peculiarity of the chemical bonds. In α-B (α-B_{12}) and

its derivative crystals, peculiar covalent bonds, i.e., intra-cluster 3-center bonds and inter-cluster bent bonds have been observed. In β-B (β-B_{105}), the intra-cluster 3-center bonds were observed, but the inter-cluster bent bonds were not. The origin of these bonds can be explained by the mismatch in the directions of the bond and lattice vector (in α-B_{12}, the bond direction is parallel to the lattice vector).

It have been shown [90, 91] by DFT calculations that α-B is the most stable phase at low temperature among icosahedron-based boron crystals. This is consistent with low-temperature crystal growth of α-B. A problem of the calculation is, however, that the conclusion would be changed if defect states in β-B, which are observed in experiment, are taken into account. This urges to suspect the perfectness of α-B crystal. Then, it was investigated possibility of imperfections of α-B from the standpoint of crystal stability: intrinsic defects of vacancy and self-interstitials have been examined. Based on the total energy calculations, it was concluded that intrinsic defects are not present at a level above ~ 0.1 %.

From the experiments, another elemental boron form – the β-B structure of boron is known to be stable over all temperatures from absolute zero to melting. However, theoretical calculations found its energy to be greater than the energy of the α-B. Furthermore, the β-B form exhibits partially occupied sites, seemingly in conflict with the thermodynamic requirement that entropy vanish at low temperature. These issues were considered by Widom & Mihalkovič [92] using electron-DFT methods and an extensive search in the configuration space. It was found a unique, energy-minimizing pattern of occupied and vacant sites that can be stable at low temperatures, but that breaks the β-rhombohedral symmetry. Even lower energies occur within larger unit cells. Alternative configurations lie nearby in energy, allowing the entropy of partial occupancy to stabilize the β-B structure through a phase transition at moderate temperature. Corresponding transition temperature was estimated as 300 K. Thus, α- and β-B are closely related structures with nearly identical stability. Unlike α-B, in which every regular site is almost fully occupied, β-B is characterized by significant partial occupancies and intrinsic disorder. Optimizing the site occupation yields [93, 94] a superstructure of β-B boron that can be called β'-rhombohedral boron (β'-B). Its energy is lower than α-B, but its symmetry is lower than β-B. The configurational entropy of partial occupation drives above mentioned β' → β transition around the room temperature (~ 300 K). Comparing the vibrational density-of-states (DOS), one can find that β'-B has an excess of low frequency modes that are strongly localized around the partially occupied sites. The vibrational entropy of these low frequency modes adds to the configurational entropy of partial occupation to further stabilize the β'-B. It should be noted that the temperature 300 K of the structural β' → β transition in boron is only a crude estimate because of several approximations made: only the coupling of two primitive cells was considered; only a small fraction of all configurations within these two cells were taken into account; atomic vibrations (which contribute strongly to the free energy and must be included in any attempt to estimate an accurate transition temperature) were neglected. Besides, this transition may be difficult to observe experimentally because atomic diffusion is slow at this temperature.

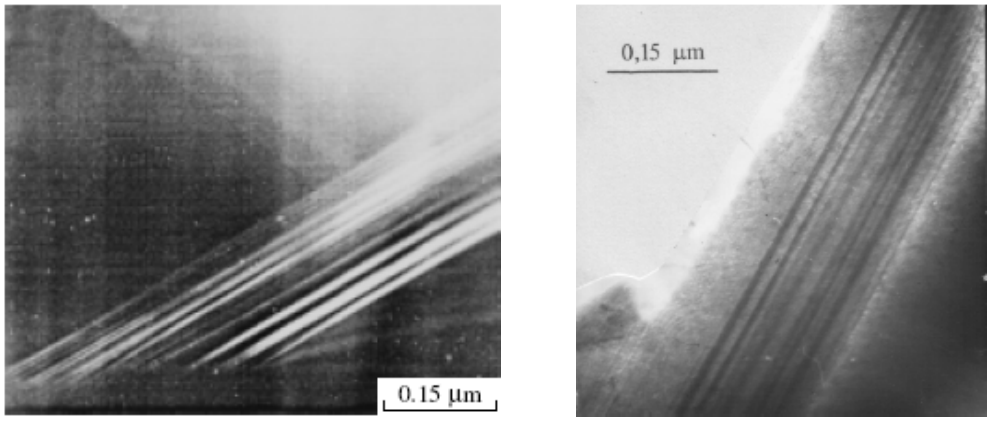

(1) (2)

Figure 2. Electron-microscopic images of (1) planar defects [100] and (2) polysynthetic twin packet [101] in single-crystal β-rhombohedral boron.

Nevertheless, around this value, at 290 K, we have indeed obtained [95-101] jumps on the temperature-dependences of the dielectric properties of β-B samples of various origins. The point is that the low-frequency charge capacitance for semiconducting boron samples proves to be "giant" – considerably higher than the geometrical value calculated from the sample sizes under assumption of material homogeneity. The explanation was found on the basis of the generalized barrier model for an inhomogeneous semiconductor within its 3-layer version. It seems that planar defects (stacking faults and polysynthetic twin packets) characteristic of real boron crystals (Figure 2) generate elastic stresses, which are sufficiently high for a local decrease in conductivity. In addition, the relatively low-conductive barrier layers can arise at the interfaces of these relatively low-conductive inclusions with a relatively high-conductive matrix. The step-wise behavior at ~ 290 K is indicative of the elimination for conditions of existence for low-conductivity barriers. The closeness of the intrinsic transition temperature ~ 300 K in the β-B structure with ~ 290 K measured for abrupt changes in β-B dielectric properties does not seem accidental. However, without detailed comparative analysis of the fine microstructure characteristic for β-B matrix and stressed inclusions, it is impossible to imagine how such transition promotes sample homogeneity by the concentration of hopping carriers.

4. Amorphous boron

4.1. Preparation techniques for boron amorphous films and powders

Early review on amorphous boron (a-B) preparation techniques as well as on its structure, and properties had been given in [102]. The Contents of this paper was restricted to amorphous films as opposed to the bulk (massive) form of a-B. However, a comparison between these two forms was carried out. It was emphasized that no precise definition of "amorphous" phase of boron exists. Though samples described as amorphous, therein degree of non-crystallinity or "amorphicity" is not clearly established. Among various thin-film-preparation

techniques – vacuum deposition, sputtering, liquid drop quenching and pyrolytic decomposition etc – vacuum deposition had proven to be the most satisfactory technique for producing amorphous films. The issues of structural and impurity analysis, electrical and optical properties, and high-field effects also were analyzed.

At the same time methods of preparation of a-B had been reviewed in [103]. The known methods of boron preparation leading to the high purity product had been divided into few groups: reduction of boron compounds by metals, hydrogen or other agents like the boron oxide, borax, metal borates, the halogenides (chloride, less frequently bromide, fluoride and iodide), and metal tetrafluoroborates, which can be used for the practical production; electrolysis; reduction in a plasma reactor; reduction in tubular electric ovens; reduction of boron halogenides in the reactor with incandescent filaments or rods; thermal decomposition of a boron compound (halogenides or hydrides). These reactions usually result in a mixture of amorphous and crystalline boron without distinctly marked structure.

In the first paper [104] by Mikheeva et al from the series of four papers, it was described reduction of the boron anhydride by the light metals. In addition to the borides of given composition (like the CaB_6 and AlB_{12}), it was formed amorphous phase with variable composition and quite high content of boron. Conclusion was made that the reduction with magnesium is practically most convenient way of producing of the a-B (in form of fine-dispersed powder composed of about 80 % boron with Mg as main impurity). Second paper [105] was especially devoted to the physical-chemical analysis of the reaction between boron anhydride and magnesium. Then, the product enrichment in boron by the vacuum distillation of magnesium from the "raw" a-B was considered [106]. It is an easy process. But, the removing of the oxygen, existing in a-B in form of lower oxides, needs long-term high-temperature annealing in vacuum close to the boron melting point [107] because the oxidation makes the particles' surfaces chemically non-active. Vacuum refinement provides with ~ 98 % purity a-B.

Elementary boron, probably with amorphous structure, had been obtained in glow discharge process as well [108].

Single crystal films of boron were prepared [109] by thermal reduction of purified BCl_3 with subsequent deposition of boron onto oriented silicon substrates: continuous α-B films about 10 μm thick were observed. But, if silicon surface was not smooth due to strains because of faceting or in case of rough surface, obtained boron films were "amorphous" – they were more irregular and revealed numerous protrusions. Films obtained at > 1000 °C or high pressures showed polycrystalline "ring" patterns.

A simple technique for deposition under vacuum of pure boron layers was suggested in [110]. It was emphasized that always exists a risk for contamination of the boron layers by evaporation of overheated electron gun components and pick-up from the support, or by evaporation resulting from scattered electrons heating parts of the vacuum enclosure. On account of this, high frequency heating had been investigated for the deposition of ultra-pure a-B layers.

Boron films on silicon and sapphire substrates were obtained [111] by the electron-beam heating in vacuum. According to the electron-diffraction studies, the films deposited on

substrates heated up to ~ 800 °C reveal amorphous structure. However, features of the diffraction pattern point on short-range order characteristic of an icosahedron and randomly distributed icosahedra. At 800 – 900 °C, formation of the crystalline – α-tetragonal boron – phase takes place. Annealing at ~ 1300 °C also transforms amorphous film into a crystalline form. One more method of obtaining of the metastable boron phases in form of thin layers is a liquid drop quenching technique [112]. By this method, 20 – 100 μm thick films with fine-crystalline structure were prepared. They are in general of β-B modification. But, very thin species showed amorphous structure according to XRD patterns.

Compact coatings of a-B were deposited [113] on smooth surface of massive substrates such as graphite, refractory metals, iron and stainless steel using the reduction of boron trichloride by hydrogen. The deposite morphology depends upon the physical aspects of the surface and is more regular on polished surfaces. It was shown 114] that non-crystalline – a-B layers grow thicker so long as the deposition rate is governed by chemical kinetics: chemical vapor deposition (CVD) brings more rapidly. It was found that on a carbon substrate boron begins to grow in the form of spheroidal nodules attached to the substrate. The drops of a-B are B_{12} clusters in α-B crystal order. In the thin layer of a-B an aggregate of tetragonal crystals is also nucleated. To obtain a flat area of a-B by CVD, the most important conditions concern the mass transportation of the reactant. The average time after which there is a nodule probability of crystallization decrease sharply when deposition temperature increases.

Process of preparation of boron film by the hydrogen-assisted reduction of boron trichloride BCl_3 in glow discharge was specially investigated in [115]. The deposition starts at ~ 900 °C, but obtained films are loose with poor adhesion with substrate. Actually they are a-B powders. At ~ 1000 °C, crystallization increases, but one can still find drop-like outgrowths of a-B. At higher substrate temperatures, the highly disordered micro-crystalline structure of the α-tetragonal boron with large residual stresses is formed.

Boron films were prepared [116] on Ti substrate by an ion plating – physical-vapor-deposition (PVD) method. Electron microscope studies of the film morphology showed that the properties of these films depend on the deposition rate and the substrate temperature.

The factors influencing the morphology of boron prepared by CVD in a closed system were specially investigated by Carlsson [117]. The formation of amorphous or crystalline deposites was found to be confined to well-separated regions defined by temperature and deposite rate of supersaturation. In the temperature range 1390 – 1640 K, a-B is formed at deposition rates higher than that given by relation $1.59 \cdot 10^6$ [μg / cm^2 · s] exp (–20070 / T[K]). At temperatures lower than 1390 K, a-B is formed at considerably lower deposition rates. Other technological conditions lead to the simultaneous growth of amorphous and crystalline boron. Heat treatment of a-B in vacuum in the temperature range 1270 – 1520 K results in the formation of β-B via the formation (by a sublimation / condensation mechanism) and subsequent decomposition of α-B. Then, the origin of various morphologies of the boron deposite was discussed [118] in connection with schematic kinetics-curve. Although the borderline between the amorphous and crystalline morphologies is fixed, the kinetics-curve can be moved to higher and lower deposition rates and to higher and lower temperatures. This

consideration was based on the investigation of the deposition rate of boron in a closed chemical system (namely rate of the CVD from a hydrogen–boron trichloride mixture, which is a complicated heterogeneous reaction) and various methods for the determination of deposition rates. Two theoretical models – quasi-kinetics and diffusion – for interpreting available boron deposition rate data from a closed CVD systems, were developed and successfully applied [119].

Pure and hydrogenated a-B films can be prepared [120] by the method employing plasma deposition of the electron-cyclotron-resonance and borane–hydrogen mixture, B_2H_2 plus H_2 (it is a technique for thin-film synthesis with many useful features).

Boron thin films were deposited by electron beam evaporation and by pyrolysis of decarbone on quartz glass substrates [121, 122]. The thickness of a film was about 0.7 μm. Films' structural characterization by X-ray and electron beam diffractions showed that they were α-B. Spectra of carbon almost disappeared after 10 min ion-etching with argon. It seemed to be more difficult to remove the oxygen from the surface of the boron film. The oxygen concentration was estimated to be about 5 %. Oxygen seemed to exist mainly at the grain boundaries.

Boron films with good quality with the aid of photo-CVD process was prepared [123, 124]. The reactant gas B_2H_6 (~ 1 % in H_2) was used. The films were grown on a single-crystalline Si plane and silica glass at various growth temperatures of 600 – 1000 °C. Obtained boron films showed both an amorphous structure and crystalline grains with sizes increased in increasing growth temperature. The activation energy for the film growth 0.14 eV for thermal CVD process decreased to 0.043 eV by using photo-CVD, which demonstrated the decomposition and excitation of B_2H_6 by deuterium lamp with radiation wave length of 115 – 400 nm. The electrical properties of boron films on silica glass showed that those obtained by photo-thermal CVD process have lower concentrations of holes and higher mobilities than those obtained by thermal CVD process. Then, Kumashiro et al prepared boron films on silica glass substrate [125, 126] by solid source molecular beam deposition (SSMBD) and gas source molecular beam deposition (GSMBD). The growth experiment was performed with cracked B_2H_6 at 300 °C under a vacuum for the deposition, where the substrate temperature of above 500 °C is necessary to desorb hydrogen from growth surface. Finally, it have been prepared [127, 128] electrodeposited boron wafers from the molten salts with $KBF_4 – KF$. The experimental apparatus consisted of graphite crucible for anode and Ni plate for cathode. Magnetic field was applied perpendicular to crucible to form homogeneous molten solution for obtaining uniform wafers. After $KBF_4 – KF$ powders were melted at the ~ 680 K, boron was deposited on the Ni plate. Then, boron wafers was peeled from these plates. XRD pattern of the boron wafers revealed their amorphous structure.

Relatively recently, for the first time a-B has been obtained [129] by using Soxhelt method: after heating the mixture of boron oxide B_2O_3 and magnesium Mg in appropriate amounts at 750 °C in a tube-furnace under argon atmosphere. The mixture obtained by heating was subjected to a purification procedure in Soxhelt apparatus with 6 M HCl. The dissolution off side products with concentrated acid was speeded up and also the purification procedure time was minimized (down to 3 – 4 h) since the product was reacted with pure acid solution in each cycle with the aid of Soxhelt apparatus. B_2O_3 and Mg (1 : 2.3 mole ratio) were mixed and

pellets were formed by 3 metric tons pressure and heated for 2 h at 750 °C under argon atmosphere. The obtained product was grinded to smaller size to increase the surface area for better dissolution of the side products. As a result, 93.1 % pure a-B was obtained by washing with 6 M HCl solution 3 times again in the Soxhelt apparatus.

There are some reports on boron films containing high concentrations of impurities. Samples of a-B films containing up to 16 at % carbon were formed [130] on fused silica substrate by an electron-beam deposition technique. Carbon was added to the samples during deposition by introducing acetylene through a leak valve. Aiming to obtain MgB_2 thin films, boron thin films were deposited [131] by using thermoionic vacuum arc technology on the Mg surfaces deposited on the glass substrate applying both sputtering and thermal evaporation methods. Thickness of the grown thin boron film was measured approximately as 1 μm. Boron–silicon amorphous films were prepared [132] by pulsed laser deposition technique. The nanoscale samples containing boron and iron were obtained [133] through chemical reactions (wet-chemical synthesis) of boron and iron sources in solutions at low temperatures. XRD revealed the amorphous character of these nanoscale products.

In review [134], discussions of fundamentals on pure boron formation leads to the following: boron being a solid with a very high melting point usually forms a powdery material. Since there is no medium for its growth in the rapidly solidified form it is amorphous in nature. In cases, where the feed material are gases (boron chloride plus H_2 or borane) boron is the only solid product. Its crystallinity is found only when ultra-high temperatures are available as in plasma or arc processes. The understanding of above fundamentals and thermo-chemical calculations indicate the possibility of forming pure boron element in molten chloride melts by metallothermic reaction of purified boron tri-chlorides. Such processes may be more economical than hydrogen-reduction of boron halides on hot filaments, as heat dissipation control is much easier in a molten salt medium.

4.2. Crystallization of amorphous boron

Process of crystallization of amorphous boron had been studied [135] within the temperature range 800 – 2200 °C in argon atmosphere. In general, gas-transport reactions yield amorphous boron (< 800 °C), α-B (800 – 1100 °C), mixture of non-stoichiometric borides and tetragonal boron (1100 – 1500 ºC), and β-B (> 1500 °C). When heated in argon environment, a-B can be transformed into α-B, but in vacuum it usually prefers β-B structure. a-B can be considered as very fine microcrystalline β-B with short-order determined by boron icosahedra. Thus, crystallization of a-B should be treated as ordering process of the icosahedral groups.

Transition of the a-B in crystalline state was specially analyzed by Pirtskhalaishvili et al [136]. It was stated that reduction of boron from its halogenides depending the reduction temperature, deposition rate, pressures of reacting gases, and impurity composition yields the different structural modifications of boron: below ~ 800 °C – amorphous; above ~ 1100 °C – crystalline; at higher temperatures – even single-crystalline. It was found that heating of the a-B leads the transition to α- and β-B and such transitions depend on initial product purity and its

annealing. Both a-B obtained by electrolysis or diborane reduction transformed into β-B with heat of transformation ~ 0.4 kcal / g · at.

An investigation of processes of structure change in thin boron films, which occurs under the influence of space-charge-limited-currents (SCLC), was performed in [137]. Initial a-B films of ~ 3 μm thick were deposited on pyroceram substrates by the thermal evaporation of a polycrystalline boron rod in vacuum and Au – B – Au film-structures were formed to obtain current–voltage characteristics at various temperatures. It appeared that the boron film structure (morphology) changed under the influence of electric fields of ~ 10^4 V / cm: the structure ordering took place.

Crystallization of a-B needs existence of the crystallization centers. This issue was considered [138] based on XRD study of the atomic radial distribution function (ARDF) in powders of a-B of various origins.

The transition of a-B into crystalline state was also investigated [139] by differential thermal analysis (DTA) at different heating rates. Obtained DTA-curves were transformed into transitional kinetic relation using the heat balance equation. Thermodynamic equations for formation processes of α- and β-Bl boron from a-B were also obtained. As a result a metastable diagram of elementary boron was constructed, which determines the regions of existence of amorphous and crystalline phases.

An investigation of sintering kinetics of boron was presented in [140]. The influence of powder size distribution on the temperature-dependence of sintering, reaching a high final density, and gaining a homogeneous grain size had been shown. The maximum sintering density was reached as the process was managed under conditions providing the successive a-B → α-B → β-B phase transitions in boron. The results of sintering of boron pellets compacted by explosive compression were considered. It was found that exposing–sintering process produces pellets of a-B and α-B.

Some characteristic features of the technology of producing α-B by the amorphous powder's crystallization were also considered [141]. Powder samples were heated to 1000 °C in a high-temperature resistance furnace and then the rate was reduced. After these heating processes, pyrolytic a-B transforms to α-B. Electrolytic a-B starts to crystallize at 1150 °C to β-B without going through the intermediate α-B phase. The investigation of the influence of impurities on the crystallization of a-B showed that carbon is more unfavorable than metallic impurities, preventing the formation of the α-B. Though the powders of pyrolytic and electrolytic a-B are distinguished by purity (electrolytic boron is more contaminated), the investigations performed lead to the speculation that the crystallization process is influenced by the short-range of the atoms of the initial powders rather than by the impurity content. In connection with this, one can note an early special method of spectrographic analysis of high purity a-B developed in [142]. It allowed the simultaneous determination of 32 element impurities in a-B with a sensitivity of 0.00003 – 0.01 % and relative error of 6 – 20 %.

Relatively recently, the problems of adaptation and application of synchrotron radiation diffraction in the study and structure determination of the solid phase products obtained during the thermal decomposition of gaseous diborane, higher cluster boron hydrides, and their

derivatives and metal-derivatives of ortho-carborane were discussed [143]. It was demonstrated that thermal decomposition process for the preparation of phases of boron proceeds at relatively low temperatures of 500 – 900 °C with formation of a-B, containing nanostructural elements. Based on a brief review of standard methods of preparing of a-B a conclusion has been made that boron, which is a refractory material, obtained at high temperatures should be mainly a crystalline product. Thus, a-B has to be produced at relatively low temperatures.

4.3. Amorphous structure of boron

As a close model for the a-B films structure can be considered that for the liquid boron (lq-B). The negative volume change of boron on melting and relatively low surface tension of lq-B should be accounted for the preservation of the icosahedral structure characteristic for boron crystalline modifications in liquid phase. A model of the structure of lq-B was built by Khantadze & Topuridze [144] using boron icosahedron as the constructional element. The arrangement of B_{12} icosahedra in the structure of β-B as well as their random, chaotic distribution were found to give an almost identical loose filling of space. As a result it was concluded that icosahedron is presented as a structural unit of the liquid phase. Thus, lq-B may be considered as a disordered mixture of icosahedra, whereas a-B, including films prepared by vacuum vaporization or by quenching from the liquid state, should be considered as a disordered packing of icosahedra.

Five-fold symmetry in liquids was considered in [145]. It was stated that a complete description of the structure of simple liquids, like the melted boron, was missed from understanding of condensed matter. But, new observations showed that liquids contain many configurations with five-fold symmetry. Understanding the structure of simple liquids is a fundamental, unsolved problem in the mathematical and physical sciences. Attempts to describe liquids theoretically as disordered crystals have failed, and their description as dense gases (fluids) remains too complex. On other hand, there are only a few experimental measurements on lq-B due to the fact that it is extremely reactive with any container. Electrostatic levitation in vacuum prevented contamination and multibeam heating overcame sample position stability problems occurring when handling boron at high temperatures. This allowed the density determination of the liquid as well as the high temperature solid states.

An *ab initio* molecular-dynamics simulation of lq-B was presented in [146]. At the density ~ 2 g / cm^3 and the temperature ~ 2600 K, icosahedra are destroyed although atoms still form an open packing with 6-fold coordination. Moreover, it was found that most 3-center covalent bonds, which make the α-B phase semiconducting, are destroyed. Furthermore, the estimated electrical conductivity shows that boron undergoes a semiconductor-to-metal transition on melting, in agreement with the previous scarce experimental information.

The structure factor and the pair distribution function has been measured for lq-B in the temperature range 2600 – 2000 K, extending over both the normal and supercooled liquid states [147]. The bond length and coordination number of the first coordination shell are similar to those reported for the crystalline and amorphous solid forms, but the second and third

coordination shells are broader and shifted to higher distances. The insulator–metal transition that takes place in boron upon melting is associated with a relatively small change in both volume and short-range order. Previously, the structure of solid and liquid boron was simulated on a computer and concluded that these icosahedra were destroyed upon melting. This result contradicted some indirect evidence that this unusual material maintains some short-range order in the liquid state. The presence of icosahedra would affect properties like the electrical conductivity of lq-B. Experimentally it has been found that at short length scales, the structure of lq-B is similar to its nonicosahedral solid forms, a comparison that the computer simulations did not address. The similarity is surprising because as a solid, boron is an insulator, while as a liquid, it behaves like a metal. But authors were unable to conclusively determine whether icosahedra remain intact above the melting temperature (whether lq-B contains icosahedra).

Over the 2275 – 2460 K interval, the density of the liquid and undercooled phases of boron was measured as $2.17 \cdot 10^3 - 0.25\ (T - T_m)$ kg / m^3, where T_m is the melting temperature (2360 K) [148]. Similarly, the density of the solid phase was measured over the 2010 – 2360 K range as $2.11 \cdot 10^3 - 0.09\ (T - T_m)$ kg / m^3. These data provided clear experimental evidence that boron contracts (nearly 3 %) upon melting.

Okada et al have designed [149] the electrostatic levitation chamber for X-ray scattering experiments (XRD and Compton scattering on lq-B were obtained).

The electrical conductivity of levitated liquid elemental boron was measured near the melting point using a contactless electrical conductivity technique [150]. A phase change is clearly detected in the course of laser heating of a 2 mm diameter boron sphere levitated aerodynamically. The value obtained for the electrical conductivity sets lq-B among the liquid semiconductors and establishes that the semiconducting behavior survives the melting process contradicting an earlier report that a semiconductor-to-metal transition occurs.

The density, surface tension, and spectral and total hemispherical emissivities of lq-B obtained with contactless diagnostics were reported for temperatures between 2360 and 3100 K [151]. It was shown that, contrary to some previous expectations, lq-B is denser than the solid at its melting point. It is also shown that the high total emissivity of 0.36 is not consistent with that of a liquid metal as claimed. Finally, good agreement is found with previously reported surface tension and spectral emissivities of lq-B.

A comprehensive study of lq-B with X-ray measurements of the atomic structure and dynamics coupled with *ab initio* molecular dynamics simulations has been performed in [152]. There found no evidence of survival into the liquid of the icosahedral arrangements that characterize the crystal structures of boron but many atoms appear to adopt a geometry corresponding to the pentagonal pyramids of the crystalline phases. Despite similarities in the melting behavior of boron and silicon, there is the evidence of a significant structural shift with temperature that might suggest an eventual liquid–liquid phase transition. Relatively poor agreement with the observed damping of the sound excitations was obtained with the simple form of mode-coupling theory that has proved successful with other monatomic liquids, indicating that higher-order correlation functions arising from directional bonding and short-

lived local structures are playing a crucial role. The large ratio of the high frequency to the isothermal sound velocity indicated the much stronger viscoelastic stiffening in lq-B.

Viscosity of lq-B was measured over the temperature range from 2325 to 2556 K using an electrostatic levitation method combined with an oscillation drop technique [153]. The results obtained revealed that the viscosity increases slowly with decreasing temperature from 2.2 mPa · s at 2550 K to 2.6 mPa · s at 2370 K, and substantially increases with further decrease in temperature below the melting temperature (2360 K), becoming as large as 6.4 mPa · s at 2325 K. Such behavior suggests that clusters with extension may appear in supercooled lq-B.

As it was mantioned above, until recently there have been few experimental measurements on lq-B since it reacts with a container. But, the advent of levitation techniques made possible to handle a sample without contamination and to carry out the measurements on the physical properties of lq-B in the temperature region down to the supercooled state. These results have been in brief reviewed in [154]. Density measurements have revealed that boron contracts by nearly 3 % upon melting. By the measuring of electrical conductivity of lq-B, it has been shown that the semiconducting property remains even in the liquid state. XRD and inelastic X-ray scattering measurements on lq-B were carried out in order to address the question whether B_{12} icosahedral units may survive into the liquid state. No evidence has been obtained on the survival of the icosahedral units into liquid. *Ab initio* molecular dynamics simulations of lq-B also suggested that icosahedral arrangements are destroyed upon melting. Both of these experimental and simulation studies seem to strongly deny the existence of B_{12} icosahedral units in lq-B. Instead, there still remains possibility that small clusters such as pentagonal units could exist in lq-B. In the more deeply supercooled state of lq-B, if realized, it is expected that small clusters may be connected together and grow larger. Authors of review have succeeded themselfs to measure viscosity of lq-B over the temperature range from 2325 to 2556 K. The results obtained revealed that the viscosity increases slowly with decreasing temperature from 2.2 MPa · s at 2550 K to 2.6 MPa · s at 2370 K and substantially increases with further decrease of temperature below the melting temperature (T_m = 2360 K), becoming as large as 6.4 MPa · s at 2325 K. The increase of the viscosity suggests that clusters with extension may appear in supercooled lq-B. At first glance, such observation coincides with above mentioned existence of small clusters with pentagonal structure which could appear in the lq-B above the melting temperature (~ 2400 K) and also in supercooled state at 2340 K. It is noticed, however, that the temperature dependence of viscosity of lq-B still follows the Arhenius' equation in the temperature range where the XRD measurements were made. Therefore, the substantial increase of the viscosity in the supercooled lq-B observed in the lower temperature range might be caused by the other origin except for the pentagonal unit. In the supercooled states below 2325 K, the growth of clusters could be favored resulting in the substantial increase of viscosity: the pentagonal units could be connected each other and grow largely and the life time of such large cluster could be long enough to increase the macroscopic viscosity as observed in the present experiments. It is possible that quenching the supercooled state of lq-B could lead to the formation of new metastable phase of boron.

The structure of evaporated boron films was studied [155] by electron diffraction. These films gave a typical amorphous pattern: 11 halos were observed. Both ARDF and the intensity comparison methods were applied to analysis of the data obtained for these thin films of boron prepared by the method of vacuum deposition. Bond distances similar to those appearing in the crystalline forms of boron were found in the evaporated film. The B_{12} icosahedra which are the structural entities common to all modifications of crystal boron existed also in the film. However, the arrangement of the icosahedra was found to be quite random. It was determined following B – B bond lengths: 1.78 (within an icosahedron), 1.70 (between icosahedra), 1.60 (between icosahedral and isolated atoms), and 2.00 Å (so-called Δ-bond). The deviation of the B – B bond length within icosahedron may originate from the fact that 1.78 Å is a mean value of the B – B distances in nearly regular icosahedra in the film, considering that it ranges from 1.73 to 1.83 Å even in crystalline boron.

The ARDF of non-crystalline boron had been computed [156] from intensities of diffracted X-rays. It was investigated boron deposites from the reduction of BCl_3 with H_2 at 1000 – 1200 °C which occur as powders, irregular plates, and aggregated needle-like crystals. Such non-crystalline forms of boron had been interpreted on the basis of α- and β-B crystalline structures. Usually, so-called a-B appeared in the form of irregular plates with metallic luster. The spherical growth was found to be characteristic of this form of material. Coordination numbers of maxima at ARDF were estimated as 6.6, 17.5, 8.0, 33.6, and 85.0. From the well defined maxima at 1.8 and 3.1 Å one can assume that in these specimens the icosahedral arrangement of boron existed in spite of the disordered non-crystalline structure. It should be considered as a metastable form of boron – the ordering occurs only above ~ 1200 °C, when β-B grains starts forming. It was found useful to compare results obtained for a-B with those for α-B. Half of atoms in an icosahedron in α-B structure are bound by a 3-center bond to neighboring icosahedra. Each of these atoms has 5 neighbors in the icosahedron at 1.73 – 1.79 Å, and 2 neighbors in a neighboring icosahedron at 2.03 Å. Remained atoms in the icosahedron are linked with the neighboring icosahedra by covalent single bonds and has 6 neighbors at 1.71 – 1.79 Å. In the second coordination space there are 17 atoms at 2.9 – 3.3 Å.

Results of the electron-diffraction studies performed on a-B films obtained by the atomization of the pressed crystalline boron tablets were suggested in [157]. The first 2 maxima on the ARDF-curve are placed at 1.75 and 3.00 Å with coordination numbers 5.6 and 17.0, respectively. As it is known, in crystalline β-B there are 5 intra-icosahedral bonds each 1.805 Å in length, and 1 inter-icosahedral bond 1.680 Å in length. Thus average value equals to $(5 \cdot 1.805 \text{ Å} + 1 \cdot 1.680 \text{ Å}) / 6 \approx 1.784 \text{ Å}$, what is close to the obtained radius of the first coordination sphere. The structure of boron films prepared by liquid drop quenching techniques was described in [158].

Boron films (~ 20 μm in thick) condensed on metal substrates was investigated in [159]. Main goal of this investigation was the determination of the nature of small-angle scattering by the electron density heterogeneities in an amorphous film in comparison with a polycrystalline one. Such scattering centers in a-B are more non-equilibrium than in polycrystals. They were found to have an elongated shape and be oriented approximately as incident molecular flux.

They are more poly-dispersive. Their volume concentration makes up ~ 1.7 %, while sizes were estimated as ~ 450 (longitudinal) and ~ 100 Å (transversal).

The purest a-B may be prepared by the gas-phase deposition, in particular, by pyrolysis. a-B can not be obtained by the super-cooling of melt because it transforms into liquid state only through crystallization process. Consequently, in this case transformation temperature coincides with crystallization temperature. Comparison of the temperature-dependences for excess-entropies of two states yields that second-order phase transition in boron takes place around 1200 K [160]. Pre-crystallization changes in a-B include insignificant relative displacements of icosahedra. As it is known $T_{Phase\,Transition} \approx 0.8\,T_{Transformation}$. Thus, temperature of crystallization of the a-B can be estimated as 1500 K, which is in good agreement with inflection point at the entropy–temperature curve.

It was found [161] that boron films (900 – 1000 Å in thick) obtained by the vacuum sublimation on various substrates of the zone-melted boron crystals in most part were characterized by the amorphous structure. Interatomic distances detected frequently are 1.78 and 2.88 Å, i.e. almost the same distances which are characteristic of boron icosahedron. Consequently, at the first icosahedra should be formed. a-B obtained at higher temperatures can be imagined as mix of various boron modifications with icosahedral structures.

The structure of vacuum-deposited thin films of boron and boron films prepared by a rolling technique from the liquid state was investigated in [162]. From structural and electron microscopic studies it was shown that, depending on the substrate temperature, the structure of thin films changes from amorphous to crystalline, but the structure of films formed by a rolling technique remains as that of β-B. Boron films prepared by vacuum evaporation technique on different surfaces (polyamide, rock-salt, mica, quartz etc) without preliminary heating had an "amorphous" structure. The heating above ~ 800 °C gave possibility of preparing crystalline state – red α-B. The X-ray and metallographic investigations of the morphology and structural imperfections of liquid-rolled films of boron showed that the structure of these films is β-B with significant imperfections of the lattice, and the presence some amorphous phase is suspected.

Palatnik et al [163] studied the structure of condensed boron films. Films were prepared by the electron-beam vacuum evaporation and condensation method using Ta and Nb substrates preheated up to 300 – 1200 °C. At < 650 °C, diffraction patterns showed only 7 halos, which is characteristic of amorphous structure. According to the ARDF, first maximum is located at 1.75 Å with coordination number of 6.5 – 7.0 atoms. These values are in satisfactory agreement with mean bond length in an icosahedron 1.78 Å and mean coordination number in a boron crystal. At 650 – 700 °C, in addition to halos one can find a line characteristic of fine-crystallized tetragonal boron. At 730 – 900 °C, it exists only tetragonal boron structure without amorphous inclusions, while at 1100 – 1200 °C, the condensed material reveals structures characteristic of β-B and boride inclusions. Annealing at ~ 1000 °C transforms tetragonal structure at first into α- and then into β-B. Annealing at temperatures higher than ~ 1400 °C transforms all films directly into β-B. Palatnik et al also considered [164] the polymorphism, substructure, and short-order in a-B films. Further, it had been once more described [165] the structure of the a-B films.

Structure and electrical properties of boron films prepared by the vacuum condensation method [166] were found to be dependent on preparing conditions. At relatively low temperatures, when substrate temperature < 620 K, it was obtained randomly orientated boron icosahedra. But, at higher temperatures, one can find some short-ordering analogous that in meta-stable tetragonal modification B_{50}, and stable boron crystalline modifications as well.

The electron microscopic study of the a-B structure had been performed by Kervalishvili et al [167] too.

Results of the XRD study of the ARDF in powders of a-B of various origins were analyzed in [138]. Radii of coordination spheres and corresponding coordination numbers found are as follows (values after thermal treatment are given in parenthesis): pyrolytic boron – 1.75 Å and 5.8 (1.75 Å and 6.0), 3.15 Å and 16.1 (3.20 Å and 17.8), [none] (3.70 Å and 4.0), 4.55 Å and 32.3 (4.50 Å and 31.3), 5.75 Å and 53.1 (5.85 Å and 60.5); electrolytic boron – 1.8 Å and 6.5, 3.5 Å and 23.0, 4.3 Å and 7.5, 5.1 Å and 33.7, 6.3 Å and 55.2. Comparing parameters obtained for first and second coordination spheres, it is possible to make a conclusion that boron atoms in a-B are bounded in icosahedra. From their part, icosahedra can be linking in various ways different from linking in any crystalline modification of boron. Besides, the character of "amophicity" of specimens differs one from another: sub-structure (short-order) of the pyrolytic a-B films differs from that of the electrolytic films. Both of them are heterogeneous, but pyrolytic boron looks more like α-B, while electrolytic boron – like β-B.

The short-range order structure of a-B was studied by Kobayashi [168]. Three sample materials of different appearances – film, whisker and fiber, were prepared by CVD by the reduction of BCl_3 with hydrogen. The reduced ARDF derived from XRD or electron diffraction patterns were found to be almost identical among three samples. The reduced ARDFs were compared with those calculated for the four crystalline modifications of boron, i.e. α-B, α-tetragonal, β-B and β-tetragonal boron. The reduced ARDFs of a-B were found to be similar to those of the β-B and β-tetragonal boron. From the similarity of physical and chemical properties and co-existence in deposition, the short-range order structure of a-B was shown to be closer to that of the β-B modification.

In [169], the structure of a-B was investigated with pulsed neutron diffraction technique. The experimental static structural factor and derived ARDF support a model based on building blocks of B_{12} icosahedra resembling those found in β-B, but with disorder occurring in the linking between these subunits (some earlier neutron diffraction studies based on reactor data also showed that the structure of a-B should be closely related to that of crystalline β-B, which consists of a complicated arrangement of icosahedral subunits; however the limited wave vector, ≤ 10.3 / Å, did not permit the derivation of a meaningful radial distribution). Because of the very large cross section of neutron capturing by boron ^{10}B isotope, such experiments can be performed only reducing its concentration. Identical measurements were made for an a-B sample consisting of 99.1 % ^{11}B contained in a metallic cylinder and powder sample of the 97.1 % isotopically enriched crystalline β-^{11}B. An overall qualitative comparison of structural factors for both samples strongly suggested that the amorphous and β-B structures are closely

related. In addition to the amorphous phase itself, the intensity data indicated that the "amorphous" sample may contain up to ~ 5 % of a mixture of crystalline α- and β-B.

Authors made simple model calculation in order to simulate the most important features in the a-B. Icosahedral units of B_{12} were assumed to be hard spheres in a random-packed arrangement (as earlier it had been done for molecular glasses). The model structural factor was calculated using hard-sphere diameter 4.8 Å and a packing fraction 0.45. The first diffraction peak at 1.5 Å was reproduced as well as a significant contribution to the largest peak at 4.2 Å. However, only little contribution to the second peak at 2.5 Å was found. This model reproduced a significant part of the oscillations at large wave vector due to short-range order within an icosahedron. Based on the effective ARDF calculations, coordination numbers were estimated. Coordination number of about 6 for the first coordinated sphere centered at 1.8 Å was found in both amorphous and crystalline cases. The a-B had about 15 atoms in the second sphere at 3.0 Å which is a slightly larger distance than for the model. This similarity supports the existence of the icosahedron as a subunit in a-B. Additional maxima appeared at radial distances of 4.7 and 5.8 Å which describe the medium-range order in the amorphous structure. Disorder occurs in the linking between icosahedra which seems to be not entirely random at medium-range distances in a-B. There seems to be no questions of the amorphous nature of vacuum deposited boron: these boron films usually consist of randomly orientated icosahedra; the estimated atomic spacing is similar to the crystalline material; the calculated coordination number of boron films is approximately 6, again in agreement with the crystalline material. The fact that short-range order is maintained accounts for the semiconducting nature of a-B.

Morphology and structure of powder particles of elementary a-B before and after following thermal treatment in vacuum at ~ 800 °C for 30 min were investigated by Kutelia et al [170] applying the method of high resolution electron microscopy (HREM). Configurations consisting of several icosahedra were found to represent the structural element of powder particles. It was studied freely-growing particles of the a-B powders prepared by plasma-chemical reduction of the boron trichloride by the hydrogen. Their special feature is a round elliptic shape with 2D structure: ratio diameter to the thickness is as ~ 20 : 1. Icosahedra were found to be randomly placed in habit-layer of particles correlating only with nearest neighbors. Short-range in a-B was studied using integral-analysis method allowing computing of the ARDF based on the Fourier-transformation (FT) of the electron-coherent-scattering intensities. Obtained coordination spheres' radii and corresponding coordination numbers are as following: 1.80 Å – 6.44, 3.00 Å – 16.8, 3.76 Å – 10.6, 4.40 Å – 23.0, and 5.76 Å – 35.0. The first 3 maxima are in good agreement with those in rhombohedral and tetragonal modifications of boron, in particular, with β-B. Thermal treatment yielded coagulation of icosahedra in spheroids with diameters ~ 20 – 50 Å. Thus, ultra-dispersed powder of the elementary boron is characterized by amorphously structured particles composed of statistically distributed icosahedra and their coagulations. Heating raises their diameters almost twice. Structure remains in whole amorphous, but within the local regions there were obtained crystalline structure characteristic for β-B. At temperatures higher than ~ 800 °C the crystallization takes place. Thus, icosahedra serve as simplest structural units, which form stable plane amorphous aggregates.

The ARDF method for the determining of the a-B structure was developed by Nakashidze [171]. Using this method, the inter-icosahedral bonds were shown to be directed along the 3-fold symmetry axis. The number of the nearest neighboring icosahedra was found to decrease with thermal treatment of boron. Both a-B films and powders are constructed from the randomly orientated and bounded icosahedra in structure close to tetragonal boron structure. Additional information gave absorption-curve analysis and its comparison with theoretical curves for various models of scattering particles. If R_1 denotes interatomic distances between neighboring atoms, atoms of the next coordination spheres will be placed at $R_2 \approx 1.618\ R_1$ and $R_3 \approx 1.903\ R_1$. The particles can exist in form of pentagons, pentagonal pyramids, polyhedrons B_{10}, and icosahedra B_{12}. Then, Nakashidze devoted a special investigation [172] to the boron amorphography – crystallographic properties of a-B. It was emphasized analogy with quasi-crystals, which are intermediate species between periodical crystals and amorphous solids. a-B powders of various origins were examined: obtained by pyrolysis of diborane; electrolysis of potassium tetrafluorineborane; plasma-chemical reduction of boron chloride. It was found that a-B uses icosahedron as a structural unit. This fact allows introducing of function of radial distribution of icosahedra, which helps to construct a geometrical model of a-B structure and to define the term "ideal amorphous structure of boron". The least is useful for quantitative characterization of defects in amorphous structure. Naturally, coordination spheres of icosahedra are almost equidistant and can be described by the symmetric cubic forms, which is a consequence of the a-B isotropy. Possible inter-icosahedral distances along 2-, 3- or 5-fold symmetry axes equal to 0.46, 0.44, and 0.51 nm, respectively. At the atomic level a-B has a close-packed structure. The first coordination number equals to 4, what reveals tetrahedral coordination of icosahedra. They should be linked along the 3-fold symmetry axes. This is a feature of amorphous structure as in boron crystals icosahedra are linked along the 5-fold symmetry axes. Powders, films and plates of a-B in first approximation possess one and same structure: 4 icosahedra forming a tetrahedron. Real structures differ from ideal amorphous structure by the defects, another rule of linking, joined icosahedra etc. Qualitative differences reveal in surface properties as well: a-B is a hydrophilic material, while crystalline boron is hydrophobic. Real structure of the a-B affects its way of crystallization (a-B → α-B → β-B or directly a-B → β-B) and quality of the obtained crystals.

Structure of the a-B obtained by the higher boranes pyrolysis was described in [173]. Further analysis of the pyrolytic boron (obtained by the complete pyrolysis of diborane B_2H_6 and higher boranes) reveals [143] a nanostructure with molecular formations of 3 connected boron icosahedra. Diffraction patterns showed smallest interatomic distance 1.75 Å and corresponding coordination number about 5, which are characteristic to an icosahedral fragment. Radius of the second coordination sphere equals to 2.10 Å, but coordination number is lower (~ 4 –5) due to distributions of icosahedra, disclinations and unoccupied icosahedral vertexes. As for the third coordination sphere, it is characterized by the values 3.00 Å and 16. Such structure can be simply explained by the 3-icosahedral aggregate with radius of ~ 5 Å. Behind this distance there exist no ordered structure.

High energy-resolution boron *K*-emission of single-crystalline α-B were measured [174] with soft X-ray emission spectroscopy (SXES) instrument attached to a conventional transmission electron microscope (TEM). The intensity profiles of the spectra, which correspond to the DOS of the valence bands with *p*-symmetry, were compared with those of a-B, single-crystalline β-B and boron carbide. A characteristic shoulder structure appears in the spectrum of α-B. This structure should be due to the inter-cluster 3-center bonding states among B_{12} clusters in α-B. Consequently, such structure does not appear in the spectrum of β-B and boron carbide crystals and a-B as well.

4.4. Physical properties of amorphous boron

Let us start from the main electrical and optical properties of a-B samples of various origin and structure. These properties of vacuum-deposited a-B films were described in [175]. The layers ~ 300 or between 1000 and 8000 Å in thick, formed on fused silica substrates by electron bombardment, remain amorphous in structure (fine-grained and with no crystalline structure) up to ~ 900 °C. Nonlinear conduction was observed under high field (> 10^4 V / cm) conditions. Acceptor state at 0.1 eV above the valence band edge was predicted. Optical measurements indicated minimum band gap of 1.32 eV, and a possible direct transition at 2.08 eV. Then, it was investigated [176] electrical conductivity of vacuum deposited a-B layers. Boron was evaporated from a zone-refined rod. These thin deposits (~ 300 Å thick) were examined by XRD and their pattern showed diffuse rings characteristic of amorphous structure. The layers exhibited p-type semiconducting properties with impurity levels within the band gap. As the voltage U across the layer increases the current I progressively follows an Ohmic ($I \sim U$), a SCLC ($I \sim U^2$) and, finally, a higher power voltage dependence ($I \sim U^n$ with $n > 2$). The existence of indirect and direct optical transitions in a-B (0.74 and 1.38 eV, respectively) were also reported [177]. These optical constants were measured on samples obtained by vacuum deposition onto fused silica substrate in vacuum. Short-order in a-B thin and massive films studied in [14] was like that in α-B. Nevertheless, they did not crystallize even being heated in argon atmosphere. On the one hand, contrary to contaminated specimens these films showed wide thermal band gap of 1.3 eV, which is almost the value measured in β-B. On the other hand, measurements of the absorption coefficient gave significantly lower value of the optical band gap, 0.62 eV. Such difference is one more argument for the amorphous structure of the vacuum deposited boron films. Resistivity of a-B films containing up to 16 at % carbon were investigated in [130]. The resistivity increased with carbon content. The increase in resistivity can be discussed in terms of a compensation model.

Temperature dependences of dark- and photoconductivity of boron films were measured in [178]. Kinetics of photoconductivity and absorption spectra at nitrogen boiling-point and room temperature were also studied. These data revealed hopping nature of conduction. Electro-physical properties of a-B films were studied in [179]. Tested boron films were obtained by the sublimation of boron atoms on the crystalline surface heated almost to the melting temperature. Due to low volatility of carbon, the main contaminator of boron, obtained films

should be pure. Thick of films grown on quartz was ~ 1 – 2 μm. The room temperature resistivity and thermal band gap of a-B were estimated as ~ 10^3 – 10^4 Ohm · cm and 1.0 eV.

Measurements of the electrical conductivity, Seebek coefficient, and thermal conductivity of a-B were made by Berezin et al [180] over wide temperature ranges (80 – 850, 300 – 850, and 80 –1100 K, respectively). The obtained temperature-dependence of the electrical conductivity can be satisfactorily described by the Mott's law. The value determined for the thermal energy gap of a-B, 1.3 eV, was found to be slightly smaller than that of crystalline β-B (~ 1.4 eV). The room temperature spectral dependence of the reflection and absorption coefficients were determined for the wave length intervals 2 – 25 and 1.3 – 25 μm, respectively. Parameter of the Ürbach-tail was found to be 0.19 eV, while static permittivity was estimated as ~ 9. In addition, current–voltage characteristics of a-B were studied and shown to be consistent with Poole–Frenkel law. Temperature dependences of the a-B electrical conductivity presented in [181] by also can be described by the Mott's law, what argues hopping mechanism of conduction. The investigation of the electrical properties of a-B in wide temperature and electrical field ranges and some its optical properties as well was carried out [182] and it was shown that the temperature- and field-dependences of the a-B conductivity are characteristic of amorphous semiconductors. The standard DOS-tail found in a-B characterized with energy-parameter ~ 0.1 eV from the Ürbach formula.

Temperature dependences of dielectric loss tangent together with internal friction (IF) were studied [183] in boron films (20 – 100 μm in thick) obtained by the liquid drop quenching method. Their microstructural studies revealed dislocations and thin twinning layers. The qualitative discussion was given for obtained IF temperature maxima. The temperature-dependence (within the interval 80 – 1000 K) and Seebeck coefficient of a-B films were studied by Samqurashvili & Tavadze [184]. The activation energy in the intrinsic conduction region (starting at temperature > 500 K what exceeds that for β-B) was determined as 0.93 eV. Room temperature resistivity of a-B was estimated as ~ 10^4 Ohm · cm.

In [120], studies were made on low-frequency refraction indexes for pure and hydrogenated a-B films prepared by plasma deposition. It was shown that the refractive indexes vary widely depending on the deposition conditions and sometimes have larger value compared with the crystal. Comparison of the absorption spectra leads to the following explanation of these features. In pure a-B, the absorption near the band edge is stronger than in the crystal and varies widely while conventional definition of the gap give nearly constant values which are slightly smaller than the crystalline gap. As a consequence, it seems reasonable that the refractive indexes of the amorphous phase are likely to be larger than those of crystalline boron. As for the hydrogenated a-B, the variation in the gap is rather clear and can contribute to the variation in the refractive indexes, the effect of which may be regarded as an essential modification of the matrix by the incorporation of hydrogen.

All thin boron films deposited by electron beam evaporation or by pyrolysis of decarbone on quartz glass substrates showed p-type conduction [121, 122]. The electrical conductivity σ increased rapidly from 10^{-3} to 1 / Ohm · cm as temperature T increased from 300 to 800 K. In the case of the film deposited by pyrolysis, the linear relation was observed in the

plots of log σ against $1 / T$. Mott's law indicating hopping conduction was observed in the electrical conductivity of the sample deposited by electron beam evaporation. The Seebeck coefficient α was positive for all samples. The value of the coefficient decreased slowly from 500 to 300 eV / K, while the power factor $\alpha^2\sigma$ increased from $\sim 10^{-9}$ to $\sim 10^{-6}$ V^2 / Ohm · cm · K, with temperature increasing from 300 to 800 K.

Thermoelectric properties were measured for boron films prepared on silica glass substrate by SSMBD and GSMBD [125, 126]. The electrical properties indicated that the GSMBD films with highest carrier mobility can be formed at substrate temperature 700 °C. All films showed to be p-type conductors with high thermoelectric power ~ 1 mV / K at entire temperature ranges although some fluctuations caused by a stress effect in the films. Temperature-dependence of electrical conductivity showed band conduction with activation energy of 1.060 for SSMBD films and 0.608 eV for GSMBD ones. The trap densities for the SSMBD films are lower than those by GSMBD one's. The GSMBD films did not contain hydrogen, but trap levels would be formed by hydrogen desorption during the film growth, which produces low electric conductivity. The electrical conductivity of SSMBD films was higher than that of GSMBD one's by two order of magnitudes. The SSMBD films had the resistivity of $\sim 10^2 - 10^3$ Ohm · cm, carrier concentration of $\sim 10^{14}$ cm^{-3}, and mobility of 0.2 – 18 cm^2 / V · s depending on the substrate temperature. The thermoelectric figure of merit for SSMBD films showed higher values (of 10^{-6} / K) than those for GSMBD one's, which is compatible to that for CVD wafer. Then, electrical and thermoelectric properties were measured [127, 128] in electrodeposited boron wafers prepared from molten salts with KBF_4 – KF. The electrical properties of the wafers showed p-type conduction. The temperature-dependencies of conductivity showed thermal activation energies of 0.2 – 0.5 eV depending on the KBF_4 / KF ratio. Thermoelectric power tended to increase with increasing temperature up to $10^{-3} - 10^{-2}$ V / K. Measured thermal-diffusivity produced thermal conductivity showing glass-like behavior in the entire temperature range. Thermoelectric figure of merit calculated by conductivity, thermoelectric power and thermal conductivity showed to be $10^{-5} - 10^{-4}$ / K at high temperatures. Kumashiro et al, who previously had prepared p-type boron films, described their thermoelectric properties [185, 186]. The conductivity for photo-thermal CVD boron films grown at 800 – 1000 K showed to be higher than that of thermal CVD one's, indicating the promotion of short-range ordering in the films. Then, photo-thermal CVD boron showed high high-temperature figure of merit 10^{-4} / K.

Band gap of the boron–silicon amorphous films prepared by pulsed laser deposition technique was estimated [132] from the optical absorption spectrum, and it increased with increasing silicon concentration. The values and concentration-dependence of the band gap are nearly the same as those measured for amorphous B – Si prepared by electron beam evaporation. Electrical direct current conductivity of these films was two or three orders of magnitude larger than that of pure a-B, and its temperature dependence revealed variable-range-hopping-type behavior (Mott's law). Concentration dependence of the direct current conductivity was similar to that of metal-doped β-B.

The local structure of a-B resembles that of the crystalline β-B. Nevertheless, one can expect a higher metal solubility in a-B than in β-B (for example, the solubility limit is about 1.5 at % in the case of V-doping) because of the structure flexibility. The metal–insulator transition of V- and Zr-doped a-B films were studied by Tanabe et al [187]. In particular, the temperature-dependences of the electrical conductivity of pure and V-doped amorphous boron were measured. It was found that transition occurs between $x = 2.9$ and 3.7 in V_xB_{100-x} and $x = 11$ and 14 in Zr_xB_{100-x}. The XRD patterns indicated that the metal–insulator transition of Zr_xB_{100-x} is a typical case, which requires a marked change of structure as in the case of V_xB_{100-x}. On the other hand, transition of V_xB_{100-x} does not require the change of the framework of the B_{12} cluster. A possible reason for the low critical concentration of the transition in V_xB_{100-x} should be the change of the bonding nature near the doped V atom from covalent to metallic.

There are few suggestions on magnetic properties of amorphous boron. In view of electron-paramagnetic-resonance (EPR) line-width data measurements performed on powdered samples, Koulmann et al give direct evidence for the existence of the paramagnetic centers in a-B [188]. In [189], magnetic susceptibility measurements of a-B samples had been performed between 80 and 1300 K. Surface impurities presented in a-B powder (according with a small particle size) had made measurements difficult. These impurity contributions being eliminated and a paramagnetic susceptibility signal rising exponentially with the temperature above room temperature was found, just as in β-B. Thus, the presence of the same sort electronic states in the forbidden gap of two materials should be considered. EPR was investigated [130] in a-B films containing up to 16 at % carbon. Signal remained essentially unchanged with increasing carbon content. Amorphous powders of boron isotopes has been studied by Tsiskarishvili et al [190] in the temperature range 100 – 400 K using EPR-method. It was shown that paramagnetic centers are the holes captured on trapping levels and they represent volume (not surface) defects. These experiments confirmed the existence of icosahedral arrangement in a-B. Then, it was studied [191] EPR in ^{10}B- and ^{11}B-isotopically enriched a-B. Obtained high concentration ($\geq 10^{20}$ / cm^3) of paramagnetic centers showed that they characterize intrinsic defects. It is difficult to recognize, what is a reason of difference between two samples: higher impurities content in ^{10}B or isotopic effect itself – because of lighter atoms the number of broken bonds in ^{10}B should be higher than in ^{11}B.

4.5. Electrical current switching in amorphous boron

Reversible current switching is a characteristic effect of a-B. Usually, a voltage increase in a-B samples leads to switching into a higher conducting state involving a change in electron capture cross section by collision ionization. This interesting phenomenon with wide perspectives of practical applications should be considered separately. The pre-switching, nonlinear current–voltage characteristics in amorphous forms of boron were analyzed by Moorjani & Feldman [192]. They investigated role played by Joule heating and its effect on switching characteristics. It was demonstrated that during switching, a conducting filament through the semiconducting film, can be formed. Study of the effect of temperature and shelf-

life on the threshold and sustaining voltages for amorphous thin films of boron had shown [193] that the threshold voltage decreases with increasing temperature while the sustaining voltage is approximately independent of temperature. Both the voltages do not vary significantly with shelf-life. In view of these experiments the hypothesis was suggested that switching is brought about by ionization across the band gap followed by the filling of traps and change in carrier capture cross-section. Sustaining voltage in this case corresponds to a voltage sufficient to keep the traps filled. Observation of the times involved in one switching cycle and the location of the conducting filament suggested [194] another possible mechanism for switching. It was postulated that Joule heating in the sample interior predetermines high conducting (avalanche) path which in turn leads to a *RC*-discharge and filament formation. With this model one can proceed from an almost purely thermal mechanism for switching to an almost purely electronic mechanism. Frenkel–Poole approach was used [130] to interpret the properties of a-B films containing up to 16 at % carbon.

Current–voltage characteristics of the a-B n films (90 – 800 μm in thick) were also studied by Zajtsev et al [195] within the temperature range 80 – 300 K in electric fields up to $2 \cdot 10^5$ V / cm. At relatively low fields, obtained curves can be described by the thermal-field emission from a Coulomb center with energy level of ~ 0.08 eV (Frenkel–Poole effect). But at fields higher than $6 \cdot 10^4$ V / cm, the effect of thermal-field tunneling seems to be preferable. Investigations of switching parameters in a-B thin films containing carbon was conducted [196] under rapid single-pulse voltage conditions. The results were discussed in terms of an electro-thermal model in which the switching process becomes less dominated by thermal effects as the duration of the applied voltage is decreased.

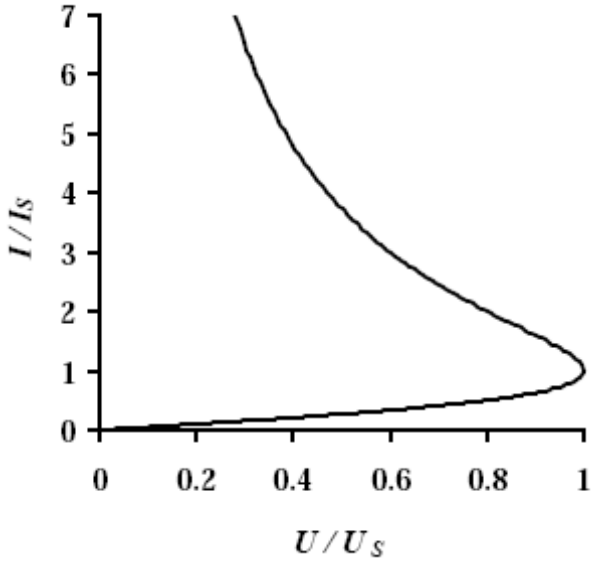

Figure 3. Normalized current–voltage characteristic of the thermal switch [198] suitable for number of samples of amorphous boron.

Summarizing earlier data available on current switching in boron it can be concluded that various switching mechanisms can take place in a-B depending on samples properties and external conditions. Moreover, mechanism can be changed during the switching process. But,

in any case thermal mechanism related to the Joule heat generated due to the current passage in the material always contribute in current switching obtained in a-B. According to our investigations [96, 197-201] the current switching observed in crystalline β-B near the room temperature possesses a thermal nature. Considering heat-balance equation for a solid semiconducting sample overheated through Joule effect, its normalized current–voltage characteristic (Figure 3) has been determined

$$\frac{1}{2}\frac{U}{U_S} = \frac{I/I_S}{1+I^2/I_S^2},$$

where I and U are the current flowing through the sample and the voltage across the sample, respectively; while Is and Us are their values in switching point related by the equation $Us / Is = R0 / 2$ with $R0$ denoting resistance of sample at ambient temperature, i.e. at zero current. On this basis, a universal correlation was established between Ohmic resistance of the sample and voltage of the predominantly thermal switching: when resistance decreases by a factor ~ 2, the current switches on. According to this simple criterion, switching effect observed not only in crystalline β-B, but also in number of samples of a-B reveal mainly thermal nature. Of course, switching in a-B should be termed as thermo-electrical as the thermal switching assists to the avalanche electrical breakdown, which occurs at currents exceeding a threshold.

4.6. Applications of amorphous boron

There are suggested some technical applications for a-B. Boron thin film can be promising thermoelectric material used at high temperatures. Besides, boron films were studied in order to produce an acoustic device, such as a loudspeaker (tweeter) membrane, forming a film composite B – Ti – B. So-called free boron films (i.e. films removed from its substrate) can serve as filters in space X-ray radiation studies. As for the powdered a-B, it is utilized in producing of various boron-based materials. In particular, due to its high chemical activity and dispersity, a-B powder is valuable product for chemical synthesis of cermets and refractory borides, which can serve as heat-resistance and semiconducting materials.

A flare which is used for signaling, illumination, or defensive countermeasures in civilian and military applications is a type of pyrotechnic that produces a brilliant light or intense heat without an explosion. A green flare contains a pyrotechnical composition illuminating in the green region of the optical spectrum used for lightening the field. One aim of the study [202] was to eliminate environmentally hazardous perchlorated oxidizers used in standard green flares. Another aim was to compare the luminous intensities and efficiencies of the standard green flare composition with green flare compositions containing a-B and Mg covered boron. It was observed that the maximum luminous intensity value of the composition containing magnesium coated boron is 26 % higher and the mean luminous intensity value is nearly the same with respect to the standard flare composition. The maximum luminous intensity value of the composition with regular boron is 7 % and the mean luminous intensity value is 34 % higher than the standard composition. However, it is further observed that boron containing compositions have lower burn time and luminous efficiencies.

5. Dispersed crystalline boron

5.1. Amorphization of boron in process of dispersion

There are known various techniques of producing of the boron powders. For instance, boron powders can be treated in induction-coupled argon plasma [203]. In this method, most of the small particles (50 to 100 μm in diameter) of microcrystalline β-B that quickly transit argon plasma are maintained within a radio-frequency induction-coupled torch element as better crystallized spheroids of the same crystalline form and nearly the same size as the starting material. In this process, a few crystals can be formed along with this general product, in particular, polycrystals of unreported "cubic" form of boron, apparently consisting of many hexagonal platelets stacked in an imprecise "amorphous" fashion.

Tsomaia & Shvangiradze [204] found out phenomenon of disappearing of the characteristic crystalline X-ray pattern during the boron dispersion, so-called "mechanical amorphization". Instead of lines one can obtain only interferential halo characteristic of substance amorphous state. According to authors, dispersion results in deep distortions and structural defects in boron. Property of disordering in process of mechanical treatment should be related with bonding nature in boron.

An effect of fine mechanical dispersion studies as applied to phase composition of boron was obtained [205] by different methods. It was established that at fine dispersion of boron obtained by depositing from a gas phase (e.g., from BBr_3) one of phase components is amorphized. An assumption was made that unstable readily amorphized phase found for the first time was a boron modification constructed of atoms with least energetically stable $s^x p^y$-configurations ($s^x p$ and sp). Powders of various origins, including dispersed crystalline boron filaments, were studies in details. In this case meta-stable components of filament easier transform into a-B than components with α- and β-B structures. Powder X-ray diagrams of the mechanically dispersed crystalline boron of various origins (in particular, deposited from BBr_3 on metallic filament) showed [206] diffusive halo and lines characteristic of the mortar material, but did not show any interferential lines characteristic of the crystalline state. Thus, fine-dispersion of boron leads to its amophization as a result of significant distortions of structure.

The results of electron-microscopic and electronographic studies of dispersed boron powders of crystalline boron were presented by Tsomaia in [207]. A model was suggested for the phenomenon of crystalline boron amorphization occurring in the process of mechanical dispersion. There were singled out 3 fractions according to the particles sizes: 14 – 7, 7 – 2, and < 7 μm. Degree of surface amorphization increases with decreasing sizes of particles. However, at very small sizes particles tend to coagulation. Then, electron-beam microscopic studies had been performed [208] for various fractions of dispersed boron. Small fraction particles revealed spongy surfaces, what points on amorphization effect. At sizes < 2 μm, amorphization again leads to the particles coagulation process. According to XRD studies, dispersed powders of β-B being melted crystallize again in β-B structure disregarded the degree of amorphization and

B_2O_3-phase inclusions (which increases with decreasing particle sizes due to boron high affinity to oxygen) [209]. Boron grinding process and classification of crystalline boron powders were described in [210]. The data of radiographic examinations of the powders were presented. A conclusion was made that in the process of fine dispersion of the crystalline boron there occurs amorphization of its particles. It was studied fractions with particles sizes 10 – 1 μm. At sizes > 7 μm, the deals of amorphized phase as well as B_2O_3 inclusions increase. For complete understanding of the process taking place during dispersion of crystalline boron it is important to undertake electron microscopic and electron diffraction examination of powders of dispersed boron. The data of the electron diffraction analysis of the dispersed and amorphous powders of boron were found almost identical [201]. The only exception was the electron diffraction patterns of fractions, where the interference lines of the β-B phase appeared. The spongy surfaces of the crystallite indicate the presence of an amorphous layer; with increase of dispersion the degree of amorphization increases further and coagulated areas can be seen. Amorphization during the mechanical dispersion was found to be almost independent both of the technique of preparation and the purity of the initial β-B crystal. Besides, it can be seen that in addition to amorphous substrate (diffuse back-ground diffraction) in the material, there are also presented crystallites ("spot" diffraction) which do not respond to grinding. From the data obtained, authors suggested a model for powder dispersion which is based on the following principle: in the process of dispersion, the surface of the crystal is deformed and fractioned, and a so-called "amorphous pillow" appears around the crystal. In some cases crystalites with "amorphous pillow" may serve as centers of coagulation of similar crystalites and also entirely amorphous particles. Then, dispersed and fractionated boron powders were fully investigated [212] by XRD and electron diffraction, electron microscope observations and chemical and spectrographic analysis. It was established that in the process of mechanical dispersion crystalline boron becomes amorphous. This change is independent of the dispersed boron. The degree of amorphism increases with the increase in the powder dispersity. Particles which usually become amorphous are 10 – 0.07 μm in size. It was assumed that the valence *p*-electrons in the amorphous layer of dispersed particles are probably delocalized and collected in less stable configurations.

Tsomaia also studied EPR in dispersed fraction classified boron powders of various dispersity from 100 to < 5 μm [213]. EPR spectra of all fractions were observed at ambient temperature. The signal was weakened with particle reduction. Low probability of localized electron states in boron powders amorphized by mechanical dispersion was determined. The deal of amorphous phase in smallest particles was up to ~ 60 %. EPR signals from a-B and particles surfaces amorphized during dispersion were compared. Signal in a-B seems to be related with unpaired electrons localized on impurities or defects of structure.

5.2. Chemical activity of boron powders

Powdered boron is a chemically active material. A thermo-kinetic method was used [214] to study the interaction of hydrogen and oxygen with boron powders at high temperature.

Investigated fine-grained boron powders were obtained using various methods: electrolysis of KBF_3; thermal decomposition of diborane; and reduction of BCl_3 with H_2 in plasma.

Thermal and thermo-gravimetric analysis was made [215] for various dispersed boron powders with grain sizes on the range of 100 to 5 μm. Experimental results showed a number of thermal effects. Their intensity increases with a decrease of boron particle size. These effects should be caused by the presence of B_2O_3 in the boron powder, the content of which increases with increasing particle dispersion. These inclusions should be connected with the dehydration process of boron acid H_3BO_3 formed as a result of the exposure of the powders to air. Usually, B_2O_3 molecules are formed on the fine-sized (less than ~ 7 μm) particles, which absorb water reacting with boron oxide and transforming it into H_3BO_3. It can be removed only by heating.

Because of boron hardness boron powders obtained by grinding or milling always contains significant amounts (up to ~ 5 %) of the reducer's material. In [216], it had been suggested method of the ultrasonic dispersion of crystalline boron powder in distilled water environment. Method was used to produce fine-grained crystalline β-B powder. The kinetics of densification of boron powders in process of sintering of different deposites was also studied and densification activation energy determined for various average particle sizes: 621, 491, and 412 kJ / mole for 20, 10, and 2 μm, respectively. Such process practically does not change material's crystalline structure: there are no traces of amorphized surface layers in powder. However, due to water environment composition of oxygen increases as a result of reactions:

$$2B + 3H_2O \rightarrow B_2O_3 + 3H_2$$

$$\underline{B_2O_3 + 3H_2O \rightarrow 2H_3BO_3}$$

$$2B + 6H_2O \rightarrow 2H_3BO_3 + 3H_2.$$

Localizations of largely oxidized impurities of iron, silicon, manganese on the surface of boron powders were detected [217] by X-ray photoelectron spectroscopy. Oxygen was found on the surface of boron particles in form of oxide films (layer thickness may vary from ~ 1 Å to a few μm) and in the adsorbed states. Apart from boron oxide B_2O_3 other oxygen compounds may also be formed on the surface of the particles. The composition and state of chemical elements on the surface of the boron particles were found to be dependent to a considerable extent on the dispersion technique and further processing of the powder. For comparison, boron powders produced by diborane pyrolysis, grinding zone-melted ingots, and purification of magneto-thermally reduced boron were studied. The appearance of boron oxide is probably related to intensive oxidation of particle surface, the latter being "amorphized" as a result of dispersion. Dispersion of boron particles to sizes smaller than ~ 10 μm resulted in appearance of boron oxides forming islands on those areas where surfaces of particles are "amorphized" in the grinding process. Samples of a-B were also oxidized on the surface.

Analyzing results of investigation of structure, composition, and properties of the fractionated dispersed (particles of sizes 100 – 40 μm together with fine-dispersed "amorphized" part) powders of boron, Badzagua stated [218] that dispersion leads to the significant surface distortion in β-B particles, where are formed inhomogeneously distributed inclusions of α-tetragonal boron and boron oxide. According to the EPR-measurements, concentrations of impurities on surface and in bulk depend on the particle size. Besides, amorphized surface

include micro-twins as twin-boundaries which in boron serve as interfacial failures. Weakening of EPR signals conditional by foreign impurities was found [219] in ground and fractionated specimens of crystalline β-B with a particle size decreased up to ~ 50 μm. But, smaller particles are characterized by an increase of amplitude of these signals. Absence of variations in the EPR spectrum of non-fractionated β-B powders with rise in their fineness suggested distribution of impurities at the grain boundaries which are places of boron ingots' failure.

5.3. Applications of boron powders

Powdered boron is known as solid fuel material. It is a reason why ignition processes in boron-particles system in oxygen-containing environment were studied theoretically and experimentally [220]. Usually powdered solid fuel is not entirely disaggregated in a combustion chamber: a gas-dredge of conglomerates and particles is formed, which is characterized with lower ignition temperature than initial powder. Corresponding conditions for boron particles were considered in [221]. Some experimental results also were presented. Boron is a hardly-ignited material. The ignition possibility in a gas-dredge of boron particles by addition small amounts of magnesium were established in [222]. Physical mechanism of the boron combustion process and its mathematical description were also suggested. Then, it was proposed ignition model for a single boron particle in humid environments [223].

There are known many other fields of utilization of dispersed boron. Boron powders can be used as abrasive materials; in high-modulus, high-temperature composites synthesized by the powder metallurgy; for coatings of machine parts with special properties; for elaboration of the energy-storage substances; as components of solid fuels for missiles etc.

6. Boron filaments and fibers

6.1. Methods of fabrication of boron filaments and fibers

In available reports on boron 1D micro-structures, they are termed "filaments" or "fibers" without a clear distinction and regardless of their sizes, structures, and properties. In present review both of them are used (according to a text) almost in one and same sense.

There are known different techniques for the preparation of boron filaments. Some of them had been described by Zhigach & Tsirlin [224]. Main technique (of practical importance) is deposition of boron on incandescent W wire ("hot-wire method") during the chemical reaction between boron trichloride and hydrogen. Obtained filaments seem to be amorphous being in fact microcrystalline (crystal sizes ~ 15 – 17 Å). They contain cracks yielded in low tensile strength of filaments. Diborane also can be used as initial product. There were reviewed as well some other methods of obtaining of boron filaments: spinning from the melt (in this way only very short filaments can be obtained); method of powder metallurgy (again with low-success); extrusion of powder from melted boron; deposition of boron on the cold polymeric

substrate from the vapor under the boron melt; and electrolysis from the melted salt. Another early overview especially on CVD of boron filament was made in [225].

Some of methods of preparation of boron fibers were discussed by Carlsson as well [226]. Brief descriptions of the following techniques had been done: direct spinning; thermal decomposition of boranes; hydrogen reduction of boron halides (usually boron tribromide or boron trichloride); and utilization of electrical (glow, corona, arc, pulse) discharges. In connection with dominating halide processes various wire-substrates (tungsten, boron nitride, carbon, titan carbide, silica, boron filament itself) were discussed together with methods for increasing the deposition rates (heating the substrate, reduction of the temperature gradient along the growing fiber etc) and those for improving the tensile strength of the fibers after their production. Finally, tensile strengths of boron fibers produced by different techniques were compared. Usually, diffraction patterns of deposited boron fibers indicate an amorphous or microcrystalline state. Boron fiber consists of an inner boride core surrounded by a-B mantle.

Massive elemental a-B was prepared [227] applying the reduction of BBr_3 vapor by H_2 in the vicinity of an incandescent W filament 25 μm in diameter. Conditions were developed for obtaining the boron in the shape of rods up to 2 mm in diameter and from 5 to 10 cm in length (temperature of rod should not exceed about 1500 K, since otherwise the boron will be deposite in polycrystalline form). This material was very hard. Obtained a-B exhibited relatively high resistivity and high-temperature coefficient of resistance. It was very opaque in visible range.

The deposition temperature for boron fibers produced by the hydrogen reduction of BCl_3 on a hot W wire is important in that below 1300 °C one obtains strong "amorphous" (according to diffuse XRD lines) fibers; whereas above 1300 °C microcrystallinity appears, resulting in appreciably weaker material [228].

Tsirlin et al experimentally investigated macro-kinetics of the gas-phase chemical deposition of boron on heated W wire (10 – 25 μm in diameter) [229]. It was performed continuous deposition from the hydrogen and boron chloride mixture according to reaction

$$2BCl_3 + 3H_2 \rightarrow 2B + 6HCl,$$

which is accompanied by the dichloroborane forming reaction

$$BCl_3 + H_2 \rightarrow BHCl_2 + HCl.$$

Obtained boron layers possessed microcrystalline (pseudo-amorphous) structure.

6.2. Filamentary and fibrous structures of boron

Observations of [230] from the interpretation of electron diffraction patterns of filamentary "amorphous" boron were as follows. X-ray studies of filaments of vapor-deposited boron showed a diffusive pattern of 6 halos. The same pattern was observed in the electron microscope in samples of crushed filament and also in chemically thinned filament. It was concluded that the structure of CVD boron consist of fcc stacking of close-packed layers of B_{12}, and profuse faulting occurs in the stacking of these layers so that the structure could readily be described as faulted hcp. Although in [231] these experimental observations considered as valid, authors felt that presented analysis and conclusions were open to question. The results of their

own research suggested the following picture of the structure of vapor-deposited boron filaments. The major portion of the material consists of α-B form having extremely small crystallite size. This structure produces the characteristic halo-patterns. Indeed, the existence of the small crystallites (< 0.1 μm diameter) had been demonstrated. Further, the structure of boron filaments deposited on a W-wire substrate in the temperature range 870 – 1260 °C, was studied [232] by XRD and TEM. The typical diffraction patterns were found to be consisted of 6 or 7 broad maxima or halos. This pattern was interpreted as arising from a microcrystalline (~ 30 Å diameter) material having an average unit-cell structure intermediate between α- and "simple"-tetragonal boron. There are also some inclusions of α- and β-B, less than ~ 1 μm in diameter, which are distributed throughout the microcrystalline material. It was emphasized that a truly amorphous material with no long-range order would not produce 6 or 7 well-defined halos as observed, but rather only 2 or 3 extremely broad maxima.

Then, the structure of non-crystalline, CVD boron fibers was investigated [233] by computer modeling the experimentally obtained XRD patterns (the diffraction patterns were computed using Debye scattering equation, while modeling was done utilizing parameters like the minimum nearest-neighbor distance, density, broadening and relative intensities of the various peaks as boundary conditions). The results suggested that the fibers mainly consist of a continuous network of randomly oriented regions of local atomic order, about 2 nm in diameter, containing boron atoms arranged in icosahedra. Part of these regions has tetragonal structure and the remaining part a distorted rhombohedral structure. This model also indicates the presence of many partial icosahedra and loose atoms not associated with any icosahedra. The partial icosahedra are in agreement with the relaxing sub-units which have been suggested to explain the anelasticity of fibrous boron. As for the loosely bound boron atoms, they have been postulated to understand the strengthening mechanism in boron fibers during thermal treatment. The coordinates of distributions of up to ~ 1400 boron atoms were used to compute theoretical diffraction patterns compared with the model developed for the fibrous boron structure. The atoms positions were then changed, i.e. distortions were introduced, as well as the size and shape of the regions, until the calculated diffraction pattern bore a fair resemblance to the experimentally obtained one. For example, out of 540 boron atoms, 276 atoms are found in 23 complete icosahedra. The remaining 264 peripheral atoms are distributed in 2 groups of 11, 18 groups of 9, 6 groups of 6, 4 groups of 4, 2 groups of 2 and 24 individual atoms.

Chemical composition of boron fibers (~ 100 μm in diameter) obtained by the deposition of boron (by boron reduction from its trichloride) on W wire (17 μm in diameter) was analyzed in [234]. Such fibers were considered as homogeneous all along the length. Method used allowed to determine all chemical elements with concentrations of $\sim 1 \cdot 10^{-4}$ at % and to analyze them with concentrations of $\sim 1 \cdot 10^{-3}$ at %. Relative precision was 5 – 20 %).

6.3. Stability and strength of filamentary and fibrous boron

Let us in-short concern the stability and strength of boron filaments and fibers. Stability of "amorphous" boron prepared by vapor thermal decomposition onto an 11 μm diameter

tungsten filament was studied in [235]. The imperfections in specimens were of a very fine scale. The obtained image suggests extensive twinning in material. Upon heating with the electron beam the boron would change from an "amorphous" form that was regarded as an extensively faulted structure to a form having a layered structure that exhibited less extensive faulting in the stacking of the layers. The distance between obtained diffraction spots corresponds to the fundamental spacing derivable from the consideration of the packing of B_{12} groups regarded as a large metal-atom. Heat treatment of such "amorphous" boron at progressively higher temperatures in evacuated capsules leads to "recrystallization", while annealing above ~ 1300 °C causes the formation of the crystalline β-B modification.

Other XRD studies of boron filament layers showed that they consist mainly α-B in a fine dispersed and in relatively coarse-grained states. Besides β-B was found in a small amount in a fine dispersed state. Heat treatment of the boron filaments is found [236] to be able to change their phase composition. As for the fracture characteristics of a-B filaments, they had been investigated in [237]. Boron filaments used were prepared by the chemical vapor plating of the a-B from a volatile halide. Tungsten wire 0.5 mm in diameter was used as a substrate. The filaments produced were of two diameter ranges 3 – 5 and 10 – 15 mm. The increase in strength demonstrated that surface defects do exist on a-B filaments. It was shown that surface flaws in a-B filaments can be eliminated by chemical polishing greatly enhancing strength properties. It was found two types of tests and the crystalline boride core seems to be responsible for the large difference in records. The point is that boron filaments are non-homogeneous structures composed of tungsten boride core ~ 0.5 mm in diameter surrounded by coating of bulk a-B. The strength of the filament is affected not only by the inherent properties of the bulk boron and the conditions on its surface, but also by the presence of the core material and interface between core and the boron. Region adjacent to the core acts as a stress concentrator because there is a structural gradient across the interface and internal stress is generated. In addition, pores had been detected. Pre-exiting flaws of some nature surface cracks, notches, inclusions etc also are presented in this brittle material. The tensile strength of boron filaments were measured [238] at elevated temperatures (up to ~ 700 °C). The tensile strength values of uncoated boron filaments decreased with air exposure. Silicon carbide had been tested as a strengthening coating material of boron filaments. Issue of the boron fibers strength was analyzed by Zhigach et al [239] based on statistical treatment of the wide experimental data. Boron fibers strength was found to be dependent on their length with averaged value about 310 kgf / mm ^{2}. This parameter is characterized by a significant spread in values due to presence in fibers different amounts of defects like the microcracks and impurity inclusions affecting their strength. In order to investigate the fracture behavior, various types of boron filaments were broken in tension in such a way that primary fracture surfaces, and fragments ejected when fracture occurred were retained [240]. Fracture surfaces observed in SEM could be placed into one of two broad categories. Type I surfaces exhibit primary fracture characteristics such as mirror, mist, and hackle zones. Flaws which initiated failure could frequently be resolved. Type II surfaces appeared to be generated by subsequent fracture immediately following

primary failure. The character of relationship between the fracture surface and the stress distributions occurring within the fibers should be a result of the manufacturing conditions.

Physical-mechanical properties of boron filaments with variable diameter (53 – 126 Å) were studied in [241]. Averaged tensile strength and shear modulus were estimated as ~ 3000 and ~ 160 000 MN / m^2, respectively. Electrical resistivity of boron fibers was presented by the empirical formula: $\rho\,[\text{Ohm}\cdot\text{cm}] = d^{2.2}\,[\mu\text{m}] / 96.5$, where d is the filaments' diameter. Explanation was related with their complex structure: during the boron deposition on W filament (12.5 μm in diameter) it takes place tungsten bronzing process (in 70 – 90 μm thick radial layer) forming internally stressed layer of borides with composition from W_2B to $WB_{6.25}$ so that increasing in d increases deal of the pure boron in filament. Aiming to obtain data on high-temperature physical-mechanical properties of boron filaments, in [242] their strength was measured at temperatures higher than ~ 400 – 500 °C. It was found drastic decrease in strength, which probably was caused by the fast oxidization and decrease in shear modulus.

Average tensile strength of boron filaments was estimated [243] as ≤ 400 kgf / mm^2, which is in 6 – 10 times less than critical theoretical value for boron. Decreasing in strength mainly should be related with imperfections of micro- and macrostructures. When a filament is grown on W filament, there exist a tungsten boride core, which seems to be almost "amorphous", may be fine-crystallized (with grains 20 – 30 Å in diameter). Structural defects like the cracks and foreign inclusions are localized at the interface zone between core and boron layers. They are possible even to reach the filament surface. Core of composition $WB_{6.25\pm0.20}$ is found to be stressed. The strength is not related with filament morphology, but with existence of a few basic types of fracturing. It was also presented [244] the results of measurements of the boron filaments elastic modulus in temperature range 300 – 1480 K. This parameter was found to be decreasing in linear-law with temperature. One can conclude that boron filament is a brittle material. Its strength is controlled by structure imperfection or flaws. In the absence of flaws due to substrate defects or contamination fracture of the wire-deposited boron filaments originated within their core. Besides, vapor deposited boron filaments exhibit high residual stresses, which strongly influence their mechanical properties. It should be mentioned that vapor-deposited a-B fibers usually display large thermally-activated anealastic deformation. Some initial results concerning the characteristics and mechanisms of this anelasticity had been described in [228].

6.4. Internal friction in boron filaments and fibers

IF-studies are a powerful method of investigation of real atomic structures of boron filaments and fibers. In particular, the extensive information on the behavior of microparticles and various defects in boron filaments can be obtained from these measurements. The IF of vapor deposited boron fibers was measured [245] at room temperature in an inverted torsion pendulum at frequency ~ 5 Hz. Two regions were observed: a relatively amplitude-independent and strong amplitude-dependent for higher oscillatory stresses. Irreversible changes in material

started within a few cycles at higher amplitude are qualitatively similar to the depining of dislocations in metals. Absolute values of the shear modulus typically were $1.4 \cdot 10^{12}$ dyne / cm^2.

Low-temperature IF and shear modulus of boron fibers (~ 100 μm in diameter) obtained by the gas-phase deposition of boron on W wire (12.5 μm in diameter), as well as boron fibers coated by the boron carbide layer (~ 5 μm in thick), was studied in [246]. The change of the height and form of the maximum was studied in dependence on the fiber diameter and purity. It was suggested that the origin of the maxima is connected with impurity displacement in a periodically applied elastic field. Then, IF of boron fibers was studied [247] from room temperature to 700 °C. The dependence on thermal treatment, fiber diameter, and its purity of the height and shape of an IF maximum was established. Fibers were obtained by the gas-phase deposition of boron on heated W wire (12.5 μm in diameter), besides boron fibers were coated by the boron carbide layer (~ 5 μm in thick). In spite of low-temperature thermal treatment, the high-temperature annealing drastically changes the decay temperature-curve. It demonstrated significant structural changes in boron fibers, which take place at high temperatures.

In [248], IF and shear modulus of boron filaments in dependence on temperature were studied aiming to understand nature of the structural defects in filaments. Results revealed significant structural changes in annealed at high temperatures filaments.

Temperature-dependence of IF in boron fibers in interval from – 120 to + 700 °C were investigated in [249]. It was studied fibers obtained by the gas-phase deposition on heated W wire. Such boron fiber possesses a microcrystalline structure, which by the high-temperature treatment is transformed in β-B. W fully spends forming its borides. Shell of the boron fiber can be considered as two-phase system – quasi-viscous amorphous and elastic polycrystalline phases. Stresses seem to be relaxed at the interfaces and / or in viscous–elastic regions.

In [250], the dependence of the IF of the boron filament on amplitude was studied in vacuum. The filament was finely dispersed and showed residual internal stress distributed in the bulk of the sample. A step-wise change in the IF was established at room temperature. The results obtained were analyzed taking into consideration the possible effects of residual internal stresses on the energy and the crystal geometry characteristics, and the nature of interaction of the admixtures with the dislocations of finely crystalline aggregates in boron filaments.

The temperature spectrum of the IF at twisting and bending vibrations in boron fibers within the temperature range 300 – 1100 K was studied [251] and a broad relaxation peak was found. A model was suggested, based on the interphase diffusion interaction in the region of the fiber core, which allows an assessment to be made of the content of borides in the core and an evaluation of the kinetic parameters determining the formation of these phases. In particular, suggested model allows to explain the experimental data obtained and to evaluate the ratio of borides in the boron fiber core.

6.5. Applications of boron filaments and fibers

One of the main areas of application of boron in form of fibers is the production of composite materials [252].

Because of their high strength and modulus to weight ratios, vapor-deposited boron fibers have found increasingly large-scale application in fiber-reinforced composite materials as reinforcing element. A rather common combination of materials utilizes boron fibers is an epoxy matrix. The excellent mechanical properties of boron fibers (average tensile fracture stress ~ 3.5 GN / m^2 and modulus of elasticity ~ 400 GN / m^2) make them very useful for fiber-strengthened materials, particularly, in light-weight constructions like the military aircraft structures and aerospace composites. For example, the strength properties of boron fibers affect the boraluminum strength. Metal-like composite materials with Al and Ti matrixes strengthened by the boron filaments are used at high temperatures: 300 – 700 °C. Besides, technological processes of fabrication of these materials and parts of machines include high-temperature (500 – 800 °C) treatments. Thus, their physical-mechanical properties at higher temperatures are not out of interest.

Boron filamentary crystals have applications for semiconductor devices as high strength filaments in fibrous composites. Boron filaments can by used as tension-wires in high-frequency oscillographic galvanometers as well.

7. One-dimensional nano-structures of boron

There is known a few early reports on fabrication of the boron one-dimensional species, which can be considered as nano-structures. Red α-B filamentary crystal was grown from the vapor by seeding [253] using the vapor–liquid–solid mechanism (reduction of BCl_3 with H_2 for transport and Pt as the liquid-forming agent). Both straight and kinked boron whisker crystals were produced. They were flexible indicating high yield strength. It was investigated [156] intensities of diffracted X-rays for boron deposites from the reduction of BCl_3 with H_2 at 1000 – 1200 °C, which can occur as aggregates of needle-like crystals. Besides, it was shown [114] that in certain conditions in the CVD thin layer of a-B an aggregate of tetragonal crystals can be nucleated, and a heap of welded nodules (whiskers) of a-B can grow as fibers normal to the substrate. The short-range order structure of a-B was studied by Kobayashi [168] using as sample materials CVD whiskers prepared by the reduction of BCl_3 with hydrogen.

7.1. Boron nanowires

Using *ab initio* QC and DFT methods to determine stable structures of bare boron clusters, in addition to other forms, it can be predicted [254] existence of the boron scroll-type filaments arising from coaxial closed layers of tubular surfaces. Actually, crystalline boron nanowires with tetragonal structure have been synthesized based on laser ablation of a B / NiCo target [255]; the nanowires were sometimes single crystals and had a droplet at one end of the nanowire; the droplet contained B, Ni and Co elements, which indicates that the vapor–liquid–solid (VLS) mechanism may play a key role in the growth of the boron nanowires.

In [256], it was reported growth of boron ninowires by CVD. The nanowires had diameters in the range of 20 – 200 nm (mean value ~ 60 nm), lengths of several μm, and were crystalline as grown. Conductivity measurements established that the nanowires are semiconducting and exhibit electrical properties consistent with those of elemental boron. An orthorhombic unit cell with $a = 9.4$, $b = 7.1$ and $c = 5.4$ Å was consistent with nano-diffraction data. These lattice parameters did not match those of any known boron polymorph or boron-rich compound. A model was suggested that C-surface coats dense cylindrical B-core. The nanowires were dense, twinned, whisker crystals rather than nanotubes.

Crystalline boron nanowires also were produced [257] through post-annealing a-B nanowires synthesized by radio-frequency magnetron sputtering. High-resolution TEM was used to characterize the microstructure of the crystalline boron nanowires. Selected-area electron diffraction studies showed that the crystalline boron nanowires belong to a β-B structure, with lattice parameters of $a = 10.95$ and $c = 23.82$ Å. Electron energy-loss spectroscopy (EELS) was used to characterize the chemical composition of boron nanowires.

Electrical transport in crystalline boron nanowires was studied [258] using Ni and Ti as the contact electrodes made on individual nanowires, in which Ni forms Ohm contact and Ti forms Schottky-barrier junction. Electrical measurements demonstrated p-type semiconductor behavior with estimated carrier mobility of 10^{-3} cm^2 / V · cm. This behavior was attributed to electric-field-induced impact ionization.

As it was demonstrated [259] boron nanowire Y-junctions can be synthesized in a self-assembled manner by fusing two individual boron nanowires grown inclined toward each other. It was showed that the presence of a second liquid, in addition the liquid Au catalyst, is critical to the inclination of the boron nanowire.

The electronic and geometric structures, total and binding energies, harmonic frequencies, point symmetries, and HOMO–LUMO gaps of small neutral boron B_n ($n = 2 – 12$) clusters has been investigated using DFT [34]. Linear boron structures have been found along with other structures.

Vertically aligned boron nanowires in self-assembled large-scale arrays with excellent uniformity and high density have been fabricated [260] using radio-frequency magnetron sputtering of boron and B_2O_3 powder onto various substrates. The produced nanowires were several tens of micrometers long and 20 – 80 nm wide, with typically platform-shaped tips.

7.2. Boron nanoribbons

Catalyst-free growth of boron nanoribbons was observed [261] by pyrolysis of diborane at 630 – 750 °C and ~ 200 mTorr in quartz tube furnace. Nano-diffraction analysis indicated that the nanoribbon is single crystalline α-tetragonal boron. TEM and SEM images showed the nanoribbon was covered by a 1 – 2 nm thick amorphous layer. Elemental analysis by EELS, energy-dispersive X-ray spectroscopy (EDXS), and X-ray photoelectron spectrometry (XPS) showed the nanoribbons consist of boron with small amounts of oxygen and carbon. FT IR spectrometric and Raman spectra were also reported.

Low-pressure CVD was used [262] to synthesize crystalline boron nanoribbons of 16 nm thickness by both uncatalyzed and Ni-catalyzed pyrolysis of diborane at relatively low temperature of 925 °C. The ribbons were characterized with SEM, TEM, XPS, Auger electron spectroscopy, and Raman spectroscopy. Obtained nanoribbons were crystalline with α-tetragonal boron structure. They consist of ~ 70 % boron, ~ 14 % oxygen, ~ 14 % carbon, and trace amounts of other impurities including nitrogen. Like the oxygen, the carbon was likely presented mainly at surface.

7.3. Boron nanobelts

Wang et al have successfully fabricated single crystalline tetragonal boron nanobelts by laser ablation method in a furnace without using a catalyst or hazardous boron vapor source at the temperature range of 700 – 1000 °C in 25 Pa of argon [263]. The obtained boron nanobelts were rectangular in cross-sectional shape with a width-to-thickness ratio of about 5, several tens nanometers to about 150 nm in width, and several micrometers to the order of millimeters in length. The interior was well crystallized in tetragonal and amorphous structures 2 – 4 nm thick can be seen along the surface. Only boron EELS peak was detected from single nanobelts.

Kirihara et al studied electrical transport in single-crystalline boron nanobelts with α-tetragonal crystalline structure using in measurements metal electrodes of Ni / Au bilayer [264]. Nanobelts were synthesized using pulse laser ablation. Thickness and lengths were approximately 25 and 100 nm, respectively. From the temperature-dependence of electrical conductance, the boron nanobelt is found to be a semiconductor. The electrical conductivity was of order of 10^{-3} / Ohm · cm at 295 K. Fitting results to variable-range-hopping conduction revealed a high density of localized states at the Fermi level compared with bulk β-B. Then, Kirihara et al measured electrical conductance of single crystalline boron nanobelts again having α-tetragonal structure [265]. The Mg-doped boron nanobelts had the same α-tetragonal crystalline structure as the pristine nanobelts. The pure boron nanobelt was a p-type semiconductor and its electrical conductivity and carrier mobility were estimated to be on the order of 10^{-3} / Ohm · cm and 10^{-3} cm^2 / V · s at room temperature, respectively, with activation energy of ~ 0.19 eV. After Mg vapor diffusion, the nanobelts were still semiconductor, while the electrical conductance increased by a factor of 100 – 500.

Catalyst-free single-crystalline boron nanobelts were successfully synthesized using pulse laser ablation [266]. The electrical conduction of an individual nanobelt was measured and it was discussed the mechanism of electrical transport in this nanobelt probed by electric field effect, chemical doping, and photoconduction. Temperature coefficients of electrical conductance and carrier mobility, obtained by current vs. bias voltage characteristics and their back-gate modulation, revealed a hopping conduction. On the other hand, doping of Mg atoms into the boron nanobelt by a vapor diffusion method increased the conductance by a factor of more than ~ 100 at room temperature. Dependence of photocurrent on the atmosphere also was observed. In ambient air, slow photoresponse under blue light illumination was observed. Rise and decay time exceeded 3 days. The magnitude of photoresponse in ambient air and oxygen

was greater than in hydrogen and argon atmospheres. In vacuum, a photo-resistivity effect consisting of the continuous decrease of conductance under blue light illumination was observed. Variation of band bending of the nanobelt surface by adsorption or desorption of oxygen and water molecules appeared to switch the photoconduction on and off by the respective trapping and recombination of photoexited carriers at the nanobelt core and surface.

The convergent-beam electron diffraction (CBED) at room temperature has been applied [267] to the boron nanobelt structural analysis. All obtained reflections can be indexed with tetragonal unit cell. The CBED pattern shows two mirror symmetries, which are consistent with space group of the α-tetragonal boron structure. The crystal structural parameters and electron density of the boron nanobelts were determined based on the last squares fitting the intensities of the CBED patterns and dynamical diffraction calculations.

EELS and *K*-SXES were used [268, 269] to investigate the electron structure of boron nanobelts with 40 and 130 nm width. The energy positions of top of valence band were found to be almost the same with the β-B. At the same time, boron nanobelt spectrum shows some new structures related with bottom of the conduction band. From these results, the boron nanobelt is expected to be a semiconductor with a narrow band gap of ~ 0.2 eV. This estimation is consistent with reported result of the electrical conductance experiment indicating typical hopping conduction. Boron nanobelts are either a semimetal or narrow-gap semiconductor. However, it is inconsistent with the theoretical band structure calculation, which predicted a metallic nature of the pure α-tetragonal boron. The point is that 1D boron materials, including boron nanobelts, posses a crystalline structure of bare α-tetragonal boron without any inclusions like the carbon and nitrogen atoms characteristic for α-tetragonal boron macrocrystalline structure.

Hyodo et al attempted Li- and Mg-doping into boron nanobelts [270], whose crystalline structure was α-tetragonal boron and discussed the possibility of metal-transition and superconductivity. The compositions, the lattice constants of the α-tetragonal boron structure, the occupancies of Mg in pure, Li- and Mg-doped boron nanobelts were presented. Li and Mg doping at high concentrations was indicated from the significant increase of the lattice constants. Besides, the current–voltage characteristics and their temperature-dependence for Li- and Mg-doped boron nanobelts were measured.

Thermal neutron transmutation of ^{10}B atom can be a method of carrier doping into boron structures because the neutron capture reaction ^{10}B (n, α) ^{7}Li. It results in significant structural damages in such structures. But, after healing the radiation damage, Li-atoms can modify the transport property. As it been mentioned above, previously the electrical transport properties of single crystalline boron nanobelts composed of α-tetragonal boron was reported and temperature coefficients of electrical conductance revealed a hopping conduction. Recently, the effects of a neutron-capture reaction of isotope ^{10}B on the structure and electrical transport of ^{10}B-enriched single-crystalline boron nanobelts were reported in [271]. Partial amorphization, particularly at the surface of the nanobelt, was observed after thermal neutron irradiation with a dose of $2 \cdot 10^{19}$ / cm^2. Carrier doping into the nanobelts by neutron transmutation is expected after post-annealing. The change in conductance was discussed based on the distribution of

localized states in the band gap of α-tetragonal boron. In [272], the effects of neutron capture reaction of isotope ^{10}B and Li ion implantation on the structure and electrical transport of ^{10}B enriched single crystalline boron nanobelts were demonstrated as well. The drastic change in the conductance was discussed based on the distribution of localized states in forbidden band of the crystalline structure.

7.4. Applications of boron one-dimensional nano-structures

Theoretical studies suggest that boron nanotubes, resembling carbon ones, should be stable. Moreover, boron nanotubes are predicted to have high metallic conductivities, exceeding those of carbon nanotubes. Consequently, boron-related 1D nano-structures might be better candidates for applications as nanoscale interconnects than are carbon-related. Any 1D structure of boron could be useful in various functional nanoscale devices because of the thermal stability and mechanical strength. The 1D structure of boron has attracted much attention also as a building block for micro electro-mechanical systems. Additionally, the electronic properties and diameters of B-based nanowires are amenable to synthetic control. Thus, both the conducting and semiconducting components necessary to build devices of nanoelectronics can be obtained from B-based nanowires.

The 1D nano-structures of boron are promising as various nano-structural devices such as a nano-probe with high strength and a nanowire chemical sensor with high sensitivity because of the thermal stability and mechanical strength of the bulk boron. The structure of the boron nanowires Y-junctions' arrays may allow construction of 3- or multiple-terminal nanowire devices directly on Si-based readout circuits through controlled nanowire growth.

Unlike carbon nanotubes, boron nanoribbons do not roll-up to multiwall tubular forms and then the dangling bonds at their surfaces may be available for bonding other elements, including hydrogen. For this reason, boron nanostructures are of interest for hydrogen storage applications too. A 1D-nanostructure of boron, like the boron nanobelt, could be useful in various functional nanoscale devices because boron-rich solids are promising candidates for thermoelectric materials and sold-state neutron sensors.

As it was mentioned, boron icosahedral cluster solids have the high DOS due to the high symmetry of the B_{12} icosahedral cluster. On the other hand, the high phonon frequency and large electron–phonon coupling constant are also characteristic features of boron-rich solids. These features give an advantage for high-T_c superconductivity. If one can dope metallic element into boron icosahedral cluster solid, in particular, in boron nanobelts, to adjust the Fermi energy to the position of the high DOS, then high-T_c superconductivity can be expected.

8. Boron sheets

There are number of theoretical studies and only few experiments predicting stability of the boron sheets' fragments – planar or quasi-planar boron clusters. Based on the investigation

[21] of geometrical structures and properties of small cationic boron clusters B_n^+ ($n = 2 - 14$) and using LSD formalism with a nonlocal correction, it was found that a part of the final structures of the cationic boron clusters prefers planar atomic arrangements and can be considered as fragments of a planar surface. The geometry optimization performed in [23] using DFT for B_n^+ clusters for $n \leq 14$, suggested that the most stable structure for each boron cluster should be planar or quasi-planar. Accurate calculations carried out on small boron clusters B_n ($n = 2 - 14$) based on *ab initio* QC methods, determined [25] that part of the final structures of the boron clusters, namely with indexes $n > 9$, results quasi-planar structures, fragments of 2D surfaces.

Very stable quasi-planar clusters of bare boron were found [273] by systematic *ab initio* DFT and QC methods. They are composed of dove-tailed hexagonal pyramids different from "classical" forms of α- or β-B crystallites. These quasi-planars are fragments of quasi-planar surfaces, which can be easily obtained and constructed from a basic unit of hexagonal pyramids. An interpretation on double layers of boron quasi-planar surfaces showed an increase in the stability of the system which can be related to the overlap of π-orbitals between the layers. Therefore, it was predicted existence of a series of parallel boron layers, as in graphite. Based on *ab initio* QC and HF approximations, DFT and LMTO (within the ASA) methods, Boustani & Quandt determined the geometric and electronic structures of atomic-scaled boron surfaces [26]. In contrast to semiconducting α-B, the boron sheets showed a metallic behavior similar to graphite. Using *ab initio* QC methods, different structures of B_{32} clusters was investigated in [27]. The part of the most stable isomers was found to have a quasi-planar structure often containing dove-tailed hexagonal pyramids. A curvature strain was found to favor their stability. Among curiously stable cationic B_{13}^+ cluster and its neutral and anionic counterparts isomers examined in [28] though the use of DFT, the planar and quasi-planar structures were seen to be more stable than 3D isomers. But, the ordering by stability of the planar and quasi-planar structures changes depending on the cluster charge-state. In particular, planar structures of boron benefit from π-delocalization.

The electronic structure and chemical bonding of boron clusters B_5^- and B_5 were investigated [29] using anion photoelectron spectroscopy and *ab initio* calculations. Extensive searches were carried out for global minimum of B_5^-, which was found to have a planar structure with a closed-shell ground state. Zhai et al reported [31] more experimental and theoretical evidences that small boron clusters prefer planar structures.

In [274], it has been suggested the results of *ab initio* calculations showing that boron can form a wide variety of metastable planar forms with unusual electronic and mechanical properties. The preferred planar structure is a buckled triangular lattice that breaks the 2-fold ground state degeneracy of a flat triangular plane. Special DFT calculations have been carried out [275] to obtain the geometric and electronic structures of boron sheets. The buckled boron sheet formed by alternating up and down rows of B atoms, with a buckling height of 0.85 Å, is found to be about 0.20 eV / atom more stable than the corresponding atomically flat sheet. Two different B – B bond-lengths characterize the buckled geometry: (1) 1.63 Å between the B-atoms in row, and (2) 1.81 Å between the B-atoms in adjacent rows. The flat and buckled sheets have different geometric and bonding characteristics, but both are metallic.

Small boron clusters as individual species in the gas phase were reviewed by Alexandrova et al [32]. Free boron clusters have been characterized using photoelectron spectroscopy and *ab initio* calculations, which have established the planar or quasi-planar shapes of small boron clusters. This was surprised as the chemistry of boron has been diversely featured by 3D structures. The planarity of the species has been further elucidated on the basis of multiple aromaticity, multiple antiaromaticity, and conflicting aromaticity. The electronic and geometric structures, total and binding energies, harmonic frequencies, point symmetries, and HOMO–LUMO gaps of small neutral boron clusters B_n ($n = 2 - 12$) have been investigated using DFT [34]. Planar and quasi-planar structures have been found along with other structures, but within the size range, planar and quasi-planar structures have the lowest energies.

Based on a numerical *ab initio* study, in [276] it was discussed a structure model for a broad boron sheet, which is the analog of a single graphite sheet, and the precursor of boron nanotubes. The sheet has linear chains of *sp* hybridized σ-bonds lying only along its armchair direction, a high stiffness, and anisotropic bonds properties. The puckering of the sheet has been explained as a mechanism to stabilize the *sp* σ-bonds. The anisotropic bond properties of the boron sheet lead to a 2D reference lattice structure, which is rectangular rather than triangular. As a consequence the chiral angles of related boron nanotubes range from 0 to 90 °. Given the electronic properties of the boron sheets, it has been demonstrated that all of the related boron nanotubes are metallic, irrespective of their radius and chiral angle, and also postulated the existence of helical currents in ideal chiral nanotubes. It was shown that the strain energy of such boron nanotubes depends on their radii, as well as on their chiral angles.

Ab initio calculations based on generalized-gradient approximation (GGA) to DFT have been performed [277] to study structural and electronic properties of the 2D sheets consisting of the elemental boron. The results found are that the boron sheet can be stable and can possess metallic or semiconducting character depending on its atomistic configuration. The unique features present in the electronic properties of the buckled {1212} and reconstructed {1221} sheets would lead to a significant variation on electronic and mechanical properties of the corresponding single-walled boron nanotubes. In [278], a comparative theoretical study of the structural, electronic and optical properties of boron sheets by *ab initio* pseudopotential (PP) calculations was presented. The results indicated that purposed 2D boron sheets are metastable. The unusual bond properties of the boron sheets lead to different 2D-lattice configurations. In addition to electronic properties of anisotropic bonds, calculated electronic band structures and DOS revealed that all purposed boron sheets are metallic.

In order to elaborate a direct experimental method available for structural determination of boron clusters, Wang has combined [36] photoelectron spectroscopy of size-selected cluster anions with quantum calculations to probe the atomic and electronic structures and chemical bonding of small boron clusters up to 20 atoms. It was found that for neutral boron clusters the planar to 3D structural transition occurs at B_{20}, which possesses a double-ring structure.

In [279], it was presented a new class of boron sheets, composed of triangular and hexagonal motifs, that are more stable than structures considered to date and thus are likely to be the precursors of boron nanotubes. A simple and clear picture of electronic bonding in boron

sheets were described, and highlighted the importance of 3-center bonding and its competition with 2-center bonding, which can also explain the stability of boron fullerenes. These findings called for reconsideration of some earlier data on boron sheets, nanotubes, and clusters. Using *ab initio* calculations, the [280] has predicted a novel stable boron sheet and boron nanotubes which show different electronic properties. The boron sheet is flat and has the structure that the 2 centers of each 3 hexagons in the hexagonal lattice are filled with additional atoms, which preserves the symmetry of the triangular lattice. The boron sheet is metal, and there are bands similar to the π-bands in the graphene near the Fermi level. Rolled from the sheet, the nanotubes with diameter larger than 17 Å are metals. Smaller nanotubes are semiconductors with the gap decreasing as the diameter and chiral angle increase. In [281], the configurations, stability and electronic structures of a new class of boron sheets have been predicted within the framework of DFT at the GGA-level. These boron sheets should be sparser than other proposals. Theoretical results showed that such kind stable boron sheet remains flat and is metallic. There are bands similar to the π-bands near the Fermi level.

The results of a study of the high pressure phase diagram of elemental boron, using full-potential density functional calculations has been presented in [282]. At high pressures ($p > 100$ GPa) boron crystallizes in quasi-layered bulk phases, characterized by in-plane multi-center bonds and out-of-plane unidimensional σ-bonds. These structures are all metallic, in contrast to the low-pressure icosahedral ones, which are semiconducting. The structure and bonding of layered bulk phases can be easily described in terms of single puckered boron sheets. These results bridge the gap between boron nanostructures and bulk phases.

Above described boron surfaces can find some practical applications. They can serve as light-weight protective armor, as a neutron-absorber material in fission reactors, or as very high-temperature semiconductors. Furthermore, it was shown that the strain energy of such boron nanotubes will depend on their radii, as well as on their chiral angles. This is a rather unique property among nanotubular systems, and it could be the basis of a different type of structure control within nanotechnology.

9. Boron nanotubes

9.1. Data on atomic and electronic structures of boron nanotubes

Like the boron sheets, there are known number of theoretical studies and few experiments predicting stability and electronic structure of boron nanotubes. Based on *ab initio* QC methods, accurate calculations on small boron clusters B_n ($n = 2 - 12$) were carried out to determine their electronic and geometric structures [25]. Part of the final structures of the boron clusters, with $n > 9$, results in convex structures, which can be considered as segments of nanotubes. Then, using *ab initio* QC and DFT methods it was determined [254] structures of bare boron clusters. In addition to other cluster forms, boron nanotubules were found to be highly stable as well. These nanotubular structures are composed of hexagonal pyramids only

and can be considered as segments of extended pips. Applying "Aufbau Principle", one can easily construct stable boron structures besides the nanotubular clusters described. Thus, "Aufbau Principle" should help in illuminating the chemical and physical nature of new boron materials based on boron nanotubules. The stability of boron tubules defined through binding energy per atom is comparable to that of the most stable quasi-planar clusters and to that of nanotubular structures found in boron quasicrystals.

Based on *ab initio* QC and HF approximations, DFT and LMTO (within the ASA) methods, the geometric and electronic structures of atomic-scaled boron nanotubes has been determined in [26]. Then using same *ab initio* QC methods Boustani et al investigated different structures of B_{32} clusters [27]. The part of the most stable isomers had a tubular structure often containing dove-tailed hexagonal pyramids. The elimination of dangling bonds was found to favor the tubular structures stability.

Ciuparu et al reported the first synthesis of pure boron single-wall nanotubes by reaction of BCl_3 with H_2 and Mg – MCM-41 catalyst over parallel cylindrical pores with uniform diameter (36 ± 1 Å) [283]. The composition of the tubular structures observed in TEM was confirmed by EELS, and the tubular geometry was also confirmed by the presence of the characteristic spectral features in the Raman breathing mode region. A pure siliceous template with a very narrow distribution of pores alone did not produce boron nanotubes suggesting the Mg incorporated into the pore walls is the catalyst or the catalyst precursor for the growth of single-walled boron nanotubes. The boron nanotubes produced were approximately 3 nm in diameter, comparable to the diameter of the catalytic template pore, suggesting the nanotube growth is physically constrained by the pores of the mesoporous molecular sieve. The initial length of a tube outside the pore of the catalyst was determined at 16 nm. Earlier boron nanotubes had been anticipated only from *ab initio* calculations and their electronic properties predicted, but they had never been reportedly produced.

A survey of novel classes of nanotubular materials based on boron was presented in [284]. Pure boron nanotubes are shown to be a consequence of a general Aufbau principle for boron clusters and solid boron phases, which postulates various novel boron materials besides the well-known bulk phases of boron based on boron icosahedra. Furthermore, several numerical studies suggest the existence of a large family of compound nanotubular materials derived from crystalline AlB_2.

It has been presentes results of *ab initio* simulations of bundled single-wall zigzag boron nanotubes (ropes) [285]. Besides the known smooth and puckered modifications, there were found new forms that are radially constricted, and which seem to be energetically superior to the known isomers. Those structures might be interpreted as intermediate states between ideal tubular phases and the known bulk phases based on boron icosahedra.

Experimental and computational simulations revealed [31] that boron clusters, which favor 2D structures up to 18 atoms, prefer 3D structures beginning at 20 atoms. Using global optimization methods, it was found that the B_{20} neutral cluster has a double-ring tubular structure with diameter of 5.2 Å. For the B_{20}^- anion, the tubular structure is shown to be isoenergetical to 2D structures, which were observed and confirmed by photoelectron

spectroscopy. The 2D-to-3D structural transition observed at B_{20} suggests that it may be considered as the embryo of the thinnest single-walled boron nanotubes.

Evans et al reported [274] the results of *ab initio* calculations showing that boron can form a wide variety of metastable planar and nanotubular forms with unusual electronic and mechanical properties. When the plane is rolled into a tube, the 2-fold ground-state degeneracy of flat triangular plane leads to a strong chirality-dependence of the binding energy and elastic response, an unusual property that is not found in carbon nanotubes. The achiral (n, 0) tubes derive their structure from the flat triangular plane. The achiral (n, n) boron nanotubes arise from the buckled plane, and have large cohesive energies and different structures. (n, n) boron nanotubes have an internal relaxation mechanism that results in very low Poisson ratio.

DFT calculations have been carried out [275] to obtain the geometric and electronic structures of boron nanotubes. Boron nanotubes formed by rolling a buckled B-sheet exhibit also buckled surface when their helicity allows for the formation of alternating up and down B rows in the surface. In all other cases, boron nanotubes exhibit only flat surfaces. Hence, all the (n, 0) boron nanotubes have buckled geometry, while not all (n, 0) boron nanotubes have the same geometry. The flat and buckled nanotubes have different geometric and bonding characteristics, but both are metallic.

As it was above mentioned, in order to elaborate a direct experimental method available for structural determination of boron clusters, [36] photoelectron spectroscopy of size-selected cluster anions was combined with quantum calculations to probe the atomic and electronic structures and chemical bonding of small boron clusters up to 20 atoms. In particular, it was found that for neutral boron clusters the planar to 3D structural transition occurs at B_{20}, which possesses a double-ring structure, even though the B_{20}^- anion remains planar. The stability of the double-ring structure is interesting, suggesting possible existence of all-boron nanotubes.

The structures of a family of multi-walled boron nanotubes, which are built from hexagonal pyramids, has been proposed by Mukhopadhyay et al at the first time [286, 287]. In addition, it was determined the geometry, electronic and structural properties of 3 cluster-families: boron spheres, double-rings and quasi-planars up to a cluster size of 122 atoms and compared the stability of the cluster families to each other, and reported a structural transition from 2D quasi-planar clusters to 3D double-rings. Transition occurs between B_{16} and B_{19}.

In [288], it was investigated the properties of nanotubes obtained from newely described boron α-sheet, using DFT. Computations confirmed their high stability and identified mechanical stiffness parameters. This allows one to further analyze the basic vibrations, including the radial breathing mode Raman frequency, 210 / cm. Careful relaxation revealed the curvature-induced buckling of certain atoms off the original plane. This distortion changes the overlap of the orbitals near the Fermi level and opens up the gap in narrow tubes, rendering them semiconducting. Wider tubes with the diameter $d > 1.7$ nm retain original metallic character of the α-sheet.

The configurations, stability and electronic structures of a new class of boron nanotubes have been predicted within the framework of DFT at the GGA level [281]. Stable boron nanotubes with various diameters and chiral vectors can be rolled from the boron sheet. Only

the thin (8, 0) nanotube was found to be semiconducting with band gap of 0.44 eV, while all the other thick boron nanotubes should be metallic independent of their chirality.

There are still many open questions on the physical properties of boron nanotubes which need to be answered on both the theoretical and experimental sides. In [289], the electronic structure and transport properties of large-diameter boron nanotubes of different structures and chiralities were theoretically investigated. Obtained results are in agreement with experimental findings and a method to control the electron transport in boron nanotubes been proposed.

In [290], it has been carried out DFT calculations using the GGA based on the PW basis set and the PP approach to study the adsorption of CO, O_2 and He to boron nanotubes. The calculations are done for a (6, 0) semiconducting boron nanotube tube with the 96 boron atoms. In calculations for adsorption of gases on the perfect tube, 7, 5 and 4 possible initial configurations for CO, O_2 and He have been considered, respectively. So, authors could find the best position for each of them. It was realized that the interaction between the nanotube and these gas molecules is weak. The electronic DOS of (6, 0) tube adsorbed with O_2 along with that of the pure one was shown. It was also found that O_2 has significant influence on the electronic structures of semiconducting boron nanotubes.

And finally, let us point to the works by Leithe–Jasper et al [291, 292] succeeded in growing hexagonal $ScB_{17}C_{0.25}$ whisker-like crystals with "inserted" boron tubes. In this crystal, boron framework is accommodated between Sc-layers. Rings of B-atoms forming tube-like structures are the key structural features. Mutually inclined boron icosahedra and large 6-membered rings are bonded to the tubular central cores around the *c*-axis. Interatomic distances of B-atoms are all in the usual range of lengths observed in higher borides (0.15 to 0.19 nm). The main structural features, the 0.35 nm diameter "tunnels", the 1.45 nm diameter 12-membered rings of Sc and the 1 nm diameter hexagonal rings of icosahedra, were resolved.

9.2. Geometrical models for boron nanotubes

For analysis of the boron nanotubular structures and future purposeful designing devices based on nanotubular boron it is important to be able to predict reliably the sizes of nanotubes with given indexes. At first such kind model was proposed in [293].

We have solved this task for the mostly regular forms with equal B – B lengths, which exhibit rolled flat surfaces. Within the frames of model proposed, we have obtained [294-298] the explicit expressions in term of B – B bond length for atomic sites coordinates and intersite distances in boron nanotubes of regular geometry. If $d_{(n,0)}$ is the B – B bonds length in a zigzag (n, 0) nanotube the tube radius $r_{(n,0)}$ is expressed as

$$r_{(n,0)} = \frac{\sqrt{3}\, d_{(n,0)}}{4\sin \pi / 2n}.$$

Let $d_{(n,n)}$ and $r_{(n,n)}$, respectively, denote the B – B bond length and radius in an armchair (n, n) nanotube, then

$$r_{(n,n)} = \frac{d_{(n,n)}}{2\sin\pi/n}.$$

Here nanotube index $n = 1,2,3,...$ determines the number of atoms because the nanotube unit cell consists of $2n$ boron atoms. At $n = 1$ zigzag nanotube degenerate in zigzag atomic chain, while armchair nanotube degenerate in straight atomic chain. Correspondingly, formula obtained for $r_{(n,n)}$ in general case, does not works; instead it should be assumed $r_{(1,1)} = 0$.

Now about the detailed regular geometries of the zigzag and armchair boron nanotubes, which we can describe using cylindrical coordinates $\vec{r}\,(\rho,\varphi,z)$. Constant of the zigzag $(n, 0)$ nanotube 1D-lattice equals to $d_{(n,0)}$. Its unit cell consists of 2 equidistant atomic rings in parallel planes perpendicular to the axis, each with n boron atoms. Evidently, cylindrical coordinate ρ for all atomic sites equals to tube radius:

$$\rho = r_{(n,0)}.$$

As for the coordinates φ and z, they equal to

$$\varphi = \frac{(4k-3-(-1)^l)\pi}{2n},$$

$$z = \frac{l\,d_{(n,0)}}{2}.$$

Here $k = 1,2,3,\ldots,n$ and $l = 0,\pm1,\pm2,\ldots$ number atomic sites in given plane and atomic planes, respectively. If $d_{(n,n)}$ is the B – B bond length in an armchair (n, n) nanotube, then its 1D lattice constant equals $\sqrt{4-1/\cos^2\pi/2n}\;d_{(n,n)}$. The unit cell also consists of two atomic rings in parallel planes perpendicular to the tube axis and, from its part, each ring consists of n boron atoms. Coordinate ρ for all atomic sites again equals to tube radius:

$$\rho = r_{(n,n)},$$

while the rest cylindrical coordinates equal to

$$\varphi = \frac{(4k-3-(-1)^l)\pi}{2n},$$

$$z = \sqrt{1-\frac{1}{4\cos^2\pi/2n}}\;l\,d_{(n,n)},$$

where again $k = 1,2,3,\ldots,n$ and $l = 0,\pm1,\pm2,\ldots$. On the basis of above obtained relations, it was found the squared distances between an arbitrary atomic site $\vec{r}\,(\rho,\varphi,z)$ and site $\vec{r}_0\,(\rho,0,0)$ of the so-called "central atom" with $l = 0$ and $k = 1$, i.e. with $\varphi = 0$ and $z = 0$, in zigzag

$$\frac{(^{kl}_{(n,0)}\mathrm{B} - {}^{00}_{(n,0)}\mathrm{B})^2}{d^2_{(n,0)}} = \frac{3\sin^2(4k-3-(-1)^l)\pi/4n}{4\sin^2\pi/2n} + \frac{l^2}{4},$$

and armchair tubes

$$\frac{(^{kl}_{(n,n)}\mathrm{B} - {}^{00}_{(n,n)}\mathrm{B})^2}{d^2_{(n,n)}} = \frac{\sin^2(4k-3-(-1)^l)\pi/4n}{\sin^2\pi/n} + \left(1-\frac{1}{4\cos^2\pi/2n}\right)l^2.$$

Independently, an analogous exact idealized polyhedral model has formulated by to describe the geometry of single-walled boron nanotubes in [299]. The boron nanotubes were

assumed to be formed by sp^2 hybridization and adopt a flat equilateral triangle pattern. Beginning from the two fundamental postulates that (1) all bond length are equal and (2) all atoms are equidistant from the common cylindrical axis, it has been derived exact formulas for the geometric parameters of the nanotube radius, bond angle and unit cell length, and presented asymptotic expansions for these quantities to the first two orders of magnitude. The fundamental variable of this model is the subtend semi-angle from which all the other parameters are derived and it is given as a root of a transcendental equation and therefore cannot be written as an explicit analytical function of tube indexes. Good agreement was demonstrated for predictions of the polyhedral model, compared with the results obtained from *ab initio* simulations. The polyhedral model allows the possible identification of an inner radius, so that the notion of boron nanotube wall thickness can be introduced. The geometric structures of some ultra-small boron nanotubes were examined. It should be emphasized that although in idealized model all bond length are adopted to be equal, a similar but more sophisticated polyhedral model of boron nanotubes might incorporate unequal bond lengths.

Authors survey [300] a number of existing nanotubular boron structures which have been proposed by them as possible exact geometric models for boron nanotubes taking into account that conventional rolled-up model of nanotubes completely ignores any effects due to curvature. It is a review of number of developments relating to the geometry of boron nanotubes, including both the traditional rolled-up model and exact polyhedral construction, also including results for the case when the bond lengths may take on distinct values.

9.3. Estimates for ground state parameters of boron nanotubes

We have developed a quasi-classical approach to the calculation substance atomic and electronic structures [301]. It was demonstrated that an atom can be considered as a quasi-classical electron system in sense of Maslov criterion and, on this basis, the quasi-classical method of the construction of interatomic pair potentials was elaborated [302, 303]. In particular, this method had been used to obtain boron–boron pair interatomic potential. Within the initial quasi-classical approximation, using quadratic polynomial expression for the electron screening factor standing in the effective atomic potential, the binding energy $E = E(d)$ between pair of boron atoms was found as piece-wise algebraic function of the interatomic distance d and known quasi-classical parameters of the electron-density and potential distributions in the interacting atoms. These parameters and electron cloud radii can be obtained by fitting quasi-classical electron energy levels and mean orbital radii of electrons to their *ab initio*, e.g. HF, values.

The proposed quasi-classical B – B binding energy function in dependence on interatomic distance $E = E(d)$ seems to be useful in calculations performed to obtain ground-state characteristics of boron structures. Part of its parameters, like the coefficients of harmonic and anharmonic terms in the corresponding interatomic potential (converted from the total energy using virial theorem), and atomic core charge (which is about 3, i.e. near the valency of boron atom) were successfully applied to interpret boron isotopic composition effect [237] on

structural [305-308] and melting parameters [309-311], respectively. As for the analysis of the binding energy curve itself based on the parameters obtained equating quasi-classical electron energy levels and mean orbital radii of the electrons with their HF values, it leads to the equilibrium B – B distance of 1.78 Å, binding energy at that distance of 2.80 eV, and relative vibration frequency of 0.131 eV. These values only by few percents are deviated from the averaged experimental B – B bond length in main structural units of boron and boron-rich compounds – icosahedra of 1.80 Å, dissociation energy of 2.69 eV, and oscillatory quantum of 0.130 eV of diboron molecule B_2, respectively.

Table 1. Tabulated boron–boron binding energy function.

d , a.u.	$E(d)$, a.u.
3.20	0.101408
3.21	0.101656
3.22	0.101887
3.23	0.102100
3.24	0.102297
3.25	0.102478
3.26	0.102642
3.27	0.102791
3.28	0.102925
3.29	0.103043
3.30	0.103147
3.31	0.103236
3.32	0.103311
3.33	0.103372
3.34	0.103420
3.35	0.103454
3.36	0.103475
3.37	0.103483
3.38	0.103479
3.39	0.103462
3.40	0.103433
3.41	0.103393
3.42	0.103341
3.43	0.103278
3.44	0.103203
3.45	0.103118
3.46	0.103023
3.47	0.102917
3.48	0.102802
3.49	0.102677
3.50	0.102542

The binding energy curve obtained in initial quasi-classical approximation for interacting boron atoms is expressed by a piece-wise analytical function. Evidently, for numerical calculations the tabulated form would be more appropriate. Here such form (in a.u.) is given in Table 1 over the range from $d = 3.20$ up to 3.50 a.u. (i.e. in the vicinity of equilibrium interatomic distance of 3.37 a.u. ≈ 1.78 Å) with step of argument of 0.01 a.u., what seems sufficient to provide accurate energy computations.

Table 2. Estimated radii of boron zigzag and armchair nanotubes.

$(n, 0)$ or (n, n)	$r_{(n,0)}$ or $r_{(n,n)}$, Å
(1, 1)	0.00
(1, 0)	0.77
(2, 2)	0.89
(3, 3)	1.03
(2, 0)	1.09
(4, 4)	1.26
(5, 5)	1.51
(3, 0)	1.54
(6, 6)	1.78
(4, 0)	2.01
(7, 7)	2.05
(8, 8)	2.33
(5, 0)	2.49
(9, 9)	2.60
(10, 10)	2.88
(6, 0)	2.98
(11, 11)	3.16
(12, 12)	3.44
(7, 0)	3.46

This curve together with obtained formulas should be useful for calculating of boron nanotubes geometrical and other parameters. On basis of these formulas, sizes of the small single-walled B-nanotubes were estimated (Table 2) assuming bond lengths as $d_0 \approx 1.78$ Å, what is the equilibrium interatomic distance value according to the quasi-classical B – B pair potential. Actually, $d_{(n,0)}$ and $d_{(n,n)}$ depend on n; and their exact values can not be determined only geometrically. In general, this task requires solving of the physical problem of the binding energy maximization for given nanotubular structure with respect B – B bond length. But, these dependences evidently have to be weak and in all cases in satisfactory approximation both $d_{(n,0)}$ and $d_{(n,n)}$ can be substituted by the mentioned value of 1.78 Å.

Analogously, one can estimate molar binding energy of a boron nanotube. Any constituent boron atom has 6 nearest neighbors and binding energy between pair of boron atoms is about 2.80 eV. So, taking into account interaction only between nearest neighbors the

tube binding energy per atom may be calculated as 2.80 eV × 6 / 2 = 8.40 eV. Of course, it is a crude estimation: actually binding energy should depend on the tube index.

Thus, using the electron-density and potential distributions in a boron atom parameterized within the initial quasi-classical approximation, it is possible to tabulate boron–boron pair binding energy curve, which leads to the boron–boron equilibrium interatomic distance, equilibrium binding energy, and relative vibration frequency values only slightly deviated from averaged bond length in structural units of boron and boron-rich solids, dissociation energy, and oscillatory quantum of the diboron molecule, respectively. On this basis, the B – B bond length and molar binding energy in a boron nanotube are predicted to be about 1.78 Å and 8.40 eV, respectively.

Note that there was presented a non-self-consistent density-functional based construction of nonorthogonal matrix elements for B and some other boron-containing species within the framework of the LCAO formalism using the local-density approximation (LDA) [312]. Despite the simplicity of the scheme considering only 2-center Hamiltonian integrals and overlap matrix elements, the method has been proven to be sufficiently accurate and transferable to all scale BN(H) structures from small clusters and molecules to crystalline solids and solid surfaces.

9.4. Applications of boron nanotubes

As for the applications of nanotubular boron, obtained theoretical results together with "Aufbau Principle" should help when searching for boron-based nanotubular or atomic-scaled microelectronic devices. It was indicated the possibility, in the design of the nanodevice, to control the electronic transport properties of the boron nanotube through the diameter. The strong variation in elastic properties of boron nanotubes makes them the mechanical analogue of carbon nanotubes, and may make them ideal candidates for application in composite materials and nano-electromechanical systems.

Novel boron-based nanotubular materials were compared to standard nanotubular systems built from carbon, and pointed out a number of remarkable structural and electronic properties. The success of future nanotechnologies will strongly depend on ability to control the structure of materials on the atomic scale. For carbon nanotubes it turns out that one of their structural parameters, the chirality, may not be controlled during synthesis. The basic reason for this defect was explained and shown that novel classes of nanotubes like boron nanotubes, which are related to sheets with anisotropic in-plane mechanical properties, could actually overcome these problems [313]. Obtained results further suggest that extended searches for nanomaterials similar to pure boron might allow for one of the simplest and most direct ways to achieve structural control within nanotechnology.

Boron nanotubes theoretically proposed to have metallic properties whether they are in armchair or zigzag structure, so they have attracted much interest. However, their real properties have been not understood because they are hard to synthesize. Recently, in [314] a large quantity of boron nanotubes, which may provide a way to master their electric and field

emission properties, have been successfully fabricated. Study on individual boron nanotubes showed that they have metallic properties with an averaged conductivity of $40 / \Omega \cdot \mathrm{cm}$. Moreover, individual boron nanotubes can sustain a high current of about 80 μA and their current density can reach $2.04 \cdot 10^{11}\ \mathrm{A} / \mathrm{m}^2$, which is very close to those of carbon nanotubes. They are also incorporated into prototype luminescent tube devices for the first time and exhibit high luminescent efficiency and stability, which suggests that boron nanotubes have a promising future in the field emission area.

Wide boron tubes rolled from α-sheet retain its original metallic character. This combination of properties could make boron α-tubes an important material for electronic, bio- and chemical sensing, and optical applications.

The study of adsorbents on nanoparticle surfaces, in particular, boron nanotubes has become of central interest in surface science because of the enormous importance of catalytic and gas sensors for industrial applications.

10. Boron cages

As it has been above mentioned, an interesting feature of elemental boron and boron compounds in solid state is the occurrence of highly symmetric icosahedral clusters. The rich chemistry of boron also dominated by other 3D cage structures. Part of the final structures of the cationic boron clusters B_n^+ ($n = 2 - 14$) obtained [21] by the linear search for minima on the LSD PES, prefers such quasi-planar atomic arrangements that can be considered as segments of a sphere. The structure and stability of small neutral boron clusters B_n ($n = 2 - 14$) was investigated [315] employing DFT. The search for minima was performed using gradient methods at the LSD. Part of final structures prefer quasi-planar forms and can be considered as segments of the surface of a sphere. From the curvature and size of the convex clusters, it was predicted that this spherical cluster should consist of 90 boron atoms, and there may exist a group of elemental spherical boron clusters. The frequency analysis was carried out for the most stable convex and quasi-planar clusters only. All these clusters have vibrational frequencies corresponding to the local minima. Most of the calculated IR vibration frequencies lie in the interval $200 - 1400 / \mathrm{cm}$. In addition to the main conclusion that most of the neutral and cationic boron clusters have similar topologies one can deduce that the evolution of most of the structures with increasing cluster size exhibits some striking regularities: (1) the participation of the pentagonal, hexagonal or heptagonal pyramids seems to be energetically favorable; (2) the convex clusters tend to converge to a definite spherical cluster consisting of about 90 atoms; (3) the quasi-planar structures tend to attain a planar surface with large number of atoms; (4) the 3D structures, which are less stable than the respective 2D structure, try to close the open spheres with a small number of atoms.

Based on a systematic *ab initio* HF SCF and direct CI methods Boustani suggested [316] that stable convex and spherical structures of bare boron clusters can easily be obtained with help of an “Aufbau Principle”: there exist only two basic units, the pentagonal and hexagonal

pyramids, which can form different boron structures (spherical clusters can be constructed only by a combination of pentagonal pyramids leading to 3D structures with hexagonal pyramids). Introduced convex and small spherical clusters differ from the "classical" forms known for boron crystals. Convex surfaces simulate boron surfaces which can be considered as segments of open or closed spheres. Two convex clusters B_{16} and B_{46} have energies close to those of their conjugate quasi-planar clusters, which are relatively stable and can be considered to act as a calibration mark. The closed spherical clusters B_{12}, B_{22}, B_{32}, and B_{42} are found to be less stable than the corresponding conjugated quasi-planar structures. As a consequence, highly stable spherical boron clusters can systematically be predicted when their conjugate quasi-planar clusters are determined and energies are compared.

Using *ab initio* QC methods, accurate calculations on small boron clusters B_n ($n = 2 - 14$) were carried out [25] to determine their electronic and geometric structures. The geometry optimization with a linear search to local minima on the PES was performed using analytical gradients in the framework of the restricted HF SCF approach. Most of the final structures of the boron clusters with $n > 9$ results in convex structures, which can be considered as segments of hollow spheres.

Some highly spherical shells of boron atoms including "supericosahedron" B_{156}, which can exist in boron-rich solids, was considered by Perkins et al [317].

Applying *ab initio* QC methods, different structures of B_{32} cluster was investigated [27]. Hollow spheres are found to be less stable than quasi-planar and tubular isomers.

The curiously stable B_{13}^+ cationic cluster and its neutral and anionic counterparts were examined [28] though the use of DFT. An intriguing atom-in-cage structure was found to be a local minimum on the cationic, neutral, and anionic surfaces. A structure was found for the B_{13}^- anionic cluster, and the 12 external boron atoms are determined to be arranged as 3 6-membered rings back-to-back.

The electronic and geometric structures, total and binding energies, harmonic frequencies, point symmetries, and HOMO–LUMO gaps of small neutral boron B_n ($n = 2 - 12$) clusters has been investigated [34] using DFT. Convex and 3D cage and open-cage structures were found along with other structures. None of the lowest energy structures and their isomers has an inner atom. i.e., all the atoms are positioned at the surface.

The geometry, electronic, and structural properties of an unusually stable boron cage made of 80 boron atoms were studied, using *ab initio* calculations [318] (see [319]). The shape of this cluster is very similar to that of the well-known C_{60} fullerene, but in the B_{80} case, there is an additional atom in the center of each hexagon. The resulting cage has a relatively large highest occupied and lowest unoccupied energy gap (~ 1 eV) and, most importantly, is energetically more stable than boron double rings, which were detected in experiments and considered as building blocks of boron nanotubes. This seems to be most stable boron cage.

Based on *ab initio* QC and DFT methods, the [286, 287] determined the geometry, electronic and structural properties of 3 cluster-families: boron spheres, double-rings and quasi-planars up to a cluster size of 122 atoms. The most stable structure is the B_{100} sphere showing

similar shape but more stability than the B_{80} cage. The structures of a family of nearly round boron cages which are built from hexagonal pyramids had been proposed at the first time.

Using *ab initio* calculations, the [320] analyzed electronic structure and vibrational modes of the boron fullerene B_{80}, a stable spherical cage similar in shape to the well-known C_{60}. There exist several isomers, lying close in structure and energy, with total energy difference within 30 meV. It was presented the detailed analysis of their electronic structure and geometry. Calculated radial breathing mode frequency turns out to be 474 / cm, which can be a characteristic of B_{80} in Raman spectroscopy. Since the B_{80} structure is made of interwoven double-ring clusters, double-rings with various diameters also were investigated, presented their structure and HOMO–LUMO dependence on the diameter, and found out that the gap alternates for different sizes and closes its value for infinite double-ring.

The symmetry of the boron buckyball and a related boron nanotube was investigated in [321]. Using large-scale *ab initio* calculations up to second-order Møller–Plesset perturbation theory, it has been determined unambiguously the equilibrium geometry / symmetry of two structurally related boron clusters: the B_{80} fullerene and the finite-length (5, 0) boron nanotube. The B_{80} cluster was found to have the same symmetry as the carbon C_{60} molecule since its 20 additional boron atoms are located exactly at the centers of the 20 hexagons. Additionally, authirs showed that the (5, 0) boron nanotube does not suffer from atomic buckling. All the boron nanotubes rolled from the α-sheet are predicted to be free from structural distortions, which has a significant impact on their electronic properties.

Ab initio electronic structure calculations showed that boron clusters B_{98}, B_{99}, B_{100}, B_{101}, and B_{102} based on icosahedral-B_{12} stuffed fullerenes are more stable than the fullerene-like boron clusters [322]. These structures are envisaged as an icosahedral B_{12} each vertex of which is connected to the apex of a pentagonal pyramid B_6 via radial σ-bonds. The resulting B_{84} ($B_{12}@B_{12}@B_{60}$) retains the same symmetry as C_{60}, and the B_n ($n = 84 – 116$) clusters are generated around it. It was considered the possibility of producing such B_{12}-based giant clusters.

In a few words about other boron-containing cage molecules.

The relative thermodynamic stability of certain boron containing fullerenes B_xC_{y-x}, $C_xB_yH_z$ and $C_xB_yF_z$ (x, y, $z > 10$) was studied by Kuznetsov & Ionov [323]. Some of the concepts of theoretical chemistry were applied to the problem of boron–carbon bonds formation upon introduction of B atoms in cluster molecules composed of carbon atoms. In such cluster molecules, one can expect the formation of multi-center bonds in different rings. The character of these bonds varies from the localized Heitler–London type bonds to the systems with the boron-mediated antiferromagnetic superexchange interaction. Introduction of B donor atoms drastically alerts the donor-acceptor properties of the fullerene C_{60}. The problem of bond energy calculation in B_xC_{y-x} was solved in frame of new semi-empirical theory which connects thermodynamic and structural properties. It was shown that the hetero-fullerenes B_xC_{y-x} with $x = 5, 10$ and $y = 60$ are less stable than C_{60}. On the other hand, the cluster B_{32} is expected to have high thermodynamic stability in comparison with C_{60} and $B_{10}C_{50}$. The results allow concluding that stability decreases with increasing interatomic distances between hetero-atoms although there are some oscillations. The thermodynamic properties (enthalpy and bond

energy) had been evaluated for the following cluster molecules: $B_{10}C_{50}$, $B_{12}C_{48}$, $B_{16}C_{44}$, $B_{18}C_{41}$, $B_{10}C_{10}$, B_{32}, B_{42}, and $B_{32}H_{32}$. The trends in stability observed upon changing composition and character of multi-center bonds in n-membered rings (n = 3, 4, 5, 6) were analyzed.

Prediction of a hollow fullerene-like boron cluster B_{80} has been provocative and motivating to rapid further research in field of boron nanostructures. A variety of competing structures, of lower symmetries and even with different topologies (stuffed, non-hollow) have been proposed and extensively studied, in theory. Authors of [324] have outlined the progress in computational and theoretical analysis of the emerging possibilities. They also have put the stability of pure-boron nanostructures in the context of broader thermodynamics, a compositional triangle of greater interest, B-C-N, where pure C allotropes are well established, pure N phase appears impossible, while pure B and various intermediate $B_xC_yN_z$ compositions and their interfaces are rich in properties, allow controllable assembly and remain a focus of active exploration.

Their previous research on nano-sized clusters of boron and boron compounds Atiş et al [325] have extended to investigate the hydrogen storage capacity of Li_nB_m ($n + m = 6$) clusters within the DFT. It was shown that the number of hydrogen increases the stability and HONO–LUMO energy gap, which indicated the lower reactivity features of the clusters. By comparing the results with available data it was stated that with the bare boron clusters alone, it is difficult to increase the capacity of the hydrogen storage.

As for the applications of boron fullerenes, as it was stated nano-sized cage clusters of bare boron and, especially, borides can serve for hydrogen storage.

11. Boron nanocrystals

Quasicrystals are intermediate species between periodical crystals and amorphous solids: on the one hand, they possess 5-fold symmetry axis materialized in structural element – icosahedron, but, at the other hand, they are not periodical. This issue takes on special significance in connection with boron because icosahedral-cluster structures are characteristic of all boron crystalline modifications. At first let us point to some studies devoted to quasicrystals of other elements and quasicrystals in general, which can be useful analyzing boron case. A model of geometrical structure of icosahedral quasicrystals that was discussed [326] is based on icosahedral clusters connected by linkages (consistent with accepted motif of the atomic structure). Such geometry should be convenient for complete atomic structure models defined by decoration, especially if configurational disorder is to be included. Using time-dependent DFT, Xie et al showed [327] that the first singlet excitations of series of icosahedral clusters are optically forbidden and that their optical absorption gaps and spectral properties are size- and composition-dependent and can be tuned broadly in the UV–visible region. It was demonstrated that optical gaps of icosahedral clusters can be tailored from the UV to near IR by properly doping them with (transition) metals, hydrogen, group VII B atoms, and organic functional groups. Thus, icosahedral clusters are suitable for tunable optical

applications. Relative stabilities of the alternative carbon nanoparticles with icosahedral symmetry (diamond-like nanocrystals and multi-shelled fullerenes – onions) have been studied [328] applying a parametric model and also by the charge-DFT within the tight-binding approximation. It was demonstrated that increasing in particles' sizes as well as their hydrogenation stabilize the diamond-like crystallites. Formation of "intermediate' nanostructures build up from the diamond-like crystallites inside the fullerene-shell was found out as well. A jellium-passivated cluster model was developed [329] to study the energetics of short-range ordering in supercooled liquid and glass systems. The energy difference between icosahedral clusters and fcc embryos in jellium was found to correlate with glass-forming ability of liquid Al alloys. Celino et al elucidated the role played by defective icosahedra on the stability of undercooled copper by using molecular-dynamics simulations [330]. It was shown that not only perfect but also defective icosahedra embedded in a disordered matrix, lower the local cohesive energy. This is the effect of stabilizing the liquid structure against crystallization. This study identified the nature of those icosahedral subunits that contribute to the stability of the undercooled liquid.

Based on a series of *ab initio* studies it had been pointed out the remarkable structural stability of nanotubular and quasi-planar boron clusters, and postulated the existence of novel layered, tubular, and quasicrystalline boron solids built from elemental subunits [331, 332]. Performed study illustrated and predicted qualitative structural and electronic properties for various models of nanotubular and layered boron solids, and compared them to well-known tubular and layered forms of pure carbon and mixed boron compounds.

An oblate rhombohedral unit cell of α-B crystal was constructed and the transition of 2 boron icosahedra B_{12} lying at the ends of its short body diagonal was estimated in [333]. Applying *ab initio* HF SCF methods it was investigated different configurations of 2 icosahedra. The obtained structure B_{24} exhibits a closed tubular form of 2 coalesced interpenetrating icosahedra. Model based on a B_{21} cluster, composed 2 icosahedra with mutual 3 interfacing atoms, was also studied. Then, it was considered [334] unit cell of hypothetical α-B quasicrystals by applying accurate *ab initio* QC methods. As it is known, atomic decoration of the α-B unit cell is based on a suitable arrangement of 8 boron icosahedra, and thus the mechanism of their cohesion is stimulated by relaxing a B_{96} supercluster composed icosahedral boron clusters located at the vertexes of the rhombohedral unit cell. Several alternative structure of B_{96} clusters were proposed and compared to the rhombohedral phase. Total energies of those structures were computed on the basis of all-electron calculations at the HF SCF level of theory. Due to the large number of degrees of freedom, the geometries of all isomers were optimized under reasonable symmetry constrains. Total energies showed that segments of nanotubes and quasi-planar sheets turn out to be more stable than the unit cell of α-B quasicrystals.

The surface energies of α- and β-rhombohedral and tetragonal boron were *ab initio* calculated [335, 336] to investigate their role in nanoscale crystal growth. Equilibrium shapes of boron crystals were obtained using Wulff's theorem. Although the existence of pure α-tetragonal boron had long been denied (as it was above mentioned) α-tetragonal boron was recently prepared in the form of a nanowire. Indeed, results of calculations showed that

α-tetragonal boron, despite its low cohesive energy, is more stable than the other structures as a result of its low surface energy when the number of atoms is less than about 216. The nanowire of α-tetragonal boron that was obtained experimentally probably was in a metastable state. The difference between the surface energy of the *ab*-plane and that of the *ac*-plane explains why the α-tetragonal boron nanowire grows in the *c*-direction. The surface energy of β-tetragonal boron was found to be higher than that of α-tetragonal boron, and lower than that of α-rhombohedral and β-rhombohedral boron. Nevertheless, β-tetragonal boron has the lowest total energy of all boron polymorphs in a region with a numbers of atoms 216 – 512. This explains why β-tetragonal boron can be obtained by gas-phase synthesis but not by liquid-phase synthesis because an appropriate number of atoms must be isolated to obtain the β-tetragonal boron structure. The real crystal was probably obtained through non-equilibrium growth. Since the surface energy of this modification is rather isotropic, it will not have a wire-like morphology.

12. Conclusions

Bare boron exhibits a variety of micro- and nano-structured forms, which can find applications in a number of wide fields of techniques and technologies. This diversity reduces to features of the electronic structure of an isolated boron atom B, which being associated in a multi-atomic network tends to the most stable electronic configuration adding one or two extra electrons from point imperfections of a structure and / or foreign impurity atoms.

Boron molecular clusters B_n (n = 2, 3, 4, …) at relatively low index n reveal a planar (flat) or quasi-planar (buckled) surfaces, which can be considered as fragments of flat or buckled boron sheets, respectively. But, at relatively high n they are open or closed convex surfaces, which are imagined as fragments of boron tubules and fullerenes or tubules and fullerenes themselves defending they are rolled cylindrically or spherically, respectively. Ordering by stability of these structures changes depending on their charge state because the stability of a boron molecular cluster increases if dangling bonds on its surface are saturated by extra electrons provided by foreign atoms associated with cluster.

Electron deficiency characteristic of boron structures leads to the clustered crystalline structures of elemental boron and most of boron-rich compounds. As a rule, constituent clusters are only slightly distorted (i.e., almost ideal) boron icosahedron B_{12} and its fragments. The preference for icosahedral cluster is based on electron requirements: it is a polyhedral building block with boron atoms at vertexes which needs minimal number (a pair) of extra electrons to stabilize its atomic structure. All main boron crystalline structures, α- and β-rhombohedral and tetragonal modifications of boron are open networks with many crystallographic voids in which icosahedra can be linked together in a variety of ways.

From the theoretical calculations α-rhombohedral boron has been shown to be the most stable phase at low temperatures among icosahedron-based boron crystals. This is consistent with low-temperature crystal growth of α-rhombohedral boron. But, on the other hand, from all available experiments the β-rhombohedral structure of boron is known to be stable over all

temperatures from absolute zero to melting. The explanation is accounted for possible structural imperfections in real crystals: unlike α-rhombohedral boron, in which every site is almost fully occupied, β-rhombohedral boron is characterized by significant partial occupancies of regular sites in lattice, self-interstitial atoms in high concentration and related intrinsic disorder. Optimizing the site occupation yields a superstructure of β-rhombohedral boron – β'-rhombohedral boron. Its energy is lower than α-rhombohedral boron, but its symmetry is lower than β-rhombohedral boron. Thus, it can be found a unique, energy-minimizing pattern of occupied and vacant sites that can be stable at low temperatures, but that breaks the β-rhombohedral symmetry.

As for the α- and β-tetragonal boron, their macro-crystals are believed to be structures stabilized by presence of point structural imperfections and certain impurities in high concentrations. But, situation changes in case of finite number of atoms in a crystal. Namely, although the existence of pure α-tetragonal boron had long been denied α-tetragonal boron was prepared in the form of a nanowire. Indeed, results of calculations showed that α-tetragonal boron, despite its low cohesive energy, is more stable than the other structures as a result of its low surface energy when the number of atoms is too small. The mentioned nanowire of α-tetragonal boron was probably in a metastable state. The difference between the surface energy of the *ab*-plane and that of the *ac*-plane explains why the α-tetragonal boron nanowire grows in the *c*-direction. The surface energy of β-tetragonal boron was found to be higher than that of α-tetragonal boron, and lower than that of α-rhombohedral and β-rhombohedral boron. Nevertheless, β-tetragonal boron has the lowest total energy of all boron polymorphs in a region with a low numbers of atoms. This explains why β-tetragonal boron can be obtained by gas-phase synthesis but not by liquid-phase synthesis because an appropriate number of atoms must be isolated to obtain the β-tetragonal boron structure. The real crystal was probably obtained through non-equilibrium growth. Since the surface energy of this modification is rather isotropic, it will probably not have a wire-like morphology.

Solid state boron can also exist in amorphous form as thin films or fine-dispersed powders. High chemical activity of dispersed amorphous boron makes it as valuable product for chemical synthesis. Features of the diffraction pattern point on short-range ordering characteristic of an icosahedron and randomly distributed icosahedra. Both amorphous films and powders are constructed from the randomly orientated and bounded boron icosahedra in structure close to tetragonal boron structure. Liquid boron may be considered as a disordered mixture of icosahedra, whereas amorphous boron is as a disordered packing of icosahedra. Boron, which is a refractory material, obtained at high temperatures mainly is a crystalline product, while amorphous boron is produced at relatively low temperatures. Amorphous boron, obtained at higher temperatures can be imagined as a mix of various boron modifications with icosahedral structures. Such kind of amorphous boron can be considered as fine microcrystalline β-rhombohedral boron with short-range order determined by icosahedra. Crystallization of amorphous boron is treated as ordering process of the icosahedral groups.

At the atomic level amorphous boron has a close-packed structure. Configurations consisting of several icosahedra were found to represent the structural element of powder

particles. In first approximation, all forms of amorphous boron possesses one and same structure: 3-icosahedral spheroidal aggregate and 4 icosahedra forming a tetrahedron. Real structures differ from ideal amorphous structure by the defects, another rule of linking, joined icosahedra etc. In amorphous boron, disorder occurs in the linking between icosahedra which is not entirely random at medium-range distances. But, long-range arrangement of the icosahedra in amorphous boron seems to be quite random.

The distance between obtained diffraction spots for amorphous boron corresponds to the fundamental spacing derivable from a consideration of the packing of B_{12} groups regarded as a "large atom". The fact that amorphous boron uses icosahedron as a structural unit allows introducing of function of radial distribution of icosahedra, which helps to construct a geometrical model of amorphous boron structure and to define the term "ideal amorphous structure of boron". The least is useful for quantitative characterization of defects in amorphous structure. In this model, coordination spheres of icosahedra are almost equidistant and can be described by the symmetric cubic forms, which is a consequence of the amorphous boron isotropy. The particles those can exist in amorphous boron in addition to icosahedra B_{12} are some relaxing sub-units: boron pentagons, pentagonal pyramids, partial icosahedra – polyhedrons B_{10}, and as well loose atoms not associated with any icosahedron.

Properties of both crystalline and amorphous boron are merged in boron powders obtained by the dispersion the boron crystals. The fine-dispersion of the crystalline boron leads to its amophization as a result of significant distortions of the surface structure. Degree of surface amorphization as well as boron compounds' inclusions in the process of mechanical dispersion increase with decreasing sizes of particles. However, at very small sizes particles tend to coagulation. The presence of an amorphous layer indicates the spongy surfaces of the crystallites. Amorphization during the mechanical dispersion was found to be almost independent both of the technique of preparation and the purity of the initial boron crystal. From the data obtained in the process of dispersion, the surface of the crystal is deformed and fractioned, and a so-called "amorphous pillow" appears around the crystal. In some cases these crystals may serve as centers of coagulation of similar crystals and amorphous particles.

Thermal treatment yielded coagulation of icosahedra in spheroids. Thus, ultra-dispersed powder of the elementary boron is characterized by amorphously structured particles composed of statistically distributed icosahedra and their coagulations. Structure remains in whole amorphous, but within the local regions there were obtained crystalline structure. The composition and state of chemical elements on the surface of the boron particles depend to a considerable extent on the dispersion technique and further processing of the powder.

More boron micro-structures merging properties of both crystalline and amorphous boron are boron filaments and fibers. Boron filaments and fibers are non-homogeneous structures. Usually, diffraction patterns of boron filaments and fibers deposited on hot-wire-substrate indicate an amorphous or core-microcrystalline state. Boron filaments and fibers consist of an inner boride core surrounded by an amorphous boron mantle. Their strength is affected not only by the inherent properties of the bulk boron and the condition on its surface, but also by the presence of the core material and interface between core and the boron layer.

1D nano-structures of boron like the nanowires, nanoribbons, and nanobelts as a rule have a crystalline structure of bare α-tetragonal boron without any foreign inclusions like the carbon and nitrogen atoms characteristic of α-tetragonal boron macrocrystalline structure.

2D nano-structures of boron are presented by flat or buckled sheets, and surfaces of nanotubes of various chirality, and cage-molecules including spheroidal fullerenes.

3D nano-structures of boron are presented by boron quasicrystals and nano-scale crystallites of all crystalline modifications of boron.

References

1. G. V. Tsagareishvili, F. N. Tavadze. Semiconducting Boron. 1978, Moscow: Nauka.
2. G. V. Tsagareishvili, D. Sh. Tsagareishvili. Thermal and Elastic Properties of Boron. 1990, Tbilisi: Metsniereba.
3. G. V. Tsagareishvili, M. E. Antadze, F. N. Tavadze. Producing and Structure of Boron. 1991, Tbilisi: Metsniereba.
4. B. Albert, H. Hillebrecht. Angew. Chem. Int. Ed., 2009, **48**, 8640.
5. B. M. Smirnov. Cluster Processes in Gases and Plasmas. 2010, Berlin: Wiley–VCH.
6. D. Emin. Phys. Today, 1987, **40**, 55.
7. G. Parakhonskiy, N. Dubrovinskaia, E. Bykova, R. Wirth, L. Dubrovinsky. Sci. Reps., 2011, **1**, 96.
8. A. R. Oganov, J. Chen, C. Gatti, Y. Ma, Y. Ma, C. W. Glass, Zh. Liu, T. Yu, O. O. Kurakevych, V. L. Solozhenko. Nature, 2009, **457**, 863.
9. V. L. Solozhenko, O. O. Kurakevych, A. R. Oganov. J. Superhard Mat., 2008, **30**, 428.
10. E. Yu. Zarechnaya, L. Dubrovinsky, N. Dubrovinskaia, Y. Filinchuk, D. Chernyshov, V. Dmitriev, N. Miyajima, A. el Goresy, H. F. Braun, S. van Smaalen, I. Kantor, A. Kantor, V. Prakapenka, M. Hanfland, A. S. Mikhaylushkin, I. A. Abrikosov, S. I. Simak. Phys. Rev. Lett., 2009, **102**, 185501.
11. U. Haussermann, A. S. Mikhaylushkin. Inorg. Chem., 2010, **49**, 11270.
12. C. Gatti, A. R. Oganov, V. L. Solozhenko. In: Abs. 17th Int. Symp. Boron, Borides & Rel. Mat. 2011, Ankara: BKM, 172.
13. S. Aydın, M. Şimşek. In: Abs. 17th Int. Symp. Boron, Borides & Rel. Mat. 2011, Ankara: BKM, 107.
14. Ch. Feldman, K. Moorjani, N. Blum. In: Boron – Obtaining, Structure, and Properties. 1974, Moscow: Nauka.
15. L. Hanley, J. L. Whitten, S. L. Anderson. J. Phys. Chem., 1988, **92**, 5803.
16. L. Hanley, J. L. Whitten, S. L. Anderson. J. Phys. Chem., 1990, **94**, 2218.
17. S. J. la Placa, P. A. Roland, J. J. Wynne. Chem. Phys. Lett., 1992, **190**, 163.
18. H. Kato, K. Yamashita, K. Morokuma. Chem. Phys. Lett., 1992, **190**, 361.
19. H. Kato, K. Yamashita, K. Morokuma. Bull. Chem. Soc. Jap., 1993, **66**, 3358.
20. A.-Ch. Tang, Q.-Sh. Li, Ch.-W. Liu, J. Li. Chem. Phys. Lett., 1993, **201**, 465.

21. I. Boustani. Int. J. Quan. Chem., 1994, **52**, 1081.
22. I. Boustani. Chem. Phys. Lett., 1995, **233**, 273.
23. A. Ricca, Ch. W. Bauschlicher Jr. Chem. Phys., 1996, **208**, 233.
24. F. L. Gu, X. Yang, A.-Ch. Tang, H. Jiao, P. von R. Schleyer. J. Comp. Chem., 1998, **19**, 203.
25. I. Boustani. Phys. Rev. B, 1997, **55-II**, 16426.
26. I. Boustani, A. Quandt. Comp. Mat. Sci., 1998, **11**, 132.
27. I. Boustani, A. Rubio, J. A. Alonso. Chem. Phys. Lett., 1999, **311**, 21.
28. J. E. Fowler, J. M. Ugalde. J. Phys. Chem. A, 2000, **104**, 397.
29. H.-J. Zhai, L.-Sh. Wang, A. N. Alexandrova, A. I. Boldyrev. J. Chem. Phys., 2002, **117**, 7917.
30. A. N. Alexandrova, A. I. Boldyrev, H.-J. Zhai, L.-Sh. Wang, E. Steiner, P. W. Fowler. J. Phys. Chem. A, 2003, **107**, 1359.
31. H.-J. Zhai, B. Kiran, J. Li, L.-Sh. Wang. Nat. Mat., 2003, **2**, 827.
32. B. Kiran, S. Bulusu, H.-J. Zhai, S. Yoo, X. Ch. Zeng, L.-Sh. Wang. Proc. Natl. Acad. Sci. USA, 2005, **102**, 961.
33. A. N. Alexandrova, A. I. Boldyrev, H.-J. Zhai, L.-Sh. Wang. Chem. Rev., 2006, **250**, 2811.
34. M. Atiş, C. Özdoğan, Z. B. Güvenç. Int. J. Quan. Chem., 2007, **107**, 729.
35. H.-J. Zhai, A. N. Alexandrova, K. A. Birch, A. I. Boldyrev, L.-Sh. Wang. Ang. Chem. Int. Ed., 2003, **42**, 6004.
36. L.-Sh. Wang. In: Abs. 16th Int. Symp. Boron, Borides & Rel. Mat. 2008, Matsue: KM, 61.
37. D. Voronovich, A. Taran, N. Shitsevalova, A. Levchenko, V. Filipov. In: Abs. 17th Int. Symp. Boron, Borides & Rel. Mat. 2011, Ankara: BKM, 106.
38. I. Boustani. In: Abs. 17th Int. Symp. Boron, Borides & Rel. Mat. 2011, Ankara: BKM, 49.
39. I. Boustani. In: Abs. 15th Int. Symp. Boron, Borides & Rel. Mat. 2005, Hamburg: UH: 41.
40. H. C. Longuet–Higgins, M. V. de Roberts. Proc. Roy. Soc. A, 1955, **230**, 110.
41. N. E. Solov'ev, E. M. Averbakh, Ya. A. Ugaj. Phys. Solid State, 1984, **26**, 195.
42. S. Lee, D. M. Bylander, L. Kleinman. Phys. Rev. B, 1990, **42**, 1316.
43. Ch. L. Beckel, J. P. Vaughan. AIP Conf. Proc., 1986, **140**, 305.
44. H. Werheit, U. Kuhlmann. Solid State Commun. 1993, **88**, 421.
45. K. Shirai, S. Conda. J. Phys. Chem. Solids, 1996, **57**, 109.
46. M. Yamaguchi, Y. Ohishi, S. Hosoi, K. Soga, K. Kimura. In: Abs. 16th Int. Symp. Boron, Borides & Rel. Mat. 2008, Matsue: KM, 106.
47. M. Yamaguchi, Y. Ohishi, S. Hosoi, K. Soga, K. Kimura. J. Phys.: Conf. Ser., 2009, **176**, 012027.
48. N. P. Konstantinidis. Phys. Rev. B, 2005, **72**, 064453.
49. H. D. Nguyen, V. S. Reddy, Ch. L. Brooks III. Nano Lett., 2007, **7**, 338.
50. S. Rovner. Chem. & Eng. News, 2011, **89** (17), 10.
51. K. Hedberg. J. Am. Chem. Soc., 1952, **74**, 3486.
52. W. Weber, M. F. Thorpe. J. Phys. Chem. Solids, 1975, **36**, 967.
53. J. V. Ortiz. AIP Conf. Proc., 1986, **140**, 274.

54. Q. Sh. Li, F. L. Gu, A. Ch. Tang. Int. J. Quant. Chem., 1994, **50**, 173.
55. N. Nogi, S. Tanaka. J. Solid State Chem., 2006, **179**, 2927.
56. Y. Ohishi, K. Kimura, M. Yamaguchi, N. Uchida, T. Kanayama. In: Abs. 16th Int. Symp. Boron, Borides & Rel. Mat. 2008, Matsue: KM, 167.
57. Y. Ohishi, K. Kimura, M. Yamaguchi, N. Uchida, T. Kanayama. J. Phys.: Conf. Ser., 2009, **176**, 012030.
58. H. Dekura, K. Shirai, A. Yanase. J. Phys.: Conf. Ser., 2009, **176**, 012005.
59. Y. Ohishi, K. Kimura, M. Yamaguchi, N. Uchida, T. Kanayama. J. Chem. Phys., 2008, **128**, 124304.
60. K. Hofmann, M. Panda, M. H. Prosenc, B. Albert. In: Abs. 16th Int. Symp. Boron, Borides & Rel. Mat. 2008, Matsue: KM, 69.
61. M. G. S. Londesborough. In: Abs. 16th Int. Symp. Boron, Borides & Rel. Mat. 2008, Matsue: KM, 70.
62. Y. Ohishi, K. Kimura, M. Yamaguchi, N. Uchida, T. Kanayama. J. Chem. Phys., 2010, **133**, 074305.
63. Y. Ohishi, K. Kimura, M. Yamaguchi, N. Uchida, T. Kanayama. In: Abs. 17th Int. Symp. Boron, Borides & Rel. Mat. 2011, Ankara: BKM, 215.
64. N. Vast, J. Sjakste, E. Betranhandy. J. Phys.: Conf. Ser., 2009, **176**, 012002.
65. K. Park, M. R. Pederson, L. L. Boyer, W. N. Mei, R. F. Sabirianov, X. C. Zeng, S. Bulusu, S. Curran, J. Dewald, E. Day, Sh. Adenwalla, M. Diaz, L. G. Rosa, S. Balaz, P. A. Dowben. Phys. Rev. B, 2006, **73**, 035109.
66. S. R. Chem. & Eng. News, 2011, **89** (13), 37.
67. R. Vandenbosch. Phys. Rev. A, 2003, **67**, 013203.
68. T. Yıldırım. In: Abs. 17th Int. Symp. Boron, Borides & Rel. Mat. 2011, Ankara: BKM, 41.
69. W. Jung, M. Weltzer, K. Petry.. In: Abs. 17th Int. Symp. Boron, Borides & Rel. Mat. 2011, Ankara: BKM, 170.
70. B. S. Krishnamoorthy, S. Kahlal, S. Ghosh, J.-F. Halet. In: Abs. 17th Int. Symp. Boron, Borides & Rel. Mat. 2011, Ankara: BKM, 269.
71. Ch. L. Beckel, I. A. Howard. Mat. Res. Soc. Symp. Proc., 1987, **97**, 51.
72. M. Böyükata, Z. B. Güvenç. Int. J. Hydr. Energy. 2011, **36**, 8392.
73. M. Böyükata, Z. B. Güvenç. J. Alloys & Comp., 2011, **509**, 4214.
74. P. Jash, K. Meaux, M. Trenary. In: Abs. 17th Int. Symp. Boron, Borides & Rel. Mat. 2011, Ankara: BKM, 234.
75. M. Böyükata, Z. B. Güvenç. In: Abs. 17th Int. Symp. Boron, Borides & Rel. Mat. 2011, Ankara: BKM, 87.
76. R. N. Grimes. AIP Conf. Proc., 1986, **140**, 31.
77. B. Albert, K. Hofmann. In: Abs. 13th Int. Symp. Boron, Borides & Rel. Comp. 1999, Dinard: CNRS, 67.
78. Sh.-I. Orimo, Y. Nakamori, J. R. Eliseo, A. Züttel, C. M. Jensen. Chem. Rev., 2007, **107**, 4111.

79. E. Yu. Koldaeva, K. Yu. Zhizhin, E. Yu. Grigorieva, N. T. Kuznetsov, A. Yu. Baryshnikov, V. N. Kulakov. In: Abs. 17th Int. Symp. Boron, Borides & Rel. Mat. 2011, Ankara: BKM, 322.
80. A. A. Lipengolts, A. A. Cherepanov, E. Yu. Grigorieva, E. Yu. Koldaeva, K. Yu. Zhizhin, N. T. Kuznetsov, Ya. Z. Voloshin, V. N. Kulakov. In: Abs. 17th Int. Symp. Boron, Borides & Rel. Mat. 2011, Ankara: BKM, 323.
81. E. D. Jemmis, D. L. V. K. Prasad. J. Solid State Chem., 2006, **179**, 2768.
82. E. D. Jemmis, E. G. Jayasree. Acc. Chem. Res., 2003, **36**, 816.
83. D. Emin. J. Solid State Chem., 2006, **179**, 2791.
84. K. Shirai, H. Dekura. In: Abs. 16th Int. Symp. Boron, Borides & Rel. Mat. 2008, Matsue: KM, 44.
85. K. Shirai, H. Dekura, A. Masago. J. Phys.: Conf. Ser., 2009, **176**, 012001.
86. R. Schmechel, H. Werheit. J. Solid State Chem., 2000, **154**, 61.
87. H. Werheit. In: Abs.16th Int. Symp. Boron, Borides & Rel. Mat. 2008, Matsue: KM, 47.
88. H. Werheit. J. Phys.: Conf. Ser., 2009, **176**, 012009.
89. Sh. Hosoi, K. Tanabe, H. Kim, K. Kirihara, K. Soga, K. Kimura, K. Kato, M. Takata. J. Phys.: Conf. Ser., 2009, **176**, 012026.
90. H. Dekura, K. Shirai, A. Yanase. In: Abs.16th Int. Symp. Boron, Borides & Rel. Mat. 2008, Matsue: KM, 116.
91. H. Dekura, K. Shirai, A. Yanase. J. Phys.: Conf. Ser., 2009, **176**, 012004.
92. M. Widom, M. Mihalkovič. Phys. Rev. B, 2008, **77**, 064113.
93. M. Widom, M. Mihalkovič. In: Abs. 16th Int. Symp. Boron, Borides & Rel. Mat. 2008, Matsue: KM, 53.
94. M. Widom, M. Mihalkovič. J. Phys.: Conf. Ser., 2009, **176**, 012024.
95. L. S. Chkhartishvili, O. A. Tsagareishvili, R. A. Khachapuridze, T. Z. Mukhraneli. In: Proc. 7th Georg. Natl. You. Sci.-Tech. Conf. 1987, Tbilisi: Metsniereba, 3.
96. L. S. Chkhartishvili, G. P. Tsiskarishvili, O. A. Tsagareishvili, G. G. Gvelesiani, J. N. Tsikaridze. In: Proc. 9th Int. Symp. Boron, Borides & Rel. Comp. 1987, Duisburg: UDG, 360.
97. L. Chkhartishvili. Trans. GTU, 2007, **466**, 64.
98. O. A. Tsagareishvili, L. S. Chkhartishvili, D. L. Gabunia, R. A. Khachapuridze. In: Proc. 1st Int. Conf. *Hi*gh *M*at *T*ech. 2007, Kiev: IPMS, 441.
99. O. Tsagareishvili, D. Gabunia, L. Chkhartishvili. In: Abs. Int. Symp. Boron, Borides & Rel. Mat. 2008, Matsue: KM, 137.
100. O. A. Tsagareishvili, L. S. Chkhartishvili, D. L. Gabunia. Semicond., 2009, **43**, 14.
101. O. Tsagareishvili, D. Gabunia, L. Chkhartishvili. J. Phys.: Conf. Ser., 2009, **176**, 012021.
102. K. Moorjani, Ch. Feldman. In: Boron and Refractory Borides. 1977, Berlin: Springer–Verlag, 881.
103. A. F. Zhigach, D. C. Stasievich. In: Boron and Refractory Borides. 1977, Berlin: Springer–Verlag, 214.
104. V. I. Mikheeva, F. I. Shamraj, E. Ya. Krylova. J. Inorg. Chem., 1957, **2**, 1223.

105. V. I. Mikheeva, V. Yu. Markina, O. N. Kryukova. J. Inorg. Chem., 1957, **2**, 1232.
106. F. I. Shamraj, V. I. Mikheeva, E. Ya. Krylova. J. Inorg. Chem., 1957, **2**, 1242.
107. V. I. Mikheeva, F. I. Shamraj, E. Ya. Krylova. J. Inorg. Chem. 1957, **2**, 1248.
108. L. Ya. Markovskij, V. I. L'vova, Yu. D. Kondrashov. In: Proc. Conf. Chem. Boron & Boron Comp. 1958, Moscow: CPSTLCh, 36.
109. E. T. Peters, W. D. Potter. Trans. Metall. Soc. AJME, 1965, **233**, 473.
110. J. van Audenhove, J. Joyeux. Nucl. Instr. Meth., 1967, **57**, 157.
111. T. V. Samqurashvili, I. A. Bairamashvili, B. V. Alexandria. In: Boron – Obtaining, Structure, and Properties. 1974, Moscow: Nauka, 142.
112. G. F. Tavadze, D. V. Khantadze, G. V. Tsagareishvili, F. N. Tavadze. In: Boron – Obtaining, Structure, and Properties. Moscow: Nauka, 1974, 145.
113. L. Vandenbulcke, G. Vuillard. J. Electrochem. Soc., 1976, **123**, 278.
114. G. E. Vuillard, A. Luque, L. Vandenbulcke. J. Less-Comm. Met., 1976, **47**, 235.
115. G. I. Kartmazov, A. P. Patokin, V. V. Sagalovich, V. L. Khrebtov. Inorg. Mat., 1979, **15**, 239.
116. K. Ishiwatari, H. Takeuchi, H. Kawabata, T. Shimizu, N. Sakamoto. J. Less-Comm. Met. 1979, **67**, 79.
117. J.-O. Carlsson. J. Less-Comm. Met., 1980, **70**, 77.
118. J.-O. Carlsson. J. Less-Comm. Met., 1980, **71**, 1.
119. J.-O. Carlsson. J. Less-Comm. Met., 1980, **71**, 15.
120. K. Shirai, S. Conda. J. Phys. Chem. Solids, 1992, **53**, 1081.
121. K. Kamimura, T. Yohimura, T. Nagaoka, M. Nakao, Y. Onuma, M. Makimura. In: Abs. 13th Int. Symp. Boron, Borides & Rel. Comp. 1999, Dinard: CNRS, 70.
122. K. Kamimura, T. Yohimura, T. Nagaoka, M. Nakao, Y. Onuma, M. Makimura. J. Solid State Chem., 2000, **154**, 153.
123. Y. Kumashiro, K. Sato, S. Chiba, S. Yamada, K. Hyodo, K. Hirata. In: Abs. 13th Int. Symp. Boron, Borides & Rel. Comp. 1999, Dinard: CNRS, 12.
124. Y. Kumashiro, K. Sato, S. Chiba, S. Yamada, K. Tanaka, K. Hyodo, T. Yokoyama, K. Hirata. J. Solid State Chem., 2000, **154**, 39.
125. Y. Kumashiro, K. Hirata, K. Sato, T. Yokoyama, T. Aisu, T. Ikeda. In: Abs. 13th Int. Symp. Boron, Borides & Rel. Comp. 1999, Dinard: CNRS, 54.
126. Y. Kumashiro, K. Hirata, K. Sato, T. Yokoyama, T. Aisu, T. Ikeda, M. Minaguchi. J. Solid State Chem., 2000, **154**, 26.
127. Y. Kumashiro, K. Hirata, K. Sato, T. Yokoyama, T. Aisu, T. Ikeda. In: Abs. 14th Int. Symp. Boron, Borides & Rel. Comp. 2002, St Petersburg: PTI, 54.
128. Y. Kumashiro, Sh. Ozaki, K. Sato, Y. Kataoka, K. Hirata, T. Yokoyama, S. Nagatani, K. Kajiyama. J. Solid State Chem., 2004, **177**, 537.
129. M. Erdoğan, T. Özgen, S. Okur, S. Okur. In: Proc. 3rd Int. Boron Symp. 2006, Ankara: NBRI, 187.
130. Ch. Feldman, H. K. Charles Jr, F. G. Satkiewicz, J. Bohandy. J. Less-Comm. Met., 1976, **47**, 141.

131. S. Okur, M. Kalkancı, M. Tanoğlu, N. Ekmer, T. Akan, S. Pat, Z. Ballağ, G. Musa. In: Proc. 3rd Int. Boron Symp. 2006, Ankara: NBRI, 349.
132. M. Takeda, M. Ichimura, H. Yamaguchi, Y. Sakairi, K. Kimura. J. Solid State Chem., 2000, **154**, 141.
133. S. Rades, J. A. Broekaert, B. Albert. In: Abs. 16th Int. Symp. Boron, Borides & Rel. Mat. 2008, Matsue: KM, 143.
134. N. R. Neelameggham. In: Abs. 17th Int. Symp. Boron, Borides & Rel. Mat. 2011, Ankara: BKM, 125.
135. Ya. A. Ugaj, N. E. Solov'ev, E. M. Averbakh, A. I. Parfenov. In: Boron – Obtaining, Structure, and Properties. 1974, Moscow: Nauka, 18.
136. R. M. Pirtskhalaishvili, I. A. Bairamashvili, T. V. Samqurashvili, G. P. Lomidze, Sh. A. Loladze, N. I. Ghudushauri. In: Boron – Obtaining, Structure, and Properties. 1974, Moscow: Nauka, 23.
137. G. V. Panteleeva, V. V. Morozkin. J. Less-Comm. Met., 1979, **67**, 205.
138. I. A. Bairamashvili, J. Sh. Jobava, G. P. Lomidze, T. G. Nakashidze, Yu. I. Soloev, D. E. Khulelidze. Inorg. Mat., 1984, **20**, 409.
139. N. E. Solov'ev, V. S. Makarov, Ya. A. Ugaj. J. Less-Comm. Met., 1986, **117**, 21.
140. G. I. Kalandadze, S. O. Shalamberidze, A. B. Peikrishvili. J. Solid State Chem., 2000, **154**, 194.
141. S. O. Shalamberidze, G. I. Kalandadze, D. E. Khulelidze, B. D. Tsurtsumia. J. Solid State Chem., 2000, **154**, 199.
142. O. F. Degtyareva, M. F. Ostrovskaya. J. Anal. Chem., 1967, **22**, 1863.
143. V. V. Volkov, G. S. Yur'ev, K. G. Myakishev, E. A. Il'inchik. In: Vacuum Nanotechnology and Equipment. 2006, Kharkiv: NSC KhPTI – PPE Contrast, 336.
144. D. V. Khantadze, N. J. Topuridze. J. Less-Comm. Met., 1986, **117**, 105.
145. F. Spaepen. Nature, 2000, **408**, 78.
146. N. Vast, S. Bernard, G. Zerah. Phys. Rev. B, 1995, **52**, 4123.
147. S. Krishnan, S. Ansell, J. J. Felten, K. J. Volin, D. L. Price. Phys. Rev. Lett., 1998, **81**, 586.
148. P.-F. Paradis, T. Ishikawa, Sh. Yoda. Appl. Phys. Lett., 2005, **86**, 151901.
149. J. T. Okada, Y. Watanabe, M. Hamaishi, T. Ishikawa, K. Kimura, M. Kohara, M. Itou, Y. Sakurai, S. Nanao. In: Abs. 16th Int. Symp. Boron, Borides & Rel. Mat. 2008, Matsue: KM, 166.
150. B. Glorieux , M. L. Saboungi, J. E. Enderby. Europhys. Lett., 2001, **56**, 81.
151. F. Millot, J. C. Rifflet, V. Sarou–Kanian, G. Wille. Int. J. Thermophys., 2002, **23**,1185.
152. D. L. Price, A. Alatas, L. Hennet, N. Jakse, Sh. Krishnan, A. Pasturel, I. Pozdnyakova, M.-L. Saboungi, A. Said, R. Scheunemann, W. Schirmacher, H. Sinn. Phys. Rev. B, 2009, **79**, 134201.
153. J. T. Okada, T. Ishikawa, Y. Watanabe, P.-F. Paradis, Y. Watanabe, K. Kimura. Phys. Rev. B, 2010, **81**, 140201(R).
154. J. T. Okada, T. Ishikawa, Y. Watanabe, P.-F. Paradis, K. Kimura, S. Nanao. In: Abs. 17th Int. Symp. Boron, Borides & Rel. Mat. 2011, Ankara: BKM, 193.

155. K. Katada. Jpn. J. Appl. Phys., 1966, **5**, 582.
156. A. R. Badzian. Elect. Technol., 1970, **3**, 143.
157. Yu. G. Poltavtsev, V. P. Zakharov, V. M. Pozdnyakova. Crystallogr.,1973, **18**, 425.
158. F. N. Tavadze, G. V. Tsagareishvili, M. E. Antadze, G. F. Tavadze. In: Abs. IME Boron – 2nd Int. Meet. Boron Chem. 1974, Leeds: UL, 14.
159. P. G. Cheremskoj, A. A. Nechitajlo. Phys. Solid. State, 1975, **17**, 3663.
160. V. S. Makarov, N. E. Solov'ev, Ya. A. Ugaj. In: Semiconducting Materials and Thin Films on Their Surfaces. 1982, Voronezh: VPTI, 15.
161. F. N. Tavadze, G. V. Tsagareishvili, N. A. Zoidze, M. E. Antadze, A. G. Khvedelidze. In: Filamentary Crystals and Non-Ferromagnetic Films. Part II: Thin Films. 1970, Voronezh: VPTI, 239.
162. M. E. Antadze, J. A. Avlokhashvili, A. G. Khvedelidze, G. F. Tavadze. J. Less-Comm. Met. 1976, 47, 243.
163. L. S. Palatnik, A. A. Nechitajlo, A. A. Koz'ma, M. Ya. Fux, K. P. Tsomaia. In: Boron – Obtaining, Structure, and Properties. 1974, Moscow: Nauka, 139.
164. L. S. Palatnik, A. A. Nechitajlo, A. A. Koz'ma. Reps. Acad. Sci. USSR, 1981, **261**, 1134.
165. L. S. Palatnik, A. A. Koz'ma, A. A. Nechitajlo. Crystallogr., 1983, **28**, 136.
166. A. A. Nechitajlo. Structure and Properties of Condensed Boron Films. 1983, Kharkiv: KhPTI.
167. P. J. Kervalishvili, E. R. Kutelia, T. A. Dzigrashvili, P. N. Dekanosidze, V. I. Petrov. Phys. Solid State, 1985, **27**, 1414.
168. M. Kobayashi. J. Mat. Sci., 1988, **23**, 4392.
169. R. G. Delaplane, U. Dahlborg, W. S. Howells, T. Lundström. J. Non-Cryst. Solids, 1988, **106**, 66.
170. E. R. Kutelia, P. J. Kervalishvili, T. A. Dzigrashvili, R. N. Dekanosidze, N. I. Maisuradze, R. Ya. Yurechko. Bull. Acad. Sci. Georg. SSR, 1988, **130**, 529.
171. T. G. Nakashidze. Bull. Acad. Sci. Georg. SSR, 1988, **130**, 297.
172. T. G. Nakashidze. Structure and Crystallization of Amorphous Boron. 1988, Tbilisi: TSU.
173. V. V. Volkov, G. S. Yur'ev, L. I. Brezhneva, K. G. Myakishev. J. Inorg. Chem., 1989, **34**, 34.
174. M. Terauchi, Y. Sato, H. Hyodo, K. Kimura. J. Phys.: Conf. Ser., 2009, **176**, 012025.
175. Ch. Feldman, F. Ordway, W. Zemmerman III, K. Moorjani. In: Boron – Preparation, Properties, and Applications. 1965, New York: Plenum Press, 235.
176. Ch. Feldman. Mat. Sci. Bull., 1968, **3**, 95.
177. K. Moorjani, Ch. Feldman. Elect. Technol., 1970, **3**, 265.
178. E. I. Adirovich, L. M. Gol'dshtejn. Semicond., 1969, **3**, 238.
179. L. M. Gol'dshtejn. Electro-Physical Properties of Boron Crystals and Films. 1971, Tashkent: Acad. Sci. Uzb. SSR.
180. A. A. Berezin, O. A. Golikova, M. M. Kazanin, T. Khomidov, D. N. Mirlin, A. V. Petrov, A. S. Umarov, V. K. Zajtsev. J. Non-Cryst. Solids, 1974, **16**, 237.

181. A. A. Berezin, O. A. Golikova, V. K. Zajtsev, L. S. Stil'bans, T. Khomidov. In: Boron – Obtaining, Structure, and Properties. 1974, Moscow: Nauka, 106.
182. O. A. Golikova, M. M. Kazanin, L. S. Stil'bans, E. N. Tkalenko, V. K. Zajtsev. In: Abs. 4th Int. Conf. Amorph. & Liq. Semicond. 1975, Leningrad: Ioffe PTI, 94.
183. G. F. Tavadze, R. A. Khachapuridze, G. Sh. Darsavelidze, G. V. Tsagareishvili, F. N. Tavadze. In: Filamentary Crystals and Thin Films. Part II: Thin Films. 1975, Voronezh: VPTI, 228.
184. T. V. Samqurashvili, F. N. Tavadze. Bull. Acad. Sci. Georg. SSR, 1976, **84**, 441.
185. Y. Kumashiro, K. Hirata, K. Sato, T. Yokoyama, Y. Abe, T. Enomoto. In: Abs. 14th Int. Symp. Boron, Borides & Rel. Comp. 2002, St Petersburg: Ioffe PTI, 98.
186. Y. Kumashiro, T. Enomoto, K. Sato, Y. Abe, K. Hirata, T. Yokoyama. J. Solid State Chem., 2004, **177**, 529.
187. K. Tanabe, K. Osumi, H. Yamaguchi, K. Soga, K. Kimura. In: Abs. 16th Int. Symp. Boron, Borides & Rel. Mat. 2008, Matsue: KM, 139.
188. J. J. Koulmann, G. Gewinner, L. Kubler, A. Jaéglé. Phys. Stat. Sol. B, 1975, **68**, K43.
189. L. Kubler, G. Gewinner, J. J. Koulmann, A. Jaéglé. Phys. Stat. Sol. B, 1975, **69**, 323.
190. G. P. Tsiskarishvili, G. V. Tsagareishvili, M. E. Antadze, F. N. Tavadze. Mat. Res. Soc. Symp. Proc., 1987, **97**, 63.
191. G. P. Tsiskarishvili, G. V. Tsagareishvili, F. N. Tavadze. Inorg. Mat., 1989, **25**, 585.
192. K. Moorjani, Ch. Feldman. J. Non-Cryst. Solids, 1970, **4**, 248.
193. Ch. Feldman, K. Moorjani. J. Non-Cryst. Solids, 1970, **2**, 82.
194. Ch. Feldman, H. K. Charles Jr. Solid State Commun., 1974, **15**, 551.
195. V. K. Zajtsev, O. A. Golikova, M. M. Kazanin. Semicond., 1976, **10**, 1256.
196. G. W. Turner, H. K. Charles Jr, Ch. Feldman. J. Appl. Phys., 1976, **47**, 3618.
197. L. S.Chkhartishvili, G. V. Tsagareishvili. Bull. Acad. Sci. Georg. SSR, 1987, **126**, 305.
198. L. S. Chkhartishvili. Mat. Sci.: An Ind. J., 2007, **3**, 18.
199. D. Gabunia, L. Chkhartishvili, O. Tsagareishvili. In: Abs. 16th Int. Symp. Boron, Borides & Rel. Mat. 2008, Matsue: KM, 104.
200. D. L. Gabunia, L. S. Chkhartishvili, O. A. Tsagareishvili. In: Proc. 5th Int. Conf. MEE. 2008, Kiev: IPMS, 203.
201. D. Gabunia, L. Chkhartishvili, O. Tsagareishvili. J. Phys.: Conf. Ser., 2009, **176**, 012023.
202. S. Yayla, L. Özmen, F. Karakulak, Ü. Önsipahioğlu. In: Abs. 17th Int. Symp. Boron, Borides & Rel. Mat. 2011, Ankara: BKM, p. 140.
203. D. B. Sullenger, K. D. Phipps, P. W. Seabaugh, C. R. Hudgens, D. E. Sands, J. S. Cantrell. Science, 1969, **163**, 935.
204. K. P. Tsomaia, R. R. Shvangiradze. Phys. Met. & Met. Sci., 1960, **10**, 791.
205. K. P. Tsomaia, G. V. Samsonov, F. N. Tavadze. Powd. Metall., 1973, **3**, 83.
206. K. P. Tsomaia, G. V. Samsonov, F. N. Tavadze. In: Boron – Obtaining, Structure, and Properties. 1974, Moscow: Nauka, 58.
207. K. P. Tsomaia. Powd. Metall., 1975, **3**, 87.
208. K. P. Tsomaia, G. V. Samsonov, D. L. Gabunia. Reps. Acad. Sci. USSR, 1975, **221**, 858.

209. K. P. Tsomaia, D. L. Gabunia, E. A. Knyshev, V. A. Kobyakov. Powd. Metall., 1975, **4**, 83.
210. K. P. Tsomaia, F. N. Tavadze, V. V. Uvarov, D. L. Gabunia, E. A. Knyshev, V. A. Kobyakov. Powd. Metall., 1975, **2**, 87.
211. K. P. Tsomaia, G. V. Samsonov, F. N. Tavadze. J. Less-Comm. Met., 1976, **47**, 249.
212. K. P. Tsomaia, D. L. Gabunia, F. N. Tavadze. J. Less-Comm. Met., 1979, **67**, 425.
213. K. P. Tsomaia, N. G. Kakazej, M. V. Vlasova, D. L. Gabunia. Powd. Metall., 1980, **9**, 104.
214. G. V. Tsagareishvili, I. A. Bairamashvili, K. A. Oganezov, M. L. Tabutsidze, O. A. Tsagareishvili. J. Less-Comm. Met., 1981, **82**, 131.
215. F. N. Tavadze, K. P. Tsomaia, D. L. Gabunia, O. A. Tsagareishvili, N. K. Svanidze, T. Sh. Badzagua. Bull. Acad. Sci. Georg. SSR, 1982, **105**, 345.
216. I. A. Bairamashvili, J. Sh. Jobava, G. I. Kalandadze, G. P. Lomidze, Sh. A. Loladze, Yu. I. Soloev. Bull. Acad. Sci. Georg. SSR, 1983, **111**, 573.
217. F. N. Tavadze, V. V. Nemoshkalenko, D. L. Gabunia, A. I. Senkevich, T. Sh. Badzagua, G. P. Tsiskarishvili, M. K. Tsomaia. J. Less-Comm. Met., 1986, **117**, 135.
218. T. Sh. Badzagua. Structure, Composition and Properties of Products of Mechanical Dispersing of β-Rhombohedral Boron. 1990, Tbilisi: IM.
219. T. Sh. Badzagua, M. V. Vlasova, D. L. Gabunia, N. G. Kakazej. Powd. Metall., 1983, **1**, 60.
220. A. N. Zolotko, L. A. Klyachko, K. M. Kopejka, D. I. Polishchuk, V. G. Shevchuk. Phys. Comb. & Expl., 1977, **13**, 38.
221. A. N. Zolotko, D. I. Polishchuk, A. I. Shvets. Phys. Comb. & Expl., 1980, **16**, 10.
222. A. N. Zolotko, A. M. Matsko, D. I. Polishchuk, S. N. Bujnovskij, L. A. Gaponenko. Phys. Comb. & Expl., 1980, **16**, 23.
223. L. A. Gaponenko, S. N. Bujnovskij, Yu. I. Tulupov, T. A. Yakovleva. Phys. Comb. & Expl., 1981, **17**, 13.
224. A. F. Zhigach, A. M. Tsirlin. In: Fibrous Dispersed-Strengthened and Composite Materials. 1976, Moscow: Nauka, 20.
225. V. Krukonis. In: Boron and Refractory Borides. 1977, Berlin: Springer–Verlag, 517.
226. J.-O. Carlsson. J. Mat. Sci., 1979, **14**, 255.
227. C. P. Talley, L. E. Line Jr, Q. D. Overman Jr. In: Boron – Synthesis, Structure, and Properties. 1960, New York: Plenum Press, 94.
228. J. A. di Carlo. Scr. Metall., 1976, **10**, 115.
229. A. M. Tsirlin, T. V. Fedorova, E. K. Florina. Phys. & Chem. Mat. Proc., 1984, **3**, 99.
230. H. M. Otte, H. A. Lipsitt. Phys. Stat. Sol., 1966, **13**, 439.
231. P. F. Lindquist, M. L. Hommond. Phys. Stat. Sol., 1966, **17**, K25.
232. P. F. Lindquist, M. L. Hommond, R. H. Bragg. J. Appl. Phys., 1968, **39**, 5152.
233. J. Bhardwaj, A. D. Krawitz. J. Mat. Sci., 1983, **18**, 2639.
234. J. Cueilleron, F. Thévenot, J. C. Viala. In: Boron – Obtaining, Structure, and Properties. 1974, Moscow: Nauka, 27.
235. H. A. Lipsitt, H. M. Otte. In: Proc. 6th Int. Cong. Elect. Microsc., 1966, **1**, 463.
236. G. Sh. Darsavelidze, G. V. Tsagareishvili, E. R. Kutelia, A. F. Zhigach, A. M. Tsirlin, E. A. Shchetilina. J. Less-Comm. Met., 1981, **82**, 89.

237. F. E. Wawner Jr. In: Boron – Preparation, Properties, and Applications. 1965, New York: Plenum Press, 283.
238. R. Veltri, F. Galasso. Nature, 1968, **220**, 781.
239. A. F. Zhigach, A. M. Tsirlin, E. A. Shchetilina, I. L. Svetlov, V. I. Grigor'ev, E. G. Shafranovich, T. I. Bulygina, V. A. Yartsev. Mech. Polym., 1973, **4**, 641.
240. G. K. Layden. J. Mat. Sci., 1973, **8**, 1581.
241. G. L. Roshkovich, A. F. Zhigach, P. A. Samosudov, A. M. Tsirlin, E. A. Shchetilina, E. K. Khodov, E. K. D'yachkin. Mech. Polym., 1976, **5**, 819.
242. B. N. Antsiferov, A. F. Zhigach, A. V. Lyudvigskij, A. I. Rabinovich, A.M. Tsirlin. Mech. Polym., 1977, **4**, 726.
243. A. F. Zhigach, A. M. Tsirlin, E. A. Shchetilina, B. M. Romanov, T. V. Fedorova, E. G. Shafranovich, N. M. Balagurova. In: Boron – Obtaining, Structure, and Properties. 1974, Moscow: Nauka, 147.
244. V. S. Erasov, E. N. Pirogov, V. P. Konoplenko, V. A. Akimkin, A. P. Marukhin, A. M. Tsirlin, E. A. Shchetilina, N. M. Balagurova. Mech. Compos. Mat., 1982, **2**, 195.
245. T. E. Firle. J. Appl. Phys., 1968, **39**, 2839.
246. G. M. Dugladze, G. Sh. Darsavelidze, G. V. Tsagareishvili, F. N. Tavadze. Bull. Acad. Sci. Georg. SSR, 1973, **69**, 397.
247. G. M. Dugladze, G. Sh. Darsavelidze, G. V. Tsagareishvili. Bull. Acad. Sci. Georg. SSR, 1973, **70**, 141.
248. G. V. Tsagareishvili, G. M. Dugladze, G. Sh. Darsavelidze. In: Boron – Obtaining, Structure, and Properties. 1974, Moscow: Nauka, 154.
249. G. M. Dugladze, G. Sh. Darsavelidze, G. V. Tsagareishvili, F. N. Tavadze. In: Mechanisms of Internal Friction in Solids. 1976, Moscow: Nauka, 66.
250. G. Sh. Darsavelidze, G. V. Tsagareishvili, M. A. Tsirlin, J. D. Nikuradze, O. A. Tsagareishvili, A. F. Zhigach, F. N. Tavadze. J. Less-Comm. Met., 1979, **67**, 471.
251. V. P. Postnikov, V. I. Lavrent'ev, V. I. Kovalevskij. J. Less-Comm. Met., 1986, **117**, 195.
252. M. Kh. Shorshorov, B.A. Aref'ev, L. E. Gukasyan, D. A. Nozadze. J. Less-Comm. Met., 1986, **117**, 183.
253. J. P. Sitarik, W. C. Ellis. J. Appl. Phys., 1966, **37**, 2399.
254. I. Boustani, A. Quandt. Euro Phys. Lett., 1997, **39**, 527.
255. Y. Zhang, H. Ago, M. Yumura, T. Komatsu, S. Ohshima, K. Uchida, S. Iijima. Chem. Comm., 2002, 2806.
256. C. J. Otten, O. R. Lourie, M.-F. Yu, J. M. Cowley, M. J. Dyer, R. S. Ruoff, W. E. Buhro. J. Am. Chem. Soc., 2002, **124**, 4564.
257. Y. Q. Wang, X. F. Duan. Appl. Phys. Lett., 2003, **82**, 272.
258. D. Wang, J. G. Lu. Appl. Phys. Lett., 2003, **83**, 5280.
259. S. H. Yun, J. Z. Wu, A. Dibos, X. Zou, U. O. Karlsson. Nano Lett., 2006, **6**, 385.
260. L. M. Cao, Z. Zhang, L. L. Sun, C. X. Gao, M. He, Y. Q. Wang, Y. C. Li, X. Y. Zhang, G. Li, J. Zhang, W. K. Wang. Adv. Mat., 2010, **13**, 1701.

261. T. T. Xu, J.-G. Zheng, N. Wu, A. W. Nicholls, J. R. Roth, D. A. Dikin, R. S. Ruoff. Nano Lett., 2004, **4**, 963.
262. P. Jash, M. Trenary. J. Phys.: Conf. Ser., 2009, **176**, 012011.
263. Zh. Wang, Y. Shimizu, T. Sasaki, K. Kawaguchi, K. Kimura, N. Koshizaki. Chem. Phys. Lett., 2003, **368**, 663.
264. K. Kirihara, Z. Wang, K. Kawaguchi, Y. Shimizu, T. Sasaki, N. Koshizaki, K. Soga, K. Kimura. Appl. Phys. Lett., 2005, **86**, 212101.
265. K. Kirihara, H. Hyodo, H. Fujihisa, Z. Wang, K. Kawaguchi, Y. Shimizu, T. Sasaki, N. Koshizaki, K. Soga, K. Kimura. J. Solid State Chem., 2006, **179**, 2799.
266. K. Kirihara, K. Kawaguchi, Y. Shimizu, T. Sasaki, N. Koshizaki, R. Soga, H. Hyodo, K. Kimura. In: Abs. 16th Int. Symp. Boron, Borides & Rel. Mat. 2008, Matsue: KM, 79.
267. K. Tsuda, K. Iwasaki, Y. Sato, M. Terauchi, K. Kimura. In: Abs. 16th Int. Symp. Boron, Borides & Rel. Mat. 2008, Matsue: KM, 127.
268. Y. Sato, M. Terauchi, K. Kimura. In: Abs. 16th Int. Symp. Boron, Borides & Rel. Mat. 2008, Matsue: KM, 107.
269. Y. Sato, M. Terauchi, K. Kirihara, T. Sasaki, K. Kawaguchi, N. Koshizaki, K. Kimura. J. Phys.: Conf. Ser., 2009, **176**, 012029.
270. H. Hyodo, K. Kirihara, K. Soga, K. Kawaguchi, Y. Shimizu, T. Sasaki, N. Koshizaki, Y. Satoh, M. Terauchi, K. Kimura. In: Abs. 16th Int. Symp. Boron, Borides & Rel. Mat. 2008, Matsue: KM, 117.
271. K. Kirihara, Y. Shimizu, Y. Yamada, F. Esaka, T. Sasaki, N. Koshizaki, H. Yamamoto, Sh.-I. Shamoto, K. Kimura. Appl. Phys. Lett., 2010, **97**, 212105.
272. K. Kimura, H. Hyodo, A. Sumiyoshi, T. Nagatochi, F. Esaka, S. Yamamoto, K. Kirihara, Y. Shimizu, T. Sasaki, N. Koshizaki, H. Yamamoto, S. Shamoto. In: Abs. 17th Int. Symp. Boron, Borides & Rel. Mat. 2011, Ankara: BKM, 282.
273. I. Boustani. Surf. Sci., 1997, **370**, 355.
274. M. H. Evans, J. D. Joannopoulos, S. T. Pantelides. Phys. Rev. B, 2005, **72**, 045434.
275. I. Cabria, J. A. Alonso, M. J. López. Phys. Stat. Sol. A, 2006, **203**, 1105.
276. J. Kunstmann, A. Quandt. Phys. Rev. B, 2006, **74**, 035413.
277. K. Ch. Lau, R. Pandey. J. Phys. Chem. C, 2007, **111**, 2906.
278. M. Şimşek, S. Aydın. In: Abs. 17th Int. Symp. Boron, Borides & Rel. Mat. 2011, Ankara: BKM, 86.
279. H. Tang, S. Ismail–Beigi. Phys. Rev. Lett., 2007, **99**, 115501.
280. X. Yang, Y. Ding, J. Ni. Phys. Rev. B, 2008, **77**, 041402(R).
281. J. Wang, Y. Liu, Y.-Ch. Li. Chem. Phys. Chem., 2010, **10,** 3119.
282. J. Kunstmann, L. Boeri, J. Kortus. In: Abs. 17th Int. Symp. Boron, Borides & Rel. Mat. 2011, Ankara: BKM, 289.
283. D. Ciuparu, R. F. Klie, Y. Zhu, L. Pfefferle. J. Phys. Chem. B, 2004, **108**, 3967.
284. A. Quandt, I. Boustani. Chem. Phys. Chem., 2005, 6, 2001.
285. J. Kunstmann, A. Quandt. Chem. Phys. Lett., 2005, **402**, 21.

286. S. Mukhopadhyay, R. Pandey, Y. Kh. Yap, I. Boustani. In: Abs. 16th Int. Symp. Boron, Borides & Rel. Mat. 2008, Matsue: KM, 62.
287. S. Mukhopadhyay, H. He, R. Pandey, Y. Kh. Yap, I. Boustani. J. Phys.: Conf. Ser., 2009, **176**, 012028.
288. A. K. Singh, A. Sadrzadeh, B. I. Yakobson. Nano Lett., 2008, **8**, 1314.
289. V. Bezugly, J. Kunstmann, G. Cuniberti. In: Abs. 17th Int. Symp. Boron, Borides & Rel. Mat. 2011, Ankara: BKM, 50.
290. F. Molani, S. Jalili. In: Abs. 17th Int. Symp. Boron, Borides & Rel. Mat. 2011, Ankara: BKM, 56.
291. A. Leithe–Jasper, L. Bourgeois, Y. Michiue, Y. Shi, Y. Bando, T. Tanaka. In: Abs. 13th Int. Symp. Boron, Borides & Rel. Comp. 1999, Dinard: CNRS, 88.
292. A. Leithe–Jasper, L. Bourgeois, Y. Michiue, Y. Shi, T. Tanaka. J. Solid State Chem., 2000, **154**, 130.
293. A. Gindulytė, W. N. Lipscomb, L. Massa. Inorg. Chem., 1998, **37**, 6544.
294. L. Chkhartishvili. In: Abs. 16th Int. Symp. Boron, Borides & Rel. Mat. 2008, Matsue: KM, 126.
295. L. Chkhartishvili. In: Proc. Mat. Sci. Days. 2009, Tbilisi: Universal, 11.
296. L. Chkhartishvili. In: Proc. 4th Int. Boron Symp. 2009, Eskişehir: OGU, 153.
297. L. Chkhartishvili. J. Phys.: Conf. Ser., 2009, **176**, 012013.
298. L. Chkhartishvili. In: New Developments in Materials Science. 2011, New York: Nova Sci. Publ. Inc., Ch. 8.
299. R. K. F. Lee, B. J. Cox, J. M. Hill. J. Phys. A: Math. & Theor., 2009, **42**, 065204.
300. R. K. F. Lee, B. J. Cox, J. M. Hill. Nanoscale, 2010, **2**, 859.
301. L. Chkhartishvili. Quasi-Classical Theory of Substance Ground-State. 2004, Tbilisi: TU.
302. L. Chkhartishvili, D. Lezhava, O. Tsagareishvili, D. Gulua. Trans. AMIAG, 1999, **1**, 295.
303. L. Chkhartishvili, D. Lezhava, O. Tsagareishvili. J. Solid State Chem., 2000, **154**, 148.
304. L. Chkhartishvili. Tr. Inorg. Chem., 2009, **11**, 105.
305. D. Gabunia, O. Tsagareishvili, L. Chkhartishvili. In: Proc. 4th Int. Conf. MEE. 2006, Kiev: IPMS, 161.
306. D. Gabunia, O. Tsagareishvili, L. Chkhartishvili, L. Gabunia. In: Abs. 16th Int. Symp. Boron, Borides & Rel. Mat. 2008, Matsue: KM, 164.
307. L. Chkhartishvili, D. Gabunia, O. Tsagareishvili. Powd. Metall. & Met. Cer., 2008, **47**, 616.
308. D. Gabunia, O. Tsagareishvili, L. Chkhartishvili, L. Gabunia. J. Phys.: Conf. Ser., 2009, **176**, 012022.
309. L. Chkhartishvili, D. Gabunia, O. Tsagareishvili, V. Metreveli. Bull. Georg. Acad. Sci., 2004, **170**, 530.
310. D. Gabunia, O. Tsagareishvili, M. Tushishvili, J. Tsikaridze, M. Tsomaia, L. Gabunia, L. Chkhartishvili, T. Machaladze. In: Abs. 15th Int. Symp. Boron, Borides & Rel. Mat. 2005, Hamburg: UH, 141.
311. L. Chkhartishvili, D. Gabunia, O. Tsagareishvili. Inorg. Mat., 2007, **43**, 594.

312. J. Widany, Th. Frauenheim, Th. Köhler, M. Sternberg, D. Porezag, G. Jungnickel, G. Seifert. Phys. Rev. B, 1996, **53**, 4443.
313. J. Kunstmann, A. Quandt, I. Boustani. Nanotechnology, 2007, **18**, 155703.
314. F. Liu, Ch. Shen, Z. Su, X. Ding, Sh. Deng, J. Chen, N. Xu, H. Gao. J. Mat. Chem., 2010, **20**, 2197.
315. I. Boustani. Chem. Phys. Lett., 1995, **240**, 135.
316. I. Boustani. J. Solid State Chem., 1997, **133**, 182.
317. G. L. Perkins, M. Trenary, T. Tanaka. Phys. Rev. B. 1998, **58-I**, 9980.
318. N. G. Szwacki, A. Sadrzadeh, B. I. Yakobson. Phys. Rev. Lett., 2007, **98**, 166804.
319. N. G. Szwacki, A. Sadrzadeh, B. I. Yakobson. Phys. Rev. Lett., 2008, **100**, 159901.
320. A. Sadrzadeh, O.V. Pupysheva, A. K. Singh, B. I. Yakobson. J. Phys. Chem. A, 2008, **112**, 13679.
321. N. G. Szwacki, C. J. Tymczak. 2010, **494**, 80.
322. D. L. V. K. Prasad, E. D. Jemmis. Phys. Rev. Lett., 2008, **100**, 165504.
323. N. T. Kuznetsov, S. P. Ionov. In: Abs. 13th Int. Symp. Boron, Borides & Rel. Comp. 1999, Dinard: CNRS, 41.
324. A. Sadrzadeh, H. Lee, B. I. Yakobson. In: Abs. 17th Int. Symp. Boron, Borides & Rel. Mat. 2011, Ankara: BKM, 196.
325. M. Atiş, M. Boyukata, C. Özdoğan, E. Yildirim, Z. B. Güvenç. In: Abs. 16th Int. Symp. Boron, Borides & Rel. Mat. 2008, Matsue: KM, 33.
326. Ch. L. Henley. Phys. Rev. B, 1991, **43**, 993.
327. R.-H. Xie, G. W. Bryant, J. Zhao, T. Kar, V.H. Smith Jr. Phys. Rev. B, 2005, **71**, 125422.
328. A. N. Enyashin, A. L. Ivanovskij. Phys. Solid State, 2007, **49**, 378.
329. Y. X. Yao, C. Z. Wang, K. M. Ho. Phys. Rev. B, 2007, **76**, 174209.
330. M. Celino, V. Rosato, A. di Cicco, A. Trapananti, C. Massobrio. Phys. Rev. B, 2007, **75,** 174210.
331. I. Boustani, A. Quandt, E. Hernández, A. Rubio. J. Chem. Phys., 1999, **110**, 3176.
332. I. Boustani, A. Quandt, A. Rubio. J. Solid State Chem., 2000, **154**, 269.
333. I. Boustani, A. Quandt, P. Kramer. Euro Phys. Lett., 1996, **36**, 583.
334. I. Boustani, A. Quandt, A. Rubio. In: Abs. 13th Int. Symp. Boron, Borides & Rel. Comp. 1999, Dinard: CNRS, 28.
335. W. Hayami, Sh. Otani. In: Abs. 16th Int. Symp. Boron, Borides & Rel. Mat. 2008, Matsue: KM, 59.
336. W. Hayami, Sh. Otani. J. Phys.: Conf. Ser., 2009, **176**, 012017.

საქართველოს ტექნიკური უნივერსიტეტის საინჟინრო ფაკულტეტის დაარსების და პროფესორ რაფიელ ჩიქოვანის იუბილეებისადმი მიძღვნილი საერთაშორისო სამეცნიერო კონფერენცია "გამოყენებითი ფიზიკის აქტუალური საკითხები"

საქართველოს ტექნიკური უნივერსიტეტის, საქართველოს საინჟინრო აკადემიის ინფორმატიკის, მართვის პროცესების და ნანოტექნოლოგიების განყოფილების, საქართველოს ტექნიკური უნივერსიტეტის ინფორმატიკის და მართვის სისტემების ფაკულტეტის ფიზიკის დეპარტამენტის თაოსნობით 2011 წლის 30 მარტს საქართველოს ტექნიკური უნივერსიტეტის გიორგი ნიკოლაძის სახელობის დარბაზში ჩატარდა საქართველოს ტექნიკური უნივერსიტეტის საინჟინრო ფიზიკის ფაკულტეტის დაარსების იუბილესა და დამსახურებული მეცნიერის, საზოგადო მოღვაწის, საქართველოს სახელმწიფო პრემიის ლაურეატის, საინჟინრო აკადემიის აკადემიკოსის, პროფესორ რაფიელ ჩიქოვანის 80 წლის იუბილესადმი მიძღვნილი საერთაშორისო სამეცნიერო კონფერენცია "გამოყენებითი ფიზიკის აქტუალური საკითხები".

კონფერენციის გახსნა

კონფერენცია გახსნა და დამსწრეთ მისასალმებელი სიტყვით მიმართა საქართველოს ტექნიკური უნივერსიტეტის რექტორმა, საქართველოს მეცნიერებათა ეროვნული აკადემიის წევრ-კორესპონდენტმა, საქართველოს საინჟინრო აკადემიის პრეზიდენტმა, პროფესორმა არჩილ ფრანგიშვილმა. მან პროფ. რ. ჩიქოვანს მიულოცა

იუბილე და ისაუბრა მისი სამეცნიერო, პედაგოგიური და საზოგადოებრივი მოღვაწეობის შესახებ, მის დიდ დამსახურებაზე საქართველოში მიკრო- და ოპტოელექტრონიკის დარგების განვითარებაში, საქართველოს ტექნიკურ უნივერსიტეტში საინჟინრო ფაკულტეტის აღორძინებაში.

სხდომათა დარბაზში

რექტორმა მოკლედ მიმოიხილა საინჟინრო ფიზიკის ფაკულტეტის ფუნქციონირების განვლილი პერიოდი, მისი როლი და დამსახურება საქართველოს საინჟინრო კადრების მომზადების საქმეში, ზოგადად ფიზიკის დარგის და, კერძოდ, გამოყენებითი ფიზიკის ახალი პერსპექტიული მიმართულებების ჩამოყალიბებისა და განვითარების სფეროში. ისაუბრა მომავალი გეგმებისა და ამოცანების შესახებ.

ფიზიკის დეპარტამენტის უფროსმა, პროფ. აკაკი გიგინეიშვილმა ვრცლად ისაუბრა რ. ჩიქოვანის სამეცნიერო, საინჟინრო და პედაგოგიურ სფეროში გაწეული ღვაწლისა და დამსახურების, მისი მრავალმხრივი ადმინისტრაციული და საზოგადოებრივი მოღვაწეობის შესახებ, აგრეთვე – საინჟინრო ფიზიკის ფაკულტეტის წარსულზე, აწმყოსა და მომავალზე.

იუბილარს მისასალმებელი სიტყვებით მიმართეს როგორც საზღვარგარეთიდან ჩამოსულმა სტუმრებმა, ასევე ქართველმა კოლეგებმა, მეგობრებმა, აღზრდილებმა.

აკადემიკოსმა თენგიზ სანაძემ პროფ. რ. ჩიქოვანს მიულოცა იუბილე და მას გადასცა საქართველოს მეცნიერების ისტორიის საზოგადოების ვერცხლის მედალი ამ საზოგადოების საქმიანობაში მის მიერ გაწეული დიდი ღვაწლის გამო.

ა. გიგინეიშვილი

თ. სანაძე

რ. ჩიქოვანს ადრესი გადასცა საქართველოს საინჟინრო აკადემიის ვიცე-პრეზიდენტმა, პროფ. გ. აბდუშელიშვილმა, იუბილარს აგრეთვე მიესალმნენ საქართველოს განათლებისა და მეცნიერების სამინისტროს უმაღლესი განათლების განვითარების სამმართველოს უფროსი, ფ.-მ.მ.კ. ნ. ჩიტაია, სოხუმის ფიზიკა-ტექნიკის ინსტიტუტის დირექტორი, დოქტორი გ. ბოკუჩავა და სხვ.

გ. აბდუშელიშვილი

გ. ბოკუჩავა

კონფერენცია იყო საკმაოდ წარმომადგენლობითი. მის მუშაობაში მონაწილეობა მიიღეს და თავიანთი ნაშრომები წარმოადგინეს როგორც საზღვარგარეთის (აზერბაიჯანი, გერმანია, ისრაელი, რუსეთი, სომხეთი და უკრაინა), ასევე თბილისის და მთლიანად საქართველოს სხვადასხვა რეგიონის უნივერსიტეტების, ინსტიტუტებისა და კვლევითი ცენტრების მეცნიერებმა. სულ კონფერენციაზე წარმოდგენილი იყო 113 ნაშრომი, აქედან 3 მოხსენება გაკეთდა პლენარულ სხდომაზე. შემდეგ კიდევ 20 ზეპირი მოხსენება იქნა მოსმენილი. ვრცელი მასალა იყო წარმოდგენილი სასტენდო მოხსენებების სახით. კონფერენციის მოხსენებები ეხებოდა გამოყენებითი ფიზიკის როლს თანამედროვე მეცნიერების, ტექნიკის, ტექნოლოგიების, მედიცინის და წარმოების სხვადასხვა დარგში; გამოყენებითი ფიზიკის სწავლების მეთოდიკას; გამოყენებითი ფიზიკის ისტორიის საკითხებს და სხვ.

პლენარულ სხდომაზე პირველი მოხსენებით გამოვიდა პროფ. ი. მარონჩუკი კრემენჩუგის ეკონომიკის, ინფორმაციული ტექნოლოგიების და მართვის უნივერსიტეტიდან (უკრაინა). მოხსენება ეხებოდა კვანტური წერტილების შემცველი ნანოჰეტეროსტრუქტურების ფორმირების თავისებურებებს და ამ ტიპის სტრუქტურების შემადგენელი თხელი ფენების ზრდის მათ მიერ დამუშავებულ თხევადფაზური ეპიტაქსიის ახალ მეთოდს. პროფ. ი. მარონჩუკთან ქართველ მეცნიერებს მრავალწლიანი (1966 წლიდან) და ნაყოფიერი ურთიერთობა აკავშირებთ. მათ ერთობლივად აქვთ შესრულებული რამდენიმე სამეცნიერო-კვლევითი და საცდელ-საკონსტრუქტორო სამუშაო. მომავლისათვის დაგეგმილია A_3B_5 ნახევარგამტარული შენაერთების საფუძველზე ჰეტეროსტრუქტურების გამოყენებით მაღალი ეფექტურობის მქონე მზის ენერგიის ფოტოელექტრონული გარდამქმნელების მისაღებად ახალი პერსპექტიული პროექტების ერთობლივად განხორციელება.

ი. მარონჩუკი

ბ. მიხელაშვილი

საინტერესო მოხსენებით გამოვიდა ბ. მიხელაშვილი – ისრაელის ტექნიკური ტექნოლოგიების ინსტიტუტის მეცნიერ-თანამშრომელი. მოხსენების თემა იყო “A non-volatile low-voltage memory transistor based on SiO_2 tuneling, HfO_2 blocking and Au nano-particle charge storage layers”. აღსანიშნავია, რომ ბ. მიხელაშვილი არის საქართველოს პოლიტექნიკური ინსტიტუტის საინჟინრო ფიზიკის ფაკულტეტის კურსდამთავრებული. შემდგომ მან გაიარა კიევში ასპირანტურა ნახევარგამტარების ფიზიკის დარგში. ასპირანტურის დასრულების და საკანდიდატო დისერტაციის დაცვის შემდეგ იგი ნაყოფიერად მოღვაწეობდა სამეცნიერო-საწარმოო გაერთიანება “მიონში”. ამჟამად იგი ისრაელის მოქალაქეა.

ასევე მეტად აქტუალური იყო პროფ. პ. თოდუას (სახელმწიფო სამეცნიერო მეტროლოგიური ცენტრის “ვაკუუმის და ზედაპირის თვისებების შესწავლის სამეცნიერო-კვლევითი ცენტრი”, რუსეთი) მოხსენება: “Нанометрология и стандартизация индустрии наносистем и материалов”. მან დამსწრეთ გააცნო ნანომეტროლოგიის მთავარი თანამედროვე ამოცანა – ნანოტექნოლოგიებში ერთიანი გაზომვის სისტემის უზრუნველყოფა. აღსანიშნავია, რომ პ. თოდუა არის ივანე

ჯავახიშვილის სახელობის თბილისის სახელმწიფო უნივერსიტეტის ფიზიკის ფაკულტეტის კურსდამთავრებული და ამჟამად მოღვაწეობს ქალაქ მოსკოვში.

პ. თოდუა

ნ. ხუჭუა

იუბილარს მიესალმა და საინტერესო მოხსენება “III–V semiconductor devices to bridge the terahertz technology gap” გააკეთა ივანე ჯავახიშვილის სახელობის თბილისის სახელმწიფო უნივერსიტეტის სამეცნიერო-საწარმოო კომპლექსის “ელექტრონული ტექნიკა” უფროსმა ფ.-მ.მ.დ. ნ. ხუჭუამ.

აქტუალურ თემას ეხებოდა ამავე უნივერსიტეტის ე. ანდრონიკაშვილის ფიზიკის ინსტიტუტის თანამშრომლის, აკად. ნ. ცინცაძის მიერ წარმოდგენილი მოხსენება “ნანოსტრუქტურები გამტარებში”. გამოყენებითი ფიზიკის სხვადასხვა მიმართულების საკვანძო საკითხებს ეხებოდა ფართო მასშტაბით წარმოდგენილი საინტერესო მოხსენებები ისეთი გამოჩენილი მეცნიერებისა და პერსპექტიული ახალგაზრდა მკვლევრების მიერ, როგორიც არიან: პროფ. ა. გერასიმოვი, პროფ. ზ. ჯიბუტი, საქართველოს მეცნიერებათა ეროვნული აკადემიის წევრ-კორესპონდენტი გ. ჯაფარიძე, პროფ. დ. ჯიშიაშვილი და ფ.-მ.მ.კ. ნ. მახათაძე, ასპირანტი ა. მკრტიჩიანი (სომხეთი), პროფ. მ. ზვიადაძე, პროფ. თ. ბუთხუზი და მეცნიერ-თანამშრომელი მ. შერვაშიძე, დოქტორანტი მ. ჩიხრაძე, პროფ. ნ. კეკელიძე და დოქტორანტი დ. ხომასურიძე, პროფ. თ. ეფრემიძე, პროფ. ნ. ღომიძე; პროფ. ე. მიმინოშვილი, პროფ. ე. ქუთელია და პროფ. თ. ძიგრაშვილი; ფ.-მ.მ.კ. ბ. კილოსანიძე და ფ.-მ.მ.კ. გ. კაკაურიძე, ფ.-მ.მ.კ. ა. დანელიანი და ტ.მ.დ. დ. ღარიბაშვილი, ფ.-მ.მ.კ. ა. თავხელიძე და მეცნიერ-თანამშრომელი ზ. ტალიაშვილი, პროფ. გ. გოდერძიშვილი, დოქტორანტი ვ. ბერაკჩიანი და პროფ. რ. ჩიქოვანი, პროფ. გ. დარსაველიძე, დოქტორი გ. ბოკუჩავა და ტ.მ.დ. ბ. შიროკოვი, დოქტორანტი კ. კობახიძე და სხვ.

კონფერენციაზე მრავლად იყო წარმოდგენილი სხვადასხვა სამეცნიერო ცენტრების თანამშრომელთა მიერ ერთობლივად შესრულებული შრომები, რაც მეტყველებს, რომ კავშირები და ურთიერთობა მეცნიერებს შორის წარმატებით გრძელდება. მთლიანობაში კონფერენციამ თბილ და კოლეგიალურ ვითარებაში ჩაიარა, სხდომებზე გაკეთებულმა მოხსენებებმა შესაბამისად დაინტერესება და ცხარე მეცნიერული სჯა-ბაასი დაიმსახურა.

რ. ჩიქოვანი

კონფერენციაზე სიტყვით გამოვიდა პროფ. რ. ჩიქოვანი. მან გულითადი მადლობა გადაუხადა საქართველოს ტექნიკური უნივერსიტეტის რექტორს, მთლიანად რექტორატს, საქართველოს საინჟინრო აკადემიას, ინფორმატიკის და მართვის სისტემების ფაკულტეტის და ფიზიკის დეპარტამენტის ხელმძღვანელობას, კონფერენციის ყველა მონაწილეს მის მიმართ გამოჩენილი დიდი ყურადღებისათვის. პროფ. რ. ჩიქოვანმა მადლიერების გრძნობით მოიხსენია ის კოლექტივები, რომლებმაც ის აღზარდეს, სადაც მან იმოღვაწევა და ჩამოყალიბდა როგორც სპეციალისტი – ივანე ჯავახიშვილის სახელობის თბილისის სახელმწიფო უნივერსიტეტი, სამეცნიერო-კვლევითი ინსტიტუტი “მიონი” ქარხნითურთ და საქართველოს ტექნიკური უნივერსიტეტი.

კონფერენციის მონაწილეთა ერთი ჯგუფი

კონფერენციის დაწყებამდე დაიბეჭდა მისი პროგრამა და მოხსენებების თეზისების კრებული. ამჟამად გამოსაცემადაა გამზადებული კონფერენციაზე წარმოდგენილ ნაშრომთა სრული კრებული.

მიღებულ იქნა გადაწყვეტილება, რომ კონფერენციები გამოყენებითი ფიზიკის აქტუალურ საკითხებთან დაკავშირებით პერიოდულად ჩატარდეს.

საერთაშორისო სამეცნიერო კონფერენციამ "გამოყენებითი ფიზიკის აქტუალური საკითხები" (2011 წლის 30 მარტი, თბილისი, საქართველო) ნათლად აჩვენა, რომ საქართველოში ჯერ კიდევ მაღალია სამეცნიერო პოტენციალი მყარი სხეულების ფიზიკისა და გამოყენებითი ფიზიკის დარგში.

გელა გოდერძიშვილი

2011 წლის 4 ოქტომბერი

ISSN 1987-8826